Turbulent Ion Heating in TCV Tokamak Plasmas

THÈSE N^{O} 4479 (2009)

PRÉSENTÉE LE 28 AOÛT 2009

À LA FACULTÉ SCIENCES DE BASE
CRPP ASSOCIATION EURATOM
PROGRAMME DOCTORAL EN PHYSIQUE

ÉCOLE POLYTECHNIQUE FÉDÉRALE DE LAUSANNE

POUR L'OBTENTION DU GRADE DE DOCTEUR ÈS SCIENCES

PAR

Christian Schlatter

acceptée sur proposition du jury:

Prof. O. Schneider, président du jury
Dr B. P. Duval, directeur de thèse
Prof. M. Cecconello, rapporteur
Prof. A. Fasoli, rapporteur
Dr S. Sharapov, rapporteur

ÉCOLE POLYTECHNIQUE
FÉDÉRALE DE LAUSANNE
Suisse
2009

Some figures in this dissertation are in colour only in the electronic version.

This document was last revised on Thursday 6th August, 2009 and has been compiled using pdfLaTeX. The official version is the printed version as registered for copyright.

Please cite this publication as:
Christian Schlatter, **Turbulent ion heating in TCV tokamak plasmas**, Ph.D. thesis, no. 4479, Ecole polytechnique fédérale de Lausanne (EFPL), CH-1015 Lausanne, Switzerland, July 2009.

Man muss sich der Idee erlebend gegenüberstellen können;
sonst gerät man unter ihre Knechtschaft.

Rudolf Steiner, *1861, †1925,
in: Die Philosophie der Freiheit (1894).

Abstract

The Tokamak à configuration variable (TCV) features the highest electron cyclotron wave power density available to resonantly heat (ECRH) the electrons and to drive noninductive currents in a fusion grade plasma (ECCD). In more than 15 years of exploitation, much effort has been expended on real and velocity space engineering of the plasma electron energy distribution function and thus making electron physics a major research contribution of TCV.

When a plasma was first subjected to ECCD, a surprising energisation of the ions, perpendicular to the confining magnetic field, was observed on the charge exchange spectrum measured with the vertical neutral particle analyser (VNPA). It was soon concluded that the ion acceleration was not due to power equipartition between electrons and ions, which, due to the absence of direct ion heating on TCV, has thus far been considered as the only mechanism heating the ions. However, although observed for more than ten years, little attention was paid to this phenomenon, whose cause has remained unexplained to date.

The key subject of this thesis is the experimental study of this anomalous ion acceleration, the characterisation in terms of relevant parameters and the presentation of a model simulation of the potential process responsible for the appearance of fast ions. The installation of a new compact neutral particle analyser (CNPA) with an extended high energy range ($\leqslant$ 50 keV) greatly improved the fast ion properties diagnosis.

The CNPA was commissioned and the information derived from its measurement (ion temperature and density, isotopic plasma composition) was validated against other ion diagnostics, namely the active carbon charge exchange recombination spectroscopy system (CXRS) and a neutron counter. In ohmic plasmas, where the ion heating agrees with classical theory, the radial ion temperature profile was successfully reconstructed by vertically displacing the plasma across the horizontal CNPA line of sight. Active charge exchange measurements, by doping the plasma with ion neutralisation targets injected with the diagnostic neutral beam (DNBI), were used to absolutely calibrate the NPA. Advanced modelling of the measured hydrogenic charge exchange spectra with the neutralisation and neutral transport codes *KN1D* and *DOUBLE-TCV* permitted a calculation of the absolute neutral density profiles of the plasma species.

The energisation and the properties of fast ions were studied in dedicated, low density, cold ion, hot electron plasmas, resonantly heated at the second harmonic of the electron cyclotron frequency. The ion acceleration occurs on a characteristic timescale in the sub-millisecond range and comprises up to 20 % of the plasma ions. The number of fast ions n_i^s and their effective temperature T_i^s are found to depend strongly on the bulk and suprathermal electron parameters, in particular $T_i^s \leqslant T_e^b$ (electron bulk) and $n_i^s \sim v_{\mathrm{de}}$ (toroidal electron drift speed). The suprathermal electrons, abundantly generated in plasmas subjected to ECCD, are diagnosed with perpendicular and oblique viewing electron cyclotron emission (ECE) antennas and the measured frequency spectra are reconstructed with the relativistic ECE radiation balance code *NOTEC-TCV*. With steady-state ECRH and ECCD, the fast ion population reaches an equilibrium state. The spatial fast ion temperature profile is broad, of similar shape compared to the bulk ion temperature profile. The hottest suprathermal temperature observed is $T_i^s \leqslant 6$ keV.

Various potential ion acceleration mechanisms were examined for relevance in the TCV parameter range. The simultaneous wave–electron and wave–ion resonances of ion acoustic turbulence (IAT) show the best correlation with the available experimental knowledge. Ion acoustic waves are emitted by the weakly relativistic circulating electrons and are mainly Landau damped onto the ions. Destabilisation of IAT is markedly facilitated by the important degree of nonisothermicity $T_e/T_i \geqslant 40$ of X2 EC heated TCV plasmas.

Efforts were undertaken to consistently model the experimental observations using a numerical experiment. The relevant physics describing IAT was implemented in a finite difference code solving the quasilinear diffusion equation describing the time evolution of the electron and ion distribution functions. The simulations, fed as far as possible with experimentally available information, confirm the growth and saturation of IAT. Electrons and ions are initially preferentially heated in the toroidal direction. As the ions gain energy, the ion waves are damped more efficiently and only modes propagating at oblique angles can still grow, thus accelerating ions into the radial perpendicular direction. The simulation shows that turbulence reaches a steady-state when the ions are sufficiently hot to permanently stabilise IAT. The parameters describing the tail of the modelled equilibrium ion distribution agree quantitatively well with the CNPA measurement.

Preliminary studies investigated on the interaction of fast ions with the sawtooth instability. It is found that the fast ion population in sawtoothing plasmas is transiently enforced with each sawtooth collapse. It is presently thought that the toroidal electric reconnection field lowers the IAT stability threshold thus producing more suprathermal ions.

Keywords:
plasma physics, plasma turbulence, waves in plasmas, neutral particle analyser, neutron detector, quasilinear diffusion equation, TCV, ECE, tokamak, nuclear fusion.

Zusammenfassung

Am Tokamak à configuration variable (TCV) ist weltweit die höchste Elektronzyklotronwellenleistungsdichte zum resonanten Heizen der Elektronen (ECRH) und zum Erzeugen nichtinduktiver Plasmaströme (ECCD) installiert. Während mehr als 15 Jahren wurden die Werkzeuge zur Beeinflussung der Verteilung der Plasmaelektronen im realen sowie im Geschwindigkeitsraum erforscht und optimiert. Unzählige Experimente haben wichtige Beiträge zum Verständnis der Physik geheizter Elektronen in Tokamakplasmen geleistet.

Bereits während den ersten Experimenten mit ECCD wurde eine wider Erwarten hohe Beschleunigung der Plasmaionen in die radiale Richtung, senkrecht zum einschliessenden Magnetfeld, bemerkt. Die Messung des Ladungsaustauschspektrums mit dem vertikal ausgerichteten Neutralteilchenanalysator VNPA zeigte, dass die Injektion der Zyklotronwellen mit dem Erscheinen einer kleinen Menge ziemlich heisser Ionen einherging. Man kam damals zum Schluss, dass die Energie, die durch Zusammenstösse mit den Elektronen auf die Ionen übertragen wird (Equipartition), nicht ausreicht, um die Entstehung der heissen Ionen erklären zu können (TCV verfügt über keine Mittel um die Ionen direkt zu heizen). Obwohl dieses Phänomen seit mehr als einem Jahrzehnt bekannt ist, waren bisher keine Versuche unternommen worden, dessen Ursache zu ergründen.

Das Hauptthema dieser Doktorarbeit ist das experimentelle Studium dieser anormalen Ionenbeschleunigung. Die relevanten Parameter, welche diese Beschleunigung beeinflussen, wurden bestummen und eine plausible Erklärung dafür wurde ermittelt. Die Beschaffung eines neuen, kompakten Neutralteilchendetektors (CNPA) mit einem erweiterten Energiemessbereich (bis 50 keV) hat diese Aufgabe erheblich erleichtert.

Der CNPA wurde in Betrieb genommen und die von den Messdaten abgeleiteten Informationen, Ionentemperatur und -dichte sowie isotopische Zusammensetzung, wurden mit den Werten anderer Ionenmessgeräte, wie z.B. aktive Ladungstauschrekombinationsspektroskopie von Kohlenstoff (CXRS) sowie ein Neutronenzähler, verglichen und bestätigt. In Plasmen mit rein ohmscher Plasmaheizung, wenn die Ionenheizung mit klassischer Theorie übereinstimmt, wurde das radiale Ionentemperaturprofil erfolgreich gemessen indem das Plasma senkrecht zur horizontalen Sichtlinie des CNPA verschoben wurde. Mit Hilfe eines Diagnostikstrahls (DNBI), welcher den lokal emittierten Ladungsaustauschfluss mit injizierten Neutralteilchen stimuliert, wurden die beiden NPA absolut kalibriert. Ein Modellieren der gemessenen Wasserstoff- und Deuterium-Ladungsaustauschspektren mit den Neutralteilchentransport-Algorithmen *KN1D* und *DOUBLE-TCV* erlaubten schliesslich die Berechnung der absoluten Neutralteilchenprofile im Plasma.

Die Beschleunigung und die Eigenschaften der schnellen Ionen wurden in speziell optimierten Plasmen mit niedriger Dichte, tiefer Ionen- aber hoher Elektronentemperatur studiert. Diese wurden mittels Zyklotronwellen an der zweiten Harmonischen der Elektronzyklotronfrequenz (X2 EC) geheizt. Die Ionenbeschleunigung geschieht während eines Bruchteils einer Millisekunde und betrifft bis zu einem Fünftel der Plasmaionen. Die Experimente zeigen, dass der Anteil schneller Ionen n_i^s und deren effektive Temperatur T_i^s stark von den Parametern der Elektronen abhängen, wir finden insbesondere thermische Elektronentemperatur $T_e^b \geqslant T_i^s$ und toroidale Elektronenströmungsgeschwindigkeit $v_{\mathrm{de}} \sim n_i^s$. Suprathermische Elektronen, in grosser Zahl hauptsächlich in Plasmen mit nichtinduktiven Strömen (ECCD) produziert, werden mit Elektronzyklotronemissionsantennen (ECE) ausgemessen.

Wir interpolieren die ECE Emissionsspektren mit dem relativistischen Strahlungsemissionscode *NOTEC-TCV*. Sind ECRH und ECCD stationär, erreicht die schnelle Ionenpopulation einen Gleichgewichtszustand. Das räumliche Temperaturprofil der suprathermischen Ionen ist breit, von der Form her ähnlich dem thermischen Temperaturprofil. Die heisseste beobachtete Temperatur der schnellen Ionen erreicht 6 keV.

Verschiedene mögliche Ionenbeschleunigungsmechanismen wurden auf deren Relevanz im Tokamak's TCV überprüft. Die gleichzeitigen Resonanzen von Ionenwellen mit Ionen und Elektronen weisen auf die sogenannte Ionen-Akustische Turbulenz (IAT) als plausibelsten Kandidaten hin. Ionen-akustische Wellen werden von den leicht relativistischen, zirkulierenden Elektronen emittiert und hauptsächlich von den kalten Ionen absorbiert (Landau-Dämpfung). Die Destabilisierung von IAT in TCV wird durch den hohen Grad an Anisothermizität ($T_e/T_i \geqslant 40$) der mit X2 EC geheizten Plasmen ermöglicht.

Die experimentellen Beobachtungen wurden mit einem numerischen Code aufwendig simuliert. Der Algorithmus beinhaltet alle relevanten physikalischen Aspekte. Er löst die quasi-lineare Diffusionsgleichung mittels finiter Differenzen und berechnet die Zeitentwicklung der Ionen- und Elektronenenergieverteilung. Die Simulation, die alle gemessenen Daten berücksichtigt, bestätigt das Wachstum und die Sättigung der IAT. Die Elektronen und Ionen gewinnen anfänglich unter dem Einfluss von IAT hauptsächlich Energie in die toroidale Richtung. Mit zunehmend heisseren Ionen werden die Ionenwellen stärker gedämpft und schliesslich können nur noch Moden mit zunehmend senkrechter (zum Magnetfeld) Wellenvektorkomponente wachsen. Diese beschleunigen die Ionen schliesslich in die Richtung senkrecht zum Magnetfeld. Die simulierten Ionengeschwindigkeitsverteilungen stimmen quantitativ gut mit den CNPA-Messungen überein.

In vorbereitenden Experimenten wurden zudem die Interaktion der schnellen Ionen mit Sägezahn-Instabili-täten untersucht. Diese zeigen, dass mit jedem Sägezahn-Kollaps vorübergehend mehr schnelle Ionen produziert werden. Überlegungen deuten darauf hin, dass durch das elektrische Feld, welches bei der Rekonnektion des Magnetfeldes entsteht, die Schwelle zur Destabilisierung von IAT verringert wird und daraus mehr schnelle Ionen resultieren.

Stichwörter:
Plasmaphysik, Plasmaturbulenz, Plasmawellen, Neutralteilchenanalysator, Neutronendetektor, quasilineare Diffusionsgleichung, TCV, ECE, Tokamak, Kernfusion.

Contents

List of Tables

Chapter 1

Introduction

1.1 The energy problem

At this point in time, the global energy problem is the talk of the town. The visibility of energy in our everyday life has fundamentally changed and has become an omnipresent actor. Green is the new buzzword and has massively found admittance to the vocabulary applied in economy and politics. Oil is becoming short in supply, prices for petrol and electricity are rising more rapidly than in the past. Despite the commonly adopted certainty that things are getting worse, our society is facing the future of energy demand with worrying composure. Access to and disposal of any sort of energy are increasingly important instruments of power. In a not so far future, the business of energy procurement and fair distribution will be an arduous challenge for mankind. Especially the highly unbalanced location of the energy resources on our planet will almost certainly cause trouble and strife on the playground of international politics.

In spite of these bleak prospects, the worldwide energy consumption is inexorably continuing to grow (worldwide by currently ∼2 % [1]), driven by the increase of the planets population, the increase of the personal consumption and the increase in number of people having access to any sort of domesticated source of energy. More than 80 % of our consumed energy is derived from the combustion of fossil fuels [1], which are claimed to be responsible of the anthropogenic **greenhouse effect**. Environmental concerns related to global warming and sustainability will hopefully move the world's energy consumption towards CO_2-free energy sources. Furthermore, the peak oil production is already passed (figure 1.1.1) and independent studies show that the suppliers *already* cannot supply the demand for oil [2]. Although energy saving is en vogue these days, a drastic reduction of our energy consumption of our own free will appears fairly improbable, although some countries are planning to impose some degree of degression. Among others, Sweden wants to become independent of fossil fuels by 2020 and Switzerland aims at a 2 kW society by 2050. Nevertheless, alternative energy sources will have to replace the fossil fuels pretty soon. New developments in solar, wind, hydro power or biomass made renewable energies progress in the energy mix [4]. The European Commission has proposed [5] that the level of renewable energy in the EU's overall market should triple to attain 20 % by 2020. But there is legitimate belief that renewable energies will never reach a share high enough to realistically replace fossil fuels. Nuclear fission plants currently produce about 6 % of world's total primary energy supply [6]. More plants are planned to be built to satisfy the increasing electricity demand, against increasing opposition from environmentalists and the fear of nuclear proliferation. The risk of accidents, terrorist attacks and the fact that solutions for the long term storage of highly radioactive waste are still missing makes the established nuclear fission industry not at all attractive. On the other hand, according to the most pessimistic estimations, usable Uranium may already be depleted in 70 years [6], unless we change the permitted reactor type (e.g. fast breeders) [7].

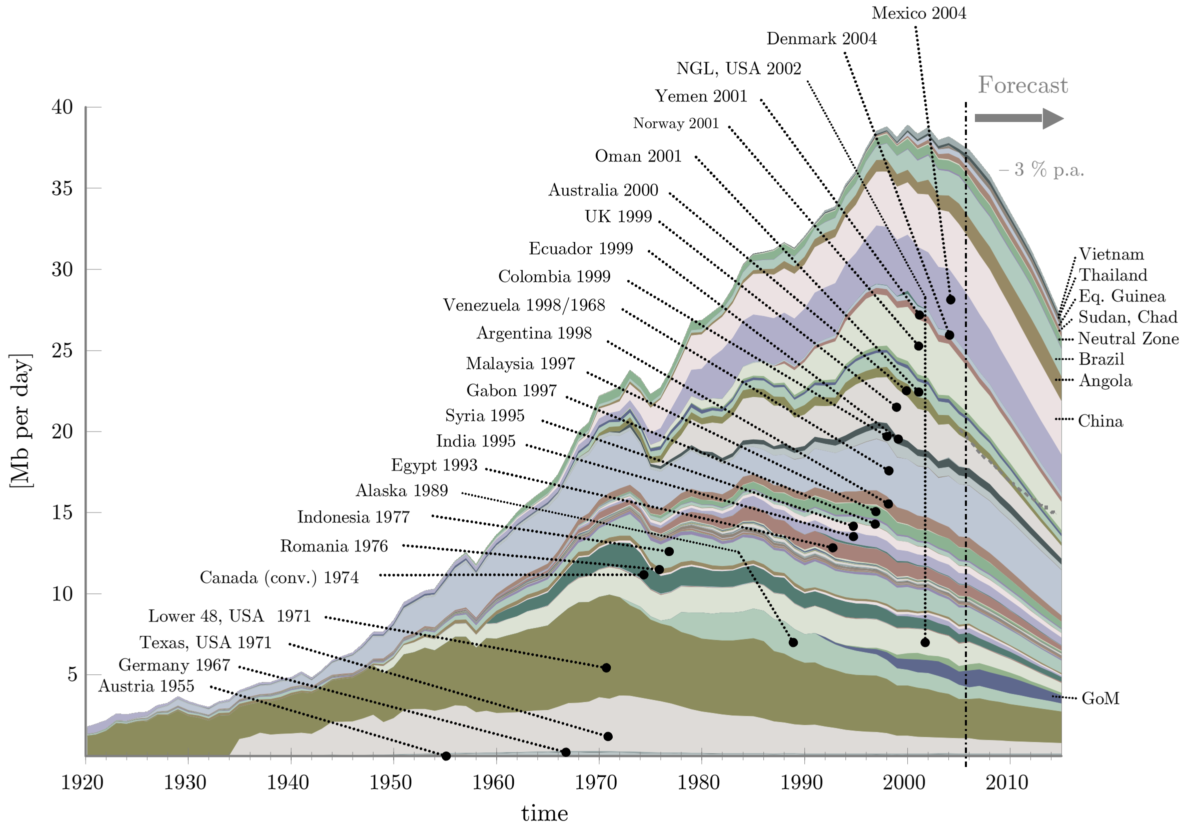

Figure 1.1.1: The oil peak has passed. Oil producing countries. Total crude oil output, classified per oil producing country. The dates printed on the plots indicate the year of maximum oil production of that particular country. Forecast estimated by Ludwig-Bölkow-Systemtechnik (LBST), courtesy of [3].

A promising avenue towards a future energy source on Earth is the nuclear fusion reaction. A first fusion reactor was patented in 1946 [8] and fusion technology was intensely developed [9] and studied since the declassification of research at the Second International Conference on the Peaceful Uses of Atomic Energy in Geneva, 50 years ago [10]. A fusion reactor burns an essentially inexhaustible fuel of light atoms, produces electricity at large scale, has a very high degree of inherent security and is environmentally benign, as very little and only short lived (half-life $\lesssim$ 100 years) radioactive waste is produced and no CO_2 is directly emitted. The resources of the raw material for fusion are spread all over the globe, making fuel procurement possible for all humanity and operation less subject to political and economical constraints.

The technology of a fusion reactor hasn't yet matured to be commercialised (in the opinion of the author due to the moderate level of funding in the past), but the way towards fusion for energy is presently paved by the **International Thermonuclear Experimental Reactor** (ITER), currently under construction in Cadarache, France, and financed by seven international parties. ITER is meant as the demonstration experiment of the scientific and technological feasibility of fusion energy exploitation for peaceful purposes. Reactor operations are currently planned to start in 2018 [11]. In parallel, the **International Fusion Materials Irradiation Facility** (IFMIF) will test the long-term behaviour of materials under conditions similar to those expected at the inner wall of a fusion reactor with the aim of reducing the radioactive activation due to neutrons impinging on the reactor structure materials. DEMO, a **DEMOnstration Power Plant**, is expected to prototype this technology within 20 years.

It is important to point out that nuclear fusion will not solve the energy problem alone, all other possibilities of energy procurement have to be explored and improved in efficiency [12] and we all will have to reduce our consumption of energy.

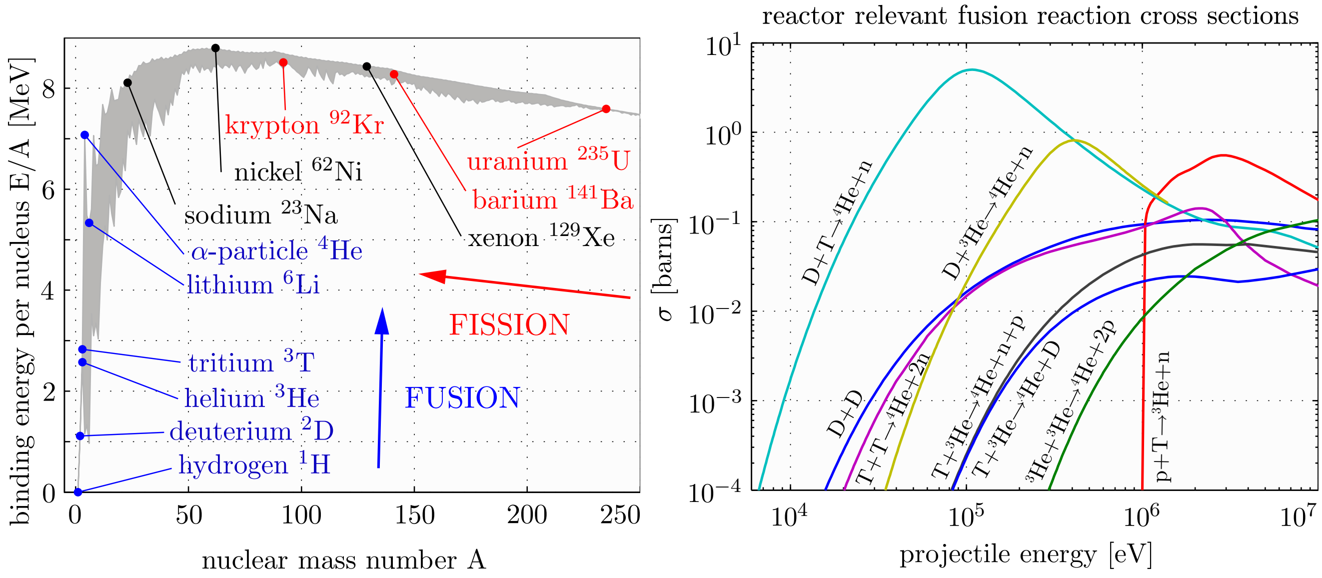

(a) Binding energy per nucleon.

(b) Fusion reaction cross section.

Figure 1.1.2: (a) For light elements (from hydrogen up to sodium) the binding energy per nucleon increases (each added nucleon increases the force exerted among nucleons, the nucleus is bound more tightly), stabilises in the sequence through xenon (attractive nuclear forces are nearly balanced by repellent electromagnetic forces between protons) and finally decreases with the heavier elements (electromagnetic repulsive forces are beginning to gain against the strong nuclear force). At the peak of binding energy, nickel-62 is the most tightly-bound nucleus [13].
(b) The fusion reaction cross section increases rapidly with energy until it maximises and then gradually drops off. The D–T cross section peaks at a lower energy (at just over 100 keV, or 1.16 billion kelvins) and at a higher value than other reactions commonly considered for fusion energy. The two D–D reactions, eq.(1.2.5) and eq.(1.2.4), have similar cross sections, the graph gives their sum. The curves are interpolations of experimental data taken from the ENDF/B-VII.0 database of the National Nuclear Data Center in Brookhaven, USA [14].

1.2 Thermonuclear fusion

Nuclear fusion is the process by which multiple like-charged atomic nuclei join together to form a heavier nucleus. The highly exothermic nuclear fusion reaction is the process that powers the Sun and other stars, where hydrogen nuclei fuse together to form helium through the following chain of reactions:

$$
\begin{aligned}
{}^{1}_{1}\mathrm{H} + {}^{1}_{1}\mathrm{H} &\rightarrow {}^{2}_{1}\mathrm{D} + \mathrm{e}^{+} + \nu_e && (1.2.1)\\
{}^{2}_{1}\mathrm{D} + {}^{1}_{1}\mathrm{H} &\rightarrow {}^{3}_{2}\mathrm{He} + \gamma && (1.2.2)\\
{}^{3}_{2}\mathrm{He} + {}^{3}_{2}\mathrm{He} &\rightarrow {}^{4}_{3}\mathrm{He} + 2\,{}^{1}_{1}\mathrm{H} && (1.2.3)
\end{aligned}
$$

The sum of mass of the products of the reaction are lighter than the sum of mass of the reactants, figure 1.1.2a, the kinetic energy given to the products corresponds to the mass deficit according to Einstein's famous formula $E = \Delta mc^2$ [15]. Each second, more than 4 million tonnes of matter are converted into energy within the Sun's core, producing neutrinos and solar radiation; at this rate, the Sun will have so far converted around 100 Earth-masses of matter into energy.

However, the cross section of the weak interaction leading to the β^{+} decay, eq.(1.2.1), is very low [16] and thus this reaction is not feasible on Earth.

To harness the energy of controlled thermonuclear fusion the heavier hydrogenic isotopes deuterium (D, one neutron in the nucleus) and tritium (T, two neutrons) are more interesting for exploitation in a fusion reactor:

$$
\begin{aligned}
{}^{2}_{1}\mathrm{D} + {}^{2}_{1}\mathrm{D} &\rightarrow {}^{3}_{2}\mathrm{He}(0.817\ \mathrm{MeV}) + {}^{1}_{0}\mathrm{n}(2.45\ \mathrm{MeV}) && (1.2.4)\\
{}^{2}_{1}\mathrm{D} + {}^{2}_{1}\mathrm{D} &\rightarrow {}^{3}_{1}\mathrm{T}(1.01\ \mathrm{MeV}) + {}^{1}_{1}\mathrm{H}(3.02\ \mathrm{MeV}) && (1.2.5)\\
{}^{1}_{1}\mathrm{H} + {}^{3}_{1}\mathrm{T} &\rightarrow {}^{3}_{2}\mathrm{He} + {}^{1}_{0}\mathrm{n} - 764\ \mathrm{keV} && (1.2.6)\\
{}^{2}_{1}\mathrm{D} + {}^{3}_{1}\mathrm{T} &\rightarrow {}^{4}_{2}\mathrm{He}(3.5\ \mathrm{MeV}) + {}^{1}_{0}\mathrm{n}(14.1\ \mathrm{MeV}) && (1.2.7)\\
{}^{2}_{1}\mathrm{D} + {}^{3}_{2}\mathrm{He} &\rightarrow {}^{4}_{2}\mathrm{He}(3.67\ \mathrm{MeV}) + {}^{1}_{1}\mathrm{H}(14.7\ \mathrm{MeV}) && (1.2.8)\\
{}^{3}_{1}\mathrm{T} + {}^{3}_{1}\mathrm{T} &\rightarrow {}^{4}_{2}\mathrm{He}(3.8\ \mathrm{MeV}) + 2\,{}^{1}_{0}\mathrm{n}(7.6\ \mathrm{MeV}) && (1.2.9)\\
{}^{3}_{2}\mathrm{He} + {}^{3}_{2}\mathrm{He} &\rightarrow {}^{4}_{2}\mathrm{He} + 2\,{}^{1}_{1}\mathrm{H} + 12.8\ \mathrm{MeV} && (1.2.10)\\
{}^{3}_{1}\mathrm{T} + {}^{3}_{2}\mathrm{He} &\rightarrow {}^{4}_{2}\mathrm{He} + {}^{1}_{1}\mathrm{H} + {}^{1}_{0}\mathrm{n} + 12.1\ \mathrm{MeV} && (1.2.11)\\
{}^{3}_{1}\mathrm{T} + {}^{3}_{2}\mathrm{He} &\rightarrow {}^{4}_{2}\mathrm{He}(4.8\ \mathrm{MeV}) + {}^{2}_{1}\mathrm{D}(9.5\ \mathrm{MeV}) && (1.2.12)
\end{aligned}
$$

where the first two processes have the same reaction probability in a deuterium plasma, the last two have a branching ratio of 59 %. The pT-fusion reaction [17], eq.(1.2.6), is endothermic.

Deuterium naturally occurs in water in the form of molecules of semiheavy water HDO, at a concentration of ∼154 ppm, enough to produce electricity for 10^{11} years(*) [18], so fusion is a practically inexhaustible source of energy. Despite the low concentration of D in water, the fusion of deuterium extracted from 1 litre of water provides 300 times more energy than the combustion of 1 litre of gasoline.
Tritium is radioactive and has a short life time of only 12.3 years and, because there is no source, therefore doesn't exist in nature. Inside a future reactor, its production is envisaged by breeding from lithium (neutron bombardment induced fission and neutron capture):

$$
\begin{aligned}
{}^{7}_{3}\mathrm{Li} + {}^{1}_{0}\mathrm{n} &\rightarrow {}^{4}_{2}\mathrm{He} + {}^{3}_{1}\mathrm{T} + {}^{1}_{0}\mathrm{n} - 2.47\ \mathrm{MeV} && (1.2.13)\\
{}^{6}_{3}\mathrm{Li} + {}^{1}_{0}\mathrm{n} &\rightarrow {}^{4}_{2}\mathrm{He}(2.05\ \mathrm{MeV}) + {}^{3}_{1}\mathrm{T}(2.73\ \mathrm{MeV}) && (1.2.14)
\end{aligned}
$$

Lithium is compounded in the crust of the Earth and dissolved in sea water, the isotope ${}^{7}_{3}\mathrm{Li}$ is the most abundant (92.6 %).
Figure 1.1.2b shows that all fusion reactions have a strong dependence on projectile energy, the fusion reaction only occurs at a sufficient rate at an impressively high energy. The D–T reaction, eq.(1.2.7), requires the least effort in terms of fuel heating, has the highest cross section and a higher energy gain than D–D fusion. ITER, DEMO and the reactors beyond will therefore burn a D–T fuel mixture. An optimum temperature is about 10 keV (∼100 millions centigrade) which is lower than the energy corresponding to the maximum of the cross section, since the fusion reactions mainly occur from particles in the high energy tail of the (mostly Maxwellian) fuel energy distribution. Note that the cross section for the fission of uranium ${}^{235}_{92}\mathrm{U}$ with a neutron at room temperature is about 500 barns, that is 50'000 times larger than the fusion cross section at 10 keV. The high temperature required and low probability for the fusion reaction dictate extremely high demands on the technical implementation of the technology of controlled nuclear fusion on Earth. The challenge of a feasible fusion reactor is how to heat the reactants to these high temperatures (section 1.6), where they are fully ionised, in other words, the ensemble of particles has become a **plasma** (section 1.3). To continually extract energy from fusion reactions, the high fuel temperature needs to be maintained (see below).

(*) estimated with a power station efficiency of 30 % and without inflation of the current annual energy consumption.

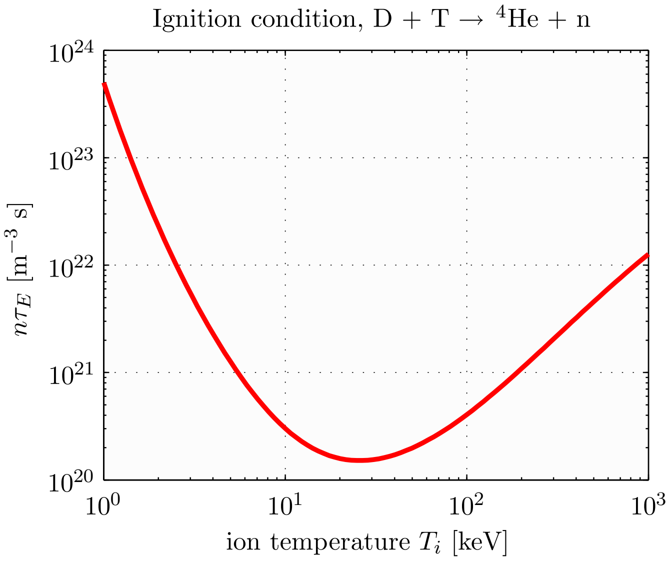

Figure 1.2.1: The value of $n\tau_E$ required to obtain ignition, as a function of temperature.

1.2.1 Ignition (fusion power plant concept)

For a steady-state operation of a fusion reactor the temperature of the fuel in a fusion power plant has not only to be raised but is required to be kept at ideally 10 keV. Fortunately, the fusion reaction, for example eq.(1.2.7), with a mixture of 50:50 D–T, provides a source of plasma self-heating through the produced charged α-particle, which carries one fifth of the reaction energy ($E_\alpha =$ 3.5 MeV). A fusion reactor strives for their confinement by means of magnetic fields (section 1.4), such that the kinetic energy is collisionally deposited in the plasma and thus transferred to the fuel particles. The hotter the plasma, the larger the fraction of plasma heating through the charged fusion products and the external heating may eventually be removed if the power provided by α-particles solely is sufficient to maintain the fuel temperature. This is called the ignition event and the plasma has become a burning one.

The condition for self-sustaining plasma burn is obtained by inspection of the plasma power balance and becomes

$$n\tau_E > \frac{12 k_B T}{E_\alpha \langle\sigma v\rangle}, \tag{1.2.15}$$

where n is the fuel density, T the fuel temperature, τ_E the energy confinement time, E_α the α-particle energy and $\langle\sigma v\rangle$ the fusion reactivity. The inequality, eq.(1.2.15), is shown in figure 1.2.1. Note that τ_E is itself a function of T and in practice the optimum condition for ignition is somewhat lower than the minimum in $n\tau_E$, typically 10 keV.

Around the optimum condition for ignition, the fusion reactivity is $\propto T^2$, such that eq.(1.2.15) is written as a triple product,

$$n\,T\,\tau_E > 5\times 10^{21}\ \mathrm{m^{-3}\ keV\ s}, \tag{1.2.16}$$

already expressed in similar form by J. D. Lawson more than fifty years ago [19]. The first fusion device had achieved a tripe product of 10^{14} m^{-3} keV s, JET, currently the world's largest fusion reactor, achieved 8.7×10^{20} m^{-3} keV s.

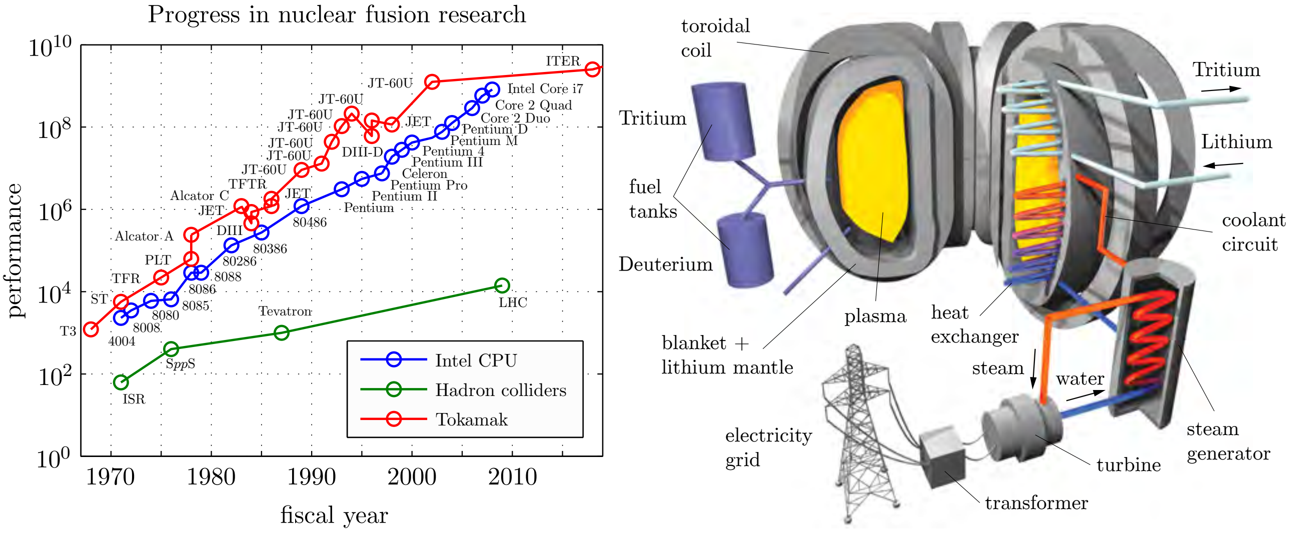

(a) Advances in science and technology.

(b) Fusion power plant.

Figure 1.2.2: (a) Measurement of the performance in the fields of hadron colliders, desktop central processing units and tokamak reactors. The vertical axis scale corresponds to the energy of the particle beam of the accelerator circuit (in GeV), the number of transistors on the processor die and the triple product in 10^{12} m^{-3} keV s respectively.
(b) Principal components of a future fusion power plant, exploiting a D–T fuel mixture.

The progress in fusion research towards ignition is commonly measured with the fusion energy gain factor Q, the ratio of thermonuclear heating power (α-particles) to heating power P_{H} provided externally,

$$Q = \frac{\dfrac{E_\alpha}{4}\displaystyle\int \langle \sigma v \rangle \, n^2 \mathrm{d}V}{P_{\mathrm{H}}} \equiv \frac{5P_\alpha}{P_{\mathrm{H}}}, \qquad (1.2.17)$$

and thus breakeven $Q = 1$ states that the α-particles provide 20 % of the applied heating power. Above $Q = 5$ the fusion heating power is greater than the external heating power. ITER is designed to achieve $Q > 5$. Figure 1.2.2a compares the history of the achieved triple product in fusion reactors to the progress achieved in the semiconductor industry and particle accelerators. The number of transistors in Intel CPU's continues to agree with the Moore law of 1965 [20], stating that its number (and therefore the calculation performance) doubles every two years. Tokamaks did somewhat better, the triple product doubled approximately every 21 months, but progress slowed down at the end of the last millennium.

Because of being an uncharged particle, the energy carried by the neutrons, the second fusion product of many fusion reactions, cannot be retained within the torus. Neutrons will traverse the reactor first wall to be stopped in the blanket surrounding the vacuum vessel. In the blanket the neutrons may breed the tritium through reactions eq.(1.2.13) or eq.(1.2.14) to replace the burnt fuel of the plasma. The neutron kinetic energy is transferred to a coolant which drives a steam turbine to finally produce electricity [21]. Figure 1.2.2b depicts the structure of a future fusion power plant.

1.3 Plasma: the fourth state of matter

Plasmas are by far the most common phase of matter in the universe, both by mass and by volume. All the stars are made of plasma, and even the space between the stars is filled with a plasma, albeit a very sparse one. Figure 1.3.1 shows the range of plasmas known today.

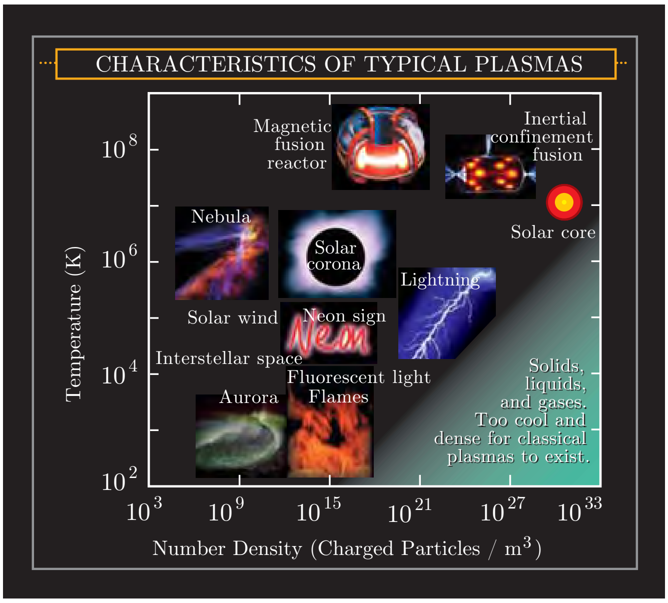

Figure 1.3.1: Zoology of plasmas, categorised by density and temperature. The volume averaged parameters of a targeted ITER plasma typically will be $n \sim 10^{20}$ m^{-3} and $T \sim 9$ keV (10^8 K).

Plasmas have very different properties from gas, which is why a plasma is often considered as the fourth state of matter. A plasma is commonly defined as being an ensemble of free charged particles, which is globally neutral and exhibits collective behaviour. Global neutrality is a result of the dominating electrostatic force that immediately restores charge equilibrium if an non-homogeneity occurs somewhere in the plasma. The potential of an ion in the plasma, written(†)

$$\phi(r) = \underbrace{\frac{e}{4\pi\varepsilon_0}\frac{1}{r}}_{\substack{\text{single charge}\\ \text{in vacuum}}} \quad \times \quad \underbrace{\exp\left\{-\frac{r}{\lambda_D}\right\}}_{\substack{\text{term due to plasma}\\ \text{collective interactions}}} , \tag{1.3.1}$$

such that the vacuum potential is screened by a cloud of electrons and

$$\lambda_D = \sqrt{\frac{\varepsilon_0\, T}{n\, e^2}} \tag{1.3.2}$$

is the *Debye* length, expressing the balance between thermal (violating neutrality) and space charge effects (restoring neutrality). Debye screening acts such that charges located at distances larger than the Debye length do not feel the potential of the screened ion. Eq.(1.3.2) is a strong evidence of collective interactions and the most remarkable feature distinguishing plasmas (range of interaction $\lambda_D \gg \sqrt[3]{n}$) from an ideal gas ($\lambda_D \ll \sqrt[3]{n}$, with n the particle density).

(†) solution of the Poisson potential equation for cold ions and thermal electrons in spherical symmetry, see for example [22].

This is sometimes called the ideal plasma approximation, that is if the average number N_d of electrons within this sphere of influence (whose radius is λ_D, thus called the Debye sphere) of a particular particle is large, i.e.

$$N_d = \frac{4}{3} n\pi\lambda_D^3 \gg 1, \tag{1.3.3}$$

then collective electrostatic interactions dominate over binary collisions, and the plasma particles can be treated as if they only interact with a smooth background field, rather than through pairwise interactions (collisions). The equation of state of each species in an ideal plasma is that of an ideal gas. In a finite plasma, λ_D must be small compared to the physical size of the plasma. In other words, the interactions in the bulk of the plasma are more important than those at its edge, where boundary effects may be influent.
Fusion reactor plasmas are essentially hot and the requirement of neutrality is therefore a strongly dynamic property, e.g. rather than exhibiting static neutrality, the plasma acts such as to shield charges very rapidly. This condition is fulfilled if the intrinsic electron plasma frequency ω_{pe} (measuring plasma oscillations of the electrons) is large compared to the electron–neutral collision frequency (measuring the frequency of collisions between electrons and neutral particles), i.e. $\omega_{\mathrm{pe}}\tau \gg 1$, where τ is the mean time between collisions with neutrals.

1.4 Magnetic confinement

At the high temperatures required for fusion the plasma cannot be confined by a recipient, since the walls would certainly melt or unacceptably cool the plasma. The plasma is strongly ionised and, although globally neutral, a soup of charged particles (electrons and ions), so magnetic fields have proven to be a popular mean to box-in plasmas. In a magnetic field $\mathbf{B}$, any charged particle of species α (mass m_α, charge q_α) is subject of the central Lorentz force $\mathbf{F} = q_\alpha (\mathbf{v} \wedge \mathbf{B})$, and its trajectory, given by the equation of motion,

$$\gamma\, m_\alpha \frac{\mathrm{d}\mathbf{v}}{\mathrm{d}t} = q_\alpha (\mathbf{v} \wedge \mathbf{B}), \tag{1.4.1}$$

is one of gyration around the magnetic field line, aka its guiding centre. $\gamma = \sqrt{1 - v^2/c^2}^{\,-1}$ is the relativistic factor. For a uniform magnetic field $\mathbf{B}$ and a particle with velocity vector component perpendicular to the magnetic field $v_\perp$, the radius of gyration is given by the *Larmor* radius,

$$\rho_{L\alpha} = \frac{\gamma\, m_\alpha\, v_\perp}{|q_\alpha| B}. \tag{1.4.2}$$

The rotation frequency is called the cyclotron frequency,

$$\Omega_{\mathrm{c}\alpha} = \frac{|q_\alpha| B}{m_\alpha} = \gamma\, \Omega_{0\alpha}, \tag{1.4.3}$$

with $\Omega_{\mathrm{c}\alpha}$ the limit of the relativistic pulsation $\Omega_{0\alpha}$ for $v \to 0$. The particle motion perpendicular to the magnetic field is now highly restricted, i.e. circular. If the particle has a non zero velocity component parallel to the magnetic field (there is no restriction on motion into this direction), the resulting particle trajectory is helical. In theory, only collisions with other particles may make the particles diffuse across the field or introduce a resistivity to the motion along the field.

Figure 1.5.1: The post of the Soviet Union published in 1987 a series of stamps commemorating science in the USSR. The 5 kopek value shows the popular T-10 tokamak at the Kurchatov institute in Moscow, in operation since 1975. Collection of Christian Schlatter.

If an additional external electric field is present (section 1.6.1), the particle guiding centres start to drift with a drift velocity

$$\mathbf{v}_{\mathrm{d}} = \frac{\mathbf{E} \wedge \mathbf{B}}{B^2}, \tag{1.4.4}$$

which is independent of particle mass or charge. Furthermore, if the magnetic field is non-uniform, an additional drift velocity appears,

$$\mathbf{v}_{\nabla \mathbf{B},\alpha} = \frac{m_\alpha\, v_\perp^2}{2\, q_\alpha\, B^3} \left(\nabla B \wedge \mathbf{B} \right), \tag{1.4.5}$$

which is of opposite direction for electrons and ions. Both drifts need to be compensated in a toroidal plasma device.

1.5 The Tokamak device

With a straight magnetic field, particles are lost at both ends of a linear configuration. In the 1950s the Soviet physicists Igor Yevgenyevich Tamm and Andrei Sakharov closed the magnetic field lines by bending them to form a torus. The successful tokamak (a transliteration of a Russian acronym made of **то**роидальная **ка**мера с **ма**гнитными **к**атушками, meaning **to**roidal **cha**mber with **ma**gnetic **c**oils) concept was born. Figure 1.5.2 shows a schematic of a tokamak. Its principal parts are

- a **Vessel** with its plasma facing first wall (not shown).

- a set of **Toroidal field coils** generating the toroidal magnetic field $\mathbf{B}_\phi$ to confine the plasma. $\mathbf{B}_\phi$ decreases as $1/R$, where R is the major radius of the machine. With this field alone, its gradient would separate the plasma species, as, according to eq.(1.4.5), the electrons would drift upwards and the ions downwards. The separation of the populations would produce a (counteracting) vertical field, which in turn would lead to the ejection, eq.(1.4.4), of the plasma towards the exterior of the torus.

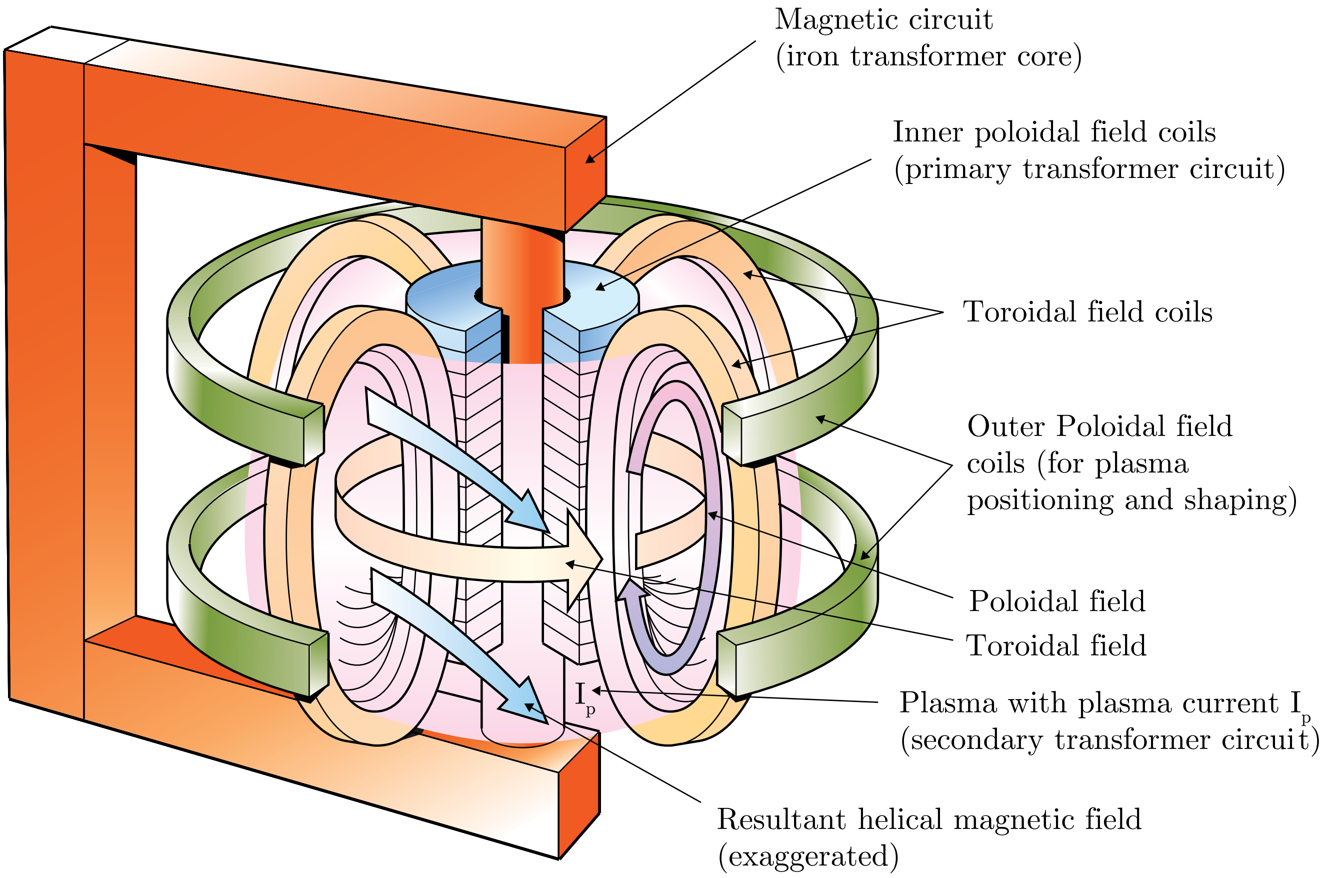

Figure 1.5.2: Experimental arrangement for controlled nuclear fusion. In a Tokamak, two superimposed magnetic fields enclose the plasma: The toroidal field generated by external coils and the field due to the plasma current. In the combined field, the field lines run helicoidally around the torus centre, ensuring the necessary twisting of the field lines to form the confining magnetic structure encapsulating the plasma. The outer poloidal field coils position and shape the plasma in the container.

- a set of **Primary transformer coils:** The continually increasing current flowing along the torus in the central solenoid induces a toroidal electric field in the plasma, which drives an inductive toroidal current I_p in the plasma (acting as a secondary transformer circuit winding). On TCV, I_p ranges from 100 kA to 1 MA. The plasma current induces in turn a poloidal magnetic field $\mathbf{B}_\theta$. The magnetic field lines resulting from the superposition of $\mathbf{B}_\phi$ and $\mathbf{B}_\theta$ are therefore helicoidal. The toroidal magnetic field is dominating in tokamaks. On TCV, $\mathbf{B}_\theta$ is approximately one order of magnitude weaker than $\mathbf{B}_\phi$. The twisting of the magnetic field lines compensates the particle drifts occurring if $\mathbf{B}_\phi$ would have been applied alone as each field line passes the upper and lower part of the torus. The net drift force, obtained by integration along the path of circulating particles (following the magnetic field lines), cancels out and there is thus no vertical drift motion.

- a set of **Poloidal field coils:** In toroidal geometry the plasma current interacts with the poloidal magnetic field, the latter is weaker at the outer side of the torus. This leads to an outward hoop force acting on the particles. In order to maintain stability, a vertical magnetic field $\mathbf{B}_v$ inducing a centripetal force $I_\mathrm{p}B_v$ of opposite direction must be applied. Further poloidal coils ensure the desired plasma positioning and shaping.

This confinement is not perfect. 50 years of research on tokamaks have shown that various magnetohydrodynamical (MHD) instabilities, collisional transport or turbulent processes may cause strong deterioration of confinement.

Nevertheless the tokamak provides a quite simple configuration to confine the plasma (it has toroidal symmetry) and no other fusion device concept (inertial fusion, stellerators) has yet reached the level of performance of a tokamak. Tokamaks are thus very popular (more than 200 tokamaks have been built worldwide [23]) and the prospects are good that the first commercial fusion power plant will operate according to the tokamak principle.

The main magnetic field is the toroidal field, in the absence of a plasma, its intensity scales as

$$B_\phi(R) \simeq \frac{B_0\,R_0}{R} \tag{1.5.1}$$

where B_0 is the field on the torus axis R_0 (the tokamak major radius). The magnetic field configuration in the tokamak is characterised by magnetic flux surfaces forming a set of nested toroids. The magnetic field lines form these magnetic surfaces. The twisting of the magnetic field lines is described by the safety factor q defined as

$$q = \frac{1}{2\pi}\oint \frac{1}{R}\frac{B_\phi}{B_\theta}\mathrm{d}l, \tag{1.5.2}$$

where the integration is performed in a poloidal section around the flux surface. For large aspect ratio tokamaks ($R_0/a \gg 1$), a the minor radius, this reduces to

$$q(r) = \frac{r}{R_0}\frac{B_\phi}{B_\theta}, \tag{1.5.3}$$

with r the radius of the flux surface. From eq.(1.5.3) the values of q on the magnetic axis and at the edge are, with μ_0 the permeability of free space, j_0 the current density on the magnetic axis

$$q_0 = q(0) = \frac{2\,B_\phi}{\mu_0\,j_0\,R_0} \tag{1.5.4}$$

and

$$q_a = q(a) = \frac{2\pi a^2 B_\phi}{\mu_0\,I_\mathrm{p}\,R_0}. \tag{1.5.5}$$

The safety factor q quantitatively indicates the number of toroidal loops a magnetic field line performs to complete a single poloidal loop. If $q = m/n$ is a rational number then the line joins up on itself after m toroidal and n poloidal rotations.

For most of the time, the plasma particles move on a specific flux surface. Energy and particle transport on a flux surface is thus extremely fast. As a consequence, most of the characteristics of the plasma are approximately identical all over the same flux surface and many parameters may be represented by a radial profile depending on the normalised radius ρ, defined as

$$\rho = \sqrt{\frac{\Psi}{\Psi_a}} \tag{1.5.6}$$

with Ψ the flux of the magnetic field through a poloidal section A_pol of the plasma (Ψ_a is the flux through the total plasma column)

$$\Psi = \frac{1}{2\pi}\int_{A_\mathrm{pol}} \mathbf{B}\cdot\mathrm{d}\mathbf{S} \tag{1.5.7}$$

1.6 External plasma heating schemes

In order to produce fusion reactions at a sufficient rate, the plasma needs to be very hot (section 1.2). Standard plasma heating schemes are summarised in this section.

1.6.1 Ohmic heating

The current driven by the induced electric field heats the electrons of the plasma through resistive dissipation (Joule effect). Energy is then transferred to the ions through collisions (elastic Coulomb interactions). For a current density j the ohmic heating power is

$$P_{\mathrm{OH}} = \eta j^2, \tag{1.6.1}$$

with η the resistivity approximately given by the Spitzer-Härm formula [24]

$$\eta_S = \frac{Ze^2\sqrt{m_e}\ln\Lambda}{4\pi\varepsilon_0^2 3\sqrt{2\pi}T_e^{3/2}} \tag{1.6.2}$$

where $\ln\Lambda \approx 24 - \ln\sqrt{n_e}/T_e = 10\ldots20$ is the Coulomb logarithm [25].
$\eta \propto T_e^{-3/2}$, thus ohmic heating becomes inefficient with higher temperature, where the plasma is less collisional and increasingly conducting. The decrease in η cannot be balanced by an increase of the plasma current, since the safety factor at the plasma edge q_a needs to be larger than 2 to avoid a disruption caused by an MHD instability. In other words, from eq.(1.5.5), the poloidal cross section average of the current is limited by

$$\langle j\rangle < \frac{1}{\mu_0}\frac{B_\phi}{R_0}. \tag{1.6.3}$$

Furthermore, an ohmically heated tokamak allows only pulsed operation, as the primary coil current cannot increase indefinitely to induce a constant plasma current (Faraday's law of induction). Ohmic heating is not sufficient to raise the plasma to fusion temperatures. Further auxiliary heating schemes were developed and successfully implemented on various plasma facilities.

1.6.2 Neutral beam heating

An additional possibility of heating a plasma is the injection of a beam of energetic atoms, for example hydrogen. The neutral atoms travel in straight lines, being unaffected by the magnetic field. The atoms become ionised through collisions with the plasma particles and the resulting hot ions and electrons are then held by the magnetic field. Once ionised the ions have orbits in the magnetic field determined by their energy, angle of injection and point of deposition. The energy of the injected ions is gradually transferred to the colder plasma electrons and ions through Coulomb collisions. That is the injected ions are initially slowed and then thermalised. Section 6.5.1 will further discuss the deposition of energetic beam particles in the plasma, albeit not for the purpose of plasma heating.

1.6.3 Heating by means of electromagnetic waves

Under certain conditions (coupling, transmission followed by absorption, i.e. the absence of cutoffs), electromagnetic waves propagate and eventually dissipate (wave-particle resonances) in the plasma. Plasmas exhibit an very rich variety of electromagnetic wave modes, therefore many different heating scenarios have been developed and implemented on various devices.

Resonant plasma heating with ion-cyclotron [26], electron cyclotron [27], lower-hybrid [28] and more recently Bernstein waves [29] were successfully employed on plasma devices. For example, a wave launched at the second harmonic electron cyclotron frequency, i.e. at twice the fundamental frequency, eq.(1.4.3), is efficiently absorbed by the electrons. This is called **E**lectron **C**ylotron **R**esonance **H**eating (ECRH). As the toroidal magnetic field decreases as $1/R$ and Ω_{ce} is proportional to B, the wave power deposition in the plasma will be localised. ECRH will be described in greater detail in chapter 5.

1.7 Motivation for this thesis

The main goal of this thesis is the experimental characterisation and eventual understanding of the mechanism causing the anomalous acceleration of a fraction of the plasma ions to suprathermal energies on TCV, whenever the plasma is subjected to the injection of waves at the second harmonic of the electron cyclotron frequency. As explained in this chapter, ion heating has always been a major topic addressed in the magnetic confinement fusion field and thus any process yielding hot ions is always welcomed and worth to be studied. The phenomena of anomalous ion energisation was observed since the early days of millimetre wave heating, but nobody has ever put forward an attempt at explanation. This work has now tried to fill this deficit.

Although the modelling of the physics involved takes an important share in the scientific efforts undertaken, this is essentially an experimental study. The acquisition of a new neutral particle analysing diagnostic coincided with the employment of the author and thus many activities were related to the commissioning, validation and integration of the diagnostic into TCV such to bring its exploitation to the best possible performance.

1.8 Outline of the dissertation

A brief introduction to magnetic confinement fusion was given in this chapter. Most of the work reported herein was carried out on the Tokamak à configuration variable (TCV), which is the subject of **chapter 2**. The principles and specifications of the TCV ion diagnostics of relevance for this work (charge exchange recombination spectroscopy, neutral particle analyser and neutron detector) are described in **chapter 3**, emphasising on the data analysis, measurement validation and the parasitic signal rejection of the horizontally looking Compact Neutral Particle Analyser (CNPA), which was commissioned in 2003–2004. Results of the commissioning are available in the journal publication:

> A. N. Karpushov, B. P. Duval, C. Schlatter, V. I. Afanasyev and F. V. Chernyshev, **Neutral particle analyser diagnostics on the TCV tokamak**, *Review of Scientific Instruments*, vol. 77, no. 3, art. 033504 (13pp), March 2006.

Chapter 4 reports on experimental studies of plasmas where the ion energy is characterised by the Maxwell-Boltzmann distribution. This includes the determination of the thermal ion parameters either directly from the measured charge exchange spectrum (ion temperature and isotopic composition) or with the assistance of codes modelling the plasma neutral emission (absolute neutral densities). The measurement of the core ion temperature with the NPA was validated against other diagnostics and the CNPA was absolutely calibrated using the diagnostic neutral beam. The ion temperature profile was measured with the single chord CNPA by displacing the plasma.

Results were reported at the 32nd EPS Conference on Plasma Physics and Controlled Fusion, Tarragona, Spain, 2005:

> C. Schlatter, B. P. Duval and A. N. Karpushov, **Reconstruction of hydrogenic ion temperature profiles on TCV**, *Europhysics Conference Abstracts (ECA)*, vol. 29C, no. P1.050

and later published in an extended journal paper

> C. Schlatter, B. P. Duval and A. N. Karpushov, **Reconstruction of ion temperature profiles from single chord NPA measurements on the TCV tokamak**, *Plasma Physics and Controlled Fusion*, vol. 48, no. 12, pp. 1765–1785, December 2006.

The physics of anomalous ion heating on TCV is governed by the interaction between waves and particles and the properties of the suprathermal ions are intimately linked to the physics of suprathermal electrons, which routinely appear whenever electron cyclotron waves are injected into low density TCV discharges. Good knowledge of the fast electron properties is therefore of paramount importance. The EC physics is addressed in **chapter 5**. Advanced analysis of the electron cyclotron emission spectra with an implementation of the *NOTEC* code on TCV gives unprecedented accuracy of the spatial and energetic fast plasma electron properties, especially in discharges with electron cyclotron current drive (ECCD), where a large number of electrons are accelerated to relativistic speeds. First results with the *NOTEC-TCV* code have been published in

> V. S. Udintsev, G. Turri, E. Asp, C. Schlatter, T. P. Goodman, O. Sauter, H. Weisen, P. Blanchard, S. Coda, B. P. Duval, E. Fable, A. Gudozhnik, P. F. Isoz, M. A. Henderson, I. Klimanov, X. Llobet, P. Marmillod, A. Mueck, L. Porte, H. Shidara, G. Giruzzi, M. Goniche and F. Turco, **Recent electron cyclotron emission results on TCV**, *Fusion Science and Technology*, vol. 52, no. 2, pp. 161–168, August 2007.

NOTEC-TCV was then extensively used to analyse oblique ECE experiments, these results were partly published in

> T. P. Goodman, V. S. Udintsev, I. Klimanov, A. Mueck, O. Sauter and C. Schlatter, **First measurements of oblique ECE with a real-time movable line of sight on TCV**, *Fusion Science and Technology*, vol. 53, no. 1, pp. 196–207, January 2008.

Chapter 6 presents the parameters of the suprathermal ions, manifesting in plasmas with auxiliary EC electron heating. Early measurements and analytic turbulence estimations were presented in two joint papers at the 33rd EPS Conference on Plasma Physics, Rome, Italy, 2006:

> A. N. Karpushov, B. P. Duval, T. P. Goodman and C. Schlatter, **Non-maxwellian ion energy distribution in ECH-heated plasmas on TCV**, *Europhysics conference abstracts (ECA)*, vol. 30I, no. P1.152

and

> C. Schlatter, B. P. Duval, A. N. Karpushov, E. Asp, S. Coda and V. S. Udintsev, **Conditions for anomalous energy and momentum transfer from electrons to ions in ECCD discharges on TCV**, *Europhysics conference abstracts (ECA)*, vol. 30I, no. P1.149.

The role played by fast electrons is discussed and candidate mechanisms for the ion acceleration are shortly reviewed. Ion-acoustic turbulence, driven by the circulating ECCD electrons, agrees with most of the experimental observations. Ion acceleration is also caused by the sawtooth instability. Due to limited availability of TCV, a last series of experiments aiming at the demystification of the physics responsible of the ion acceleration could unfortunately not yet be carried out, the end of the chapter thus makes do with the description of the pending experiments, namely the measurement of the turbulence frequency spectrum and the anisotropy assessment of the ion distribution function.

Chapter 7 makes an attempt to model the ion-acoustic turbulence and the associated ion acceleration for TCV parameters by solving the quasilinear diffusion equation numerically. Preliminary results were presented at the 49th Annual Meeting of the Division of Plasma Physics, Orlando, Florida, USA, 2007:

> C. Schlatter, B. P. Duval, A. N. Karpushov, T. P. Goodman, **Ion-Acoustic Turbulence in ECCD-driven TCV plasmas**, *Bulletin of the American Physical Society*, vol. 52, no. 11, poster GP8.00023.

Chapter 8 summarises the main results and draws conclusions.

A number of appendices consolidates the matter presented in the chapters. The independent appendix F reports on the diagnosis of the fast ions with the high energy NPA on JET. This analysis of the accuracy of the calculation of the fast ion temperature was presented at the 15^{th} topological conference on high-temperature plasma diagnostics, April 2004, San Diego, California, USA and published in Review of Scientific Instruments:

> C. Schlatter, D. Testa, M. Cecconello, A. Murari and M. Santala, **Error estimation and parameter dependence of the calculation of the fast ion distribution function, temperature, and density using data from the KF-1 high energy neutral particle analyser on Joint European Torus**, *Review of Scientific Instruments*, vol. 75, no. 10, pp. 3547–3549, October 2004.

A further appendix G reports on the successful deployment and operation of wiki technology on the intranet of the Plasma Physics Centre in Lausanne and how an open, collaborative documentation platform enriches the scientific exchange among researchers and technicians and how organisational aspects of tokamak operation and administrative tasks are greatly facilitated.

Chapter 2

The TCV experiment

2.1 TCV tokamak

The *Tokamak à configuration variable* (TCV), shown in figure 2.1.1, is a mid sized machine with a rectangular, strongly elongated torus [30] (the vessel is three times higher than large). Operational since November 1992, TCV was mainly built to study the impact of the plasma shape on the particle confinement and plasma stability against Magnetohydrodynamic (MHD) properties. In almost 17 years of operation, more than 37'000 plasma discharge sequences, known as 'shots', have been fired.

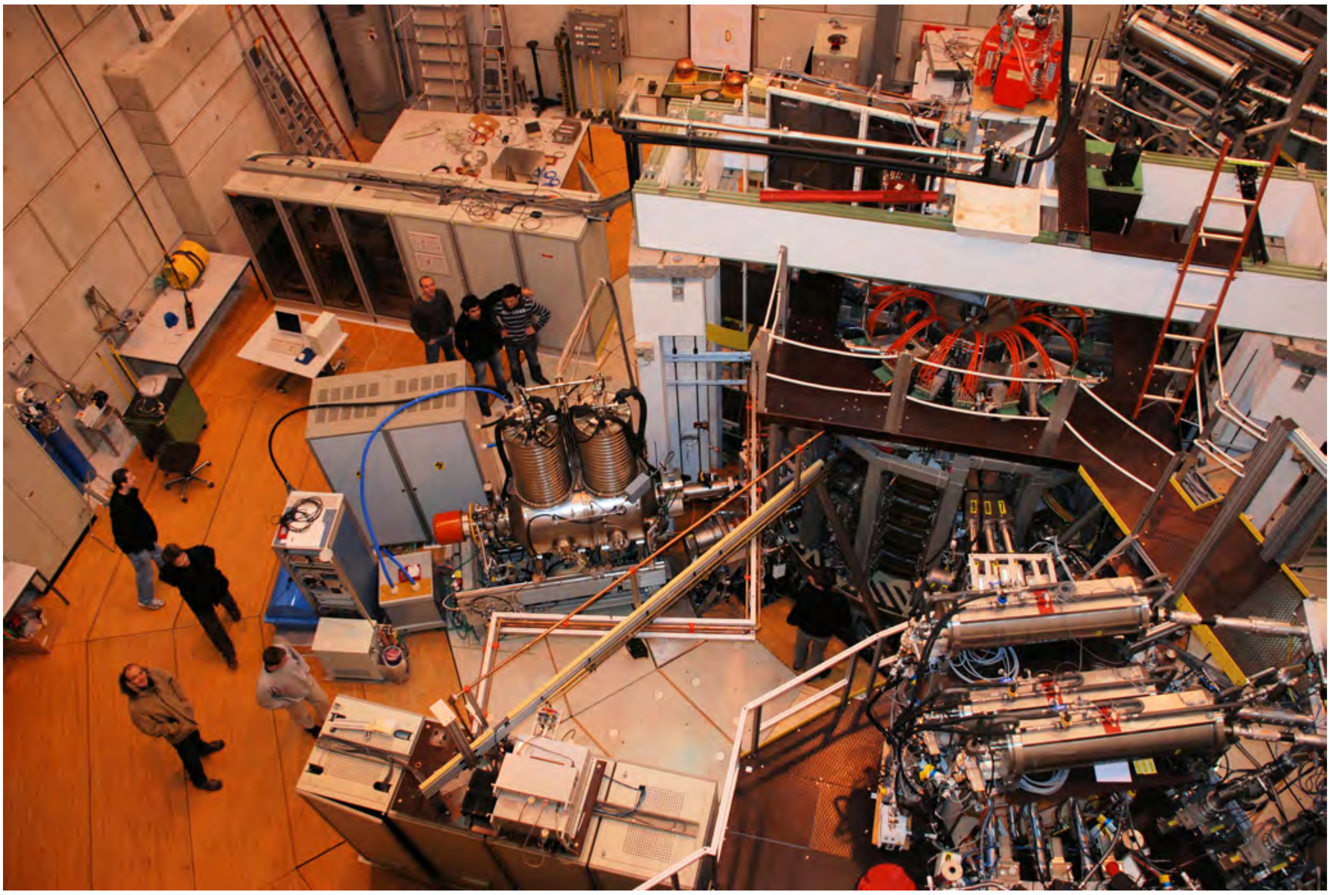

Figure 2.1.1: Picture of the TCV tokamak taken from above. The diagnostic neutral beam (DNBI) is located on the left. The tubes containing the electron cyclotron wave guides are discernable on the right. The thin copper lines in front of the DNBI are the transmission lines of the ECE low field side radiometers.

Some key parameters of TCV are listed in tables 2.1 and 2.2. Figure 2.1.2 shows a sketch of its main components. The toroidal magnetic field is generated by 16 coils connected in series, the inductive current is driven by an air core transformer consisting of 7 coils, their position minimises the perturbation of the magnetic field inside the torus. The induced electric field is typically 0.25 V/m on the magnetic axis, whose length is typically 5.5 m.

Parameter	Symbol	Value
first plasma	t_0	November 1992
major radius	R_0	0.88 m
maximum minor radius	a	0.255 m
internal height of vessel	h	1.5 m
aspect ratio	$\epsilon = R_0/a$	2.9…3.6
toroidal vessel resistance	Ω_{TCV}	45 mΩ
vessel time constant	τ_{vessel}	6.7 ms
toroidal magnetic field on axis	$B_{\phi 0} = B_\phi(R_0)$	$\leqslant$ 1.54 T
plasma current	I_{p}	$\leqslant$ 1 MA
transformer flux	Φ_{T}	3.4 Vs
loop voltage	V_{loop}	$\leqslant$ 10 V
Vessel elongation	κ_{TCV}	3
Pulse duration	T_S	$\leqslant$ 4 s
Intershot delay	T_D	$\geqslant$ 400 s
OH heating power	P_{OH}	1 MW
X2 RF heating power	P_{ECH} X2	2.8 MW
X3 RF heating power	P_{ECH} X3	1.4 MW
vessel base vacuum	p_0	$< 10^{-7}$ mbar
Helium cleaning glow discharge	t_g	300 s
Maximum vessel temperature	T_g	350 ℃

Table 2.1: System parameters of the TCV tokamak (specifications as of January 2009).

Parameter	Symbol	Value
plasma width	w	$\leqslant$ 0.48 m
plasma height	h	$\leqslant$ 1.44 m
electron density	n_{e0}	$\leqslant 20 \times 10^{19}$ m^{-3}
electron temperature (OH)	T_{e0}	$\leqslant$ 1 keV
electron temperature (ECH)	T_{e0}	$\leqslant$ 15 keV
ion temperature	T_{i0}	150…1000 eV
electron plasma frequency	f_{pe}	28…120 GHz
electron cyclotron frequency	f_{ce}	41 GHz
ion cyclotron frequency	f_{ci}	11 MHz
electron Larmor radius	ρ_e	70…250 μm
ion Larmor radius	ρ_i	2.5 …4 mm
edge plasma elongation	κ_a	0.9…2.8
edge plasma triangularity	δ_a	−0.8…1

Table 2.2: Plasma parameters of the TCV tokamak (specifications as of January 2009).

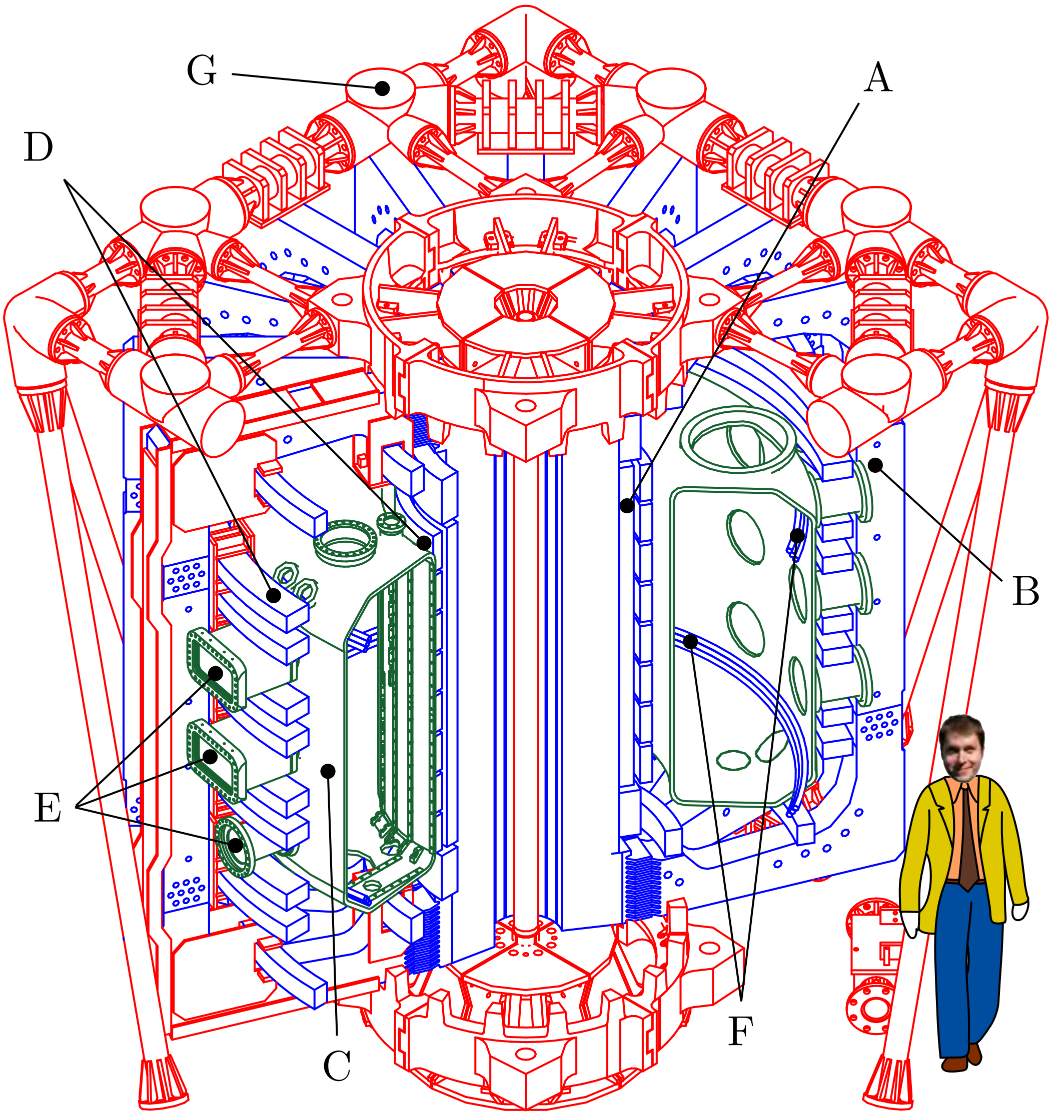

Figure 2.1.2: Sketch of the TCV tokamak. Labelled are: (A) primary transformer circuit (ohmic coil) to drive the inductive plasma current, (B) poloidal coil for the generation of the main toroidal field, (C) the vacuum vessel, (D) plasma shaping coils, (E) diagnostic ports, (F) internal toroidal coils for the vertical stabilisation of elongated plasmas, (G) supporting mechanical structure.

2.2 First wall

Plasma-wall interactions continually lead to the exchange of particles between plasma and wall. Wall eroded material constitutes the main source of impurities in the plasma. The penetration of high-Z impurities into the plasma has to be avoided, since their strong line radiation results in an inadmissible cooling of the plasma. On TCV, the compromise between a light material, sufficiently withstanding high heat loads and of enough tensile strength led to the selection of carbon for the first wall cover. Currently about 90 % of the vessel interior (surface area $\sim$23 m^2) are covered by a total of $\sim$1700 graphite tiles. Figure 2.2.1 shows a recent photo of the interior of the TCV tokamak. To further limit the contamination of the plasma by erosion of deposited impurities from the wall, the vessel is sporadically baked out at 250 °C and coated by boron to cover impurities and getter oxygen. The boronisation with a mixture of helium and B_2D_2 creates a 10 μm thick layer by chemical vapour deposition. Between plasma pulses, the chamber is conditioned by glow discharges with helium (typically running for 300 seconds).

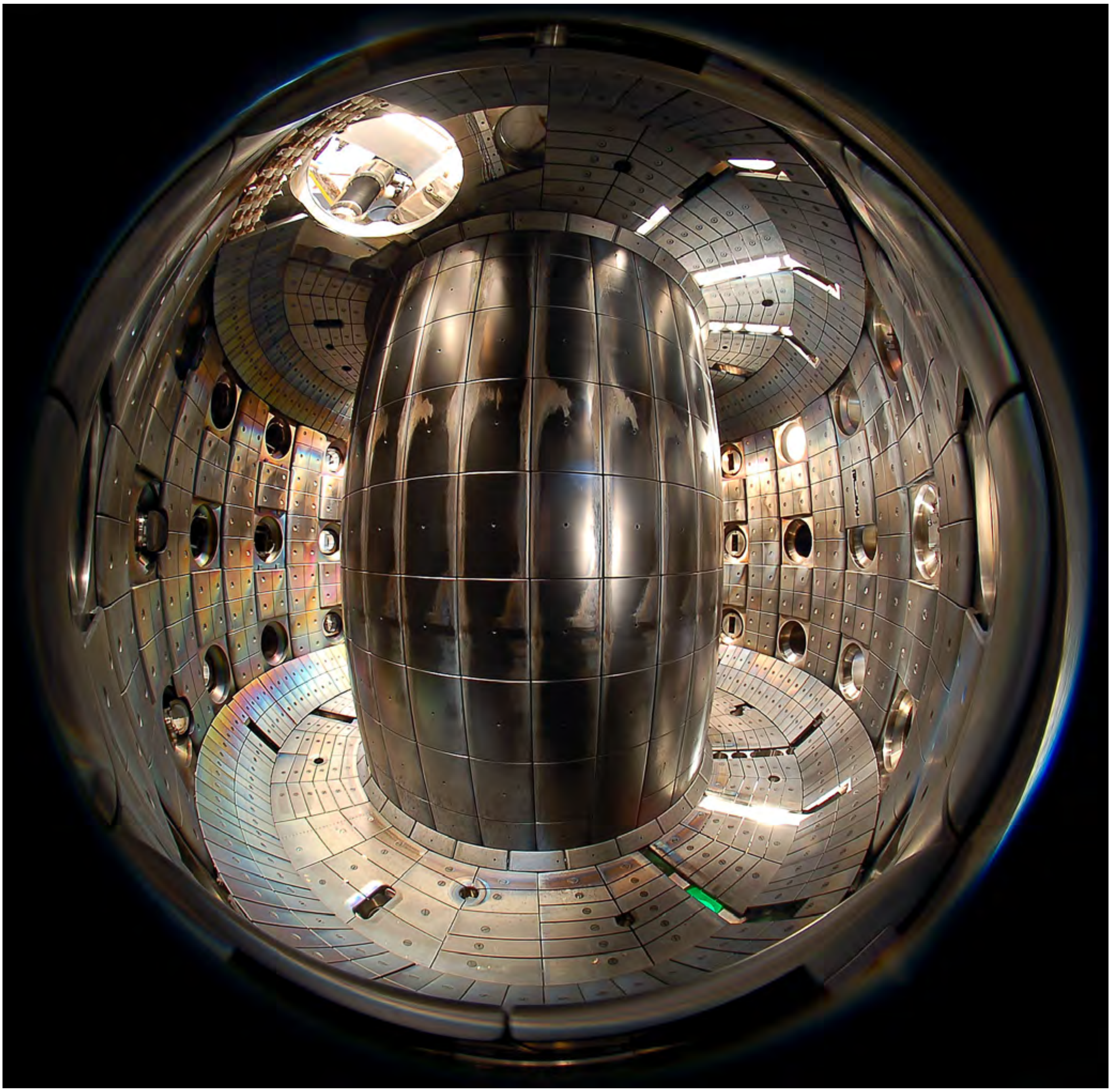

Figure 2.2.1: Fisheye view of the TCV vessel. The picture was taken in March 2007, after 15 years of tokamak operation. Areas of erosion and thin film deposition are clearly visible. Courtesy of Alain Herzog, EPFL.

2.3 Plasma shaping

A set of 16 independently controllable poloidal field shaping coils closely surround the vacuum vessel on the in- and outside and guarantee, for TCV, a unique flexibility in plasma shaping, positioning and control. Two additional poloidal field coils located inside the vessel permit better control of otherwise vertically unstable configurations. The coil arrangement is shown in figure 2.3.1.

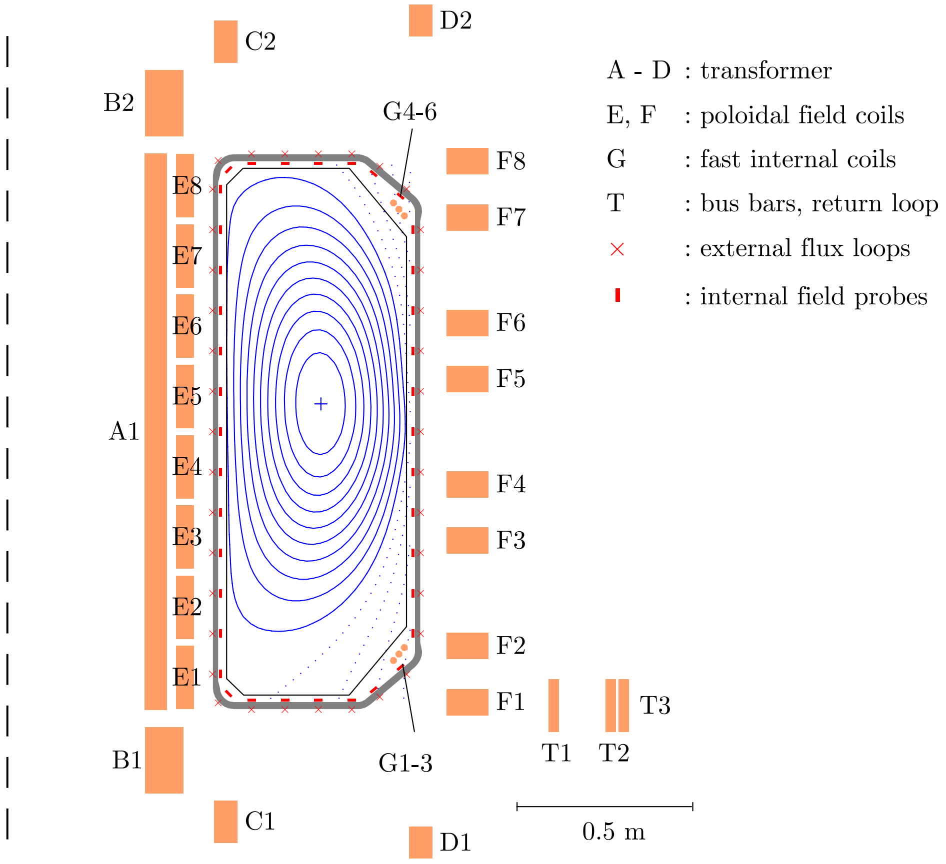

Figure 2.3.1: Representation of the transformer windings (A, B, C and D), the poloidal field coils (E and F) and the internal fast coil (G). The bus bars (T1 and T2) interconnect the toroidal field coils and are compensated by the return loop (T3). The magnetic configuration of the plasma is investigated using the external flux loops and the internal poloidal field coils (see figured legend).

Figure 2.3.2 shows a subset of the achieved zoology of plasma shapes. The shape parameters κ (elongation), δ (triangularity) and λ (squareness) are defined by the following formulae, parameterising a flux surface contour in real space,

$$\begin{cases} R = R_0 + a\cos\big(\theta + \arcsin(\delta\sin\theta)\big) & \text{and} \\ z = z_0 + \kappa a \sin\big(\theta + \lambda\sin 2\theta\big), & \end{cases} \tag{2.3.1}$$

where R is the machine major radius, z the vertical coordinate, θ the poloidal angle and a the plasma minor radius. The index 0 labels the magnetic axis coordinates. For an illustration of κ and δ see figure 2.3.3. Achieved values for κ and δ are shown in table 2.1. Elongated plasmas allow for a higher plasma current in respect to circular plasmas, as the edge safety factor (which is required $q_a > 2$ for ideal MHD stability) and thus the plasma current scale as $\propto (1+\kappa^2)/2$ [32]. A higher current allows then to operate at higher density (Greenwald density limit) [33]. TCV has demonstrated that elongated and triangular plasmas have better stability and reduced radial particle transport [34], thus improving the cost-effectiveness of the experience.

Impurities in the plasma give rise to radiation losses and also dilute the fuel. The restriction of their entry into the plasma therefore plays a fundamental role in the successful operation of tokamaks. This requires a separation of the plasma from the vacuum vessel. TCV uses two techniques: limited and diverted plasmas, figure 2.3.4. In the limited configuration a rather small fraction of the last closed flux surface (LCFS) is in contact with the vessel wall.

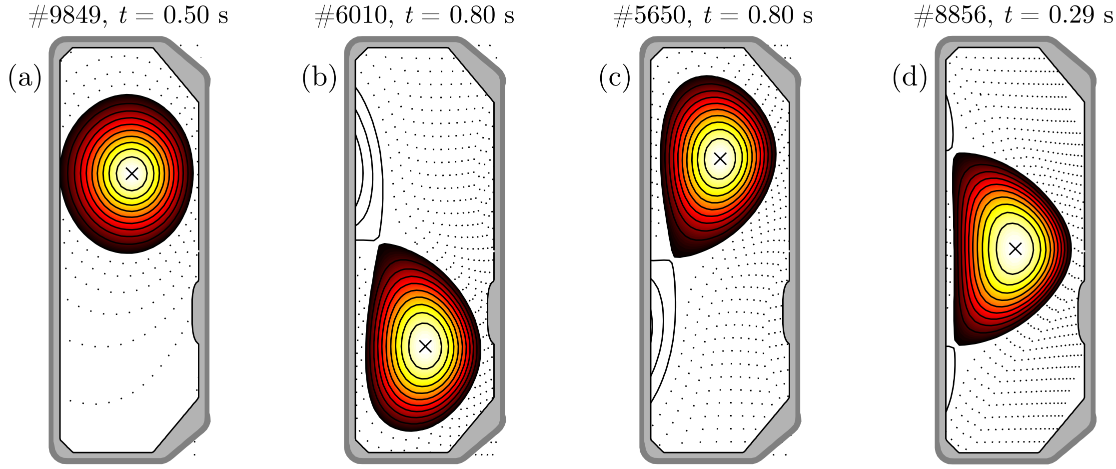

#9849, $t = 0.50$ s #6010, $t = 0.80$ s #5650, $t = 0.80$ s #8856, $t = 0.29$ s

Limited $\kappa = 1.2$, $\delta = 0.0$, $I_\mathrm{p} = 230$ kA

SND upper $I_\mathrm{p} = 330$ kA

SND lower $I_\mathrm{p} = 335$ kA

DND $I_\mathrm{p} = 325$ kA

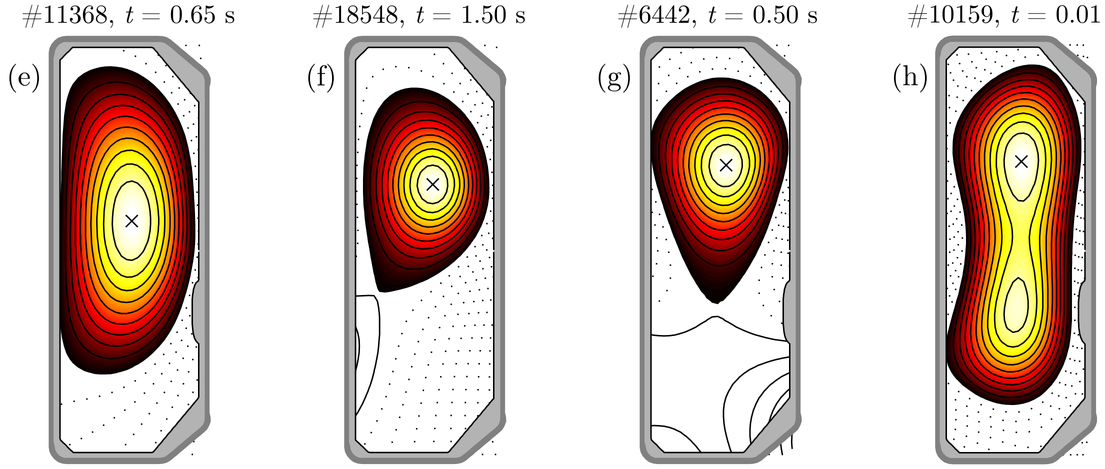

#11368, $t = 0.65$ s #18548, $t = 1.50$ s #6442, $t = 0.50$ s #10159, $t = 0.01$ s

Highest current, $I_\mathrm{p} = 1.06$ MA

Highest fully ECCD driven current, $I_\mathrm{p} = 210$ kA

Pear shape $I_\mathrm{p} = 360$ kA

Doublet shape $I_\mathrm{p} = 115$ kA

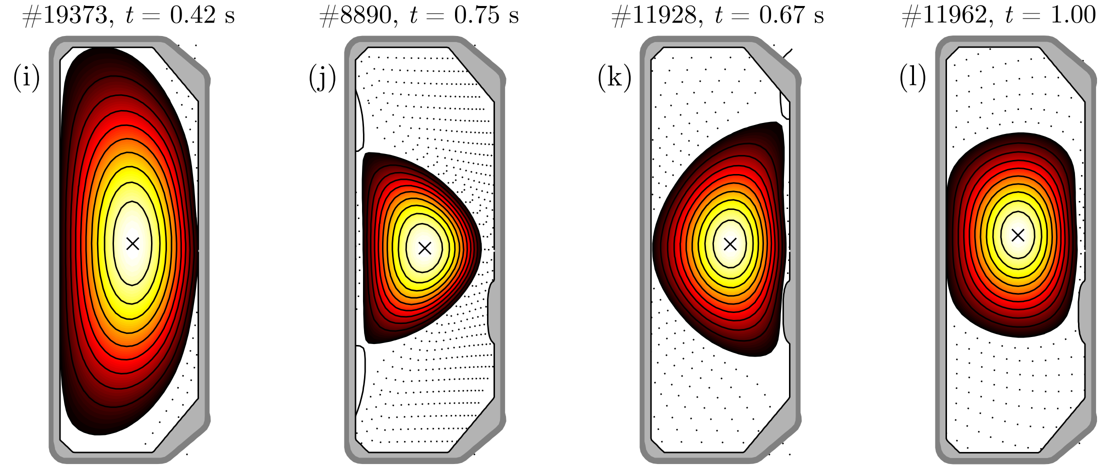

#19373, $t = 0.42$ s #8890, $t = 0.75$ s #11928, $t = 0.67$ s #11962, $t = 1.00$ s

Highest elongation, $\kappa = 2.80$

Highest triangularity, $\delta = 0.86$

Lowest triangularity, $\delta = -0.77$

Highest squareness, $\lambda = 0.5$

Figure 2.3.2: Omnium gatherum of plasma shapes achieved on TCV. The first line shows standard limited (a) and diverted configurations with a single null on top (b), below (c) and a double null (d). Divertor legs may be put on the inner (as shown) or outer wall. The last line shows extremely shaped stable plasmas of (i) highest elongation, maximum (j) and minimum (k) triangularity and (l) maximum squareness. The middle line shows achieved record ohmic (e, anno 1996) and non-inductive (f, anno 2000) currents and (g) near snowflake [31] and (h) doublet configurations. The colour scale is proportional to the temperature (black: cold, white: hot).

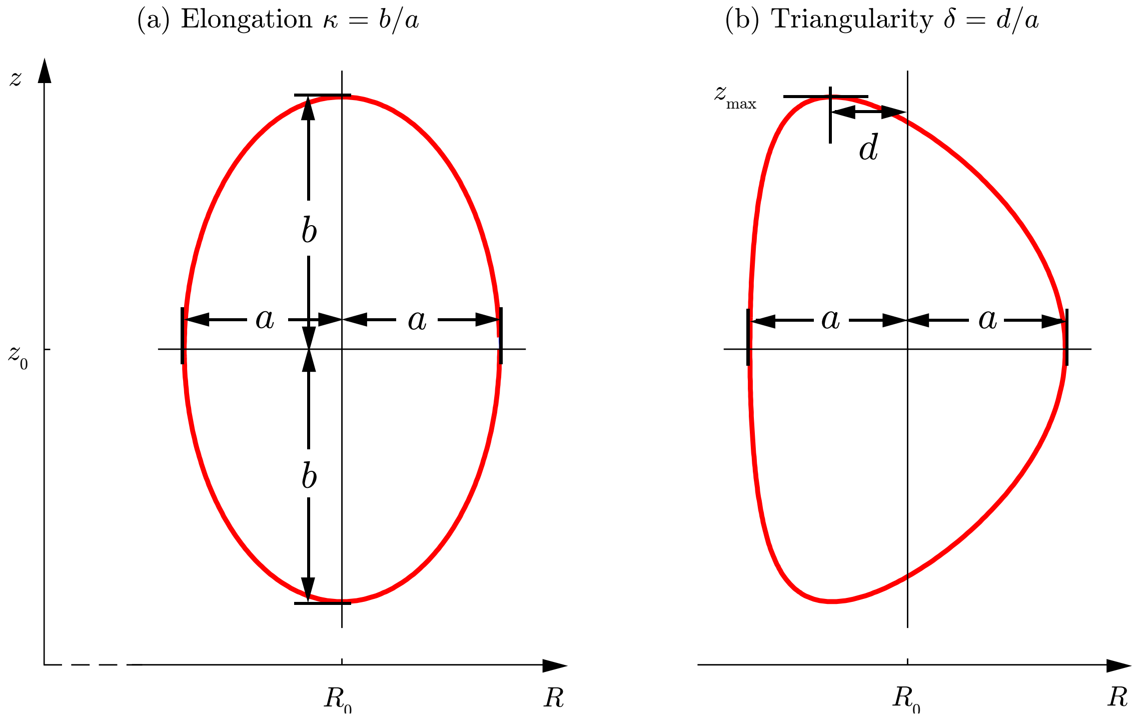

Figure 2.3.3: Higher order moments of the poloidal plasma geometry.
(a) defines the elongation $\kappa = b/a$ and
(b) the triangularity $\delta = d/a$.

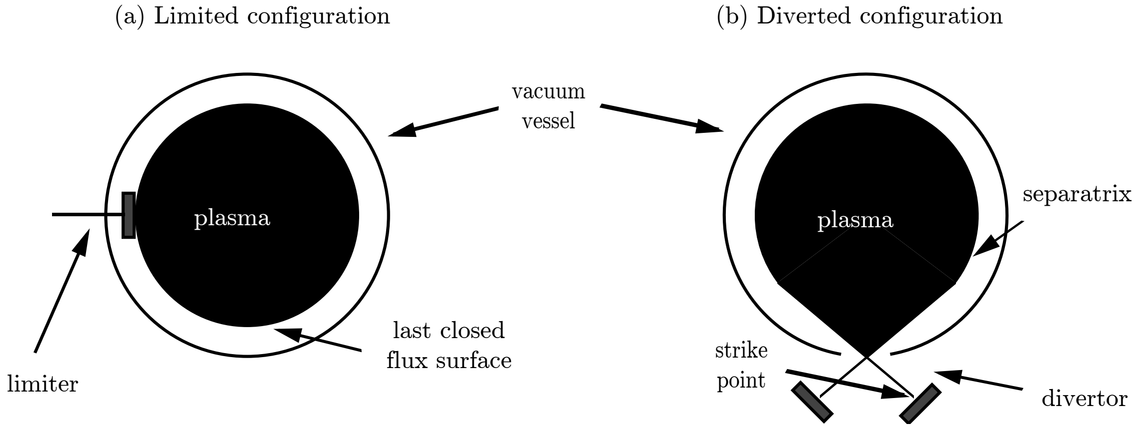

Figure 2.3.4: Configuration of plasmas in a tokamak.
(a) A limiter scrapes the plasma off and defines the last closed flux surface (LCFS). On TCV the walls are limiting the plasma in this configuration.
(b) In diverted configurations the LCFS is determined through additional magnetic coils that shape the magnetic flux surfaces such as to create an X-point, where the poloidal magnetic field has a null. The magnetic flux surface passing through this X-point is called the separatrix. The region below the X-point may be loosely defined as the divertor. The points at which the separatrix strikes the wall are known as the strike points.

In the diverted configuration the LCFS is not determined by the interference of a solid surface with the main plasma, but by additional magnetic coils that shape the magnetic flux surfaces such as to create one or more X-point(s), where the poloidal field vanishes (see figure 2.3.2). This can be obtained using an external conductor whose current is parallel to the main plasma current. The magnetic flux surface passing through the X-point is called the separatrix. The points at which the separatrix strikes the wall are known as the strike points. Diverted plasmas are generally cleaner since the interaction between plasma and wall takes place at a larger distance from the plasma bulk.

2.4 Auxiliary heating

TCV employs auxiliary plasma heating by means of electron cyclotron waves. 9 gyrotrons working at the second or third harmonic of the electron cyclotron frequency provide a total power of 4.2 MW. An well thought-out system of wave launchers allows for localised plasma heating or toroidal injection for current drive. The EC system is described in detail in chapter 5.

2.5 Diagnostics

TCV has a versatile set of diagnostics to measure most of the parameters relevant for experimental studies. The flexibility in plasma shaping and positioning requires diagnostics with a good coverage of the vessel cross section. Due to the rich variety of plasmas achievable on TCV, most of the diagnostics are designed to measure a parameter over a large range. These diagnostics are

TS The Thomson scattering diagnostic, providing profiles of thermal electron density and temperature.

FIR The Far-Infrared Interferometer, measuring the line integral of the electron density at high temporal resolution.

ECE Various electron cyclotron emission antennas for fast electron temperature profile measurements and the characterisation of suprathermal electrons.

DMPX, XTOMO, XTE various soft-X ray diagnostics with different spatial setups for the characterisation of electron temperature profiles and/or the determination of the effective charge.

HXRC, HXRS, PMTX Hard X-ray diagnostics for the assessment of the keV energy tail of the electron distribution function.

DNBI+CXRS, VNPA, CNPA, NEUT ion diagnostics measuring ion temperature, isotopic compositions, impurity concentrations and ion rotation profiles.

LIUQE et al. magnetic diagnostics used for the reconstruction of the equilibrium and the analysis of Magnetohydrodynamic (MHD) fluctuations.

BOLO, AXUV, PD Single line and broad range radiation diagnostics in the visible and ultraviolet frequency range.

SPRED, PHA Plasma spectroscopy

and many more. . .

A short description of the diagnostics essential to this thesis are given below, measurements of ion parameters are described in more detail in a separate chapter 3 and the radiometers for the detection of the electron cyclotron emission are introduced later in section 5.3.5.

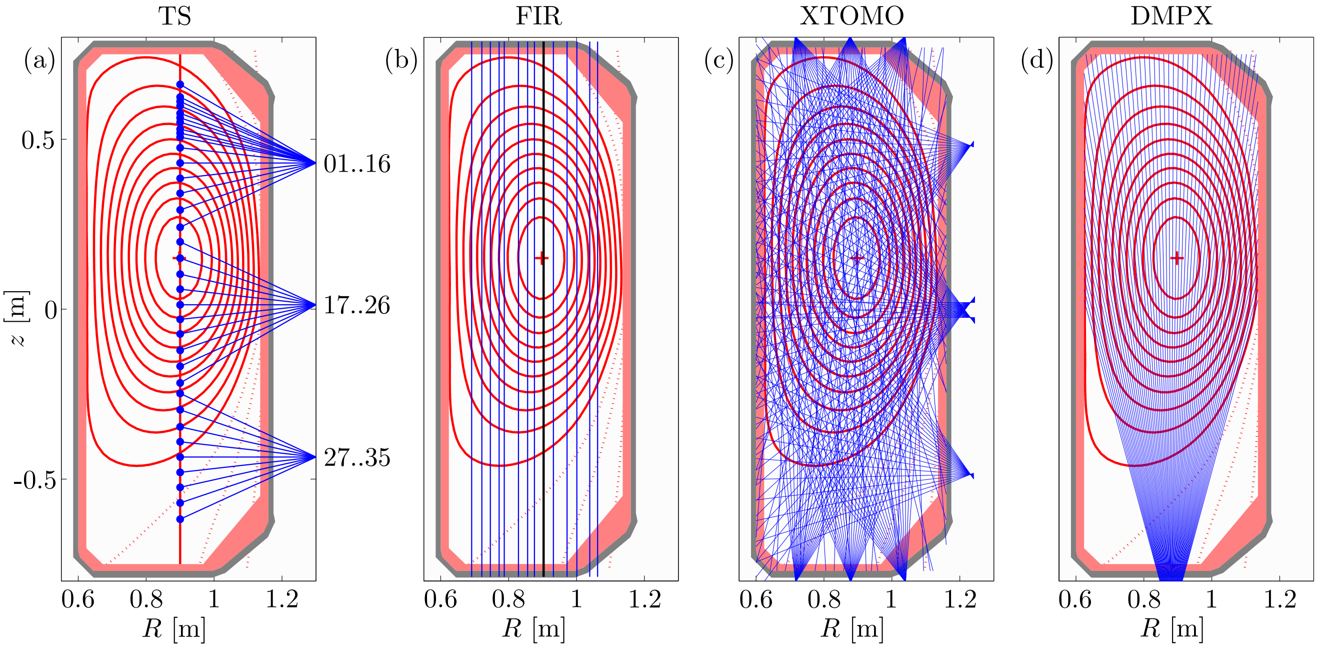

Figure 2.5.1: Diagnostic setups on TCV:
(a) Lines of sight of the optical fibres of the Thomson scattering system before the 2007 upgrade (featuring a higher spatial resolution at the upper plasma edge),
(b) 14 vertical chords of the far infrared interferometer, the measurement of the central chord (#9) acts as reference for the density preset,
(c) the 200 chords of the soft X-ray system XTOMO cover the whole poloidal cross section (geometry as after the camera upgrade in 2008) and
(d) the multiwire proportional X-ray detector with 64 channels achieving a spatial resolution better than 1 cm at the midplane.

2.5.1 Thomson Scattering (TS)

TCV features a powerful Thomson scattering diagnostic [35–38] routinely providing radial profiles of electron temperature $T_e(\rho)$ in the range from 50 eV to 20 keV and electron density $n_e(\rho)$. The measurement is derived from the local analysis of light from a laser beam (incident wave vector $\mathbf{k}_i$, frequency ω_i) scattered by the electrons of the plasma (scattered wave vector $\mathbf{k}_s$, frequency ω_s). If the wave vector of the laser beam is large enough, essentially the scattering parameter $(k_i\lambda_D)^{-1} \ll 1$, the correlation between electrons may be ignored. This means that the scattering is incoherent and the total scattered power is simply the sum of the power scattered by the individual electrons. The frequency of the scattered light is double Doppler shifted and becomes

$$\omega_s = \omega_i + (\mathbf{k}_s - \mathbf{k}_i) \cdot \mathbf{v}. \tag{2.5.1}$$

The shift is due to (a) the motion of the electron towards the laser beam and (b) its motion towards the observation optics. In the non-relativistic approximation (valid for $T_e \lesssim 1$ keV) the frequency spectrum scales with the one-dimensional velocity distribution along the direction of $\mathbf{k} = \mathbf{k}_s - \mathbf{k}_i$. If the electron velocity distribution is Maxwellian, the local temperature is determined by the width of the measured spectrum (Doppler line broadening).

On TCV, the laser beam is injected vertically at $R = 0.9$ m and $\mathbf{k}$ is in a plane perpendicular to the toroidal magnetic field $\mathbf{B}$, thus the measured temperature is the perpendicular temperature $T_{e\perp}$. In the presence of suprathermal electron populations the Thomson scattering diagnostic measures in principle the temperature of the thermal bulk population. The intensity of the scattered light is given by the integral over the spectral peak and is proportional to the local electron density.

The Thomson scattering cross section is extremely low, requiring powerful and therefore pulsed lasers. TCV operates 3 collinear Q-switched Nd:YAG (neodymium–yttrium aluminium garnate) lasers ($\lambda = 1.06$ μm) at a repetition rate of 20 Hz. By sequentially triggering the lasers, the repetition rate may be increased up to 60 Hz. Each pulse has an energy of about 1.5 J. The scattered light is observed through 3 lateral ports at 35 vertical locations shown in figure 2.5.1a, the spatial resolution is $2\dots4$ cm. For plasmas of moderate elongation ($\kappa \sim 1.7$) at least 25 points are inside the plasma. The collected light enters optical fibers which feed the light to polychromators consisting of broadband filters connected to avalanche silicon photo-diodes.

The diagnostic is periodically absolutely calibrated by Raman scattering from a nitrogen gas introduced into the torus. A cross calibration to the line integrated density obtained from a multi-chord FIR interferometer (section 2.5.2) is performed for consistency. Uncertainties of the measurements are typically better than 10 %. Statistical errors dominate due to the scattered light fraction.

2.5.2 Multi-chord Far Infrared Interferometer (FIR)

The interferometer installed on TCV [39,40] is of the Mach-Zehnder layout [41,42]. It determines the phase shift $\Delta\phi$ between two collimated beams from a coherent light source, one of which travels through the plasma and the other outside the tokamak (reference beam). The refractive index of an electromagnetic wave of frequency $\omega \gg \{\omega_{\text{pe}}, \Omega_{ce}\}$ in a plasma is approximately(*)

$$N^2 = 1 - \left(\frac{\omega_{\text{pe}}}{\omega}\right)^2 = 1 - \frac{n_e}{n_c}, \tag{2.5.2}$$

where

$$n_c = \frac{\varepsilon_0\, \omega^2\, m_e}{e^2} \tag{2.5.3}$$

is the cutoff density. The density, integrated along the beam path through the plasma, $\overline{n}_e = \frac{1}{L}\int n_e\, \mathrm{d}l$, is proportional to the phase shift of the wave traversing the plasma,

$$\Delta\phi = \int (k_{\text{plasma}} - k_{\text{reference}})\, \mathrm{d}l = \int (N-1)\frac{\omega}{c}\, \mathrm{d}l \approx \frac{\omega}{2\, c\, n_c}\int n_e\, \mathrm{d}l, \tag{2.5.4}$$

where for the reference beam $k_{\text{reference}} = \omega/c$. The last term in eq.(2.5.4) was obtained using $n_e \ll n_c$. The heterodyne interferometer on TCV consists of a far infrared difluormethane (CH_2F_2) laser emitting at $\lambda = 214.6$ μm (some mW) and is optically pumped by a continuous wave CO_2 laser working at $\lambda = 9$ μm (power ~40 W). The probing beam is superposed with a reference beam with a slight frequency offset ($\Delta\omega/2\pi = 100$ kHz) provided by a local oscillator (LO) using the Doppler shift caused by diffraction from a rotating grating.

(*) in the limit of $\mathbf{B} \to 0$, see section 5.1.2.

The coherent electric field vectors $\mathbf{E}_{\text{probe}} = \widehat{\mathbf{E}}_{\text{probe}} \exp\big(\mathrm{i}\,(\omega_0 t + \Phi(t) + \phi_{\text{probe}})\big)$ as well as $\mathbf{E}_{\text{LO}} = \widehat{\mathbf{E}}_{\text{LO}} \exp\big(\mathrm{i}\,(\omega_0 t + \Delta\omega t + \phi_{\text{LO}})\big)$ are mixed and the detector measures the mixed beam intensity,

$$\begin{aligned} I_{\text{plasma}} &\propto (\mathbf{E}_{\text{probe}} + \mathbf{E}_{\text{LO}})(\mathbf{E}_{\text{probe}} + \mathbf{E}_{\text{LO}})^{\mathrm{T}} \\ &= |\widehat{\mathbf{E}}_{\text{probe}}|^2 + |\widehat{\mathbf{E}}_{\text{LO}}|^2 + 2|\widehat{\mathbf{E}}_{\text{probe}}||\widehat{\mathbf{E}}_{\text{LO}}| \cos\big(\Delta\omega t - \Phi(t) + \phi_{\text{LO}} - \phi_{\text{probe}}\big), \end{aligned} \tag{2.5.5}$$

whose amplitude oscillates at the beat frequency $\Delta\omega$. A filter removes any DC component and the remaining signal is

$$S_{\text{plasma}} = |\widehat{\mathbf{E}}_{\text{probe}}||\widehat{\mathbf{E}}_{\text{LO}}| \cos\big(\Delta\omega t - \Phi(t) - \phi_{\text{setup}}\big), \tag{2.5.6}$$

with $\phi_{\text{setup}} = \phi_{\text{probe}} - \phi_{\text{LO}}$, independent of time. The phase shift $\Phi(t)$ is obtained by comparison of S_{plasma} with the reference signal

$$S_{\text{reference}} = |\widehat{\mathbf{E}}_{\text{probe}}||\widehat{\mathbf{E}}_{\text{LO}}| \cos\big(\Delta\omega t - \phi_{\text{reference}}\big), \tag{2.5.7}$$

where $\phi_{\text{reference}}$ is ideally a constant (e.g. in absence of mechanical vibrations). The signal is captured by liquid helium cooled InSb hot electron bolometers on the top of the machine with a frequency response as high as 750 kHz, currently sampled at 20 kHz. For the chosen wavelength, a phase shift of 2π requires a change of the line integrated density of the order of 10^{19} m^{-2}, see eq.(2.5.4). The accuracy of the phase analysis is ∼20 degrees, giving an impressive accuracy of about 1 % of the line density. A total of 14 vertical beam path go through the plasma, shown in figure 2.5.1b. The measurement of the central chord ($R = 0.9$ m) enters the feed back loop of the plasma gas valve and is used to control the plasma density in real time. The non-local FIR signals have to be mathematically inverted to obtain density profiles. The most promising method currently applied is SVD-I [43], using singular value decomposited Thomson density profiles as base functions for the inversion [44].

2.5.3 Soft X-ray production and diagnostics

Relevant radiation emission from a plasma in the range of soft X-rays (120 eV to 12 keV) originates mainly from three processes [45]:

Bremsstrahlung arises from small-angle scattering of electrons due to electron–ion Coulomb collisions. The collision is free–free, i.e. the free electron is not captured by the ion and the radiation spectrum is therefore continuous in frequency.

Recombination radiation is resulting from a free–bound collision, the initially free electron is bound as a result of the interaction with the ion. The spectrum is mostly a continuum.

Line radiation is the product of a bound–bound transition from an excited state to one of lower energy. The emitted photon has an energy $h\nu = \Delta E$ equal to the difference in energy of the involved levels.

The radiation in the soft X-ray range constitutes the most important channel of radiation power losses of the TCV plasma. There are other sources of radiation commonly involved in plasmas (cyclotron radiation, Čerenkov radiation) but they are far less important than the processes listed above. Spectroscopic studies showed that for plasmas containing light impurities only (e.g. carbon, oxygen), the power lost through line radiation is only important in the ultra soft-X ray spectral range [46] and above 1 keV the emitted radiation is largely due to continuum radiation. Heavy ions however (e.g. iron, nickel, molybdenum), strongly radiate into the keV energy range and need therefore to be kept away from the plasma.

The Bremsstrahlung spectrum essentially depends on the local electron density, electron temperature and impurity content. For a Maxwellian electron distribution of temperature T_e and ions of charge Z, the continuum Bremsstrahlung spectrum is [47],

$$\frac{\mathrm{d}N}{\mathrm{d}E_X} \propto Z^2 n_e n_Z \frac{g_{\mathrm{ff}} e^{-E_X/T_e}}{E_X\sqrt{T_e}}, \tag{2.5.8}$$

with N being the number of emitted photons of an energy E_X, n_Z the ion density and g_{ff} the Maxwell-averaged Gaunt factor, tabulated in the literature [48].
The calculation of the electron–impurity–ion recombination radiation requires detailed knowledge of the atomic structure of the impurity ion and usually dominates eq.(2.5.8). The sum of braking and recombination radiation may be expressed as [49]

$$\frac{\mathrm{d}N}{\mathrm{d}E_X} = 1.5 \times 10^{-38}\, n_e^2 \frac{\exp\left(-\dfrac{\hbar\omega}{T_e}\right)}{\sqrt{T_e}} \zeta(T_e), \tag{2.5.9}$$

where $\zeta(T_e)$ represents the enhancement of the radiation by the presence of impurities (in respect to a comparable pure hydrogen plasma).

2.5.3.1 X-ray tomography (XTOMO)

TCV has some complex diagnostics to measure soft X-ray emission. Available since early operations of TCV, the soft x-ray tomographic system XTOMO consists of 10 pinhole cameras. Each camera is equipped with a linear array of 20 p-n junction silicon photodiodes resulting in 200 lines of sight covering the whole plasma cross section (see figure 2.5.1c). Each camera features 47 micron Be filters for efficient detection of photons with energies between 1 keV and 10 keV (but not visible or UV light) which covers the thermal spectrum of most TCV plasmas. Since 2008 the diode signals are acquired at a frequency of 200 kHz.

2.5.3.2 Duplex Multiwire Proportional X-ray detector (DMPX)

The compact 64 channel Duplex Multiwire Proportional soft X-ray detector (DMPX) combines high spatial and temporal resolution [50, 51]. The DMPX is installed on a helium filled slot aperture camera under the TCV vacuum vessel and views the plasma through two beryllium windows (total thickness of 100 μm). The DMPX measures soft X-ray emission in the 1–30 keV range with a radial resolution of about 8 mm at the equatorial plane of TCV (see figure 2.5.1d). The beryllium filters remove photons with energies below 1 keV. An additional 308 μm thick aluminium foil may be used to observe higher energy photons (exceeding 15 keV). The DMPX is acquired at 200 kHz.

The DMPX detector consists of a plane of 64 independent sensitive parallel anode wires placed between two cathode plates. A constant negative voltage is applied to the cathodes. An incident soft X-ray photon interacts with an atom of the detection gas filling the chamber, creating a pair of electron and ion (photo-ionisation) which are then accelerated by the electrical field. While migrating towards the closest wire-anode, the primary electron will collide with detection gas atoms and ionise them, thus creating more electron–ion pairs which will in turn be accelerated and collide with neutral atoms. This avalanching chain-reaction takes place near the wire (corona effect).

The chamber output voltage U_{out} satisfies the conservation of the energy,

$$\frac{1}{2}CU_{\text{HV}}^2 = \frac{1}{2}CU_{\text{out}}^2 + \Delta W, \tag{2.5.10}$$

where U_{HV} is the applied wire high voltage, C the chamber capacity and ΔW the work done by the free charged particles (mainly the ions) moving in the electric field of the chamber. The change of the output voltage is thus

$$\Delta U = U_{\text{HV}} - U_{\text{out}} = \frac{\Delta W}{CU_{\text{HV}}}. \tag{2.5.11}$$

ΔW is maximum when all charges have been collected by the anode and cathode. Depending on the time constant $\tau = RC$ of the system, ΔU is limited by the current flowing in the circuit which is restoring $\Delta U = 0$ after a time of the order of τ. The chamber output amplitude is proportional to the number of free charges created in the detector volume (and thus to the incident X-ray intensity). The wires are connected to amplifiers.

Since the X-ray emissivity has a strong dependence on the electron temperature and density as well as on the impurity mixture, see eq.(2.5.9), the X-ray diagnostics are very sensitive to the presence of MHD instabilities. The XTOMO system is routinely exploited for MHD analysis. XTOMO and DMPX are precious tools to determine the location of the sawtooth inversion radius (sections 5.4.4 and 6.6), the high spatial resolution of the DMPX camera allows the detection of the small scale structure of the perturbations with good accuracy.

To recover the local soft X-ray emissivities, the measured soft X-ray signals are tomographically inverted. The inversion is based on the method of the Minimum Fisher Information (MFI) [52], which has its foundation in information theory. In conjunction with measurements of electron densities and temperature profiles, the local X-ray emissivities are used to obtain local relative values of the effective plasma charge Z_{eff} (see next section).

2.5.3.3 Measurements of the plasma effective charge

Knowledge of the overall isotopic composition of the plasma is of importance in all aspects of the physics of plasmas. Especially transport and turbulence codes require a more or less rigourous estimation of the charged plasma components, determined by the concentration of impurities contaminating the plasma. In many cases the densities of the various ion species and isotopes are not of importance and the ionic configuration is sufficiently described by an effective charge Z_{eff}, ascribed to a single imaginary "ion species". The effective charge is defined as enhancement factor of the plasma resistivity η of the impurity contaminated plasma over that of a pure hydrogen plasma, η_S, given by eq.(1.6.2), thus

$$\eta = \eta_S \, Z_{\text{eff}}, \tag{2.5.12}$$

giving [24]

$$Z_{\text{eff}} = \frac{\sum n_i \, Z_i^2}{n_e} = \frac{\sum n_i \, Z_i^2}{\sum n_i \, Z_i}, \tag{2.5.13}$$

where the summation is taken over all ion species/isotopes in the plasma and for the last term the condition for quasi-neutrality,

$$n_e = \sum n_i \, Z_i, \tag{2.5.14}$$

was used.

On TCV, data from at least four different diagnostics are (or were) exploited to extract the effective plasma charge. These include

☞ **Bremsstrahlung:** The total continuum Bremsstrahlung emission, eq.(2.5.8), using the definition of Z_{eff}, eq.(2.5.13), writes (Watts per m^3 and eV)

$$I(\omega) = 1.54 \times 10^{-38}\, n_e^2\, Z_{\text{eff}} \frac{\exp\left(-\dfrac{\hbar\omega}{T_e}\right)}{\sqrt{T_e}}, \tag{2.5.15}$$

where the Gaunt-factor was approximated by 1. In the visible range of frequencies $\hbar\omega \gg T_e$ and the exponential may be neglected. Two telescopes look vertically into TCV at $R =$ 0.9 m and 1.054 m [53]. Fabry-Perrot filters ($\lambda_0 = 536$ nm, $\lambda_{\text{FWHM}} = 6$ nm, transmission 70 %) ensure operation without pickup of lines. The light is analysed by photomultipliers (bialkali, quantum efficiency of 8 %). This system was absolutely calibrated but has ceased to provide valuable data after 2005.

☞ **Soft X-ray:** The wide spectral range of radiation analysed by the soft X-ray systems on TCV requires the contributions to the spectral emissivity to be calculated properly using an ionisation equilibrium code like IONEQ [54] and assuming a coronal equilibrium [55]. This yields the energy integrated local spectral emissivity ε_Z for each considered ion species. The total local plasma emissivity is obtained from

$$g(\mathbf{x}) = \sum_Z n_e(\mathbf{x})\, n_Z(\mathbf{x})\, \varepsilon_Z(\mathbf{x}), \tag{2.5.16}$$

which is reconstructed from the experimentally measured soft x-ray chord brightness f by inversion of the matrix of Fredholm equations,

$$\mathbf{f} = \mathbf{T} \cdot \mathbf{g}, \tag{2.5.17}$$

with the matrix element T_{ij} representing the length of sight line i in pixel j.

In the case of a deuterium plasma contaminated by carbon the local effective charge is then [56]

$$Z_{\text{eff}}(\mathbf{x}) = 1 + 30\, g(\mathbf{x}) \frac{\varepsilon_{\text{D}}}{\varepsilon_{\text{C}} - \varepsilon_{\text{D}}}. \tag{2.5.18}$$

☞ **Plasma conductivity:** The conductivity of a cylindrical plasma linearly depends on the plasma effective charge, see the Spitzer formula for the plasma resistivity, eq.(1.6.2),

$$\sigma_{\text{Spitzer}} = 1.9 \times 10^4 \frac{T_e^{3/2}}{Z_{\text{eff}} \ln\Lambda}. \tag{2.5.19}$$

In a tokamak, however, the toroidal geometry implies the trapping of a fraction of the electrons (banana orbits) in the magnetic field and the plasma current is therefore reduced by a factor depending on the aspect ratio $\varepsilon = r/R$, approximately [57]

$$\sigma = \sigma_{\text{Spitzer}} \left(1 - \sqrt{\varepsilon}\right)^2. \tag{2.5.20}$$

More complete calculations including interactions between trapped and circulating electrons were conducted by Hirshman [58] and Hinton–Hazeltine [59]. Analytical scalings of the calculations of these papers are available from [60] as

$$\sigma_{\text{neo}} = \sigma_{\text{Spitzer}} + 1 - \left(1 - \frac{0.36}{Z_{\text{eff}}}\right) f_t + \frac{0.59}{Z_{\text{eff}}} f_t^2 + \frac{0.23}{Z_{\text{eff}}} f_t^3, \tag{2.5.21}$$

where f_t is the fraction of trapped particles, corrected by the collisionality of the electrons. Z_{eff} is then derived from the measurement of the total plasma current,

$$I = \int \left(\sigma_{\text{neo}} E_{\parallel} + j_{\text{CD}} + j_{\text{BS}}\right) \mathrm{d}A, \tag{2.5.22}$$

including the inductive, the EC driven j_{CD} and the bootstrap j_{BS} contribution(†).

☞ **Beam-plasma charge exchange:** In plasmas with injection of a beam of energetic neutrals (section 3.2.1), the carbon density n_C is recovered with the absolutely calibrated Charge eXchange Recombination Spectroscopy (CXRS) diagnostic (section 3.2.4) from the charge exchange induced emissivity (photons per m^3 per second),

$$\varepsilon = n_b n_{\text{C}} \left\langle \sigma v \right\rangle_{\text{CX}}, \tag{2.5.23}$$

knowing the local neutral beam density n_b and the effective (cascade and excited neutral corrected) charge exchange rate coefficient.

In practice, if available, an average of the different Z_{eff} is determined. Each method is no more precise than about 30 %. Agreement within this error is generally found when comparing the various methods [61].

2.6 Equilibrium reconstruction

A magnetic configuration is in equilibrium if, in any point of the plasma, the kinetic pressure force is compensated by the magnetic forces. Describing the plasma as incompressible fluid and a perfect conductor, i.e. using the ideal MHD model [62], the condition for a static equilibrium may be written as

$$\nabla p = \mathbf{j} \wedge \mathbf{B}, \tag{2.6.1}$$

with p the plasma pressure and $\mathbf{j}$ the current density. By transcription into cylindrical coordinates, the problem of the equilibrium reconstruction consists of finding a solution $\psi(R, Z)$ to the nonlinear elliptic differential **Grad-Shafranov equation**,

$$R\frac{\partial}{\partial R}\left(\frac{1}{R}\frac{\partial \psi}{\partial R}\right) + \frac{\partial^2 \psi}{\partial Z^2} = -\mu_0\, R^2 \frac{\partial p(\psi)}{\partial \psi} - R\, B_\phi(\psi) \frac{\partial\big(R B_\phi(\psi)\big)}{\partial \psi}, \tag{2.6.2}$$

with the stream function $\psi = RA_\phi = \psi_{\text{pol}}/2\pi$, where A_ϕ is the toroidal component of the vector potential and $\psi_{\text{pol}} = \int_{A_{\text{tor}}} \mathbf{B} \cdot \mathrm{d}\mathbf{A}$ is the poloidal flux through an arbitrary toroidal cross section of a flux surface.

The magnetic equilibrium of TCV plasmas is reconstructed every 2 ms by the Grad-Shafranov solver *LIUQE*(‡) [63, 64], based on measurements of the poloidal flux provided by various flux loops and internal poloidal field coils [65] inside and outside the vacuum vessel (shown on figure 2.3.1). The plasma is supposed to have axisymmetry and eq.(2.6.2) is solved iteratively until the description of the poloidal flux reproduces the measurements to within the requested accuracy. To increase the quality of the reconstruction, the code optionally accepts further constraints such as the total plasma energy measured by a one turn diamagnetic loop (DML) [66], the pressure profile obtained from the Thomson scattering diagnostic or the location of the sawtooth inversion radius derived from the tomographic reconstruction of the soft X-ray emissivity.

(†) If the plasma pressure is greater in the core than at the edge, this pressure differential spontaneously drives a toroidal current in the plasma. This current is called the bootstrap current. It's origin is due to the diffusive momentum exchange between trapped and current carrying electrons (see section 5.2.4).

(‡) reads *EQUIL* when spelt backwards.

2.7 Lines of research

The main topics presently investigated on TCV are

☞ The impact of plasma shaping on plasma performance, transport and MHD stability,

☞ Plasma real time control,

☞ Plasma intrinsic rotation,

☞ Stabilisation of edge localised modes and sawteeth,

☞ Suprathermal electron physics in discharges with EC injection, particularly noninductive current drive mechanisms,

☞ Development of enhanced confinement regimes (H-mode, transport barriers) and

☞ Plasma edge and SOL physics and plasma–wall interactions.

Chapter 3

Ion diagnostics on TCV

3.1 Introduction

Knowledge of the parameters characterising the various species of ions present in a plasma is of great importance in a hot plasma physics device. Ion parameters are essential in order to assess ion confinement, particle transport or various turbulence phenomena in an experimental reactor. In a future fusion power plant, knowledge of the parameters of the burning ion population (only ions contribute to fusion energy!) and alpha particles are of paramount importance to achieve and maintain the fuel temperature at the optimum value for ignition.

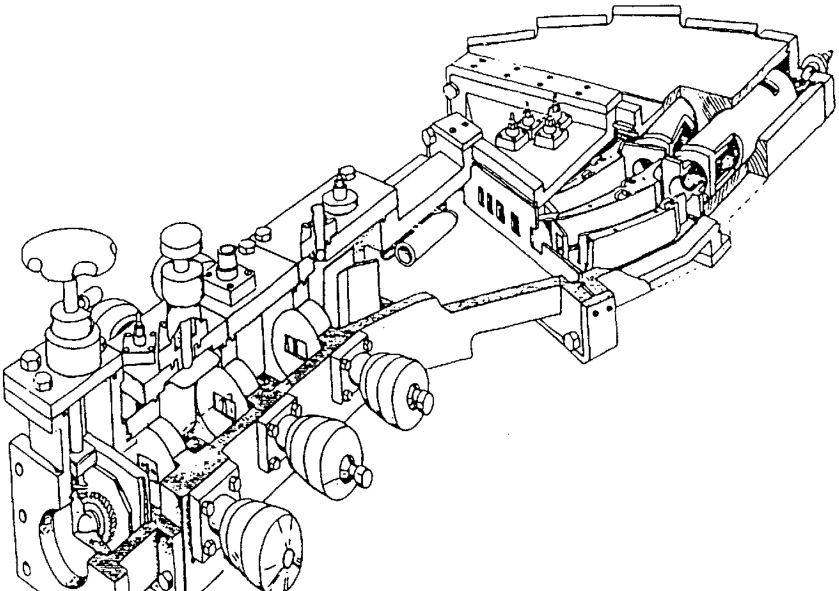

Figure 3.1.1: Stereoscopic view of the vertical neutral particle analyser (VNPA).

In most fusion devices the ion temperature is significantly different from the electron temperature because the ion–electron equilibration time is comparable or longer than the ion energy confinement time. Often the species are unequally heated, ohmic heating acts on the electrons or resonant heating schemes like ion cyclotron heating are tuned to the cyclotron frequency of a specific ion species and the other particle species share this energy only through Coulomb collisions.

Many plasma physics models require precise expressions for ion and atomic densities, ion temperature profiles or a description of a more sophisticated velocity distribution of the ions. The ratio of the peak temperatures T_e/T_i characterises most of the transport processes studied so far [67] and many turbulence phenomena in a plasma [68]. For example, gyrokinetic simulations of Ion Temperature Gradient (ITG) driven turbulence (and resulting transport) need a good spatial description of the ion temperature [69]. Neutral heating beams [70] deposit hot monoenergetic ions in the plasma, their relaxation exhibits a strongly non-thermal velocity distribution (slowing down distribution). Wave–particle interactions (heating or turbulence) produce supra-thermal ion populations (chapters 6 and 7), the latter being often satisfactorily described by a sum of two Maxwellian distributions (referred to as bi-Maxwellian distribution). These phenomena require spectrometric diagnostics able to unfold the ion energy distribution.

Various diagnostic principles have been used to study ions on tokamaks. Lower energy thermal ion populations are mostly measured using Charge Exchange Recombination Spectroscopy (CXRS) [71] relying on a Diagnostic Neutral Beam Injector (DNBI) [72]. For low and high energetic ions in lower density plasmas Neutral Particle Analysers (NPA) are commonly exploited. Hot and dense plasmas can be diagnosed by their fusion neutron rate using neutron detectors or γ-ray detectors [73]. Cross beam CXRS directly measures local properties, all other diagnostics mentioned measure line- or volume-integrated quantities and require Abel inversion or tomography methods to unfold the local properties from the measurements.

Here the description of ion diagnostics is restricted and specific to the diagnostics currently available on TCV. These are CXRS (section 3.2), NPA (section 3.3) and neutron detector (section 3.5).

3.2 Charge Exchange Recombination Spectroscopy and Diagnostic Neutral Beam

A low power diagnostic neutral beam provides an elegant opportunity to measure ion parameters in a plasma. When the beam injected particles enter the plasma radiation is produced as a result of excitation of the beam and following charge exchange reactions between beam neutrals and plasma ions. If this radiation is observed at an angle to the beam, localised measurements of plasma parameters can be made. Observation of radiation in the visible region are often preferable since instrumentation at these wavelengths is particularly simple and versatile.

In the visible range, the spectrum emitted by the tokamak plasma is dominated by line radiation of heavy impurities. In contrast, light impurities like carbon ($Z = 6$) are completely ionised and don't exhibit line radiation. However, their excited states may be populated through recombination. Charge exchange reactions between the intrinsic impurity ions and intrinsic plasma neutrals (whose density is extremely low in tokamak plasmas) or stimulated with injected beam neutrals are an efficient mean to do this.

TCV features such a tandem of Diagnostic Neutral Beam Injector and Charge Exchange Recombination Spectroscopy diagnostic. As a consequence of its graphite first wall, the most abundant impurity in TCV is carbon. The carbon concentration in the plasma, after a long period of operation, is typically 3 %.

Hence the DNBI injected energetic hydrogen neutrals induce the charge exchange reaction

$$\mathrm{H}^0_{\mathrm{beam}} + \mathrm{C}^{6+}_{\mathrm{plasma}} \rightarrow \mathrm{H}^+_{\mathrm{beam}} + \mathrm{C}^{5+}_{\mathrm{plasma}}, \tag{3.2.1}$$

where the fully ionised intrinsic carbon impurity ion receives an electron which, most likely, will end up in a state with a high principal quantum number, e.g. $n = 8$. The relaxation time for the excited state is generally short (∼ns) [74–76] and the hydrogenic carbon ion C^{5+} relaxes before being reionised (the ionisation time τ_i is ∼ms) and emits a photon whose energy corresponds to the difference in energy of the level n and n' of the transition. The CXRS diagnostic is tuned to measure the spectrum of the emission of the transition involving the principal quantum numbers $n = 8 \rightarrow 7$,

$$\mathrm{C}^{5+}(n = 8) \rightarrow \mathrm{C}^{5+}(n = 7) + h\nu. \tag{3.2.2}$$

This line has a wavelength of $\lambda = 5291$ Å (green visible light). CXRS goes hand in hand with the DNBI, which is described first.

3.2.1 Beam injector

The diagnostic neutral beam injector on TCV was manufactured by the Budker Institute of Nuclear Physics, Novosibirsk, Russian Federation [77]. Installed in 2000, major upgrades were conducted in 2002-2003 [78] and 2006-2008 [79]. The description presented here reflects the current state of the injector. Figure 3.2.1 shows the various parts of the installation.

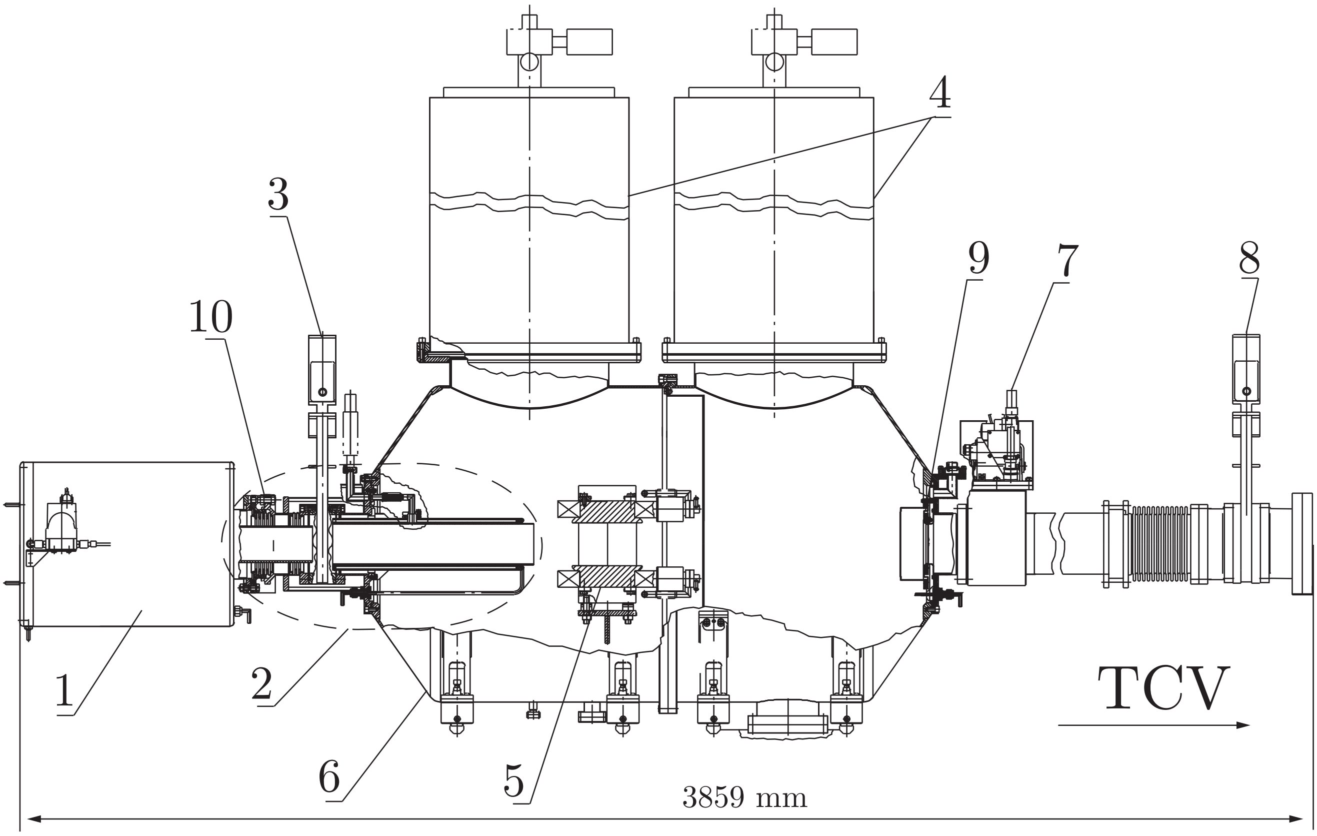

Figure 3.2.1: Lateral view of the DNBI. The beam interfaces to TCV on the right. The labelled components are ① ion source; ② neutraliser; ③ ion source gate valve; ④ cryogenic pumps; ⑤ magnetic separator with diaphragm; ⑥ vacuum tank; ⑦ retractable calorimeter; ⑧ TCV gate valve; ⑨ aiming target; ⑩ turning gear.

The beam consists of

- A cold cathode arc-discharge plasma source from which hydrogen ions and charged molecules are extracted,
- An ion optical grid system to focalise and accelerate all charged particles to the beam energy,
- A neutraliser tube where the charged molecules are dissociated and neutralised (50 % efficiency for the protons and better for the other extracted particles),
- An electric magnet and dump to remove the residual ions and
- A short beam duct interfacing with the TCV chamber.

The beam is injected at the horizontal vessel mid-plane, almost perpendicular to the torus to reduce toroidal momentum to be given to the plasma, but nevertheless slightly inclined at an angle of 11.25° to reduce particle trapping in the toroidal ripple of the magnetic field.

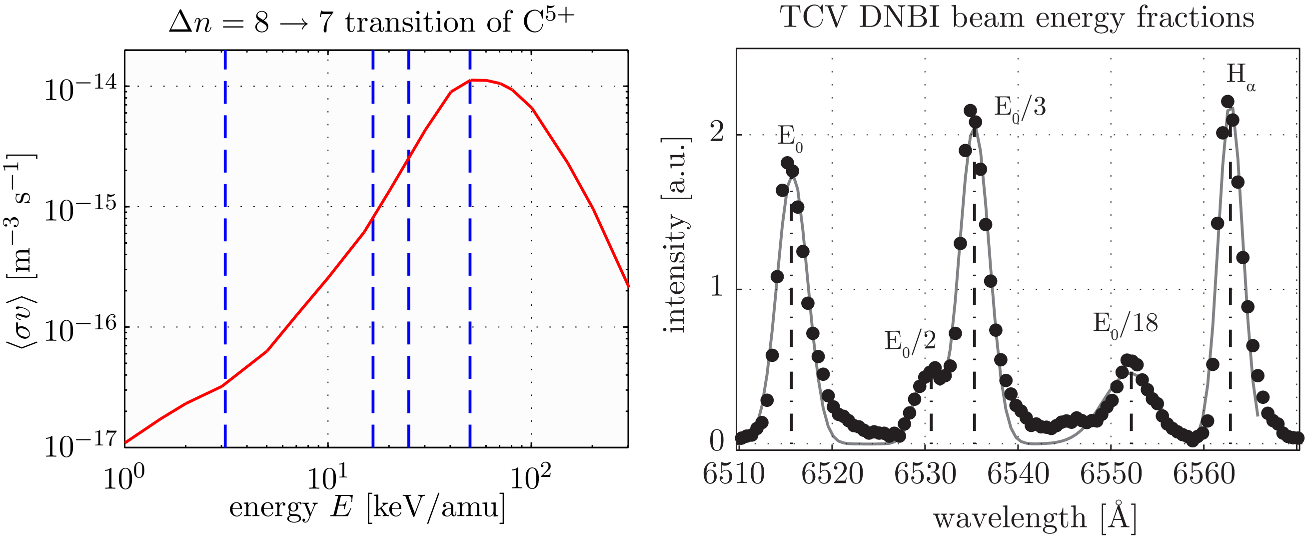

(a) transition in hydrogenic carbon.

(b) neutral beam energy components.

Figure 3.2.2: (a) Rate coefficient [80] of the $\Delta n = 1$ transition $n = 8 \rightarrow 7$ of the C^{5+} ion. The vertical lines indicate the DNBI nominal, half, third and 1/16 energy components.
(b) Observation of the H_α emission of the neutral beam when observed at an angle of 45° (resulting in the energy dependent Doppler shift of emission wavelength due to the four beam energy fractions) [81]. The peak at $\lambda = 6562.85$ Å corresponds to the (unshifted) H_α emission of the quiescent background gas in the beam tank after the magnetic separator, see figure 3.2.1.

The beam atoms are normally hydrogen, deuterium is an option. The beam nominal energy is $E_0 = 50$ kev/amu (per atomic mass unit), that is a compromise between sufficient plasma penetration and the a sufficient cross section for the transition, eq.(3.2.2), shown in figure 3.2.2a. The beam is unfortunately not mono-energetic, the H^0 originating from the acceleration of the charged molecules H_2^+, H_3^+ and H_2O^+ are present at energy components of respectively $E_0/2$, $E_0/3$ and $E_0/18$ (see figure 3.2.2b). The full energy component has a proportion of about 85 % in beam density and its equivalent hydrogen particle current is higher than 1 A. However, the lower energy components do not significantly contribute to the transition eq.(3.2.2), as the cross section strongly decreases with decreasing energy (see again figure 3.2.2a).

The beam has gaussian shape and a little divergence of 0.5° in order to reduce the beam $1/e$ width to approximately 8 cm at the focal point on the magnetic axis. A small beam size results in a strong beam density and is therefore providing more light yield per unit volume.
The beam is operated in pulsed mode to separate the active beam induced CXRS signal from the background radiation (see below) with a duty cycle of generally 30 % and typical pulse length of 10. . . 60 ms. The maximum uninterrupted beam pulse duration is limited to 1.5 s. Typical current rise and fall times are 2.5 and 0.2 ms respectively.

3.2.2 Beam profile and attenuation (BEAT)

For absolute calibrations of the CXRS and NPA diagnostics (section 4.8.2.2) the beam geometry and current density along its path through the plasma have to be known [82]. As a first approximation, the beam is considered to be gaussian in the focus vicinity (i.e. inside the plasma). With

$$\frac{1}{z^*} = \frac{1}{z} - \frac{1}{z_{\text{foc}}} \tag{3.2.3}$$

the vacuum beam current density on the beam axis z is

$$j(z,0) = \frac{I}{\pi a^2}\frac{(z^*)^2}{z^2}\left[1 - \exp\left(-\frac{\alpha a^2}{(z^*)^2}\right)\right], \tag{3.2.4}$$

where $\alpha = v_b^2/v_{\text{th},b}^2$ is the ratio of the (axial) beam velocity to the (transverse) thermal beam velocity(*), a is the homogenous DNBI plasma source radius and I is the total neutral beam current. The beam has cylindrical symmetry and the radial vacuum profile writes

$$j(r,z) = j(z,0)\exp\left(-\frac{\pi r^2}{I} j(z,0)\right). \tag{3.2.5}$$

The beam halo, composed of the secondary thermal neutrals produced as fall-out of the charge-exchange between the beam and plasma fuel ions (no impurities), for example deuterium,

$$\mathrm{H}^0_{\text{beam}} + \mathrm{D}^+_{\text{plasma}} \rightarrow \mathrm{H}^+_{\text{beam}} + \mathrm{D}^0_{\text{plasma}}, \tag{3.2.6}$$

surrounds the beam and has an impact on its width and intensity. However, the energy of the halo neutrals is much less than the beam energy (the plasma particles are supposed to be thermalised) and their impact on the CXRS signal is thus small. For TCV, neglecting halo neutrals leads to an overestimation of the ion temperature of the order of 10 % [83]. On the other hand, halo neutrals will be more important for the absolute calibration of the NPA (see section 4.8.2.2). Due to collisions with the plasma particles, the beam component densities are attenuated,

$$n_b(z) = n_b(z_a)\exp\left(-\int_{z_a}^{z}\lambda\,\mathrm{d}l\right), \tag{3.2.7}$$

with z_a the first point of intersection between the beam and the plasma and with the attenuation coefficient given by

$$\lambda \approx n_e\left(\frac{\langle\sigma_e v_e\rangle}{v_b} + \frac{6 - Z_{\text{eff}}}{6-1}\sigma^{\text{D}}_{\text{tot}} + \frac{Z_{\text{eff}} - 1}{6(6-1)}\sigma^{\text{C}}_{\text{tot}}\right), \tag{3.2.8}$$

where n_e is the electron density, $\sigma_{\text{tot}} = \sigma_{\text{CX}} + \sigma_i$ and $v_{\text{ion}} \ll v_b \ll v_e$ was used.

(*) α is linked to the beam divergence ϑ through $\tan\vartheta = 1/\sqrt{\alpha}$.

The first term describes electron impact ionisation, the collision rate coefficient is integrated over the electron distribution function, the other two terms describe charge-exchange reactions and ion impact ionisation of beam neutrals with deuterium plasma ions or carbon impurity ions. The charge-exchange process dominates for all energies of the beam components (see figure 3.3.1a). The absolute beam profile is then obtained by multiplying eq.(3.2.5) by an attenuation factor $n_b(z)/n_b(z_a)$ defined by eq.(3.2.7) and eq.(3.2.8).

3.2.3 Plasma perturbation by the DNBI

The parameters of the DNBI limit the total injected power to 80 kW, of which only a fraction is finally absorbed by the plasma. The lower energy beam components are more strongly attenuated in the plasma and therefore dominate the plasma perturbation. Using eq.(3.2.3) to eq.(3.2.8), the absorbed power ranges from 20 % ($n_e = 1{\times}10^{19}$ m^{-3}) to 80 % ($n_e = 6{\times}10^{19}$ m^{-3}). An evaluation of the thermal plasma particle distribution averaged collision frequency for energy loss shows that most of the absorbed power goes into the electrons, the ions absorb only a fraction of about 10 %. With a beam duty cycle of 30 % the beam power absorbed by the ions is about 2 kW. This is 10. . . 100 times less than the electron–ion equipartition power (see section 4.9.1). A measurement of the ion temperature using the NPA during beam firing shows that the increase in ion temperature due to the beam energy deposition is fairly below 10 % of T_i (see section 4.9.5).

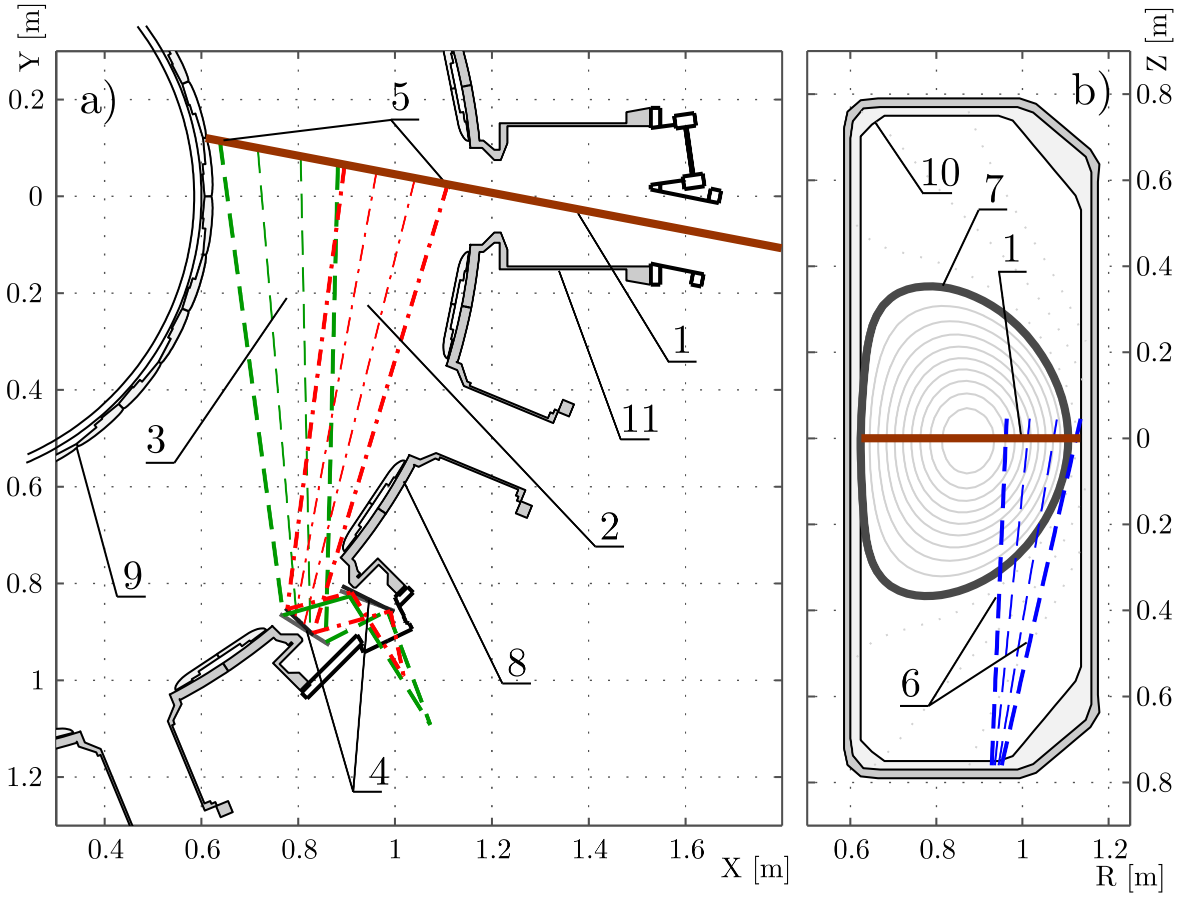

Figure 3.2.3: Toroidal (a) and poloidal (b) views of the CXRS diagnostic. Labels show: ① The DNBI beam; ② toroidal LFS CXRS view lines; ③ toroidal HFS CXRS view lines; ④ toroidal CXRS observation head with mirrors; ⑤ extent of the toroidal beam observation region; ⑥ poloidal CXRS view lines; ⑦ plasma last closed flux surface (LCFS); ⑧ TCV vacuum vessel; ⑨ tokamak central column; ⑩ first wall; ⑪ DNBI diagnostic port.

3.2.4 CXRS spectrometry

The implementation of the CXRS diagnostic on TCV currently comprises three beam observation subsystems: (a) the toroidal low field side (LFS) and (b) high field side (HFS) system and (c) a poloidal LFS system. The CXRS observation chord geometry is depicted in figure 3.2.3.

The toroidal systems cover together the whole beam path in the plasma. Each system has 20 pairs of optical fibers collecting the light emitted at 40 radial locations of the beam path (the radial resolution is about 1 cm). The light is then transported to Czerny-Turner monochromators where it is dispersed by a holographic grating to illuminate a Charge Coupled Device (CCD). The radial resolution is about 1 cm. The dispersion unit is designed to map the $\mathrm{C}^{\mathrm{VI}}(n = 8 \rightarrow 7)$ line, eq.(3.2.2), and its surroundings onto the CCD.

A complicating feature of the exploitation of a CXRS diagnostic on TCV is the pronounced transport of carbon from the plasma core towards the edge, estimations derived from measurements with a ultra soft X-ray spectrometer revealed a strong increase of carbon diffusivity towards the plasma periphery [84].

Fully ionised carbon is therefore found throughout the plasma column, even in the very edge region where the temperature is far below the ionisation energy! The fully ionised carbon which has migrated there is suspected to produce a strong passive line radiation background by undergoing a charge exchange reaction with the thermal neutrals in fundamental ($n = 1$) and mainly excited ($n = 2$) state [85] whose concentration is maximum at the edge (see section 4.1.2).

As a result the passive signal collected along each diagnostic chord exceeds the emission stimulated by the beam by a factor ∼1.5, requiring the operation of the DNBI in pulsed mode. The active signal is then obtained by subtracting the passive background radiation level (obtained by interpolation of the spectrum), which is acquired before and after the beam pulse. The beam injection is in the range of 10...60 ms. The lower limit is dictated by the achievable CCD readout rate(†). If the light yield is low, the statistical noise on the CCD may require a longer exposition time.

From the acquired spectrum the ion temperature profile $T_i(\rho)$ is obtained by fitting a gaussian line envelope, broadened by the Doppler effect with prior deconvolution of the spectrometer's instrumental function. Figure 3.2.4 shows the image of the line during a DNBI pulse, the ratio of active to passive signal is about AP ∼35 %.

If the carbon ion velocity distribution is Maxwellian, the full width at half maximum (FWHM) of the Gaussian peak is linked to the population temperature through

$$T_i = \frac{m_{\mathrm{C}}\, c^2}{8\, e \ln 2} \left(\frac{\Delta\lambda_{\mathrm{FWHM}}}{\lambda_0} \right)^2 , \tag{3.2.9}$$

with T_i given in eV. The accuracy of the deduced ion temperature is generally believed to be 10 % or better, the main source of error is the low signal to noise ratio, requiring long exposure of the CCD to improve the photon statistics.

(†) A fast acquisition mode (∼ 2 ms) is available for the observation of repetitive features like sawteeth collapses but requires coherent averaging of the CXRS signal over the sawtooth period at the price of a drastic reduction of the spatial resolution (typically less than 6 radial observation points).

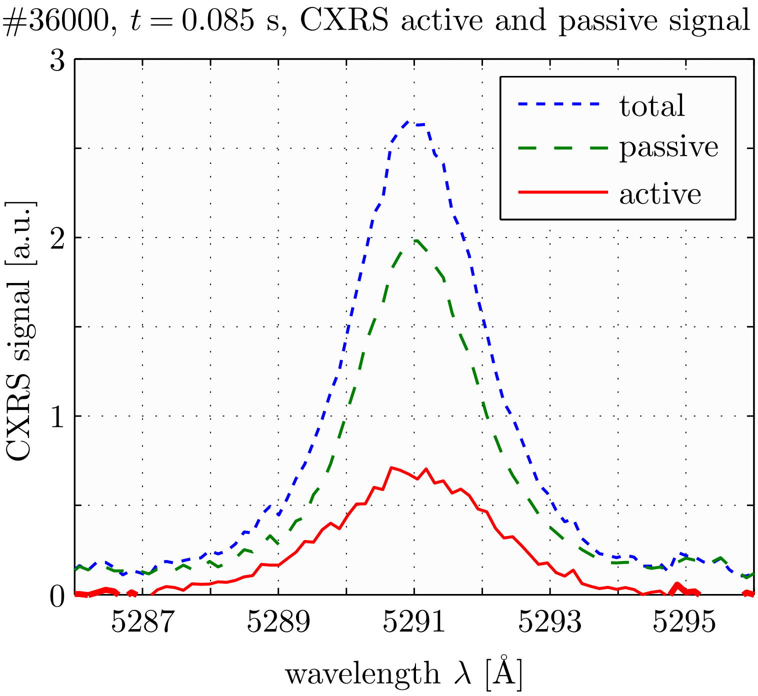

Figure 3.2.4: The total signal (top line) measured with the CCD comprises active (beam) and passive (background) contributions. The passive signal is interpolated from the measurement before and after the beam. The difference is the active signal (lowest line).

Toroidal (respectively poloidal) carbon rotation velocity $v_i(\rho)$ profiles are derived from the Doppler shifted peak centre wavelength. The rotation velocity is linked to the wavelength displacement through

$$\frac{\Delta\lambda}{\lambda_0} = \frac{v_i}{c}\cos\alpha, \tag{3.2.10}$$

where α is the angle between the velocity vector $\mathbf{v}_i$ and the direction of observation. The precision of the velocity measurement essentially depends on the wavelength calibration of the spectrometer and the goodness of fit of the spectrum. The CXRS diagnostic is absolutely calibrated in wavelength and intensity (against a source of light of known emission spectrum). This allows the carbon density profile $n_{\mathrm{C}}(\rho)$ be derived from the measured intensity I_λ of the line transition through

$$I_\lambda = \frac{1}{4\pi}\int\sum n_{\mathrm{C}}(\ell)n_b(\ell)\left\langle\sigma v\right\rangle_{\lambda_0}(T_e,n_e)\mathrm{d}\ell \qquad \left[\frac{\text{photons}}{\text{sm}^2\text{sr}}\right], \tag{3.2.11}$$

where the sum is taken over all beam energy components and the integration is carried out along the viewing path of the spectrometer across the beam. The beam densities are evaluated from eq.(3.2.3) to eq.(3.2.8).

Note that the CXRS only measures the parameters of thermal bulk ions. Impacts of suprathermal ion populations or other non-thermal features in the ion distribution function on the broadening of the spectral profile are negligible.

The duo of DNBI and CXRS provide direct profile measurements of $T_{i\mathrm{C}}$, $v_{i\mathrm{C}}$ and $n_{i\mathrm{C}}$ for plasmas of electron densities up to 1×10^{20} m^{-3} at sampling rates ranging from 2 to 20 Hz.

3.3 Neutral particle analysers

The quantitative physics underlying the neutral particle analysis will be copiously developed in chapter 4. Here we shall restrict the discussion to a qualitative summary of the main principles necessary to understand how a neutral particle analyser is working.

3.3.1 Diagnostic principles

A widely used principle to measure the plasma fuel ion temperature (hydrogen, deuterium, tritium or helium) is the analysis of the energy distribution of charge-exchanged fast neutrals escaping across the plasma edge.

This will only work if a certain concentration of neutral atoms exist inside the plasma, especially in the hot core. Fortunately this is often the case in TCV, although in medium and large sized tokamaks most of the plasma particles are fully ionised. The neutrals arise from atoms and molecules released from the vessel wall or simply through gas supply in the plasma periphery (to increase the plasma density or to replace particle losses) and are produced through many processes, for example dissociation by electrons

$$H_2 + e \rightarrow H + H + e, \tag{3.3.1}$$

where the wall molecule and the so called Frank-Condon neutrals formed have an energy of a few eV, characteristic for the conditions at the wall. The neutral may penetrate into the plasma, experience a charge-exchange reaction producing a new secondary neutral following

$$H_{cold} + H^+_{hot} \rightarrow H^+_{cold} + H_{hot}. \tag{3.3.2}$$

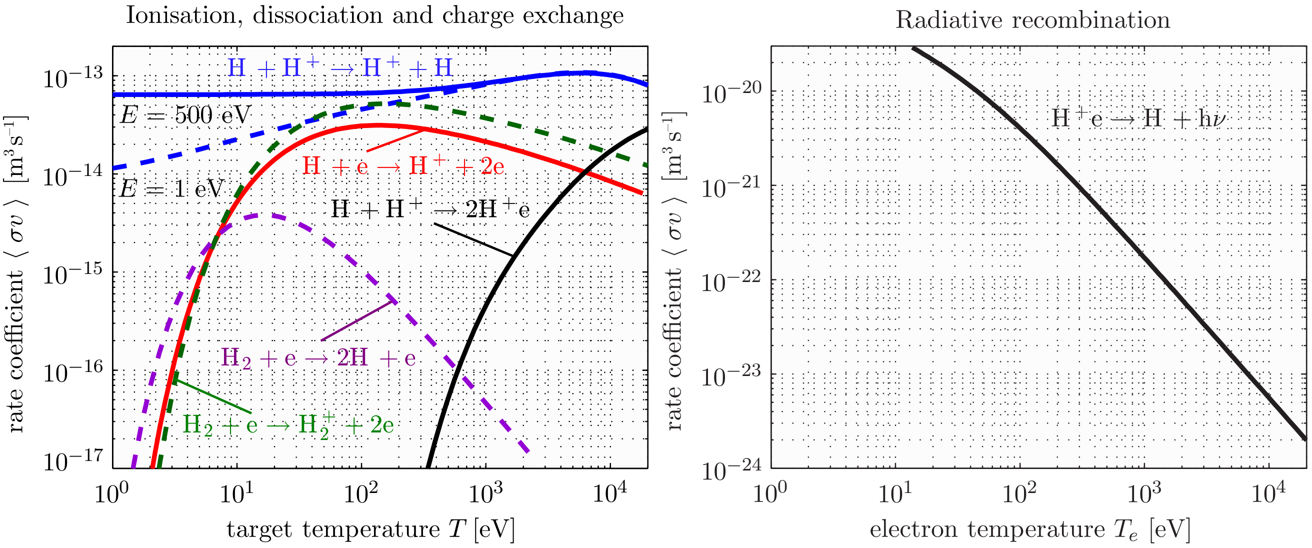

(a) ionisation, charge-exchange and dissociation.

(b) recombination.

Figure 3.3.1: Reaction rates averaged over a Maxwellian distribution function as a function of temperature of the target hydrogen. (a) shows electron impact ionisation of atomic (red) and molecular hydrogen (green), electron impact molecule dissociation (violet), ion impact ionisation (black) and charge exchange (blue), (b) shows radiative recombination. The influence of the energy of the projectile hydrogen on the rate coefficient for charge exchange is depicted for two different energies. The first symbol denotes the test particle, the second refers to the thermal population. All data was taken from the IAEA ALADDIN database [86].

Consecutive multiple charge-exchange reactions may line up a sequence of neutral particle generations which migrate deeper and deeper towards the interior of the discharge and, according to reaction eq.(3.3.2) gain thermal energy. This process stops when the neutral gets ionised or leaves the plasma. Figure 3.3.1 shows that charge-exchange is much more probable than ionisation at low to intermediate energies, hence neutrals have a good change of being transported even to the very centre of the discharge.
In the plasma core, the reaction eq.(3.3.2) produces hot neutrals which, due to the high mass ratio of electron and ion, conserve energy and momentum of the ion which has now become a secondary neutral. Hence this neutral carries the signature of the ion population in the plasma centre and there is some chance (section 4.3) for this neutral to escape the plasma without further interaction with the plasma. Neutral Particle Analysers (NPA) capture such neutrals and analyse their velocity distribution parameters (section 4.3.2).

NPA's collect neutrals born all along the diagnostic chord and therefore all measurements represent line-integrated quantities. However, multi-chord NPA measurements (section 4.4.1) or integrated modelling of the measured neutral fluencies (section 4.2.1) may assist the recovery of the local parameters.

An important feature of the NPA is its capability to record a large energy range of the plasma ion velocity distribution. NPA's are thus frequently operated in present day tokamaks, where a plethora of phenomena are giving rise to non-thermal features in the velocity distribution function, even on machines without auxiliary ion heating (like TCV, see chapter 6).

Most NPA installed on tokamaks have a view line perpendicular to the toroidal magnetic field and thus measure $T_{i\perp}$ and $n_{i\perp}$.

Conventional NPA comprise a collimation system (a restriction of the solid angle with diaphragms), a unit to strip the electrons off the incoming neutrals, a dispersion system employing electromagnetic fields for the energy and/or mass separation and a detector array to count the particles of a specific mass and energy within a certain range.

TCV disposes of two complementary neutral particle analysers,

a) the **VNPA**, [87, 88] a robust *vertical NPA* (section 3.3.2) which was already used [89–91] on TCV's predecessor, the *Tokamak à chauffage d'Alfvén* (TCA) and

b) the **CNPA**, a *Compact NPA* (section 3.3.3), implemented at the beginning of this thesis.

Table 3.1 summarises relevant parameters of both analysers whose setup and capabilities are concisely described in the following subsections. More instrumental details are available in a technical paper [92]. Both analysers were manufactured by the Ioffe Physico-Technical Institute of the Russian Academy of Sciences in St. Petersburg, Russian Federation. Ioffe has a long tradition in NPA design and production (the first single channel analyser was built in 1960 [93]) and both analysers on TCV are still available for purchase, albeit in revised form.

Up-to-date reviews of contemporary NPA principles and design were recently published in [94] and [95]. Although NPA are classic diagnostic in tokamaks, they become of increasing importance with increasing plasma temperature. NPA's will be a key diagnostic in ITER and beyond [96].

Analyser	**VNPA**	**CNPA**
availability on TCV	1996	2004
dispersion scheme	double analysis	$E \parallel B$
energy dispersion	electrostatic	permanent magnet
energy coverage	voltage sweep	fixed energy
mass separation	no, H+D	H/D or D/He
mass suppression	none	1000
Detection	**VNPA**	**CNPA**
# channels	5	11+17+2(‡) (2 arrays)
stripping	N_2 gas	carbon foil
detectors	EMT	CEM
Operation	**VNPA**	**CNPA**
# setups	1	2
energy range	0.6...8 keV	0.5...50 keV
time resolution	0.05...2 ms	0.5...4 ms
maximum count rate	10 MHz	500...800 kHz
sweep period	10...20 ms	-
energy resolution	7 %...20 %	60 %...10 %

Table 3.1: Key parameters of the NPA on TCV (specifications as of October 2006).

3.3.2 Vertical NPA (VNPA)

The VNPA [97] is an older version of the currently commercially available ACORD-12 NPA from Ioffe [98]. Since its design in 1975 [99], more than 50 NPA of this type have been implemented on magnetic fusion devices. The VNPA is installed below the TCV torus and views the plasma along a vertical chord located at a major radius $R = 0.88$ m. The spatial resolution on the machine axis is about 4 cm. Figure 3.3.2 shows a schematic representation of the VNPA.
The incoming neutral particles emitted from the plasma are purified by a capacitor (to remove charged particles) and then partially stripped in a molecular nitrogen gas cell (impact ionisation). The gas pressure in the stripping cell (in the range $3 \ldots 5 \times 10^{-4}$ mbar) is optimised such that only single collisions between particles and gas molecules occur. The emerging ions are deflected downstream by the electric field of condenser plates. The electrostatic analysis alone doesn't separate different hydrogen isotopes. The ions enter cylindrical deflectors, guiding the ions to the 5 detection channels equipped with open electron multiplier tube (EMT) detectors. When the ions collide with the conversion dynode at the entrance of the EMT, secondary electrons are generated which avalanche down through the dynode cascade. Figure 3.3.3 illustrates the assembly of the core of the VNPA. The electronic signals from the output of the EMT pass through pre-amplifiers that generate TTL pulses if above a certain thresholds, which in turn are counted by a CAMAC housed multichannel scaler. The voltages on the analysing condenser plates and cylindrical deflectors are supplied by a dual power supply. The latter is commanded by a DAC, whose waveform (amplitudes and sweeping frequency) is fully programmable before each plasma discharge. By sweeping the analyser voltage, the energy spectrum of the incoming neutrals is scanned. This extends the energy range of the VNPA to 0.5...8 keV and provides cross channel calibration. Typical energy scanning periods are 10...20 ms (the maximum sweep frequency is 2 kHz). Better time resolutions down to 50 μs are achieved by maintaining a fixed deflector voltage (the energy dynamic range is then reduced from >13 to <4). The detection and acquisition path is able to resolve up to 5000 counts per ms.

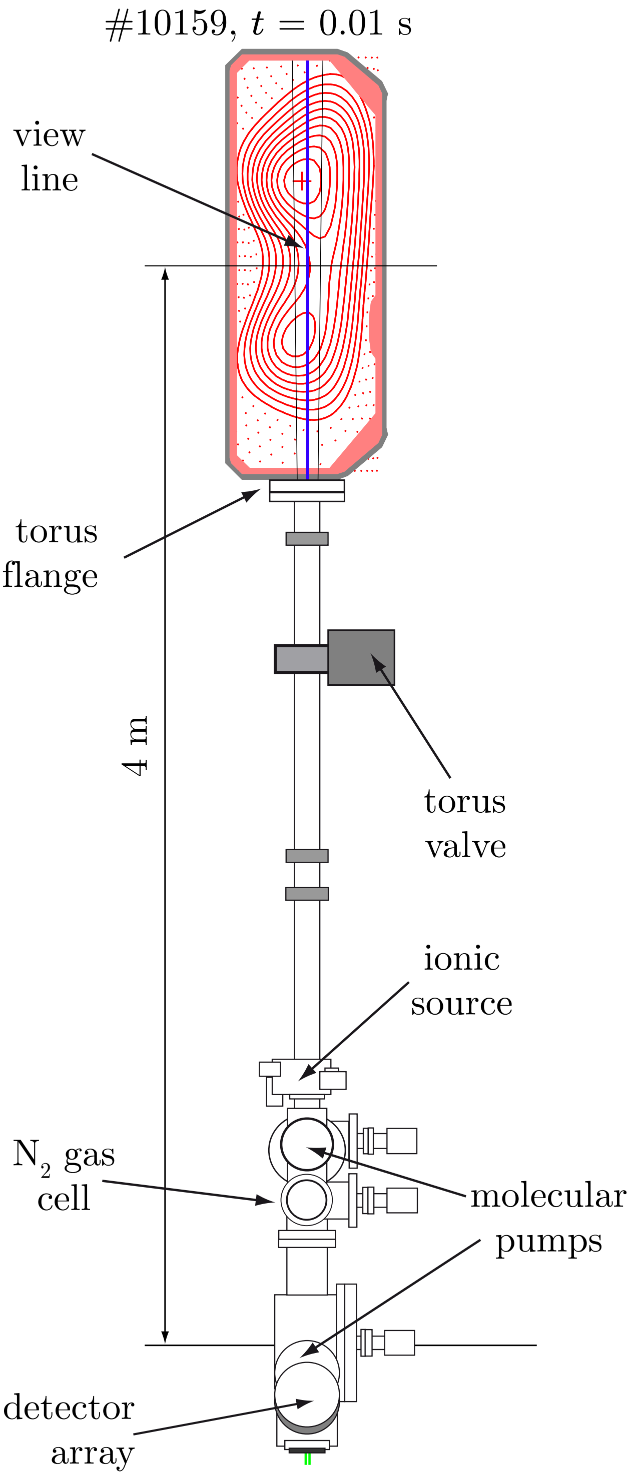

Figure 3.3.2: Schematic representation of the vertical NPA (VNPA) on TCV showing the NPA duct, calibration source, stripping element and detection housing. The width of the solid angle is indicated by the two thin lines. The distance between vessel midplane and dispersion element is 4 m.

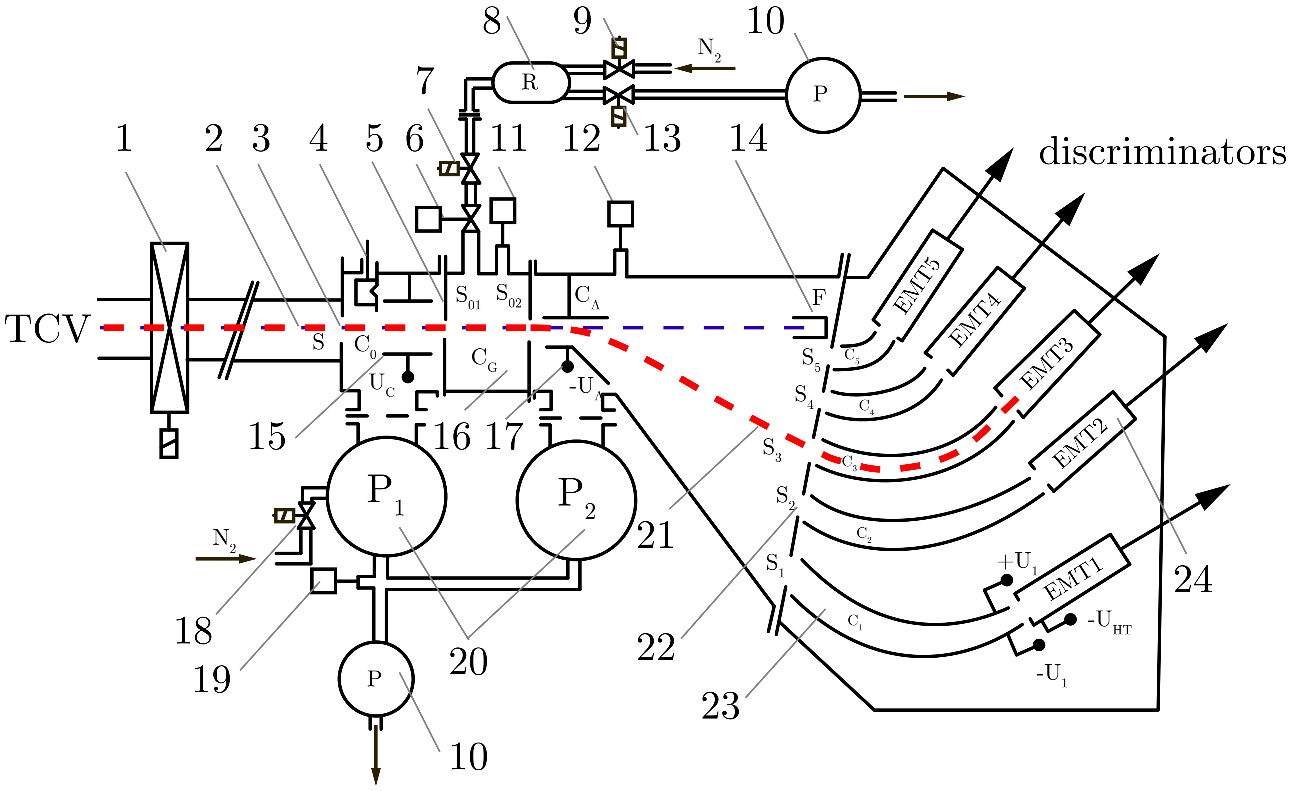

Figure 3.3.3: Pumping and electrical configuration of the VNPA. In particular, the labels highlight the following elements: ① TCV torus valve; ② neutral particle path; ③ entrance slit; ④ retractable ionic source; ⑤ adjustable gas cell diaphragm (S_{01}, S_{02}); ⑥ nitrogen gas flow regulator; ⑦ nitrogen valve; ⑧ nitrogen reservoir; ⑨ nitrogen reservoir supply valve; ⑩ primary pumps; ⑪ gas cell gauge; ⑫ VNPA gauge; ⑬ nitrogen reservoir pressure valve; ⑭ neutral dump; ⑮ purification condenser; ⑯ stripping gas cell; ⑰ analysing condenser; ⑱ pump security valve; ⑲ primary vacuum gauge; ⑳ turbomolecular pumps; ㉑ trajectory of secondary ions; ㉒ detection entrance slits; ㉓ cylindrical condensers; ㉔ electron multiplier tubes.

3.3.3 Compact NPA

The acquisition of the Compact NPA (CNPA) was driven by a requirement of the experimental program on TCV. The assessment of suprathermal features due to current-driven turbulence (chapter 6) or DNBI deposited particles (section 6.5.1) required a spectrometer with energy range up to 50 keV.

Observation of fast features in the ion distribution function like the rapid anomalous energisation of the suprathermal ion population in ECCD plasmas (section 6.1.3) or the effect of sawteeth on the ion confinement (section 6.6) require a diagnostic with high spatial resolution and high particle detection efficiency to reduce the counting period duration. Studies of the transport of plasma bulk ions in multi-isotope plasmas using gas puff experiments [100] required a separate recording of at least two particle isotopes or species. Observation of different plasma regions (section 4.4.1) or directions need a compact, more or less simply displaceable diagnostic design and assembly. All these requirements are met by the CNPA [101]. This new type of compact (smaller than 200×400×500 mm^3) and lightweight (<50 kg) NPA was developed at the beginning of this millennium and has since then been installed and exploited on various plasma physics devices, namely the Wendelstein 7-AS stellerator in Germany [102], the LHD heliotron in Japan [103], TCV [92], the TJ-II heliac stellerator in Spain [104], the SSPX dynamo spheromak in California [105] and the Mega Amp Spherical Tokamak (MAST) in the UK [106].

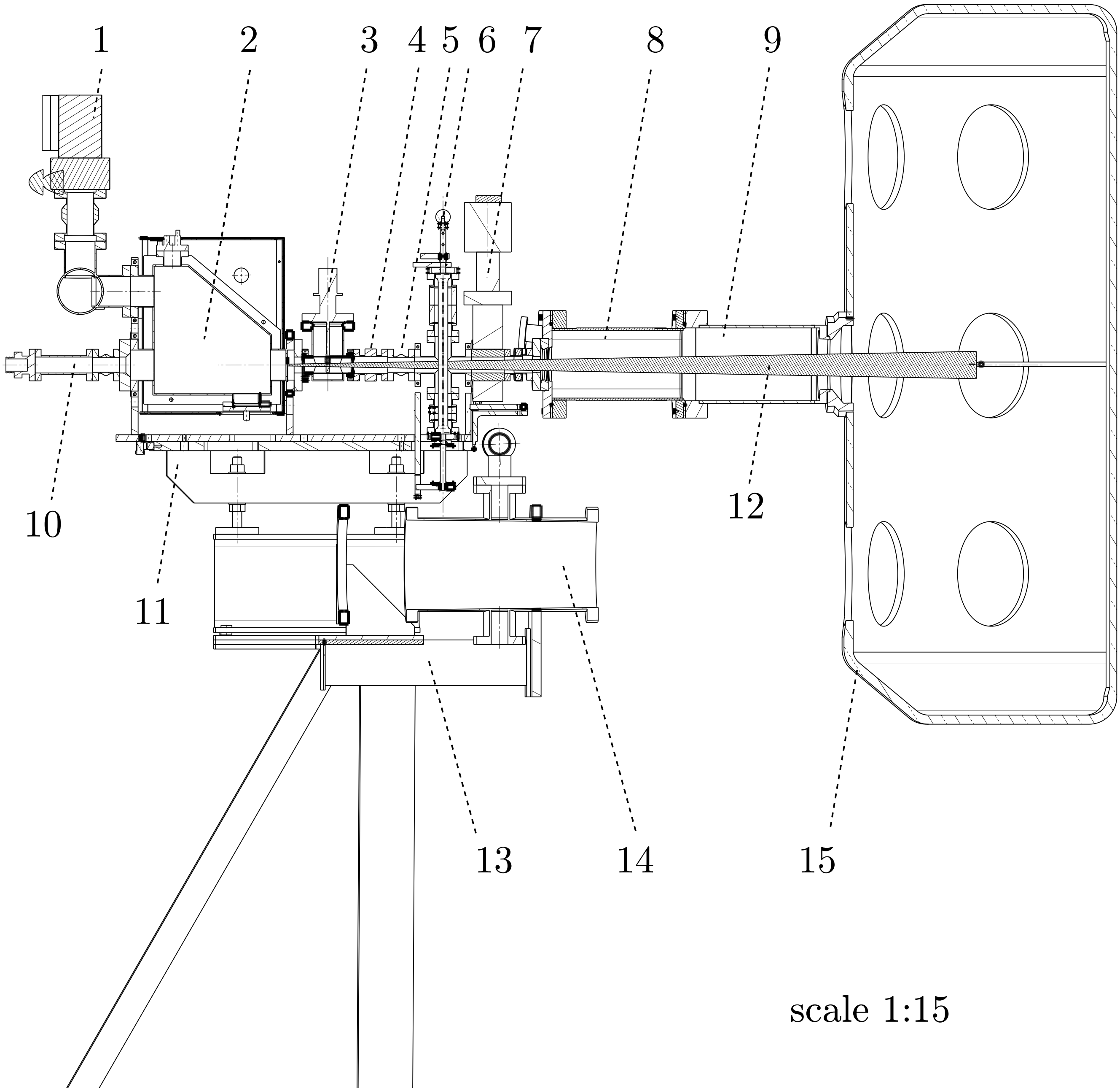

Figure 3.3.4: Side view of the integration of the CNPA in TCV. The labels designate: ① turbodrag pump and secondary pressure gauge; ② CNPA housing with soft iron shield; ③ alkali ion source; ④ bellow for horizontal CNPA orientation; ⑤ insulating ceramic; ⑥ rod with three input diaphragms; ⑦ gate valve; ⑧ CNPA duct; ⑨ TCV midplane port; ⑩ bypass line for primary pumping; ⑪ vertically adjustable CNPA support; ⑫ CNPA maximum solid angle; ⑬ supporting structure; ⑭ TCV pump; ⑮ TCV chamber. The view shown corresponds to the location in toroidal sector 14 (prior to 2008).

3.3.3.1 CNPA biviewline setup on TCV

TCV's CNPA collects neutrals along a horizontal view line at the vessel mid-plane. The diagnostic was initially installed next to the DNBI with its view line being of grazing incidence on the beam path inside the plasma (see figure 4.8.1). For the 2008 experimental campaign (and onwards), the diagnostic was displaced to another location on the torus, where a new support and torus flange allow measurements at normal incidence or at an inclination of 60° in respect to the toroidal direction. This setup was designed to address the anisotropy of the fast ion population (section 6.9.1).

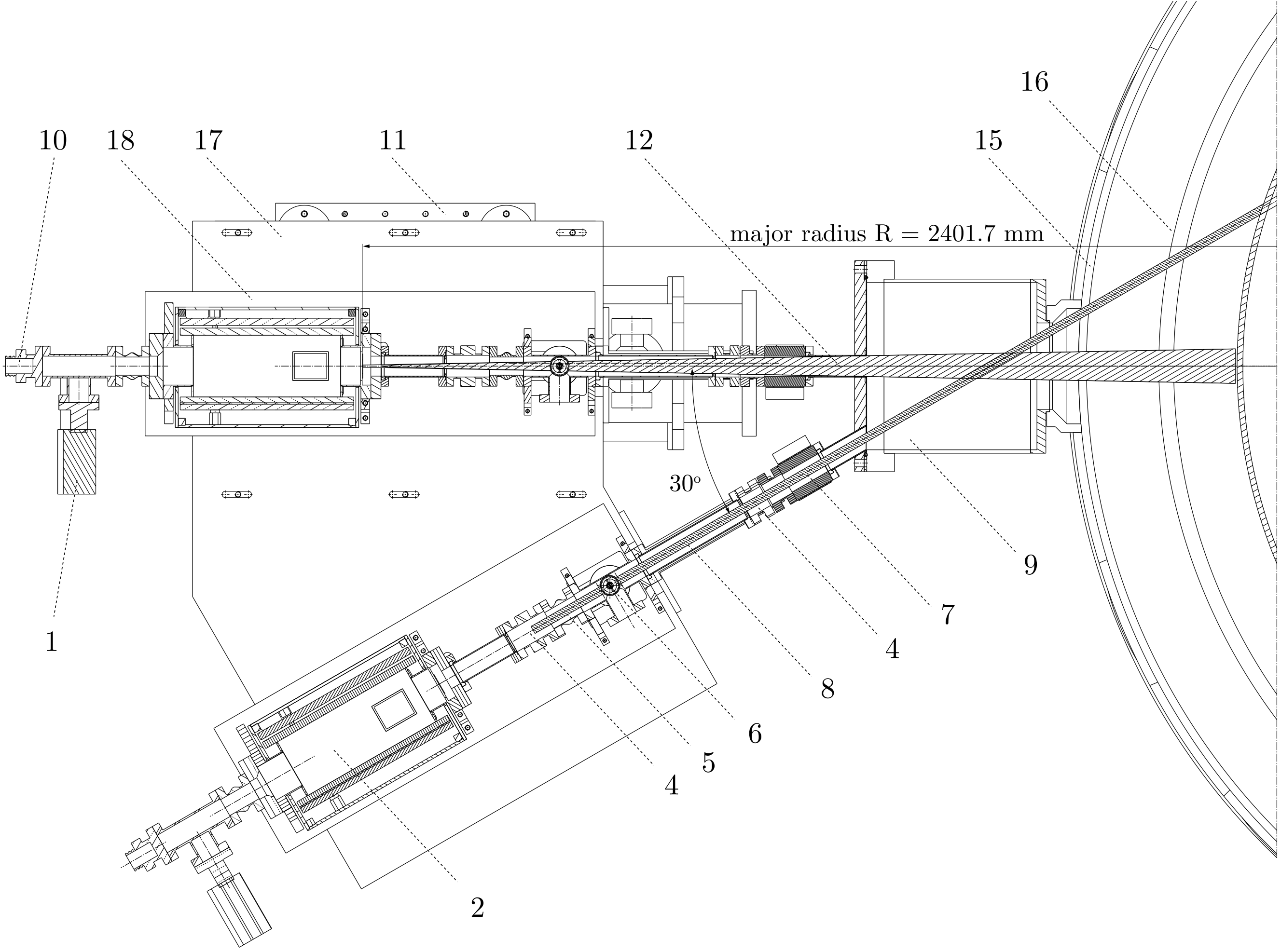

Figure 3.3.5: Top view of the integration of the CNPA in TCV. For labels ① to ⑮ see the caption of figure 3.3.4, ⑯ magnetic axis; ⑰ CNPA platform; ⑱ movable CNPA table. The view shown corresponds to the location in toroidal sector 10 (since 2007) with the two possible view line configurations. The alkali ion source is not represented in the drawing.

Figures 3.3.4 and 3.3.5 show how the CNPA interfaces with TCV. The maximum solid angle is $>10^{-8}$ m^{2}sr wide and is normally reduced by one of three inlet collimators(§) which are mounted on a movable rod in order to diagnose various levels of neutral fluencies.

Both TCV port holes are equipped with a gate valve, so that the position of the diagnostic may be changed without breaking the torus vacuum. However the vacuum inside the CNPA is broken during this operation and the subsequent pumping takes some time (to prevent any damage of the carbon stripper foil, see below) – typically 2 days.

(§) The available diaphragm diameters currently are 1.38, 4.6 and 13.8 mm. The rod, figure 3.3.4, label ⑥, is located at a distance of 35 cm from the CNPA input diaphragm, figure 3.3.6, label ①. The latter is located at a major radius of $R = 2.4$ m.

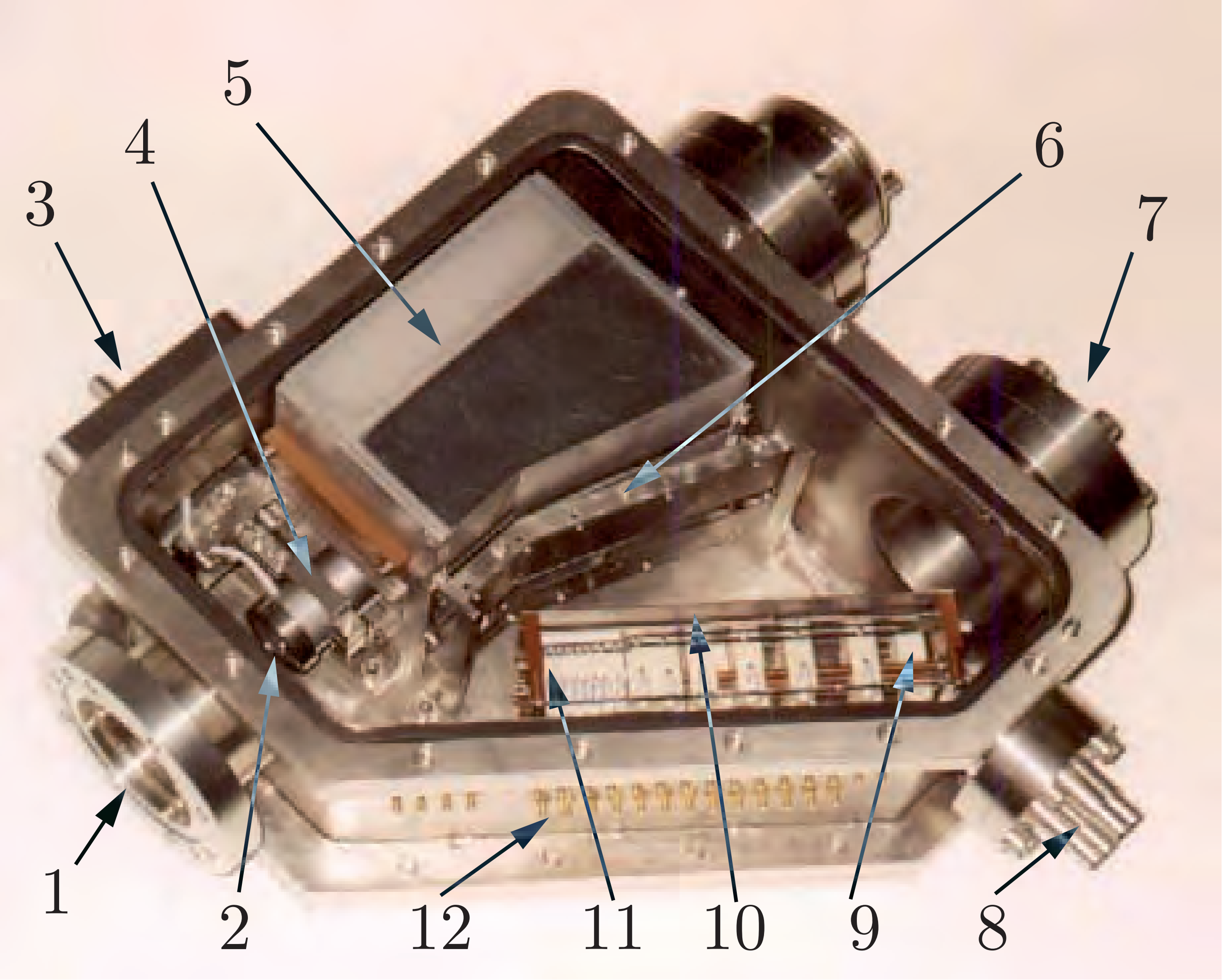

Figure 3.3.6: Photograph of the CNPA core, ① particle beam entrance flange and fixed input diaphragm with diameter of 1.38 mm; ② combined stripping and acceleration unit; ③ access window for stripping foil replacement; ④ carbon stripping foil; ⑤ permanent magnet of the analyser; ⑥ electrostatic condenser of the analyser; ⑦ pumping port; ⑧ high voltage feed through; ⑨ detector for secondary hydrogen ions with $E = 50$ keV; ⑩ detector mask; ⑪ detector for secondary hydrogen ions with $E = 644$ eV; ⑫ detector output signal connectors.

3.3.3.2 Diagnostic core

Figure 3.3.6 depicts the core components of the CNPA. The analyser employs a diamond like carbon (DLC) foil [107] to strip the electrons from the incident neutrals. The foil is produced by thermal sputtering, has a thickness of 100 Å and is mounted on a fine grained mesh of high transmission.

Foil strippers are simpler to implement (no need of gas supply and handling) but induce an important scattering of the particles at lower energies. To correct this, the foil is supplemented by a cylindrical electrostatic acceleration unit to achieve an efficient refocusing of the particle stream. The resulting ions are dispersed by momentum and energy using collinear **E** and **B**-fields.

The **B**-field is produced by two rare-earth $Nd_2Fe_{14}B$ permanent magnets (residual magnetisation $\sim$1.2 T) whose geometry is optimised to focus the particles onto the detector plane.

The detector plane is equipped with two parallel arrays of open-ended channeltron electron multiplier (CEM) detectors [108] manufactured by Dr. Sjuts Optotechnik, Göttingen, Germany [109]. These are operated in the pulse counting mode, in a vacuum of $<10^{-5}$ mbar, obtained with a group of fore- and turbodrag pumps (this pressure prevails in the whole volume behind the torus gate valve).

The CEM's are sensitive to charged particles, hard and soft X-rays, as well as ultraviolet radiation. The continuous dynode of these channeltrons is made of hydrogen-reduced lead oxide glass coated on a ceramic support. The secondary electron cloud is collected by an anode, producing a pulse shorter than 10 ns. The linear electron avalanche gain is about 10^8, but is strongly degraded if more than $\sim$500 ions/ms are impacting on the inner wall of the detector (note that this is a factor 10 below the limit of the VNPA).

This counting rollover is primarily due to the limited CEM bias current (sustaining the secondary electron emission process) and, if the incoming secondary ion flux becomes still more important, due to the channel capacitance, resulting in lower pulse amplitudes, that now fall below the discrimination level of the multichannel charge amplifier (MCA) with integrated discriminators, connected to the CEM's in outgoing circuit.

The MCA delivers LS-TTL-pulses which are then counted using a multichannel CAMAC scaler with a memory of 1024 counting cells per discharge. The raw counts are stored to the MDSplus database [110] holding all the measurement data of the TCV experiment. The diagnostic is integrated into the TCV plant control system and is controlled through a Vista GUI window on the OpenVMS cluster of CRPP.

Two types of particles with different mass/charge ratio are simultaneously recorded, the detected particle pair is chosen by the adjustment of the acceleration unit and analysing condenser voltages. These voltages are kept constant during an experiment (i.e. no dynamic energy scanning like with the VNPA). The mass crosstalk rejection is better than 10^3. Two setups are available, with simultaneous H/D or D/He detection. The lower mass row has 11, the higher mass row has 17 detectors. Detectors with three different sized acceptance slits are used to partially compensate for the exponential decay of the particle fluency with increasing energy (section 4.3.2).

To reduce the perturbation of the ion trajectories by the tokamak magnetic field, a soft Armco iron box (wall thickness 5 mm) encapsulates the diagnostic to limit the interior stray field to a value below the maximum allowed 5 mT.

The channel energy resolution $\Delta E/E$, detection efficiency α and instrumental function were absolutely calibrated using mono-energetic neutral beams in the lab of the manufacturer [111]. To verify the correct diagnostic operation and calibration, a movable thermal source for alkali ions may be inserted into the CNPA line of sight. A salt powder containing a blend of potassium or lithium is heated such that K^+ or Li^+ ions are produced by thermoemission. An adjustable potential is then applied to the source to bring the emitted ions to energies in the range of 100 eV to 2 keV, with their velocity vector directed into the CNPA collimator. This permits the detector response to be checked using a multichannel pulse height analyser. Note that this is a relative calibration (against channel neighbours), the (slow) disintegration of the radioactive salt requires its sporadic replacement. Thus the overall evolution of the detector response (e.g. precipitate ageing) may not be assessed. A procedure for the absolute calibration of the NPA will be described in section 4.8.2.

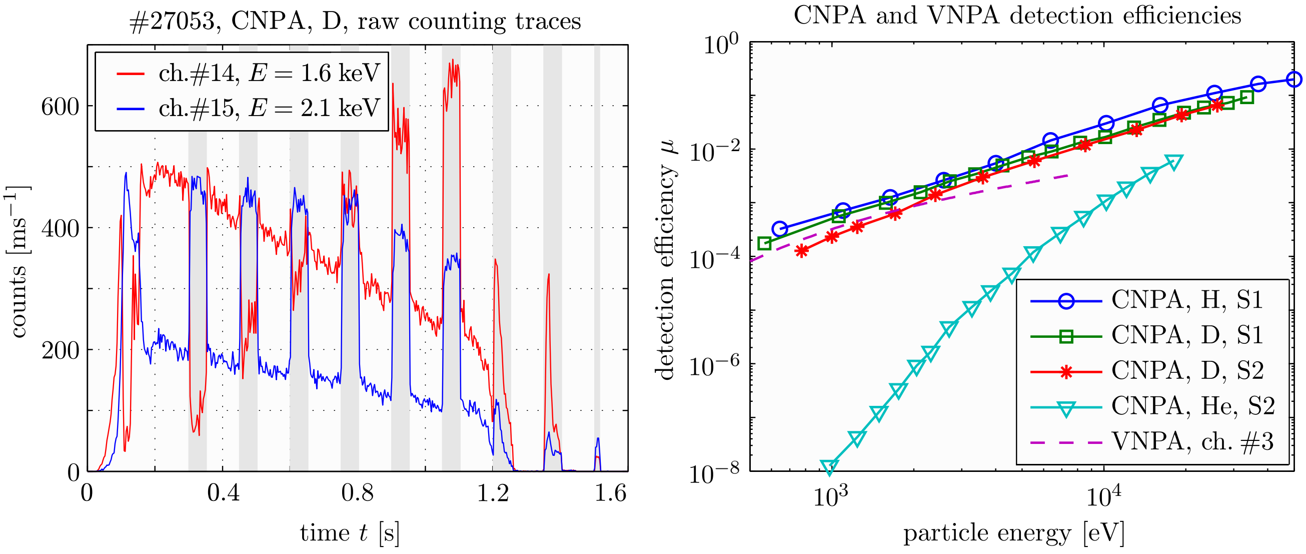

(a) Overloading of the CNPA. (b) Detection efficiency.

Figure 3.3.7: (a) CNPA channel #14 and #15 (deuterium array) raw counting traces. The signal of channel #15 scales linearly with the incoming neutral flux at energy $E = 2.1$ keV and ranges below the pulse counting limit of typically 500 events per ms. The flux into channel #14 ($E = 1.6$ keV) exceeds this limit at $t = 0.1$ ms and during each DNBI blip (shaded regions). The stronger the flux the weaker the detector response – clearly a signature of capacitive saturation.
(b) VNPA and CNPA detection efficiencies. S1 and S2 designate the two possible setups of the CNPA. The calibration factors for energies above 20 keV were calculated using a Monte Carlo code [111]. All VNPA channels have very similar detection efficiencies, only detector #3 is shown.

3.3.4 Comparison of the capabilities of VNPA and CNPA

The compact size of the CNPA permits installation closer to the magnetic axis than the VNPA and thus the spatial resolution is better (the particle collection volume at the magnetic axis is smaller).

The neutral flux intensity can vary over several orders of magnitude at the energies typically diagnosed with NPA. The large energy range covered by the CNPA, despite the application of CEM's of increasing acceptance at higher energy, results in a counting dynamic range exceeding a factor of 10^3. Satisfactorily high count rates at high energy are then sometimes paid for by the saturation of the detectors at lowest energy (and/or those of intermediate size). Nonlinear detector responses are also observed in the high energy hydrogen channels when the DNBI is fired. Figure 3.3.7a shows an example. Due to its capacitive nature, channeltron saturation depends on the transient flux behaviour and its history. The maximum count rate is therefore limited to less than 1 MHz. Such problems do not occur with the VNPA diagnostic (count rates up to 10 MHz).

At higher particle energies the foils are better ionisers than the gas cells, the stripping efficiency is increasing with the incoming atom energy whereas gas cells become almost inefficient above ~10 keV [112]. Although the particle scattering becomes significant at low particle energies, the subsequent acceleration and refocusing unit of the CNPA ensures an acceptable detection efficiency. The higher detection efficiency allows for higher spatial resolution without degradation of the detection statistics. Figure 3.3.7b compares the detection efficiencies of CNPA and VNPA. The very low detection efficiency for helium should be noted.

The horizontal view line of the CNPA, together with the flexibility of vertical plasma positioning of TCV, opens the way to diagnose different parts of the plasma. The outcome of neutral particle flux measurements with systematic vertical plasma displacements can be used as pseudomultichord measurements (see sections 4.4.1 and 6.3).

However, the VNPA provides complementary information in such experiments since for example the plasma-wall interactions, the plasma shape or the location of deposition of EC power may be altered undesirably in a plasma that is vertically displaced. The VNPA measurement thus becomes a monitor of the stationarity and reproducibility of the discharge in this case.

Last but not least, the VNPA is further away from the plasma core, such that the intensity of parasitic signals that surround a tokamak is reduced in respect to the CNPA and the EMT of the VNPA have the advantage of being relatively insensitive to hard radiation (good Russian design and more than 25 years of operation). The CNPA requires lavish shielding (see the next section).

3.4 Parasitic signal rejection (diagnostic shielding issues)

During the first session exploring the fast ion physics on TCV with the CNPA (chapter 6), strong but, apparently parasitic signals, in the high energy channels of the CNPA were observed (figure 3.4.1).

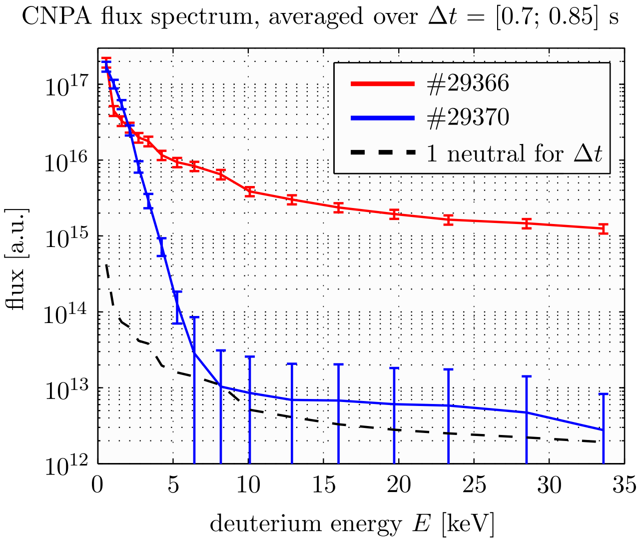

Figure 3.4.1: CNPA signal spectrums averaged over $t = [0.7; 0.85]$ s. Both discharges shown are strictly ohmically heated up to the time interval shown, electron density is as low as $\langle n_e \rangle = 1.3 \times 10^{19}$ m^{-2}. The spectrum of discharge #29366 is not the result of incoming neutrals, as the accelerator and analysing condenser high voltage were switched off. No secondary ion could therefore reach the channeltrons. All hits are due to parasitic interactions between the CEM and X-rays. A change in the design of the initial phase of the discharge successfully prevent the triggering of parasitic signal contributions (discharge #29370, see discussion in section 3.4.2.1).

In order to exclude this contribution from the signal due to neutral particles, the accelerator and analyser voltages were switched off and the CNPA gate valve closed (to prevent potential ultraviolet light from the plasma to penetrate into the detectors through multiple reflections) during a discharge. Strong perturbations of the channeltrons were clearly identified, as they leave an identical signature in all CNPA channels, shown in figure 3.4.2 for the channeltrons at low, mid- and high energy for the hydrogen (left) and deuterium (right) detector array. All traces are plotted to the same scale. To get rid of this unwanted signal contribution, each discharge had to be repeated, first with and second without the CNPA analyser voltages being applied. The neutral part of the signal was then obtained by substraction of the signals of the second from the first discharge. Of course, this was not a feasible long-term solution since shot repetitions are costly and often are not that reproducible.

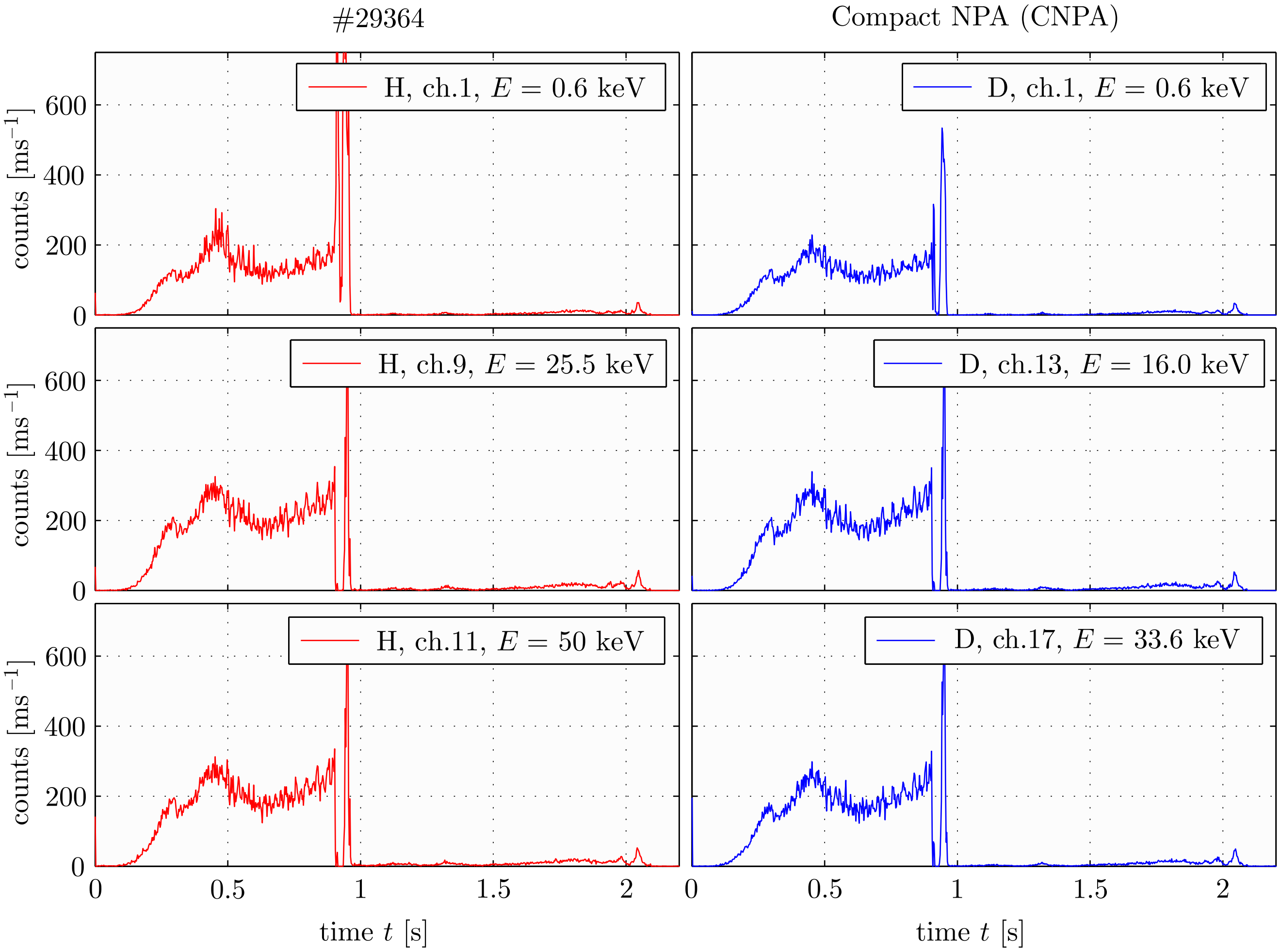

Figure 3.4.2: Parasitic CEM events occur in all CNPA channels, independent of the channel energy. For the discharge shown the parasitic signals are reduced when the electron cyclotron waves are injected into the plasma (modulated, 3 pulses of 100 ms length each, duty cycle 50 %, starting at $t = 0.9$ s). During the first auxiliary heating pulse the discharge starts to disrupt, but recovers and weaker parasitic signal reappear. For the ohmic plasma period the CEM response is essentially due to runaway electrons (emission of hard X-rays when they collide with the vessel wall or with ions). For the EC heated phase suprathermal electrons are produced by Electron Cylcotron Current Drive (see discussion in section 3.4.2.1).

Visible or ultraviolet stray light as a possible perpetrator is excluded since the signal pollution is observed regardless whether the CNPA gate valve was open or closed.
The channeltrons of the compact NPA were found to be remarkably sensitive to X-rays. If the radiation is sufficiently hard, the photons traverse the materials surrounding the torus and interact with the detectors of the CNPA. Weaker parasitic signals, as observed during ECCD phases (see second half of the discharge shown in figure 3.4.2), are more difficult to identify and compensate. Reliable operation of the diagnostic requires careful monitoring and, should the occasion arise, proper shielding of the potential radiation source from the CNPA.

3.4.1 Hard X-ray production on TCV

The most important source of hard X-rays on TCV is Bremsstrahlung radiation emitted by electrons with energies above ∼10 kiloelectronvolts [113], upon collisions with plasma ions or absorption in a solid target (so called thick-target radiation). The photon energy depends on the impact parameter of the collision and may be as high as the electron energy prior to the collision.

Electrons gain such high energies in plasmas with electron cyclotron current drive (section 5), with the injected wave being in resonance with the gyration motion of the electron around the magnetic field line, resulting in efficient electron acceleration in the direction along the torus. A second avenue to high energy electrons are low density plasmas, where the electrostatic force due to the loop voltage may overcome the drag and the electrons may accelerate continuously. The upper limit in energy within reach for the electrons is dictated by the amount of energy lost through radiation or the loss of confinement.

3.4.1.1 Runaway electrons

Runaway electrons circulate toroidally with drift velocities $v_{\rm de}$ in excess the thermal speed of the bulk electron population $v_{\rm the} = \sqrt{T_e/2\,m_e}$. Their equation of motion may be written

$$m_e \frac{{\rm d}v_{\rm de}}{{\rm d}t} = -e\,E - \nu_p^{e/i}(v_{\rm de})\,m_e\,v_{\rm de}, \tag{3.4.1}$$

where E is the toroidal electric field induced by the transformer and

$$\nu_p^{e/i}(v_e) = n_i \frac{Z^2 e^4}{4\pi\,\varepsilon_0^2} \frac{\ln\Lambda}{m_e^2\,v_e^3} \tag{3.4.2}$$

is the momentum loss rate of electrons due to Coulomb collisions with ions, evaluated at the electron drift velocity [114]. The first term of eq.(3.4.1) describes the acceleration of the electrons (ohmic heating), the second the deceleration by the drag force. If now $e|E| > \nu_p^{e/i}\,m_e\,v_{\rm de}$, the electrons accelerate, and as $\nu_p^{e/i} \propto v_e^{-3}$, the drag decreases and the electrons accelerate even more, i.e. they are running away…

The previous inequality may be written as

$$\frac{1}{2}\frac{m_e\,v_{\rm de}^2}{T_e} > \frac{E_D}{E}, \tag{3.4.3}$$

with E_D, the Dreicer field [115], defined as

$$E_D = \frac{n_e\,Z\,e^3\ln\Lambda}{8\pi\,\varepsilon_0^2\,T_e}. \tag{3.4.4}$$

Eq.(3.4.3) states that if $|E| = E_D$, the runaway regime is reached at $E_{\rm drift} = m_e\,v_{\rm de}^2/2$. For toroidal electric fields below E_D, the electron acceleration is eventually balanced by the collisional drag exerted by the ions.

The generation of hard X-rays on TCV was studied with diagnostics described below.

3.4.2 Hard X-ray diagnostics on TCV

A multichord hard X-ray camera (section 3.4.2.1) was installed on TCV (with interruptions) from 1999 to 2005 [116]. The camera was on loan from CEA Cadarache. Unfortunately the camera was returned to France soon after the commissioning of the CNPA, so only preliminary tests concerning the CNPA shield against hard X-rays could were performed. Most of the tests to design and optimise the CNPA hard X-ray shield were undertaken with a simple photomultiplier/scintillator tube (section 3.4.2.2).

A new hard X-ray spectrometer (HXRS) is currently under development [117, 118] and will comprise 4 cameras, each housing 30 detectors for a complete imaging of a poloidal cross section. The current design strives for an energy resolution of $\Delta E \sim 5$ keV, energy range 10. . . 200 keV, temporal resolution of maximum $\Delta t = 1$ ms and spatial resolution $\Delta r = 2$ cm for neighbouring chords. A tomographic reconstruction of the detector signals would then unfold the hard X-ray emissivity profile and the underlying suprathermal electron distribution function.

3.4.2.1 Hard X-ray camera (HXRC)

The hard X-ray detector system from Tore Supra is a single multichord camera comprising detector diodes made of cadmium telluride (CdTe) [119]. The system was installed on TCV to study the dynamics of suprathermal electrons during electron cyclotron current drive experiments [120]. The analysed range of Bremsstrahlung energy lies approximately between 5 and 200 keV. 14 partly overlapping observation chords capture the photons emitted from roughly the outboard half of the TCV plasma. Figure 3.4.3 shows the diagnostic geometry.

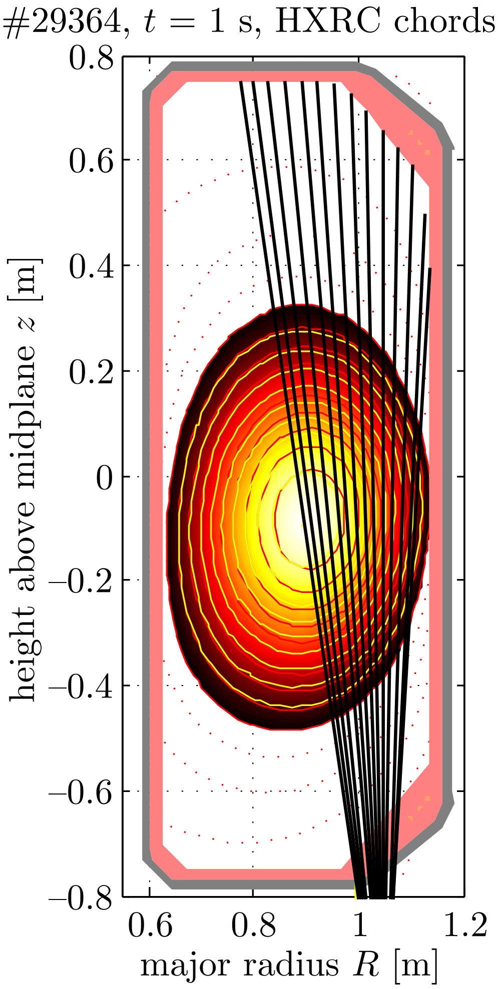

Figure 3.4.3: Equilibrium reconstruction for discharge #29364 showing the geometry of the hard X-ray camera available during the initial commissioning of the Compact NPA.

The spatial resolution is about $\Delta r = 2$ cm on the torus midplane. Each chord collects photons which are discriminated into 8 energy channels with adjustable energy discrimination thresholds. At most 1024 acquisition periods are available in a discharge, although the temporal resolution is mostly limited by the poor photon statistics (typically a couple of milliseconds).

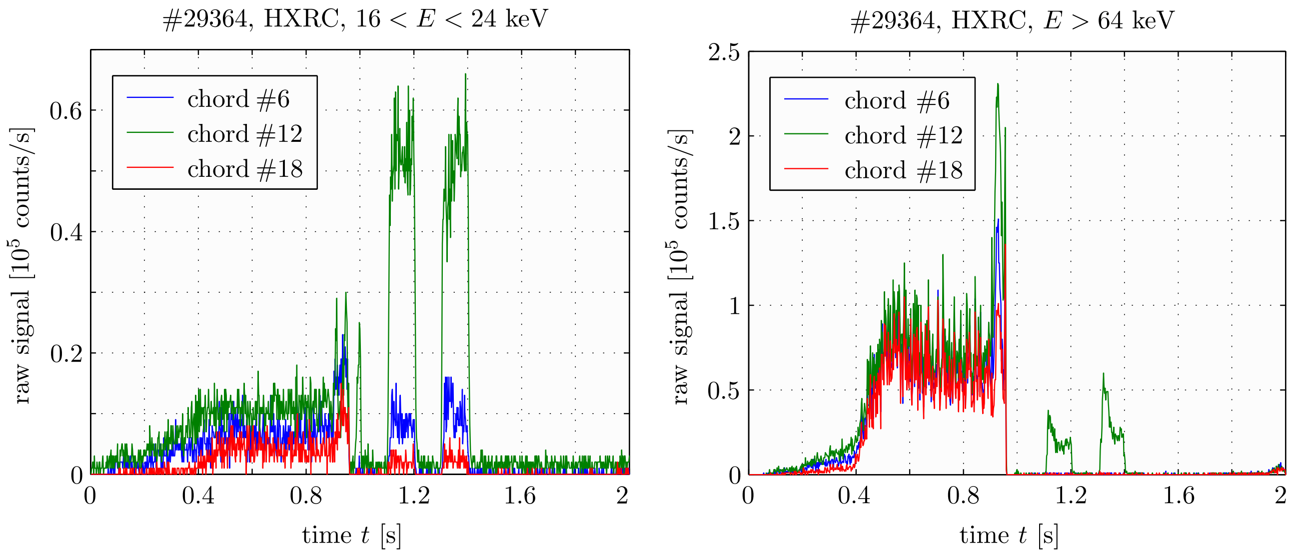

(a) low energy hard X-rays.

(b) high energy hard X-rays.

Figure 3.4.4: Hard X-ray camera traces of photons binned in the lowest (a) and highest (b) available energy windows. Chord #6 intersects the plasma edge, chord #18 the plasma core, as shown in figure 3.4.3. High energy hard X-ray photons are emitted from all locations inside the plasma during the electron runaway phase prior to the EC injection. During the current drive intervals hard radiation is only seen at the location where the EC power is absorbed (inside the q=1 safety factor surface, located at normalised radius $\rho \approx 0.4$).

Figure 3.4.4 shows HXRC measurements during the discharge already shown for the CNPA (figure 3.4.2). Figure 3.4.4a shows weakly hard photons with energies around 20 keV, figure 3.4.4b such with energies between 64 and 200 keV. Signals from three chords are shown, chord #6 is the outermost (looking at the edge), chord #18 the innermost (looking at the plasma core) view line (see figure 3.4.3)(¶). Obviously plenty of hard X-ray photons are found throughout this experiment.

Figure 3.4.5a shows the radiation intensity spectrum of some chords averaged over the ohmic time interval $t = [0.7; 0.9]$ s, showing that the peak of the photon energy distribution lies above 64 keV. These photons are emitted everywhere inside the plasma, as all HXRC chords detect them. At these energies the photons easily penetrate into the CNPA housing and yet deposit part of their energy in the channeltron detectors (figure 3.4.2).

The discharge discussed here has a very low density of $\langle n_e \rangle < 6 \times 10^{18}$ m^{-3}, a strong loop voltage (-3 V at $t = 0$, -1 V at $t = 0.4$ s) and runaway electrons were inevitable since the prefill density just after the plasma breakdown at $t = 0$ was low. If the density upon ionisation of the gas is too low then the toroidal electric field may overcome the Dreicer field, eq.(3.4.4), and the produced electrons immediately start to run away. Close collisions between thermal and keV-electrons, although much less frequent than those with large impact parameters, continuously increase the runaway electron population.

This route to hard X-rays may often be suppressed by careful tweaking of the gas programming at the start of the discharge (figure 3.4.5b).

(¶) The camera has 20 detectors, but on TCV number #1–#5 and #19/#20 are obstructed by the port aperture.

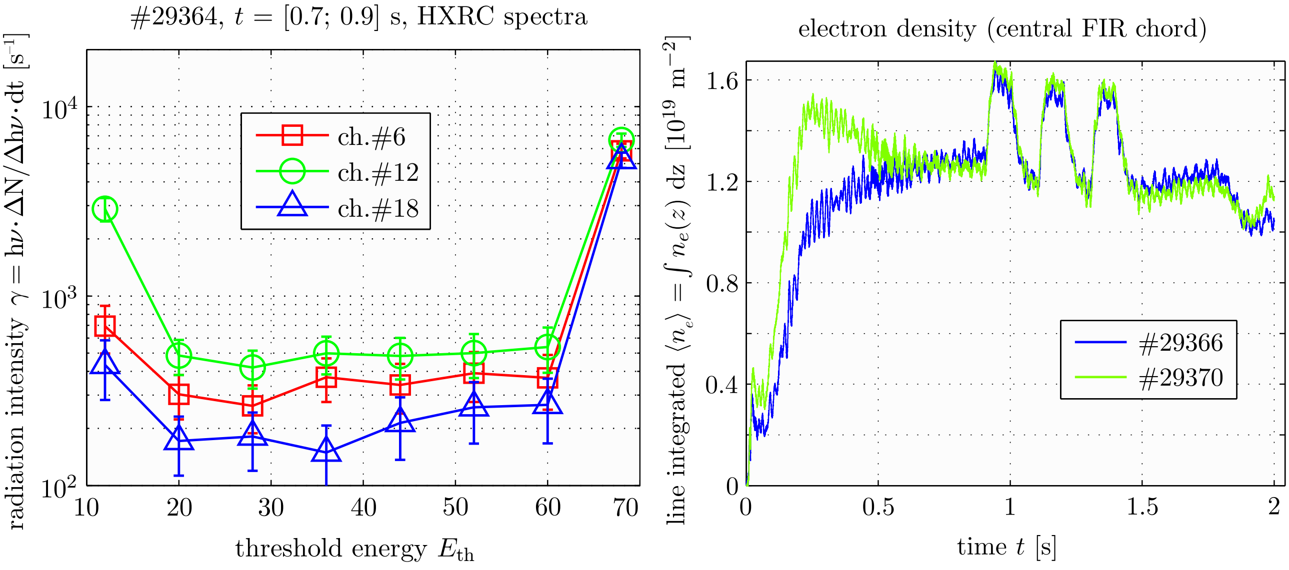

(a) very hard X-rays. (b) prefill density tweaking.

Figure 3.4.5: (a) Hard X-ray energy spectrum typical for the runaway regime. The spatial emission profile is flat and the photons have high energies (the last energy channel collects photos with energies between 64 and ∼200 keV).
(b) Measured line integrated density (central FIR chord) for the two discharges #29366 and #29370. The runaway electrons which were present in the first experiment are not produced in the second and the CNPA (figure 3.4.1) measures a real thermal neutral flux distribution.

There is however a far more troublesome source of hard-X rays. In discharge #29364 (look again at figure 3.4.2), the density rapidly increases as an UFO is falling inside the plasma at $t = 0.96$ s. The plasma disrupts but recovers. The runaway signal disappears due to the increased electron drag after this event. At $t = 0.9$, 1.1 and 1.3 three gyrotrons (on axis: 1 pure ECH, 1 ECCD at $\rho < 0.4$, off-axis: 1 pure ECH at $\rho \sim 0.5$) started to inject a total power of 1.5 MW during three gyrotron pulses lasting 100 ms each. The auxiliary heating periods are clearly visible on the HXRC traces (figure 3.4.4), mainly on those chords intercepting the region of absorption of the radiofrequency power.

Figure 3.4.6a shows the photon intensity energy spectrum $\gamma(E_\gamma)$ of some chords, where the photon temperature T_γ was derived from a linear regression of the slope of the spectrum,

$$\frac{d\gamma}{dE_\gamma} \propto \exp\left(-\frac{E_\gamma}{T_\gamma}\right) . \tag{3.4.5}$$

Figure 3.4.6b plots these temperatures against the minimum normalised radius intercepted by the chord. The photon temperature obtained correlates with the period of auxiliary heating. During ECH/ECCD the parasitic signals in the CNPA channels rise here to about 10. . . 20 counts per millisecond. This is too much for studies of suprathermal ion populations with poor neutral particle fluxes at high energies (section 6.1), worse, in plasmas with stronger ECCD (up to three gyrotrons instead of just one here) the hard X-ray production was found to be substantially stronger. With the return of the HXRC to CEA, the potential of shielding was examined with a simple hard X-ray monitor.

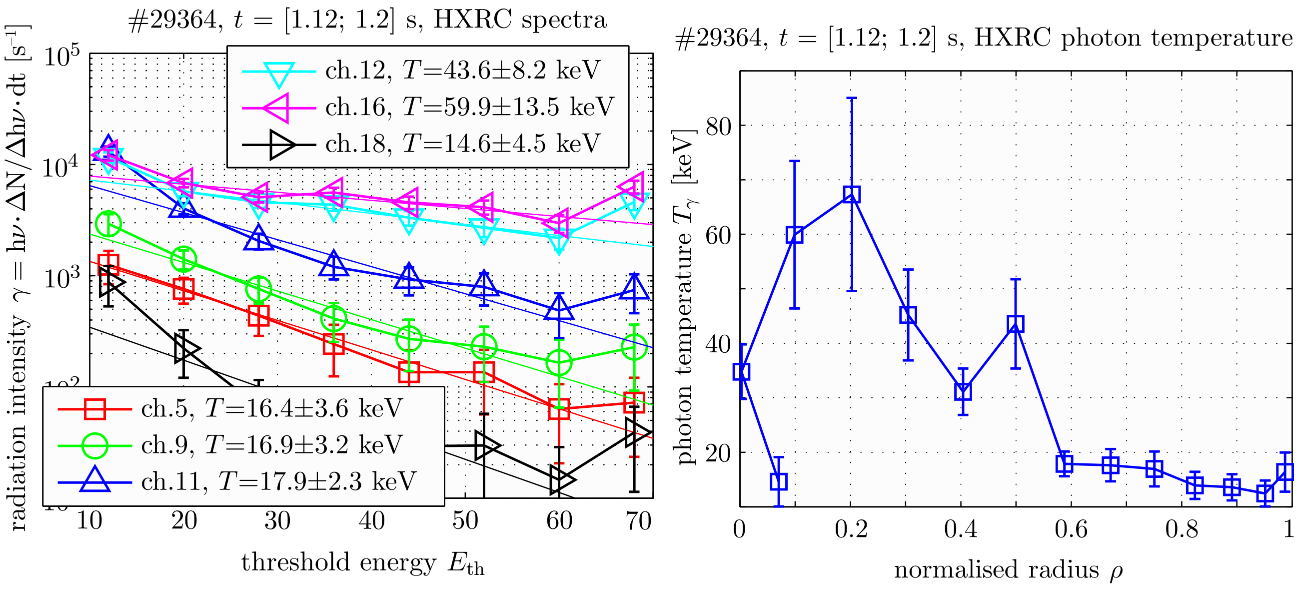

(a) photon energy spectrum.

(b) photon temperature profile.

Figure 3.4.6: (a) Photon energy spectrum obtained with the hard X-ray camera during an ECCD phase of discharge #29354 for a subset of the available view lines. The photon temperature was inferred from the slope of the photon energy distribution (thin straight lines).
(b) Photon temperature for all available chords as a function of radius (channel #5 close to the LCFS, channel #18 lies on the low field side with respect to the magnetic axis.

3.4.2.2 Hard X-ray monitor (PMTX)

The PMTX diagnostic is a standard Hamamatsu photomultiplier tube (PMT) encapsulated by a soft iron cylinder to shield the PMT against soft X-ray photons (of energies lower than 50 keV) and the magnetic stray field. The scintillator at the end of the tube is covered by 2 cm of aluminium.

The tube was connected to a remotely programmable high voltage power supply to adjust the tube dynode supply voltage and thus avalanche gain to diagnose various levels of hard X-ray fluencies. The tube output signal is acquired through a digitiser typically working at a frequency of 20 kHz. However no information about the absolute photon flux or photon energy spectrum is available.

For the design of a shield for the CNPA a sufficient number of specially shaped bricks made of lead (length of a side 5 or 10 cm) were procured(‖). Lead is the best attenuator for photons up to 500 keV due to its high density ($\rho = 11.33$ g/cm^3) and its heavy nucleus (atomic number $Z = 82$) ensuring the presence of many bound electrons. A series of low density discharges designed to provoke the generation of runaway electrons were executed with various variants of lead shields built around the PMTX. The PMTX is smaller than the CNPA, easier to handle and may be placed freely. First, the PMTX was placed behind a lead wall of thickness $\Delta x = 5$ cm. The unshielded CNPA measured an almost unchanged influx (figure 3.4.7a), whereas the PMTX registered photon fluency was reduced by a factor ~20 (figure 3.4.7b).

This attenuation was still considered as insufficient, so the PMTX was completely wrapped in a lead shield housing of minimum thickness $\Delta x = 10$ cm (photograph 3.4.8a). Now the X-ray flux was decreased by a factor of ~250 (figure 3.4.8b).

(‖) Foundry André Neeser SA, Morges, Switzerland.

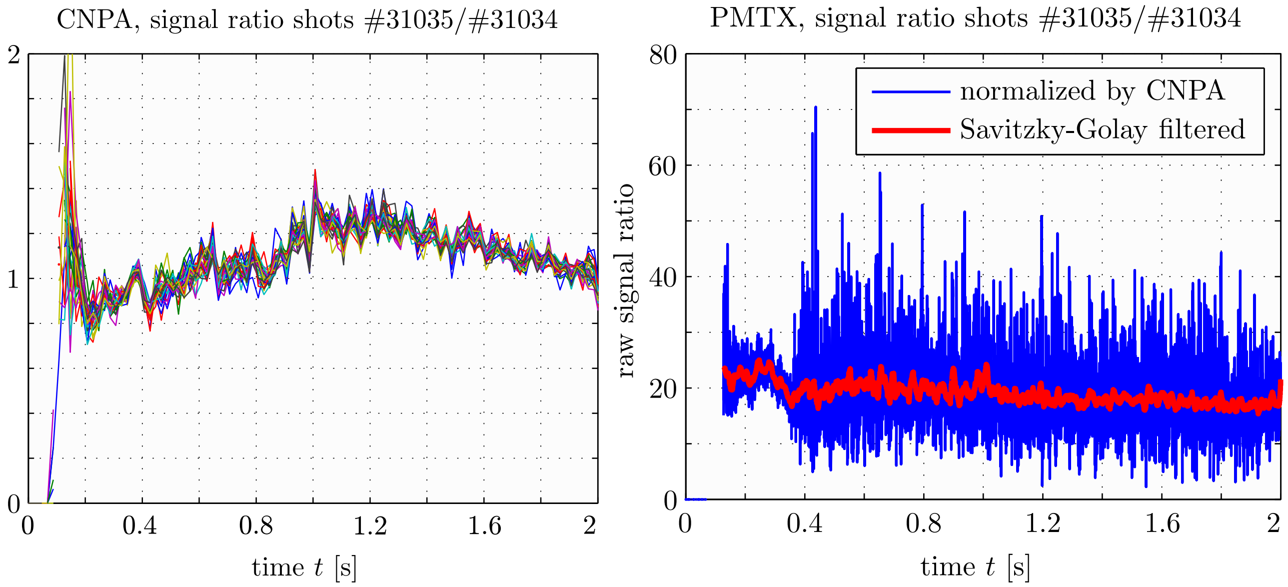

(a) CNPA signal ratios.

(b) PMTX signal ratios.

Figure 3.4.7: Raw signal ratios of (a) the CNPA and (b) the PMTX diagnostics for two identical very low density plasma discharges. The CNPA was unshielded to monitor the reproducible HXR production, the PMTX was only shielded in discharge #31034. The signal ratio of the PMTX is renormalised with the flux ratio measured with the CNPA.

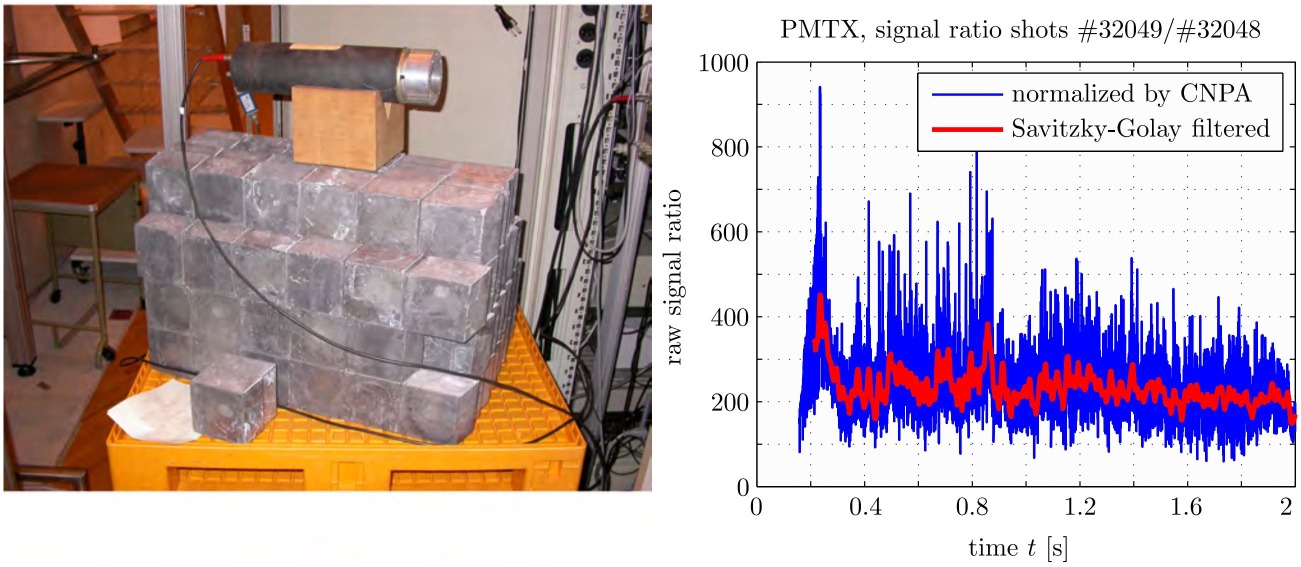

(a) Picture of PMTX and test shield.

(b) PMTX ratio with full shield.

Figure 3.4.8: (a) PMTX tube on top of the lead brick housing used for the X-ray attenuation tests.
(b) With the PMTX inside the mountain of lead the parasitic signals were reduced by a factor better than 200.

The same value was obtained with an open and a closed housing on the side away from the torus so backscattered X-rays do therefore not significantly contribute and the shield may be reduced to only cover the diagnostic from direct exposure.

The energy of the photons was estimated from the observed X-ray intensity attenuation in lead,

$$\gamma = \gamma_0 \exp\left(- \left(\frac{\mu}{\rho}\right) \rho \Delta x \right), \tag{3.4.6}$$

where γ_0 is the measured photon intensity without shield, Δx the linear thickness of the shield, ρ the mass density of the absorber and (μ/ρ) the mass absorption coefficient, whose value as a function of X-ray energy is available from tables published by the National Institute of Standards and Technology (NIST) [121], shown in figure 3.4.9a. Eq.(3.4.6) gives $(\mu/\rho) \approx 0.6\ \mathrm{cm}^2/\mathrm{g}$ for both wall thicknesses, thus requiring photon energies of 250 keV, consistent with the observations of the HXRC camera.

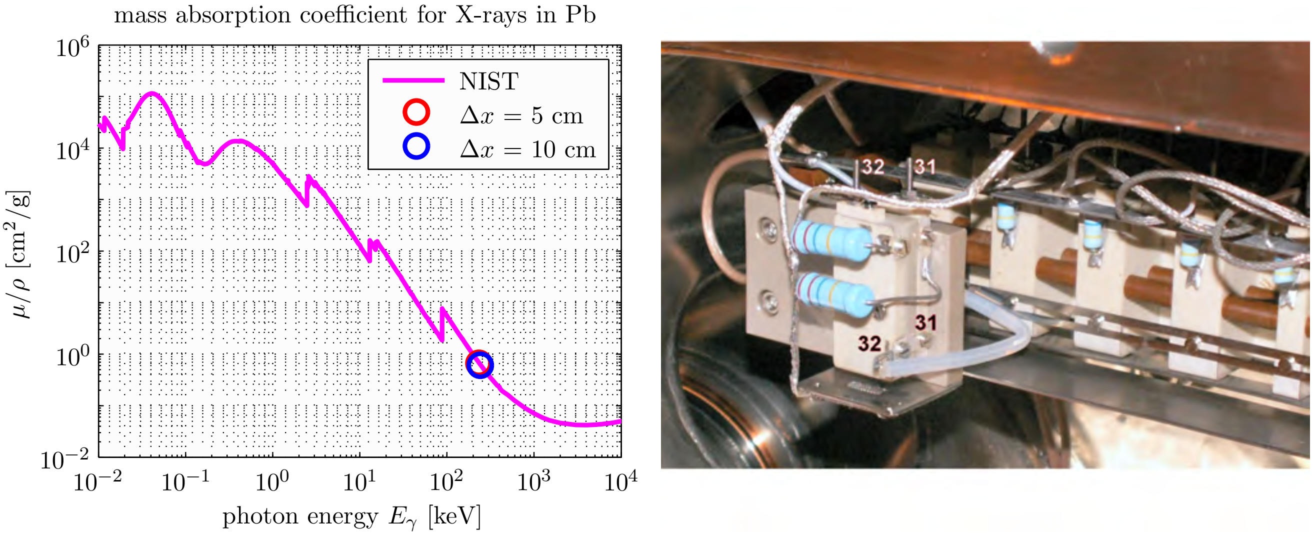

(a) X-ray absorption in lead.

(b) CNPA X-ray survey detectors.

Figure 3.4.9: (a) Linear mass absorption coefficient (μ/ρ) of lead [121]. The two (overlapping) circles represent the observed X-ray attenuation with a lead shield of $\Delta x = 5$ and 10 cm thickness respectively, indicating photon energies in the neighbourhood of 250 keV.
(b) Photograph of the additionally installed channeltrons inside the CNPA. The rail in the background supports the hydrogen array, particles enter the detectors from below. The X-ray detectors are connected to the preamplifier channels #31 (blinded entrance window) and #32 (open window). The negative detector voltage is applied to the detector entrance through the wire in the teflon hose, the anode output signal is lead out of the detector on its top end. The entrance mask is at ground potential. The 10 MΩ resistors connect to the system mass, ensuring a potential difference of approximately 100 V between the anode and the output end of the CEM such that the secondary electron clouds are efficiently transferred to the anode.

After these tests the PMTX was placed into an electronics shelf in the TCV hall, at a distance of approximately 3 m from the torus, where it is used as a hard X-ray survey monitor without calibration. The output signal U_{PMTX} scales as $(U_{\mathrm{HV}})^8$, such that the tests performed lead to the definition of a PMTX signal threshold. If exceeded, the CNPA measurement should not be taken as a valid neutral particle measurement.

3.4.2.3 X-ray channeltrons in the CNPA

The possibilities of X-ray surveys were completed by the installation of two spare CEM detectors inside the CNPA locations where particles with a mass that would have to be less than hydrogen would impact. These channeltrons monitor the X-ray radiation background in situ (detector with masked acceptance) and stray light potentially reflected on the interior of the CNPA housing or internally generated UV scintillation light (open detector). Figure 3.4.9b shows a picture of these channeltrons (channels #31 and #32).

3.4.3 CNPA shield design

After the displacement of the CNPA to its new location in 2008 (section 3.3.3.1), more free space was available around the diagnostic. A lateral and frontal shield built with lead bricks is currently installed, the lead in place weighs about one ton. To further shield the 5×5 cm^2 hole left for the vacuum tube linking to the torus, a machined cylinder of INERMET™ [122], contributed by Plansee, an Austrian high performance material company, was inserted into the bellows between the thermal ion source and the ceramic insulator, see label ④ on figure 3.3.4.

INERMET™ is an iron free tungsten alloy with a high mass density (17…18 g/cm^3) and is therefore a strong X-ray absorber. Contrary to pure tungsten, INERMET™ is easily machinable. With all the described shielding measures in place, perturbations of the CNPA measurement by X-rays were only merely observed.

3.5 Neutron yield monitor

3.5.1 Diagnostic principles

Together with γ-ray spectroscopy [73], neutron measurements [123] are the diagnostic of choice for the measurement of the ion parameters of a burning plasma, where the number of escaping neutrons is impressively high. But also in machines like TCV, with plasmas far from the ignition point, neutron detectors may be used to recover the fuel temperature and density as the fusion rate is measurable even at low temperatures.

TCV is fuelled with hydrogen or deuterium, but only the deuterium fusion reaction, eq.(1.2.4), produces neutrons, whose energy is 2.45 MeV. From figure 3.5.1b it is clear that only ions in the tail of the deuterium distribution function will undergo a fusion reaction(**), as the fusion cross section decreases exponentially towards lower energies and may be interpolated [47] by

$$\sigma_n = \frac{71}{E_{\mathrm{D}}} \exp\left(-\frac{44}{\sqrt{E_{\mathrm{D}}}}\right), \tag{3.5.2}$$

with E_{D} the energy in keV in the lab frame of the projectile deuterium ion colliding with a target ion at rest and the cross section is given in the units of barns.

(**) indeed the mean energy of the reacting deuterium ions is approximatively given by

$$\overline{E_{\mathrm{D}}} \approx \frac{7}{6} T_i + 3.1\, T_i^{2/3} \tag{3.5.1}$$

with T_i in keV [124]. For a plasma with $T_i = 1$ keV, the mean energy of the reacting particles is $\overline{E_{\mathrm{D}}} \simeq 4.3$ keV.

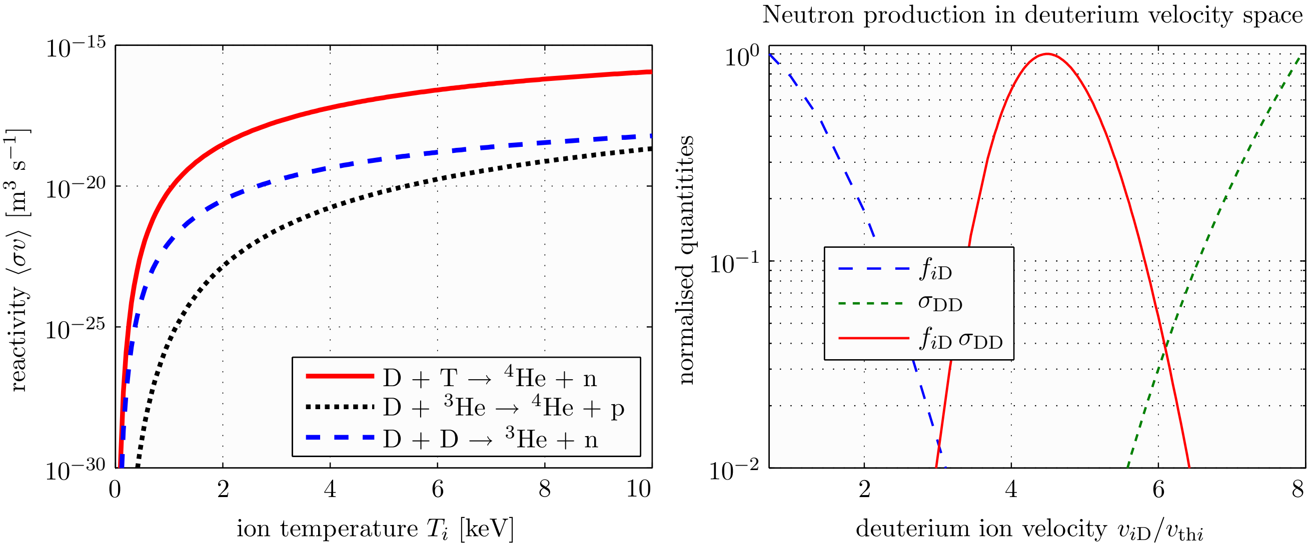

(a) Fusion reaction rates.

(b) Velocity range of fusing Deuterium.

Figure 3.5.1: (a) Nuclear fusion reactivities for thermal plasmas as a function of the plasma ion temperature. Data taken from [125, 126].
(b) Convolution of fusion cross section and deuterium velocity distribution function ($T_i = 400$ eV).

The neutron production rate per unit volume is then

$$d\Phi_n = \frac{1}{2} n_{\mathrm{D}}^2 \langle \sigma_n v \rangle, \tag{3.5.3}$$

where the reaction rate coefficient is integrated over the velocity distribution of the deuterium ions. Shown in figure 3.5.1a, the averaged reaction rate $\langle \sigma_n v \rangle$ has a strong dependence upon T_i, an experimental evaluation of eq.(3.5.3) by measuring the number of neutrons produced allows then T_i to be determined provided that n_{D} is known. Assuming carbon as the only impurity in the plasma, $n_{\mathrm{D}}(\rho)$ is defined by quasi-neutrality,

$$n_e = n_{\mathrm{D}} + 6\, n_{\mathrm{C}}, \tag{3.5.4}$$

where, from the definition of the effective charge, eq.(2.5.13),

$$n_{\mathrm{C}} = n_{\mathrm{D}} \frac{Z_{\mathrm{eff}} - 1}{6\,(6 - Z_{\mathrm{eff}})} \tag{3.5.5}$$

and finally

$$n_{\mathrm{D}}(\rho) = \frac{n_e(\rho)}{1 + \frac{Z_{\mathrm{eff}}-1}{6-Z_{\mathrm{eff}}}}. \tag{3.5.6}$$

Although the accuracy of the experimentally measured (profile averaged) Z_{eff} is often worse than 30 % (section 2.5.3.3), the impact of n_{D} on the ion temperature is not overly critical. Indeed, from eq.(3.5.2), integrated over a thermal ion velocity distribution, the propagation of the error on n_{D} into the error on T_i gives

$$\frac{\Delta T_i}{T_i} = \frac{\sqrt[3]{T_i}}{3.3} \frac{\Delta n_{\mathrm{D}}}{n_{\mathrm{D}}}. \tag{3.5.7}$$

That is, for $T_i = 1$ keV, less than 30 % of the relative error on n_{D} contribute to the error on T_i.

On the other hand, parasitic non-fusion reactions producing neutrons may represent non-negligible sources of errors in the estimation of the ion temperature. Very energetic electrons produced by resonant interactions with electron cyclotron waves or by electric fields exceeding the runaway threshold (section 3.4.1.1) effectively incite the disintegration of deuterium [127]. Direct disintegration,

$$\mathrm{D} + e \rightarrow \mathrm{H} + n + e, \tag{3.5.8}$$

may occur anywhere in the plasma. Indirect disintegration is caused when the energetic electrons impinge on the structure materials at the vessel wall and emit thick-target Bremsstrahlung (γ-rays). The γ's induce then photodisintegration in the surrounding solid structures,

$$\mathrm{D} + \gamma \rightarrow \mathrm{H} + n. \tag{3.5.9}$$

Both disintegration reactions have a threshold given by the deuterium binding energy (2.2 MeV). On TCV the neutron detector measurements are only processed if the runaway production is small, i.e. if the PMTX hard X-ray detector (section 3.4.2.2) signal is negligibly small. Otherwise the proper isolation of the 2.45 MeV fusion born neutron contribution from the measured signal would require a neutron energy spectrometer [128].

The total flux of neutrons through a space point x_i is then obtained by integration over space points being potential sources of neutrons (i.e. the plasma volume)

$$\Phi_n(\mathbf{x}_i) = \frac{1}{4\pi} \int_{V_{\text{plasma}}} \frac{\mathrm{d}\Phi_n}{(\mathbf{x}_j - \mathbf{x}_i)^2}\, \mathrm{d}\mathbf{x}_j \tag{3.5.10}$$

where the neutrons scattered by light atoms (air in the torus hall, concrete structure of the reactor bioshield) are neglected. The first contribution is in general negligible, the second is partly avoidable with a detector neutron shield for incidence directions other than those originating from the plasma.

The neutron flux recorded by an absolutely calibrated neutron detector located at x_i is then modelled by eqns.(3.5.2)–(3.5.10). The parameters of the ion distribution function in the modelled flux are iteratively adjusted for convergence to the experimental value.

This T_i recovery procedure is simple for a plasma with Maxwellian ion velocity distribution, where only the two parameters characterising the ion population (n_D and T_i) have to be iterated. In this case, the reaction rate coefficient is well approximated [129] by

$$\langle \sigma_n v \rangle \approx \frac{3.5 \times 10^{20}}{T_i^{3/2}} \exp\left(-\frac{20.1}{\sqrt[3]{T_i}} \right). \tag{3.5.11}$$

Through the strong energy dependence of its cross section, neutron production susceptibly depends on the detailed structure of the distribution function. For non-thermal distributions, further assumptions must be made (bi-Maxwellian distribution, suprathermal population strength) and eq.(3.5.3) needs eventually numerical integration. Useful analytic expressions for anisotropic velocity distribution functions are available in [130].

The error bar on the deuterium ion temperature is calculated from the error on the experimental profiles for n_e, Z_{eff} and the statistical error $1/\sqrt{N}$, with N the number of recorded neutrons, as the neutron production follows a Poissonian distribution.

3.5.2 ^{3}He tube

Neutrons can penetrate deeply into matter without experiencing any collisions. Direct detection of a neutron is therefore impossible and a neutron diagnostic relies on the detection of the emission of secondary charged particles released upon a nuclear reaction triggered by an incoming neutron inside a target volume [131], typically filled with a noble gas.

^{3}He is the most important isotope in instrumentation for neutron detection. A neutron entering the gas undergoes the nuclear reaction

$$^3_2\text{He} + {}^1_0n \rightarrow {}^3_1\text{T}(191\text{ keV}) + {}^1_1p(573\text{ keV}) \tag{3.5.12}$$

and the charged reaction products ionise surrounding ^{3}He gas molecules along their trajectories. The released electrons are accelerated towards the axis of the cylindrical tube, where an electrode at high positive potential creates an intense radial electric field. On their way towards the anode the electrons collide with the filling gas molecules and may ionise more of them giving rise to a townsend avalanche. The electron cloud is then collected on the anode. As explained in the section about the DMPX (section 2.5.3.2), each avalanche causes a surge in the detector output signal, which, if the high voltage was chosen appropriately, can be made approximately proportional to the energy deposited by the nuclear reaction products in the filling gas.

Reaction (3.5.12) has a large cross section at thermal energies ($E \simeq 1/40$ eV) and strongly decays with increasing neutron energy (figure 3.5.2a). Fusion born neutrons (in our case $E_n = 2.45$ MeV) are far too energetic for detection in a He^3 tube and must first be thermalised. This is conveniently performed by elastic collisions with light nuclei contained in materials surrounding the helium tube, that is moderators containing hydrogen.

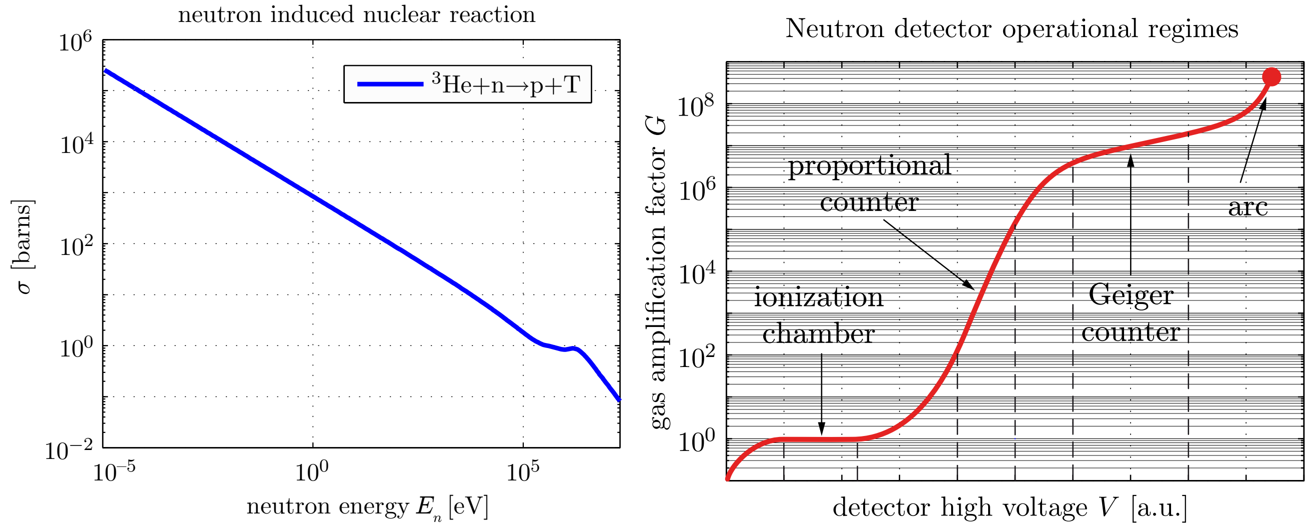

(a) Neutron detection principle.

(b) Neutron detector regimes.

Figure 3.5.2: (a) Behaviour of the nuclear reaction, eq.(3.5.12), playing the key role in the neutron detection. (b) Gas amplification factor G (e.g. the number of electrons collected on the anode per incident neutron) as a function of the anode high voltage. The neutron detector on TCV is operated in the proportional counting regime, where each neutron causes an avalanche such that the number of secondary electrons has a linear dependence on the neutron energy. The tube works as an ionisation chamber ($G = 1$, no avalanche) at lower voltage and as a Geiger-Müller counter (multiple avalanching leading to anode pulses which are independent of the neutron energy) at higher voltage.

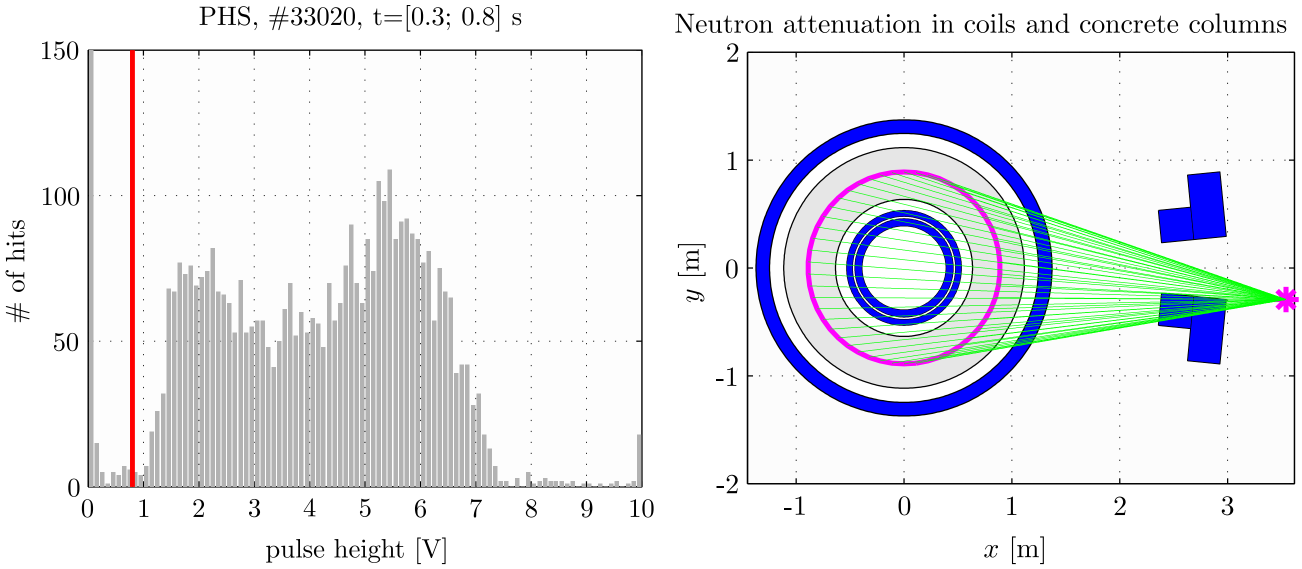

(a) Pulse height spectrum.

(b) Measurement matrix.

Figure 3.5.3: (a) Pulse height distribution of the neutron detector output signal, accumulated over half a second. Most of the pulses are of low amplitude, the lowest bin has seen more than ten times the pulses recorded in all other bins. The total number of neutron encounters is obtained by summation of the pulse height spectrum on the right hand side of the vertical red line (representing the threshold voltage $U_{\text{thres}} = 0.85$ V).
(b) Geometrical arrangement of the neutron detector on TCV. Sampling of the magnetic axis (circle in magenta) as seen from the detector. Neutron attenuation in the transformer coils A (innermost blue ring), and inner (E) and outer poloidal coils (F), see figure 2.3.1, are considered. The detector solid angle partly intercepts a massive concrete column (on the right).

The neutron detector on TCV consists of a helium filled tube (type 18NH10) manufactured by Canberra [132]. The detector has a diameter of $\o = 2.5$ cm, an active length of $\ell = 100$ cm and the gas pressure is $p = 6$ bar. The tube is surrounded by a moderator made of polyethylene with a wall thickness of $\Delta x = 6.5$ cm, optimised for effective neutron thermalisation without exaggerated scattering and absorption losses [133]. Detector and moderator are encapsulated in a soft iron cylinder to remove the residual magnetic field. The tube is vertically oriented and mounted on a movable support at a height to have its tube centre at the tokamak midplane. High count rates without saturation are obtained at a distance of approximately $x = 2.2$ m from the torus.

The anode high voltage is configured for proportional neutron counting such that the anode pulse peak is proportional to the energy of the incident neutron (proportional counting regime, see figure 3.5.2b). The anode signal is DC filtered, processed using a Canberra ACHNA98 charge amplifier and acquired with a transient digitiser sampling at a frequency up to 1 MHz. The ionisation of the filling gas by means of X-rays generates many output pulses with low amplitude. Real neutron hits are identified from the acquired signal by pulse height analysis. Figure 3.5.3a shows an example, the threshold for pulse counting has to be set to approximately $U_{\text{thres}} = 0.5 \ldots 1$ V here, the pulses in the bins below have to be discarded. Note that the lowest bins are mostly populated by electronic noise in the charge amplifier. For proportional counters one may expect to see the neutron contribution as a narrow peak on the pulse height spectrum, as the kinetic energy deposited in the gas amounts to 764 keV, see reaction (3.5.12). The broad measured neutron contribution shown is due to the finite size of the gas chamber as the reaction products may be partially absorbed by the detector chamber wall before their whole kinetic energy is deposited in the gas.

Neutron detector measurements are not exploited if the parasitic counts overlap the neutron contribution or if the count rate exceeds the detector saturation limit ($>5\times10^4$ neutrons/second).

3.5.3 Detector calibration

The effective surface and absolute sensitivity of the detector were determined ten years ago [133] using the decay of Americium ^{241}Am/Be [134]. A source with an activity of 10 mCu (>2×10^4 n/s) was used.

Depending on the placement of the detector in the torus hall, the neutron attenuation in the most relevant tokamak structure elements, namely coils and concrete columns [135], are modelled knowing their materials, position and geometries. Elastic scattering was neglected in these attenuators. The geometrical arrangement of these structures is depicted in figure 3.5.3b.

3.6 Comparison summary of T_i diagnostics on TCV

The measurement principles and some technical details of the ion diagnostics available on TCV were presented in this chapter. For a tokamak, whose experimental program is strongly devoted to explore the physics of the electrons, the available set of ion diagnostics is quite formidable.

Table 3.2 summarises the capabilities and limitations of the various diagnostic techniques.

Diagnostic	**DNBI+CXRS**	**VNPA**	**CNPA**	**NEUT**
measurement principle	charge exchange recombination luminance	hydrogenic neutral flux	light atoms flux	neutron flux
measured ion parameters	T_{iC}, n_{iC} v_{iC}	$f_{iH+D\perp}$	$f_{iD\perp}$, $f_{iH\perp}/f_{iHe\perp}$	fusion reactivity
derivable parameters	Z_{eff}	n^0_{H+D}	n^0_D, n^0_H/n^0_{He}	T_{iD}, n_{iD}
spatial measurement	local 20/40 locations	vertically line integrated	horizontally line integrated	global
diagnosed ion population	bulk	rather bulk	bulk+tail	mainly tail
typical time resolution	30 ms	13 ms	2.5 ms	1 ms
electron densities [m^{-3}](††)	$< 6 \times 10^{19}$	$< 3 \ldots 4 \times 10^{19}$	$< 6 \ldots 8 \times 10^{19}$	$> 2 \times 10^{19}$
spurious detection	green light	Hard X-rays	HXR, ultra-violet, light	Hard X-rays
operated	on demand	by default	by default	on demand
current availability	78 % (when requested)	> 90 %	> 85 %	< 2 % (average of ten years)

Table 3.2: Comparison of key parameters of the ion diagnostics on TCV. Except for the neutron detector, which is rarely used, the numbers of availability for operation represent the score of successful measurements whenever the diagnostic was selected by the operator.

(††) for the retrieval of the core ion temperature.

Strong effort was expended to successfully exploit the measurements of the Compact NPA under extreme experimental conditions. Over the five last years, the measures taken for appropriate shielding against parasitic signal sources have been advanced strongly and the diagnostic is now outstandingly well fitted to operate safely and satisfactorily during practically all recent experimental campaigns on TCV.

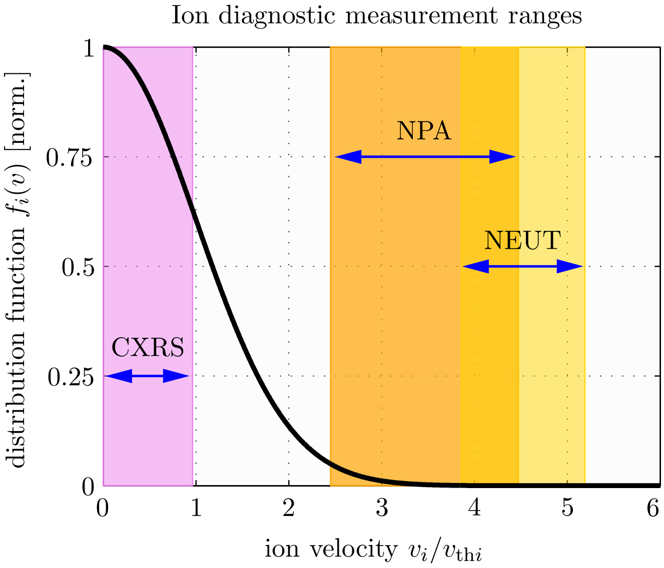

Figure 3.6.1: Example of the experimental investigation of a Maxwellian distribution function ($T_i = 400$ eV) in velocity space with the ion diagnostics available on the TCV tokamak. The hatched velocity ranges illustrate the approximate region of operation of the corresponding diagnostics. For CXRS this corresponds to the wavelength domain mapped onto the active CCD area, $\Delta v = c\Delta\lambda/\lambda_0$. The NPA range is representative of the particle velocity span of the CNPA deuterium array. The neutron detector velocity range was chosen to correspond to the FWHM of the neutron production spectrum $f_{i\mathrm{D}}\sigma_{\mathrm{DD}}$ (shown in figure 3.5.1b).

Although the quantities derived from the measurements of the different ion diagnostics are somewhat redundant, each technique has its own peculiarities, making them complementary. Note that each type of diagnostic probes the ions in different ranges of energies. In the ideal case the plasma ion velocities are distributed according to a Maxwell-Boltzmann distribution. The different diagnostic measurement ranges illustrated in figure 3.6.1 are then linked by a known function, parameterised by one single parameter – the ion temperature – and the determination of its value with the different techniques will agree. Various examples illustrating either agreement or disagreement will be discussed in the next chapters.

Chapter 4

Neutral particle analysis of thermal TCV plasmas

This chapter describes various results obtained with neutral particle measurements of thermal TCV plasmas. The first section introduces selected elements of the physics of neutral particle analysis. The underlying theory is verified using simple one-dimensional modelling in sections 4.2 (plasma permeation by cold neutral gas) and 4.3 (plasma neutral particle exit flux measured with the neutral particle analysers). A diagnostic experiment is discussed in section 4.4, where the ion temperature profile was directly measured by a displacement of the plasma across the NPA line of sight. Section 4.6 demonstrates that integrated modelling of the NPA measurement is sufficient to iteratively extract the ion temperature profile from one single charge exchange flux spectrum. More advanced modelling of the neutral emissivity using a 2D particle code is presented in section 4.7 and applied to active charge exchange measurements (section 4.8), used for the absolute calibration of the NPA. The NPA ion temperature measurement is then validated against the other ion diagnostics (section 4.9). The behaviour of the ions in thermal TCV plasmas is finally summarised in section 4.10.

	reaction	E(*) [eV]	$\langle\sigma v\rangle$(*) [m^3 s^{-1}]	**type**
(a)	$H_2 + e \rightarrow 2\,H + e$	15	1×10^{-14}	dissociation
(b)	$H_2 + e \rightarrow H + H^+ + 2\,e$	125	2.5×10^{-15}	dissociative ionisation
(c)	$H_2^+ + e \rightarrow H + H^+ + e$	$\sim$100	1×10^{-14}	dissociation
(d)	$H_2^+ + e \rightarrow 2\,H^+ + 2\,e$	$\sim$100	1×10^{-13}	dissociative ionisation
(e)	$H_2^+ + e \rightarrow 2\,H$	10	1×10^{-14}	dissociative recombination
(f)	$H_2 + H_2^+ \rightarrow H + H_3^+$	1	1×10^{-15}	
(g)	$H_3^+ + e \rightarrow 3\,H$	1	6×10^{-14}	recombination
(h)	$H + H^+ \rightarrow H_2^+$	10^5	5×10^{-14}	
(i)	$H^+ + H_2 \rightarrow H_3^+$	10^5	8×10^{-14}	
(j)	$H + e \rightarrow H^+ + 2\,e$	100	3×10^{-14}	ionisation
(k)	$H_2 + e \rightarrow H_2^+ + 2\,e$	100	5×10^{-14}	molecular ionisation
(l)	$H^+ + H_2 \rightarrow H + H_2^+$	-	-	charge exchange
(m)	$H + H^+ \rightarrow H + H^+$	-	-	charge exchange
(n)	$H_2 + H_2^+ \rightarrow H_2 + H_2^+$	-	-	charge exchange

Table 4.1: Listing of the reactions relevant for neutral particle analysis in a tokamak plasma.

(*) the tabulated energy corresponds to the location of the maximum in the rate coefficient.

4.1 Neutral targets for charge exchange reactions

Thus far the origin of the neutral flux escaping the plasma was discussed rather qualitatively (section 3.3.1), here a more quantitative discussion is given. For this, the mechanisms that take neutrals into and out of a hot plasma are briefly reviewed. These processes are, in turn, governed by a number of collisional interactions between neutrals and charged plasma particles.

4.1.1 Collision processes involving neutrals

The description of the survival of neutral particles inside the plasma column is quite complicated due to the large number of possible interactions with the charged particles of the background plasma [136]. Ionising collisions are a sink of neutrals, recombination a source and charge exchange reactions alter the energy of the neutral population.

Table 4.1 shows a list of tokamak relevant reactions, figure 3.3.1 shows the corresponding rate coefficients as a function of temperature for some of the most important reactions inside the plasma, namely:

- **electron-impact ionisation** doesn't occur if the energy of the impacting electron is below the ionisation potential (13.6 eV for a hydrogen atom), but then dramatically increases to attain a maximum value of $\sim\pi a_0^2$ (hence the analogy with a spatial section, as a_0 is the Bohr radius of the hydrogen atom) at an energy where the deBroglie wavelength of the electron has approximately the dimension of the hydrogen atom. Because electrons move generally more rapidly than ions the motion of the atom will not affect this type of collision until the translational energy of the atom exceeds that of the electrons by a factor m_i/m_e. One can thus usually approximate the ionisation rate as independent of velocity. The effective cross section for an atom moving through a distribution of electrons therefore is

  $$\sigma_{\text{ion}} = \frac{\langle \sigma_{ei} v_e \rangle}{v_a}, \tag{4.1.1}$$

  where $\langle \sigma_{ei} v_e \rangle$ is the electron ionisation rate coefficient and v_e and v_a are the electron and atom velocity respectively.

- **ion-impact ionisation** ejects the electron from the target atom. The cross section of this process has a dependence on energy similar to the electron-impact ionisation, but the projectile ion must have an energy that is a factor m_i/m_e higher in this case.

- **charge-exchange**, as already mentioned in section 3.3.1, transfers the electron from the atom to the impacting ion. If the atom formed is of the same species as the incident atom, the process need involve no change in energy of the bound electron other than the transitional energy change associated with the different atomic velocities. The charge-exchange process is then resonant between atomic levels of the same energy (usually the ground state). The transfer probability is high even for slow encounters and with impact parameters up to $10 \times a_0$, the cross section is as high as $50\pi a_0^2$ [137] and increases for lower relative kinetic energies, since the interaction time is then longer. Since ions move more slowly than electrons by the ratio m_e/m_i, the translation will have a small effect for collision energies less than about $R_y m_i/m_e \simeq 25$ keV for hydrogen. If the relative velocity exceeds the electron orbital velocity, the resonance breaks and the cross section drops rapidly.

In the absence of neutral transport, the local neutral particle balance equation is a sum over all possible reactions of neutrals with plasma particles and each other,

$$\frac{\mathrm{d}n_0(\rho)}{\mathrm{d}t} = \sum f_0\, n_0(\rho)\, f_j\, n_j(\rho)\, \langle \sigma_{0j} v_j \rangle\,, \tag{4.1.2}$$

where f_j is the reacting particle and f_0 the unknown neutral velocity distribution function, normalised by the number of particles in the population. Eq.(4.1.2) is valid if the density and temperature of the particles do not significantly change over the neutral mean free path between collisions.

As shown in figure 3.3.1, the charge exchange rate dominates over the ionisation processes, a neutral inside the plasma may therefore undergo multiple charge exchange reactions before ionising.

4.1.2 Plasma penetration by neutrals

There are three possibilities for neutrals to penetrate inside an ionised plasma:

(a) transport of vessel wall recycled neutrals into the plasma,

(b) radiative recombination of plasma ions with plasma electrons and

(c) injection of neutral beams.

The additional neutral deposition by the diagnostic neutral beam on TCV was described in section 3.2. An application of such a local neutral density enhancement will be discussed in section 4.8 (active charge exchange). However the DNBI source rate ($\sim 10^{19}$ neutrals per second) is insignificant in comparison with the total neutral influx from the plasma edge.

Radiative recombination occurs when a ion captures a free electron, which is then in a bound state, reactions (e) and (g) in table 4.1. Light is emitted to compensate the loss of kinetic energy of the electron. But recombination is a less probable process, with a recombination rate six to seven orders of magnitude smaller than the sum of the ionisation rates (figure 3.3.1). Recombination has to be considered for high density plasmas only [138], say above 8×10^{19} m^{-3}.

For the rather low density plasmas studied with NPA on TCV, recombination may often be neglected. The most relevant neutral source is therefore from the plasma periphery, where lost plasma particles are soon neutralised at the intersection of the open magnetic field lines with the vacuum vessel wall and then reenter the plasma as neutral molecules (particle recycling). Molecular replacement gas (hydrogen, deuterium or helium) is also puffed at the edge, highly unionised particles are therefore by far the most abundant occupants of the plasma surroundings. Chemical reactions with other ion species (oxygen, carbon) may also influence the neutral population at the plasma edge [139]. Cold ($\sim$ambient temperature) wall desorbed neutrals have velocities typically $v_0(a) = 10^3$ m/s when they cross the last closed flux surface (LCFS) where electron densities of $0.5 < n_e < 5 \times 10^{19}$ m^{-3} and electron temperatures of $20 < T_e < 200$ eV are typically found. For these conditions the rate for direct ionisation of molecular hydrogen is $\sim 2 \times 10^{-8}$ m^{3}s^{-1} and the mean free path,

$$\lambda = \frac{v_0}{n_e \langle \sigma v \rangle_{\text{ion}}}, \tag{4.1.3}$$

is of the order of a centimetre, much smaller than the size of the plasma (TCV has a minor radius $a = 25$ cm).

Molecular neutrals are therefore only found at the very edge of the plasma. But ionisation is not the only fate of molecular neutrals, at typical edge temperatures (5…50 eV), H_2 are efficiently dissociated by electron impact, reaction (a) in table 4.1. The resulting Frank-Condon atoms have a mean free path of 10 cm and higher at low edge densities, as for X2-ECRH heated discharges (chapter 5). Moreover, unlike molecular neutrals, atomic neutrals may penetrate into the plasma in a diffusive-like manner by a sequence of charge-exchange interactions until ionisation occurs. As the charge exchange cross section is larger than the atomic ionisation cross section this sequence may persist for some time. Too, with each charge exchange the slow neutral is replaced by a faster one. With subsequent increase in v_0, λ is enlarged and may become larger than the plasma column. λ therefore depends on the ion temperature.

To summarise, the neutral concentration in the plasma core is essentially determined by the balance between ionisation and neutrals entering the plasma from the wall. The balance depends on neutral velocity v_0, neutral n_0 and electron density n_e. On TCV the electron properties are determined from measurements inside (Thomson scattering or interferometry) and outside the plasma (Langmuir probes). The neutral properties are difficult to determine experimentally inside the plasma (optical measurements with large uncertainties), the neutral velocity may be estimated from vessel tile temperature measurements and the neutral gas pressure (measured using gauges).

4.1.3 Neutral pressure gauge (IOMAN)

Mainly for studies of diverter detachment [140], TCV was equipped with fast pressure gauges of the type installed on ASDEX [141]. One of those was located at the outer midplane, with its gauge head aligned with the magnetic field and standing out from the wall by a few cm.

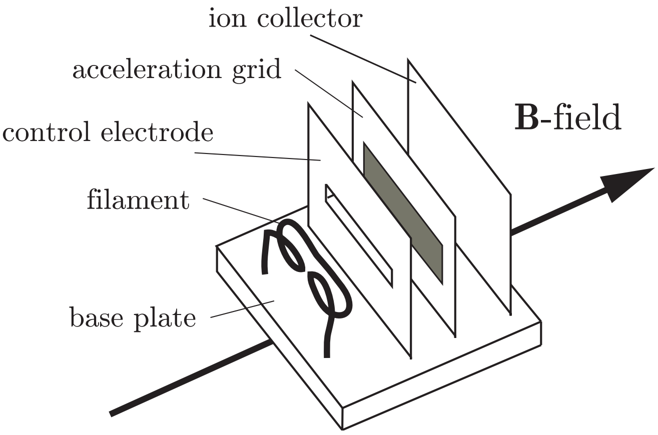

Figure 4.1.1: Sketch of the fast pressure gauge head.

A schematic of the gauge head is sketched in figure 4.1.1 and consists of:

- A filament as thermal electron source ($U_\mathrm{F} = 50$ V, $I_\mathrm{F} \leqslant 20$ A),
- a control grid with horizontal slit whose potential is chopped at some kHz between 25 and 105 V,
- an acceleration grid (potential at 250 V) with multiple vertical slits and
- an ion collector plate

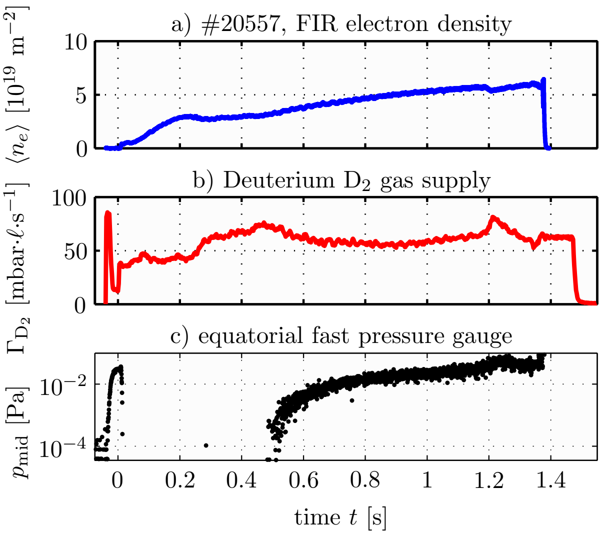

Figure 4.1.2: Time traces of (a) electron density, (b) gas supply and (c) edge neutral pressure measured with the midplane fast gauge.

The electrons emitted by the filament oscillate in the potential between filament and the collector plate until they collide with other particles or with the acceleration grid, where they give rise to the measured electron emission current I_{ce}. The tokamak magnetic field amplifies the electron emission and enhances the electron lifetime in the ionisation volume. The measured ion collector current I_{ci} is proportional to the neutral density in the gauge,

$$p_{\rm neutral} = S\frac{I_{ci}}{I_{ce} - I_{ci}}, \tag{4.1.4}$$

where the calibration coefficient S is determined off line by immersion of the gauge into a magnetic field similar to TCV and thermal gas of known density. The gauge head is equipped with a metallic cover to protect the electrodes against arcs. Neutral gas penetrates through a small orifice, limiting the time resolution of the gauge measurement to 2. . . 4 ms. Figure 4.1.2 shows the line integrated electron density (measured by FIR), gas puff flowmeter and calibrated fast pressure gauge measurements for a deuterium discharge on TCV. Unfortunately the collector current noise level is too strong for a valuable determination of the neutral density at $\overline{n}_e < 4 \times 10^{19}$ m^{-3}, i.e. most of the discharges studied within this thesis. The gauge was damaged in 2003 and has yet to be repaired.

4.2 Modelling of neutral particle transport

Proper calculation of the neutral density profiles requires numerical codes which follow the neutral trajectories from the edge to the plasma core. Within closed flux surfaces of a steady state plasma, the neutral fluid transport equations

$$\begin{aligned} \nabla\left(-D\nabla n_e + V n_e\right) &= n_e n_0 S_{\rm ion} - n_e^2 S_{\rm rec} && (4.2.1)\\ \nabla\left(n_0 v_0\right) &= -n_e n_0 S_{\rm ion} + n_e^2 S_{\rm rec} && (4.2.2)\end{aligned}$$

describe the electron n_e and neutral n_0 densities. $S_{\rm ion}$ is the neutral particle sink due to ionisation processes, $S_{\rm rec}$ the neutral source term due to recombination, D and V are the radial electron diffusivity and pinch velocity and v_0 the neutral fluid velocity.

As neutrals are not confined by the magnetic field some of the available codes are 2D or even 3D in real space. The linear transport solver *EIRENE* [142], for example, uses the Monte Carlo technique to track neutrals entering the plasma and includes a very precise 2D description of the plasma facing surfaces. *EIRENE* provides realistic results for the low temperature plasma edge within a reasonable computation time, but the computational effort increases tremendously for calculations covering regions deeper inside the plasma.

The simulation of the NPA measurement requires the neutral concentration in the plasma core to be assessed properly. Fortunately the number of atomic processes of relevance inside the LCFS is strongly reduced and the neutral flux can be satisfactorily calculated using spatially one-dimensional kinetic or fluid codes. Such codes show reasonable agreement with sophisticated multidimensional codes beyond the LCFS [143].

4.2.1 Kinetic neutral transport algorithm (*KN1D*)

KN1D [144] is a kinetic transport solver for atomic and molecular hydrogen or deuterium velocity distribution functions in a one dimensional, slab-like geometry for a plasma with known background profiles. The numerical algorithm includes charge exchange collisions, electron-impact ionisation and dissociation, elastic self-collisions (atomic and molecular), and a variety of elastic cross-collisions among heavy particles (atoms, ions and molecules). *KN1D* is written in IDL and was implemented at CRPP for the TCV geometry interfacing with the experimental database.

The geometry adopted are (a) the chamber wall surface, (b) the scrape-of-layer (SOL) and (c) the core plasma. The code calculates the neutral properties along the diagnostic chord of the CNPA or VNPA.

To take account of the real (elongated) plasma geometry, the neutral penetration for each point on the diagnostic chord inside the plasma is calculated along a straight spatial grid aligned along the **shortest** distance from the LCFS, that is not necessarily along the diagnostic chord. This is especially important for the vertical viewing VNPA in elongated plasmas (core neutrals come predominantly from the in- or outboard side depending on the plasma shape) and for plasmas above the midplane investigated using the CNPA (core neutrals enter from the bottom). This approach is justified by the short mean free path of wall neutrals inside the plasma, most of the neutrals present at a certain plasma location have arrived there along the shortest path from the boundary. However, the 1D simulated core neutral concentration will be the upper limit for the experiment, in 2D (large edge and small core volumes) the real neutral influx to the core is expected to be smaller than predicted in this way.

L-mode discharges on TCV are limited on the inner vessel wall, the inner SOL length is therefore set to zero. The upper, lower or outer SOL lengths correspond to the distance from the intersection of the NPA chord with the LCFS to the upper, lower or outer vessel wall.

The experimental plasma profiles are mapped to the diagnostic chord using the geometry of the reconstructed equilibrium using the Ψ-toolbox [145]. Electron density and temperature profiles are mostly taken from the Thomson scattering diagnostic, the ion temperature profile from CXRS (this will be justified in section 4.9.2). The profiles outside the LCFS are not routinely measured, exponential decay profiles in agreement with Langmuir probe data [146] are usually adopted, with typical wall temperature $T_e(a) = 10$ eV and density $n_e(a) = n_e(\rho = 1)/3$. The recycled neutrals are at ambient temperature when they leave the wall. All particles are assumed to have Maxwellian velocity distribution functions. The free parameter of the simulation is the neutral edge gas pressure p_a, which is taken to be uniform everywhere around the plasma. Note that the calculated *KN1D* density profiles are linear in p_a.

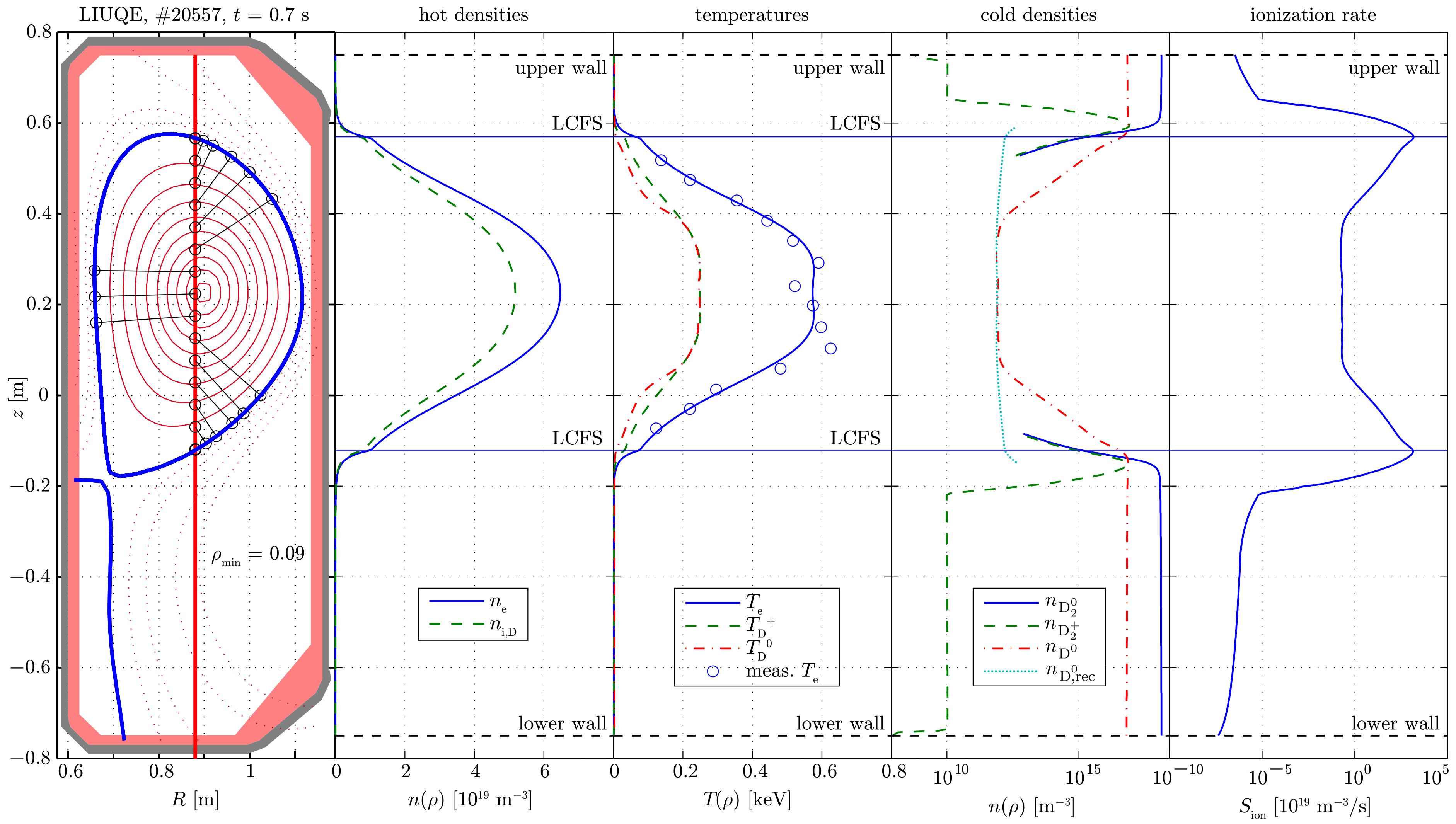

Figure 4.2.1: Modelling of the neutral density profiles along the view line of the VNPA with the *KN1D* code for the diverted discharge #20557. To obtain the neutral profiles (forth subplot), *KN1D* was run 15 times, with its geometry aligned along the lines of the barbells shown in the poloidal cross section. For each highlighted point along the VNPA line of sight, these lines connect to the closest location on the LCFS. n_e (SVD-I FIR), T_e, T_i and n_i are code input parameters, the neutral temperature T_D^0, the "cold" molecular ion, molecular neutral and atomic neutral densities plus the ionisation rate are returned by *KN1D*. The case shown is a higher density discharge, the neutral density in the core is uniquely due to recombination, *KN1D* reproduces the recombination level (dotted curve) estimated from eq.(4.2.3).

Figure 4.2.1 shows results obtained with *KN1D* for a diverted Deuterium plasma of mid range core electron density, #20557, $t = 0.7$ s, $n_e(0) = 6 \times 10^{19}$ m^{-3}, where the neutral profiles were calculated along the view line (vertical line at $R = 0.88$ m) of the VNPA (the CNPA was not installed yet on TCV). At the modelled time instant the divertor leg is detached from the plasma wall. The second sub-figure shows electron (SVD inverted FIR measurement) and hydrogenic ion density profiles mapped to the VNPA chord, the ion density profile was obtained from eq.(3.5.6) using $Z_{\text{eff}} = 2.1$ (constant over the profile), derived from the measured plasma Bremsstrahlung radiation and assuming carbon as the only plasma impurity. The positions of intersection of the LCFS with the diagnostic chord are indicated by the two stroked horizontal lines. The efficient separation of the plasma from the vessel exhibits a considerable electron density even at the LCFS, $n_e(\rho{=}1) = 1 \times 10^{19}$ m^{-3}. The third sub-figure shows the electron temperature measured with the Thomson scattering diagnostic (round symbols) together with the interpolated profile inputted to *KN1D*. Measurement of the ion temperature profile using CXRS was not yet available for this discharge, the ion profile (- -) was taken to be of the same shape as the electron temperature profile, scaled by $T_i(0)$ determined from the VNPA (section 4.3.3). The neutral temperature profile (-·-) shown is calculated by *KN1D*. The forth sub-figure shows the *KN1D* calculated deuterium molecular neutral (straight line), molecular ion (- -) and atomic neutral (-·-) density profiles and the last sub-figure the ionisation rate S_{ion} entering eq.(4.2.1) and eq.(4.2.2). Note that the neutral edge pressure taken by *KN1D* was $p_{\text{D}_2}(a) = 0.01$ Pa, this is the value measured with the fast pressure gauge at the midplane (figure 4.1.2). The lines linking some points on the VNPA chord to the LCFS (first sub-figure) indicate the 1D calculation grid of *KN1D*, the profiles shown in sub-figure four were actually concatenated from the neutral density obtained from 15 individual runs of *KN1D*. As shown, the shortest distance from the plasma edge to the locus on the VNPA view line runs from the outboard side of the plasma, except at plasma core.

Figure 4.2.2 shows another *KN1D* simulation for a more rarified, $n_e(0) = 1 \times 10^{19}$ m^{-3}, and limited plasma (#27182, $t = 1$ s) almost vertically centred (magnetic axis at $z_{\text{mag}} = 3$ cm) in the vessel. The magnetic configuration is such that the plasma is limited simultaneously on the inner and outer walls, resulting in zero width of the SOL. Here, the neutral particle density profiles were calculated along the horizontal view line of the CNPA and the shortest path from any point of the chord to the LCFS coincides with this chord. *KN1D* required only two runs per isotope species, once for each half of the plasma, considering neutral penetration from the right or left.

Figure 4.2.2 shows *KN1D* simulations for hydrogen and deuterium, the hydrogen concentration was less than 1 % for this discharge (determined using the CNPA, see section 4.9.6.1). Experimental points from Thomson were used for the definition of electron density and electron temperature profiles. Plasma purity was derived from XTOMO ($Z_{\text{eff}} = 1.8$). This time the ion temperature profile was measured using CXRS (circles in the second sub-figure). The ratio of the similar looking neutral profiles, deuterium (top) and hydrogen (bottom), reflect the ratio in the respective neutral edge pressures. The calculated molecular deuterium density profiles are shown in detail in figure 4.2.3.

From the *KN1D* simulations shown so far the following conclusions may be drawn:

- ☞ Molecular neutrals play an important role in neutral fuelling of the plasma only at the very edge, especially at high electron density the molecular density drops to zero within a few centimetres.
- ☞ For TCV conditions, neutral densities vary, from the plasma edge to the plasma core, by a factor $>10^5$.

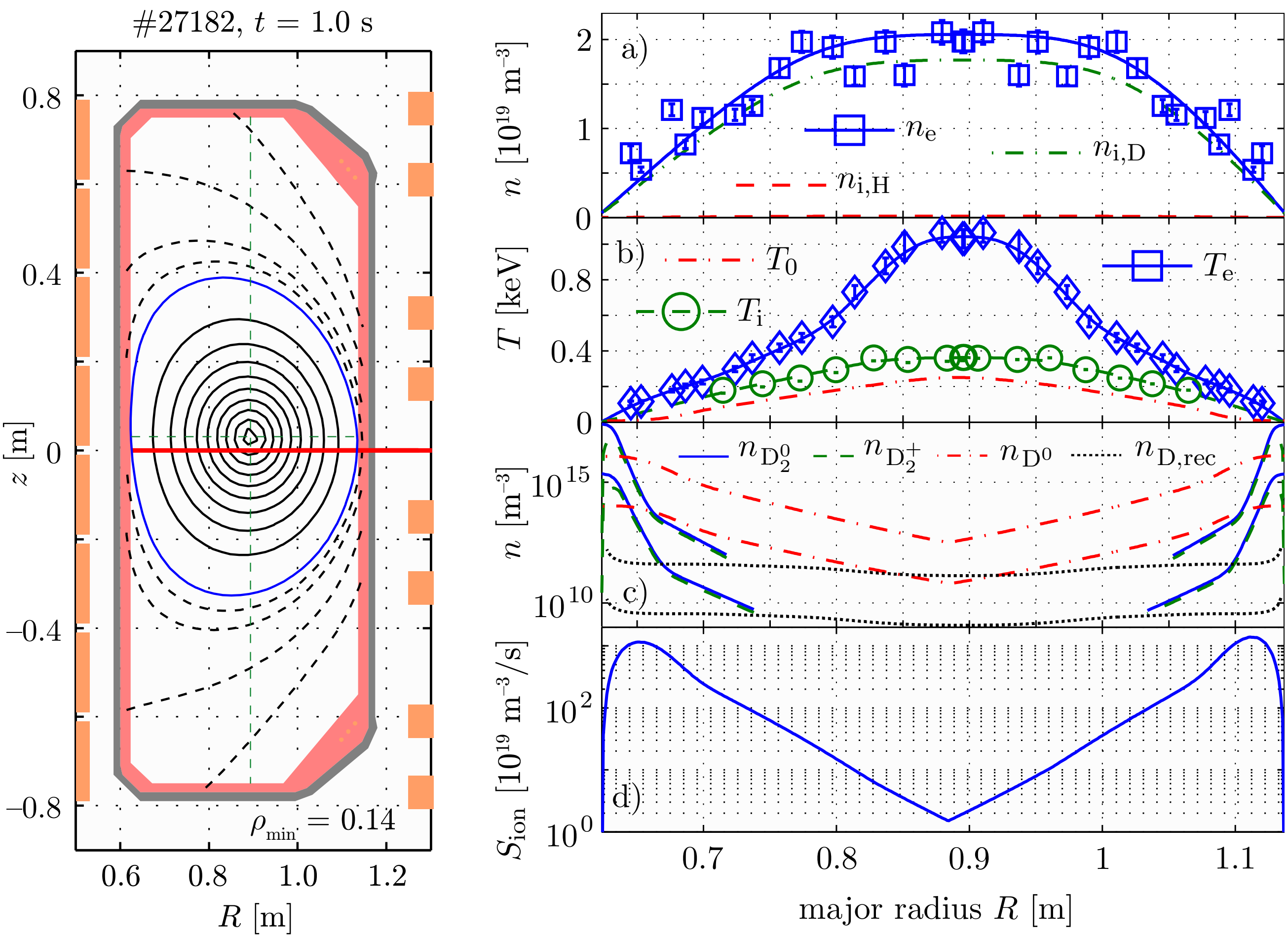

(a) Equilibrium.

(b) *KN1D* inputs and outputs.

Figure 4.2.2: Low density *KN1D* modelling along the line of sight of the CNPA.
(a) The plasma is simultaneously limited on inner and outer walls, such that the SOL profile calculation is omitted. The magnetic axis is located at about 3 cm above the vessel midplane, neutrals found along the CNPA chord came there along that same direction.
(b) *KN1D* was run for H and D separately, the upper set of profiles in the third subplot represents D, the lower H (very low concentration, <1 % of deuterium density).

☞ Multiple charge exchange reactions efficiently heat the neutral particles, at high electron density the ion and neutral populations are thermalised throughout the plasma. This is due to frequent charge exchange at high density and therefore small mean free path between collisions. A neutral arriving at the magnetic axis in a low density plasma has undergone far fewer charge exchange reactions than in a high density discharge and is therefore much colder. The difference in electron and ion temperature will be discussed in section 4.9.1.

☞ At high density, no edge neutrals arrive at the core, the low neutral density in a vast part of the bulk is entirely due to volume recombination. This is due to the strongly enhanced atomic ionisation rate $n_e\, n_i\, S_{\text{ion}}$; for S_{ion} see the last graphs in figures 4.2.1 (subplot 5) and 4.2.2 (subplot 4). The competition between ionisation and recombination yields

$$n_0^{\text{rec}} = n_i \frac{\langle \sigma v \rangle_{\text{rec}}}{\langle \sigma v \rangle_{\text{ion}}}. \tag{4.2.3}$$

The contribution of recombination born neutrals n_0^{rec} is shown in figures 4.2.1 (subplot 4) and 4.2.2 (subplot 3). Volume recombination may be neglected at low density.

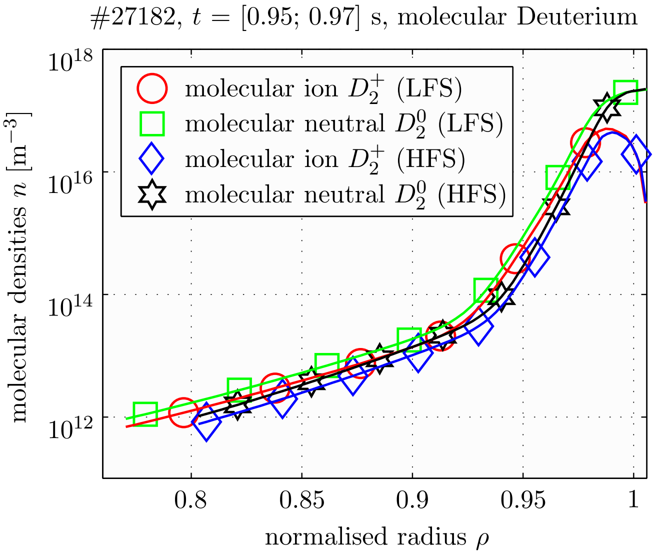

Figure 4.2.3: Densities of molecular neutral deuterium D_2^0 and molecular deuterium ions D_2^+ for the low (LFS) and high field sides (HFS) of the plasma.

4.3 Plasma fast neutral emission

Now we have explained how neutrals get into the plasma, how do they get back out? In the very core of the plasma, a charge exchange collision transfers the captive electron from the neutral atom to a hot ion. The nucleus of the "old" atom is now trapped by the magnetic field whereas the "new" atom continues in the same direction as prior to the charge exchange and carries "memory" of its life as an ion in the vicinity of the collision. We shall call this atom a **fast neutral**, to distinguish it from the more numerous neutrals surrounding the plasma. With the knowledge of the radial neutral particle profile, the local emissivity of fast neutrals may now be calculated from

$$S(\mathbf{v}_i) = f_i(\mathbf{v}_i) \int \sigma_{\mathrm{CX}} \left(|\mathbf{v}_a - \mathbf{v}_i|\right) |\mathbf{v}_a - \mathbf{v}_i| \, f_a(\mathbf{v}_a) \, \mathrm{d}^3 v_a \equiv f_i(\mathbf{v}_i) \left\langle \sigma_{\mathrm{CX}} v_a \right\rangle_{v_i} n_a, \tag{4.3.1}$$

where the subscript i refers to the ion that becomes the neutral and a refers to the atom from which it gains the electron. However, at least for low density plasmas (see the respective temperatures in figure 4.2.2), prior to the collision, the hot ion has an energy significantly in excess of the cold neutral, the relative velocity may be approximated by $|\mathbf{v}_a - \mathbf{v}_i| \approx v_i$ and the local neutral emissivity simplifies to

$$S(\mathbf{v}_i) = f_i(\mathbf{v}_i) \, \sigma_{\mathrm{CX}} \, v_i \, n_a. \tag{4.3.2}$$

4.3.1 Plasma thickness for neutrals

Although the fast neutral has a high velocity v_a, the plasma is not fully transparent to it. The electron loss mechanism discussed in section 4.1.1 may occur along its new trajectory. Thus the probability of a neutral to survive from point A to B without suffering a collision is

$$P_{\mathrm{A}\rightarrow\mathrm{B}} = \exp\left[-\int_{\mathrm{A}}^{\mathrm{B}} \alpha(l) \, \mathrm{d}l\right] \equiv 1 - \gamma, \tag{4.3.3}$$

where γ is the absorption probability and α the mean number of collisions per unit path length, defined as

$$\alpha = \frac{1}{v_a}\left[n_e \left\langle\sigma_{ei} v_e\right\rangle_{v_a} + \left(n_i \left\langle\sigma_{ii} v_i\right\rangle_{v_a} + \left\langle\sigma_{\mathrm{CX}} v_i\right\rangle_{v_a}\right)\right] \approx \frac{n_e \left\langle\sigma_{ei} v_e\right\rangle}{v_a} + n_i\big(\sigma_{ii} + \sigma_{\mathrm{CX}}\big), \qquad (4.3.4)$$

where σ_{CX}, σ_{ei} and σ_{ii} are respectively the cross sections for charge exchange, ionisation by electron and ion impact. Here the charge exchange process has to be considered also, as it replaces the fast neutral by a slow, and from the diagnostic point of view, uninteresting neutral. Figure 3.3.1 shows the reaction rates as a function of electron respectively ion temperature. The charge exchange reaction is the most important fast neutral loss channel for ion temperatures below 10 keV. Note that the neutral mean free path λ increases towards the periphery of the plasma as the ion density n_i decreases. The approximation of α made in eq.(4.3.4) is justified because the background neutrals are much slower than the thermal electrons but usually significantly faster than the ion thermal speed. It is clear that the electron impact ionisation plays a secondary role, at most at low neutral velocities, due to the factor $1/v_a$ in eq.(4.3.4).

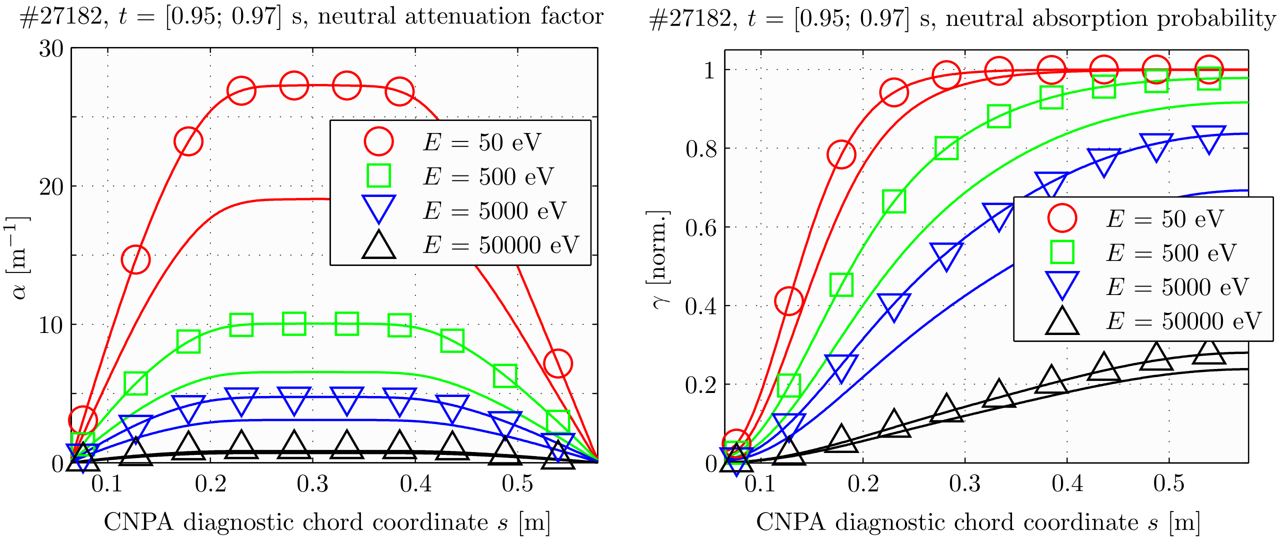

(a) attenuation factor.

(b) absorption probability.

Figure 4.3.1: Survival of neutrals on their journey towards the CNPA pinhole. The abscissae is the CNPA chord length, with its origin coinciding with the CNPA port flange. The lower (upper) limits of the plot match the outer (inner) vessel wall. The curves illustrate again the low density discharge #27182. For each energy shown there are two curves, the upper (labelled with symbols) stands for deuterium, the lower for hydrogen.

Figure 4.3.1a shows the attenuation factor α across a TCV poloidal cross section. The attenuation length $1/\alpha$ for a neutral of energy $E = 5$ keV traversing a plasma of density $n_e = 10^{19}$ m^{-3} is 0.2 m, about the minor radius of a TCV plasma. Figure 4.3.1b shows γ, i.e. the probability for a neutral being absorbed before passing the CNPA gate valve and demonstrates that neutrals with $E \lesssim 1$ keV are quite efficiently reabsorbed. The neutral flux collected by an NPA thus doesn't contain neutrals born in the plasma centre if the line integrated density $\langle n_e\rangle = \int n_e\,\mathrm{d}l$ is too high. On TCV the NPA cannot recover the centre ion temperature for $\langle n_e\rangle \gtrsim 5\times10^{19}$ m^{-2} (see section 4.9.3).

4.3.2 CX spectrum and inference of the core ion temperature

The charge exchange induced production of fast neutral particles throughout the plasma with an outward velocity vector gives rise to a particle flux leaving the plasma. The fraction of the emitted particles detected by an NPA is obtained by integration of the local neutral emissivity over the plasma volume seen by the detector, retaining only particles flying into the cone of acceptance of the NPA.

If the detector solid angle Ω is small, the emissivity in a plane at a certain distance to the detector is approximately constant and the integration is carried out along the detector central view line. For an NPA with étendue $A\Omega$, the neutrals of energies within the interval $\mathrm{d}E$ generate a neutral flux per second (at the NPA entrance window)

$$F(E)\,\mathrm{d}E = v^2\,\mathrm{d}v\,A\Omega \int_{-\rho_{a,\mathrm{HFS}}}^{\rho_{a,\mathrm{LFS}}} \exp\left[-\int_{\rho}^{\rho_{a,\mathrm{LFS}}} \alpha(l)\,\mathrm{d}l\right] S(\rho,\mathbf{v})\;\mathrm{d}\rho, \tag{4.3.5}$$

where $\rho_{a,\mathrm{HFS}}$ and $\rho_{a,\mathrm{LFS}}$ are the normalised chamber wall radii at the high field and low field side respectively. For NPA detector j with central channel energy E_j, channel energy window width ΔE_j and detection efficiency μ_j the relationship between the flux and the N_j secondary ions counted during a period of time Δt is

$$F(E_j) = \frac{N_j}{\Delta t\,\Delta E_j\,\mu_j}. \tag{4.3.6}$$

From the point of view of the NPA diagnostician, as will be shown below, the charge exchange spectrum $G(E)$, is a far more useful quantity, as there is a simple relationship between $G(E)$ and the ion temperature of the diagnosed plasma. The **charge exchange spectrum** is defined as

$$G(E) = \frac{F(E)}{\sigma_{\mathrm{CX}}\,E}. \tag{4.3.7}$$

Indeed, if the velocity distribution function of the ions $f_i(E)$ is thermal, i.e.

$$f_i(E) = n_i\left(\frac{m_i}{2\pi\,T_i}\right)^{3/2} \exp\left(-\frac{E}{T_i}\right), \tag{4.3.8}$$

meaning that an ion temperature T_i is well defined, the charge exchange spectrum, using eq.(4.3.1), for a uniform plasma, may be written

$$G(E) = n_i\,n_a\frac{A\Omega}{(\pi\,T_i)^{3/2}\sqrt{2\,m_i}} \exp\left(-\frac{E}{T_i}\right) \int_{-\rho_{a,\mathrm{HFS}}}^{\rho_{a,\mathrm{LFS}}} \exp\left[-\int_{\rho}^{\rho_{a,\mathrm{LFS}}} \alpha(l)\,\mathrm{d}l\right] \mathrm{d}\rho \tag{4.3.9}$$

and, after differentiation of its logarithm with respect to the energy, one obtains

$$\frac{\mathrm{d}}{\mathrm{d}E}\ln|G| \approx -\frac{1}{T_i} - \left[\int_{\rho_{a,\mathrm{HFS}}}^{\rho_{a,\mathrm{LFS}}} \alpha(l)\,\mathrm{d}l\right] \frac{\mathrm{d}}{\mathrm{d}E}\ln|\alpha|. \tag{4.3.10}$$

The last term is small and may be neglected, as α is largely governed by σ_{CX}, the latter being weakly dependent on energy up to 20 keV (see again figure 3.3.1).

Eq.(4.3.10) shows that, in theory, the ion temperature may be obtained as the negative reciprocal slope of a semi-logarithmic plot of the charge exchange spectrum versus energy, i.e. through

$$T_i^{\mathrm{NPA}}(E) \equiv -\left(\frac{\mathrm{d}}{\mathrm{d}E}\ln\left|\frac{F_{\mathrm{CX}}^{\mathrm{NPA}}(E)}{\sigma_{\mathrm{CX}}(E)\,E}\right|\right)^{-1}. \tag{4.3.11}$$

However, a more realistic plasma exhibits a temperature profile that is not spatially uniform and the flux emanated at the cold edge would thus have a steeper slope on the plot than the contribution from the hot core. In steady state TCV discharges, without additional heating or diagnostic beam injection, the plasma particle energy distribution functions are essentially Maxwellian(†), eq.(4.3.8), with the ion temperature monotonically increasing towards the magnetic axis.
The slope of the measured charge exchange spectrum is representative for the plasma region contributing most to the flux, weak contributions are obscured. To estimate the maximum contribution to the flux the maximum of the integrand of eq.(4.3.5) has to be found. Differentiating in respect to the radial coordinate ρ yields

$$\alpha + \frac{1}{n_a}\frac{\mathrm{d}n_a}{\mathrm{d}\rho} + \frac{1}{n_a}\frac{\mathrm{d}n_a}{\mathrm{d}\rho} + \left(\frac{E}{T_i^2} - \frac{3}{2\,T_i}\right)\frac{\mathrm{d}T_i}{\mathrm{d}\rho} = 0, \tag{4.3.12}$$

where the contribution containing E is the most important if $E \gg T_i$. Roughly speaking, most of the neutral flux is emitted in the region where the temperature profile is flat, that is the plasma core. Another property of the charge exchange spectrum is that at a certain energy $\overline{E}$, the absolute value of the $G(E)$ is not modified when the ion temperature changes. This energy is found by differentiating eq.(4.3.9) with respect to T_i and setting the derivative equal to zero, giving $\overline{E} = \frac{3}{2}T_i$. This means that for energies above $\overline{E}$ the logarithmic slope of the charge exchange spectrum is thus characteristic of the hottest temperature probed by the NPA chord.

4.3.3 Measured spectrum slope fit and accuracy of $T_i(0)$ estimation

Figure 4.3.2a shows the CNPA charge exchange spectrum (hydrogen and deuterium detector array) measured for discharge #27182.

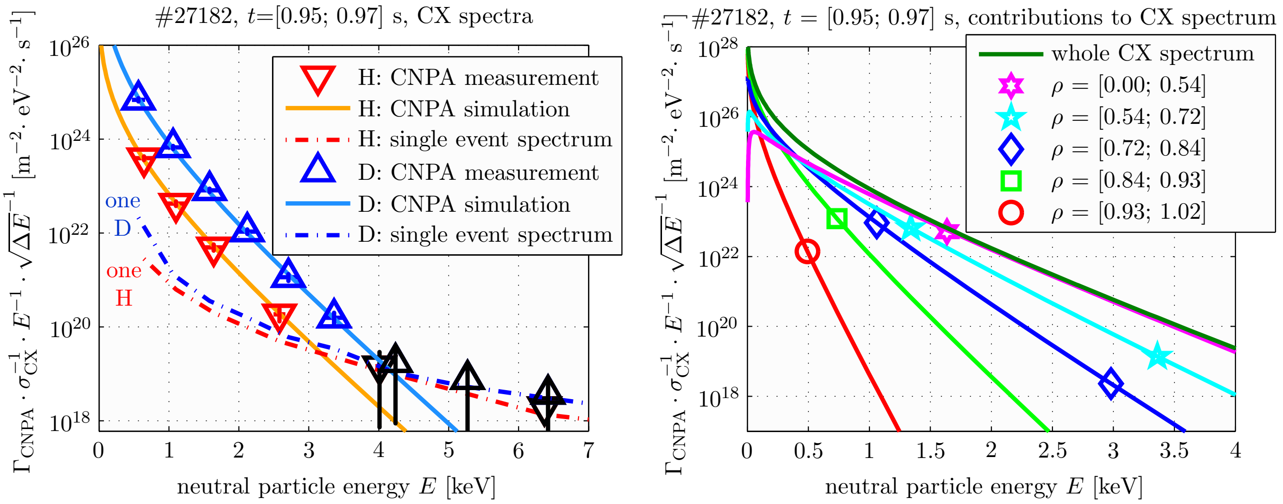

(a) measured CX spectrum.
(b) contributions to the CX spectrum.

Figure 4.3.2: (a) CNPA charge exchange spectrum for discharge #27182, averaged over $t = [0.95; 0.97]$ s (triangles). The lower curve shows the hydrogen flux, the upper deuterium. The statistics of counted particles in channels above 4 keV is insufficient, the events "one counted particle in the time interval considered" are indicated by the discontinuous lines.
(b) Decomposition of the calculated charge exchange spectrum (upmost curve) into contributions from distinct spatial regions. The calculation was performed with the *KN1D* code (section 4.2.1), supplemented with the equations presented in section 4.3.2.

(†) For such distributions, neutral particles of a particular energy will originate from all plasma radii.

Evidently, as the slope of the spectrum is not entirely linear, the inferred effective temperature will depend on the particle energy considered; furthermore, the inferred ion temperature increases with particle energy, suggesting that the more energetic neutrals are coming from the hotter plasma regions. At lower energies the spectrum has a steeper slope, indicating a lower temperature. It is the cold plasma edge, surrounded by plentiful neutrals, that contributes most to the flux at these energies (section 4.5). The slope increase is partially compensated by the stronger attenuation of low energy neutrals (figure 4.3.1). Nevertheless, $T_i^{\text{NPA}}(E)$ depends on the energy interval over which the slope is measured that, in ohmic heated plasma discharges on TCV, may lead to differences in the NPA effective ion temperature as high as ∼70 % between the slope obtained for low, $\sim 2{\cdot}T_i(0)$ and high, $\sim 8{\cdot}T_i(0)$ neutral energies. In practice, the slope of the charge exchange spectrum measured by the VNPA or CNPA on TCV is usually determined in the range

$$3 \cdot T_i \leqslant E \leqslant 10 \cdot T_i. \tag{4.3.13}$$

This is common practice of many tokamak NPA operators [147] and is justified by looking at figure 4.3.2b, where the charge exchange spectrum was classified into individual contributions originating from a set of spatial shells of the plasma volume. The extent of these shells correspond to regions where the ion temperature decreases by 20 % each. The core temperature for this discharge is $T_i(0) = 350$ eV (figure 4.2.2), T_i is therefore fitted from the slope of the CX spectrum – according to eq.(4.3.13) – in the range $E = [1; 3.5]$ keV. In this energy range the whole CX spectrum correlates well with the spectrum of the flux contribution from the plasma core. For Maxwellian velocity distribution functions, eq.(4.3.8), the CX flux falls off exponentially with energy, hence the upper energy limit of eq.(4.3.13) takes into account the statistical dispersion of the high energy neutrals, with the result that the charge exchange spectrum flattens (see figure 4.3.2a).

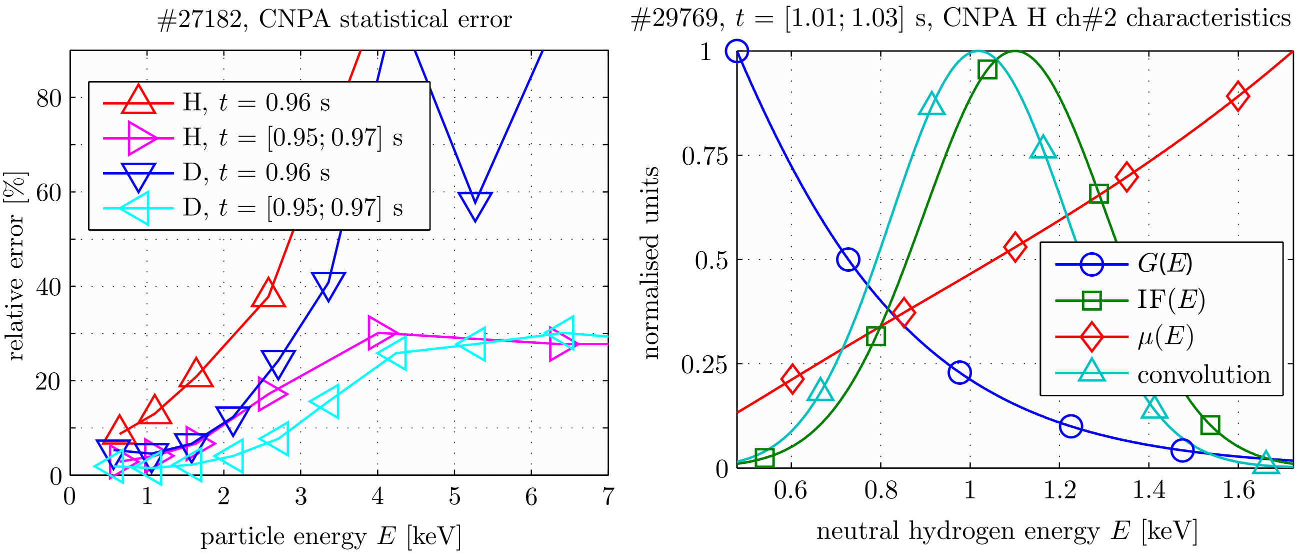

(a) CNPA relative error.

(b) CX spectrum energy correction.

Figure 4.3.3: (a) Error bars on the raw CNPA counts for discharge #27182. Shown is the relative error for the low energy channels of hydrogen and deuterium for a single measurement ($t = 0.96$ s, vertically oriented triangles) and if the detector pulses are summed up during 20 ms.
(b) Correction of the CNPA nominal channel energy at the example of hydrogen channel #2 ($E_{\text{H}}^{\text{c}} = 1.1$ keV). The true channel energy response (triangles) is obtained by convoluting the charge exchange spectrum (circles) with the channel instrumental function (squares) and overall detection efficiency (diamonds). The correction results in a channel centre energy lowered by ∼10 %. The dependence of the detection efficiency is obtained by interpolation of μ between neighbouring channels (figure 3.3.7b).

The slope of the CX spectrum is determined by linear regression. As the ion temperature is often, a priori, unknown, an iterative approach for the correct selection of the energy range according to eq.(4.3.13) is adopted.

The straight-line fit is weighted by bi-dimensional uncertainties; these are

- ☞ σ_G: Charge-exchange interactions at the origin of the plasma emitted neutral flux occur at an average rate given by the cross section and each interaction is independent of the others. Such neutrals follow therefore a Poisson distribution. The statistical uncertainty on the counts N is

$$\sigma_N = \frac{1}{\sqrt{N}}. \tag{4.3.14}$$

  The neutral count rate is usually high at low energies such that the Poisson distribution converges nicely towards a Gaussian. For higher energies Poisson predicts events that are much more likely than a Gaussian, high energy channels with low count rates may falsify the temperature inference if they are given too much weight.

  In figure 4.3.2a the dashed line indicates the charge exchange spectrum produced if each detector of the CNPA would have recorded exactly 1 neutral during a period of 20 ms. Of course there is no plasma that would correspond to such a spectrum, but this curve becomes handy whenever the measured charge exchange spectrum drops below this limit. If this happens the ion temperature is inferred only from channels lying above this limit. How this works will be shown in section 4.4.

  The vertical error bar of the charge exchange spectrum σ_G is dominated by eq.(4.3.14), systematic errors (uncertainty of charge exchange cross section σ_{CX}, estimation of the NPA solid angle Ω or detection efficiencies μ) play a minor role, even when σ_N is small). Figure 4.3.3a shows the statistical error of a single CNPA measurement and its reduction when the charge exchange flux is averaged over a time window where the plasma conditions are steady-state. These are the error bars drawn on the charge exchange spectrum in figure 4.3.2a.
  The rate coefficients in the neutral attenuation calculation (section 4.3.1) are double polynomial fits (depending on density and temperature) taken from [148].

- ☞ σ_E: The channel energy width ΔE of the lowest energy hydrogen detector ($E^c_{\mathrm{H}} = 500$ eV) of the CNPA is as large as 70 % of its central value. The minimum channel energy width is more than 10 % ($E^c_{\mathrm{H}} = 50$ keV). The channel instrumental function IF(E) were determined using the in-situ alkali ion source (section 3.3.3.2). For a thermal plasma, as already mentioned, the number of particles entering the diagnostic aperture exponentially decreases with energy, eq.(4.3.9). The maximum flux contribution in a detector therefore doesn't normally occur at the channel centre energy E^c, but somewhat below (above) for high (low) energies. Figure 4.3.3b shows the convolution of the simulated particle flux of discharge #29769, ion temperature $T_i(0) = 600$ eV, and the detection efficiency of hydrogen channel #2. The nominal channel energies E are then corrected to correspond to the energy representing the maximum particle influx to the detector. The error bar on that corrected energy is then chosen to be $\sigma_E = 5$ % to reflect the channel's energy acceptance range (but to a value lesser than the lowest channel energy width). The correction depends on the individual channel's characteristics and the local ion temperature and generally lowers the inferred temperature by less than 20 %.

Following eq.(4.3.10), the straight line model to be fitted is

$$\ln G(E) = \ln G_0 - \frac{E}{T_i} \tag{4.3.15}$$

and the goodness-of-fit is checked through the χ^2 merit function [149],

$$\chi^2(T_i) = \sum_m \frac{\left(G(m) - G_0 + \dfrac{E(m)}{T_i}\right)^2}{\sigma_G^2(m) + \left(\dfrac{\sigma_E(m)}{T_i}\right)^2}, \tag{4.3.16}$$

with m the set of data points in agreement with eq.(4.3.13). The iterative code starts by fitting the slope to the three lowest energy CNPA channels, the obtained temperature is then used to reevaluate the energy interval according to eq.(4.3.13) and a new temperature is inferred from that new energy range. This procedure iteratively increases the considered energy interval until convergence of T_i towards a value compatible with eq.(4.3.13) is achieved. The procedure is similar for the VNPA, where all measurements within the energy interval of interest are considered.
The code calculates the propagation of the vertical and horizontal error bars σ_G and σ_E into the calculation of T_i (σ_{T_i}) and the probability Q that a value of χ^2 as poor as eq.(4.3.16) would occur statistically [150].

Figure 4.3.4a shows the charge exchange spectrum measured with CNPA and VNPA for discharge #29370, which was centred on both diagnostic view lines (the magnetic axis has the coordinates $R = 89$ cm, $z = -2$ mm). To improve the particle statistics, the measurements were averaged over 100 ms and the VNPA performed almost eight scans across the diagnosable energy range. The electron density is also low, $\langle n_e \rangle = 1 \times 10^{19}$ m^{-2}, so the neutral attenuation in the plasma is low and the neutral flux entering both NPA is strong. It is possible to deduce the ion temperature from the hydrogen flux, whose concentration is only ∼10 % of the deuterium population. The straight lines in the figure symbolise the energy interval, compatible with eq.(4.3.13), used for the retrieval of the ion temperature on the magnetic axis. The three temperatures measured (see the figure caption) agree within 5 %.

Figure 4.3.4b shows the time traces of the ion temperature obtained with the VNPA and CNPA of a hot ($T_e \simeq 1$ keV) low density discharge with strong EC heating. In this case, the neutral fluencies are strong (low attenuation) and the ion temperature is low (only the low to intermediate energy channels are required for the CX spectrum slope fit), such that poor particle counting statistics is not an issue.

NPA channels with events below the statistical confidence level or saturated by too many particles (figure 3.3.7.a) are ignored. A calculation of T_i is not attempted unless at least three channels satisfy these requirements. The question is now: Which statistical confidence level should be used? An answer will be given with the experimental studies presented in the next section. Further justification for the T_i inference rule, eq.(4.3.13), will be validated by statistical benchmarks, to be discussed in section 4.9.4.

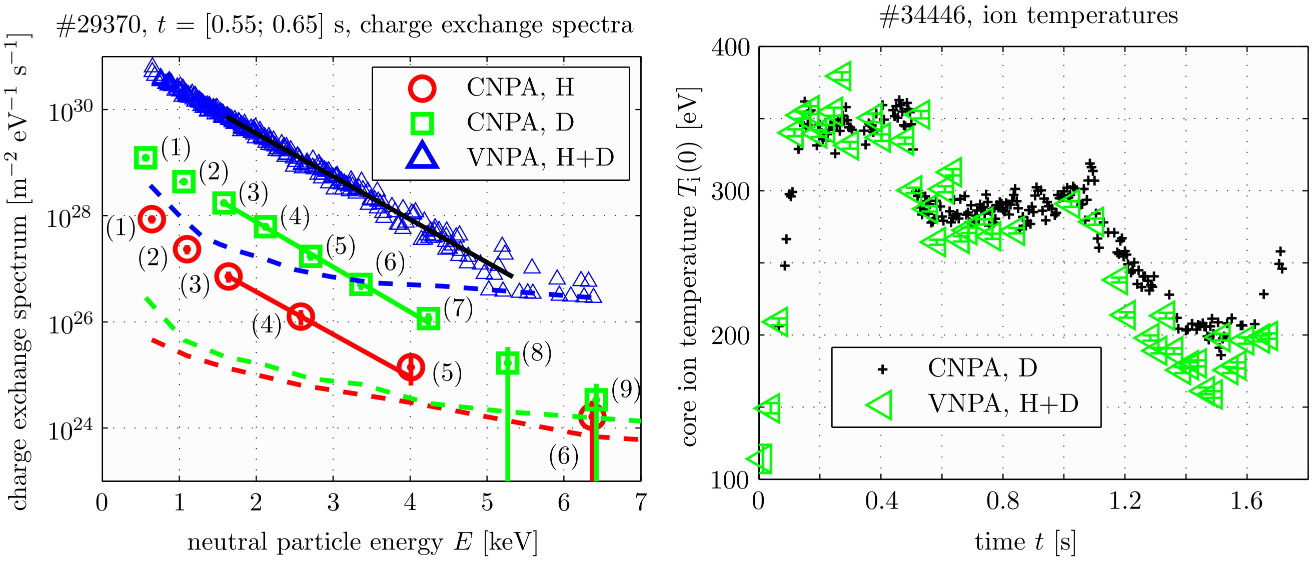

(a) NPA charge exchange spectra.

(b) NPA ion temperature traces.

Figure 4.3.4: (a) Charge exchange spectra measured with CNPA and VNPA for discharge #29370, averaged over the steady-state plasma phase $t = [550; 650]$ ms. The numbers refer to the CNPA array channels. The straight lines indicate the fitted slope and the energy subinterval used for the calculation of the core ion temperature. These are: VNPA, $E = [1.61; 5.35]$ keV, $T_i(0) = 535 \pm 32$ eV; CNPA, hydrogen, $E = [1.64; 4.01]$ keV, $T_i(0) = 542 \pm 26$ eV; CNPA, deuterium, $E = [1.58; 4.24]$ keV, $T_i(0) = 513 \pm 6$ eV. The broken lines indicate the "one count per integration period" event.
(b) Low density (1×10^{19} m^{-2}) high electron temperature (1 keV) discharge #34446. At $t = 0.5$ s a total of 2 MW of electron cyclotron power is injected into the plasma, increasing to 2.5 MW from 1.1 s onwards. The plasma is vertically centered in the vessel up to 1.3 s and moves upwards later on. Up to this time the temperatures measured by VNPA and CNPA are expected to agree.

4.4 Ion temperature profile reconstruction

4.4.1 Quasi multichord measurement by plasma displacement

The freedom of plasma shaping and placement inside the vessel of TCV may be exploited for diagnostic purposes. In order to verify the assumptions that the charge exchange spectrum is characteristic of the hottest temperature along the diagnostic view line (section 4.3.2) and that this temperature is correctly derived from the spectrum energy range, eq.(4.3.13), the recovery of the ion temperature profile in a moving plasma experiment was performed. This exercise will also finalise the analysis of the minimum level of counting statistics required by the NPA measurement for reliable retrieval of the core ion temperature (section 4.3.3).

First attempts to probe different regions of the plasma with the CNPA were aimed at reproducing a discharge at different vertical positions inside the vessel. By displacing the plasma across the CNPA line of sight a temperature profile was concatenated from multiple discharges [151]. The plasma parameters of these shots have, however, proven not sufficiently reproducible. The exercise was successfully repeated by displacing the plasma configuration vertically during a single discharge. The displacement of the magnetic axis was performed for a fixed plasma configuration with stationary plasma parameters (elongation $\kappa = 1.5$, triangularity $\delta = 0.6$) from $z = 25$ cm down to the vessel midplane.

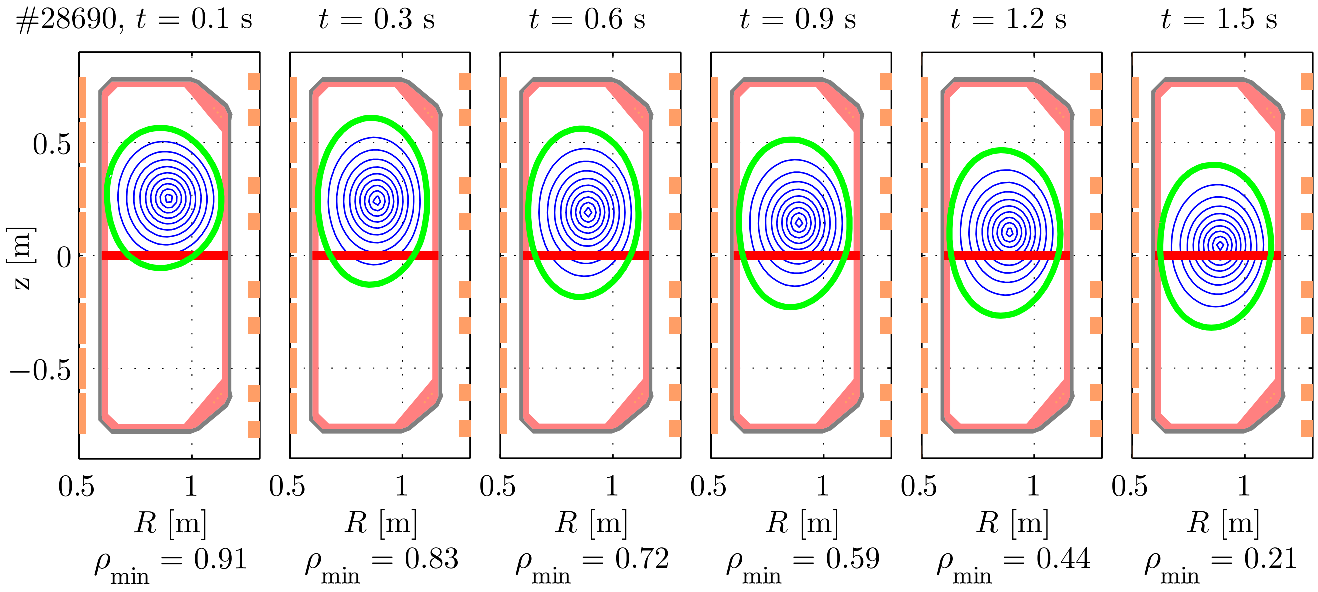

Figure 4.4.1: Reconstruction of the poloidal topology of the magnetic flux surfaces for the vertically displaced discharge #28690 (moving plasma experiment) for t = 0.1, 0.3, 0.6, 0.9, 1.2 and 1.55 s. The horizontal line at $z = 0$ represents the view line of the CNPA, the minima of the normalised radius ρ intercepted are drawn below the figure. The nested flux surfaces are depicted for $\rho = 0.1 \ldots 1.0$ (last closed flux surface, LCFS).

Figure 4.4.1 shows the poloidal cross section of TCV together with the reconstruction of the magnetic topology by the *LIUQE* code. The minimum of the magnetic flux coordinate intercepted by the view line of the CNPA decreases linearly from $\rho = 0.8$ @ $t = 0.3$ s to $\rho = 0.2$ @ $t = 1.5$ s. To monitor the target plasmas constance, the vertical NPA monitored the core plasma temperature taking advantage of its relative insensitivity to a vertical plasma displacement.

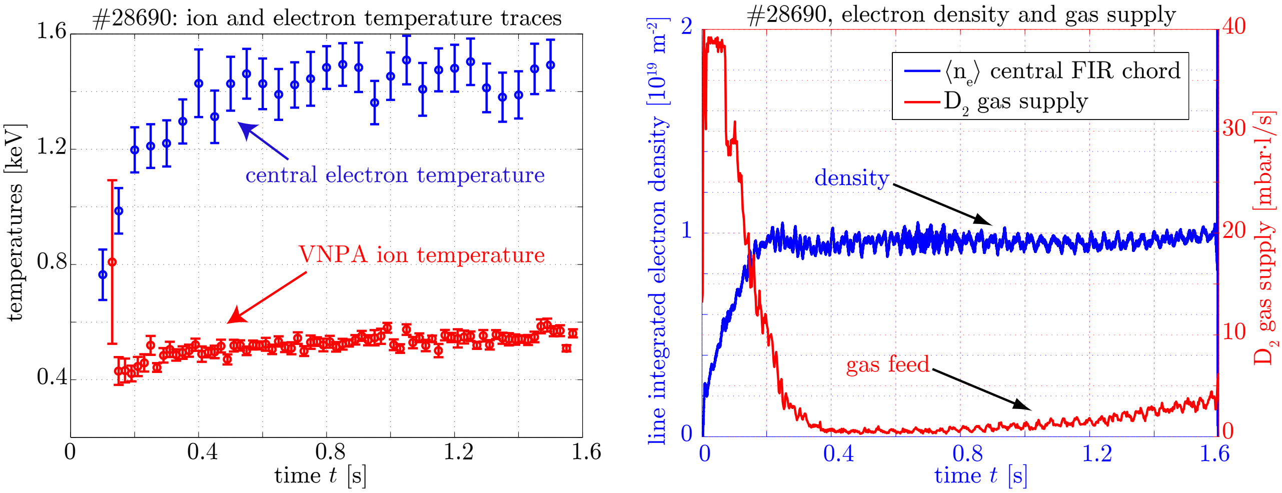

(a) T_e and T_i in the plasma core.

(b) Electron density and gas feed.

Figure 4.4.2: (a) Time traces of central electron temperature derived from a reconstructed profile of the electron temperature measured with Thomson Scattering (upper points) and the ion temperature derived from the charge exchange flux measured by the VNPA, whose line of sight crosses almost the centre of the plasma (lower points). The temperatures are constant from t = 0.4 s onwards.
(b) Time traces of line integrated electron density measured with the FIR (left axis) and deuterium gas supply (right axis).

The ion temperature from the VNPA is shown together with the central electron temperature measured by the Thomson Scattering system in figure 4.4.2a. The temperatures $T_e(\rho{=}0)$ and $T_i(\rho{\approx}0)$ are deemed sufficiently constant from $t = 0.4$ s onwards.

Figure 4.4.2b shows the thermal deuterium gas feed (toroidally $\phi = 45°$ from the CNPA, 112° from the VNPA), injected from the top and the bottom of the plasma to maintain a constant electron density. The measured electron density (line integrated FIR measurement, used for feedback of the gas control) is also shown.

To exclude a possible perturbation of the NPA measurement by the strong neutral density surrounding the plasma (section 4.2.1), the influence of the difference in instrument to plasma distance (defined by the LCFS) for the two NPAs (which is less than 1 m for the CNPA but more than 4 m for the NPA) was investigated by horizontally shrinking a plasma configuration by several centimetres in a separate experiment.

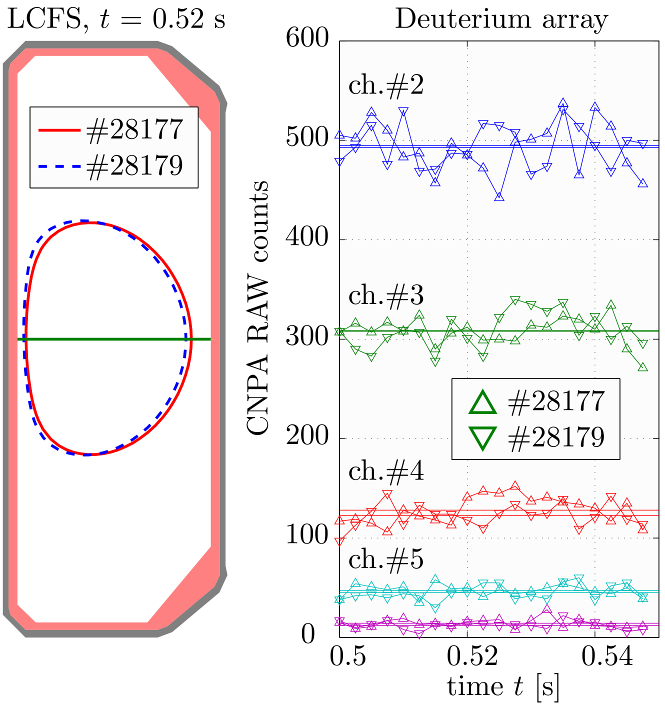

Figure 4.4.3: Discharge #28177 and #28179, with the latter being displaced horizontally by 3 cm, illustrated by the LCFS contours. Both plasmas have otherwise similar parameters (not shown). The CNPA counting traces (on the right with the horizontal lines representing the average counts in the shown time window) do not exhibit any difference between the two discharges, although the neutral particles have to traverse a dense cold neutral edge layer which has been enlarged by 25 % for the second discharge. Only CNPA deuterium channels #2 to #6 are shown.

Figure 4.4.3 shows the LCFS of two plasmas (left), one has a LFS SOL path length of 4 cm along the CNPA line of sight, the other of about 7 cm. Both plasma configurations are, otherwise, identical. On the right the raw CNPA count rates (counts per 2.5 ms of counting) of some of the lower deuterium energy channels are shown. Little change in the measured flux is observed which implies that there is no significant particle absorption in the volume between the plasma edge and the CNPA. The orientation of the view line is, however, found to be important since neutrals created in the plasma core must traverse a longer distance within the plasma (especially with high elongation) and scrape-off layer before entering the VNPA and are thus more strongly attenuated than the neutral flux reaching the CNPA.

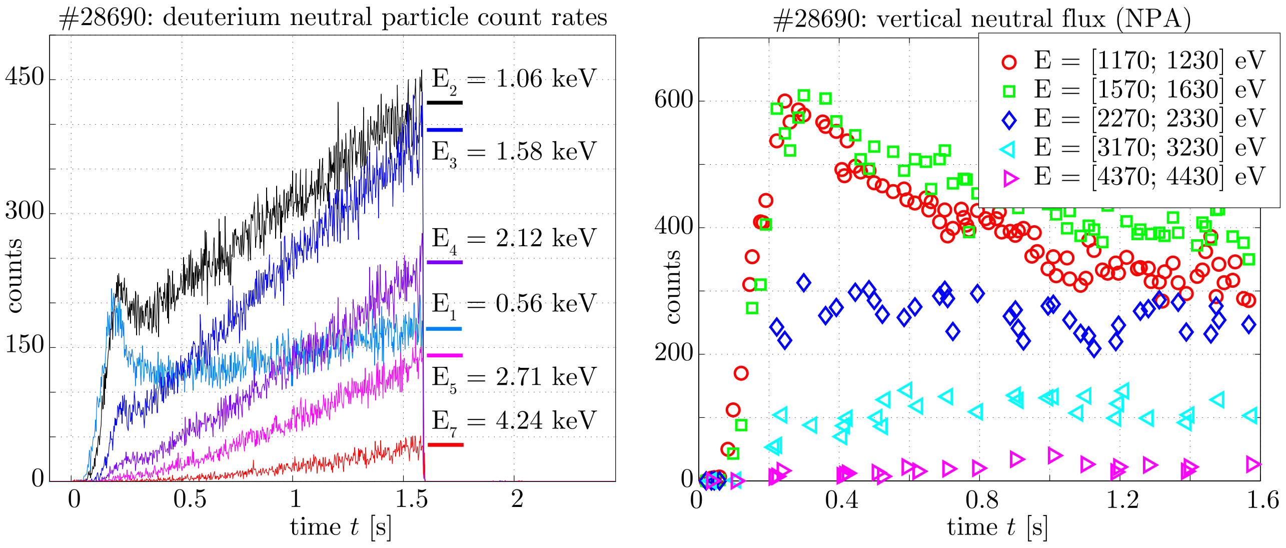

(a) CNPA flux time traces.

(b) VNPA flux time traces.

Figure 4.4.4: (a) Time traces of the charge exchange flux for six of the lower energy CNPA deuterium channels. (b) Time traces of the charge exchange flux within some narrow energy windows acquired by the energy sweeping VNPA.

In the moving plasma experiment, discharge #28690, the CX fluxes measured by the CNPA increase linearly in time for all energies for $t > 0.4$ s, see figure 4.4.4a, whereas the fluxes at the energies fulfilling eq.(4.3.13), detected by the VNPA, are unchanged (figure 4.4.4b).
The CX spectrum, derived from the measured fluxes of figure 4.4.4a for the 9 lowest energy deuterium channels, is shown in figure 4.4.5 at five different times (the straight lines show the fitted slope for the temperature determination). The higher the analysed energy range, the hotter the inferred temperature, which is thus concluded to correspond to the preponderance of a plasma region closer to the plasma centre.

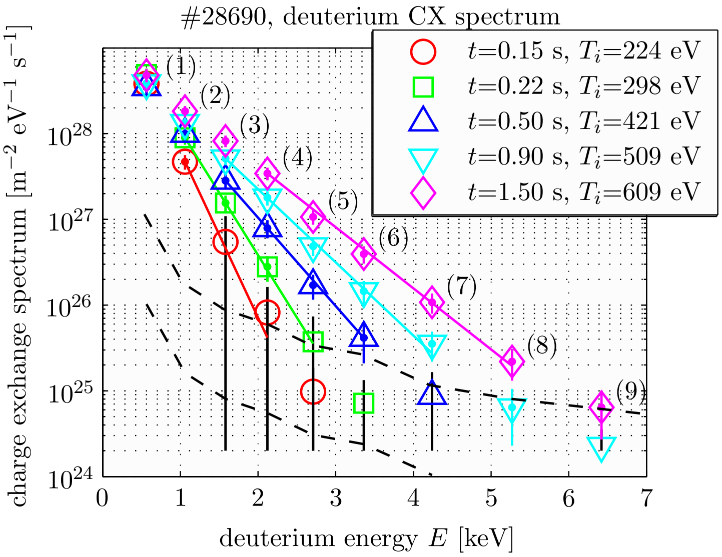

Figure 4.4.5: Charge exchange spectra averaged over intervals of 50 ms for the time slices t = 0.4, 0.8, 1.1 and 1.5 s. The upper dotted line corresponds to a count rate of 25 counts per bin, the lower to one count per bin. The straight lines show the channels retained in the calculation of T_i, the obtained values are printed in the figure legend. The numbers in brackets label the CNPA deuterium channels.

As the temperature of the hottest part of the plasma covered by the solid angle of the NPA is not a priori known, the temperature was iteratively determined according to the procedure described in the previous section. However, the restricted number of the fixed energy channels of the CNPA require sometimes the inclusion (or not) of a channel outside but close to the interval defined by eq.(4.3.13), especially when some of the included channels show saturation.
The neutral flux in ohmic discharges of higher densities is drastically reduced (section 4.3.1) and the counting statistics of the high energy channels are poor. In such discharges, the ion temperature is high (see section 4.10.2) and eq.(4.3.13) requires the ion temperature to be derived from NPA channels of higher energy. Even for the low density discharge discussed here, if an important number of ions with energy $\gtrsim$ 7 keV would be neutralised in the plasma, most must then be reionised on their trajectory to the CNPA since the higher energy channels observe essentially noise which is not statistically significant (large Poisson error). This was confirmed by a repetition of the discharges with the NPA accelerator and deflector high voltage power supplies switched off (to measure the noise background).
The statistical error of the counted neutrals in channels at the upper energy limit must be properly assessed otherwise the measurement is worsened by the inclusion of those channels. The criteria for selection (or not) of the high energy channels uses a time independent (but CX flux intensity dependent) statistical argument to determine the ion energy range from which the ion temperature is calculated. If too many high energy channels must be discarded the temperature inference is abandoned.

The ion temperature was calculated for a range of counting statistics $\Upsilon = \sum \text{counts}/\Delta t$ such that the CX flux measured by the energy channels, whose counting rates exceeded this limit, were used in the linear regression of the CX spectrum.

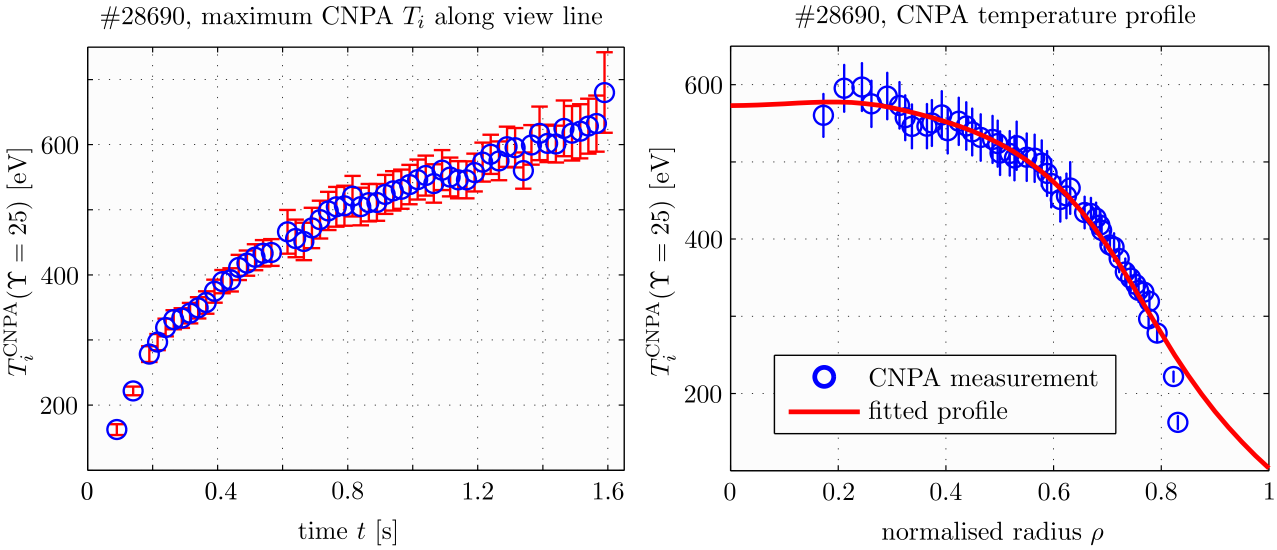

(a) CNPA inferred ion temperature trace.
(b) T_i as a function of minimum intercepted ρ.

Figure 4.4.6: After integration over time slices of 50 ms, the ion temperature was calculated from the CNPA measurement. (a) shows the time trace of the temperature for $\Upsilon = 25$ counts per time slice, in (b) the temperature is plotted against the minimum of the intercepted ρ at every time slice, in order to obtain a temperature profile. A smooth profile, fitted to the CNPA measurement and further used in the simulations (section 4.2.1), is also shown.

For a counting limit of $\Upsilon = 25$ counts per 50 ms, the obtained ion temperature trace is plotted in figure 4.4.6a.

The value of the obtained temperature is within a range of 3–10 times the particle energy of the CX flux for the measurement, for the entire discharge. Figure 4.4.6b shows the ion temperature profile obtained from plotting T_i against the minimum of ρ intercepted by the CNPA. The solid line in the figure shows a weighted interpolation of the passive CNPA measurement (points) setting a zero first derivative at the plasma centre. The final choice of the statistical limit, i.e. the limit that will result in the best estimation of the temperature profile, was addressed by modelling the measured charge exchange flux spectrum based on the interpolation of the recovered ion temperature profile using the method described in section 4.2.1.

4.4.2 Modelling of the moving plasma experiment

Using the method described in sections 4.2.1 to 4.3.2, the CX flux in the moving plasma experiment was modelled for the various ion temperature profiles calculated for different upper ion energy limits, defined by levels of count rates ranging from $\Upsilon = 5$ to 50 counts per 50 ms (section 4.4.1). The simulated CX spectrum was then compared to the measured spectrum and characterised by the figure of merit function X^2 defined by

$$X^2(m) = \sum_{k=1}^{m} \frac{\Big(\Gamma_{\text{sim}}(k) - \Gamma_{\text{exp}}(k)\Big)^2}{\Gamma_{\text{exp}}(k)}, \tag{4.4.1}$$

summed to the $m = 8^{\text{th}}$ CNPA channel. The fit of the temperature profiles inferred from the CNPA CX spectrum and the corresponding relative error between simulated and measured charge exchange flux, defined by

$$\delta\Gamma_{\text{CX}}(i) = \frac{\Gamma_{\text{sim}}(i) - \Gamma_{\text{exp}}(i)}{\Gamma_{\text{exp}}(i)}, \tag{4.4.2}$$

with i the CNPA channels, are shown in figure 4.4.7. Only channels with count rates higher than the chosen Υ are shown.

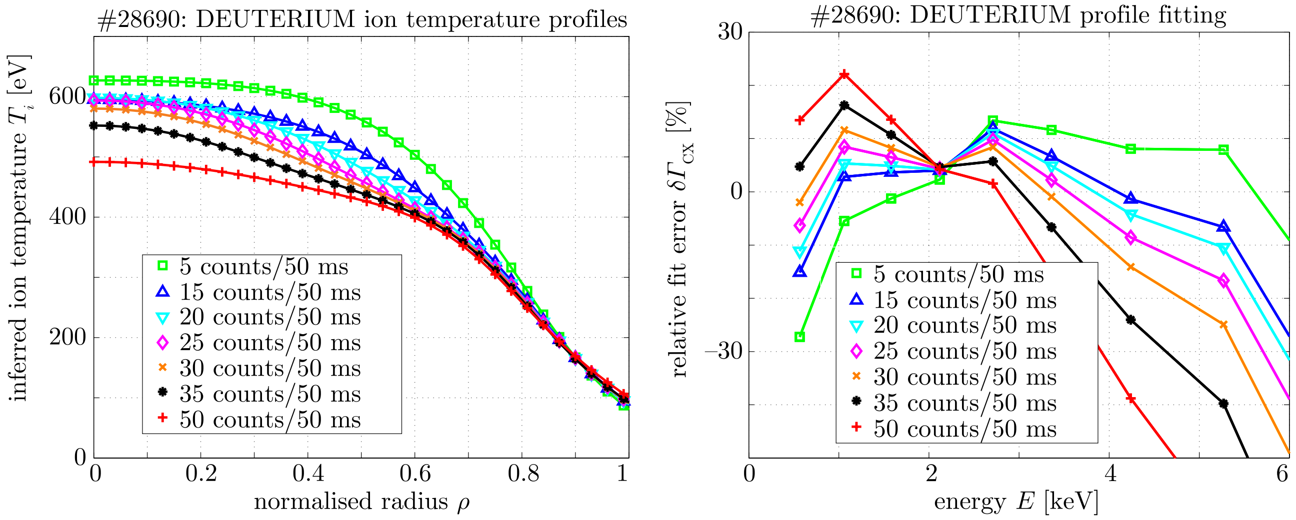

(a) reconstructed ion temperature profiles.

(b) relative fit error for different T_i profiles.

Figure 4.4.7: (a) Fit of the temperature profile reconstructed from the CNPA CX spectrum of the moving plasma experiment (section 4.4.1, #28690) for different levels of the statistical limit Υ used to determine the set of CNPA channels to derive the temperature from.
(b) Fit error $\delta\Gamma_{\text{CX}}$, eq.(4.4.2), between simulated and measured charge exchange flux spectrum for the different temperatures shown in (a).

The X^2 defined in eq.(4.4.1) is shown in figure 4.4.8a. The best match between experiment and simulation is achieved with a reconstructed temperature profile inferred from ion energies corresponding to CNPA channels with count rates exceeding $\Upsilon = 25$ counts per 50 ms. The simulated and measured charge exchange spectrum for this statistical level is shown in figure 4.4.8b. The agreement of the simulation with the measurement is surprisingly good, with a relative error $\delta\Gamma_{\mathrm{CX}} \lesssim 10$ percent for the 8 lowermost deuterium energy channels over the complete CNPA!

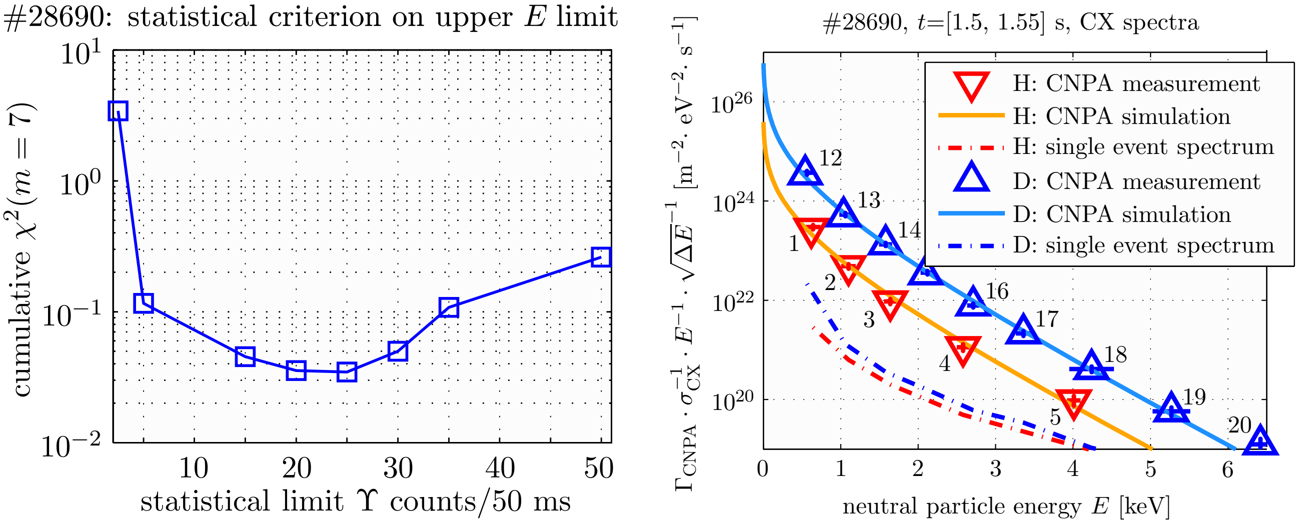

(a) Goodness of fit.

(b) Charge exchange spectrum.

Figure 4.4.8: (a) Goodness of fit quantified by the X^2, eq.(4.4.1). The model recovers the charge exchange flux for a temperature profile calculated for ion energy count rates just above the statistical limit of $\Upsilon = 25$ counts/50 ms.
(b) Modelling of the charge exchange spectrum (continuous lines) with the upper energy limit $\Upsilon = 25$ counts/50 ms.

4.5 Modelling of the neutral source energy distribution

In the moving plasma experiment (section 4.4.1), the ion temperature was inferred from the CNPA CX spectrum at the energy of particles supposed to originate from the hottest region of the plasma. Figure 4.3.2b, where the total charge exchange flux was separated into contributions from different nested shells of the plasma column, has already demonstrated that the slope of the measured CX spectrum is a reasonable approximation of the ion temperature in the plasma core.
This section explains how the birth place of the neutrals detected by the NPAs are recovered from the model of the neutral source of the neutrals (section 4.2.1).

4.5.1 Place of birth

The primary place of birth, i.e. the dominant contribution to the flux of neutrals of energy E, is given by the position of the maximum emissivity, eq.(4.3.1). The terms in this formula peak at different radial positions: on the source side the neutral density (figure 4.2.2) and the charge exchange rate coefficient peak at the plasma edge (low particle energy), whereas the sinks, described by the plasma attenuation coefficient α (figure 4.3.1a), increase towards the centre and decrease in strength with particle energy.

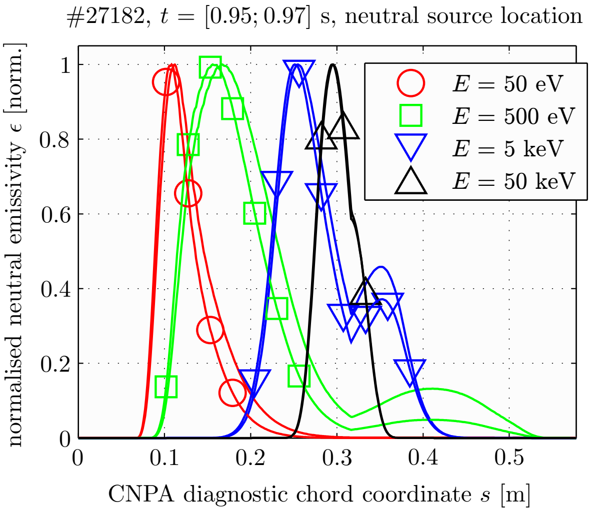

Figure 4.5.1: Normalised neutral deuterium (curves with symbols) and hydrogen emissivities $\varepsilon(\rho, E)$ for arbitrarily chosen neutral particle energies, plotted against the CNPA chord coordinate. The discontinuities in the curves coincide with the magnetic axis. Discharge #27182, t = [0.95; 0.97] s.

The competition between particle sources and sinks leads to peaked emissivity profiles, whose radial position maxima are a function of energy (shown in figure 4.5.1 for arbitrarily chosen particle energies of discharge #27182) where the vertical scale of the plots was normalised to facilitate comparison. Put simply, the hotter neutrals have a deeper place of origin. Even if, locally, the ions D^+ have a broad energy distribution, characterised by the local temperature, the maxima of the neutral emissivities of the CNPA channel energies remain well separated in space and may be used to determine the preferential radial origin of the detected particles. Figure 4.5.2a plots the spacing $\Delta\rho$ of the channels with respect to their higher energy neighbour channel.

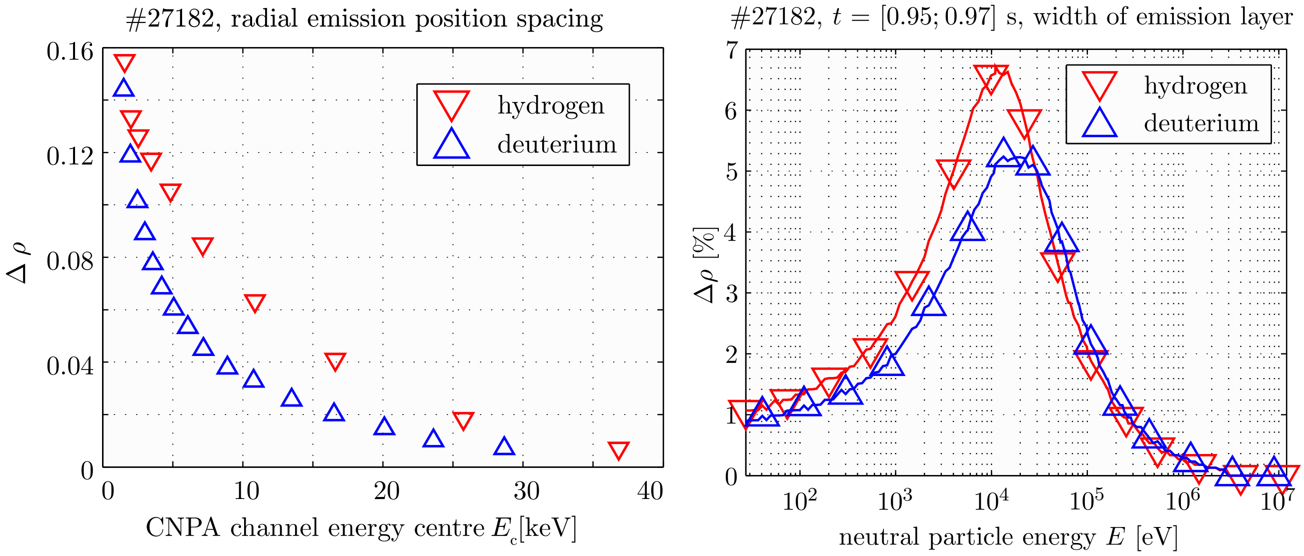

(a) Radial spacing of the emissivity maxima.

(b) Radial width of the emissivity maxima.

Figure 4.5.2: (a) Neutral particle emission maxima are well separated in ρ. The separation is highest for the lowest energy channels, the high energy channels cover the plasma centre. Discharge #27182, t = [0.95; 0.97] s.
(b) The radial width of the emissivity peaks is maximum for intermediate energies, at the edge the width is limited by the strong gradients of neutral atomic density and charge exchange rate coefficients, in the centre of the plasma the emission is localised but also small.

Increasing the plasma density leads to a displacement of the maxima away from the plasma centre. The flatter the profile, the closer the peak separation and the wider they become, as shown in figure 4.5.2b. The widths are largest for the intermediate channel energies (where the gradient of the ion temperature profile is smallest).

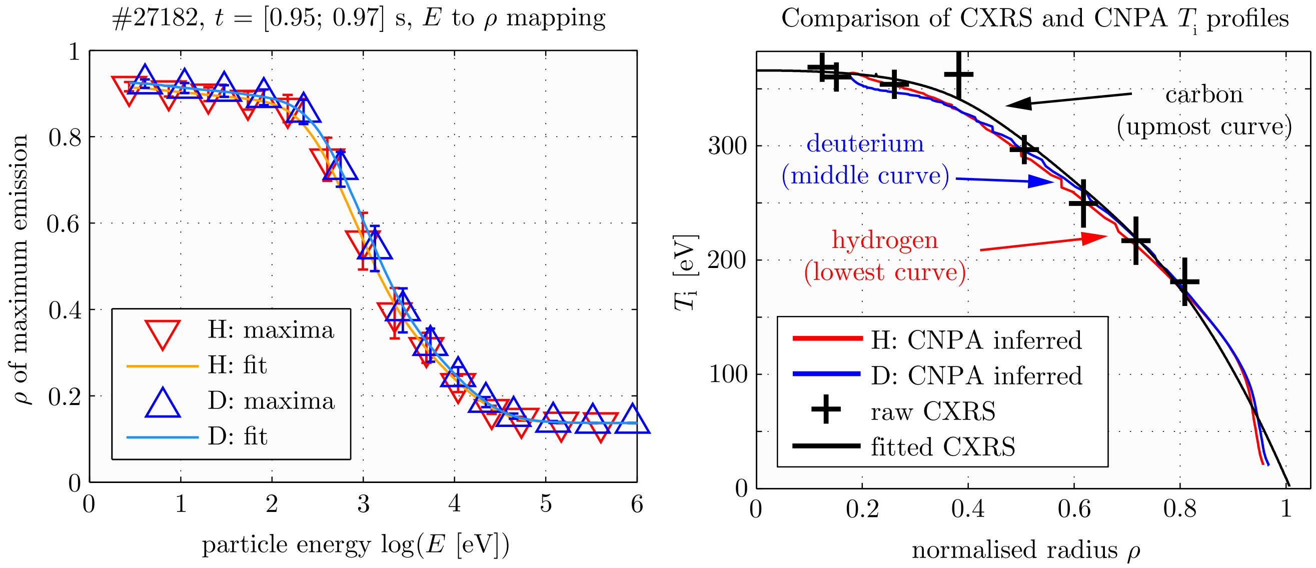

(a) energy to radius mapping

(b) CNPA inferred ion temperature profiles

Figure 4.5.3: (a) Origin of maximum emissivity versus corrected CNPA channel energies for discharge #27182, t = [0.95; 0.97] s, for hydrogen and deuterium. The maxima are fitted with weights given by the radial width of the emissivity.
(b) CXRS carbon ion temperature measurements (t = 0.86 s) and corresponding fitted profiles. CNPA/*KN1D* ion temperature profiles for hydrogen (red) and deuterium (blue) with radial coverage of ρ = [0.15; 0.95] averaged over t = [0.95; 0.97] s.

4.5.2 Hydrogenic ion temperature profile

Using the deduced flux energy spectrum and the probable spatial origin (chosen to be the radial positions of the maxima of the neutral emissivities shown in figure 4.5.1), the energy of the neutrals may be mapped into radial space, $\rho = g(\mathrm{E})$, figure 4.5.3a. The simulated CX spectrum of figure 4.3.2a is a smooth function, so the ion temperature from eq.(4.3.11) may be obtained at every point on the curve. A hydrogenic ion temperature profile is obtained in the range ρ = [0.15; 0.95] by plotting these values against the flux surface coordinate. Figure 4.5.3b shows the profiles obtained for the hydrogen and deuterium isotopes, together with the CXRS measurement at $t \simeq 0.86$ s. The fitted CXRS profile, used as input for the codes, is also shown. Excellent agreement, within the error bars of deuterium and carbon ion temperatures, is found (as previously described, the ions are thermalised for this scenario).

Figure 4.5.3b is taken as confirmation of the assumption that the NPA temperature inferred from the CX spectrum at a particular energy E is equal to the value of the ion temperature profile at the radial position contributing most particles to the CX flux of that energy E.

4.6 Inversion of single chord NPA measurements

TCV ion temperature profiles are reasonably approximated using parabolic expressions. Using functional expressions for the ion temperature in the neutral transport codes, the temperature profile may be iteratively recovered by fitting the measured CX spectrum with a functional temperature profile – without a priori knowledge of the ion temperature profile shape.

For this purpose, an initial temperature profile is constructed by

$$T_i(\rho) = \left[\ T_i(0) - T_i(1)\ \right] \left(1-\rho^2\right)^{\kappa_{T_i}} + T_i(1), \tag{4.6.1}$$

where $T_i(1)$ is the value of the ion temperature at the LCFS, $T_i(0)$ is the central ion temperature and κ_{T_i} the peaking coefficient of the profile. For this procedure, $T_i(0)$ is usually estimated from the measured CX spectrum. This initial profile is then input to *KN1D* to calculate the neutral density profile. The modelled charge exchange spectrum is calculated using eq.(4.3.1) to eq.(4.3.12) with an unconstrained nonlinear optimisation of the functional ion temperature profile, eq.(4.6.1), based on the Nelder-Mead simplex method in order to reproduce the measured spectrum. The deduced temperature profile is then returned to the neutralisation codes and the procedure repeated with the new neutral density profile until a convergent solution is found. Figure 4.6.1 illustrates the results of this method for discharge #29769 employing *KN1D*. Plasma profiles are shown in figure 4.6.2.

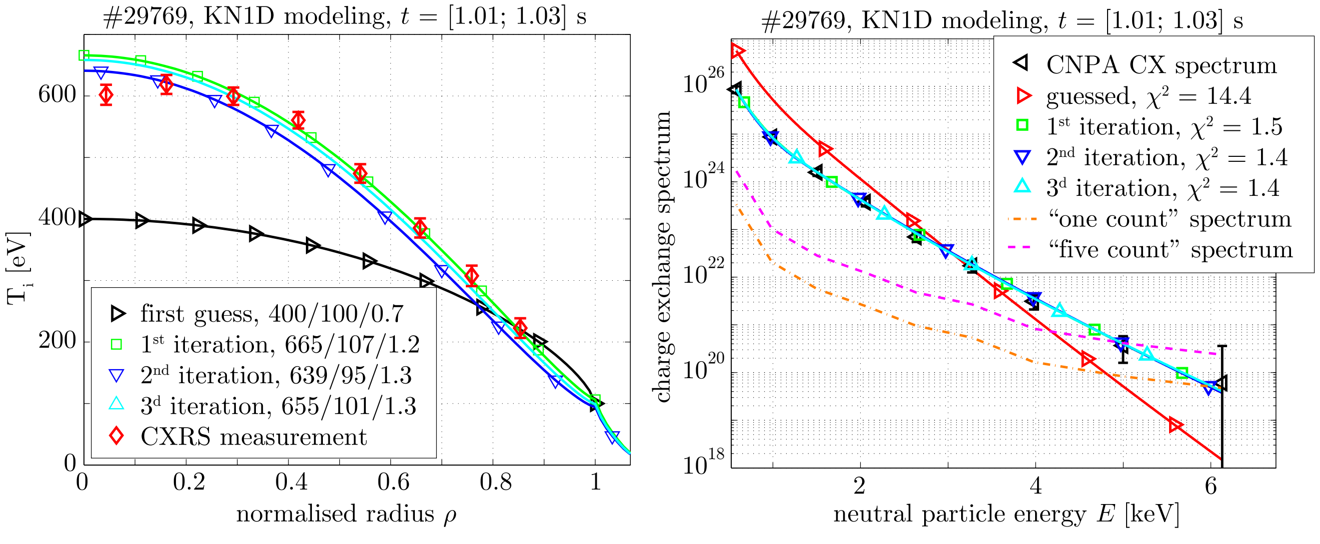

(a) ion temperature profile recovery (b) CX spectrum fit

Figure 4.6.1: CNPA signal inversion using *KN1D*.
(a) Arbitrary initial guess of the ion temperature profile and subsequent iterations with parameters giving the best interpolation of the measured CX spectrum. The legend indicates the core and edge ion temperature, the last number is the profile peaking factor.
(b) Measured and iteratively improved approximation of the CX spectrum using the temperature profiles shown in (a).

Starting with an initial (arbitrarily bad) guess profile of parameters $T_i(0) = 400$ eV, $T_i(1) = 100$ eV and $\kappa_{T_i} = 0.7$, a convergent solution is found after only two iterations. The parameters of the best fit profile are $T_i(0) = 660$ eV, $T_i(1) = 100$ eV and $\kappa_{T_i} = 1.3$. For comparison, the measured CXRS profile is shown. It should be recalled that the procedure described here is independent of the knowledge of this profile! The solution is largely insensitive to the initial profile parameter approximation. Convergence is often obtained within 1…3 iterations.

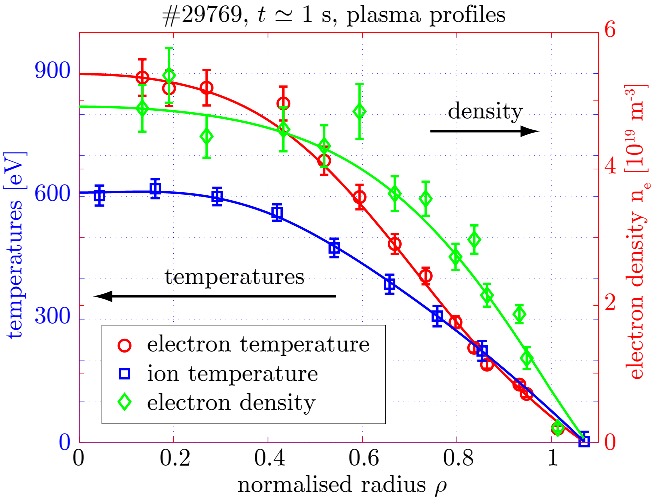

Figure 4.6.2: Measured electron density and temperature (Thomson scattering) as well as ion temperature (CXRS) profiles for discharge #29769. The Thomson scattering measurements were made at $t = 1.02$ s, the ion temperature was measured during a DNBI beam blip lasting from $t = 1.04$ to 1.06 s.

This exercise was also performed with the Monte Carlo code *DOUBLE-TCV*, to be described in the next section. For this code, the numerical noise in the calculated neutral density limits the convergence precision. Figure 4.6.3 shows an example of the temperature profile recovery using the VNPA (the CNPA was not available for this discharge). However, the lack of a CXRS measurement for this discharge doesn't allow for a validation of the profile obtained.

The recovery of the central ion temperature is restricted to charge exchange spectra with sufficient contributions from the centre of the plasma, i.e. with significant CX flux up to energies $10 \cdot T_i(0)$. If this condition is fulfilled, the central ion temperature is generally recovered to within $\lesssim$10 % of the CXRS measured carbon ion temperature (for scenarios where agreement is to be expected, of course).

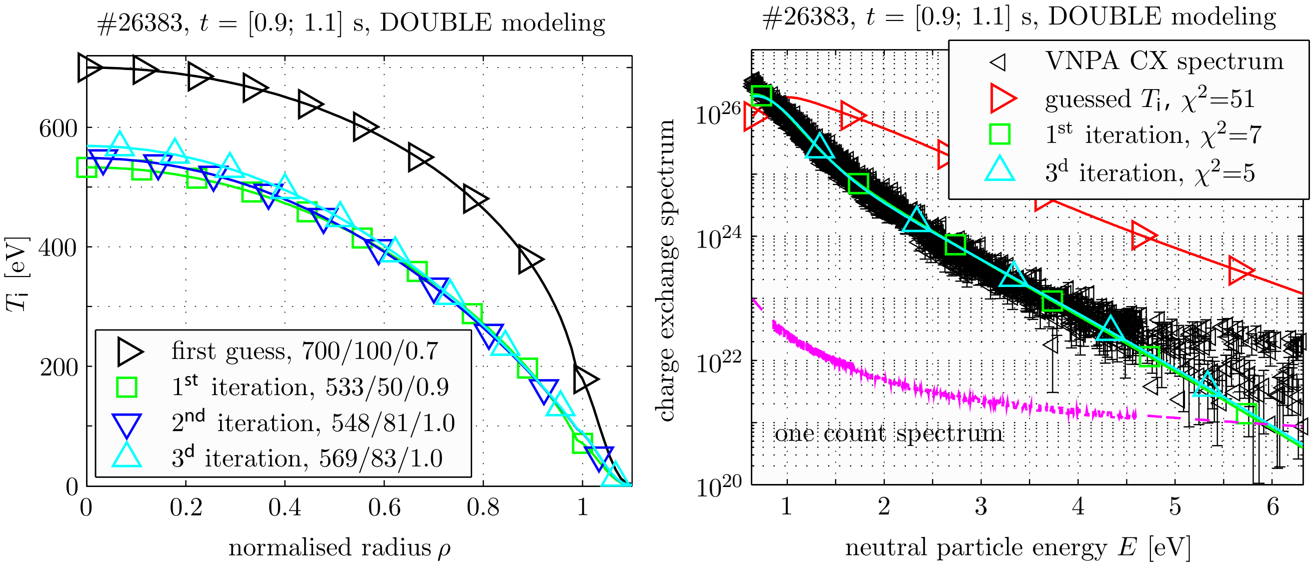

(a) ion temperature profile recovery (b) CX spectrum fit

Figure 4.6.3: VNPA signal inversion using *DOUBLE-TCV*. (a) shows the temperature profile iteration, (b) the corresponding CX spectra.

4.7 2D neutral emissivity simulations

KN1D was designed to calculate the neutral particle penetration at the plasma edge. In section 4.2.1 it was shown how the neutral density profile is obtained requiring laborious multiple runs of the code, especially when profiles along vertical directions are called for. Further, TCV plasmas have a significant impurity content and multiple species have been modelled by individual runs of *KN1D*. This is, however, only valid as a first approximation, as collisions between different species are neglected. For TCV's needs, a neutral transport code with the following additional requirements was desirable:

- A correct 2D description of the plasma, with the ability to model the zoo of TCV plasma shapes,
- the ability to describe a non-homogenous neutral density distribution in the SOL,
- the execution of simultaneous simulations of multiple plasma species (hydrogen, deuterium, helium isotopes and impurity ions), especially the proper accounting of atomic processes between particles of different species or isotopes,
- a description of neutrals injected by the DNBI,
- the ability to handle non-thermal particle distribution functions,
- the direct calculation of the fast neutral attenuation, including a direct modelling of the NPA measurements and
- to avoid proprietary software (e.g. IDL).

4.7.1 Multi-species neutral transport modelling with DOUBLE-TCV

The neutral particle diagnostics group at the Ioffe institute offered an upgraded version of their *DOUBLE* code [152–154], which was finally purchased and installed at CRPP. The *DOUBLE-TCV* upgrade(‡) included [155]:

- A re-implementation of the neutral distribution calculation using the Monte Carlo technique,
- an implementation of the focusing DNBI beam (equations of section 3.2.2), of circular shape with a gaussian radial profile, including a calculation of the cold beam halo neutrals. The true beam geometry (divergence, width, position, direction, focal length) is described and up to three beam components (species, energy and equivalent current) may be specified,
- a description of a non-homogenous (but monoenergetic and isotropic) neutral distribution surrounding the plasma column (density at the LCFS), the non-homogeneity may be obtained for example from *EIRENE* [142],
- a definition of the real plasma geometry through a convex poloidal flux map (function of vertical and horizontal coordinate), last closed flux surface (particle source location) and the vessel first wall (particle recycling and refuelling),
- the treatment of mixed fuel plasmas, e.g. simultaneous simulation of two hydrogen isotopes (out of H, D and T), one helium isotope (^{3}He or ^{4}He) and carbon ^{6}C impurity,

---

(‡) features implemented as of October 2006

- ☞ the inclusion of recombination neutrals and
- ☞ a description of plasma ions of arbitrary distribution (pitch angle and energy) to describe suprathermal ion populations.

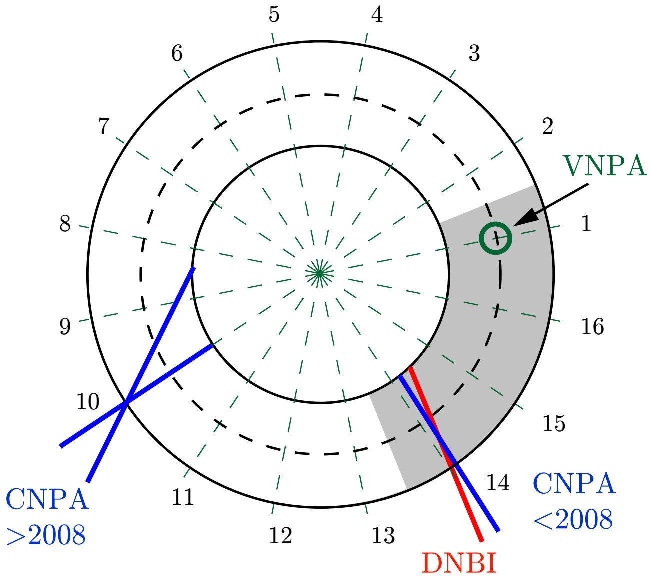

Figure 4.7.1: Disposition of the neutral beam (DNBI) and diagnostics modelled with the *DOUBLE-TCV* code. Beam and CNPA don't intersect anymore since the displacement of the latter in 2007. The grey area indicates the plasma volume covered by the simulation.

The output of the code are 2D neutral particle distributions in a poloidal plane and 1D neutral density and emissivity profiles along the NPA view lines as well as charge exchange spectra as measured by NPAs. DNBI and NPA chords are specified by a reference location, by toroidal and poloidal orientation angles and need not be located in the same toroidal sector (TCV is divided into 16 toroidal sectors, VNPA is located in sector 1, CNPA now in sector 10 and the DNBI in sector 14, see figure 4.7.1). The code is written in Fortran 90 and presently runs on a IBM eServer p5 with POWER5 processor running IBM AIX 5.3 and interfaces with Matlab and the MDS database. Results are stored in a container in the self-describing Hierarchical Data Format HDF5 [156].

With respect to *KN1D*, the *DOUBLE-TCV* code doesn't model the molecular atomic processes and elastic collisions at the plasma edge but these are not expected to strongly influence the fast neutral particle emission (see section 4.7.3 below). Each bulk ionic plasma species is defined by its density profile and an energy distribution in space and energy. Atomic reactions between particles of different species or isotopes are considered. The impurity component is defined through a profile of the effective charge, eq.(2.5.13), and does not contribute to the charge exchange flux, as this contribution is negligible for particle energies below 500 keV. Only electron impact and ion impact ionisation of carbon are implemented, the latter plays the role of a neutral hydrogen loss channel. The plasma column is assumed to be surrounded by atomic gas only. The code launches a specified number of particles from the LCFS. The particle starting points are uniformly distributed along the plasma boundary, with varying weighting factor to address non-homogenous conditions. Each particle trajectory is tracked until the particle hits the first wall or its weighting evolves to below a certain threshold level.

The contribution of recombination to the neutral density is calculated upon completion of the tracking of the edge neutrals assuming a coronal model, e.g.

$$n_x^0 = \frac{n_e n_x^i \left\langle \sigma v \right\rangle_{\text{rec}} \left(\left(n_x^i + n_y^i\right) \left\langle \sigma v \right\rangle_{\text{CX}}^{y \to x} + \Sigma_{\text{loss}}^y \right)}{n_x^i \left\langle \sigma v \right\rangle_{\text{CX}}^{y \to x} \Sigma_{\text{loss}}^x + n_y^i \left\langle \sigma v \right\rangle_{\text{CX}}^{x \to y} \Sigma_{\text{loss}}^y + \Sigma_{\text{loss}}^x \Sigma_{\text{loss}}^y}, \tag{4.7.1}$$

where

$$\Sigma_{\text{loss}} = \sum n \, \sigma \, v \tag{4.7.2}$$

is the sum over all considered loss processes. x and y are the first and second hydrogen component respectively. Equation eq.(4.7.1) is supplemented with a second equation of the same form, but x and y permutated.

The computation domain of *DOUBLE-TCV* for the calculation of the wall neutral penetration is 2D in space, with rectangular particle cells filling the whole poloidal section of the vessel. The obtained density is then virtually extended to 3D and superimposed by the beam particle cells (which do not necessarily lie in a poloidal plane).

The beam particles are launched separately, once the wall particle penetration has been completed. For each tracked beam particle, the cloud of produced halos is evaluated immediately after each propagation step. Simultaneous modelling of VNPA and CNPA fluxes in plasmas with neutral beam require the particle cells to fill approximately a slice as large as $\phi = 90°$ of the torus (grey shaded sector in figure 4.7.1). The initial particle integration step must be smaller than the neutral mean free path. A typical code setup comprises a cell grid composed of $50 \times 210 \times 80$ elements in radial, toroidal and vertical direction respectively. A reasonable setup of the number of launched edge, beam and halo particles is typically 10^5, 10^3 and 10.

Figure 4.7.2 shows an example of the beam attenuation in the plasma. The plasma neutrals are not shown on the contour plots. The FWHM of the beam profile is 10 cm at the magnetic axis. The cold halos have a spatial distribution that is almost twice as large as the beam profile. In this example, the beam was already attenuated by a factor of two at the plasma centre and the halo driven density is almost as large as that of the beam and the maximum halo density occurs at the intersection of beam and CNPA. This is beneficial for the active charge exchange measurements (section 4.8). The statistical noise on the beam axis in the *DOUBLE-TCV* calculation results from the small beam volume at the beam core.

4.7.2 Validation of beam neutral fuelling

The calculation of the spatial distribution of the diagnostic neutral beam with *DOUBLE-TCV* was compared to the simple beam attenuation code *BEAT* expounded in section 3.2.2. The halo calculation was switched-off in *DOUBLE-TCV* as *BEAT* doesn't take them into account. *DOUBLE-TCV* evaluates only three beam components, therefore the H_2O^+ component (contribution of less than 2 % to the ion current) is reasonably neglected in *BEAT*.
The vertical grid size was refined to ~1 cm and the number of launched wall and beam particles was one and two million respectively. The *DOUBLE-TCV* calculation was restricted to the toroidal angle domain $\phi = [-45; -65]°$ to just cover the plasma region affected by beam particles. The radial and vertical extent of the grid are not constrainable.

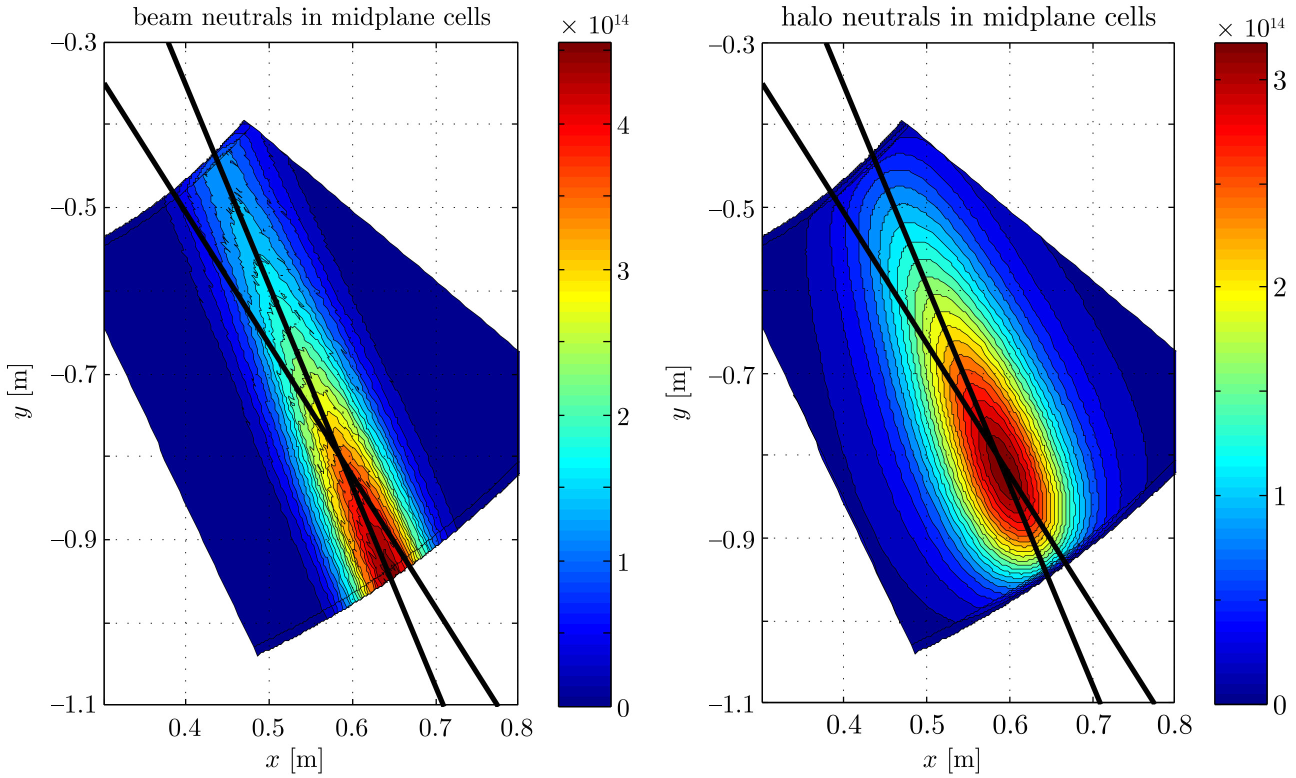

(a) beam at midplane (b) halo at midplane

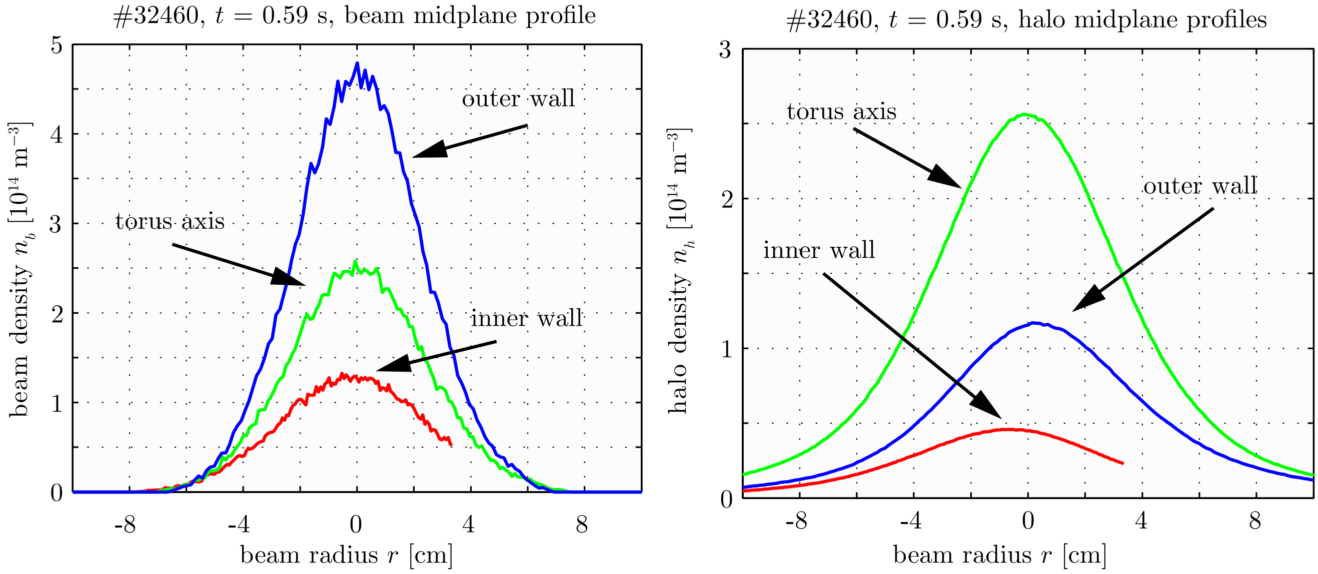

(c) beam profiles (d) halo profiles

Figure 4.7.2: Simulation of the plasma penetration of the diagnostic neutral beam with *DOUBLE-TCV*.
(a) and (b) show contour plots of the population of beam and halo particles in the vessel midplane cells (vertical view). The straight lines indicate beam axis and its intersection with the CNPA view line (setup prior to 2008). The blue background is delimiting the toroidal and radial extent of the particle cells.
(c) and (d) show profile cuts of beam and halo particles at plasma entrance, exit and at beam focus close to the torus axis.

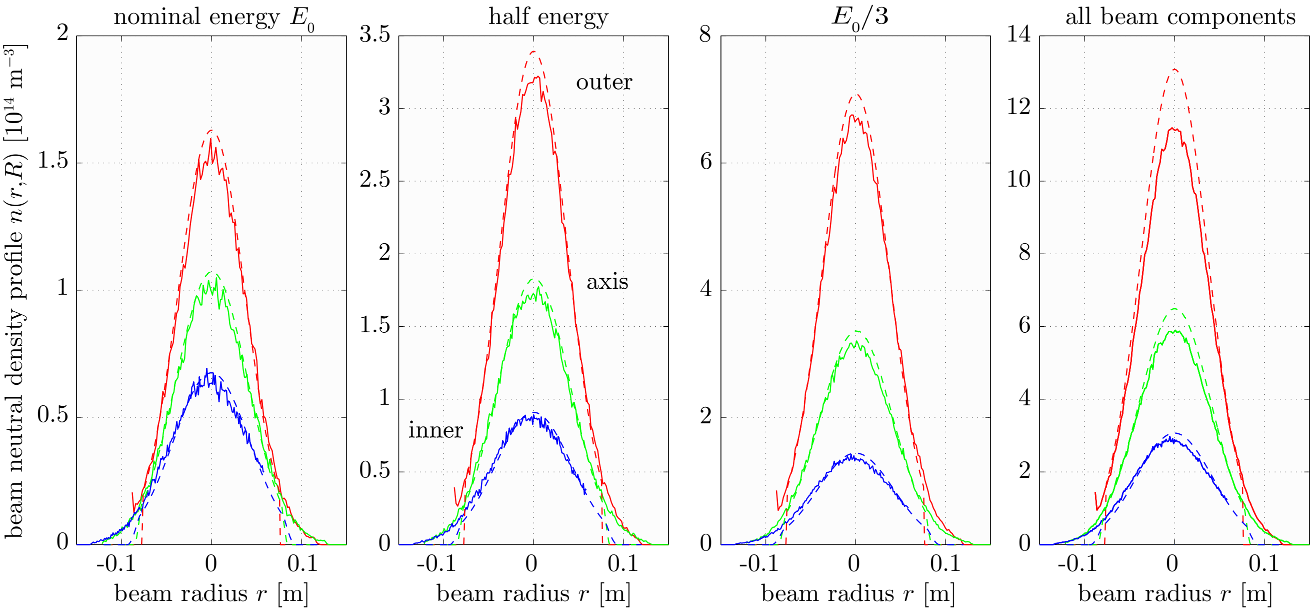

Figure 4.7.3: Gaussian beam profile shapes before, at the plasma centre and after the plasma traversal. The dashed lines are analytical calculations with *BEAT*, the solid curves are the numerical results obtained with *DOUBLE-TCV*.

Figure 4.7.3 compares the projection of the gaussian beam density profile on the cylinder normal surface (plane normal vector in radial direction) at the vessel entrance window ($R = 1.136$ m, upmost), the beam focal point ($R = 0.91$ m, middle) and central solenoid wall ($R = 0.634$ m, lowest curve) during an injected DNB beam blip at around $t = 0.6$ s of discharge #32460 obtained from *BEAT* and *DOUBLE-TCV*. Full lines represent *DOUBLE-TCV* simulations, dotted lines the analytical beam profile convoluted with the beam absorption probabilities (*BEAT*). The beam nominal energy is 51.4 keV, the equivalent total current 3.67 A and the beam power fractions of full, $\frac{1}{2}$ and 1/3 energy component are respectively 38 %, 28 % and 32 %. The DNBI-CNPA intersection major radius was $R = 0.994$ m. The beam setup in the codes corresponds to the experimentally determined parameters of beam geometry, that is Abel inversion of lateral visible imaging measurements with a web cam [157], current profile measurement with thermocouples inside the calorimeter at the beam dump and spectroscopic H_α emission measurements after the beam neutraliser to determine the beam composition, see section 3.2.2.

Discharge #32460 was performed shortly before the beam plasma RF generator [158] was replaced by the arc-discharge source [159] (section 3.2). The old ion supply was replaced because most of the extracted beam particles had one third of the nominal energy. Figure 4.7.4 compares the old and new beam source, demonstrating that the new source has a nominal energy beam density fraction exceeding 85 %.

Poloidal maps of total hydrogen neutral density distribution (beam and wall sources) at the location of beam injection are shown in figure 4.7.5. The beam is clearly discernable on the hydrogen background density. Note that the neutral density distribution outside the plasma is not meaningful, *DOUBLE-TCV* ignores potential molecular and flow processes in the plasma SOL.

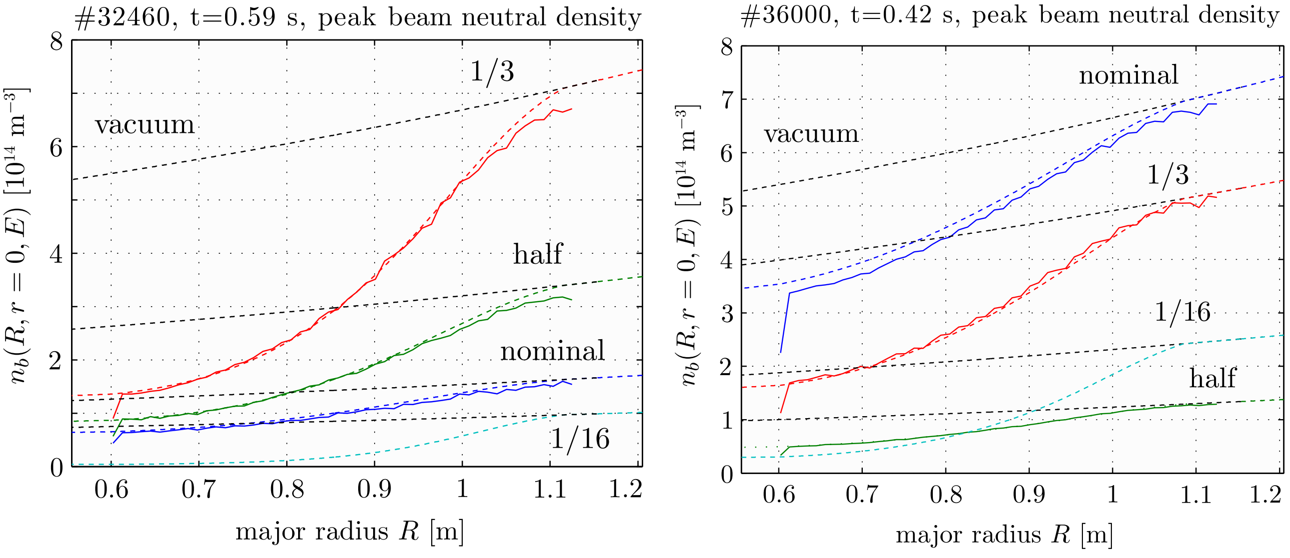

(a) prior to beam upgrade (b) after beam upgrade

Figure 4.7.4: Peak beam density on the beam axis. (a) shows the beam condition with the RF plasma box for discharge #32460, (b) with the new arc source for discharge #36000, demonstrating the improved beam energy distribution. Shown are again calculations with *BEAT* and *DOUBLE-TCV*. Both codes agree reasonably well.

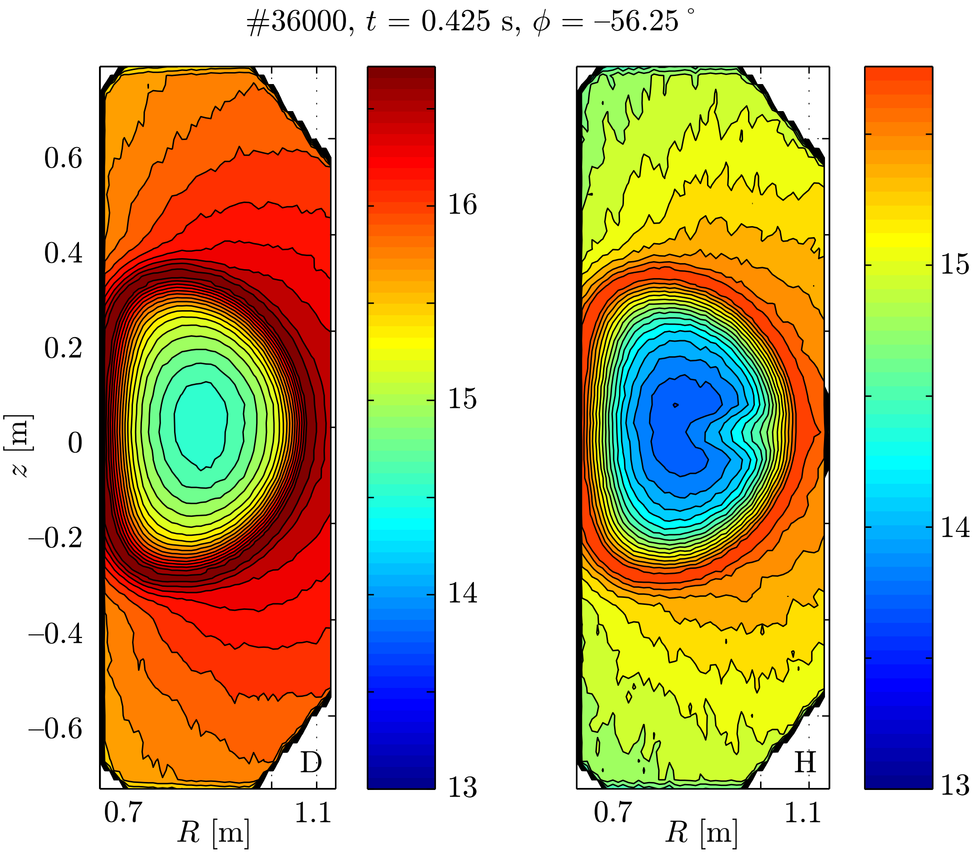

Figure 4.7.5: Neutral density distribution in a poloidal plane for the conditions of discharge #36000. The colour bar scales with the logarithm of the neutral density (in m−3). The toroidal location shown ($\phi = -56°$) coincides with the location of the DNBI. The left cross section shows deuterium, the right hydrogen. The simulation includes 2’000’000 wall, 100’000 beam and 10 halo particles (per beam particles). Particles were tracked down to densitites that were a factor 10^{-9} than the initial density.

4.7.3 Comparison of *DOUBLE-TCV* and *KN1D*

In order to benchmark *DOUBLE-TCV*, both neutral transport codes were run for many thermal discharges of TCV [160]. Each time, the atomic neutral density and energy at the LCFS, calculated by *KN1D*, were taken by *DOUBLE-TCV* and both codes calculated the neutral density profile along the vessel midplane against the same background plasma profiles. The edge neutral density was taken to be uniform. High density discharges require *KN1D* to be executed with a larger number of iterations of the calculation of the neutral distribution function to avoid the neutral density to be truncated in the plasma centre. The number of launched particles in *DOUBLE-TCV* requires a massive increase and the initial particle maximum attenuation has to be chosen accordingly, otherwise the number of particles tracked down to the core was often too small. The agreement is excellent with a discrepancy of neutral density in the core as low as a factor of 2. As an example, figure 4.7.6 shows the neutral density profiles provided by *KN1D* and *DOUBLE-TCV* for the moving plasma experiment (section 4.4), calculated along the view line of the CNPA.

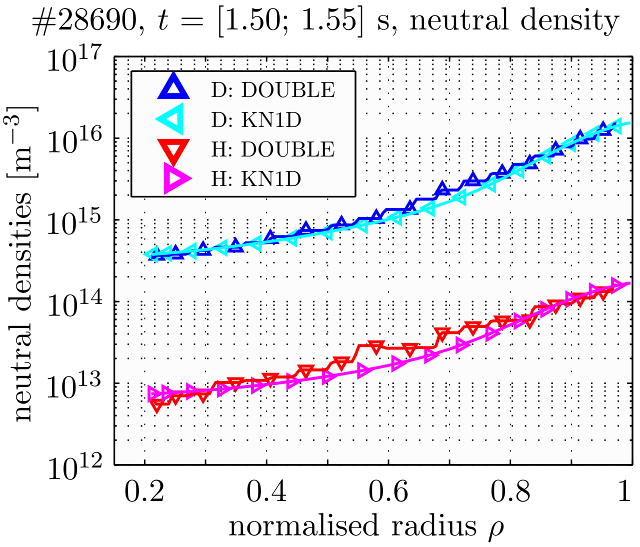

Figure 4.7.6: Simulated profiles of atomic hydrogen and deuterium for t = [1.50; 1.55] s of discharge #28690. Comparison of results from *DOUBLE-TCV* and *KN1D* for identical situations. The profiles are for the low field side of the plasma. The ratio between the hydrogenic isotope densities is ∼2 %.

4.8 Active charge exchange measurements

At the beginning of the 1960s, neutral beams injected into plasmas were first used to measure the electron line density [161] where the beam shine-through was compared to the beam intensity before entering the plasma. The first application of a beam for the local measurement of the ion temperature was obtained on the Russian T-6 tokamak in 1973 [162]. In this technique a diagnostic neutral beam is used to dope the plasma locally with a time-modulated neutral density. The doping gives rise to a modulation in the neutral flux at the analyser, resulting from the increment in charge exchange production at the point in the plasma along the detector sight-line where it crosses the doping beam path. The slope of the measured charge exchange flux spectrum is then characteristic of the temperature at that position and hence a local measurement. The local character of the measurement is maximised by a narrow neutral beam width, a low NPA acceptance and a perpendicular crossing of beam and NPA directions. Many fusion devices (e.g. TFTR [163], Alcator C-Mod [164], HT-7 [165], TJ-II [166]) have been equipped with such an active charge exchange diagnostic setups.

4.8.1 Benefits from active charge exchange on TCV

Although TCV features a diagnostic beam (section 3.2.1) and a CNPA intersecting its beam path until 2007, the active charge exchange measurement is not local. The reason for this is the flat incidence (about 10° only) of the directions of beam and CNPA (figure 4.8.1). As a result the active volume for beam charge exchange extends almost through the whole plasma column and the measurement is mostly global (figure 4.7.2).

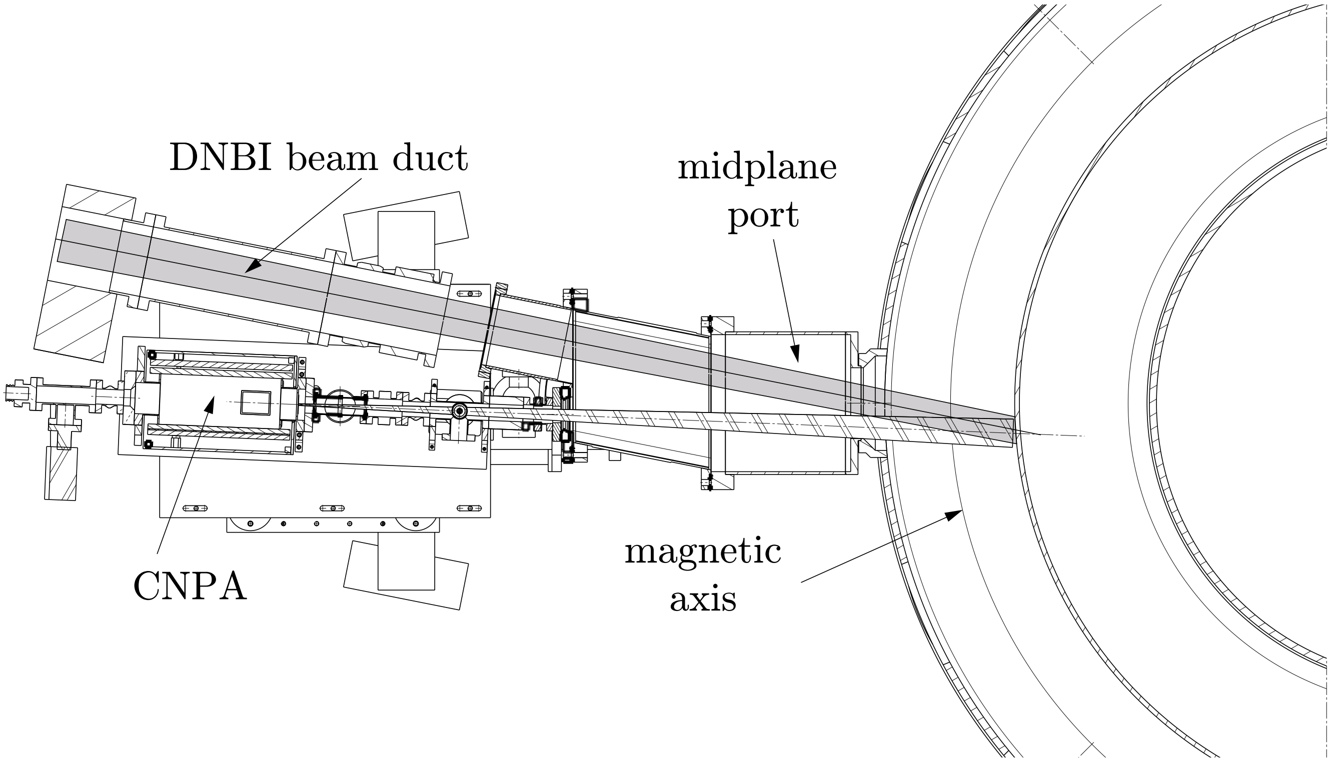

Figure 4.8.1: Setup for active charge exchange measurements on TCV. From 2004–2007 the CNPA was intersecting the DNBI. The position shown corresponds to the minimum angle of intersection between beam and CNPA view line, such that the intersection with the beam axis is located at the inner wall. The CNPA may be slightly turned on its table, the maximum major radius of intersection accessible is approximately $R = 1$ m.

Figure 4.8.2a shows active and passive charge exchange spectra measured by VNPA and CNPA averaged over periods of 20 ms before and during a neutral beam blip, discharge #27094, $\langle n_e \rangle = 2 \times 10^{19}$ m^2, $T_e(0) = 900$ eV, figure 4.8.2b shows the corresponding ion temperature profile obtained with the CXRS diagnostic.

The DNBI mostly injects hydrogen, a fraction of the injected neutrals get ionised in the plasma (section 6.5.1) and these beam deposited particles strongly perturb the charge exchange spectra measured by the hydrogen array of the CNPA, impeding a core ion temperature measurement.
On the other hand the deuterium neutral flux registered by the CNPA is enhanced by approximately an order of magnitude, depending on the electron density. This flux increase is due to charge exchange between beam hydrogen and plasma deuterium ions. The VNPA doesn't gain from the beam doping as its line of sight doesn't intersect the beam. However the beam deposited ions, following their orbits, occasionally get neutralised in front of the VNPA and pollute the high energy tail of the charge exchange spectrum, though the perturbation is less pronounced than on the CNPA (as the hydrogen contribution is masked by the stronger superimposed deuterium flux).

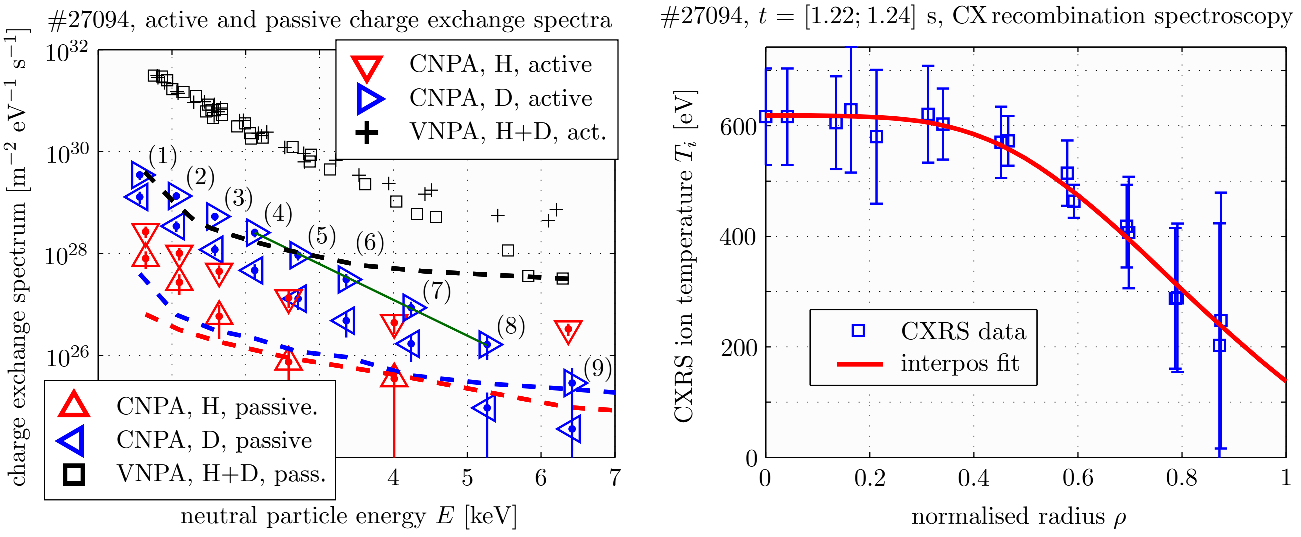

(a) Active charge exchange spectrum (b) CXRS ion temperature profile

Figure 4.8.2: Illustration of global charge exchange measurements on TCV. (a) depicts the NPA charge exchange spectra during a passive (averaged over t = [1.19; 1.2] s) and an active (averaged over t = [1.23; 1.24] s) charge exchange phase. The fitted slope (during the active phase, see the straight line) indicates a core deuterium temperature of 618 ± 12 eV, in agreement with the peak ion temperature profile measured with the CXRS diagnostic (b).

Nevertheless the measured charge exchange spectrum is still slightly curved, due to the non-locality of the measurement. Anyway, the increased flux permits improved statistics for the temperature inference and extends the range of diagnosable core ion temperatures to ∼20 % higher electron densities in respect to the density limit of passive charge exchange. As shown in figure 4.8.2a, the charge exchange spectrum is noisier without the additional neutrals from the beam, the core ion temperature is only reliably determined during the beam blip and agrees well with the CXRS value: $T_i(0)^{\mathrm{CXRS}} = 620 \pm 60$ eV, $T_i(0)^{\mathrm{CNPA}} = 618 \pm 12$ eV. The rather large error bar on the CXRS measurement results from a low recombination light yield.

The constructive constraints of the TCV vessel would actually allow to perpendicularly intersect a horizontal beam with a vertical NPA if installed in the same toroidal sector, but the availability of free ports on TCV in the past years has not (yet?!) permitted such a layout.

4.8.2 NPA absolute calibration

The NPA measurement scales linearly with the background neutral densities and the absolute profiles might thus be determined if the NPA is absolutely calibrated.

4.8.2.1 VNPA calibration against neutral pressure gauge

An absolute calibration of the VNPA was not accomplished in the past, although the stripping gas pressure is kept fairly constant (typically 4×10^{-4} mbar), such that the calibration should not evolve in time. A relative calibration is effectively achieved with every discharge diagnosed in sweep mode, as the channel overlapping is typically 50. . . 70 % of the energy swept by each channel. The measurement of the edge neutral pressure, as described in section 4.1.3 (figure 4.1.2), was used to model the absolute neutral density profile (with *KN1D*, figure 4.2.1).

The measured VNPA neutral flux spectrum was then scaled to agree with the modelled spectrum, both are shown in figure 4.8.3. All data derived from VNPA measurements shown in this thesis is scaled in this way.

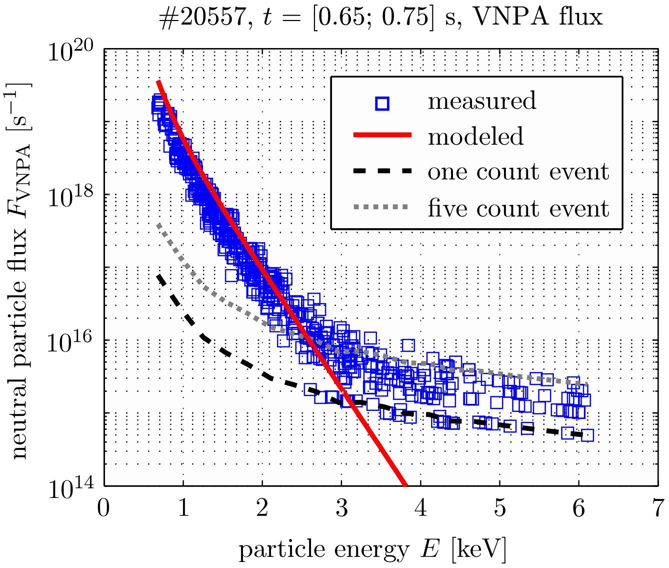

Figure 4.8.3: Calibrated energy spectrum of the neutral flux measured with the VNPA (squares) and its simulation using *KN1D*. The *KN1D* result is absolutely scaled by the neutral pressure measured with the fast pressure gauge. The VNPA measurement was then scaled to reproduce the modelled neutral particle measurement in the statistically relevant energy range.

The gauge pressure measurement is expected to be close to the background vessel pressure. However, the uncertainties in the measurement technique are quite large and there may be large variations of the neutral pressure in the periphery due to the wall geometry, local pumping points, local gas injection and SOL gas fluxes (the gauge is in sector 3, the VNPA in sector 1). The unavailable measurement of the isotopic composition of the plasma (before the CNPA became available, see section 4.9.6.1) further complicates the unbundling of contributions form hydrogen and deuterium to the measured flux.

4.8.2.2 CNPA calibration using the diagnostic beam

Prior to delivery, the CNPA manufacturer characterised the detector response using a mono-energetic particle beam providing calibration coefficients (detection efficiency, energy instrumental function). Provided that the geometrical parameters (diagnostic alignment and solid angle) are known with sufficient precision, the CNPA is therefore absolutely calibrated. However, the coefficients for channels with energy above 30 keV were not determined experimentally (restriction on the manufacturers beam energy) and were estimated by modelling the ion trajectories in the dispersion element. An in-situ absolute calibration on the tokamak was therefore most welcome. When the CNPA was installed the neutral pressure gauge had ceased operation. But the intersection of CNPA and DNBI path allowed for a new calibration based on the beam modulated increase of the charge exchange targets. For this purpose, both NPA were simultaneously modelled with the *DOUBLE-TCV* code for a phase without and a phase with DNBI. Figure 4.8.4 shows the excellent results, for the hydrogen (left) and deuterium (middle) arrays of the CNPA and the VNPA (right). The modelling took all available experimental data into account, i.e. $T_e(\rho)$ from Thomson scattering, $T_i(\rho)$ from CXRS, $n_e(\rho)$ SVD-I reconstructed from the FIR, average Z_{eff} from conductivity measurements and the neutral edge densities were adjusted to achieve agreement with the NPA measurements.

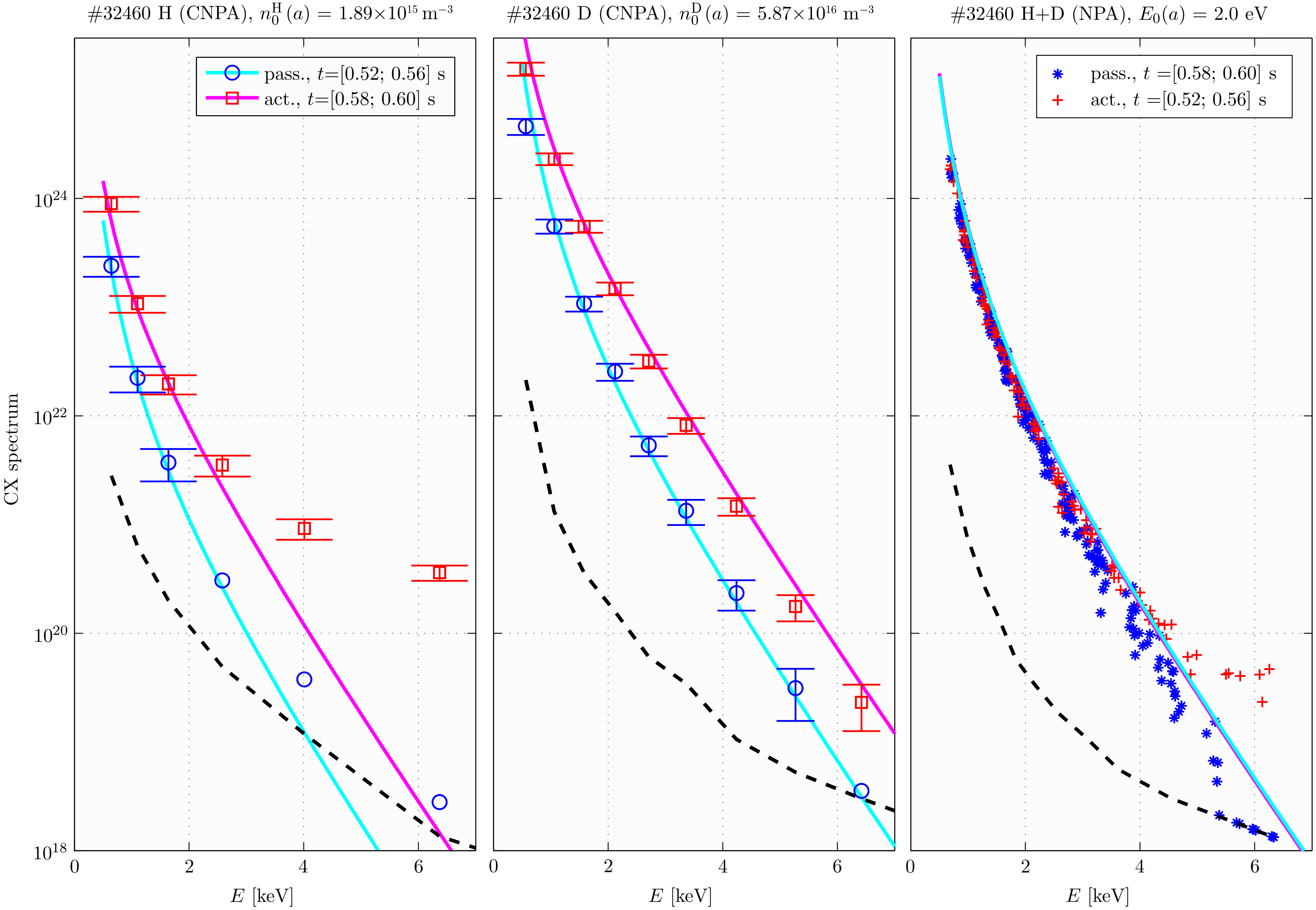

Figure 4.8.4: Simulation of the absolute number of neutrals provided by the DNBI for discharge #32460 at $t \approx 0.6$ s. The CNPA charge exchange spectrum is scaled by the absolute calibration coefficients provided by the manufacturer, the VNPA is calibrated using the method described in section 4.8.2.1.

The VNPA measurement was modelled by the sum of the hydrogen and deuterium flux using the previously determined calibration coefficients (see preceding section). The ion temperature profile and the density of the neutrals surrounding the plasma before and during the beam blip were assumed to be the same. The wall particle energy was taken $E_0(a) = 2$ eV. The beam energy was 50 keV.
Note again that the ionised beam hydrogen is visible on the VNPA and the CNPA hydrogen array. Proper modelling of the neutral flux due to the beam ions would require the calculation of the (magnetically confined) ion orbits in the whole plasma torus (including all probable orbit loss mechanisms). The computational investment for such an analysis would be disproportionate and the corresponding calculations are thus not implemented in *DOUBLE-TCV*.
The two VNPA spectra overlap well, confirming the assumptions that the wall particle pressure and the plasma ion temperature do not considerably change between the two time intervals considered.

The same exercise of the NPA calibration with the beam was successfully repeated for various historical setups of the DNBI (e.g. also with the new ion optical system installed in 2007–2008) and the absolute beam neutral source simulations were always consistent with the NPA and CXRS (recombination luminosity) measurements. The conclusion from what has been shown in this section is that the description of the DNBI beam is correctly implemented in *DOUBLE-TCV* and is considered as confirmation of an acceptable absolute calibration of VNPA and CNPA.

4.9 Diagnosis of thermalised ion populations in steady-state inductive discharges

Thus far the ion temperatures of various ionic species have been compared numerous times and their agreement was generally noted. This section recapitulates, after all, the reasons why.

4.9.1 Relaxation processes

The long-range Coulomb forces induce frequent elastic collisions between the charged particles of a strongly ionised plasma. Collisions are responsible for the loss or transfer of energy or momentum among the charged particle species of a plasma and are responsible for the isotropisation and thermalisation of particle populations. The rate at which a collision produces a certain effect (e.g. energy transfer) is commonly obtained by considering a succession of frequent small angle two-body collisions and by integration over all possible collision impact parameters [167]. An effective collision frequency for the loss of kinetic energy E from projectile particle species j with velocity v_j on target particles at rest of species k may be defined as

$$\nu_E^{j/k} = \frac{1}{E}\frac{\mathrm{d}E}{\mathrm{d}t} = n_k \frac{Z_j^2\, Z_k^2\, e^4}{2\pi\, \epsilon_0} \frac{\ln \Lambda_k}{m_j\, m_k\, v_j^3}. \tag{4.9.1}$$

An average collision frequency for a population of particles of a certain velocity distribution is then obtained by integration of eq.(4.9.1) over the distribution function of the projectile particles. For the case of energy transfer from electrons to ions, this becomes

$$\overline{\nu}_E^{e/i} = \frac{1}{n_e\, E} \int \nu_E^{e/i} f_e(\mathbf{v})\, \frac{1}{2} m_e \mathbf{v}^2\, \mathrm{d}\mathbf{v} = \frac{2}{3}\sqrt{\frac{2}{\pi}}\, n_i \frac{Z^2\, e^4\, \ln \Lambda}{4\pi\, \varepsilon_0^2} \frac{\sqrt{m_e}}{m_i\, T_e^{3/2}}. \tag{4.9.2}$$

Figure 4.9.1 summarises the hierarchy of the characteristic time scales $\tau = \nu^{-1}$ for the isotropisation (momentum transfer) and thermalisation (energy transfer) for ions and electrons.

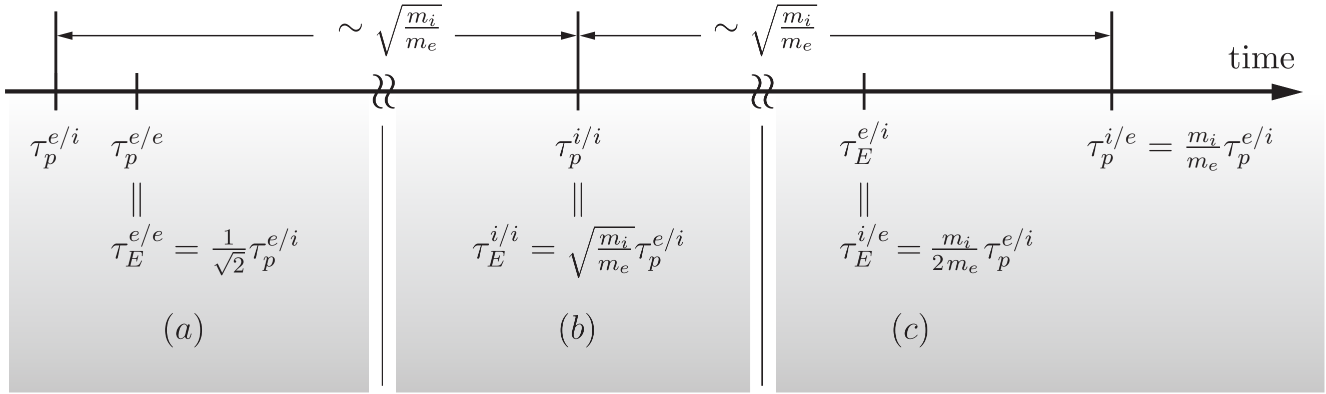

Figure 4.9.1: Characteristic time scales for momentum (τ_p) and energy exchange (τ_E) in terms of the fastest collision process ($\tau_p^{e/i}$). There are three classes of time scales at play: (a) electrons lose momentum on ions and other electrons, electrons lose energy on other electrons (electrons become Maxwellian), (b) ions lose momentum and energy on other ions (ions become Maxwellian) and (c) electrons and ions reach thermal equilibrium.

The following three time scales are distinguishable:

a.) the electrons loose momentum first on the ions, then energy and momentum on other electrons. For example, for an ohmically heated low density deuterium TCV plasma, $n_e(0) = 1 \times 10^{19}$ m^{-3}, $T_e(0) = 1$ keV, $T_i(0) = 500$ eV, $\tau^{e/e} = 60$ μs. The electron population is rapidly thermalised.

b.) A time of the order $\sim\sqrt{\frac{m_i}{m_e}}$ later, ions have thermalised. For the example above, this happened after $\tau^{i/i} = 1$ ms. That is, particles of the same species have reached thermal equilibrium, but $T_e \neq T_i$ yet.

c.) Only a time again $\sim\sqrt{\frac{m_i}{m_e}}$ later, electrons and ions have thermalised $T_e = T_i$. The equipartition of the energy between electrons and ions would take more than $\tau_E^{e/i} = 120$ ms for the plasma considered.

However, tokamak plasma confinement is not perfect and losses (by transport or radiation) may occur on time scales comparable or faster to those of collisional processes. An energy confinement time is commonly defined by the balance between energy input and losses to a certain species. The plasma heating schemes on TCV (inductive or injection of electron cyclotron waves) primarily heat the electrons only.

The energy of the electron population,

$$E_e = \frac{3}{2}\int n_e T_e \, \mathrm{d}V, \tag{4.9.3}$$

varies as

$$\frac{\mathrm{d}E_e}{\mathrm{d}t} = P_{\mathrm{OH}} + P_{\mathrm{ECH}} - \frac{W_e}{\tau_E^e}, \tag{4.9.4}$$

where P_{OH} and P_{ECH} are the ohmic and electron cyclotron wave heating powers respectively and τ_E^e is the electron energy confinement time.

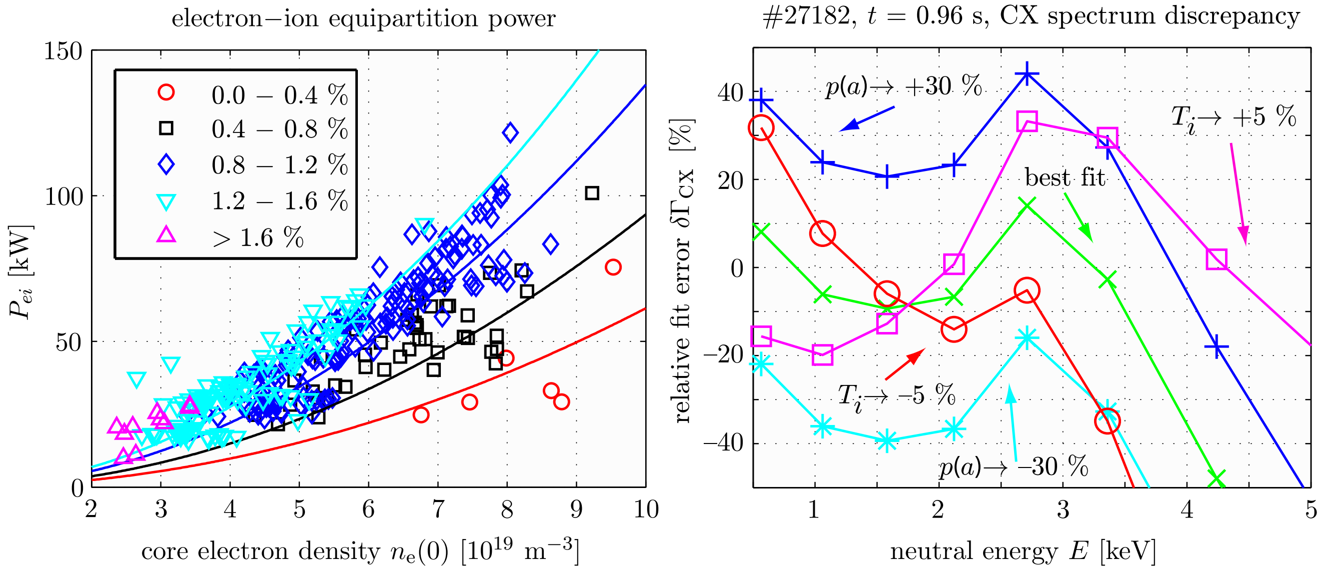

(a) Power equipartition. (b) Quality of CX spectrum fit.

Figure 4.9.2: (a) Electron–ion equipartition power for TCV plasmas (symbols) as a function of the core electron density. The ion temperature was obtained with the CNPA, the electron temperature and density were extrapolated from profile fits to Thomson scattering data. The legend labels the values of the fraction in eq.(4.9.8). The solid curves represent robust quadratic fits of the data.
(b) Relative fit error $\delta\Gamma_{\mathrm{CX}}$ for deuterium. The best fit is obtained for $T_i = T_{i\mathrm{C}}^{\mathrm{CXRS}}$. The linearity the charge exchange spectrum with particle edge density $p(a)$ is demonstrated with *KN1D* runs with the edge pressure modified by ± 30%. The influence of the ion temperature on the slope of the mismatch as function of particle energy is also shown ($T_i \pm 5\%$).

Ions gain energy through collisions with the electrons, the balance of the ion energy is written

$$\frac{\mathrm{d}E_i}{\mathrm{d}t} = P_{ei} - \frac{E_i}{\tau_E^i}, \tag{4.9.5}$$

where P_{ei} is the equipartition power between electrons and ions, defined as

$$P_{ei} = \frac{3}{2}\int n_i \frac{\mathrm{d}T_i}{\mathrm{d}t}\,\mathrm{d}V \tag{4.9.6}$$

and τ_E^i is the ion energy confinement time. Using the equipartition time $\tau_E^{e/i} = 1/\nu_E^{e/i}$ defined in eq.(4.9.1), the increase in ion temperature may be written as

$$\frac{\mathrm{d}T_i}{\mathrm{d}t} = \frac{T_e - T_i}{\tau_E^{e/i}}. \tag{4.9.7}$$

Eq.(4.9.6) depends therefore strongly on electron density and temperature, namely

$$P_{ei} \propto n_e^2 \frac{T_e - T_i}{T_e^{3/2}}, \tag{4.9.8}$$

illustrated in figure 4.9.2a.

The energy losses of electrons and ions are phenomenologically characterised by energy confinement times τ_E^e and τ_E^i. They are defined by eq.(4.9.4) and eq.(4.9.5) by setting $\frac{\mathrm{d}E_i}{\mathrm{d}t} = 0$. For typical TCV plasmas τ_E^e is of the order of 10 ms, τ_E^i ~100 ms.

To summarise, the energy time scale ordering of TCV plasmas is as follows:

$$\tau_E^{e/e} < \tau_E^{i/i} < \tau_E^e < \tau_E^i \simeq \tau_E^{e/i} \tag{4.9.9}$$

This in turn implies that

- ions equilibrate their energy more than 100 times faster than they are heated by collisions with the electrons. The ion temperatures of the various ion species (essentially hydrogen, deuterium, carbon) in TCV plasmas are therefore expected to be thermalised among themselves, e.g. $T_i^{\mathrm{H}} = T_i^{\mathrm{D}} = T_i^{\mathrm{C}}$. Measurements with diagnostics measuring the temperature of different ion species confirm this (see the following sections).

- At low densities, the energy confinement time of ions is of the order or less than the electron–ion equipartition time and the equipartition power is low and electrons and ions are not expected to have time to thermalise.

- $\tau_E^{e/i}$ decreases and P_{ei} increases with density, their heating rate exceeds the loss rate and $T_e = T_i$ may be achieved (section 4.9.4). Note that burning plasmas (e.g. ITER) or neutral beam/ICRF heated plasmas (e.g. JET) generally have $T_i > T_e$.

4.9.2 Validation of the NPA against the CXRS temperature profile

So far it was shown that the ion temperature profile inferred from the CNPA CX spectrum agrees with the integrated model of neutrals in the plasma. We now compare the hydrogenic ion temperature profiles to a simulation obtained with profiles of the carbon ion temperature measured with charge exchange recombination spectroscopy. The comparison was thus made with a stationary, ohmically heated discharge (shot #27182) at $z \simeq 0$ featuring a high-quality CXRS measurement and a strong passive charge exchange flux. The constancy of the plasma parameters permitted a reduction of the Poisson statistical error by integrating the CNPA signals over several tens of milliseconds, obtaining error bars below ∼10 %, even for higher particle energies (see figure 4.3.3a). T_i^{CXRS} was measured at $t \approx 0.95$ s, close to the time interval selected for averaging the CNPA signals in order to keep the temperature measurements comparable, but sufficiently delayed from neutral injection to allow the injected hydrogen beam particles decelerate to thermal velocities.

The profiles used in the neutralisation codes are shown in figure 4.2.2. For the ion temperature, the experimental profile from CXRS was directly used in the codes this time. For the analysis of time intervals far from a CXRS measurement, a small ion temperature scaling factor, close to 1, and constant over the radial profile, accounts for the possibility of having $T_i^{\mathrm{C}} \neq T_i^{\mathrm{D}}$ or the heating or cooling of the plasma in respect with the CXRS measurement and may thus improve the agreement of the simulation with the experiment over the considered time interval.

The effect of a small ±5 % change of T_i^{D} with respect to T_i^{C} in the simulation is illustrated in figure 4.9.2b (□, ⊙), showing the relative error $\delta\Gamma_{\mathrm{CX}}$, eq.(4.4.2), between simulated and measured neutral flux Γ_{CX}. The figure shows deuterium channels #1 to #7 ($E = 500\ldots5'000$ eV) where the statistical Poisson uncertainty of the averaged CNPA signals, shown in figure 4.3.3a, is below ∼20 %. Ion temperature changes lead to a positive (negative) slope in the relative error $\delta\Gamma_{\mathrm{CX}}$ when the temperature is increased (decreased).

The best agreement with the CNPA measurement was obtained by setting $T_i^{\mathrm{code}} = T_i^{\mathrm{CXRS}}$. The modelled charge exchange spectrum was already shown in figure 4.3.2a (solid lines). For the shown energy interval, the simulation recovers the experimental charge exchange flux again with a mismatch $\lesssim$10 %.

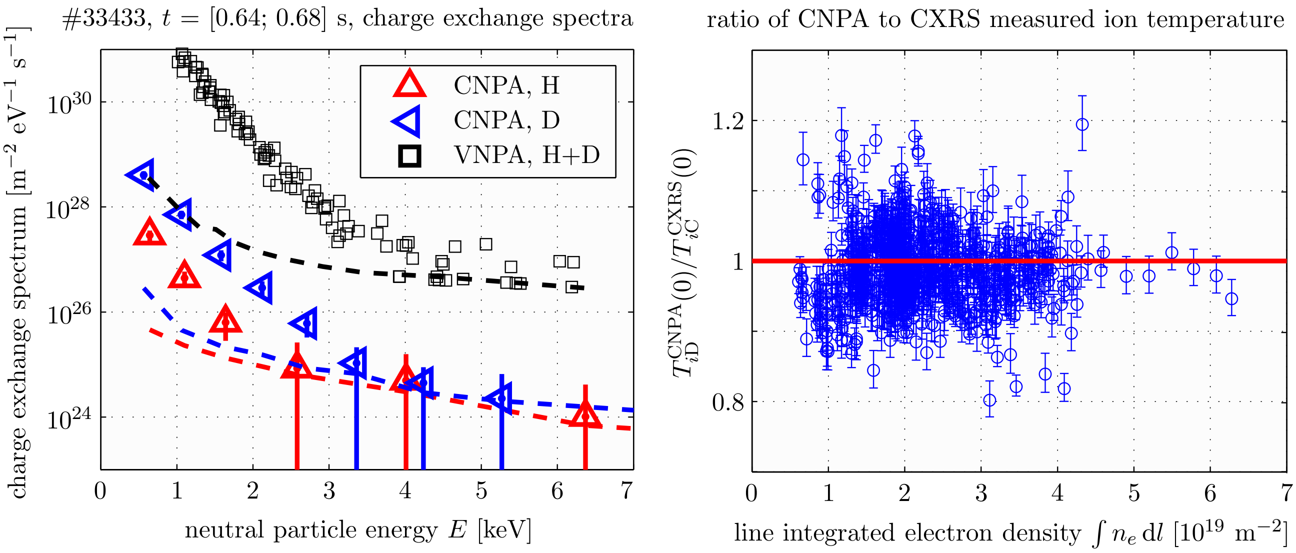

(a) High density CX spectrum.

(b) Comparison of CNPA and CXRS.

Figure 4.9.3: (a) Charge exchange spectrum of the high density discharge #33433 with $T_i(0)$ = 750 eV. Flux components with energies above 4 keV are statistically irrelevant and the core temperature is not retrievable, as this would require to fit the slope of the spectrum at energies up to 7.5 keV.
(b) Ratio of CNPA and CXRS temperature as a function of line integrated electron density. The absorption of core neutrals during their journey towards the CNPA increases with density, but this has no influence on the correct ion temperature calculation.

The quality of the agreement between simulation and experiment vindicates the model presented in section 4.2.1 and implies that the deuterium and carbon ion temperatures are essentially the same, which is to be expected since the ion thermalisation time is ~0.5 ms for these plasma conditions (incidentally also vindicating the use of the CXRS profile from carbon as the hydrogenic ion temperature in the simulation).
To demonstrate the charge exchange flux linearity and solution sensitivity to neutral wall parameter changes, figure 4.9.2b illustrates further code simulations with the same conditions but $p_{D_2^0}(r{=}a)$ modified by 30 % respectively.

4.9.3 Density limit for neutral particle analysis

Any comparison of the measurement of a plasma physics parameter obtained with different experimental techniques must deal with the limitations of applicability of the latter. Table 3.2 summarised the capabilities of CXRS and NPA for the central T_i measurement in terms of density. The quite low density limit of the VNPA is explained by the long path that core neutral particles must cover inside the plasma to reach the diagnostic. Figure 4.8.3 illustrates a spectrum, although averaged over 100 ms, with the statistical limit lying below the energy necessary to fit the core ion temperature. Things are less strict with the CNPA, where this limit now extends to $n_e(0) \leqslant 6 \times 10^{19}$ m^{-3}. Active charge exchange measurements extend its operational domain even to $n_e(0) \leqslant 8 \times 10^{19}$ m^{-3}. Figure 4.9.3a shows the charge exchange spectrum for a discharge with $n_e(0) \simeq 1.7 \times 10^{20}$ m^{-3}, close to the highest density achievable on TCV. The ion temperature is expected to approximate 750 eV but the CNPA records only neutrals up to energies half the energy necessary to successfully infer the temperature from the spectrum.
As the CXRS diagnostic nowadays has a similar high density limit, $n_e(0) \leqslant 8 \times 10^{19}$ m^{-3}, the following analysis is naturally limited to a comparison of many discharges at low and intermediate densities.

4.9.4 Statistical benchmark of CXRS and CNPA T_i measurement

To further justify the energy range for the temperature inference from the charge exchange spectrum, the CXRS ion temperature measurement made during ∼2500 hydrogen DNBI beam blips extended over the last four years of TCV operation (2005–2008) were compared to the core ion temperature derived from the CNPA charge exchange spectrum.

CNPA and CXRS signals were both integrated over the whole DNBI beam pulse length. Figure 4.9.4a shows the excellent agreement of the ion temperature measurement, over a wide range of ion temperatures. Most of these measurements represent steady-state plasma phases. All the ion populations, hydrogen, deuterium and carbon are strictly heated by collisions with electrons and are thus expected to be thermalised with each other (section 4.9.1).

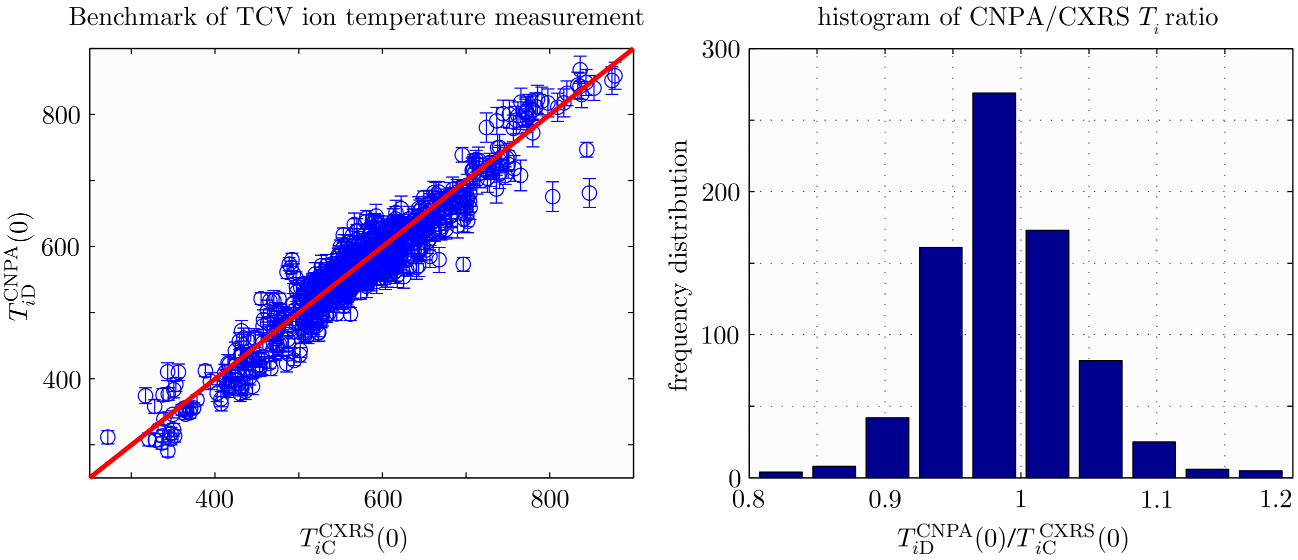

(a) CNPA and CXRS $T_i(0)$

(b) CXRS ion temperature profile

Figure 4.9.4: Benchmark of CXRS and CNPA core ion temperature measurements.
(a) compiles 2500 measurements made from TCV experiment #27053 to #34972 and demonstrates the agreement between the two diagnostics.
(b) shows the distribution of the mismatch between the two diagnostics.

For CXRS, the central ion temperature was extrapolated from an interpolated profile if a believable measurement at $\rho = 0.2$ or below was available. The core ion temperature was determined from the CNPA measurement according to eq.(4.3.13). All possible TCV scenarios are represented, as long as the bulk ion temperature was determinable with the CNPA (e.g. in absence of suprathermal ion species, see section 6.1).
Figure 4.9.4b illustrates the histogram to the ratio of CNPA to CXRS temperature, 90 % of the measurements give values in agreement to within 10 % !

Figure 4.9.3b shows the ratio of the ion temperatures as a function of electron density, demonstrating that NPA may correctly determine the core ion temperature for low and mid range electron densities (remember, this is active charge exchange).

Figure 4.9.5b illustrates the typical agreement of the CXRS and CNPA ion temperature measurement within a single discharge (for the density ramp of experiment #30556, figure 4.9.5a).

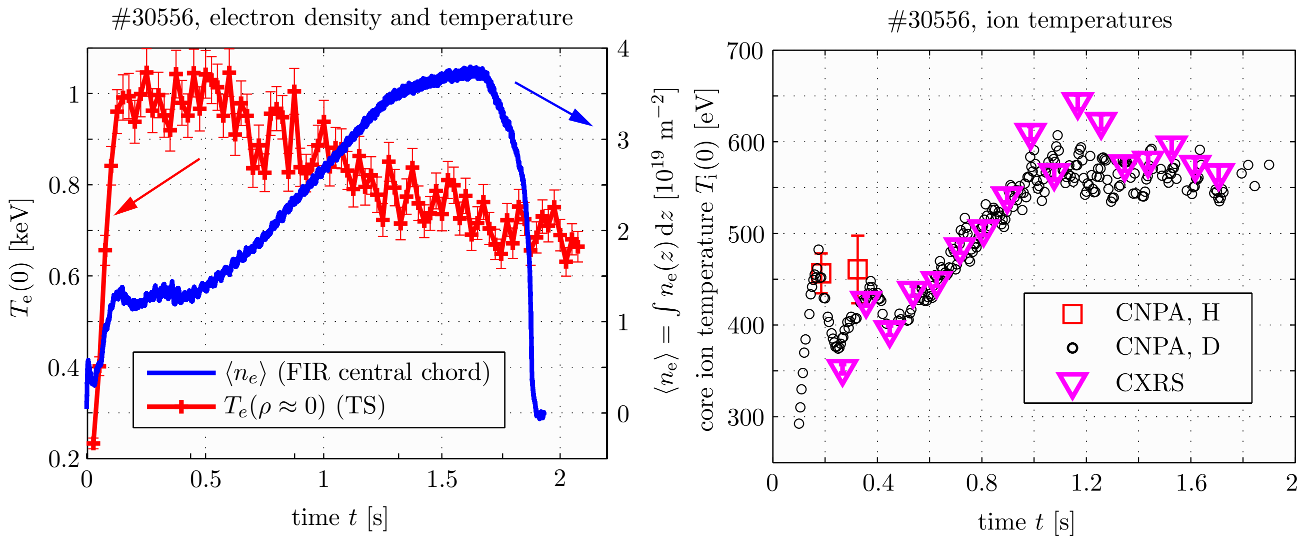

(a) (b)

Figure 4.9.5: Comparison of T_i measurement with CNPA and CXRS diagnostics (discharge #30556).
(a) The electron density keeps increasing from $\langle n_e \rangle = 1 \times 10^{19}$ m^{-2} @ 0.4 s to $\langle n_e \rangle = 4 \times 10^{19}$ m^{-2} @ 1 s, the electron temperature is high and slightly decreases during the plasma lifetime.
(b) Ion temperatures ramp measurement. The hydrogen flux is very weak, its intensity is only sufficient for the temperature calculation at the beginning of the discharge. The deuterium temperature is calculated every 5 ms, independently of the hydrogen beam blips.

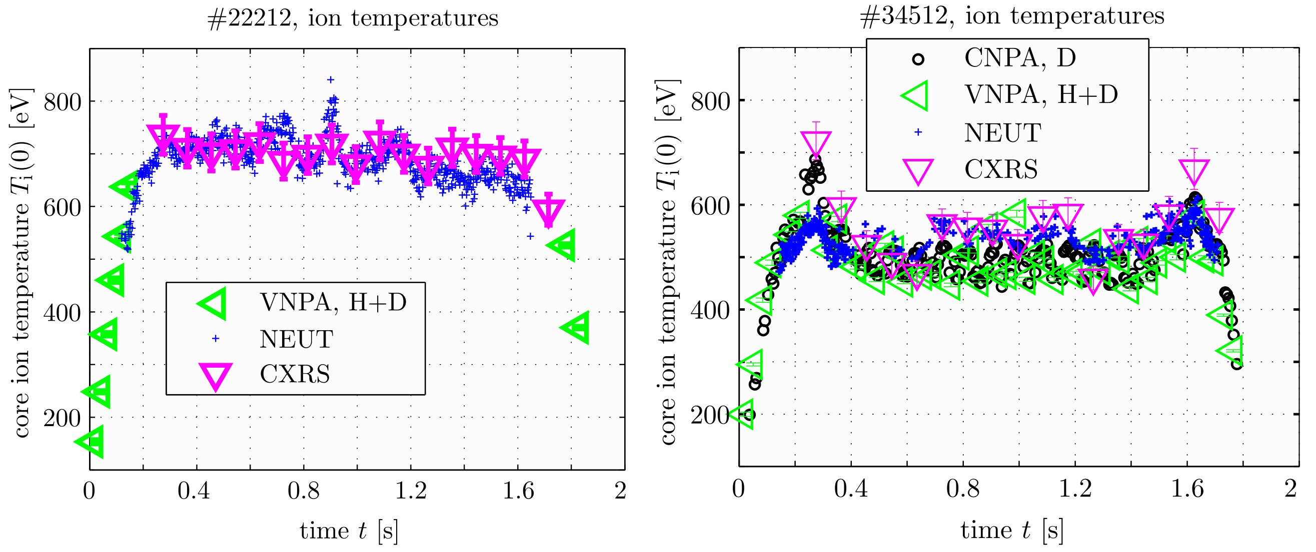

(a) #22212 (b) #34512

Figure 4.9.6: Comparison of T_i measurement with CNPA and CXRS diagnostics.
(a) limited discharge #22212, $T_e(0) = 1.1$ keV, $\langle n_e \rangle = 2.5 \times 10^{19}$ m^{-2}. The CNPA was not yet available, T_i is too high to be calculated from the VNPA during the flattop.
(b) diverted, single upper null discharge #34512, $T_e(0) = 800$ eV, $\langle n_e \rangle = 2.0 \times 10^{19}$ m^{-2}. Good neutron statistics is only available at the beginning and at the end of the discharge, where the density peaks to $\langle n_e \rangle = 3 \times 10^{19}$ m^{-2}. The CNPA measures the ion heating by the beam.

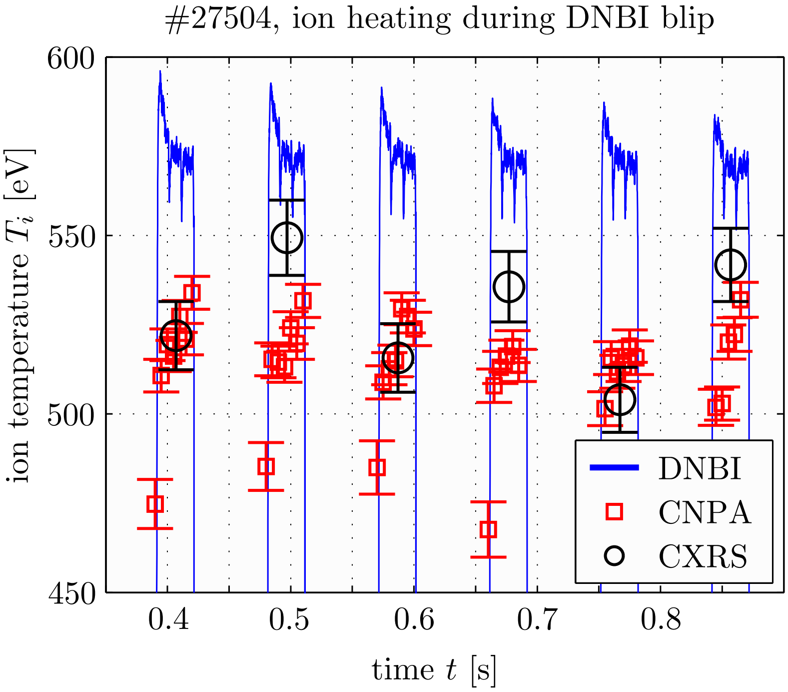

Figure 4.9.7: Ion heating during DNBI beam blips. The DNBI trace corresponds to the neutral current (arbitrary units). Due to the beam deposited ions the plasma temperature (deuterium is shown here) increases by approximately 10 %. Discharge #27504, $T_e(0) = 650$ eV, $\langle n_e \rangle = 4 \times 10^{19}$ m^{-2}.

4.9.5 Overall comparison of ion diagnostics in thermal plasmas

The third type of ion temperature measurement on TCV, the neutron detector, gives reliable estimations for $T_i(0)$ at high ion temperatures (where the fusion reactivity strongly increases) and the neutron statistics increases with the square of the deuterium ion density (section 3.5). High thermal ion temperatures are only attainable at high electron density on TCV (section 4.10.2). The neutron detector is namely used to estimate $T_i(0)$ at high density, where the exploitation of NPA and CXRS are not suitable. At intermediate densities, none of the diagnostics perform well but such plasmas are interesting as a comparison of diagnostic methods.

Figure 4.9.6 shows two examples of ion temperature traces obtained with neutron detector, CXRS and CNPA. The first was calibrated in 1997, discharge #22212 (figure 4.9.6a) was obtained five years, discharge #34512 (figure 4.9.6b) ten years after the calibration. The calibration seems not to have evolved with time. The 'neutron' ion temperature was calculated using the ion temperature profile shape measured by CXRS, but not its absolute value.

During DNBI beam blips a small fraction of the neutrals are ionised. These ions transfer most of their energy to the electrons during their slowing down. The energy directly transferred to the plasma ions results in an increase of the hydrogenic ion temperature of less than ten percent (confirmed by modelling of the CNPA hydrogen charge exchange spectrum before and during a beam blip). This value is within the typical error bars of the CXRS measurement. This effect is seen in figure 4.9.6b and shown in greater detail in figure 4.9.7.

4.9.6 Ion and neutral density profiles

4.9.6.1 Experimental determination of the isotopic composition

The experimental assessment of the isotopic composition of the bulk plasma is still lacking on many tokamaks, although it is required for the analysis of many aspects of tokamak physics, especially transport issues. Recent experiments with trace isotopes (tritium at JET [168]) made high demands on exact measurement of the isotope concentrations. Isotope monitoring will be indispensable in burning mixed fuel plasma operation, like in ITER. New NPA monitoring multiple plasma ion species were developed, like the isotope separator (ISEP), which has successfully measured the three hydrogenic isotopes, again on JET [169].

On TCV the radial profile of the fuel isotopic composition is obtained from the CNPA hydrogen and deuterium efflux measurements using the relation between particle energy and position of maximum emissivity, as discussed in section 4.5.2. The particle flux of species j, eq.(4.3.5), approximated by considering only the contribution from the maximum emissivity x_0, may be written

$$\Gamma_j(E) = \gamma_j(E) \int_{-a}^{a} n^0(x) \left\langle \sigma v_j^0 \right\rangle_{\mathrm{CX}} (E)\, f_j^i(x,E)\, \delta(x-x_0)\, \mathrm{d}x = \\ \gamma_j(E)\, n^0(x_0) \left\langle \sigma v_j^0 \right\rangle_{\mathrm{CX}} (E) \int_{-a}^{a} f_j^i(x,E)\, \mathrm{d}x = \gamma_j(E)\, n^0(x_0) \left\langle \sigma v_j^0 \right\rangle_{\mathrm{CX}} (E)\, n_j^i(E), \quad (4.9.10)$$

where the fast neutral attenuation, eq.(4.3.4), appearing in the emissivity function, eq.(4.3.1), is approximated by a transmission coefficient evaluated at x_0, e.g.

$$\gamma_j = \exp\left(- \int_{x_0}^{a} \alpha_j(l)\, \mathrm{d}l \right). \quad (4.9.11)$$

In the energy range below 10 keV the charge exchange rate coefficient is flat (figure 3.3.1) and is species independent.

From the ratio of the neutral fluxes, measured at the same energy for species j and k, the isotopic composition is then derived through

$$\frac{n_j}{n_k} = \frac{m_j}{m_k} \frac{\Gamma_j}{\Gamma_k} \frac{\gamma_k}{\gamma_j} \quad (4.9.12)$$

and the factor involving the masses comes from the comparison of the two fluxes at the same energy ($v_j = \frac{m_k}{m_j} v_k$).

For hydrogen and deuterium, x_0 almost coincides and the absorption probabilities α are quite close (see figure 4.3.1), thus $\gamma_{\mathrm{H}}/\gamma_{\mathrm{D}} \approx 1$. The radial profile of the isotopic composition is then readily available, although the neutral energy to plasma radius conversion needs some modelling. Figure 4.9.8a shows the radial isotopic composition profile for the E-to-ρ mapping obtained in the moving plasma experiment (section 4.5). One profile was obtained by assuming $\gamma_{\mathrm{H}} = \gamma_{\mathrm{D}}$, the other is corrected by the calculated ratio of the transmission coefficients. The profiles generally indicate that the hydrogen concentration increases towards the plasma centre.

Figure 4.9.8b shows the evolution of the hydrogen population density since the installation of the CNPA (after a TCV restart in June 2004). Only measurements from TCV standard discharges (first prototype plasma shot each morning) at $t = 0.3$ s are shown.

The counted particles in the two lowermost energy channels of the hydrogen and deuterium detector arrays were interpolated at an intermediate energy of 840 eV to calculate the neutral flux ratio from. The isotopic measurement is therefore representative for the outer part of the plasma. The considered CNPA counts were accumulated over a time window of 30 ms.

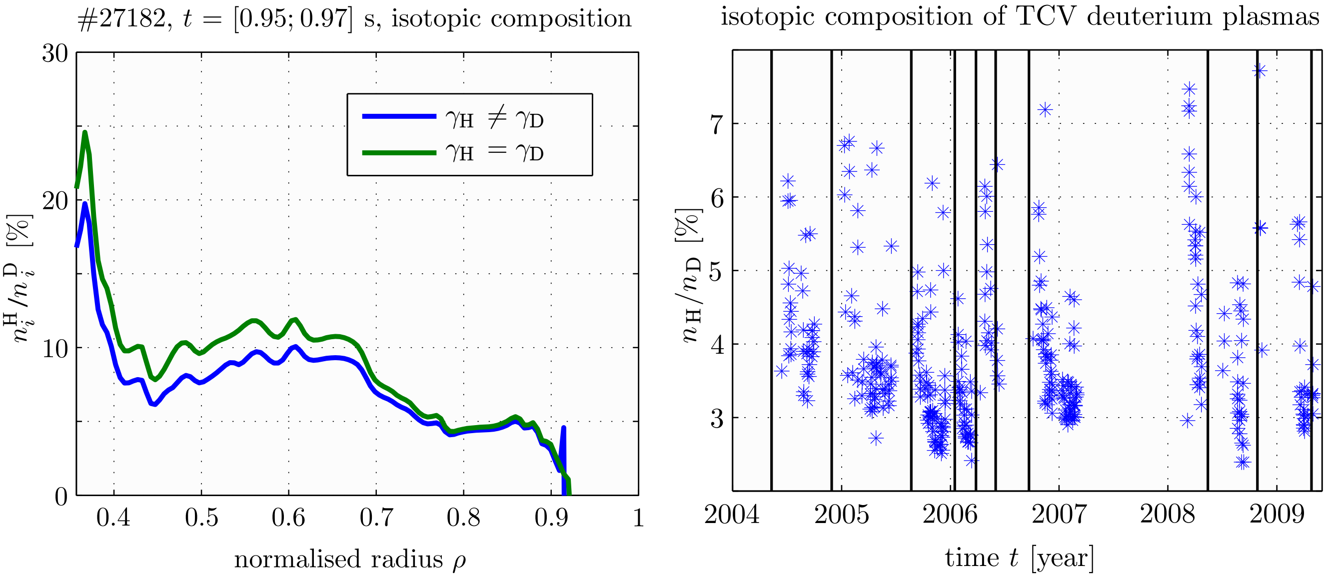

(a) isotopic composition profile. (b) isotopic composition history.

Figure 4.9.8: (a) Profile of the isotopic plasma fuel ion composition of discharge #27182.
(b) Time history of the hydrogen concentration of TCV deuterium plasmas. Periods without discharges indicate tokamak openings for maintenance and upgrades. The vertical lines represent occasional wall conditioning by boronisation.

During the last five years, TCV has been operating with deuterium gas only (pure hydrogen and helium plasma campaigns [170] were performed earlier). Hydrogen is therefore an impurity on TCV. ~90 % of the TCV first wall is tiled with polycrystalline graphite. Hydrogen atoms cannot deeply diffuse into graphite. However, the tile surfaces and the non-graphite materials of the first wall are good absorbers of hydrogen, mainly in their bound form as hydrocarbons or water molecules. The trapped hydrogen gets released by outgassing, erosion (sputtering) and is continually recycled into the plasma. Efficient wall desorption may give hydrogen concentrations as high as 10 %. During experimental campaigns without air leaks the hydrogen slowly decreases through continuous pumping and is replaced by deuterium, but never decreases below some 2–3 %.

Helium was sometimes injected additionally to assist in cleaning the wall surface layers of gas after strong disruptions or air leaks, but the CNPA setup was not switched to observe helium because due to the very bad electron stripping efficiency of helium in the carbon foil at low energy (figure 3.3.7b), the helium setup has poor statistics even in pure helium plasmas. The first wall of TCV is routinely – particulary after a major shutdown – reconditioned using a vessel vacuum bake-out at 250°C followed by a thin film boronisation using a mixture of diborane (B_2H_6) and helium. These conditioning cycles are represented by the vertical lines in figure 4.9.8b. No boronisation was carried out prior to the operation restart March 2008. During the long machine opening in 2007 all the TCV carbon protection tiles were removed, sandblasted and cleaned and the plasma was facing an unconditioned, uncoated wall in early 2008. The hydrogen reduction with operation is well portrayed on figure 4.9.8b, during two month of operation the hydrogen content reduces from 8 % to the TCV asymptotic 3 %.

4.9.6.2 Modelling of absolute neutral density profiles

The absolute value of the charge exchange spectrum (but not its slope and thus the inferred temperature) changes linearly with the neutral density at the plasma edge, as the equations governing neutral penetration (section 4.2.1) and neutral escape (section 4.3.1) are all linear with the plasma edge gas pressure p_a. This has already been reported in section 4.9.2, where *KN1D* was run with artificial modification of the neutral edge pressures. With the absolutely calibrated NPA and the isotopic composition of the plasma known, the absolute atomic neutral (output of *KN1D* or *DOUBLE-TCV*), molecular ion and neutral profiles (output of *KN1D*) and edge pressures (inputs) are obtained by matching the modelled charge-exchange flux $\Gamma_{\text{CX}}^{\text{sim}}(E)$ to the measurement of the CNPA, $\Gamma_{\text{CX}}^{\text{CNPA}}(E)$. Examples of such profiles, obtained following this procedure, are shown in figures 4.2.1, 4.2.2b and 4.7.6 with absolute scales.

4.10 The behaviour of T_i in inductive TCV discharges

4.10.1 Temperature profile shape

The behaviour of the ion temperature profile was also extensively studied with the CXRS diagnostic [171]. Ion temperature profiles are typically flatter than electron temperature profiles measured with the Thomson scattering diagnostic (e.g. figure 4.6.2) and may reasonably be approximated by a parabolic profile, eq.(4.6.1), with peaking factors κ_{T_i} between 0.2 and 0.5. The profile shape is similar to the deduced plasma current profile with the profile flattening in the plasma core mainly due to the action of sawteeth (section 5.4.4).

4.10.2 Plasma energy balance

The energy balance between electrons and ions of inductively heated discharges on TCV depends on the plasma density and charge. With direct heating of the electrons, the electron temperature is in excess or at most close to the ion temperature, depending on the efficiency of collisional energy transfer between the plasma particles. Following eq.(4.9.6), the coupling between electrons and ions is strongly enhanced in denser plasmas. Figure 4.9.2a shows how P_{ei} scales with the line averaged density.

P_{ei} shows that the energy influx to the ion population and the fraction of the plasma energy sustained by the ions therefore varies with density. $E_i/(E_i + E_e)$, shown in figure 4.10.1a, varies from 20 % at low density and stabilises at a fraction of ∼40 % when the plasma approaches global thermodynamic equilibrium, in agreement(§) with typical effective charges of TCV plasmas, $Z_{\text{eff}} \sim 2 \ldots 3.5$. Finally figure 4.10.1b demonstrates the discrepancy of electron and ion temperature at low density. For electron densities close to (and above) the high density limit for the CNPA, T_e and T_i agree, as P_{ei} is sufficiently high to thermalise electrons and ions.

(§) from the definition of the effective charge, eq.(2.5.13), assuming carbon and deuterium being the only plasma constituents, $n_{\text{D}} + 36\,n_{\text{C}} = Z_{\text{eff}} n_e$, plasma neutrality $n_{\text{D}} + 6\,n_{\text{C}} = n_e$ and for a flat temperature and density profile,

$$\frac{E_{\text{D}}}{E_e + E_{\text{D}}} \simeq \frac{n_{\text{D}}}{n_e + n_{\text{D}}} = \frac{1}{1 + \frac{5}{6 - Z_{\text{eff}}}} = 44\ \% \ldots 37\ \%, \qquad \text{corresponding to } Z_{\text{eff}} = 2 \ldots 3.5, \quad (4.10.1)$$

where the definition of particle stored energy, eq.(4.9.3), was used for E_e and E_i.

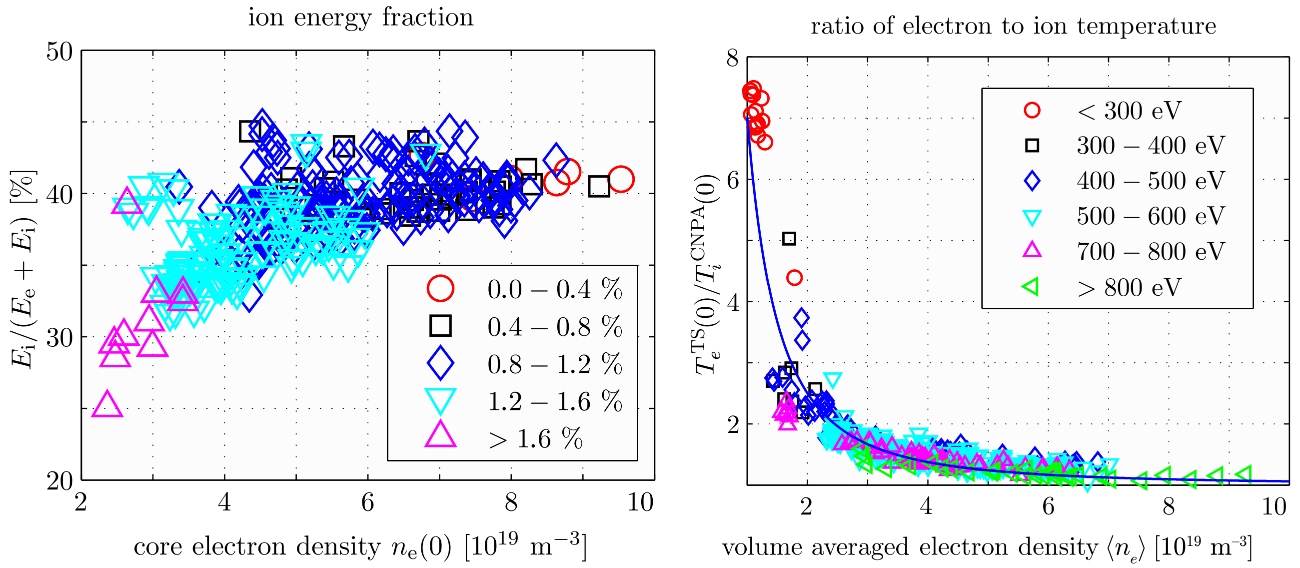

(a) Ion energy.

(b) isotopic composition profile.

Figure 4.10.1: (a) Ion stored energy fraction. The legend labels indicate again the value of the quotient in eq.(4.9.8). The ion energy fraction saturates towards higher densities because of global thermodynamic equilibrium ($T_e = T_i$).
(b) Ratio of measured core electron (TS) to core ion (CNPA) temperature of thermal TCV plasmas as a function of the plasma volume averaged electron density. The symbols show different classes of ion temperatures. Electron and ion populations are decoupled at low density but approach thermodynamic equilibrium at high densities.

4.10.3 Impact of plasma shape

TCV was designed to study the impact of the plasma shape on plasma performance, such as energy confinement and MHD stability and detailed studies have revealed the importance of plasma elongation and triangularity on particle and heat transport (see [172] and the references therein).

The electron confinement time τ_E, section 4.9.1, was characterised in several series of ohmic and second harmonic EC-heated L-mode discharges, where κ and δ were varied whilst keeping the density and the edge safety factor q constant. At intermediate densities (line averaged, $5\ldots9\times10^{19}$ m^{-3}), τ_E was found to increase with κ with little dependence on δ [34, 173].
At higher elongation ($\kappa > 2$) a saturation of τ_E is observed [174].

The behaviour of τ_E at intermediate densities is ascribed solely to geometrical effects, as an increase in the elongation involves a compression of the flux surfaces and thus a steepening of the gradient of the electron temperature profile. Assuming no poloidal variation, the flux surface averaged conducted radial heat flux may be written

$$\langle Q_\alpha\rangle = -\chi_\alpha n_\alpha \frac{\mathrm{d}T}{\mathrm{d}r}\frac{\mathrm{d}r}{\mathrm{d}\psi}\langle\nabla\psi\rangle\,, \qquad (4.10.2)$$

where the heat diffusivity χ (due to collisions and turbulence) is independent of κ.

The increase in τ_E is correctly predicted by the shape enhancement factor (SEF), the ratio of the confinement time of a shaped plasma to that of a cylindrical plasma(¶),

$$H_S = \frac{\tau_E^e(\kappa)}{\tau_E^e(0)} = \frac{S_0 \displaystyle\int \left(\int \frac{Q_{\text{in}}}{n\chi} \frac{1}{\langle \nabla\psi \rangle} \frac{\mathrm{d}\psi}{\mathrm{d}r} \mathrm{d}r' \right) \mathrm{d}V}{S \displaystyle\int \left(\int \frac{Q_{\text{in}}}{n\chi} \mathrm{d}r' \right) \mathrm{d}V_0} \tag{4.10.3}$$

where the index 0 makes reference to a unshaped (cylindrical) plasma, S is the poloidal section of the plasma and $Q_{\text{in}} = P_{\text{OH}}/S$ is the energy input due to ohmic heating. The confinement enhancement is due to the purely metric term $\frac{\mathrm{d}r}{\mathrm{d}\psi} \langle \nabla\psi \rangle$ appearing in eq.(4.10.2) and eq.(4.10.3).

On TCV, the main energy loss channel is thermal conduction. The maximum energy released by internal disruptions (sawtooth instability) is less than 25 % of the electron stored energy E_e and radiation losses (mostly impurity line radiation) reach 30 % of E_e at most. Conduction is most efficient through the electrons. From eq.(4.10.2), the ratio of the thermal conductivities is expressed as

$$\frac{\lambda_e}{\lambda_i} = \frac{n_e \chi_e}{n_i \chi_i} = \frac{P_e \frac{\mathrm{d}T_i}{\mathrm{d}r}}{P_{ei} \frac{\mathrm{d}T_e}{\mathrm{d}r}}, \tag{4.10.4}$$

where P_e is the total electron input power (inductive and auxiliary heating). With the temperature gradients averaged over the outer region of the plasma (typically $\rho > 0.7$), the ratio, eq.(4.10.4), varies from ∼2 at high to ∼10 at low current (where the coupling between electron and ions is weak and P_{ei} is small in respect to P_e).

At low line averaged densities, e.g. $<2 \times 10^{19}$ m^{-3}, with central X2 EC heating, in contrast to the higher density case, a strong dependence of confinement on triangularity was observed. An asymmetric scaling of τ_E as $(1+\delta)^{-0.35}$ was calculated [175] that could not be explained in terms of geometrical effects since the SEF, eq.(4.10.3), doesn't depend on δ. An influence of plasma shape on heat diffusivity was invoked and new experiments revealed that the heat transport decreases with decreasing triangularity [176]. χ_e was eventually found to decrease with increasing collisionality, defined as the ratio between electron–ion collision frequency ν_{ei} and electron curvature drift frequency ω_{De} [177], that is

$$\nu_{\text{eff}} = \frac{\nu_{ei}}{\omega_{De}} \propto \frac{R_0\, n_e\, Z_{\text{eff}}}{T_e^2}. \tag{4.10.5}$$

Gyrokinetic simulations [178] revealed that Trapped Electron Modes (TEM) are responsible for the major part of the electron heat flux. The TEM growth rates were found to be substantially lower at negative than at positive triangularity.

The ion confinement characteristics are similar to those of the electrons [83]. Common scaling laws for the ion temperature like the formula of Artsimovich [179] are therefore not applicable to TCV plasmas. However, it is not possible to determine a dependence of the ion confinement time on κ (due to the large uncertainties accompanying the assessment of τ_E^i), but the strong decrease of τ_E^i with triangularity at low collisionality is also seen for the ions.

(¶) Shaped and unshaped plasma need to have the same n_e, χ_e and the electron edge heat flux in order to be comparable.

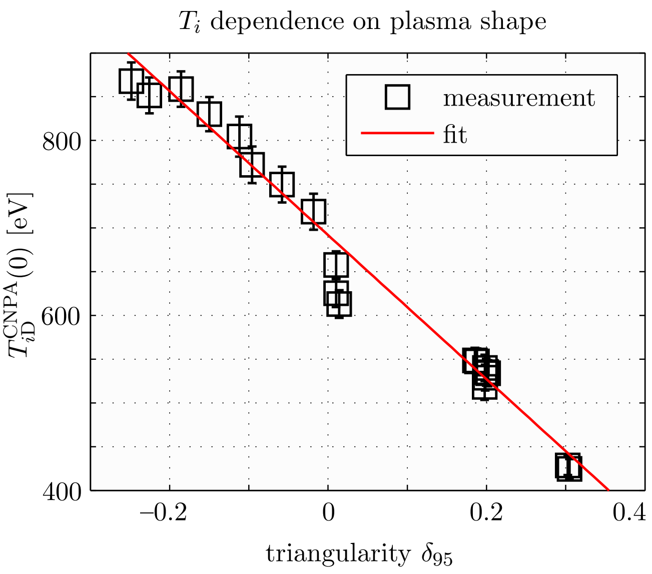

Figure 4.10.2: Core ion temperature measured with the CNPA in low collisionality plasmas of various triangularities. The abscissae is the triangularity calculated for the flux surface having a normalised radius of $\rho = 0.95$. T_i decreases linearly with δ.

Figure 4.10.2 shows the CNPA core ion temperature measured during five ohmic discharges(‖) covering a large range of δ (±0.3), besides other parameters $\kappa \sim 1.4$, $q_0 < 1$, $4 < q_a < 5.5$, $B_{\mathrm{T}} \sim 1.25$ T, $I_{\mathrm{p}} \sim 23$ kA, $\langle n_e \rangle \in [1; 1.4] \times 10^{19}$ m^{-3}.

Some of the equilibria for the measurements shown in figure 4.10.2 are depicted in figure 4.10.3.

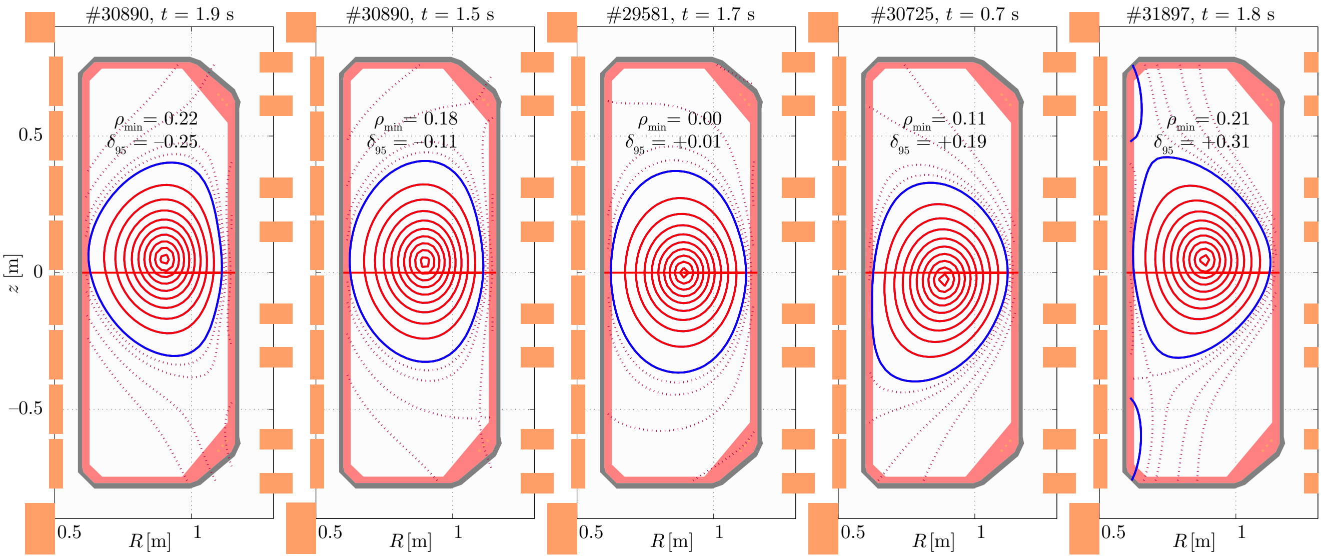

Figure 4.10.3: TCV equilibria with triangularities spanning $\delta_{95} \in [-0.3; +0.3]$. The ion temperature profiles are sufficiently flat in the plasma centre such that the core ion temperature may be derived with the CNPA even if its line of sight is not crossing the magnetic axis (see the labels for ρ_{min}).

Note that the observed change in T_i is not due to a change in P_{ei}, which is even slightly higher for the case of positive triangularity. The ion heat diffusivity must therefore decrease as well at negative triangularity.

(‖) #29581, #30724, #30725, #30890 and #31897.

4.11 Summary and conclusions

The following topics were addressed in this chapter:

☞ The ion temperature profile of an ohmically heated low density discharge was experimentally determined by displacing the plasma rather than the chord of the diagnostic (moving plasma experiment).

☞ The considered processes for cold neutral penetration into the plasma, ion neutralisation and attenuation of the escaping hot neutrals were sufficient to successfully model the measured charge-exchange spectrum.

☞ The carbon impurity ion temperature profile calculated from CXRS agrees with the hydrogenic $T_i(\rho)$ in plasmas with thermalised ion populations. A comparison of CNPA and CXRS shows good agreement (within the expected error bars) between the measured core ion temperatures.

☞ A procedure to recover the ion temperature profile without requiring plasma displacement was developed and successfully applied. The method combines NPA measurements with iterative modelling of the charge exchange spectrum by subsequent adjustment of the parameters of a functional ion temperature profile.

☞ Simulations of the absolute charge exchange spectrum provide estimations of the hydrogenic atomic neutral density and molecular neutral and ion density profiles, consistent with the main plasma parameters and code models. These profiles are important for transport studies, since they have a strong influence on the particle diffusion coefficients and pinch velocities [180], which are, in turn, important in the understanding of the plasma ion confinement.

☞ Using active charge exchange, the NPAs on TCV were absolutely calibrated for their particle flux intensity.

☞ Combined simulations of both plasma fuel species with *DOUBLE-TCV* provide absolute density profiles of the hydrogenic plasma species.

☞ Ion confinement shows a behaviour similar to the electron confinement. The ion confinement time strongly degrades with triangularity at low collisionality.

The applicability of moving plasma experiments is limited to TCV, whose flexibility in plasma shaping and positioning is unique. Machines without this ability have applied similar procedures to reconstruct ion temperature profiles, either using rotatable analysers [181] or employing multiple NPAs for instantaneous profile measurements [182].

Using the iterative ion temperature recovery method, $T_i(\rho)$ was reliably retrieved for a large variety of ohmic plasmas for which a sufficient counting statistics on CNPA channels up to energies $\leqslant 10 \cdot T_i(0)$ was measured. Here two examples have been shown (discharges #27182 and #28690). The method breaks down for densities above $n_e(0) = 6 \times 10^{19}$ m^{-3}, where neutrals emitted in the centre of the plasma are absorbed before reaching the NPA. Close to this density limit, averaging of the charge-exchange flux over longer time intervals may be necessary to improve the counting statistics, requiring steady state plasmas. The lower the density, the stronger the charge-exchange flux. Time resolutions of the recovered ion temperature profile as high as the CNPA sampling rate were achieved ($\leqslant$2 kHz).

This is more than 100 times shorter than the time resolution of CXRS, as the diagnostic beam on TCV has a repetition rate $\geqslant$10 Hz (provided that the carbon line light yield is good enough to permit such short DNB pulses). The NPA may therefore be used to study ion temperature fluctuations.

An iterative recovery procedure was presented using a parabolic profile to interpolate the ion temperature, which is a good choice in ohmic scenarios at high q. Since TCV ions are heated indirectly through interactions with electrons, the temperature profiles are monotonic and peaked. At low safety factor, sawteeth flatten the central profile and more parameters may be required to describe the ion temperature profile. The method is flexible enough to admit a user defined functional expression for the ion temperature profile.

In general, the presence of suprathermal ion populations make the methods described within this chapter impracticable. In plasmas with Electron Cyclotron Resonance Heating (ECRH) or Electron Cyclotron Current Drive (ECCD), an anomalous energy transfer from electrons to ions is observed (see chapters 6 and 7). The charge exchange flux of the suprathermal ion population appears as a fast ion tail in the charge exchange spectrum for the highest CNPA energies, superimposed on the flux from the neutralisation of the thermalised ions. The presence of the tail does not appear to affect the underlying bulk ion temperature profile, since the flux to the low energy CNPA channels does not change strongly. However, suprathermal populations, comprising 20 % of the ions, have been observed and the highest energy CNPA channel unaffected by the tail is generally well below the $E = 10 \cdot T_i(0)$ criterion, rendering a reliable iterative retrieval of the bulk $T_i(0)$ no longer possible. The NPAs on TCV are, however, well suited to study the properties of suprathermal ions, which are not diagnosable with CXRS, as their contribution to the Doppler broadening of the impurity radiation line is negligible [83]. Eq.(4.3.11) may be applied to the tail of the charge-exchange spectrum to estimate an effective “tail” temperature. This will be discussed in chapter 6.

Chapter 5

Electron cyclotron (EC) wave resonance heating (ECRH), current drive (ECCD) and emission (ECE)

This chapter is an excursion into the physics of nonthermal electrons. It constitutes the basis for the fast ion studies (chapters 6 and 7), as the behaviour of the latter is found to strongly correlate with the parameters of the suprathermal electrons(*).
Profound knowledge of the spatial and energetic electron distribution are thus prerequisites for the qualitative and quantitative analysis of the fast ion energy redistribution. A certain period of this thesis is thus devoted to a better experimental assessment of the electron population properties.

All charged particles of a plasma are sources for the Maxwell equations, eqns.(5.1.1), and their oscillatory solutions. Therefore most dynamical processes in plasmas are related to electromagnetic waves and oscillations. Applied externally, waves are used to heat plasmas and to drive current non-inductively. Another example of the importance of waves is the role that microscopic electromagnetic waves and instabilities play in producing transport of particles and energy in plasmas well above levels expected by collisions alone.

Some elements of electron cyclotron physics, including wave theory, wave propagation and absorption modelling are introduced first. A short description of the millimetre wave sources employed on TCV is then followed by a presentation of the available electron cyclotron diagnostics and an analysis of their measurements. A last paragraph deals then with some topics of the EC physics on TCV, notably internal electron transport barriers, electron velocity distribution function modelling, non-thermal electron effects and internal disruptions. Many of the plasmas shown and analysed in this chapter are those of the dedicated fast ion experiments to be presented later (next chapter).

(*) Suprathermal electrons have velocities such that

$$\frac{1}{2}m_e v^2 > \frac{1}{2}k_{\mathrm{B}}T_e. \tag{5.0.1}$$

They represent an important fraction of the electrons of a thermal Maxwellian velocity distribution. Suprathermals of special interest in tokamak plasmas are nonthermal electrons populating suprathermal energies such that the tail of the electron distribution function considerably exceeds the number of thermal bulk electrons at higher energies, i.e. their tail 'temperature' $T_e^t \gg T_e^b$. Such electron energy distributions are known to be the source of various kinetic instabilities.

5.1 Elements of electromagnetic wave theory

5.1.1 The wave dispersion relation

A plasma, described by a charge density ρ and current density $\mathbf{j}$, generates electric $\mathbf{E}$ and magnetic $\mathbf{B}$ fields according to the Maxwell equations

$$\begin{aligned} \nabla \wedge \mathbf{E} &= -\frac{\partial \mathbf{B}}{\partial t}, & \nabla \wedge \mathbf{B} &= \mu_0 \mathbf{j} + \frac{1}{c^2}\frac{\partial \mathbf{E}}{\partial t}, \\ \nabla \cdot \mathbf{E} &= \frac{\rho}{\varepsilon_0}, & \nabla \cdot \mathbf{B} &= 0, \end{aligned} \tag{5.1.1}$$

where the vacuum permeability μ_0 and dielectric constant ϵ_0 satisfy the relation $c^2 = 1/(\epsilon_0 \mu_0)$. Taking the curl of the first Maxwell equation, the **wave equation** is obtained:

$$\nabla \wedge (\nabla \wedge \mathbf{E}) = -\mu_0 \frac{\partial \mathbf{j}}{\partial t} - \frac{1}{c^2}\frac{\partial^2 \mathbf{E}}{\partial t^2}. \tag{5.1.2}$$

To be self-consistent, the Maxwell equations need to be completed with a constitutive relation describing the link between wave and propagation medium, e.g. the plasma. Assuming a constitutive relation between $\mathbf{j}$ and $\mathbf{E}$ totally general,

$$\mathbf{j}(\mathbf{x}, t) = \int \mathrm{d}t' \int \mathrm{d}^3 x' \, \underline{\boldsymbol{\sigma}}(t, t'; \mathbf{x}, \mathbf{x}') \cdot \mathbf{E}(\mathbf{x}', t'), \tag{5.1.3}$$

where $\underline{\boldsymbol{\sigma}}$ is the conductivity tensor which contains the model for the plasma dynamics, which is, in general, a non–local relation. However, if the unperturbed system is *uniform* and *stationary*, then, as a consequence of translation invariance,

$$\underline{\boldsymbol{\sigma}}(t, t'; \mathbf{x}, \mathbf{x}') = \underline{\boldsymbol{\sigma}}(t - t'; \mathbf{x} - \mathbf{x}') \tag{5.1.4}$$

and Fourier decomposition may be applied,

$$\mathbf{j}_{\omega,\mathbf{k}} = \underline{\boldsymbol{\sigma}}_{\omega,\mathbf{k}} \cdot \mathbf{E}_{\omega,\mathbf{k}}. \tag{5.1.5}$$

In writing eq.(5.1.4) it is assumed that the electric field of the wave doesn't affect the dispersive properties of the plasma. Using plane waves for the fields, i.e.

$$\mathbf{E}(\mathbf{r}, t) = \mathbf{E}_{\omega,\mathbf{k}} \exp\big(\mathrm{i}\,(\mathbf{k}\cdot\mathbf{r} - \omega t)\big) \tag{5.1.6}$$

$$\mathbf{B}(\mathbf{r}, t) = \mathbf{B}_{\omega,\mathbf{k}} \exp\big(\mathrm{i}\,(\mathbf{k}\cdot\mathbf{r} - \omega t)\big) \tag{5.1.7}$$

the Fourier transform of eq.(5.1.2) is

$$-\frac{c^2}{\omega^2}\mathbf{k} \wedge (\mathbf{k} \wedge \mathbf{E}) = \mathrm{i}\,\frac{c^2 \mu_0}{\omega}\,\underline{\boldsymbol{\sigma}} \cdot \mathbf{E} + \mathbf{E} = \left(\frac{\mathrm{i}\,\underline{\boldsymbol{\sigma}}}{\varepsilon_0\,\omega} + \mathbb{1}\right) \cdot \mathbf{E} \equiv \underline{\boldsymbol{\epsilon}} \cdot \mathbf{E} \tag{5.1.8}$$

where $\mathbf{k}$ is the wave vector and ω the wave frequency, $\mathbb{1} = \delta_{ij}$ is the identity dyad and

$$\underline{\boldsymbol{\epsilon}} \equiv \frac{\mathrm{i}\,\underline{\boldsymbol{\sigma}}}{\varepsilon_0\,\omega} + \mathbb{1} \tag{5.1.9}$$

is the *dielectric tensor* describing the wave propagation and absorption properties. Finally the wave equation becomes

$$\left\{ N^2 \left[\frac{\mathbf{k} : \mathbf{k}}{k^2} - \mathbb{1}\right] + \underline{\boldsymbol{\epsilon}} \right\} \cdot \mathbf{E} = 0 \tag{5.1.10}$$

with N the *index of refraction*

$$N^2 \equiv \frac{k^2\,c^2}{\omega^2} = \frac{c^2}{v_{\text{ph}}^2} \tag{5.1.11}$$

and

$$v_{\text{ph}} = \frac{\omega}{k} \tag{5.1.12}$$

the wave phase velocity. Eq.(5.1.10) only has a non–trivial solution $\mathbf{E} \neq 0$ (i.e. a condition for waves to propagate) if $\omega = \omega(\mathbf{k})$ or equivalently $\mathbf{k} = \mathbf{k}(\omega)$ are solutions of the *dispersion relation*

$$\Lambda(\omega, \mathbf{k}) = \det\left\{ N^2 \left[\frac{\mathbf{kk}}{k^2} - \mathbb{1} \right] + \underline{\boldsymbol{\epsilon}} \right\} = 0 \tag{5.1.13}$$

Frequency and wavelength are thus related in a way that depends on plasma dynamics.

5.1.2 Wave propagation in a cold magnetised plasma

A general treatment of the electromagnetic waves in plasmas is a very complicated subject. Numerous phenomena observed in magnetically confined plasmas (e.g. the wave propagation) are sufficiently described by considering a zero temperature, frictionless plasma. This so-called cold plasma approximation considers the anisotropy due to an external confining magnetic field $\mathbf{B_0}$ (introducing a privileged direction), but treats the plasma as a frictionless fluid neglecting the thermal particle motion. The fluid approach ignores the motion of gyration of the charged particles around the magnetic field. The cold plasma approximation therefore does not describe the wave absorption by the plasma.

The Newton equation of a plasma described as a fluid of two species $\alpha = e, i$ at static equilibrium (fluid velocity $\mathbf{u}_{\alpha 0} = 0$) and spatially uniform ($n_{\alpha 0} \equiv n_0$), with an external unperturbed and uniform magnetic field aligned with the axis z ($\mathbf{B}_0 = B_0 \mathbf{e}_z$), is written

$$m_\alpha \left\{ \frac{\partial \mathbf{u}_\alpha}{\partial t} + (\mathbf{u}_\alpha \cdot \nabla)\, u_\alpha \right\} = q_\alpha \Big(\mathbf{E} + \mathbf{u}_\alpha \wedge \mathbf{B} \Big). \tag{5.1.14}$$

Linearisation and Fourier transformation yields

$$-\mathrm{i}\,\omega\, m_\alpha\, \mathbf{u}_{\alpha 1} = q_\alpha\, \mathbf{E}_1 + q_\alpha\, \mathbf{u}_{\alpha 1} \wedge \mathbf{B}_0, \tag{5.1.15}$$

or, introducing the *mobility tensor* $\underline{\boldsymbol{\mu}}_\alpha$,

$$\mathbf{u}_{\alpha 1} = \underline{\boldsymbol{\mu}}_\alpha \cdot \mathbf{E}_1. \tag{5.1.16}$$

The perturbed quantities (index 1) are of the form $\propto \exp\big(\mathrm{i}\,(\mathbf{k}\cdot\mathbf{r} - \omega t)\big)$. From the current density,

$$\mathbf{j} = \sum_\alpha q_\alpha\, n_{\alpha 0}\, \mathbf{u}_{\alpha 1} = \sum_\alpha q_\alpha\, n_{\alpha 0}\, \underline{\boldsymbol{\mu}}_\alpha \cdot \mathbf{E}_1 \equiv \underline{\boldsymbol{\sigma}} \cdot \mathbf{E}_1, \tag{5.1.17}$$

using eq.(5.1.9), the dielectric tensor in the cold plasma approximation is obtained

$$\underline{\boldsymbol{\epsilon}} = \begin{pmatrix} \epsilon_1 & -\mathrm{i}\,\epsilon_2 & 0 \\ \mathrm{i}\,\epsilon_2 & \epsilon_1 & 0 \\ 0 & 0 & \epsilon_3 \end{pmatrix}, \tag{5.1.18}$$

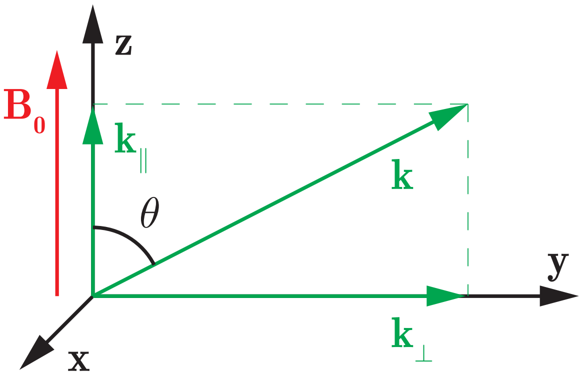

Figure 5.1.1: Stix frame notation: Geometry of magnetic field and wave.

that is two uncoupled sub-systems, one for the components perpendicular to $\mathbf{B}_0$, the second for the parallel component. The coefficients ϵ are

$$\epsilon_1 = 1 + \sum_\alpha \frac{\omega_{\mathrm{p}\alpha}^2}{\Omega_\alpha^2 - \omega^2}; \qquad \epsilon_2 = -\sum_\alpha \frac{\Omega_\alpha}{\omega}\frac{\omega_{\mathrm{p}\alpha}^2}{\Omega_\alpha^2 - \omega^2}; \qquad \epsilon_3 = 1 - \sum_\alpha \frac{\omega_{\mathrm{p}\alpha}^2}{\omega^2}; \tag{5.1.19}$$

with

$$\omega_{\mathrm{p}\alpha} = \sqrt{\frac{n_\alpha\, q_\alpha^2}{\varepsilon_0\, m_\alpha}} \tag{5.1.20}$$

the plasma frequencies and

$$\Omega_{c\alpha} = \frac{|q_\alpha| B_0}{m_\alpha} \tag{5.1.21}$$

the cyclotron frequencies.

For a cold plasma, $\underline{\boldsymbol{\epsilon}}$ does *not* depend on $\mathbf{k}$, but only on ω. For $\mathbf{B} \to 0$ we have $\epsilon_2 \to 0$ and $\epsilon_1 \to \epsilon_3$, thus $\underline{\boldsymbol{\epsilon}}$ becomes a diagonal matrix, e.g. there is no privileged direction.
Considering a wave vector $\mathbf{k}$ in the yz–plane and defining the angle θ with respect to the z–axis as shown in figure 5.1.1, the wave equation, eq.(5.1.10), and its solutions given by eq.(5.1.13) then become

$$N^2\left[\frac{\mathbf{kk}}{k^2} - \mathbb{1}\right] + \underline{\boldsymbol{\epsilon}} = \begin{pmatrix} -N^2+\epsilon_1 & -\mathrm{i}\,\epsilon_2 & 0 \\ \mathrm{i}\,\epsilon_2 & -N^2\cos^2\theta + \epsilon_1 & N^2\sin\theta\cos\theta \\ 0 & N^2\sin\theta\cos\theta & -N^2\sin^2\theta + \epsilon_3 \end{pmatrix}, \tag{5.1.22}$$

whose non–trivial solutions for $\mathbf{E}_1$ are defined by the **Appleton-Hartree dispersion relation**

$$AN^4 + BN^2 + C = 0, \tag{5.1.23}$$

where A, B and C depend on the *angle* θ between $\mathbf{k}$ and $\mathbf{B}_0$, but not on $|\mathbf{k}|$ and on ω. Explicitly

$$\begin{cases} A = \epsilon_1 \sin^2\theta + \epsilon_3\cos^2\theta, \\ B = (\epsilon_1 - \epsilon_2)^2 \sin^2\theta + \epsilon_1\epsilon_3\left(1+\cos^2\theta\right), \\ C = \epsilon_3\left(\epsilon_1+\epsilon_2\right)\left(\epsilon_1 - \epsilon_2\right). \end{cases} \tag{5.1.24}$$

The wave experiences a **cut-off** if $N \Longrightarrow 0$, i.e. is *reflected* [183]. That is if the wave phase velocity ω/k diverges. This is the case if the wave frequency is either

$$\begin{cases} \omega_{\mathrm{p}}, & \text{or} \\ \omega_{\mathrm{R,L}} = \pm\dfrac{\Omega_{\mathrm{ce}}}{2} + \sqrt{\left(\dfrac{\Omega_{\mathrm{ce}}}{2}\right)^2 + \omega_{\mathrm{pe}}^2 + \Omega_{\mathrm{ce}}\,\Omega_{ci}}. \end{cases} \tag{5.1.25}$$

Cut-offs do not depend on the propagation angle θ.

There is no general expression for the solutions $\omega(k,\theta)$. In terms of electron cyclotron wave heating and diagnosis, wave propagation perpendicular to the tokamak main magnetic field ($\theta = \pi/2$) is the interesting case. The dispersion relation is then considerably simplified and has two solutions,

$$\begin{cases} N_\perp^2 = \epsilon_3, \\ N_\perp^2 = \dfrac{\epsilon_1^2 - \epsilon_2^2}{\epsilon_1}. \end{cases} \tag{5.1.26}$$

The first solution may be written as

$$\omega^2 = \omega_{\mathrm{pe}}^2 + k^2 c^2, \tag{5.1.27}$$

with electric wave field components(†) $E_x = E_y = 0, E_z \neq 0$ and is thus a longitudinal wave, $\mathbf{E} \parallel \mathbf{B_0}$. This wave is linearly polarised and is called the **ordinary (O) mode**. The second solution may be written as

$$N_\perp^2 = \frac{(\omega^2 - \omega_{\mathrm{R}}^2)(\omega^2 - \omega_{\mathrm{L}}^2)}{(\omega^2 - \omega_{\mathrm{UH}}^2)(\omega^2 - \omega_{\mathrm{LH}}^2)}, \tag{5.1.28}$$

where

$$\omega_{\mathrm{UH}}^2 = \omega_{\mathrm{pe}}^2 + \Omega_{\mathrm{ce}}^2 \tag{5.1.29}$$

and

$$\omega_{\mathrm{LH}}^2 = \Omega_{\mathrm{ce}}\,\Omega_{ci} \frac{1 + \dfrac{m_e}{m_i}\left(\dfrac{\Omega_{\mathrm{ce}}}{\omega_{\mathrm{pe}}}\right)^2}{1 + \left(\dfrac{\Omega_{\mathrm{ce}}}{\omega_{\mathrm{pe}}}\right)^2} \tag{5.1.30}$$

are the **upper** and **lower hybrid frequencies** respectively. This time $E_z = 0$, therefore $\mathbf{E} \perp \mathbf{B_0}$ and the transverse wave is elliptically polarised in the plane perpendicular to the magnetic field with

$$\frac{E_x}{E_y} = \mathrm{i}\,\frac{\epsilon_1}{\epsilon_2} \tag{5.1.31}$$

and is called the **extraordinary (X) mode**.

A wave resonance occurs if $N \Longrightarrow \infty$, i.e. where the phase velocity, eq(5.1.12), vanishes. A resonance leads to the *absorption* of the wave by the plasma. This is the case if $A = 0$, eq.(5.1.24), therefore the resonance depends on the angle of propagation θ. For propagation perpendicular to the magnetic field the extraordinary wave enters resonance at $\omega = \omega_{\mathrm{LH}}$ or $\omega = \omega_{\mathrm{UH}}$.

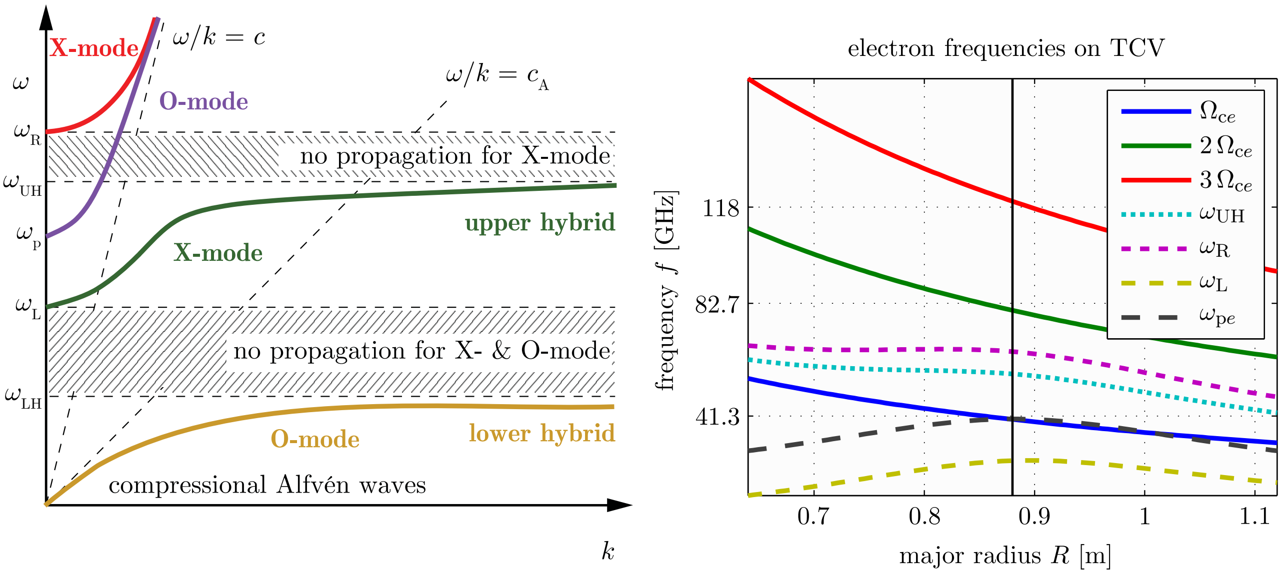

(a) Dispersion relation. (b) Electron frequencies.

Figure 5.1.2: (a) Summary of the dispersion relation for an indefinitely extended, magnetised ($\mathbf{B}_0 \neq 0$), cold ($T = 0$) plasma for propagation perpendicular to the confining magnetic field ($\mathbf{k} \perp \mathbf{B}_0$).
(b) Spatial dependence of the electron frequencies of a plasma with $n_e(0) = 2 \times 10^{19}$ m^{-3}, $T_e(0) =$ 2 keV, $B_T = 1.43$ T and $I_p = 260$ kA. Shown are the three first harmonics of the electron cyclotron resonances, the upper hybrid resonance (X-mode) and the cut-off frequencies ω_{pe} (O-mode), ω_R and ω_L (both X-mode). The vertical line indicates the torus axis and the labels of the vertical axis coincide approximately with the on-axis fundamental as well as second and third harmonic of the electron cyclotron frequency.

The dispersion relation for ordinary and extraordinary modes are summarised in figure 5.1.2a. For the case of a low density TCV plasma, typical values of the electron frequencies and their spatial profiles are shown in figure 5.1.2b.
For a wave propagating in a direction oblique to the magnetic field, the solution of the dispersion relation, eq.(5.1.22), usually gives two modes of propagation (elliptically polarised). Even though the X-mode is only defined with $\theta = \pi/2$ also oblique waves are usually called X-mode if their polarisation is X-mode in the limit $\theta \to \pi/2$.

5.1.3 Wave absorption in a hot magnetised plasma

The cold plasma approximation treats the plasma particles as immobile and therefore all kinetic effects having an impact on the wave behaviour are missing. One such feature are strong wave-particle resonances at the harmonics of the cyclotron frequencies (shown in figure 5.1.2b), due to the movement of gyration of the charged particles around the magnetic field lines (section 1.4). At the layer where wave and cyclotron frequency match, the electric field in the rest frame of the electrons is approximately constant and, if the electron density is sufficiently high, efficient transfer of energy from the wave to the electrons occurs. To properly describe the wave behaviour in the vicinity of the resonant absorption layer a microscopic description of the plasma, including thermal particle motion, is required. Temperature is a statistical quantity, so the plasma is described by a probability distribution function representing the instantaneous number of particles in a infinitesimal volume element in the 6D phase space,

$$f(\mathbf{r}, \mathbf{v}, t)\, \mathrm{d}\mathbf{r}\, \mathrm{d}\mathbf{v}. \tag{5.1.32}$$

(†) by substitution of eq.(5.1.26) into eq.(5.1.22).

Kinetic theory leads to a correction $\widetilde{\underline{\boldsymbol{\epsilon}}}$ of the cold plasma dielectric tensor of the form

$$\underline{\boldsymbol{\epsilon}}^{\text{hot}} = \underline{\boldsymbol{\epsilon}}^{\text{cold}}(\omega, \mathbf{B}_0, n_{e0}) + \widetilde{\underline{\boldsymbol{\epsilon}}}(\omega, \mathbf{k}, \mathbf{B}_0, n_{e0}, T_{e0}), \tag{5.1.33}$$

involving the wave vector and the equilibrium electron temperature. The electrons are described by a relativistic distribution function $f_e(\mathbf{r}, \mathbf{p}, t)$ with $\mathbf{p} = m_{e0}\gamma\mathbf{v}$ the momentum, m_{e0} the electron rest mass and $\gamma = 1/\sqrt{1-(v/c)^2}$. The plasma is then macroscopically described by the zeroth- and first order moment of the distribution function,

$$n_e(\mathbf{r}, t) = \int f_e(\mathbf{r}, \mathbf{p}, t)\, \mathbf{j}(\mathbf{r}, t)\, \mathrm{d}\mathbf{p} = -e\, n_e \int \frac{\mathbf{p}}{\gamma m_{e0}} f_e(\mathbf{r}, \mathbf{p}, t)\, \mathrm{d}\mathbf{p} \tag{5.1.34}$$

and the distribution function evolves under the influence of the active forces according to the relativistic Vlasov equation [184],

$$\frac{\partial f_e}{\partial t} + \frac{c^2}{\sqrt{p^2c^2 + m_{e0}^2c^4}}\mathbf{p} \cdot \frac{\partial f_e}{\partial \mathbf{r}} - e\left(\mathbf{E} + \frac{c^2}{p^2c^2 + m_{e0}^2c^4}\mathbf{p} \wedge \mathbf{B}\right) \cdot \frac{\partial f_e}{\partial \mathbf{p}} = 0 \tag{5.1.35}$$

As a first approximation, collisions may be neglected because the characteristic time of the wave-particle interaction is considerably smaller than the characteristic particle collision time. The determination of the dielectric tensor follows again a perturbative Ansatz, the distribution function is split into a stationary, spatially uniform and a perturbed part,

$$f_e(\mathbf{r}, \mathbf{p}, t) = f_{e0}(\mathbf{p}) + f_{e1}(\mathbf{r}, \mathbf{p}, t) \tag{5.1.36}$$

and a first order development of eq.(5.1.35) for a frame of reference streaming with the electrons, $\mathbf{E}_0 = \mathbf{j}_0 = 0$, yields

$$\frac{\mathrm{d}f_e}{\mathrm{d}t} = \frac{\partial f_{e1}}{\partial t} + \frac{\mathbf{p}}{m_e} \cdot \frac{\partial f_{e1}}{\partial \mathbf{r}} + \frac{e}{m_e}(\mathbf{p} \wedge \mathbf{B}_0) \cdot \frac{\partial f_{e1}}{\partial \mathbf{p}} = -e\left(\mathbf{E}_1 + \frac{\mathbf{p} \wedge \mathbf{B}_1}{m_e}\right) \cdot \frac{\partial f_{e0}}{\partial \mathbf{p}}, \tag{5.1.37}$$

where m_e is the relativistic electron mass and it was assumed that $B_1/B_0 \ll 1$. f_{e0} is conveniently described by a relativistic Maxwell distribution [185],

$$f_{e0} = \frac{\mu}{4\pi\, (m_{e0}c)^3\, K_2(\mu)} \exp\left(-\mu\gamma\right), \tag{5.1.38}$$

with $\mu = mc^2/(k_B T_e)$ and $K_2(z)$ the McDonald function. Eq.(5.1.37) is then solved for f_{e1} by integration along the characteristics (unperturbed particle orbits), in Fourier space (see appendix A). The perturbation current is then obtained from eq.(5.1.34) by integration over f_{e1} and the electric tensor is expressed by [185]

$$\epsilon_{ij}(\mathbf{k}, \omega) = \delta_{ij} - \frac{\omega_{\text{pe}}^2}{\omega^2}\frac{\mu^2}{2\,K_2(\mu)}\int_{-\infty}^{+\infty} \mathrm{d}\overline{p}_{\|} \int_0^{+\infty} \overline{p}_{\perp}\mathrm{d}\overline{p}_{\perp}\, \frac{\exp\left(-\mu\gamma\right)}{\gamma} \sum_{n=-\infty}^{n=+\infty} \frac{P_{ij}^n\left(\overline{p}_{\perp}, \overline{p}_{\|}\right)}{\gamma - N_{\|}\overline{p}_{\|} - n\left(\Omega_{\text{ce}}/\omega\right)}, \tag{5.1.39}$$

where $\overline{p} = p/(m_{e0}\,c)$, $N_{\|}$ the refractive index for propagation parallel to $\mathbf{B}_0$ and P_{ij}^n the coefficients resulting from the expansion in Bessel functions of the integration along the non-perturbed orbits. The matrix has 6 independent components, namely

$$\begin{aligned}
P_{xx}^n &= p_{\perp}^2 \frac{n^2}{\xi^2} J_n^2(\xi), & P_{xy}^n &= -P_{yx}^n = \mathrm{i}\, p_{\perp}^2 \frac{n}{\xi} J_n(\xi)\, J_n'(\xi), \\
P_{yy}^n &= p_{\perp}^2 J_n'^{\,2}(\xi), & -P_{yz}^n &= P_{zy}^n = \mathrm{i}\, p_{\|}\, p_{\perp} J_n(\xi)\, J_n'(\xi), \\
P_{zz}^n &= p_{\|}^2 J_n^2(\xi), & P_{zx}^n &= P_{zy}^n = p_{\|}\, p_{\perp} \frac{n}{\xi} J_n^2(\xi).
\end{aligned} \tag{5.1.40}$$

As in the cold plasma approximation, the solution of the dispersion relation yields two solutions, corresponding to an electrodynamic (the electron cyclotron wave) and an electrostatic mode (the Bernstein wave), whose real parts describe the wave propagation and its imaginary parts the wave absorption.

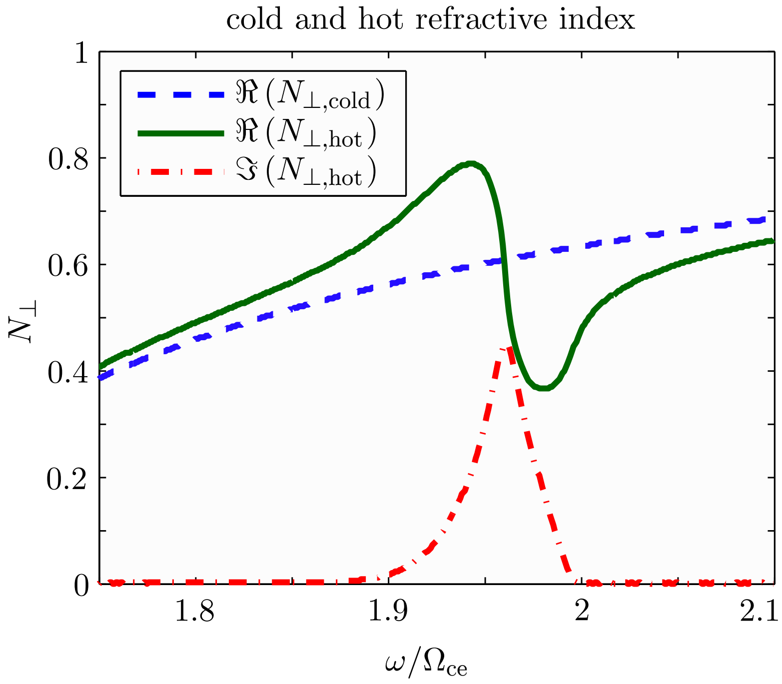

Figure 5.1.3: Real and imaginary components of the refractive index (electromagnetic electron cyclotron mode) for a plasma of density $n_e = 2 \times 10^{19}$ m^{-3} around the second harmonic of Ω_{ce}. Wave absorption only occurs in a hot plasma model.

Figure 5.1.3 compares the refractive indexes representative of a cold and a warm plasma ($T_e =$ 2 keV) for propagation perpendicular to the magnetic field.

The resonance condition is given by the diverging denominator of eq.(5.1.39), i.e.

$$\omega = n\,\Omega_{\mathrm{ce}}/\gamma + k_\parallel v_\parallel = 0 \tag{5.1.41}$$

5.2 EC injection system on TCV

The development of the gyrotron [186] in the seventies of last century paved the avenue to heat a plasma by the absorption of millimetre waves at the electron cyclotron frequency [187]. The availability of powerful and reliable gyrotrons matured the technology of electron cyclotron resonance heating (ECRH) that has progressed constantly over a period of forty years, particularly as a tool in magnetic confinement fusion. ECRH technique has seen a steady increase in the sophistication of its applications in plasma physics, from bulk heating through profile tailoring and finally to distribution function engineering. In comparison with other techniques, ECRH combines the significant advantages of good coupling, localised power deposition, easy launch and precise directionality.

As $\Omega_{\mathrm{ce}} \gtrsim \omega_{\mathrm{pe}}$, the wave energy is only absorbed by the electrons. Gyrotrons constitute the only available auxiliary heating system at TCV. EC waves are electromagnetic waves, hence they propagate in vacuum and the wave source may be placed away from the tokamak with the energy transported through wave guides with negligible losses. On TCV the length of wave guides exceeds 30 m and the losses are smaller than 5 % [188].

5.2.1 EC wave source (gyrotron)

TCV currently features 9 gyrotrons for the auxiliary heating of TCV plasmas [189]. The working frequency of the gyrotrons is fixed, 6 of them (available since 1996/1999) work at $f = 82.7$ GHz (wave length $\lambda = 3.6$ mm in the vacuum), matching the second harmonic electron cyclotron frequency close to the torus axis for a magnetic field of $B_{\mathrm{T}} = 1.43$ T [188]. Three further gyrotrons were purchased in 2002 [190] and work around the third harmonic ($f = 118$ GHz). A total of 4.2 MW nominal EC power (465 kW at the second, 480 kW at the third harmonic of Ω_{ce} per gyrotron) is simultaneously available. The maximum heating pulse length is limited to 2 s (thermal constraints on the diamond window at the gyrotron output). Three gyrotrons are grouped in a cluster with a common power supply and each gyrotron is operated independently.

Power is directed to the plasma from two upper lateral launchers ($z = 46$ cm) and one equatorial launcher. Each gyrotron can be independently switched to the torus or to a calorimetric load from shot to shot, such that power is delivered from any combination of up to six launchers for a given shot. Wave guides connect the gyrotrons to lateral (2^{nd}) and top (3^{d} harmonic) launchers (figure 5.2.1).

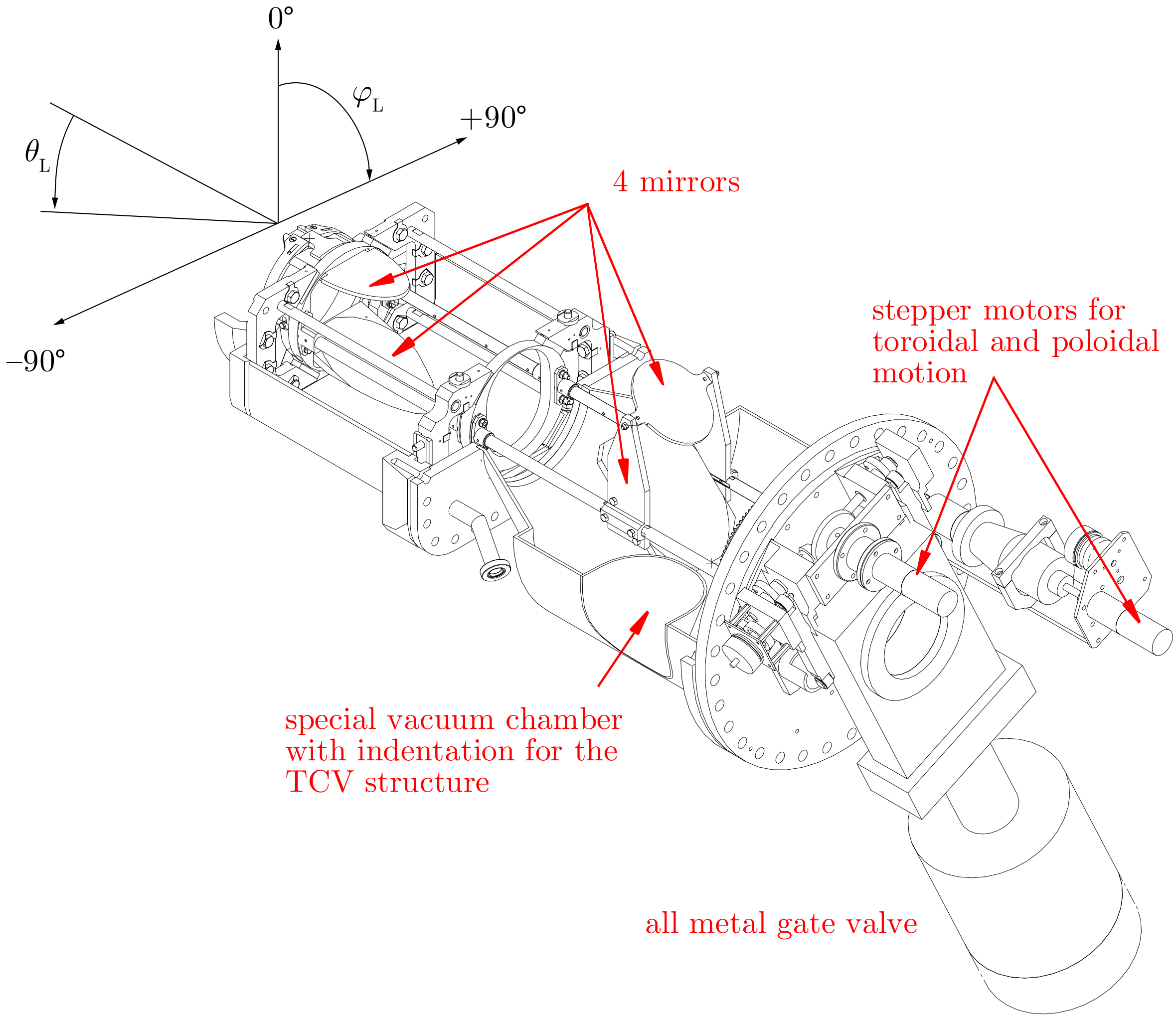

Figure 5.2.1: Drawing of the 2^{nd} harmonic EC wave launcher. The wave travels from right to left. The plasma facing mirror is tiltable by $\theta_L = 55°$. Toroidal aiming is achieved by rotating the whole launcher ($\phi_L = \pm 90°$). At a given θ, the beam path describes a cone as ϕ is swept through 360°. The mirror stepping motors are controllable in real time.

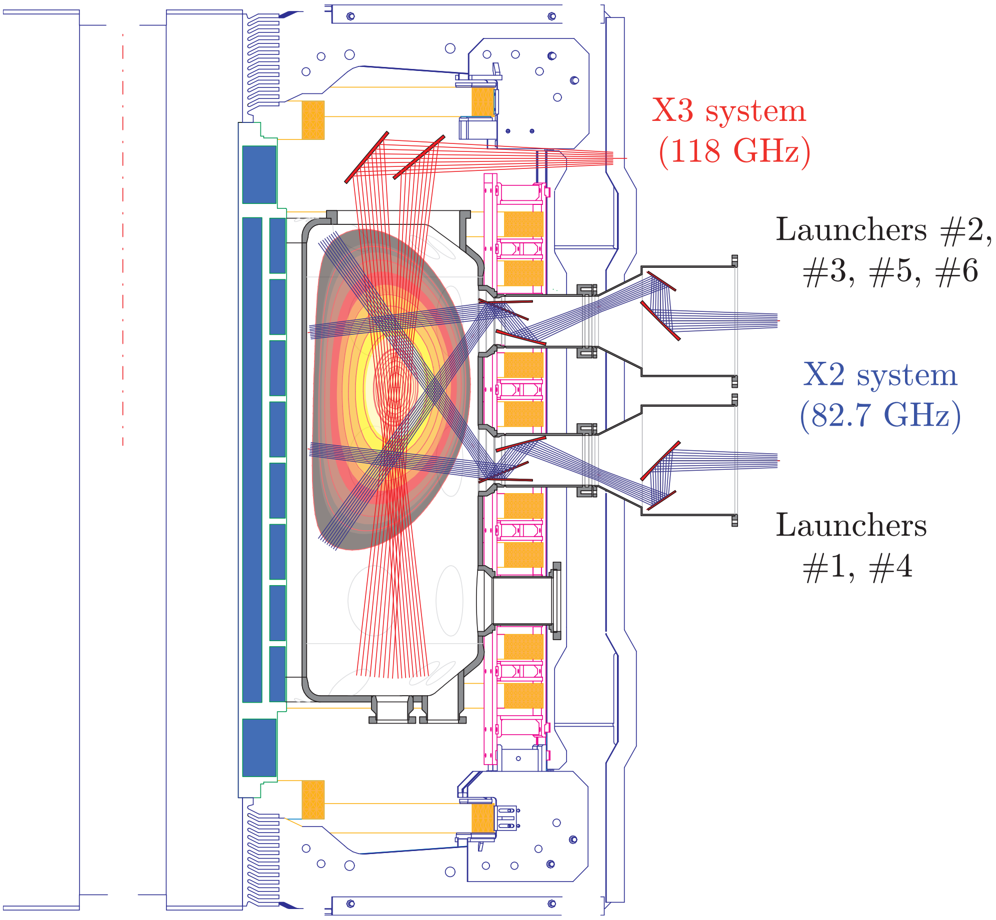

Figure 5.2.2: Poloidal drawing of the launcher locations and the steerability of the X2 and X3 beams. The X3 mirror is horizontally displaceable. The colour contours of the plasma represent the nested flux surfaces. Note that the wave trajectories are representative for a vessel without plasma.

For maximum flexibility, the launchers are steerable in real time in both toroidal and poloidal directions, such that a range of plasma configurations may be heated (the beam aiming covers almost the entire poloidal plane of TCV). For the 2^{nd} harmonic beam, when operated in X-mode, whose absorption is strong, the energy deposition is very localised. The short EC wavelength and unique localisation and directionality properties of the EC system afford an unprecedented degree of phase space manipulation. By changing the poloidal launcher angle, θ_L, the deposition layer is displaced across a plasma flux surface, whilst a non-zero toroidal launcher angle, ϕ_L, results in a finite parallel wave number, $N_\parallel \propto \sin(\phi_L)$, causing electron cyclotron current drive (ECCD). In the remainder of this manuscript, pure heating ($\phi_L = 0$) is termed electron cyclotron resonance heating (ECRH), although, due to the twist of the magnetic field lines, $\phi_L = 0$ doesn't imply $N_\parallel = 0$ in general. This is particularly true for off-axis absorption, where, due to the poloidal field, the projection of the k-vector on the total magnetic field $\mathbf{B}$ may have a non-negligible component [191, 192] (the driven current is small though). For the beam to reach the plasma centre, an angle $\theta_L \sim 55°$ is typically required. Figures 5.2.2 and 5.2.3 illustrate the possibilities to direct the EC waves poloidally respectively toroidally into the vessel.

In this thesis only the gyrotrons working at the second harmonic have been used, in the following the description is therefore limited to this system only.

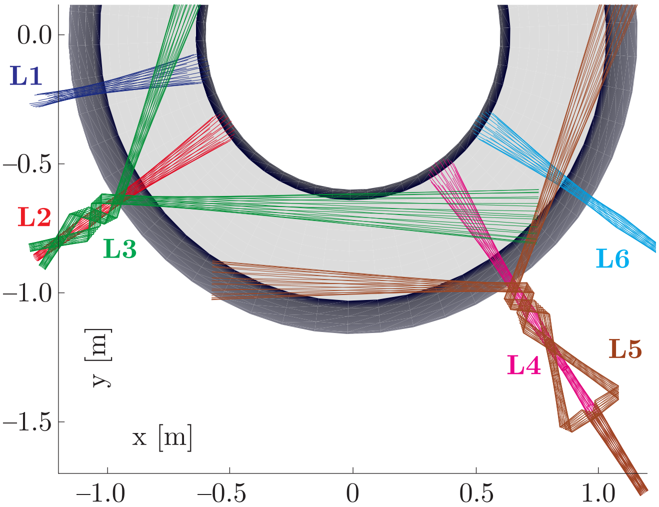

Figure 5.2.3: Sketch of the vertical view of the launcher locations demonstrating the toroidal steerability of the X2 EC beams. The trajectories are representative for a vessel without plasma.

5.2.2 EC wave accessibility

Heating or diagnosis of a plasma by means of electron cyclotron waves is drastically limited by the presence of cut-offs between the plasma edge and the desired location of power deposition or radiation emission respectively. According to section 5.1.2, the X2-mode cannot propagate if $\omega \leqslant \omega_{\mathrm{R}}$, i.e. $N = 0$. ω_{R} depends on the density (through ω_{pe}) and therefore, if the density increases, ω_{R} will overlap the second harmonic (see figure 5.1.2b) such that the resonance is no longer accessible as the wave is reflected before reaching the targeted absorption layer. Eq.(5.1.25), for $\omega \approx \omega_{\mathrm{R}}$ and neglecting $\Omega_{ce}\,\Omega_{ci} \ll \Omega_{ce}^2, \omega_{\mathrm{pe}}^2$, translates the cut-off condition to

$$\omega\,(\omega - \Omega_{ce}) = \omega_{\mathrm{pe}}^2. \tag{5.2.1}$$

Using the definitions eq.(5.1.20) and eq.(5.1.21), the maximum density at the resonance location is therefore

$$n_c = m\,(m-1)\,\frac{\varepsilon_0\,B^2(r)}{m_e}, \tag{5.2.2}$$

which is plotted in figure 5.2.4a for the second ($m = 2$) and third ($m = 3$) harmonic. The core of the vessel is therefore inaccessible for EC waves if the core electron density exceeds $n_e(0) = 4.1 \times 10^{19}\ \mathrm{m}^{-3}$.

Wave accessibility is conveniently discussed on the Clemmow–Mullaly–Allis (CMA) diagram shown in figure 5.2.4b. The abscissae of this plot is proportional to density, the ordinate to the magnetic field squared. The left branch of the X-mode cut-off corresponds to ω_{R}, the right to ω_{L}. The stroked lines on the left show the wave trajectory of an electron cyclotron wave with frequency close to the second harmonic of Ω_{ce}, launched from the low field side for propagation towards the high field side. Calculations were performed in the cold plasma approximation, so no absorption is present at $2\,\Omega_{ce}$. In a real plasma, the wave would be absorbed upon crossing the Ω_{ce} region. The second stroked line corresponds to the density $n_e(0) = 4.1 \times 10^{19}\ \mathrm{m}^{-3}$, this is the critical density and thus the wave trajectory touches the cut-off at the resonance. If the density is further increased, the wave cannot come across the resonance but is reflected at the cut-off.

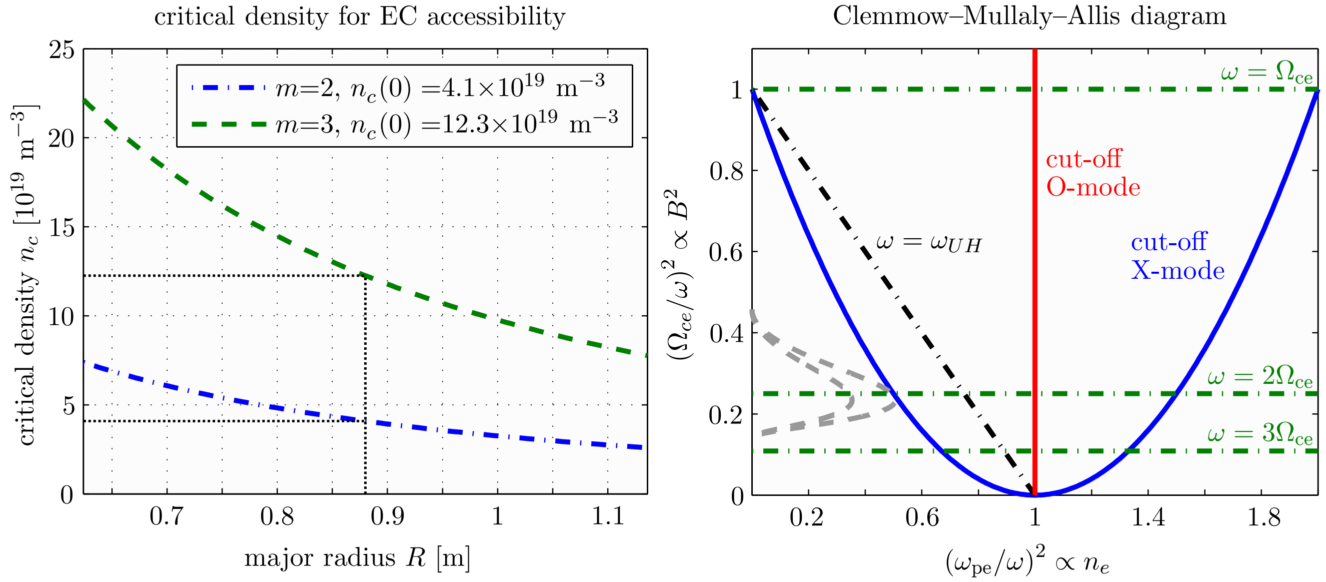

(a) Critical density. (b) CMA-diagram.

Figure 5.2.4: (a) Local critical density for the second and third harmonics due to the cut-off ω_R for a toroidal magnetic field $B_{\mathrm{T}}(0) = 1.45$ T on the torus axis. The centre critical densities are given for the second and third harmonic of the cyclotron frequency.
(b) CMA-diagram for electron cyclotron waves of perpendicular propagation in respect to the magnetic field. Solid lines represent cut-offs, dash-dotted lines resonances. The stroked lines on the left illustrate access to the second harmonic of the electron cyclotron resonance with low field side launch.

5.2.3 EC wave ray tracing

When a wave propagates through an anisotropic, non-homogenous plasma, the gradients of the main plasma parameters, such as the density n_e, temperature T_e, magnetic field $\mathbf{B}_0$, pressure p_0 etc., cause the dispersion relation to depend on the spatial position $\mathbf{x}$ and the plane wave approximation breaks down. Wave raytracing treats these difficulties using the Wentzel-Kramers-Brillouin (WKB) approximation [193–195], applicable if $\mathbf{k}$ is only a slowly varying function in space (i.e. the variations occur over scales that are much longer than the wavelength), $\lambda_0 \ll w_0 \ll \mathfrak{L}$, where λ_0 is the wave length in vacuum, w_0 the size of the wave beam and $\mathfrak{L} = N/|\nabla N|$ the characteristic length of non-homogeneity of the plasma. In the WKB-approximation, the plane wave description of the wave field $\mathbf{E_1} \propto \exp\big(\mathrm{i}\,(\mathbf{k}\cdot\mathbf{x} - \omega t)\big)$ is replaced by

$$\mathbf{E_1} = \Re\Bigg(\widetilde{\mathbf{E}}_\mathbf{1}(\mathbf{x})\exp\Bigg(\mathrm{i}\Big(\int_0^{\mathbf{x}} \mathbf{k}(\mathbf{x}')\cdot \mathrm{d}\mathbf{x}' - \omega t\Big)\Bigg)\Bigg) \equiv \Re\Bigg(\widetilde{\mathbf{E}}_\mathbf{1}(\mathbf{x})\exp\Bigg(\mathrm{i}\Big(\frac{2\pi}{\lambda_0}\phi(\mathbf{x}) - \omega t\Big)\Bigg)\Bigg). \tag{5.2.3}$$

This means that the wave propagation is considered as a single ray propagating according to the laws of geometrical optics. Ignoring the wave nature of the wave beam implies that absorption does not occur. Since absorption occurs mainly at the EC resonance (section 5.1.3), being very small elsewhere, propagation is safely calculated up to the resonance layer.
The phase $\phi(\mathbf{x})$ in eq.(5.2.3) is solution of the Maxwell equations [196],

$$(\nabla\phi)^2 = N^2(\mathbf{r}) \tag{5.2.4}$$

and N is determined locally by solving the Appleton-Hartree dispersion relation, eq.(5.1.23). With the choice $\mathbf{k} = 2\pi\nabla\phi/\lambda_0$ the wave propagation is described by a succession of localised plain waves.

The dispersion relation, 5.1.13, has now a spatial dependence,

$$\Lambda(\mathbf{k},\mathbf{r},\omega) = \mathbf{k}^2 - \left(\frac{\omega}{c}\right)^2 N^2(\mathbf{r}) = 0 \tag{5.2.5}$$

and the hamiltonian ray-tracing system

$$\begin{cases} \dfrac{\mathrm{d}\mathbf{r}}{\mathrm{d}t} &= -\dfrac{\partial\Lambda/\partial\mathbf{k}}{\partial\Lambda/\partial\omega} \equiv \mathbf{v}_g, \\ \dfrac{\mathrm{d}\mathbf{k}}{\mathrm{d}t} &= -\dfrac{\partial\Lambda/\partial\mathbf{r}}{\partial\Lambda/\partial\omega}, \end{cases} \tag{5.2.6}$$

describes the propagation speed of the ray, defined by the group velocity v_g (first equation), and the direction of propagation (second equation).

On TCV, the electron cyclotron wave beam has a width $w_0 \simeq \mathfrak{L}$, that is divergent along the beam path. The wave propagation inside the plasma is then correctly described by a set of rays filling the beam volume and calculated independently according to the ray-tracing equations.

5.2.3.1 EC heating (ECRH)

The plasma heating by EC waves is described by the absorption coefficient α. A rigourous derivation of α is available in [184].
The dispersion relation obtained for a hot plasma,

$$\Lambda = \Re\Lambda + \mathrm{i}\Im\Lambda, \tag{5.2.7}$$

has a complex solution

$$\mathbf{k} = \Re\mathbf{k} + \mathrm{i}\Im\mathbf{k}, \tag{5.2.8}$$

where $\Im\mathbf{k}$ describes the absorption of the wave by the plasma. If the absorption is weak, i.e. $\Im\mathbf{k} \ll \Re\mathbf{k}$, a Taylor development of the dispersion relation yields, to first order,

$$\Im\mathbf{k}\cdot\Re\frac{\partial\Lambda}{\partial\mathbf{k}} = -\Im\Lambda(\Re\mathbf{k},\omega), \tag{5.2.9}$$

whose projection on the group velocity defines the **absorption coefficient**,

$$\alpha = -2\,\Im\mathbf{k}\cdot\frac{\partial\Re\Lambda/\partial\Re\mathbf{k}}{\mid\partial\Re\Lambda/\partial\Re k\mid} = -2\,\Im\mathbf{k}\cdot\frac{\mathbf{v}_g}{v_g}. \tag{5.2.10}$$

For a plasma described by the electron distribution function f_e, with the wave propagation at an angle θ with respect to the magnetic field, the absorption coefficient may be written [45]

$$\alpha(\theta,t) = -\frac{8\pi^3\,c^2}{N_r^2\,\omega^2}\int_0^\infty\int_{-\infty}^{\infty}\eta_\omega(p_\parallel,p_\perp,\theta)\times \left[\frac{E}{c^2}\frac{\partial f}{\partial p_\perp} - N(\theta)\cos\theta\left(\frac{p_\parallel}{c}\frac{\partial f}{\partial p_\perp} - \frac{p_\perp}{c}\frac{\partial f}{\partial p_\parallel}\right)\right]2\pi\,p_\perp\,\mathrm{d}p_\perp\,\mathrm{d}p_\parallel, \tag{5.2.11}$$

with $E = (pc)^2 + (m_e c^2)^2$ and N_r the refractive index along the ray,

$$N_r = \Re N\sqrt{\left|\frac{\sin\theta}{\cos\beta\frac{\partial}{\partial\theta}\left[\cos(\theta-\beta)\right]}\right|}, \tag{5.2.12}$$

where

$$\tan\beta = \frac{1}{\Re k}\frac{\partial \Re k}{\partial \theta} \tag{5.2.13}$$

and with η_ω given by the Schott-Trubnikov formula,

$$\eta_\omega(\mathbf{v},\theta) = \frac{e^2\,\omega^2}{8\pi^2\,\varepsilon_0\,c}\sum_{m=1}^{\infty}\left[\left(\frac{\cos\theta - \frac{v_\parallel}{c}}{\sin\theta}\right)^2 J_m^2(\xi) + \left(\frac{v_\perp}{c}\right)^2\frac{\mathrm{d}J_m^2(\xi)}{\mathrm{d}\xi}\right]\times$$
$$\delta\left(m\,\Omega_0 - \omega\left(1-\frac{v_\parallel}{c}\cos\theta\right)\right), \tag{5.2.14}$$

where

$$\xi = \frac{\omega}{\Omega_0}\,\beta_\perp\sin\theta. \tag{5.2.15}$$

The dirac of eq.(5.2.14) contains the condition of the cyclotron resonance,

$$\omega - k_\parallel v_\parallel - \frac{m\,\Omega_{ce}}{\gamma} = 0, \tag{5.2.16}$$

where $k_\parallel v_\parallel$ is due to the Doppler shift and the factor γ, correcting the electron mass, results in a relativistic frequency upshift of the resonance. In velocity space, $\mathbf{u} = \gamma\mathbf{v}/c$, the resonance condition is represented as half-ellipses,

$$\frac{\left(u_\parallel - u_{\parallel 0}\right)^2}{\alpha_\parallel^2} + \frac{u_\perp^2}{\alpha_\perp^2} = 1, \tag{5.2.17}$$

where

$$u_{\parallel 0} = \frac{N_\parallel\,(m\Omega_{ce}/\omega)}{1-N_\parallel^2}, \tag{5.2.18}$$

$$\alpha_\parallel = \frac{\sqrt{N_\parallel^2 + (m\Omega_{ce}/\omega)^2 - 1}}{1-N_\parallel^2}, \tag{5.2.19}$$

$$\alpha_\perp = \frac{\sqrt{N_\parallel^2 + (m\Omega_{ce}/\omega)^2 - 1}}{\sqrt{1-N_\parallel^2}}. \tag{5.2.20}$$

Figure 5.2.5a shows a resonance map for various frequency ratios $m\,\Omega_{ce}/\omega$ (m is the harmonic number) for the case $N_\parallel = 0$ (pure ECRH). The resonance curves are circles centred at the origin of the axes. The resonance curve collapses to a point at the origin of the velocity space if the wave frequency is a multiple of the electron cyclotron frequency.
Figure 5.2.5b shows the absorption coefficient at the second harmonic (X-mode, $\theta = \pi/2$) for three different temperatures. The higher the temperature, the stronger the Doppler broadening of the absorption layer and the stronger the relativistic downshift of the maximum of the absorption away from the cold resonance $\omega = 2\,\Omega_{ce}/\gamma$.

Integrating the absorption coefficient, eq.(5.2.10), along the ray trajectory, eqns.(5.2.6), the **optical thickness** is defined as

$$\tau = 2\int \Im\mathbf{k}\cdot\mathrm{d}\mathbf{s} = -\int \alpha\,\mathrm{d}s, \tag{5.2.21}$$

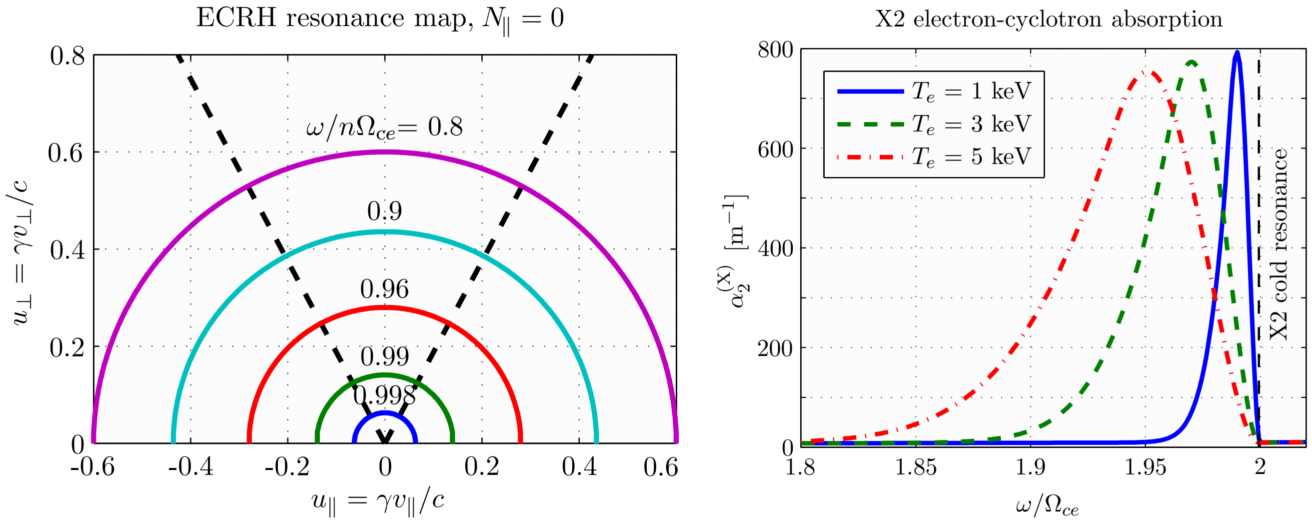

(a) ECRH resonance map. (b) Absorption coefficient.

Figure 5.2.5: Resonance and absorption at the electron cyclotron frequency.
(a) Resonance curves at different points along a perpendicular ray in a tokamak magnetic field geometry. The resonant curve becomes imaginary for $\omega > n\Omega_{ce}$ and the wave can in general propagate but no energy exchange occurs for the n^{th}-harmonic.
(b) Broadening and displacement of the X2 resonance layer in respect to the cold resonance location for an electron density $n_e(0) = 2\times10^{19}$ m^{-3}.

which is useful to calculate the absorbed EC power fraction

$$\frac{P_{\text{abs}}}{P_{\text{inj}}} = 1 - \exp\left(-\tau\right), \tag{5.2.22}$$

where P_{inj} is the injected power and P_{abs} is the power absorbed by the plasma after one single pass of the wave beam through the resonance layer.
If the electrons are considered non-relativistic, i.e. $v_{\text{the}}/c \ll 1$, where v_{the} is the thermal speed of the electrons, that is for electron temperatures up to say 5 keV, the optical thicknesses for $\theta = 0$, as a function of major radius R, are respectively [184],

O-mode:

$$\tau_m^O(R) = \frac{\pi}{2\,c}\frac{m^{2(m-1)}}{2^{m-1}(m-1)!}\left[1-\left(\frac{\omega_{\text{pe}}}{m\Omega_{\text{ce}}}\right)^2\right]^{m-1/2}\left(\frac{\omega_{\text{pe}}^2}{\Omega_{\text{ce}}}\right)\left(\frac{k_B\,T_e}{m_e\,c^2}\right)^m R, \tag{5.2.23}$$

X-mode:

$$\tau_m^X(R) = \frac{\pi}{2\,c}\frac{m^{2(m-1)}}{2^{m-1}(m-1)!}\left(\frac{\omega_{\text{pe}}^2}{\Omega_{\text{ce}}}\right)\left(\frac{k_B\,T_e}{m_e\,c^2}\right)^{m-1} R, \tag{5.2.24}$$

where $m \geqslant 2$ is again the harmonic number. For typical tokamak parameters, the previous equations imply $\tau_2^X \geqslant 1$ and $\tau_3^X \approx \tau_2^O < 1$. Thus the TCV 2nd harmonic electron cyclotron wave system is operated most of the time in X-mode polarisation, as the beam absorption efficiency is much higher than in the O-mode branch [197]. The absorption of the wave at the third harmonic is far smaller (the absorbed power fraction is reduced by roughly a factor k_BT_e/m_ec^2).
A wave launched from the LFS towards a harmonic of the electron cyclotron frequency penetrates the plasma until it reaches the cold resonance layer, where absorption is still weak. In a tokamak, the cyclotron frequency scales as $1/R$, see eq.(5.1.21), the wave is therefore moving from the right to the left on figure 5.2.5b and the absorption becomes stronger.

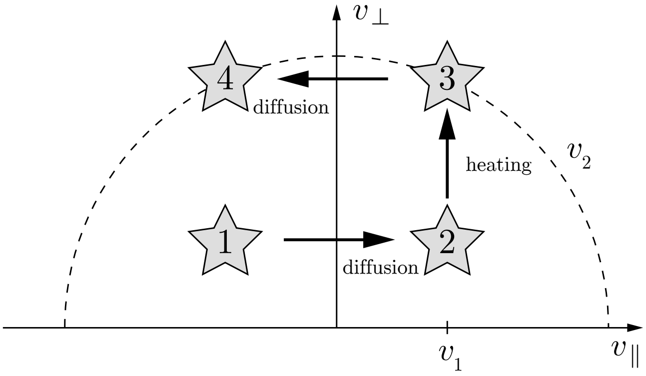

Figure 5.2.6: Fisch–Boozer mechanism of electron cyclotron current drive (ECCD).

If the plasma is optically thick (say $\tau \geqslant 3$), the wave energy has been deposited completely upon passing the resonance layer. This is generally the case for X2, so the absorption layer is spatially narrow. The interaction is strongest with (suprathermal) electrons having an energy(‡)

$$E_{\mathrm{res}} = (\gamma - 1)\, m\, c^2 = \left(\frac{m\, \Omega_{ce}}{\omega} - 1 \right) m_e\, c^2. \tag{5.2.25}$$

To change the radial location of absorption the magnetic field of the tokamak must change.

TCV features the EC system with currently the highest wave power density worldwide (40 MW/m^3). In 1999, using the full power of 6 gyrotrons, low density plasmas were heated to bulk electron temperatures reaching almost 15 keV.

5.2.3.2 EC current drive (ECCD) [198]

One might think that injecting the EC waves toroidally would transfer momentum to the plasma and drive a non-inductive current. The wave, however, carries practically no longitudinal momentum and the effect of its absorption by the plasma is roughly limited to an increase of the transverse electron energy. Toroidal EC injection nevertheless generates a toroidal current in the plasma, albeit through a more complex interplay between the plasma particles. The principle of this process is illustrated in figure 5.2.6 and works as follows [199]: Consider a wave propagating at an angle $\cos\theta = k_\parallel / k$. Electrons with longitudinal velocity v_1 (zone 2 in the figure) fulfill the resonance condition, eq.(5.2.16), if

$$v_1 = \frac{\omega - m\, \Omega_{ce}}{k_\parallel}, \tag{5.2.26}$$

such that, after absorption (heating),

$$v_2 \simeq \sqrt{v_1^2 + \frac{\Delta E}{2\, m_e}}, \tag{5.2.27}$$

the electrons are in zone 3 in velocity space, where ΔE is the increase in transverse energy (the longitudinal energy is barely augmented). Diffusion results in the density of particles removed from zone 2 being replenished from zone 1.

(‡) using the resonance condition, eq.(5.2.16).

The particle balance equations between these two zones may be written

$$\begin{cases} \dfrac{\mathrm{d}n_2}{\mathrm{d}t} & = -\dfrac{P_{\mathrm{abs}}}{\Delta E} + \nu_\mu(v_1)\big[\overline{n}_2 - n_2\big], \\[2ex] \dfrac{\mathrm{d}n_3}{\mathrm{d}t} & = -\dfrac{P_{\mathrm{abs}}}{\Delta E} + \nu_\mu(v_2)\big[\overline{n}_3 - n_3\big], \end{cases} \tag{5.2.28}$$

where $\overline{n}$ and n are the equilibrium and perturbation densities respectively and $\nu_\mu(v)$ is the angular electron diffusion frequency due to electron–electron collisions, equal to the characteristic frequency for energy loss, eq.(4.9.1), and thus proportional to v^{-3}. This dependence is the origin of the current generated with ECCD, which, for stationary conditions, is

$$j_{\mathrm{ECCD}} = -e\, v_1\, (n_1 - \overline{n}_1 + n_2 - \overline{n}_2) = \frac{e\, v_1\, P_{\mathrm{abs}}}{\Delta E\, \nu_\mu(v_2)} \left(1 - \frac{\nu_\mu(v_2)}{\nu_\mu(v_1)}\right). \tag{5.2.29}$$

Hence j_{ECCD} is due to the faster particles being more slowly scattered in pitch-angle, resulting in an anisotropy of the electron distribution function. If the injected EC power equals P_{inj}, the ECCD efficiency is [200],

$$\eta_{\mathrm{ECCD}} = \frac{j_{\mathrm{ECCD}}}{P_{\mathrm{inj}}} = \frac{3\, e\, v_1^2}{5\, \nu_0\, m_e\, v_{\mathrm{the}}^2\, Z_{\mathrm{eff}}}, \tag{5.2.30}$$

where ν_0 is given by eq.(4.9.1), evaluated at $v = v_{\mathrm{the}}$.

The toroidal geometry of the tokamak leads to particle trapping. The magnetic moment $\mu_m = \frac{1}{2} m_e v_\perp^2 / B$ is an adiabatic invariant^(§). The helical particle orbits imply that $\nabla B \neq 0$ along a magnetic field line, but if the total kinetic energy $W = W_\parallel + W_\perp$ is constant, the conservation of the magnetic moment requires $v_\parallel$ to decrease when $v_\perp$ increases. For some particles, as they follow the field lines, $v_\parallel$ may become zero, i.e. the particle changes direction and is thus trapped by the magnetic field. The projection of the particle orbit on a poloidal cross section has the rough shape of a banana. A particle is trapped if $v_\parallel \leqslant \sqrt{\zeta} v_\perp$, where $\zeta = a/R$ is the aspect ratio. The wave energy absorbed by resonant particles only contributes to the noninductive current if their orbits are not trapped. Worse, if passing particles become trapped (see figure 5.2.6), the depletion of the electron energy distribution function gives rise to a return current, opposite to the EC driven current, reducing the overall efficiency of the ECCD [201]. The calculation of the total EC driven current needs these toroidal effects to be taken into account.

Figure 5.2.7 illustrates the resonance curves in velocity space in the ECCD case ($k_\parallel \neq 0$). Due to the Doppler shift, the resonance curves become ellipses which are asymmetric in $v_\parallel$. The wave may be either absorbed at the low ($\omega / n\Omega_{ce} < 1$, shown in figure 5.2.7a) or high field side of the cold resonance ($\omega / n\Omega_{\mathrm{ce}} > 1$, shown in figure 5.2.7b). Low field side absorption exhibits a reduced ECCD efficiency because the wave is interacting with a higher proportion of trapped particles. In the second case the overlapping of resonance curve and passing/trapped particle boundary is avoidable.

TCV was the first tokamak to achieve steady-state fully non-inductively EC driven discharges in 1999 [202] (albeit at relatively low plasma currents and with a high bootstrap component, see below). Such discharges have since then been routinely achieved.

(§) A quantity that remains approximately constant when the magnetic field changes (in time or space).

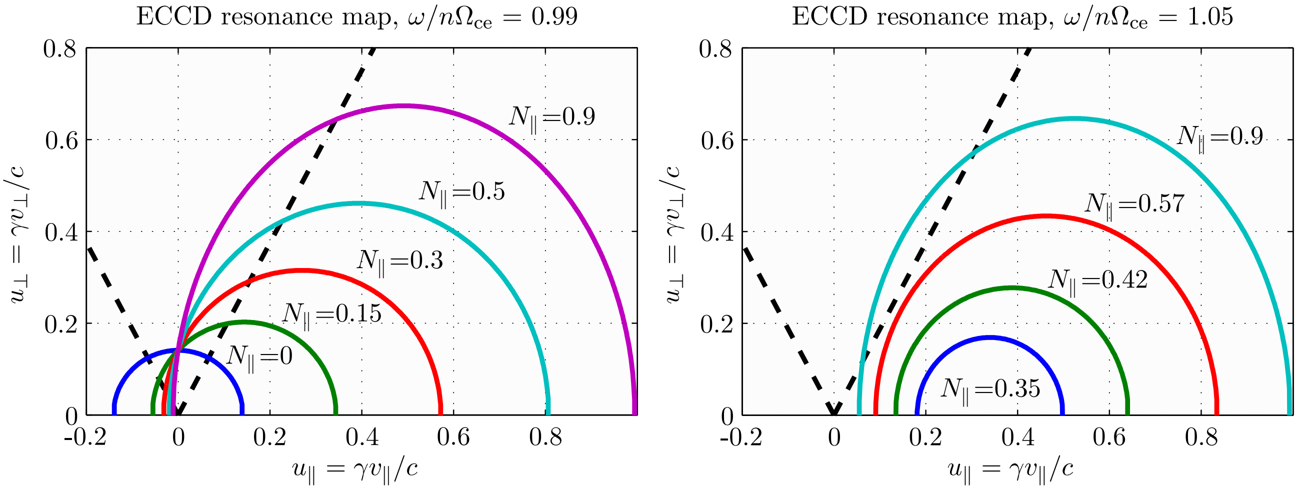

(a) High field side absorption.

(b) Low field side absorption.

Figure 5.2.7: Asymmetric ECCD resonance maps for TCV with the wave absorption occurring at (a) the high field side and (b) on the low field side of the cold resonance. In the first case the wave is always interacting with the trapped particle population, whereas with a frequency $\omega/n\Omega_{ce} > 1$ and sufficiently small $k_\parallel$ the resonance involves only passing particles. Particles having velocity components lying inside the upside down cone are trapped, those outside are passing (see discussion in section 5.2.3.2).

5.2.4 Bootstrap current

Strong ECCD is often accompanied by strong radial plasma pressure gradients (section 5.4.1), which are the origin of the so called bootstrap current [203, 204]. Trapped particles, oscillating toroidally back and forth on their banana orbits, experience the magnetic field gradient ∇B provoking a radial drift force, eq.(1.4.5), which points inwards (outwards) for electrons moving in the same (opposite) direction to the toroidal magnetic field. The turning points of the orbits on the high field side are therefore located closer to the main torus axis for electrons with $v_\parallel > 0$ than those with $v_\parallel < 0$. In the presence of density and temperature profiles falling off towards the edge, the number of electrons of positive velocity, on a given flux surface, will therefore be larger than those moving opposite, hence there is a net trapped electron banana current causing the trapped distribution function to become asymmetric in $v_\parallel$. The stronger the density gradient, the stronger this asymmetry and thus the flowing current. Although this current is fairly small, the collisional diffusion (mainly through pitch-angle scattering) across the trapped-untrapped boundary in the velocity space extends this asymmetry to the untrapped-electron region with the result of a net parallel plasma current, dubbed the 'bootstrap current'.

The total plasma current density j_p is therefore the sum of the components

$$j_\mathrm{p} = j_\mathrm{OH} + j_\mathrm{ECCD} + j_\mathrm{BS}, \tag{5.2.31}$$

where the bootstrap current j_BS amounts approximately to

$$j_\mathrm{BS} = -\frac{\sqrt{\varepsilon}}{B_\theta} T_e \frac{\mathrm{d}n_e}{\mathrm{d}r}. \tag{5.2.32}$$

Note that the bootstrap current is driven by the plasma itself, it is even envisaged to replace the inductive current component by j_BS and thus render continuous tokamak operation possible. The bootstrap current production was studied on TCV [205], and steady-state discharges fully sustained by j_BS were achieved recently [206].

5.2.4.1 EC penetration calculations with *Toray-GA*

The calculation of the EC wave propagation and absorption on TCV is routinely performed with the linear ray-tracing code *Toray-GA* [207–210]. *Toray-GA* helps in the pre-shot model design of a TCV discharge (mandatory check to prevent wave reflections or wrongly configured launcher angles) and provides the post-shot calculation of the absorbed power and current drive efficiency based on the experimental data (LIUQE equilibrium and radial profiles for electron density and temperature fitted to Thomson scattering data).

Toray-GA models the wave propagation (trajectory, refractive indices) in real tokamak geometry using typically 12 rays, each carrying a fraction of the total injected power, representative of a gaussian radial beam power profile. The propagation is calculated using the cold dispersion relation, eq.(5.1.23), whereas the absorption is calculated locally using the hot dispersion relation but with a weakly relativistic approximation. The ECCD current drive efficiency is calculated considering particle trapping by the magnetic field, using the equations published in [207]. *Toray-GA* calculations were extensively benchmarked against TCV experiments and good agreement was found [211]. The data analysed in the following is taken from a few discharges which were part of the TCV fast ion mission executed in 2005. The information obtained about the parameters of the electrons presented in the remainder of this chapter will be required later in chapters 6 and 7 to characterise the properties of suprathermal ions.

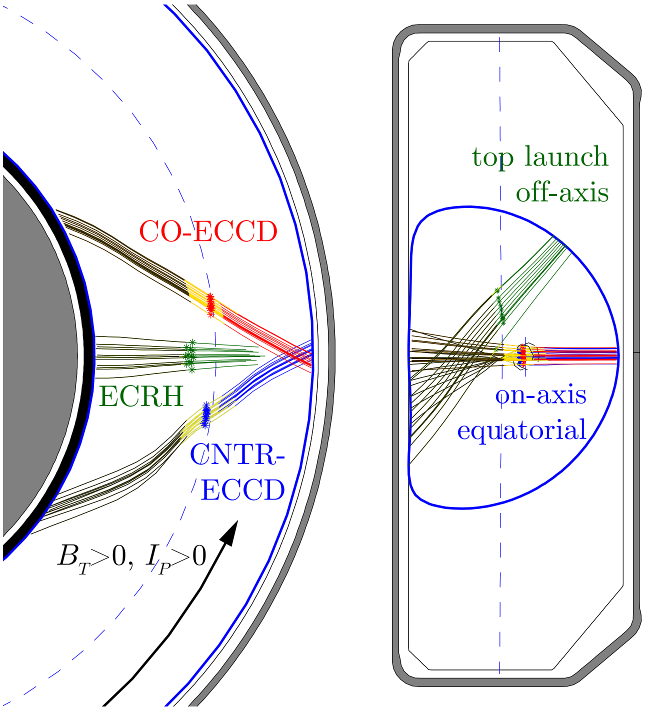

Figure 5.2.8: Top (left) and poloidal (right) view of the wave trajectories in plasma discharges #31175 and #31176, $t = 1$ s. The upper launchers #2 and #6 heat the plasma off-axis without current drive, the equatorial launchers #1 and #4 are configured for co- (#31176) or counter-current drive (#31175). Note that in reality the launchers are not located in the same toroidal sector (refer to figure 5.2.3). The lighter segments along the beam path indicate the region where 99 % of the wave power is absorbed, the stars represent the locus where the absorption is maximum. The vertical line on the right plot indicates the position of the cold X2 resonance.

Figure 5.2.8 shows ray trajectories calculated by *Toray-GA*. The plot compiles data from two discharges, #31176 with non-inductive current drive aligned with the inductive plasma current I_p, referred to as co-ECCD and #31175, where the equatorial wave launchers were turned by $\Delta\phi_L = 180°$, such that the driven current was opposite (counter-ECCD).

Although the wave is fully absorbed at the resonance layer during the first pass through the plasma (*Toray-GA* calculates a fraction exceeding 99 %), the wave trajectories continue beyond the absorption layer because the cold plasma approximation is used to calculate the wave propagation. Figure 5.2.9 plots the evolution of some important plasma parameters for discharge #31175.

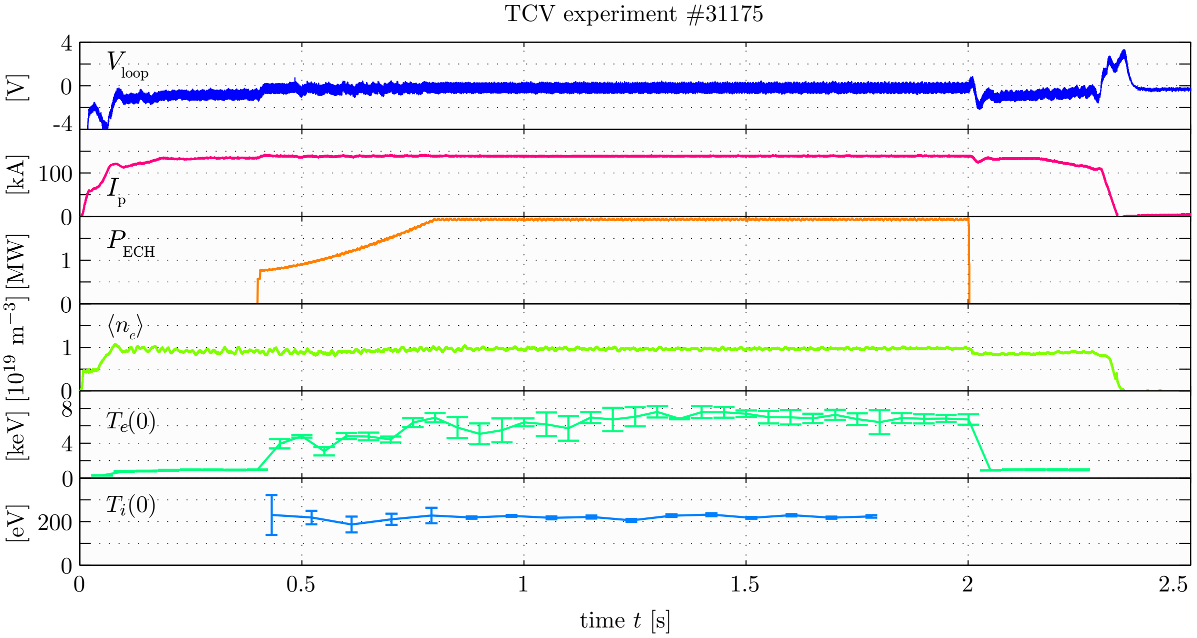

Figure 5.2.9: Temporal traces of, from top to bottom, loop voltage (estimated from the derivative of the current in the ohmic transformer), plasma current, EC power, line integrated central electron density (FIR), core electron (TS) and ion temperature (CXRS) for discharge #31175 (counter-ECCD). During the steady-state flat top the EC power reaches 1.94 MW, $V_\mathrm{loop} = -0.2$ V, $I_\mathrm{p} = 140$ kA and the electron and ion temperatures peak at 7.5 keV and 220 eV respectively.

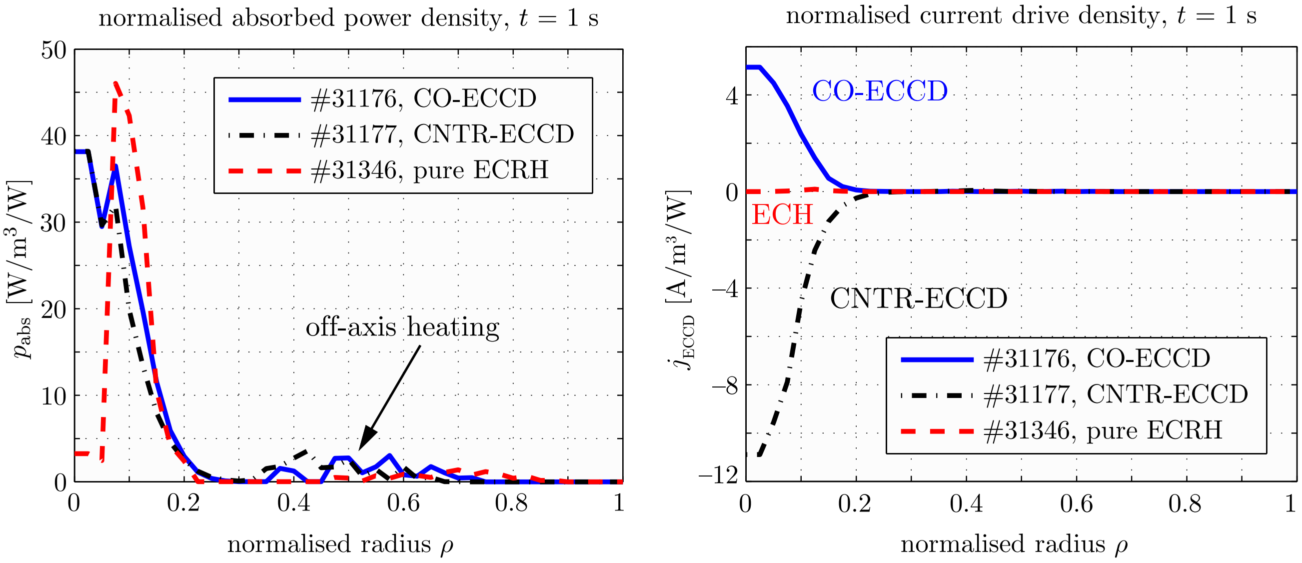

(a) Absorbed power.

(b) Driven current density.

Figure 5.2.10: Absorbed EC power (a) and resulting EC driven current density (b) calculated with *Toray-GA* for the wave trajectories shown in figure 5.2.8. The profiles shown are representative for three different discharges, namely #31176 (noninductive current aligned with the inductive current, co-ECCD), #31175 (j_ECCD antiparallel to I_p, counter-ECCD) and #31346 (ECRH only, i.e. $k_\parallel = 0$).

Figure 5.2.10 shows the corresponding power absorption and current drive densities for co- and counter-ECCD. Both figures are normalised by the EC injected power, which was 1.93 kW in total. The driven current is located inside a narrow region around the magnetic axis ($\rho < 0.2$). The off-axis heating improves the confinement of the discharge (section 5.4.1), the absorbed power density is much smaller off-axis due to a substantially larger absorption volume.

5.3 EC wave emission diagnosis

Charged particles in a magnetised plasma, owing to gyromotion around the magnetic field lines, emit synchrotron radiation. The first measurement of the electron cyclotron emission (ECE) dates back in 1964 [212] and the diagnostic techniques for its detection matured in the seventies of the last century [213]. Today almost all tokamaks are equipped with ECE diagnostics.
ECE was first exploited to locally measure the temperature of the bulk plasma. ECE is a passive measurement technique and is advantageous over active techniques like Thomson scattering, mainly because its high temporal resolution. More recently, ECE has been successfully employed to study non-thermal features of the plasma particle energy distribution. The measurable signals are much stronger than any other comparable diagnostic technique, e.g. do not suffer the poor (and time resolution limiting) statistics of hard X-ray detectors (section 3.4.2), primarily due to a much smaller energy of the diagnosed photons [214].

5.3.1 Plasma EC wave source

A point charge q, at position $\mathbf{r}(t)$ and of velocity $\mathbf{v}(t)$, observed from a space point $\mathbf{x}$ at a distance $\mathbf{R} = \mathbf{x} - \mathbf{r}$, may be described in terms of charge $\rho = q\,\delta\big(\mathbf{x} - \mathbf{r}(t)\big)$ and current density $\mathbf{j} = q\,\mathbf{v}\,\delta\big(\mathbf{x} - \mathbf{r}(t)\big)$. The electromagnetic effect of the relativistically moving charge is, according to the Maxwell equations, eqns.(5.1.1), and the Lorenz gauge, described by the Liénard-Wiechert potentials [215], that is the scalar ϕ and vector $\mathbf{A}$ potential fields

$$\phi = \frac{q}{4\pi\varepsilon_0}\left(\frac{1}{R}\right); \qquad \mathbf{A} = \frac{\mu_0 q}{4\pi}\left(\frac{v}{R}\right). \tag{5.3.1}$$

The electric field is then

$$\mathbf{E} = -\frac{\partial \mathbf{A}}{\partial t} - \nabla\phi = \frac{e}{4\pi\,\varepsilon_0\,\kappa^3\,R}\left[\frac{\mathbf{R}}{R} - \frac{v}{c}\frac{1-\left(\frac{v}{c}\right)^2}{R} + \frac{\mathbf{R}}{R} \wedge \left\{\left(\frac{\mathbf{R}}{R} - \frac{\mathbf{v}}{c}\right) \wedge \frac{1}{c}\frac{\partial v}{\partial t}\right\}\right] \tag{5.3.2}$$

where $\kappa = 1 - \mathbf{R}\cdot\mathbf{v}/Rc$ and the first term is the close field (not interesting for ECE). The far field ($R \gg r$), with its spectrum unfolded by a Fourier transform, becomes

$$\begin{aligned}
&\mathbf{E}(\omega) = \frac{-\mathrm{i}\,e\,\omega}{8\pi^2\,\varepsilon_0\,c\,R}\int_{-\infty}^{+\infty}\frac{\mathbf{R}}{R} \wedge \left(\frac{\mathbf{R}}{R} \wedge \frac{\mathbf{v}}{c}\right)\exp\left(\mathrm{i}\,\omega\left(t' - \frac{\mathbf{R}\cdot\mathbf{r}}{rc}\right)\right)\mathrm{d}t' = \\
&\frac{\mathrm{i}\,e\,\omega}{4\pi\,\varepsilon_0\,c\,R}\sum_{m=-\infty}^{+\infty}\delta\Bigg(\left(1 - \frac{v_\parallel}{c}\cos\theta\right)\omega - m\,\Omega_0\Bigg)\times \\
&\quad\left\{\mathbf{e}_x\left(-\frac{\cos\theta}{\sin\theta}\left(\cos\theta - \frac{v_\parallel}{c}\right)\right)J_m(\xi) - \mathbf{e}_y\frac{\mathrm{i}\,v_\perp}{c}\frac{\mathrm{d}J_m(\xi)}{\mathrm{d}\xi} + \mathbf{e}_z\left(\cos\theta - \frac{v_\parallel}{c}\right)J_m(\xi)\right\},
\end{aligned} \tag{5.3.3}$$

where $\xi = (\omega/\Omega_0)\,v_\perp/c\sin\theta$ and a frame of reference with a uniform B_0 along $\mathbf{e}_z$, $\theta = \angle(\mathbf{R}, \mathbf{e}_z)$ and $\mathbf{R} = R(\sin\theta, 0, \cos\theta)$ was chosen.

The emitted radiation is therefore limited to the Doppler shifted harmonics of the cyclotron frequency, i.e.

$$\Omega_m = \frac{m\,\Omega_0}{1 - v_\parallel \cos\theta / c}; \qquad m \in \mathbb{N}^*. \tag{5.3.4}$$

An inverse Fourier transform yields the Schott-Trubnikov spectral density formula, eq.(5.2.14), which gives the energy emission rate at the observation point. In a plasma, in the absence of correlations between electron trajectories, the total emission coefficient (per unit volume, unit frequency and unit solid angle) is obtained by integration over the velocity distribution function,

$$j_\omega(\theta, t) = 2\pi \int_0^\infty \int_{-\infty}^\infty \eta_\omega(p_\parallel, p_\perp, \theta)\, f(p_\parallel, p_\perp, t)\, p_\perp \mathrm{d}p_\perp \mathrm{d}p_\parallel. \tag{5.3.5}$$

At a given location, the plasma not only emits but also absorbs radiation. If the electron distribution function is Maxwellian, the ratio between emission, eq.(5.3.5), and absorption, eq.(5.2.11), equals the intensity of the black body emission in vacuum [45],

$$\frac{1}{N_r^2} \frac{j_\omega}{\alpha_\omega} = \frac{\omega^2}{8\pi^3 c^2} k_B T. \tag{5.3.6}$$

5.3.2 EC radiation transport

The interplay between emission and absorption of the wave propagating along its trajectory s is described by the transfer equation [45],

$$N_r^2 \frac{\mathrm{d}}{\mathrm{d}s}\left(\frac{I_\omega}{N_r^2}\right) = j_\omega - \alpha_\omega I_\omega, \tag{5.3.7}$$

where I_ω is the radiation intensity (Watts per unit surface, unit frequency and unit solid angle). The solution of this equation, in the absence of radiation sources outside the plasma, may be written

$$I_\omega = \int_0^{\tau_0} S_\omega(\tau)\, e^{-\tau}\, \mathrm{d}\tau = \frac{\omega^2}{8\pi^3 c^2} k_B T_{\mathrm{rad}} \left(1 - e^{-\tau_0}\right), \tag{5.3.8}$$

where τ_0 is the result of the integration of eq.(5.2.21) along the whole wave trajectory inside the plasma. Two limits of eq.(5.3.8) need now to be discussed:

- ☞ $\tau_0 \ll 1$: The emitted radiation is poorly reabsorbed by the plasma, this is the optically thin case. The whole plasma contributes to the radiation intensity

  $$I_\omega = \int j_\omega \,\mathrm{d}s. \tag{5.3.9}$$

- ☞ $\tau_0 \gg 1$: Most of the radiation gets reabsorbed (optically thick case), except the radiation from a thin layer whose location depends on frequency. The radiation temperature is an average over the emitting layer and, if the plasma is thermal, $T_{\mathrm{rad}} = T_e$. That is, a linear correspondence between I_ω and $T_e\big(\rho(\omega)\big)$. An ECE based electron temperature diagnostic needs therefore the measurement of I_ω at multiple frequencies covering the plasma cross section, see figure 5.1.2b. In practice, a plasma is considered optically thick if $\tau_0 \geqslant 3$, corresponding to 95 % of absorption.

Figure 5.3.1a shows profiles of τ for some typical electron temperature amplitudes representative of TCV low density plasmas. The dotted horizontal line indicates the limit of proportionality between radiated spectral power and local radiation temperature ($\tau = 3$). Note that the HFS plasma edge is always optically thin.

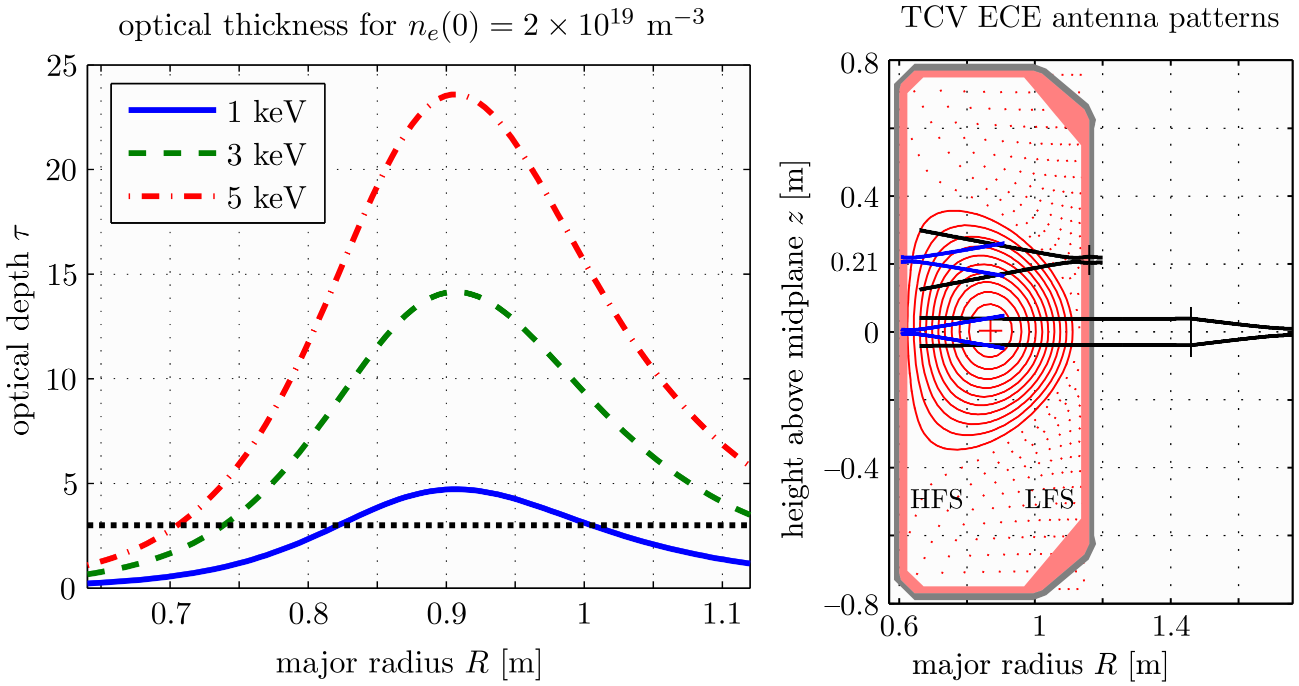

(a) τ dependence on T_e.

(b) ECE antennas on TCV.

Figure 5.3.1: (a) Optical thickness along the radius for a core electron density $n_e(0) = 2{\times}10^{19}$ m^{-3} with a toroidal magnetic field on the torus axis of $B_{\mathrm{T0}} = 1.43$ T. Three different core electron temperatures are represented (see legend label). Parabolic electron density and temperature profiles were assumed. (b) View line optics for the perpendicularly viewing ECE chords since January 2006. For the HFS and upper LFS antenna, a combination of a Gaussian feed horn and an elliptical mirror has been used as a receiver. The Gaussian beam waists in the plasma centre have an $1/e^2$-folding radius of 5 cm, the midplane LFS antenna consists of a methylpentene (TPX) focusing lens and an oversized waveguide connecting to the radiometer. The beam waist is 2.5 cm in the plasma centre.

5.3.3 ECE diagnostic principle

The principle of classic ECE spectrometry relies on the radial dependence of the electron cyclotron frequency (through the dependence $B \sim 1/R$ of the main magnetic field). From eqns.(1.5.1) and (1.4.3),

$$\Omega_{ce}(R) \simeq \frac{e\,B_0\,R_0}{m_e\,R}, \tag{5.3.10}$$

with B_0 the toroidal magnetic field at the axis of the torus R_0. For a given emission frequency the condition of resonance is thus met at a particular radial position whose locally emitted radiation intensity is proportional to the electron temperature, eq.(5.3.6), provided the plasma is optically thick. A radial temperature is then obtained by simultaneously measuring the radiation intensity at various frequencies.

5.3.4 Perpendicular versus oblique observation

The geometrical setup of any ECE diagnostic is of capital importance when it comes to diagnosis of non-thermal plasmas. The presence of suprathermal electrons causes the EC emission to deviate from the black-body ideal and the detectable deviations strongly depend on the direction of observation. The fundamental resonant angular frequency, eq.(5.3.4), may be written as

$$\omega = \Omega_{ce} \frac{\sqrt{1-\left(\frac{v}{c}\right)^2}}{1-\frac{v_\parallel \cos\theta}{c}}, \tag{5.3.11}$$

such that high perpendicular velocities $v_\perp$ (eg. if strong ECRH is applied) cause a relativistic frequency downshift. As a consequence, the radiation emitted by the electrons populating the suprathermal tail of the distribution function is only detectable on the HFS [216] as the radiation transported towards the LFS is reabsorbed at the cold resonance layer further outside (follow the radiation path on figure 5.1.2b for example). The opposite is true for high forward electron velocities $v_\parallel$ (e.g. if strong ECCD is applied), eq.(5.2.16) implies then a Doppler upshift of the emission frequency. For a optically thick plasma, this upshift is only observable for $k_\parallel \neq 0$, that is with oblique ECE [217, 218].

Electron cyclotron emission is therefore a very sensitive detector of suprathermal populations in geometries that place the resonant suprathermal electrons closer to the receiving antenna than the thermal population. The horizontal perpendicular ECE view is not able to separate the spatial and energetic location of the emitting electrons as, for a given frequency, only the product γR is defined. Only oblique ECE is able to resolve radial and energetic distributions of the optically thin suprathermal EC emission independently. The reason for this is given by eq.(5.2.16): For a given $k_\parallel$ and ω, there is a maximum major radius $\rho_{\max}$ from which radiation emission is permitted. The spatial resolution is then achieved by the choice of the observation angle, such that the radius of tangency $\rho_{\min}$ of the refracted ray with the flux surface is close to $\rho_{\max}$.

5.3.5 ECE diagnostic setup on TCV

The radiometers analysing the ECE radiation on TCV work according to the heterodyne scheme [219], i.e. mixing the measured signal with a fixed frequency signal provided by a Gunn local oscillator, such that the electron cyclotron signal frequency is brought to a lower frequency (below 20 GHz), which is then analysed. The following lines of sight exist on TCV:

- ☞ two lines of horizontal perpendicular view, looking from the high field side, at $z = 0$ and $z = 21.2$ cm respectively. This system was commissioned in 2000 [220].
- ☞ identical setup, but viewing from the low field side. This system was commissioned in 2003 [221, 222].
- ☞ a steerable view, using a launcher of the type employed for the X2 gyrotron beams (figure 5.2.1), from the low field side, at the midplane, operational since 2005 [221]. An independent 7th launcher, for exclusive use as receiving antenna for the purpose of oblique ECE, was installed in 2007 [223]. During the discharge, the receiver may be swept in the poloidal, toroidal or any inclined plane with the launcher mechanics. Two toroidal sweeps between $\phi = 7°$ and $55°$ are achievable per discharge.

The current setup permits to use only one line of sight per field side. HFS and LFS antennas are located in different toroidal locations. Figure 5.3.1b shows the antenna geometry of the perpendicular ECE view lines. This geometry limits the collected radiated power to 50 μW for an electron temperature of $T_e = 10$ keV. Each radiometer has 24 channels, the HFS radiometer has a frequency range of 78–114 GHz, the LFS radiometer 65–99 GHz, such that the whole plasma cross-section is covered. Each radiometer has an IF bandwidth of 750 MHz and each frequency channel has a video bandwidth of 100 kHz (LFS) and 40 kHz (HFS) respectively with sampling rates ranging 10. . . 200 kHz. The spatial resolution is, for a magnetic field of $B_0 = 1.45$ T, 4 mm at the edge and 8.5 mm in the centre. Notch filters at the second and third harmonic of the electron cyclotron frequency protect the radiometers from power coming directly from the gyrotrons.

5.4 EC physics on TCV

This section very briefly reviews some effects of the EC waves on the background plasma. These include experimental evidence of improved confinement due to transport barriers (section 5.4.1), quasi-linear modelling of the evolution of the electron velocity distribution function in phases with strong wave-particle interactions (section 5.4.2.2) and the generation of highly suprathermal electrons by ECCD (section 5.4.3). The discussion is restricted to features exploited in the fast ion plasma mission.

Although merely heating electrons, ECRH has become an important tool for the localised modification of plasma parameters, e.g. current profile tailoring [224], neoclassical tearing mode (NTM) stabilisation or sawtooth control [225]. The selectivity in energy and space made of EC physics a highly regarded mean of distribution function engineering. Recent developments in plasma feedback control hardware promote these tools even available in real time [226, 227].

5.4.1 Internal transport barriers

In the mid-nineties, a new improved operational regime was discovered on the Tokamak Fusion Test Reactor TFTR [228], showing substantial enhancement in confinement. This regime exhibits internal transport barriers (ITB), e.g. strong gradients on the density and temperature profiles. Such advanced scenarios for better performance are interesting for future fusion reactors, ITER currently aims at steady state operation with weak ITBs [229]. ITBs were therefore extensively studied on various tokamaks, a recent review is available in [230]. The key ingredient for the formation of the barrier is the provision of a central region of negative magnetic shear(¶) [231]. TCV has produced electron internal transport barriers (eITB) in discharges with inductive current and localised ECRH [232], but also achieved fully noninductive scenarios where the current was entirely sustained by ECCD [205]. The improvement in energy confinement over the ohmic TCV L-mode [175] is commonly parameterised by the Rebut-Lallia-Watkins scaling factor $H_{\mathrm{RLW}} = \tau_E^e/\tau_{\mathrm{RLW}}$ [233], whose value ranges up to 6 on TCV. The barrier formation [234] and strength [231] strongly depend on the current profile, such that the EC absorption must be localised. TCV has no direct measurement of the current profile, but wave driven current distributions are routinely calculated using self-consistent models of wave absorption, current drive and diffusion (see next section).

(¶) In a tokamak, the direction of the magnetic field changes from flux surface to flux surface, the pitch of the helical field lines and therefore their twist is measured by the profile of the safety factor q, eq.(1.5.2). The magnetic shear s is the radial rate of change of q,

$$s = \frac{r}{q}\frac{\mathrm{d}q}{\mathrm{d}r}. \tag{5.4.1}$$

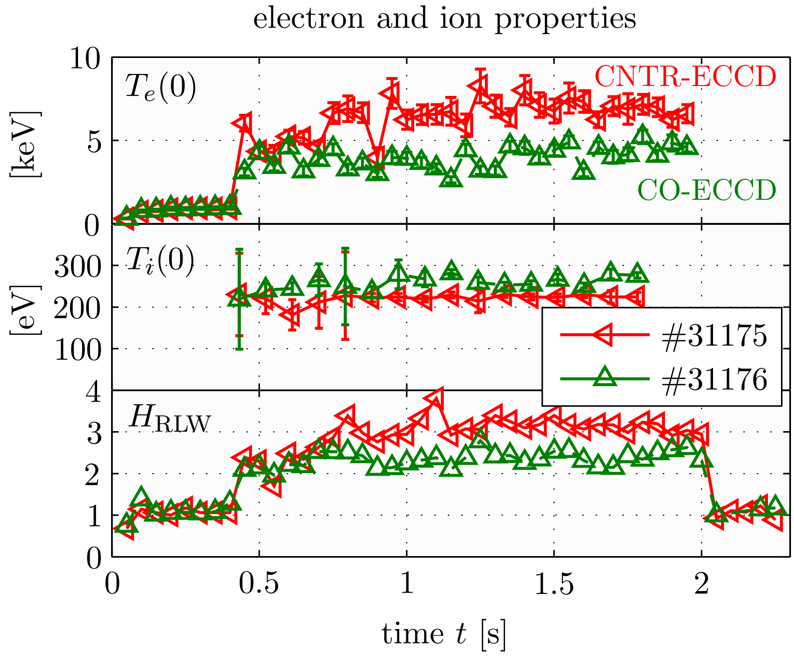

Figure 5.4.1: Temporal traces of core electron (TS, top), core ion temperature (CXRS, middle) and H_{RLW} (bottom) for the counter- and co-ECCD discharges #31175 and #31176 ($\langle n_e \rangle = 1 \times 10^{19}$ m^{-3}). The gyrotrons are switched on at $t = 0.4$ s, reach full power at $t = 0.8$ s and are switched off at $t = 2$ s (see figure 5.2.9). Except the sign of the toroidal EC injection angle the setup of both discharges is identical. $H_{\mathrm{RLW}} = 1$ during the ohmic phase, as expected, but increases to 2–2.5 in the co- and 3–4 in counter-ECCD case. The high T_e of the counter-ECCD discharge reduces the energy coupling between electron and ions, the core T_i is thus slightly lower.

Figure 5.4.1 shows the behaviour of bulk electron and ion temperature in the two ECCD discharges already shown in figures 5.2.8 to 5.2.10, targeted to study the formation of fast ion populations (chapter 6) and designed to exhibit high core electron temperature and strong central ECCD current. In discharge #31175 the ECCD beam is injected in opposite direction of the inductive plasma current (counter-ECCD), in #31176 the two currents align (co-ECCD). As shown, the injection of EC waves considerably increases the core electron confinement.

Figure 5.4.2a shows the corresponding electron temperature profiles prior and during the EC heating phase, demonstrating their evolution from classic L-mode near parabolic profiles to high gradient peaked profiles. However, in the co-ECCD discharge the strong ITB gradient does not appear, whereas the counter-ECCD clearly exhibits a barrier, although a weak one (H_{RLW} exceeds only 3), resulting in a high core electron temperature. The off-axis ECRH serves to improve the barrier in the counter-ECCD discharge and stabilises sawteeth (section 5.4.4.2). Stronger internal barriers may be obtained with off-axis ECCD [235]. Simulations confirm [236] that the injection of counter-ECCD on-axis provides a negative current source in the plasma centre, which increases the depth of the reversed current density profile hollow and causes a reduction in the core transport due to micro-turbulence. Electron confinement is therefore improved (with regard to H_{RLW}) and the ECCD current drive efficiency is higher. Also the ohmic current is increased in the region of absorption because of the higher conductivity of the hotter electrons [237] which compensates the counter-ECCD. There is a feedback loop on the time derivative of the plasma current to maintain I_{p} constant and the loop voltage is decreased upon EC injection and barrier formation (figure 5.2.9).

Note that the barriers are eITBs, the ion confinement is not affected. This is demonstrated in figure 5.4.2b.

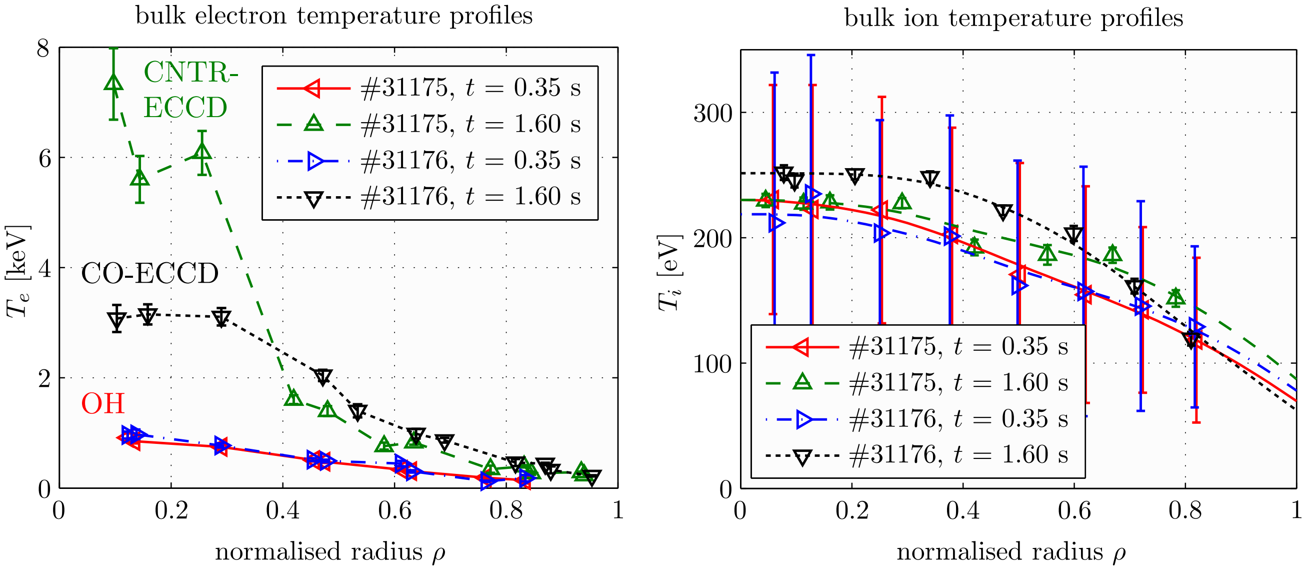

(a) TS electron temperature profiles.

(b) CXRS ion temperature profiles.

Figure 5.4.2: Measured profiles of electron (a, TS) and ion (b, CXRS) temperature profiles. In the two discharges shown, the ohmic profiles ($t = 0.35$ s) are the same, with ECCD, the core T_e of the counter-ECCD discharge exceeds the value in the co-ECCD case by more than two ($t = 1.6$ s), thanks to the eITB located somewhere between $\rho = 0.3 \dots 0.4$. On the other hand the ions (b) are decoupled from the destiny of the electrons, their temperature profiles do practically not change in the high electron confinement phase.

5.4.2 Background plasma distribution function modelling

5.4.2.1 Quasilinear (QL) theory

Wave propagation and weak absorption are well described by linear models. If absorption becomes important, the background plasma is strongly modified and, due to the selectivity in energy of the resonant interaction between wave and electrons, may no longer be considered as thermal. Quasilinear [238], i.e. lowest order nonlinear kinetic models have been extremely successful in describing the evolution of the plasma in such circumstances.

The starting point of the quasilinear treatment is the QL ordering, i.e. the separation of the plasma distribution function into a slowly varying part F and a part $\tilde{f}$ which is fluctuating with the wave fields. The wave-particle interaction is then described as a diffusion process in velocity space,

$$\frac{\partial F(\mathbf{p},t)}{\partial t} = \frac{\partial}{\partial \mathbf{p}} \cdot \mathbf{D}_{\mathrm{QL}} \cdot \frac{\partial F}{\partial \mathbf{p}}, \tag{5.4.2}$$

with a quasilinear diffusion tensor

$$\mathbf{D}_{\mathrm{QL}} = \begin{pmatrix} D_{\perp\perp} & D_{\perp\parallel} \\ D_{\parallel\perp} & D_{\parallel\parallel} \end{pmatrix}, \tag{5.4.3}$$

with components

$$
\begin{aligned}
D_{\perp\perp} &= \pi q^2 \lim_{V\to 0} \frac{1}{V} \int_k \sum_{n=-\infty}^{+\infty} \delta\left(\omega - n\,\hat{\Omega}_{ce} - k_\parallel v_\parallel\right) \left|\mathcal{E} + J_n\, E_\parallel \frac{v_\parallel}{v_\perp}\right|^2 \left(\frac{n\,\hat{\Omega}_{ce}}{\omega}\right)^2 \mathrm{d}^3k, \\
D_{\parallel\parallel} &= \pi q^2 \lim_{V\to 0} \frac{1}{V} \int_k \sum_{n=-\infty}^{+\infty} \delta\left(\omega - n\,\hat{\Omega}_{ce} - k_\parallel v_\parallel\right) \left|\mathcal{E} + J_n\, E_\parallel \frac{v_\parallel}{v_\perp}\right|^2 \left(\frac{k_\parallel v_\perp}{\omega}\right)^2 \mathrm{d}^3k, \qquad (5.4.4) \\
D_{\perp\parallel} &= \pi q^2 \lim_{V\to 0} \frac{1}{V} \int_k \sum_{n=-\infty}^{+\infty} \delta\left(\omega - n\,\hat{\Omega}_{ce} - k_\parallel v_\parallel\right) \left|\mathcal{E} + J_n\, E_\parallel \frac{v_\parallel}{v_\perp}\right|^2 \frac{n\,\hat{\Omega}_{ce}}{\omega} \frac{k_\parallel v_\perp}{\omega} \mathrm{d}^3k, \\
D_{\parallel\perp} &= D_{\perp\parallel}.
\end{aligned}
$$

To improve continuity, the QL diffusion equation is derived in appendix A.

Eqns.(5.4.4) demonstrate that in the case of pure ECRH where the wave is injected perpendicular to the magnetic field, i.e. $k_\parallel = 0$, only $D_{\perp\perp} \neq 0$, that is electrons gain only perpendicular energy.

5.4.2.2 The *CQL3D* Fokker-Planck code

To obtain an experimentally viable description of the plasma response to the wave absorption, other effects influencing the particle velocity distribution require consideration, such as parallel electric fields, electron transport and particle collisions. The mechanism of the EC current drive relies itself on the collisional diffusion in velocity space (section 5.2.3.2), it is therefore natural that popular quasilinear codes solve the Fokker-Planck equation [239], that is the Vlasov equation (5.1.35) with a relativistic Fokker-Planck collision operator.

Many TCV experiments were modelled with the collisional Fokker–Planck code *CQL3D* [240], solving the bounce averaged Fokker–Planck equation using finite differences (1D in real space, 2D in velocity space). Wave ray-tracing is treated with a *Toray-GA* plug-in. Wave–particle interactions are treated quasilinearly. Experimentally observed current drive efficiencies, systematically underestimated by the linear *Toray-GA* code, were, due to quasi-linear enhancement by the impressive power densities on TCV, historically strongly overestimated with *CQL3D*. The level of current drive calculated with *CQL3D* matched to the experimental value by the inclusion of radial diffusion ($D = 0.5\ldots 5$ m^2/s, of the order of the thermal energy diffusivities) of the hot electrons [236, 241]. That is, current carrying electrons are pitch angle scattered within a deflection time of approximately 10 ms ($E = 100$ keV) such that they no longer contribute to the current.

Experimental and simulated I_{ECCD} are brought into agreement by adjusting a (flat) diffusion coefficient, the current is monotonically decreasing with D. Typical values of the diffusion coefficient were experimentally confirmed using modulated EC injection [242], analysis of hard X-ray emission profiles [120, 243] or high field side ECE to monitor the presence of fast electrons [244]. However, if the EC power is large enough, the energy of the suprathermal electrons is so high that they can diffuse to the plasma edge, where they are still carrying current [245].

Although having the highest wave power density, TCV is still below the quasilinear saturation level and absorption is not affected by the radial electron transport (so the *Toray-GA* model remains valid).

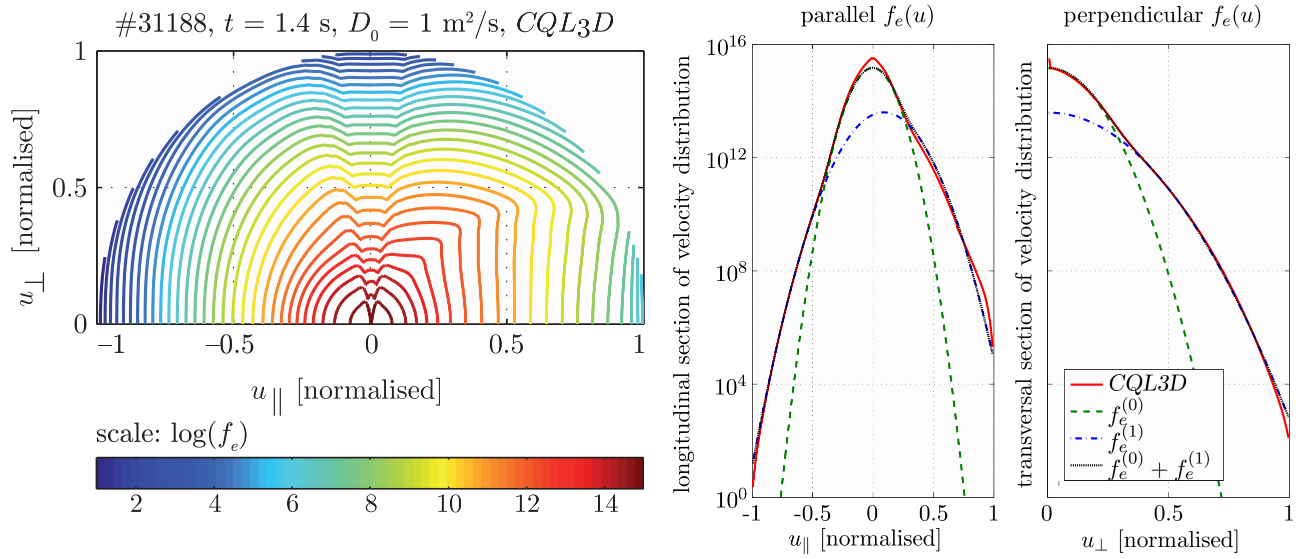

(a) Modelled 2D electron distribution function.
(b) Parallel and perpendicular distribution function.

Figure 5.4.3: (a) Pitch angle dependence of the electron distribution function calculated by *CQL3D* based on experimental data for discharge #31188 at $t = 1.4$ s. A radial suprathermal electron diffusion coefficient of $D_0 = 1\ \mathrm{m}^2/\mathrm{s}$ was sufficient to bring the modelled and measured current drive efficiency into agreement. The contour lines scale with the logarithm of the distribution function f_e and are equispaced. The velocity coordinates are normalised by a relativistic electron energy of 200 keV. The trapping/passing boundary is clearly visible.
(b) Attempts to describe the *CQL3D* calculated distribution by a two-dimensional set of Maxwellians. Anisotropic longitudinal and transversal distributions with the best fit parameters are shown.

Figure 5.4.3a shows the result of a *CQL3D* run for the counter-ECCD discharge #31188 (similar to #31177 shown previously) for experimental conditions on the magnetic axis. The distortion of the distribution function into the direction of the ECCD is clear and extends to relativistic speeds. Although the pitch angle dependence of the distribution function is complicated, a description in terms of a bi-Maxwellian distribution is feasible. A 2D-fit of the distribution shown in figure 5.4.3a yields

- ☞ a thermal electron bulk denoted by $f_e^{(0)}$, isotropic and symmetric in respect to the parallel direction. $T_e^{(0)} = 6.5$ keV (consistent with TS) and

- ☞ a shifted (along the parallel direction) suprathermal electron population $f_e^{(1)}$ with a modest drift velocity parallel to the magnetic field, compatible with the current driven by ECCD and high perpendicular temperature due to ECRH. $T_e^{(1)} = 15$ keV (consistent with ECE), suprathermal population strength $n_e^{(1)}/n_e^{(0)} = 0.1$, parallel drift velocity $v_\mathrm{d}^{(1)} = 0.7\, v_\mathrm{the}$ with v_the the thermal electron velocity. The last two parameters are consistent with the driven current density $j_\mathrm{ECCD} = e\, n_e^{(1)} v_d^{(1)} \lesssim 10\ \mathrm{MA/m^2}$.

Longitudinal and transversal distribution functions, defined respectively as

$$F_{e\|}(v_\|) = \int_0^{2\pi} \mathrm{d}\theta \int_0^{\infty} v_\perp\, f_e(\mathbf{v})\, \mathrm{d}v_\perp, \tag{5.4.5}$$

$$F_{e\perp}(v_\perp) = \int_0^{2\pi} \mathrm{d}\theta \int_{-\infty}^{+\infty} f_e(\mathbf{v})\, \mathrm{d}v_\|, \tag{5.4.6}$$

are, together with the analytic bi-Maxwellian expression and parameters stated above, shown in figure 5.4.3b.

5.4.3 Observation and simulation of non-thermal ECE emission

Relativistic electrons accompanying strong ECCD were observed from the early days of compatible fast electron diagnostics [246], currently preferentially investigated by ECE diagnostics. During ECRH, the lowest energy electrons are in resonance with the full power of the beam and strong attenuation leads to less power being available to heat the higher energy electrons. During ECCD, conversely, the higher energy electrons are primarily in resonance (see figure 5.2.7b) [247]. The non-thermal electrons carry the non-inductively driven current. The distortion of the electron distribution function (modelled using *CQL3D*) during strong current drive and the associated suprathermal tail are clearly visible on figure 5.4.3a. The HFS and LFS ECE systems do radially overlap and simultaneous measurements with both radiometers provide complementary quantitative and qualitative information about the electron distribution function due to the asymmetry of the ECE spectra emitted into opposite radial directions. The HFS radiometer partially covers the third harmonic frequency range, which provides additional information on suprathermal electrons.

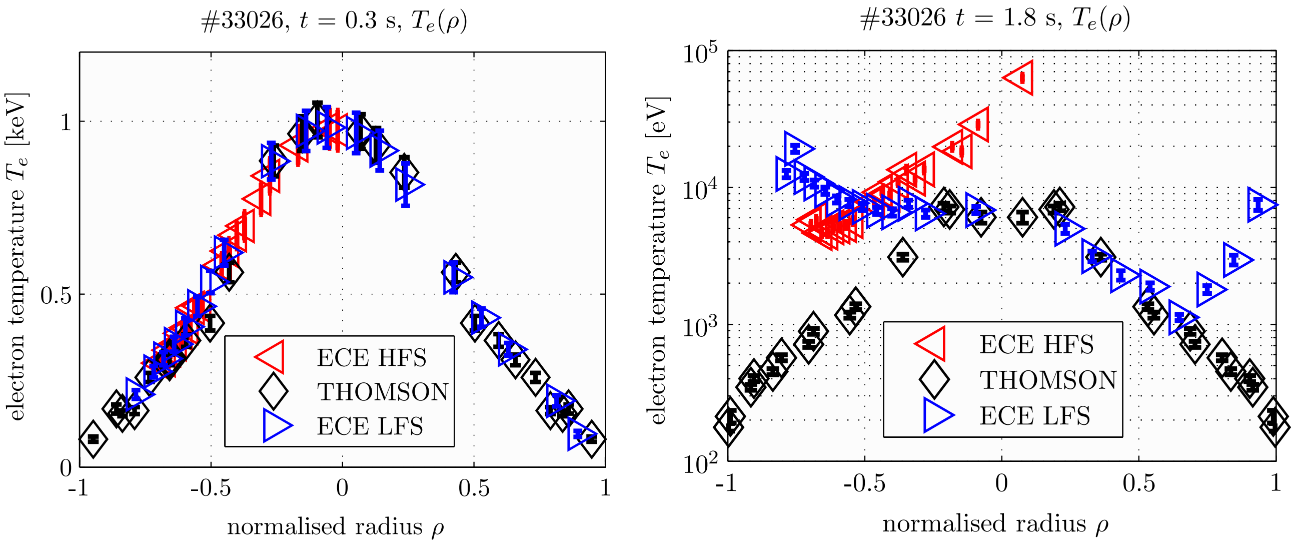

(a) Ohmic electron temperature profiles.

(b) ECCD electron temperature profiles.

Figure 5.4.4: Profiles of measured electron temperature during a purely inductive phase (a) and with 1 MW counter-ECCD on axis plus 1 MW off-axis ECRH (b). Note that the temperature scale is logarithmic in the second plot. In the ohmic plasma the three temperature diagnostics agree. During the phase of auxiliary heating, the LFS radiometer measures core bulk temperatures in agreement with Thomson scattering, whereas the HFS radiometer indicates fairly suprathermal temperatures. Negative ρ parameterise the HFS side of the plasma, the vertical Thomson scattering measurement points were mapped to the normalised radius grid.

Figure 5.4.4 shows profiles of electron temperature measured with the LFS and HFS radiometers (perpendicular view) and the Thomson scattering diagnostic. At the beginning of 2006, the midplane LFS antenna lens was replaced to achieve better focusing properties in the near field. The poloidal focal spot is now 1.2 cm at $r/a = 0.85$, compared to 6 cm before. As a result, perpendicular LFS observation of the circulating suprathermal on-axis ECCD electrons doesn't show the Doppler upshifted radiation and the core LFS ECE temperature agrees with the Thomson scattering measurement. The HFS radiometer measures temperatures well above the thermal level, channel #1 ($f = 79.6$ GHz), whose cold resonance lies close to the magnetic axis, indicates $T_e^{(1)} \approx 60$ keV. A suprathermal density of only 2×10^{16} m^{-3} is sufficient to make the HFS signal departure from the thermal intensity visible.

Relativistically downshifted radiation from the tenuous suprathermal tail of the electron distribution function is observed throughout the plasma. The behaviour of the ECE intensity at high frequencies is due to downshifted third harmonic radiation. Radiometer channels above approximately 100 GHz overlap the resonance band of the third harmonic (see figure 5.1.2b), whose optical depth is typically too low for the associated radiation to be absorbed before reaching the pickup antenna (figure 5.4.5a).

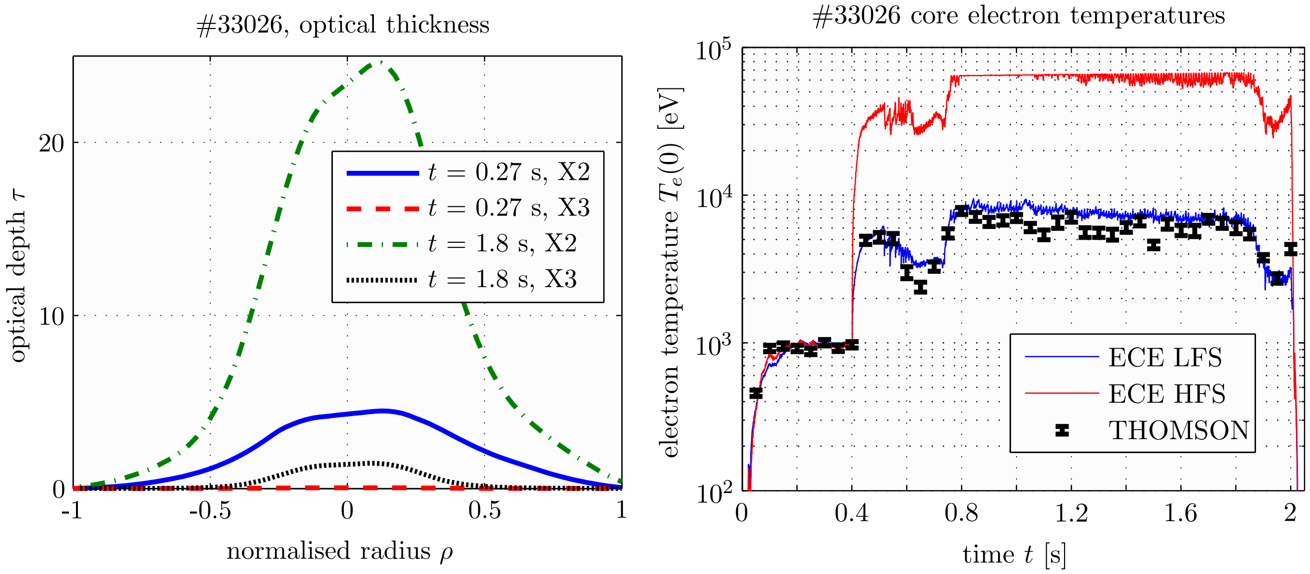

(a) Optical depth of X2 and X3. (b) Core temperature traces.

Figure 5.4.5: (a) Optical thickness of the second and third harmonic X-modes during phases of purely ohmic (t = 0.27 s) and partly non-inductive current drive (t = 1.8 s). The high electron temperature guarantees the high optical thickness during EC injection, the plasma bulk efficiently shields the LFS antenna from radiation emitted by suprathermal electrons. The third harmonic is optically thin and pollutes the high frequency radiometer channels.
(b) Core electron temperature traces. The LFS measurement follows the black-body ideal is thus close to the Thomson scattering value. The HFS measurement is strongly influenced by the presence of suprathermal electrons and exceeds the thermal temperature by a factor of 10.

Figure 5.4.5b finally illustrates the time traces of the core electron temperatures for the same discharge.

When ECE temperatures are compared to Thomson scattering values it should be mentioned that the analysis of the latter assumes a monothermal electron population. The presence of non-thermal electrons falsifies the calculated temperature, although a precise analysis of its impact is difficult to estimate. It is currently believed that in plasmas with strong ECCD (1.35 MW toroidally injected power), the temperature derived from the scattered laser beam may be in error by 20 % at most [248].

In the past, the emission of suprathermal electrons was modelled using bi-Maxwellian electron distribution functions [249] or the sum of two Maxwellians truncated at cutoff energies in the range of 5–10 keV [222]. We can now model the ECE spectra with a more sophisticated code, *NOTEC-TCV*.

5.4.3.1 The non-thermal ECE emission code *NOTEC-TCV*

The three dimensional, fully relativistic *NOTEC* radiation balance code was developed at Stichting voor Fundamenteel Onderzoek der Materie (FOM), The Netherlands, in the 1980ies to calculate ECE spectra of JET tokamak plasmas, taking into account the real ECE antenna pattern, refraction, the polarisation scrambling multiple vessel wall reflection coefficient, and non-thermal electron populations described by drifting Maxwellians, temperature anisotropy and particle loss- and anti-loss cones [250]. It was later adapted for TEXTOR [251, 252] and was implemented at CRPP to study TCV plasmas in 2006 [253]. *NOTEC* is coded in Fortran 77.
The calculation of an ECE spectrum is carried out in the following way: When the antenna pattern is known, several rays, describing the characteristics of this pattern, are launched into the plasma. Calculating the total radiation emitted along a ray in the direction of the antenna, i.e. going from the source to the antenna or going in the opposite direction, is equivalent. Starting the ray tracing from the antenna gives a great numerical advantage. To calculate a ray path through a plasma in the approximation of geometrical optics, wall reflections at frequencies for which the plasma is optically thin after one pass through the plasma must be modelled. For the ray tracing, the cold plasma approximation is used throughout. In the case of strong absorption, e.g. at the second harmonic resonance, the ray tracing calculation can be stopped before the critical range(‖) is reached as a large value of τ builds up over a fraction of the resonance layer. Numerically the ray tracing is done in the same way as in the *RAYS* code [254].
Simultaneously with the calculation of a ray, the equation of radiative transfer may be solved if the absorption and emission coefficients are locally known along the ray path (defined by the electron temperature and density profiles, magnetic field and wave vector direction). Besides the plasma equilibrium and the parameters of the thermal plasma, non-thermal populations may be specified.

Because non-thermal emission spectra do not uniquely correspond to one electron distribution function, additional assumptions for interpreting the non-thermal features need to be introduced. In practice, the diagnostician is forced to consider a limited class of distributions only and a convincing interpretation also has to rely on additional information from other diagnostics.

EC frequencies whose resonance layer lie at the plasma boundary or outside the plasma are optically thin after one pass through the resonance layer. Then not only the second harmonic X-mode, but multiple harmonics and, as a consequence of reflection of the radiation at the wall, both polarisations can contribute to the emission. The measured radiation now comes from several plasma layers. Furthermore, the antenna pattern and, if the density is high enough, refraction become particularly important.

For the requirements of TCV, the current implementation of *NOTEC-TCV* was modified to interface with the experimental MDS database. A graphical user interface helps to keep control over the large number of adjustable parameters. Instead of analytical profiles for electron density and temperature, the code uses the profiles measured with the Thomson scattering diagnostic. Accurate antenna patterns for all ECE antennas are correctly implemented. The description of the magnetic equilibrium in *NOTEC-TCV* is currently only circular in the poloidal plane but includes a Shafranov shift. This should not be a problem as long as only plasma configurations centred in front of the ECE antenna are considered. The wall reflection coefficient is 97 % (graphite tiles). All calculations are normally performed using 5 rays per antenna.

(‖) that is the region where the geometrical optics approximation breaks down.

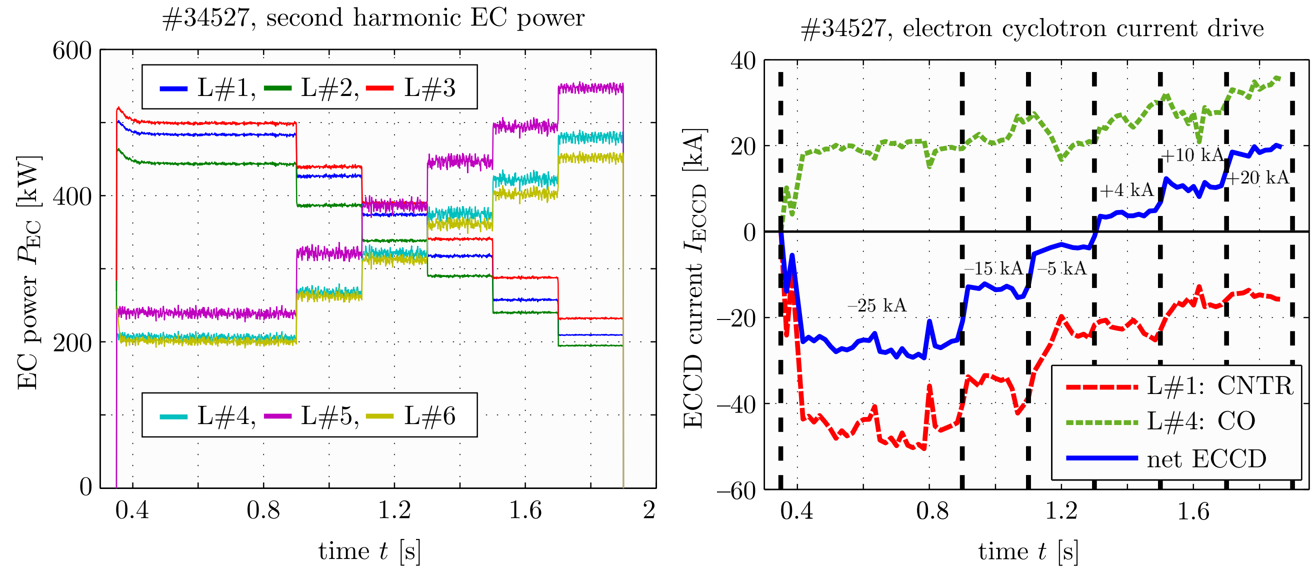

(a) Gyrotron power traces. (b) ECCD traces.

Figure 5.4.6: (a) X2 Gyrotron power stepping. The power injected through launchers #1–#3 is gradually reduced whereas the other three gyrotrons do the opposite. The traces measure the power extracted at the gyrotrons.
(b) ECCD launchers #1 and #4 point into opposite toroidal directions. With the programmed power ramps, the net driven EC current is initially in the counter direction and becomes finally co. Although the gyrotron powers are symmetric at the beginning and at the end of the discharge, the current drive efficiency is smaller in the co-direction, as discussed in section 5.4.1. The driven current was calculated using *Toray-GA*.

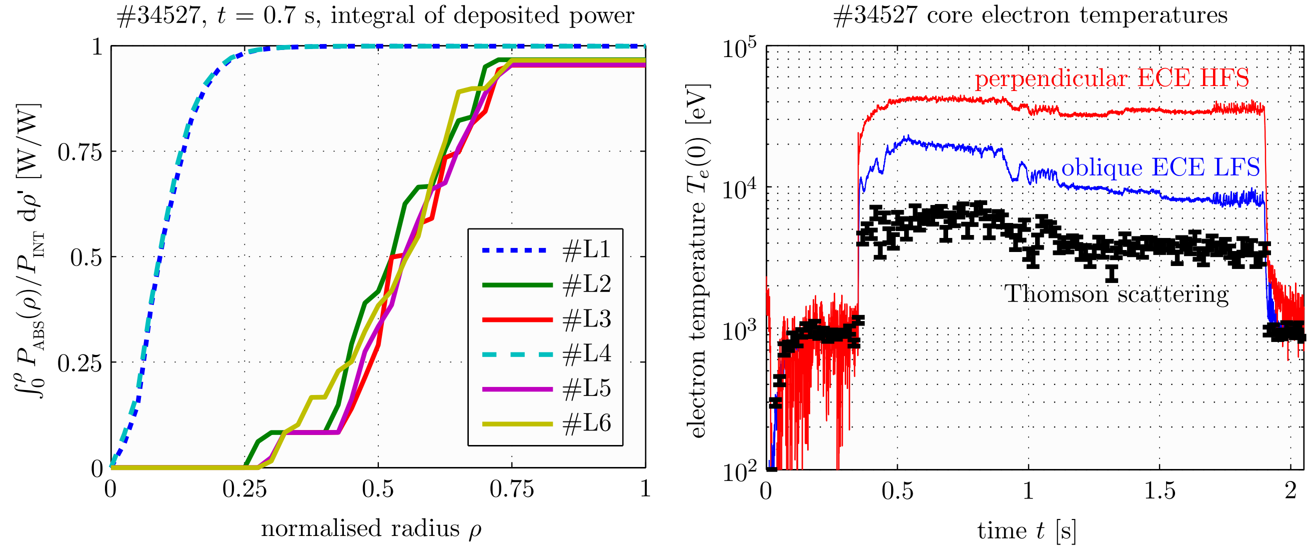

(a) Power absorption profile. (b) Core electron temperature traces.

Figure 5.4.7: (a) Integral profile of absorbed power (evaluated from the magnetic axis) for the individual gyrotrons at $t = 0.7$ s. The ECCD launchers deposit 90 % of the EC power inside $\rho = 0.2$. The ECRH launchers deposit off-axis, with quite uniform power deposition in the interval $\rho \in [0.25; 0.75]$.
(b) Time traces of on-axis electron temperature measured by Thomson scattering (bulk), low field side oblique ECE (Doppler upshifted emission) and perpendicular high field side ECE (relativistically downshifted radiation).

5.4.3.2 Simulation of oblique ECE spectra

Oblique ECE was only exploited on TCV recently. A series of experiments directly demonstrated the asymmetry of the electron distribution function in ECCD plasmas by looking into co- and counter directions with a steerable LFS ECE receiver [255]. One discharge (#34527) out of this mission was analysed in great detail using *NOTEC-TCV*. Figure 5.4.6 shows the setup of the gyrotrons for this experiment.

EC heating starts at $t = 0.35$ s and ends at $t = 1.9$ s. Cluster A (launcher #1 has on-axis counter-ECCD, launchers #2 and #3 pure ECRH) starts with full power and gradually steps down to half power (every 200 ms the power-per-gyrotron is decreased by 50 kW starting at 450 kW/gyrotron), cluster B (launcher #4 has co-ECCD, launchers #5 and #6 also ECRH) powers an ascending staircase starting at 200 kW/gyrotron. The total delivered EC power is nearly constant, about 2 MW. The net ECCD current is initially -25 kA and then increases into the opposite direction in 5 steps to reach $+20$ kA. The total plasma current of 140 kA is held constant by inductive feedback control. With the 7^{th} launcher antenna oriented at a fixed angle of $+65°$ in respect to the magnetic field (co-view) during the whole discharge the distortion of the distribution function was directly evidenced [255]. Figure 5.4.7a illustrates the location of the power absorption of the individual launchers, ECCD is driven on-axis, the four ECRH launchers deposit in a large volume off-axis. Figure 5.4.7b shows the electron temperature traces for the different diagnostics. Other than in the perpendicular LFS observation (shown in figure 5.4.5b), the oblique view captures the Doppler upshifted radiation, the LFS temperature measurement is thus in disagreement with the Thomson scattering measurement.

Thermal profiles of the bulk plasma electron density and electron temperature are shown in figure 5.4.8. The electron density profiles become slightly hollow during the EC phase. As expected, the temperature profile is the most peaked with the highest temperature during the counter-ECCD phase.

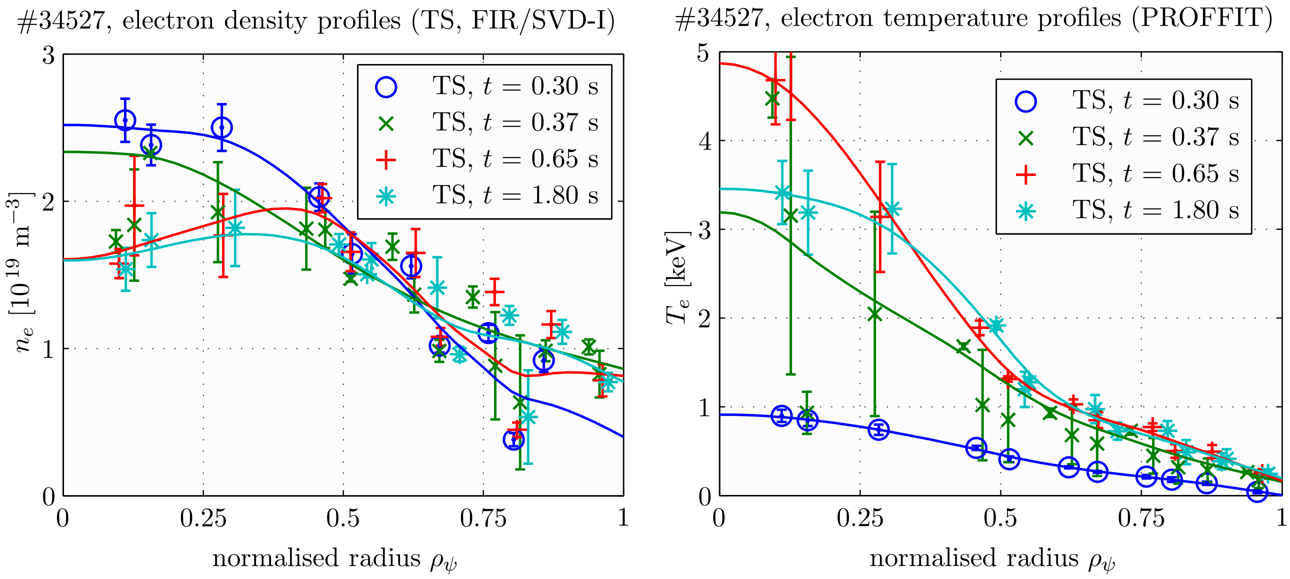

(a) Bulk n_e profiles.

(b) Bulk T_e profiles.

Figure 5.4.8: (a) Bulk Thomson scattering (symbols) and SVD-inverted interferometer electron density profiles during the ohmic phase ($t = 0.3$ s), shortly after the switch on of the gyrotrons ($t = 0.37$ s), towards the end of the counter-ECCD injection, $j_{\mathrm{ECCD}} = -25$ kA period ($t = 0.7$ s) and during the co-ECCD phase, $j_{\mathrm{ECCD}} = +20$ kA interval ($t = 1.8$ s).
(b) Bulk Thomson scattering electron temperature profiles including profile fits.

Figure 5.4.9 shows the results of extensive modelling of the ECE spectra using *NOTEC-TCV*, based on knowledge of the parameters of the background plasma and the calculation of the EC properties with *Toray-GA*.

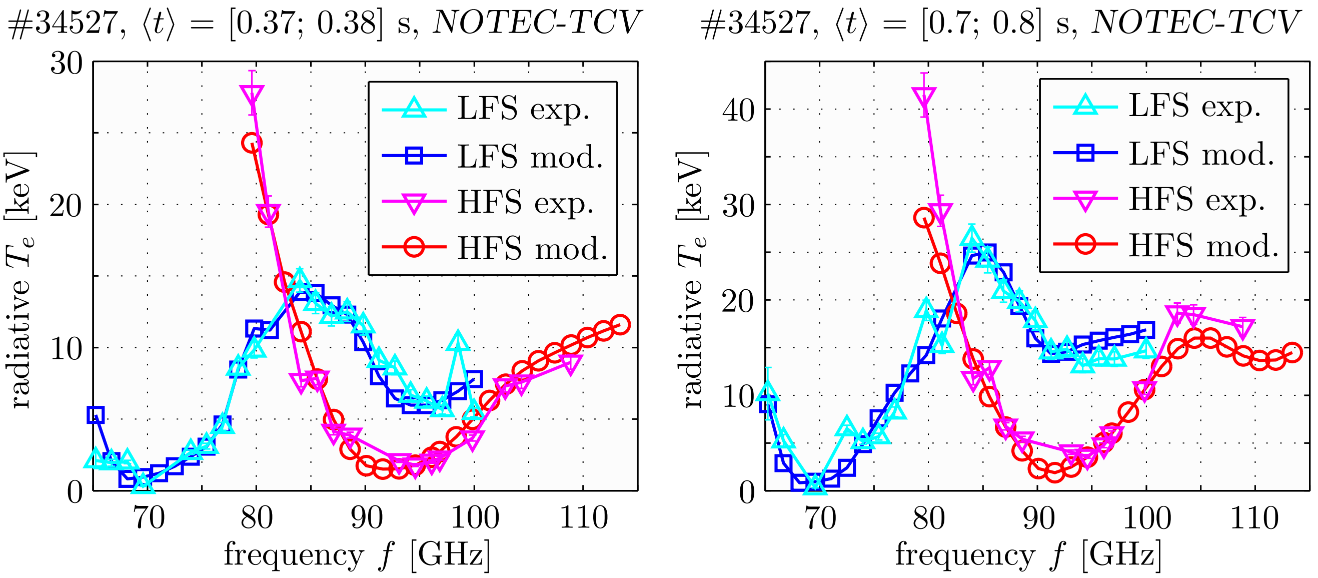

(a) *NOTEC-TCV* at heating onset.

(b) *NOTEC-TCV* at steady-state.

Figure 5.4.9: *NOTEC-TCV* simulation of the measured HFS and LFS ECE spectra shortly after the start of the EC injection (a, $t = 0.37$ s) and later when the fast electrons were radially redistributed (b, $t = 0.7$ s). The parameters to fit the experimental data are given at the bottom of this page.

The radiometer measurements were labouriously reproduced in copious runs of the code. This approach corresponds to reverse engineering the suprathermal populations present in the plasma. The difficulty lies in the large number of parameters which can be changed. Modifications of the properties of the electron populations drive the modeler inexorably to despair as the parameters change not only the emission properties but also the transport of radiation across the population. The result of small changes of the parameters is often an improvement in the agreement with the radiometer on one field side but large discrepancies with the other side. Put simply: the plots of figure 5.4.9 are the result of long and patient scan and provide the following electron parameters:

★ $t = 0.37$ **s, early after gyrotron switch-on:**

- bulk: $n_e^{(0)}(0) = 2.3 \times 10^{19}$ m^{-3} (TS, FIR), $T_e^{(0)}(0) = 3.2$ keV (TS, SXR)
- on-axis electron beam: $n_e^{(1)} = 80$ %, $T_{e,\parallel}^{(1)} = 5$ keV, $T_{e,\perp}^{(1)} = 15$ keV, $\rho^{(1)} \in [0; 0.05]$, $\beta^{(1)} = 0.15$
- extended on-axis beam: $n_e^{(2)} = 50$ %, $T_{e,\parallel}^{(2)} = 5$ keV, $T_{e,\perp}^{(2)} = 15$ keV, $\rho^{(2)} \in [0.1; 0.2]$, $\beta^{(2)} = 0.1$
- off-axis hot electrons: $n_e^{(3)} = 2$ %, $T_{e,\parallel}^{(3)} = 4$ keV, $T_{e,\perp}^{(3)} = 35$ keV, $\rho^{(3)} \in [0.2; 0.5]$, $\beta^{(3)} = 0$

★ $t = 0.70$ **s, at steady-state:**

- bulk: $n_e^{(0)}(0) = 1.7 \times 10^{19}$ m^{-3} (TS, FIR), $T_e^{(0)}(0) = 4.8$ keV (TS, SXR)
- on-axis electron beam: $n_e^{(1)} = 9$ %, $T_{e,\parallel}^{(1)} = 5$ keV, $T_{e,\perp}^{(1)} = 25$ keV, $\rho^{(1)} \in [0; 0.1]$, $\beta^{(1)} = 0.4$
- off-axis hot electrons: $n_e^{(2)} = 2$ %, $T_{e,\parallel}^{(2)} = 4$ keV, $T_{e,\perp}^{(2)} = 80$ keV, $\rho^{(2)} \in [0.2; 0.5]$, $\beta^{(2)} = 0$

The bulk profiles are input to the code as shown in figure 5.4.8. The density of each population is given as a fraction of the total density. For the sake of simplicity, the suprathermal population profile is simply scaled from the bulk profile and its spatial extent is parameterisable in normalised radius ρ and poloidal angle θ. The suprathermal temperature profiles are flat across the plasma.

The first simulation ($t = 0.37$ s) models the conditions 20 ms after the start of EC injection. The majority of the electrons in the volume where the ECCD power is absorbed are taken to the suprathermal tail of the distribution function. The hollowness of the bulk electron density profile shortly after EC injection may be ascribed to this transfer (the analysis of the TS signal doesn't really take the suprathermal electrons into account). Initially, the driven current is still small ($\beta = v_{\|}/c = 0.1 \ldots 0.15$, in agreement with figure 5.4.6b). The perpendicular temperature of the off-axis electrons has already risen to 35 keV. The strong ECE intensity on the high frequency end of the HFS spectrum is again due to relativistically downshifted third harmonic radiation. Note that agreement on the low frequency end is not very good, which is ascribed to the low intensity in the ohmic phase, when the radiometer was calibrated (see next paragraph). Only radiometer channels with physically meaningful signals are shown.

A second simulation reproduces conditions after redistribution of the fast electrons ($t = 0.7$ s). The perpendicular temperature of the off-axis population has reached a maximum value of 80 keV. The parallel temperatures of the suprathermals have not evolved and have values close to the thermal temperature of the electron bulk. The other properties (relative density, radial extent) of the off-axis population have not changed (neither have the EC heating properties). The on-axis population carrying the non-inductive current has now reached the maximum drive efficiency. The drift velocity of this population has more than tripled ($\beta = 0.4$), but its strength has strongly reduced, i.e. less than 10 % of the electrons in the core are sustaining this current. These parameters agree with the *Toray-GA* calculation of the ECCD current profile in this region. The electrons which were redistributed further outwards are not visible (the *CQL3D* simulation looks similar to the pitch angle map shown in figure 5.4.3a and matches the experimentally observed current with a quite small radial diffusion coefficient $D_0 = 0.2$ m^2/s). The reproduction of the increased radiation registered in the high frequency HFS channels required the consideration of up to 5 wall reflections per traced ray. A higher number of reflections didn't enhance the signal further. Note that oblique ECE measures a radiation temperature that is a weighted average of $T_{e\|}$ and $T_{e\perp}$, the perpendicular HFS ECE view fixes $T_{e\perp}$ and the oblique ECE LFS view provides a constraint for the $T_{e\perp}/T_{e\|}$ ratio.

5.4.3.3 ECE radiometry calibration

A final word on the subject of ECE radiometer calibration: An absolute calibration would usually be performed by means of a microwave noise source. The amplifiers in the RF stage of the radiometer do unfortunately not have a feedback control of the gain, and are thus sensitive to temperature fluctuations of the surrounding air. Radiometer calibration on TCV is therefore performed in the post-shot analysis, historically against calibrated Thomson scattering temperature profiles. For the HFS radiometer, this calibration only uses the ohmic plasma phase such that no non-thermal electrons are present(**). The oblique LFS ECE receiver may also be calibrated in a pure ECRH phase (but not with ECCD, see discussion in section 5.3.4).

(**) This may be verified by looking at the ECE emission at a frequency that corresponds to a radial location outside the plasma.

Sawtoothing plasmas (see next section) are often not suitable for this calibration [256], as the electron temperature may locally change by more than 10 % during a sawtooth cycle and the ECE shows a strong component from electrons accelerated by the sawtooth crash. Further, the poloidal symmetry assumed when vertical Thomson scattering data and horizontal ECE data are mapped to the common grid of normalised radius breaks down during the sawtooth crash [257]. Optically grey or thin plasma regions have, of course, to be excluded as the radiation from such regions is not proportional to the radiation temperature. For the data shown in this chapter, a more suitable calibration procedure was adopted: The ECE emission spectra of the ohmic phase of the plasmas were modelled with *NOTEC-TCV* and the radiometer signals were scaled accordingly. This greatly improved the calibration of the edge channels, which are sometimes optically too thin to represent the local electron temperature. Figure 5.4.4a shows the agreement of the temperature diagnostics for the ohmic phase of discharge #33026. The calibration was calculated with *NOTEC-TCV* by averaging over three Thomson scattering profiles ($\Delta t \simeq 50$ ms).

5.4.4 Internal disruptions (sawteeth instability)

The sawtooth instability was first observed in the early 1970ies on the ST tokamak in Princeton [258] and on T-4 in Moscow [259]. The observation of the soft X-ray emission in these devices revealed repetitive internal disruptions, that is a slow increase (over a couple of milliseconds) in emissivity, terminated by a rapid crash ($\sim$100 μs) in the plasma core – the time history is thus shaped like a sawtooth. The behaviour reverses in plasma regions outside the so-called inversion radius (rapid increase and slow decay). Sawteeth are observed in density and temperature and at each relaxation event, particles and energy are expelled from the core region.

A first explanation for the sawtooth instability (especially its fast collapse) was given with the Kadomtsev full reconnection model [260, 261], which is a solution of resistive MHD. According to this theory an instability with poloidal/toroidal mode numbers $m/n = 1/1$ becomes unstable at the $q = 1$ magnetic surface due to a pressure driven instability that is excited by an increase in the plasma current in the core region (such that the central value of the safety factor q_0 drops below 1). The pressure driven instability reconnects the magnetic field [262, 263], and as a consequence the influx of cooler plasma from outside the inversion radius into the core region results in the formation of a cold island. The island grows in time and eventually pushes the hot region of the plasma (i.e. the region with $q < 1$) out of the core.

Extensive sawtooth studies on various fusion devices and new developments in diagnostics enabling investigation with higher spatial and temporal resolution have shown various inconsistencies with the Kadomtsev model. These include the predicted scaling of the collapse time with machine size, which is not observed. The behaviour of the q-profile in the plasma core, first investigated on TEXTOR [264], showed that, in some situations, q stays below 1 in the core during the whole sawtooth cycle. This finding was not in line with the full reconnection model that was based on the hypothesis that the sawtooth becomes unstable as soon as $q_0 < 1$ in the plasma centre and leads to a restoration of the current density profile such that $q > 1$ over the full profile.

Reviews of the progress in experimental and theoretical studies of the sawtooth instability are available in [265] and [266]. But more than 30 years after their discovery, the physics of sawteeth is still not satisfactorily understood.

5.4.4.1 Sawteeth parameters on TCV

On TCV, the confinement and transport in sawteething plasmas were extensively investigated using tomographic reconstructions of the XTOMO measurements during the complete sawtooth period (section 2.5.3.1). The discharges investigated employed intense localised ECRH [257, 267] and allowed for a comparison with theory and a validation of the dynamics of the $m = n = 1$ magnetic island associated with the resistive internal kink mode [268], as predicted by the Porcelli model [269, 270] (a modified version of the Kadomtsev model in the presence of localised heat sources [271, 272]).

Internal kink modes may trigger the sawtooth crash. The type of mode at play and the properties of the resulting sawteeth (period and crash amplitude) strongly depend on plasma shape. At low triangularity and with sufficient elongation, ideal MHD significantly contributes to the trigger whereas, at high triangularity and low elongation, the ideal mode is stable and resistive MHD is responsible for kink dynamics [273–275]. Sufficient elongation or low triangularity plasmas exhibit frequent small sawteeth with long and large sawteeth observed in the opposite limits. The sawtooth period increases with particle density and heating power. At high elongation, sawteeth disappear abruptly [276].

5.4.4.2 Sawteeth stabilisation with EC wave deposition

One method of controlling the sawtooth instability in tokamaks relies on the accurate deposition of ECRH power in the vicinity of the $q = 1$ surface, resulting in large controllable variations in the sawtooth period by local modification of the current profile [277]. The flexibility of the electron cyclotron heating and current drive systems on TCV have been successfully used to modify the sawtooth period in such a way by tailoring the local current profile. Localised current is injected either by reducing the resistivity of the local plasma through heating (ECRH) or by direct current drive (ECCD). Transport modelling indicates that sawtooth stabilisation is responsible for the increased confinement time and the accompanying enhancement of the central temperature over co-ECCD in counter-ECCD plasmas [278]. Sawtooth stabilisation is caused in turn by the central safety factor q_0 rising above 1 for counter-ECCD; by contrast, the simulation results show that $q_0 < 1$ in the sawtoothing co-ECCD and ECRH cases.

In particular, two heating locations exist at opposite sides of the $q = 1$ surface which allow for most efficient sawtooth stabilisation and destabilisation [279]. By placing this current source immediately inside/outside the $q = 1$ surface, the magnetic shear is enhanced/decreased, reducing/increasing the time until the shear limit is achieved and therefore shortening/lengthening the sawtooth period. Moreover, the modelling shows that counter- and co-current drive alone, without the presence of heating, have opposite effects on the sawtooth period at symmetrical locations as compared with the position of the $q = 1$ surface. The main features of the experimental behaviour can be explained as due to the modification of the local plasma parameters involved in the linear resistive stability threshold of the internal kink, in particular the dynamics of the magnetic shear at the $q = 1$ surface [225].

Recently TCV demonstrated the ability to exercise continuous real time feedback control of the sawtooth period by varying the EC injection angle [227]. In the sawtooth control algorithm the instability threshold is described by a crash triggering condition whereby the shear at the $q = 1$ surface has a critical value.

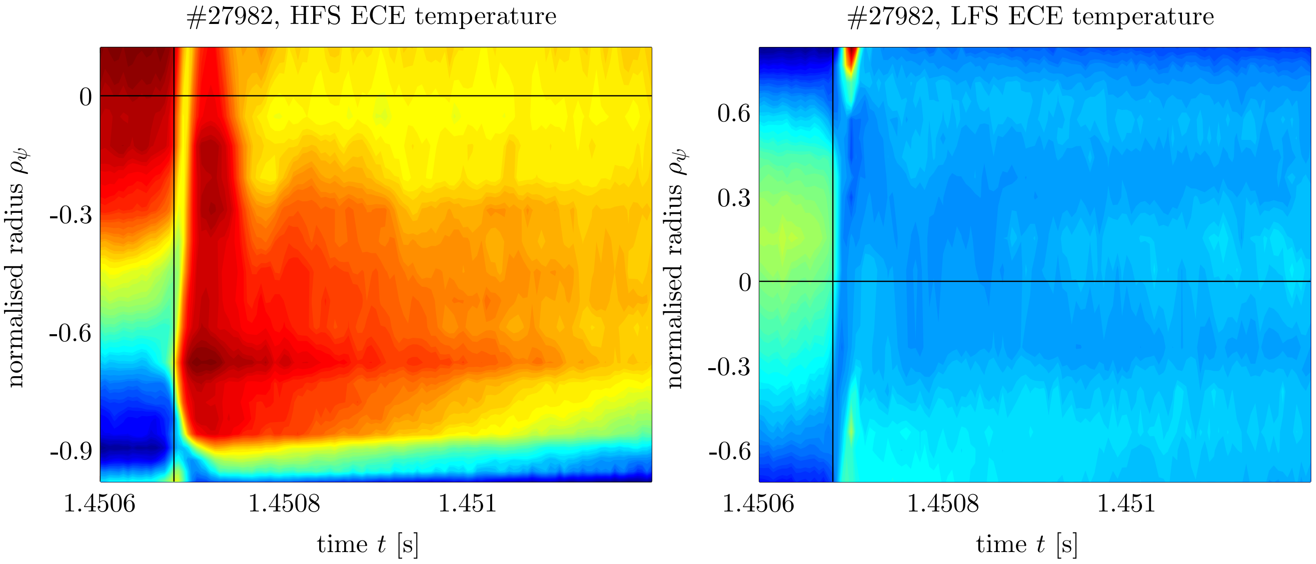

(a) High field side ECE.

(b) Low field side ECE.

Figure 5.4.10: Contour plots of the HFS (a) and LFS (b) ECE temperatures. The crash is triggered at $t = 1.45068$ s (the vertical line indicates the start of the crash). Negative normalised radii refer to the high field side.

5.4.4.3 Weak suprathermal electron acceleration by sawteeth

In magnetised plasmas, electric fields accompany the phenomenon of magnetic reconnection and any resulting acceleration produces suprathermal tails observed widely in the solar corona, in the aurora region and in laboratory plasmas, where this phenomenon was observed for the first time on the T-10 tokamak [280]. These events typically occur in connection with the formation of magnetic islands such as in sawtooth and disruptive instabilities in tokamaks. The same effect was also investigated on TCV [281, 282]. Figure 5.4.10 shows contour plots of the HFS and LFS ECE temperatures around a sawtooth crash ($t = 1.45068$ s). Temperature profile time slices prior, during and after the collapse are shown in figure 5.4.11. At the crash, the temperature profile is immediately flattened in the core (LFS ECE). At the same time, on the HFS ECE channels, hot electrons appear off-axis, outside the $q = 1$ surface (located at $\rho = 0.57$). Note that the radiation in the core may also come from relativistically downshifted off-axis radiation. Note further that these fast electrons are also observed on the DMPX (not shown), whose minimum photon detection energy was increased with filters (blocking radiation emitted by electrons with energies below 15 keV). The radiative temperature at the $q = 1$ location is less than 2 keV prior to the crash but then reaches almost 4 keV with a delay of about 20 μs. These hot electrons decay on a time typically <500 μs which is the average lifetime of electrons in the plasma with energies <30 keV. The presence of fast electrons is also detected by the LFS ECE, indicating large electron drift speeds. The LFS signals decay more quickly than the HFS signals, they probably disappear once the reconnection process has completed. The slower evolution of the HFS signals may be due to the pitch angle scattering of the electrons (recall that HFS ECE is most sensitive to perpendicular electron energy), whose characteristic time is <100 μs for energies <30 keV. Figure 5.4.10a shows that the maximum of the non-thermal emission doesn't move spatially with time.

The measurements shown were taken during a phase of auxiliary heating (ECRH only, as ECCD would itself produce runaway electrons) to maximise the sawteeth amplitudes, but the same effect is also observed in purely inductive sawteething discharges. The departure of the ECE HFS signals from the thermal level scales with the measured sawtooth amplitude.

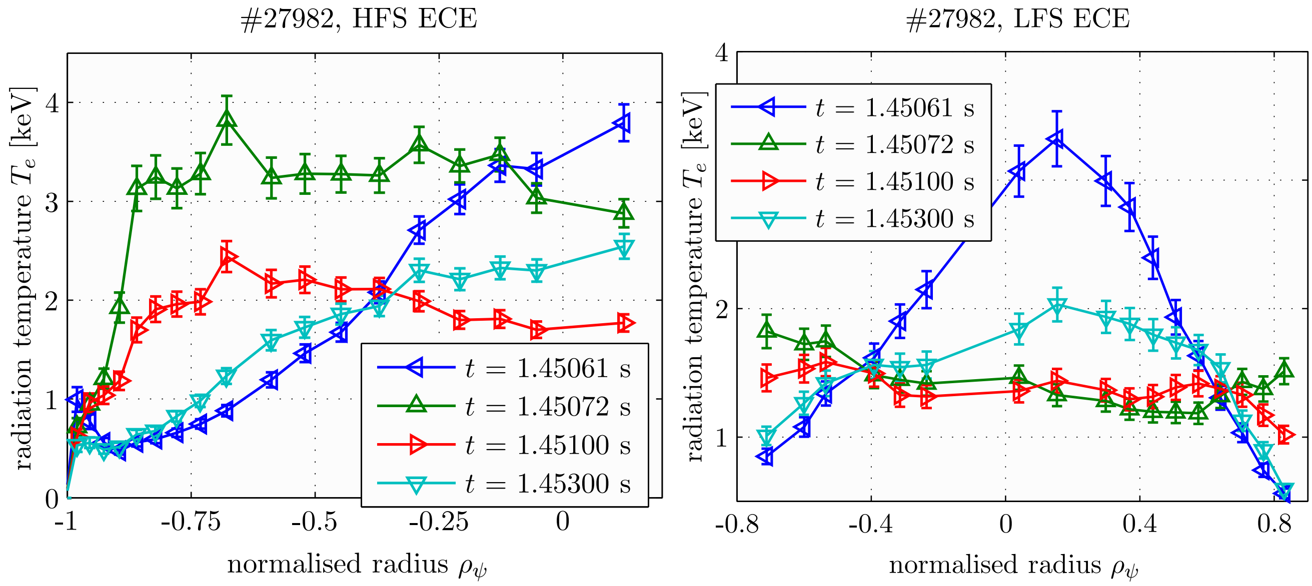

(a) High field side ECE.

(b) Low field side ECE.

Figure 5.4.11: ECE temperature profiles measured with the HFS (a) and LFS (b) radiometers. Negative normalised radii refer to the high field side. The four times shown represent conditions just before the crash, during the crash with maximum off-axis HFS temperature, minimum core temperature and during the ramp towards the next sawtooth crash.

The measured HFS ECE signals were modelled with a simple bi-Maxwellian distribution function [222]. The bulk temperature and density correspond to the LFS ECE and Thomson scattering measurements. The fit parameters of the suprathermal population require the fast electrons to be situated outside the $q = 1$ surface. Confinement is expected to be poor up to this location (the q-profile is very flat down to the core). The best fit is achieved with $T_{\text{hot}} = 11$ keV and $n_{\text{hot}} = 2 \times 10^{17}$ m^{-3}. The energy dissipated for the acceleration of the electrons is approximately 40 % of the magnetic energy released by reconnection and represents up to 10 % of the plasma stored energy.

The production of the fast electrons was explained by Dreicer acceleration [222]. That is, upon reconnection, the reduction of the poloidal magnetic field flux B_θ generates, according to Faraday's law, first equation of eqns.(5.1.1), a toroidal electric field

$$\frac{\partial E_\phi}{\partial \rho} = \frac{\partial B_\theta}{\partial t}. \tag{5.4.7}$$

The rate of change of the poloidal field may be estimated from the rate of change in B_θ and the duration of the sawtooth crash. ΔB_θ is estimated through eq.(1.5.2) using the q-profile prior and after the sawtooth crash. Since on TCV the current profile is not measured, the q-profile was approximated from its value at the edge, eq.(1.5.5), which doesn't change (determined by the total plasma current), the position of the $q = 1$ surface (by looking at the ECE or soft X-ray signals) and assuming a reasonable evolution of $q_0 < 1$. With a typical crash time of 100 μs the resulting electric field is about 10 V/m (maximum on the magnetic axis) [222]. This electric field exceeds the Dreicer electric field E_{D}, eq.(3.4.4). The number of runaway electrons produced is estimated from [283]

$$\frac{n_{\text{hot}}}{n_e} \approx \exp\left(-\frac{E_{\text{D}}}{2\,E}\right) \tag{5.4.8}$$

A value of the electric crash field $E = 1.5$ V/m at the reconnection site ($q = 1$) would produce a fast electron density of approximately 3×10^{17} m^{-3}, sufficient to explain the HFS ECE signal behaviour discussed above.

5.5 Final remark

The analysis of the electron properties of the plasmas presented in this chapter will be supplemented by the analysis of the ion properties in the following chapter. It will be shown that the understanding of the ion behaviour requires precise knowledge about the electron velocity space distribution, this information is provided by the tools used to control the EC actuators and to analyse the ECE measurements, which were the subject of this chapter.

Chapter 6

Neutral particle analysis of suprathermal TCV plasmas

Suprathermal ions have been deliberately introduced into high performance fusion devices for plasma heating (by means of radio-frequency waves, neutral beams or as fusion products) for some decades and their investigation have paved the path towards a basic understanding of the behaviour of burning plasmas, i.e. plasmas with strong self-heating [284] by fusion products. This understanding is the primary scientific challenge faced by ITER and fusion research in general, and is a necessary step towards the demonstration of fusion as a source of energy. The scientific progress achieved in this area of research is impressive, but a lot of work is still required [285]. Apart from technological and non-scientific aspects, the controllability of fast ions, by minimising their impact on turbulence, transport and confinement, is probably the most critical potential stumbling block in bringing the fusion adventure to fruition.

Irrespective of the mainstream fusion track, plasma physics research was, and is, also exploring other areas where fast ions are found. An important property of plasmas is the ability to accelerate ions to very high energy themselves (e.g. without fusion reactions). Strongly non-thermal ions are frequently observed in the outer space plasmas, e.g. solar flares [286], astrophysical shocks [287] or the ion conics in the magnetosphere [288], and were also discovered in early laboratory plasmas [289]. The scientific literature is full of treatises of odd ion acceleration phenomena. However, the acceleration mechanisms in numerous of the investigated plasmas are uncertain, many theoretical possibilities have been put forward but rarely provide a complete or persuasive picture of the observations. Sadly, observations are often unable to distinguish between the theories.

Suprathermal ions appear on TCV and these are the subject of the remainder of this dissertation. Anomalous ion acceleration was discovered during the initial experiments with injection of electron cyclotron waves on TCV in 1996 [290]. Investigations with the VNPA have shown that fast ions appear in ECCD plasmas and that their effective temperature is hotter when the ECCD current is injected in the direction opposite to the inductive current(*). Systematic studies of the fast ion properties were first conducted by Karpushov et al. [291] with such experiments greatly facilitated by the procurement of the CNPA in 2004. After the CNPA X-ray shield was completed (section 3.4.3), comprehensive experimental investigations were conducted in 2005–2006 [292, 293], that are presented in this chapter. After discussing some general phenomenological aspects in section 6.1, dedicated parameter scans are used to provide an idea of the conditions under which fast ions appear.

(*) see TCV discharge #11155

Sections 6.2 to 6.4 explore the parametric dependence of the fast ion population on the background plasma conditions and the auxiliary heating properties. Section 6.5 validates the probing of the fast ion population parameters by comparison with other diagnostics. Section 6.6 presents introductory studies on the impact of sawtooth collapses on the fast ion energy distribution. The described properties are then summarised in section 6.7 in order to identify a candidate mechanism responsible for the ion energisation (section 6.8). Further experimental work, initially scheduled for execution in 2007–2008, was unfortunately – due to force majeure – not performed before the redaction of this manuscript, so section 6.9 gives a short overview of the pending studies. The results of an attempt to model the experimental observations follows in chapter 7.

6.1 Phenomenology of suprathermal ions in X2 EC heated TCV plasmas

6.1.1 Ingredients for generation and detection

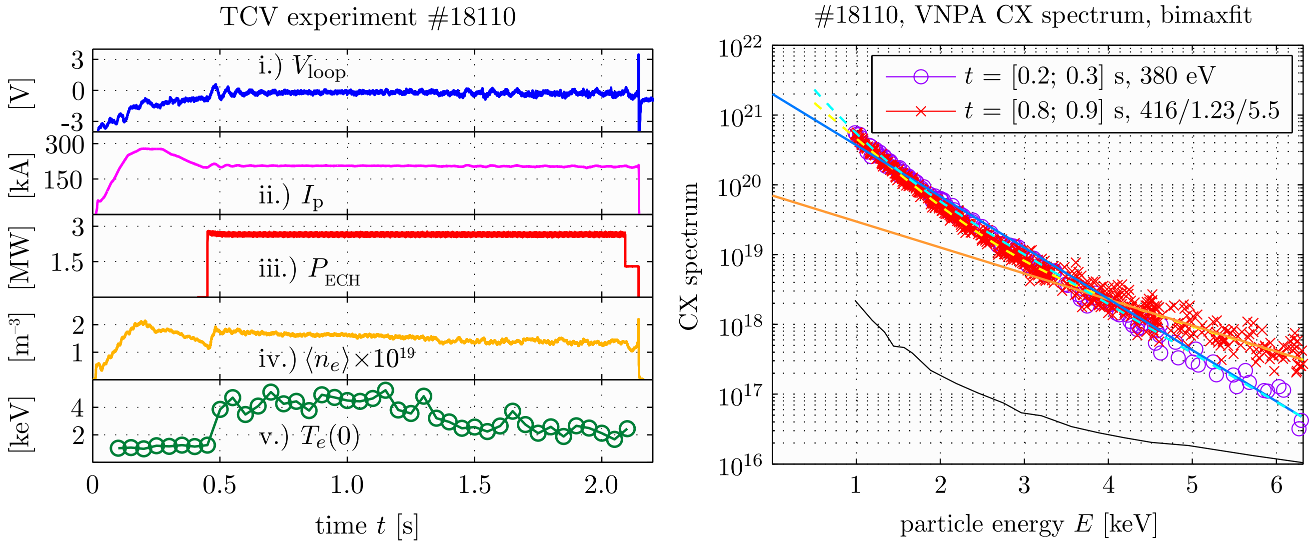

(a) Plasma evolution.

(b) VNPA spectrum.

Figure 6.1.1: Left figure: Time traces of (i) loop voltage, (ii) total plasma current, (iii) total injected EC power, (iv) average electron density and (v) core electron density.
Right figure: Charge exchange spectra prior (circles) and during (crosses) the auxiliary heating phase. The legend label indicates the bulk (in eV) and tail (in keV) temperature of the ion distribution function and the density ratio between the tail and bulk population (in percent).

Suprathermal ions are observed on TCV whenever a sufficiently low density plasma is subjected to injection of electron cyclotron waves. The parameters of fast ion populations (e.g. their strength and distribution in energy) can be studied with neutral particle analysers. Figure 6.1.1 shows an example after an upgrade of the auxiliary X2 heating equipment to six gyrotrons in 1999. This discharge has a diverted configuration, situated at z = 26 cm and features a total of 2.7 MW of co-current injection, with a wide power absorption profile extending from the core to half normalised radius. The noninductively driven current reaches 80 kA (approximately half of the total plasma current). The ion energy distribution, measured with the VNPA, is shown in figure 6.1.1b.

The VNPA acquires the neutral flux with an energy scanning configuration with a sweep period of $\tau = 13$ ms. The two spectra shown incorporate 8 energy scans each. During the ohmic heating phase the spectrum is thermal, but deviates from a Maxwellian distribution when the EC power is injected. The lower energies of the spectrum are not modified, with a slope representative of the temperature of the majority of the ions in the plasma, i.e. the bulk. A fit of the high energy spectrum yields an effective temperature exceeding 1 keV that is more than double that of the bulk temperature. The strength of the tail is measured by the ratio of the population specific contributions to the charge exchange spectrum $G(E)$, eq.(4.3.7), at the origin of the energy axis, namely

$$\frac{n_i^s}{n_i^b} = \frac{\ln G^s(E=0)}{\ln G^b(E=0)} \left(\frac{T_i^s}{T_i^b}\right)^{3/2} . \tag{6.1.1}$$

For the spectrum shown in figure 6.1.1b, this estimation gives a fast ion fraction of 5.5 % in number density. The energy range of the VNPA is too restricted to properly determine the parameters of the suprathermal population, since the knee between cold and hot population is located too close to the upper energy limit of the diagnostic.

The extended energy range of the CNPA is more suitable for the analysis of fast ions or non-thermal ion energy distributions, but requires the discharge to be vertically centred in the vessel. Figure 6.1.2a shows a non-thermal deuterium charge exchange spectrum measured with the CNPA. This is the hot electron discharge with electron transport barrier already shown in figures 5.2.8 to 5.2.10 and 5.4.1. The measured spectrum was not averaged in time, but results from a single measurement at $t = 1.215$ s (the CNPA counter integration time was 2.5 ms). Time averaging was not required due to the strong high energy neutral fluxes entering the diagnostic, only the highest energy channel lies close to the usual 'one count' limit.

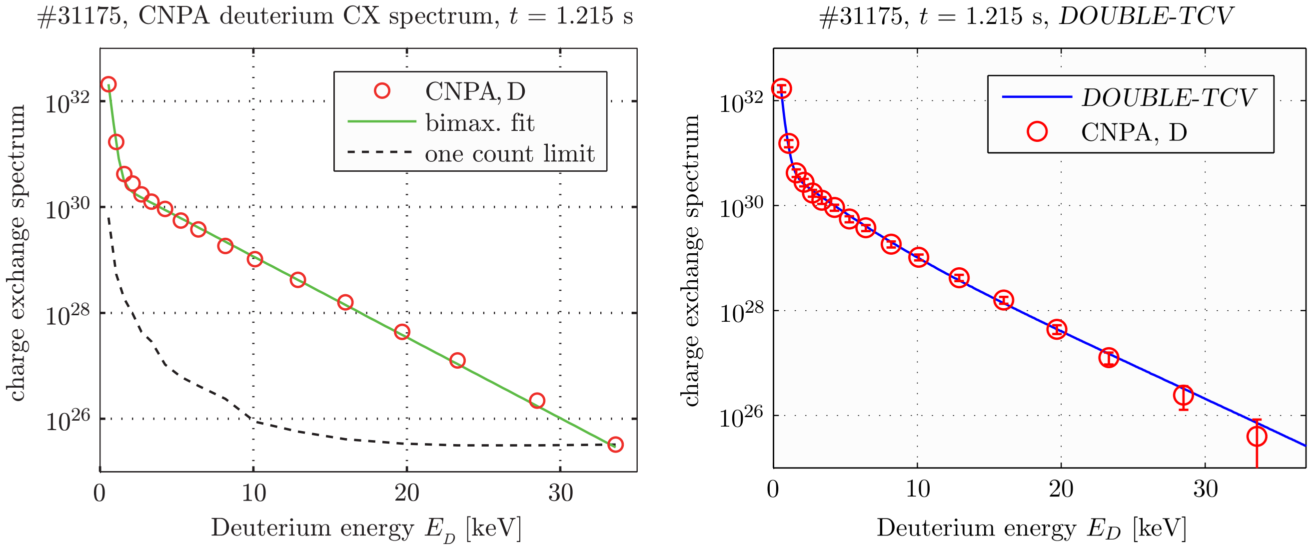

(a) Bi-Maxwellian fit.

(b) *DOUBLE-TCV* simulation.

Figure 6.1.2: (a) Bi-Maxwellian fit of the deuterium charge exchange spectrum measured with the CNPA assuming the ion temperature being constant along the plasma radius. The best fit parameters are thermal $T_i^b = 185$ eV, suprathermal $T_i^s = 2.84$ keV and the ratio between suprathermal and thermal ion densities $n_i^s/n_i^b = 5.7$ %.
(b) Simulation of the CNPA charge exchange spectrum for the measurement shown in (a) using *DOUBLE-TCV* based on the parameters from the crude bi-Maxwellian fit.

If the measured spectra are steady-state, they are well described by a sum of two Maxwellian ion energy distributions,

$$f_i(E) = f_i^b(E) + f_i^s(E) = 2\,n_i^b \sqrt{\frac{E}{\pi\,\left(T_i^b\right)^3}}\,\exp\left(-\frac{E}{T_i^b}\right) + 2\,n_i^s \sqrt{\frac{E}{\pi\,\left(T_i^s\right)^3}}\,\exp\left(-\frac{E}{T_i^s}\right). \tag{6.1.2}$$

The data in figure 6.1.2a was interpolated by multidimensional unconstrained nonlinear minimisation (thick line) and the agreement with the data is good. Such a description neglects temperature profile effects, but here the curvature of the bulk charge exchange spectrum is hidden below the suprathermal tail. The parameters of the maximum likelihood estimation of the measurement are $T_i^b = 185$ eV, $T_i^s = 2.84$ keV and $n_i^s/n_i^b = 5.7$ %. The bulk temperature T_i^b is not equal to the core ion temperature, the slope for the fit of the bulk temperature must be fitted at energies far below the usual inference rule, eq.(4.3.13), typically with the data below CNPA channel #3 or #4, depending on the tail strength. For the example shown here, the obtained T_i^b is the ion temperature found at $\rho = 0.5$ (CXRS profile, see figure 6.1.3b), the true core temperature is 230 eV.

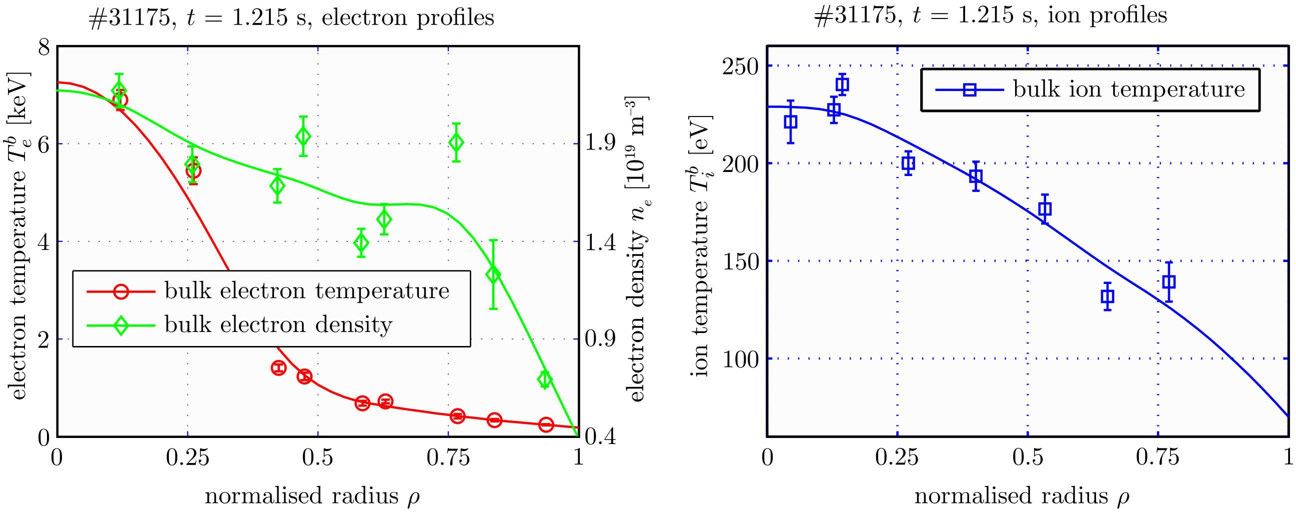

(a) Electron profiles. (b) Ion profiles.

Figure 6.1.3: (a) Calibrated Thomson scattering data and interpolated profiles of bulk electron density and temperature for discharge #31175, $t = 1.215$ s.
(b) Measured charge exchange recombination spectroscopy bulk ion temperature profile and its interpolation. The measurements were performed with the LFS CXRS system.

A zero-dimensional bi-Maxwellian fit may appear as a crude approximation of the real ion velocity distribution. The *DOUBLE-TCV* code was thus used to model the measured charge exchange spectrum of discharge #31175 using this fit. All available experimental data was used by the code (figure 6.1.3). The bulk ion temperature profile was measured with CXRS during the beam blip lasting from $t = 1.23$ to 1.26 s. The fast ion population was described by a temperature profile of the same shape as the bulk temperature profile, with the peak value determined from the crude bi-Maxwellian fit. The tail density was taken to be flat, with the concentration again taken from the bi-Maxwellian fit, but truncated at $\rho = 0.8$, as fast ions are poorly confined at the plasma edge. A justification for these choices will be given later in section 6.3.

The effective plasma charge of $Z_{\mathrm{eff}} = 2.5$ was determined from the XTe diagnotic(†). The output of *DOUBLE-TCV* is shown in figure 6.1.2b. Within the statistical error bars, the modelled spectrum agrees with the measurement. This demonstrates that the bi-Maxwellian fit gives a sufficiently accurate measurement of the fast ion population and advanced modelling with a code such as *DOUBLE-TCV* is not generally required.

6.1.2 The TCV fast ion database

A database of discharges exhibiting fast ions was compiled to characterise the general dependencies of the fast ions on plasma, confinement and heating parameters. The entries comprise more than 3000 single CNPA measurements within 45 dedicated TCV discharges obtained between 2005 and 2007. CNPA measurements prior to the installation of the complete X-ray shield (section 3.4) were excluded, as the presence of hard X-rays seriously hindered the determination of reliable fast ion parameters. Older experiments with the VNPA were also not considered because of the intrinsic inaccuracy in the determination of the tail parameters.

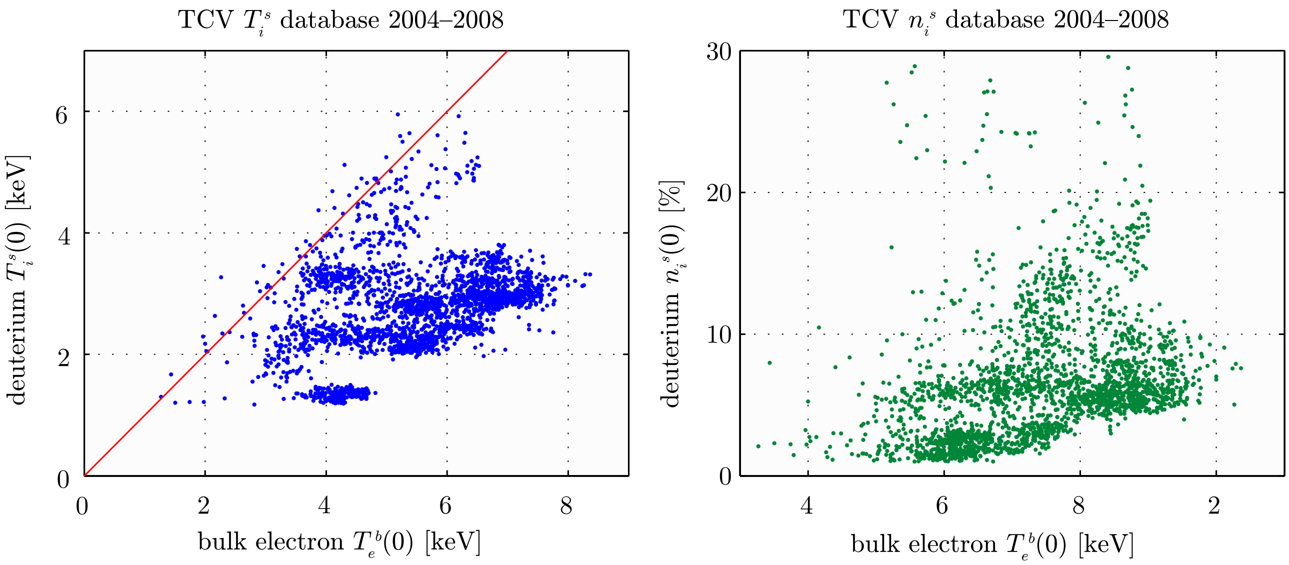

(a) T_i^s database. (b) n_i^s database.

Figure 6.1.4: Database of suprathermal TCV plasmas (period 2004–2008).
(a) shows the suprathermal temperature, (b) the corresponding suprathermal density. Both parameters are plotted against the bulk electron temperature.

Figure 6.1.4 shows the occupation of the fast ion parameter space. The fast ion tail strength ranges from typically below 10 % but occasionally exceeded 20 % of the bulk density. Density ratios below 1 % were not considered as being suprathermal, since the bi-Maxwellian fit then only represents the hot core and the colder edge of a thermal ion temperature profile. The dependence of the suprathermal ion temperature on the bulk electron temperature (measured with the Thomson scattering diagnostic) is striking. The hotter the electrons, the higher the suprathermal proportion. Although the points are scattered into a large part of the parameter space, the maximum ion temperature reached appears limited by the bulk electron temperature (the straight line indicates $T_i^s = T_e^b$). Again, the hotter the electrons, the hotter the suprathermal ions.

(†) XTe consists of a set of four silicon diodes, looking through the plasma along vertical chords at $R = 0.9$ m. Each diode is equipped with a Beryllium filter screening the radiation from suprathermal electrons and the effective charge is determined using the foil-absorption technique [294].

The fast ion generation is a complex multivariable problem and general features other than the electron–ion temperature correlation are not readily extracted from the whole database. Experiments that aim to vary only single parameters were therefore necessary and will be discussed in section 6.2.

6.1.3 Fast ion population dynamics

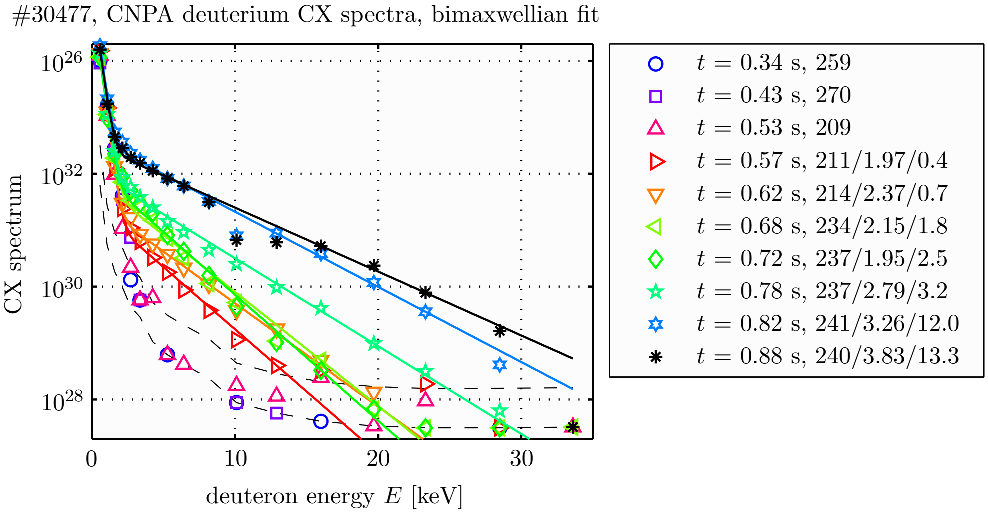

Figure 6.1.5: Evolution of the ion energy distribution during an EC power ramp-up (figure 6.1.6a). The legend shows the fit parameters of a bi-Maxwellian interpolation of the charge exchange spectra.

Multiple time scales govern the temporal properties of the fast ions. An example of the rather slow evolution of the fast ion population is shown in figure 6.1.5 (discharge #30477). Relevant plasma time traces are shown in figure 6.1.6a.

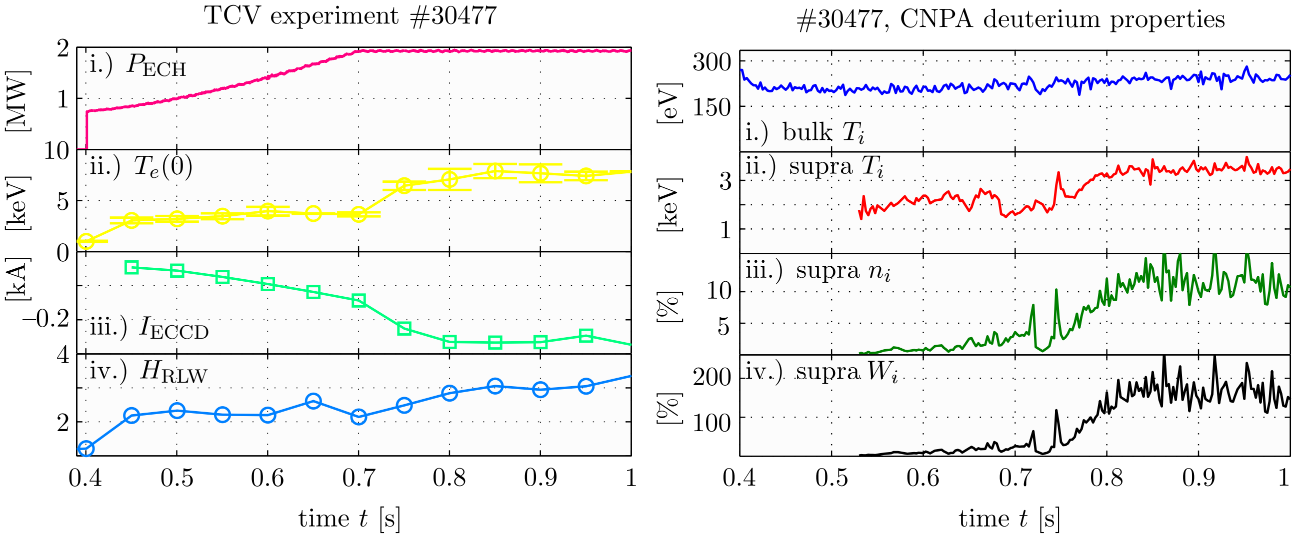

(a) Electron parameters.

(b) CX spectrum evolution.

Figure 6.1.6: (a) Time traces of (from top) the total EC power increase, measured core electron temperature (Thomson scattering), total driven EC current (*Toray-GA*) and the confinement scaling factor H_{RLW}. (b) Build up of the suprathermal ion population during the same period of time. The CNPA flux at suprathermal energies prior to $t = 0.53$ s is too small to identify a bi-Maxwellian distribution (compare with figure 6.1.5).

ECH power was initiated at $t = 0.4$ s. 2 launchers drive counter-current on-axis (absorption within $\rho = 0.2$) and 2 launchers aim perpendicularly off-axis (absorption in the range $\rho = 0.2 - -0.5$). The coupled gyrotron power starts at 180 kW each and reaches full power at $t = 0.7$ s. During the power ramp, the electron temperature increases first rapidly, then more slowly, whereas the driven noninductive current steadily increases. Initially there are few fast ions, or, their number is not sufficient to be detected by the CNPA. At $t = 0.5$ s the signature of fast ions exceeds the noise level, but a tail fit is only possible after $t = 0.55$ s. The extracted hot ion tail temperature is high from the start, with a tail strength increasing with time. As soon as the EC power flattop is reached, a transport barrier develops. The improved core confinement raises the electron temperature by a factor of two and the current drive efficiency almost doubles. This is accompanied by a strong increase of the fast ion temperature and density. Note that the high energy neutral fluxes are very strong, with the intermediate CNPA channels #11 and #12 (figure 6.1.5) being saturated from $t = 0.8$ s onwards(‡) (these channels were of course excluded from the bi-Maxwellian fit).

Each CNPA measurement (sampling time $\Delta t = 2.5$ ms) was fitted with the bi-Maxwellian model with parameters shown in figure 6.1.6b. The bulk ion temperature does not change at first but increases slightly with the improved confinement. The suprathermal ion temperature is roughly constant during the EC power ramp and increases afterwards. T_i^s seems to correlate with T_e^b. Fast ion density and energy increase linearly during the power ramp and considerably increase when the barrier is formed (the figure shows the ratios between suprathermal and thermal density respectively energy). n_i^s and the fast ion energy $W_i^s = \frac{3}{2} n_i^s T_i^s$ seem to correlate with I_{ECCD}. The fast ion parameters increase up to $t = 0.85$ s and remain constant thereafter (up to the EC power switch off at $t = 1.7$ s). The time scale of the evolution after $t = 0.7$ s is of the order of the current redistribution time (some hundreds of milliseconds), typical for the formation of a transport barrier.

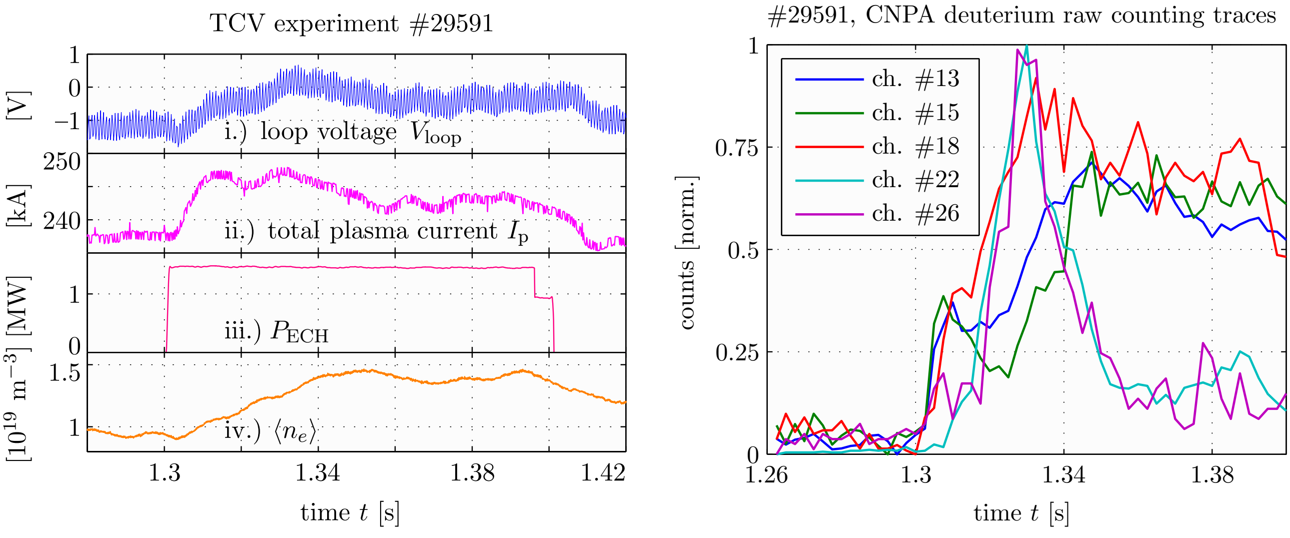

(a) Plasma parameters.

(b) CNPA counting traces.

Figure 6.1.7: (a) Time traces of measured loop voltage, measured plasma current, EC waveform and line integrated electron density.
(b) Neutral flux behaviour upon injection of 1.5 MW of EC power (only some deuterium channels are shown).

(‡) Deuterium channels #1–#6 have an opening window as large as 3 mm, channels #7–#10 of 5 mm and channels #11–#17 of 1 cm.

If, on the other hand, the full EC power is injected from the start, the creation of the fast ion population exceeds the 1 ms time resolution of the CNPA, with plenty of hot ions already seen in the first measurement, see figure 6.1.7b. Discharge #29591 features a EC beam blip of three gyrotrons injecting counter-ECCD on axis ($I_{\rm ECCD} = 140$ kA), lasting for 100 ms. Some of the plasma parameters are shown in figure 6.1.7a. The impact of the EC power on the particle temperatures is shown in figure 6.1.8, where only measurements with acceptable error bars are shown (the bi-Maxwellian fits are often noisy at the start). Electron temperatures are normalised against the maximum HFS ECE temperature, ion temperatures against the maximum fast deuterium temperature. Here, even the hydrogen neutral fluxes are strong enough to apply a bi-Maxwellian fit of the charge exchange spectra (the hydrogen concentration was ~8 %).

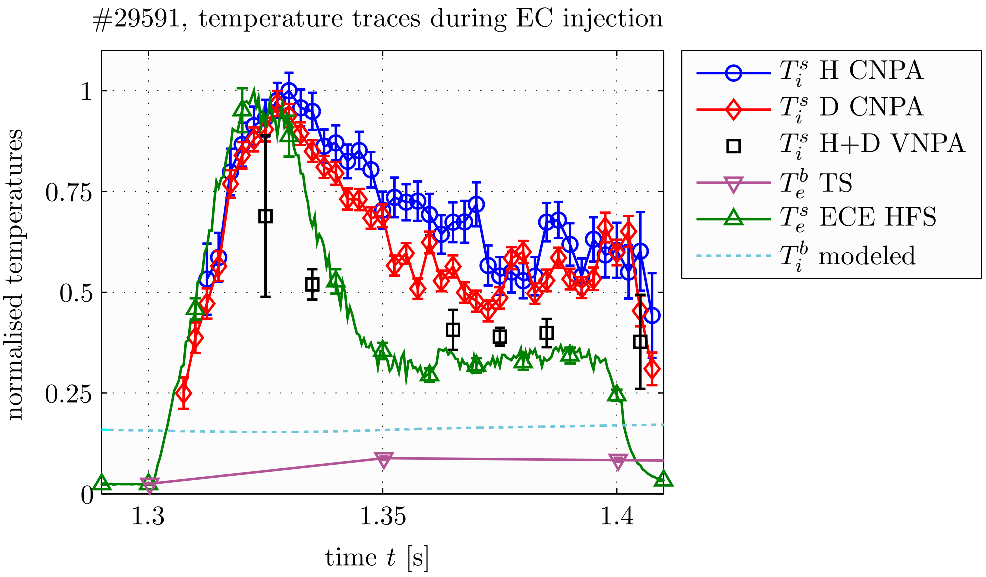

Figure 6.1.8: Rapid fast ion acceleration upon injection of 1.5 MW of EC power. Fast electron and ion temperatures rise rapidly within 20 ms to relax within another 20 ms to finally stabilise for the rest of the wave power pulse.

CNPA deuterium and hydrogen ion temperatures follow the same temporal evolution (also in absolute values) and are strongly correlated with the high field side ECE temperature measured on the magnetic axis. The VNPA was in scanning mode (period of 13 ms) and a fit of the data after each completion of an energy sweep gives only mediocre results.

The behaviour of the temperature illustrates a reproducible mechanism of self-regulation of the plasma. Although the injected EC power absorption properties are not altered, the energy distribution of the fast electrons is fundamentally modified after 30 ms, probably following redistribution of the ECCD current. This is supported by the behaviour of the loop voltage, which is steadily decreasing, such that almost the whole plasma current is sustained by ECCD and bootstrap contributions by $t = 1.33$ s. The drop of the ECE temperature that follows is observed in all ECE channels. Again after 30 ms, the temperatures stabilise, with the same behaviour seen for other EC blips in the discharge.

This quick energisation of the ions is not of a collisional nature. The coupling between ions and electrons is very weak at these densities compatible with second harmonic EC heating (here $\langle n_e \rangle = 1 \times 10^{19}$ m^{-3}) and the electron–ion energy equipartition time $\tau_{ei} = 1/\bar{\nu}_E^{e/i}$, eq.(4.9.2), is long (figure 6.1.9a).

To illustrate the weakness of collisional heating in low density plasmas, the ion energy balance equation, eq.(4.9.5), can be written in terms of temperatures,

$$\frac{\mathrm{d}T_i}{\mathrm{d}t} = \frac{T_e - T_i}{\tau_{ei}} - \frac{T_i}{\tau_i} \tag{6.1.3}$$

and solved using the Euler method. At $t = 0.8$ s, before the first EC power blip, the plasma is in steady state and the ion energy confinement time $\tau_i = 98$ ms is determined from eq.(6.1.3) setting $\frac{\mathrm{d}T_i}{\mathrm{d}t} = 0$. τ_i is then kept constant when advancing the solution in time, but τ_{ei} is calculated at each time step (as shown in figure 6.1.9a). The initial value of the temperature of $T_i(0) = 510$ eV was determined from the CNPA.

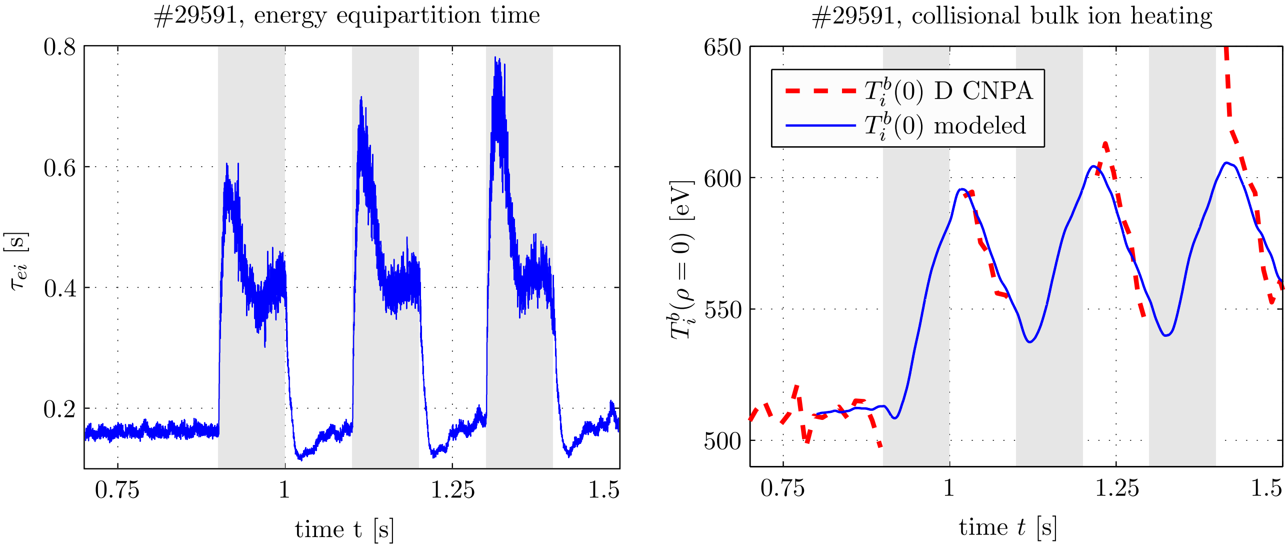

(a) Equipartition time.

(b) Bulk ion heating.

Figure 6.1.9: (a) Electron–ion energy equipartition time τ_{ei}. The grey zones indicate three phases of EC heating. (b) Modelled bulk ion heating due to collisional energy transfer from the electrons.

Figure 6.1.9b shows the obtained evolution of the bulk ion temperature heating (straight line). Between the EC injection phases the core bulk ion temperature was successfully measured with the CNPA and its relaxation agrees very well with the model. Note that this is not possible during the EC phase as the fast ions mask the core bulk temperature. During 100 ms of auxiliary heating, the bulk ion temperature rose by 20 % at most. This is a factor 25 below the observed fast ion temperature, which reaches $T_i^s = 3$ keV within 10 ms.

6.2 Plasma parameter scans

To assist in the understanding of the hot ion acceleration and to characterise the apparent importance of the electron parameters in the establishment of a steady state in the fast ion population, plasmas with scans of single plasma or heating parameters were carried out, namely

- ☞ plasma density (section 6.2.1),
- ☞ toroidal EC injection angle (section 6.2.2),
- ☞ EC power deposition location (section 6.2.3) and
- ☞ plasma geometry (section 6.2.4).

6.2.1 Electron density scan

Figure 6.2.1 shows time traces of electron and ion properties during an electron density ramp from $\langle n_e \rangle = 1.0$ to 1.5×10^{19} m^{-3}. A part from the density increase, discharge #31338 uses the same model as its reference discharge #31175, which was illustrated in figures 5.2.8ff. The line averaged density was programmed to increase linearly, controlled by a gas injection density feedback loop (measurement of the central FIR channel).

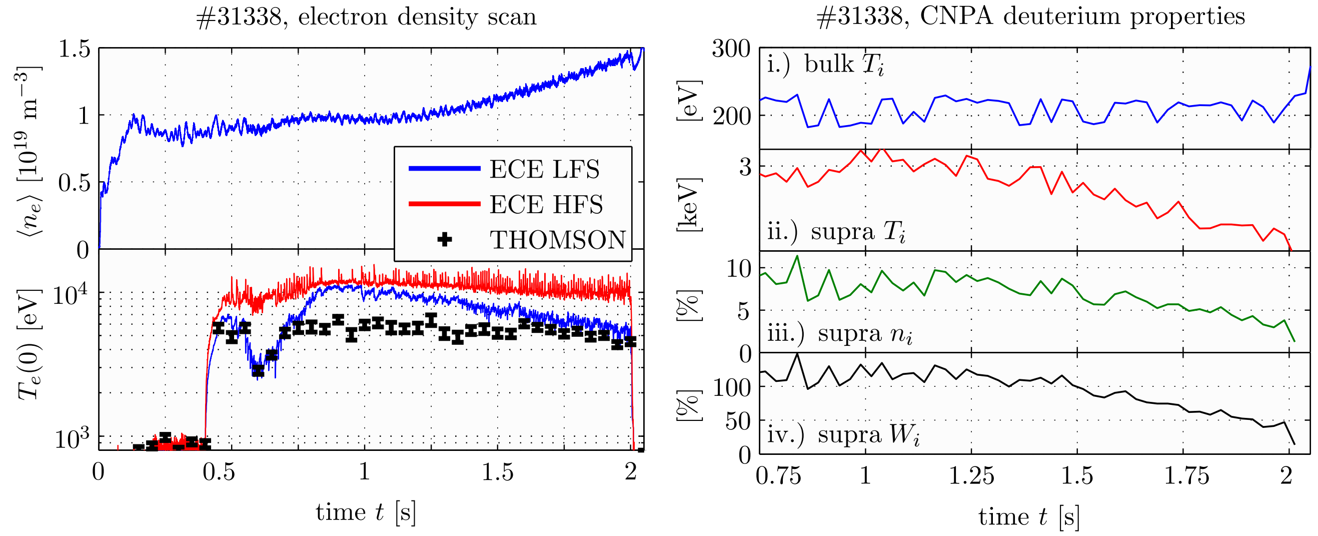

(a) Electron density and temperature.

(b) Fast ion properties.

Figure 6.2.1: Scan of the electron density.
Left figure: At $t = 1$ s, a linear increase of the line averaged density was programmed. The density increases by 50 %. The lower plot shows traces of calibrated HFS and LFS ECE temperatures and core bulk electron temperature (Thomson scattering).
Right figure: Fast ion parameter evolution during the density scan.

The electron temperature traces demonstrate that the EC power absorption remains high, as the bulk and HFS ECE suprathermal electron temperatures do practically not change. This discharge was run before the LFS ECE antenna was replaced for better focusing (section 5.3.5) and retains a non-negligible oblique ECE radiation pick-up. This explains why the LFS ECE temperature diverges from the Thomson temperature at $t = 0.75$ s. This difference is due to the Doppler upshifted radiation of the electrons sustaining the ECCD current. When the density increases, the LFS ECE temperature steadily decreases, hence the electron drift velocity decreases. This is expected since, as explained in section 5.2.3.2, current drive relies on the collisionality of the plasma and the drive efficiency scales therefore as [199]

$$\eta_{\text{CD}} \sim \frac{T_e}{n_e \left(Z_{\text{eff}} + 5\right)}. \tag{6.2.1}$$

However, the ECCD total current does practically not change (*Toray-GA* calculation), the loss of electron velocity (drive efficiency) is compensated by the current density increase (number of electrons contributing to the current). The fast ion temperature and density decrease, although the electrons remain hot. This again indicates that the fast ion population correlates with the electron drift velocity.

6.2.2 Scan of toroidal EC injection angle

One important question is that of the mechanism for fast ion production being linked directly to the interaction with the EC wave or if its origin is rather to be found in the behaviour of the electrons. Figure 6.2.2 shows the charge exchange spectra for hydrogen and deuterium for three toroidal EC injection angles(§) ϕ_L (#31175: counter-ECCD, #31176: co-ECCD and #31346: pure ECRH) and central EC power deposition. The plasma and gyrotron configuration, except the launcher angle ϕ_L, were identical for these three experiments, see figures 5.2.10.

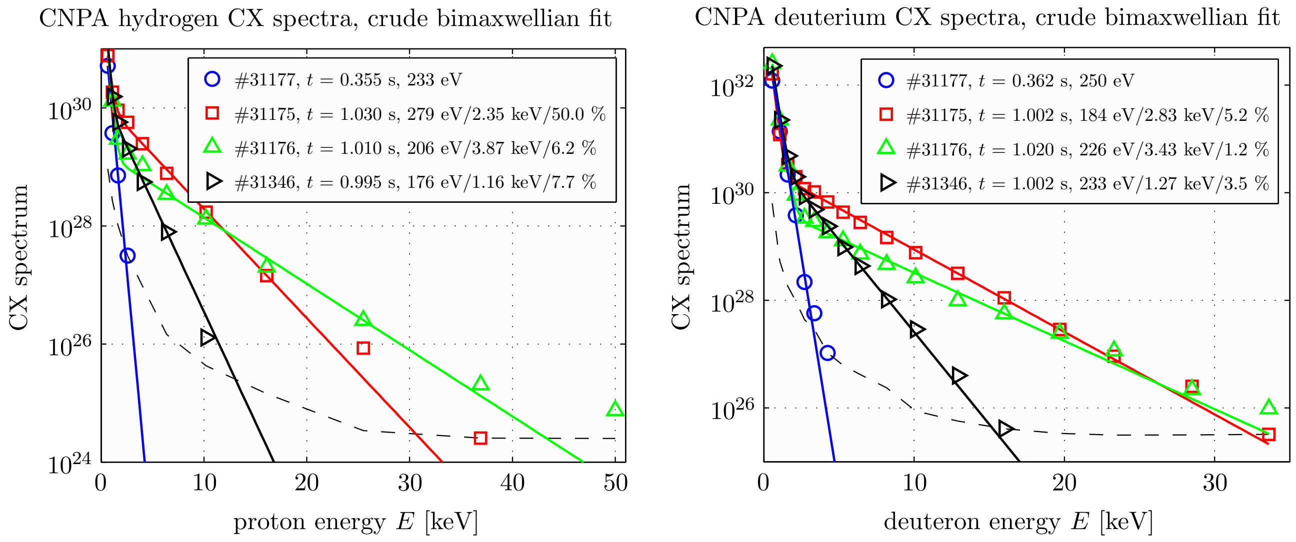

(a) Hydrogen spectra.

(b) Deuterium spectra.

Figure 6.2.2: Hydrogen (a) and deuterium (b) charge exchange spectra for solely ohmic heating (discharge #31177), ECRH only (discharge #31346), co-current (discharge #31176) and counter-current EC injection (discharge #31175). The discharge parameters are otherwise identical.

The fast ion population is more prominent for the counter-ECCD case. This is not a surprise, as the electron temperature is considerably higher due to the eITB, which is absent in the co-ECCD case. However, the fast ion population is present also in the pure ECRH case, albeit with considerably weaker strength than with ECCD.

A series of discharges was dedicated to scan the toroidal injection angle within the discharge. This is summarised in figure 6.2.3. All plasmas were centred at $z = 0$. Launchers $\#L1$ and $\#L4$ are toroidally aligned and perform the ECCD, all figures are plotted against ϕ_L of these two launchers. Two discharges were scanning the co-, two others the counter-injection, starting at $\phi_L = \pm 23°$. Two further discharges with perpendicular injection complete the picture of the scan. Discharge #31190 unfortunately has no Thomson measurement, some derived quantities could thus not be calculated. At all angles, the EC power is fully absorbed on the first pass (a). The on-axis deposited EC power density (b, *Toray-GA*) is maximum for launcher angles in the range $15 \ldots 25°$, where the wave direction aligns with the toroidal direction, such that the volume of absorption is located along the magnetic axis. For smaller angles the absorption takes place in a radially more extended region, for larger angles the absorption becomes more off-axis and refraction becomes important.

(§) ϕ_L is defined as the angle between the EC beam and its projection on the poloidal plane at the launcher, and is positive for co-ECCD.

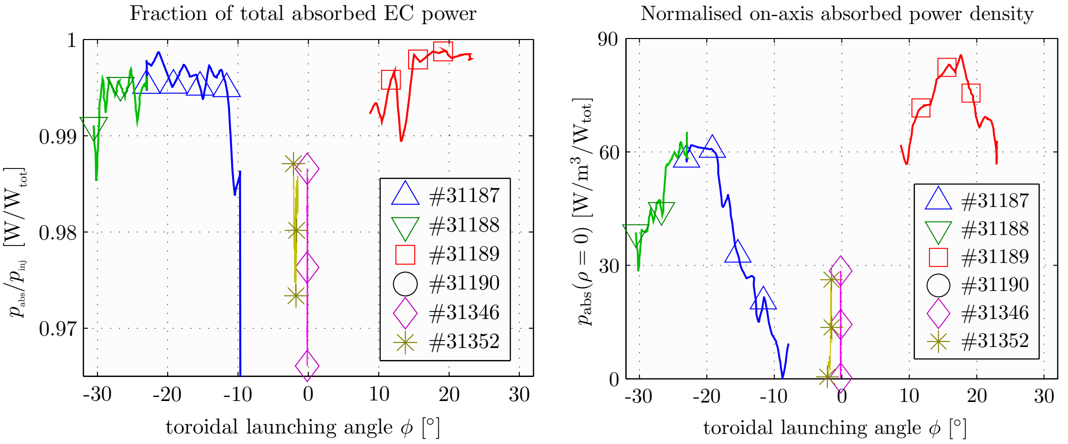

(a) Absorbed EC power. (b) EC power density.

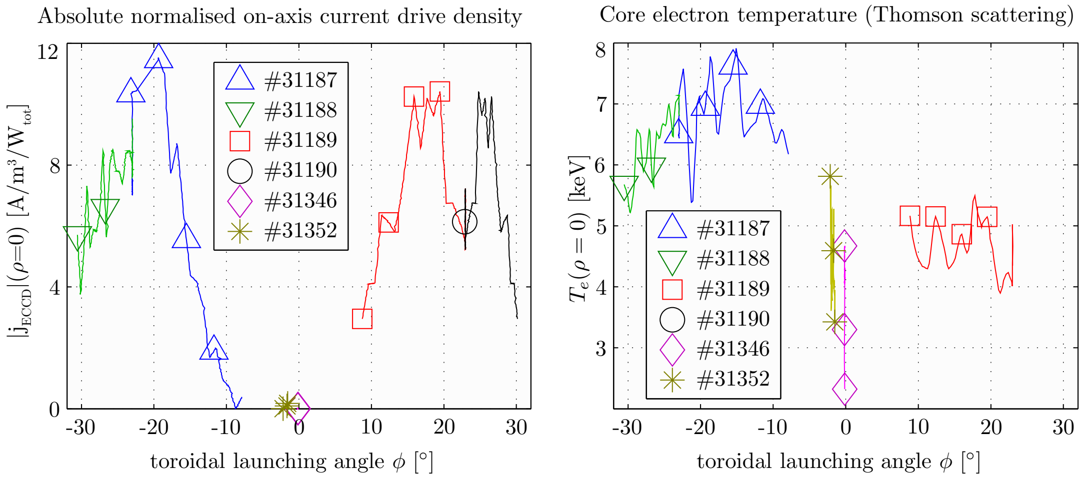

(c) Current drive density. (d) Bulk electron temperature.

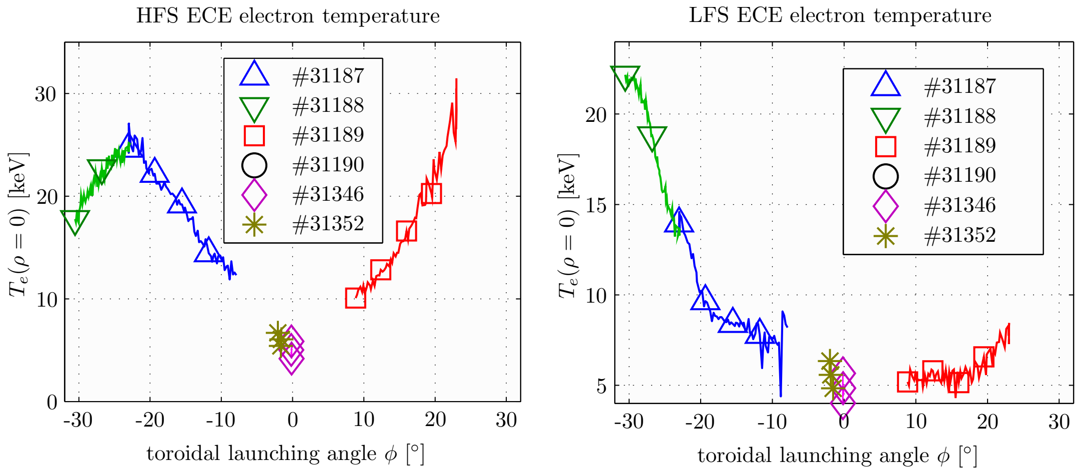

(e) HFS ECE electron temperature. (f) LFS ECE electron temperature.

Figure 6.2.3: Scan of the toroidal launcher angle (#$L1$ and #$L4$) and its impact on the fast electron population. (a) Ratio between injected and first pass absorbed EC power. The coupling between wave and electrons is pretty good. (b) Power density in the plasma core, normalised by the injected power. Note that the power density is higher in the co-injection case. (c) Current drive efficiency on the magnetic axis. The current drive densities are similar in co- and counter direction. (d) Bulk electron temperature measured by the Thomson scattering system. As usual, the counter-current driven plasmas are substantially hotter than the co-driven ones. (f) and (g) high (channel #1) and low field side (channel #11) ECE core temperature, temperature calibration using *NOTEC-TCV*.

These effects are observed in the modelled(¶) current drive density (c, again *Toray-GA*). The electron temperatures measured by Thomson scattering (d), LFS (e) and HFS ECE (f) show different behaviour, the bulk electron temperature is higher in the counter-ECCD case, because of the transport barrier (figure 5.4.2), which is absent in the co-ECCD case. Note that the toroidal angle of central ECCD also changes the steepness of the eITB. The HFS ECE is quite symmetric in the launching angle, which means that the perpendicular electron energy is the same for co- and counter-case, since the absorbed EC power is the same for both directions. The LFS ECE emission behaves completely differently, the electron drift speeds in the counter current direction seem to largely exceed the co-speeds, although the calculated current drive densities are similar. The total plasma volume integrated EC driven currents peak at -150 (counter-ECCD), $+100$ (co-ECCD) and -7 kA (ECRH). Note the different angles of peaking of the various temperatures in the counter-ECCD shots: The bulk electron temperature is highest at $\phi_L = -15°$, the HFS ECE peaks beyond $-20°$ (as the current drive density) and the LFS ECE temperature continues to increase up to the largest toroidal angle explored.

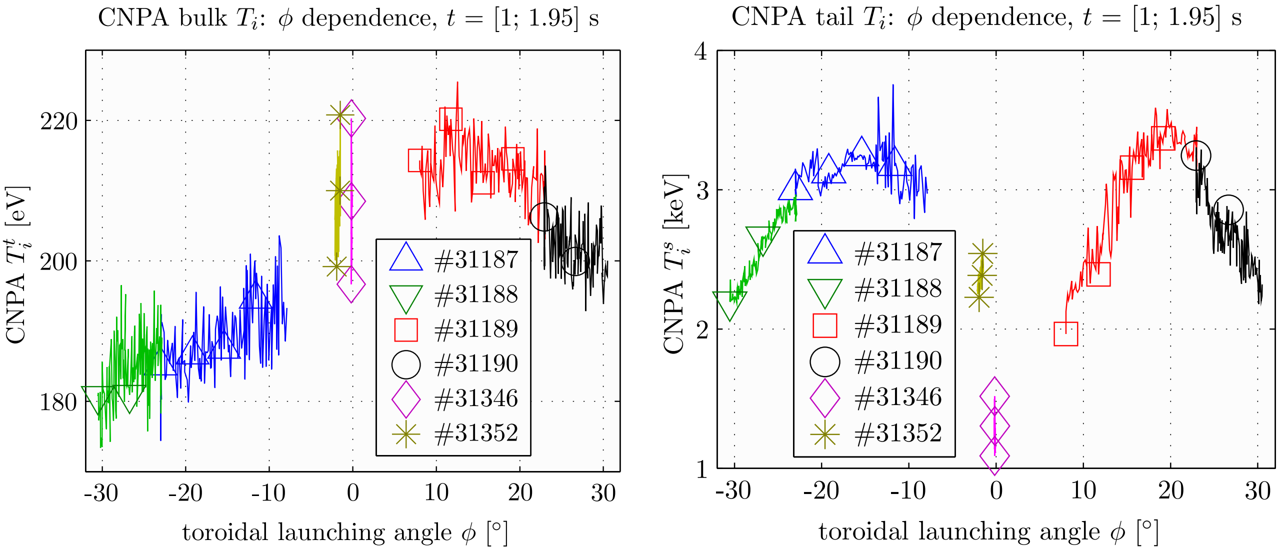

(a) Bulk ion temperature.

(b) Fast ion temperature.

Figure 6.2.4: Scan of the toroidal launcher angle (#$L1$ and #$L4$) and its impact on the fast ion population.
(a) Bulk ion temperature as determined from the crude bi-Maxwellian interpolation.
(b) Temperature of the hot ion population, again determined with the crude fit. T_i^s is symmetric in ϕ_L.

Figure 6.2.4 and 6.2.5 shows the injection angle dependence of the deduced ions parameters. The bulk ion temperature changes marginally with ϕ_L, the high electron temperature at negative angles increases the electron–ion equipartition time, thus lowering the ion temperature. The suprathermal ion temperature is symmetric in ϕ. The population develops mainly when counter-ECCD is applied. Discharge #31352 demonstrates that already a very small negative toroidal angle causes a well pronounced fast ion population, this is not the case for the electrons. The maximum of beam temperature and density occur at $\phi_L = -15\ldots20°$, as for the bulk electrons.

(¶) An experimental evaluation of the ECCD efficiency using the measured loop voltage [295] yields the same result [296].

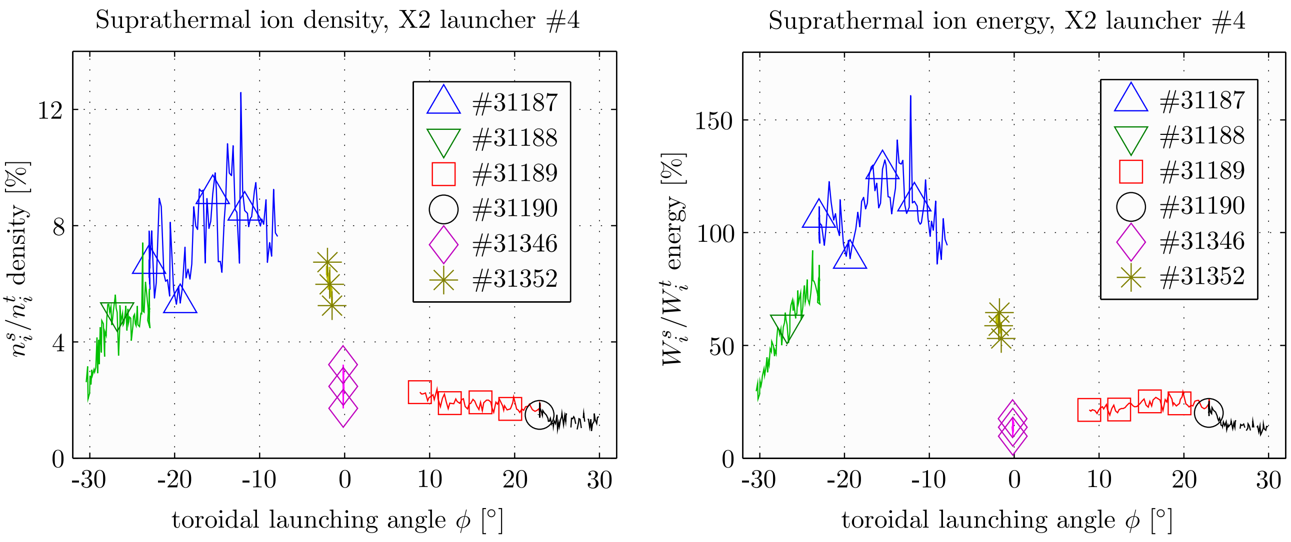

(a) Fast ion density. (b) Fast ion energy.

Figure 6.2.5: Scan of the toroidal launcher angle (#$L1$ and #$L4$) and its impact on the fast ion population.
(a) Ratio of the suprathermal to the thermal ion population. In the co-case the suprathermal population is barely measurable.
(b) Ion energy ratio.

6.2.3 Scan of the EC deposition location

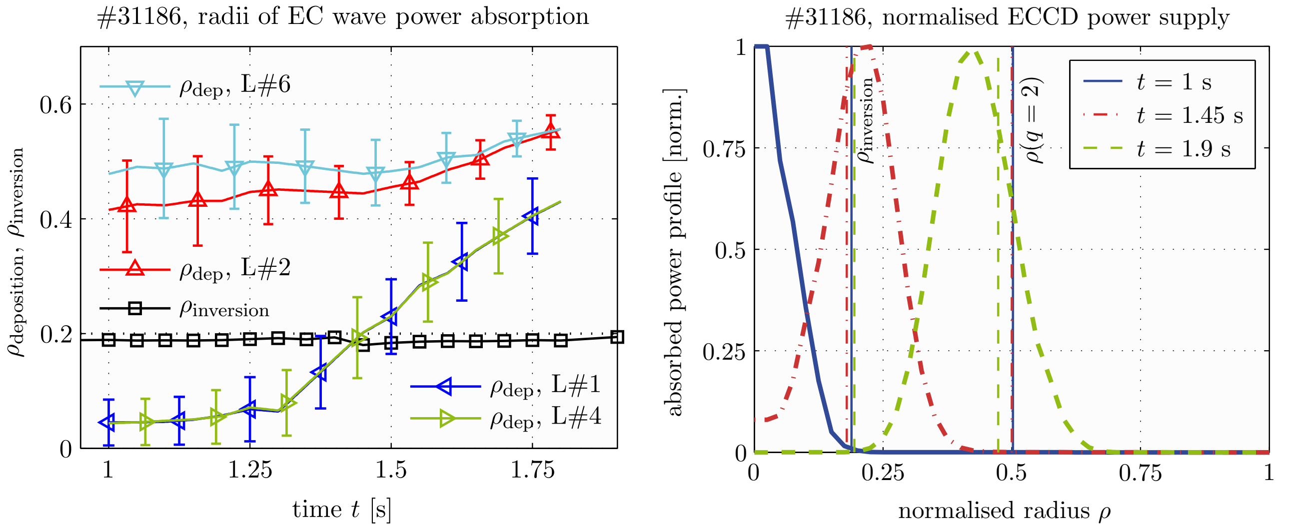

(a) Maximum EC absorption location. (b) EC absorption profiles.

Figure 6.2.6: (a) Time traces of the location of maximum EC power absorption for the wave beams launched by the four launchers. At $t = 1.43$ s the launchers L#1 and L#4 traverse the inversion radius.
(b) Profiles of the EC power deposition calculated with *Toray-GA*. At the beginning of the absorption location scan, the full power is deposited inside the volume delimited by the inversion radius.

Most of the plasmas studied were designed to drive the noninductive current on the magnetic axis, as the strongest fast ion population parameters were found with central EC absorption. No fast ions were observed with peripherically located heating.

The experiment illustrated in the following figures was conducted to study the role of the wave power deposition location. The ECCD current deposition location (launchers #$L1$ and #$L4$), initially configured as for discharge #31177, were moved outwards during the experiment, whereas the absorption location of the off-axis beams (perpendicularly injected) were kept constant. The toroidal injection angle was also kept constant during the scan, which was initiated at $t = 1.3$ s and crossed the inversion radius at $\rho = 0.2$ at $t = 1.43$ s (figure 6.2.6a). The inversion radius was calculated from the scaling law for shaped TCV plasmas [297],

$$\rho_{\text{inv}} = \frac{\langle j \rangle}{j_0\, q_0}, \tag{6.2.2}$$

with j_0 and q_0 the axial current density and safety factor respectively and $\langle j \rangle$ the cross section averaged toroidal current density. The corresponding radial profiles of the plasma absorbed EC power are shown in 6.2.6b. The usual ion parameters are shown in figure 6.2.7, now plotted against the difference between maximum EC absorption position and inversion radius. When the EC beams are moved outwards, the fast ion properties do not change until the beam is localised at a distance corresponding to the half of its FWHM in respect with ρ_{inv}. The fast ion population gradually decreases and then abruptly drops when more of the absorbed power is deposited outside. The current profile changes when the beam traverses ρ_{inv}, as the latter steps inwards (figure 6.2.6a).

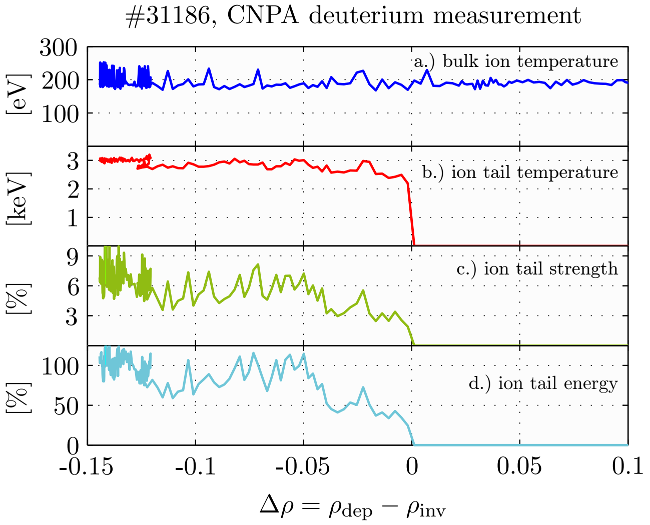

Figure 6.2.7: Ion parameters, namely (a) thermal ion temperature, (b) suprathermal ion temperature, (c) fast ion density and (d) energy fraction. The density and energy of the suprathermal population start to drop as soon as a considerable part of the EC power is deposited outside the inversion radius. As soon as more power is deposited outside, the fast ions disappear.

6.2.4 Impact of plasma geometry

In section 4.10.3 it was shown that the thermal ion confinement exhibits trends similar to the behaviour of the thermal electron bulk, namely a strong degradation with triangularity at low collisionality. An attempt to study the confinement properties of the fast ions using the VNPA was first undertaken in 2002. Figure 6.2.8 shows the response of the fast ion parameters during a discharge whose elongation was swept out from $\kappa = 1.2$ in $t = 0.9$ s to $\kappa = 1.6$ in $t = 1.6$ s and back in to the initial value in $t = 1.9$ s. Two EC beams with counter-ECCD ($\phi_L = -30°$) at a power level of 450 kW each, no other (e.g. perpendicular) EC power were injected. The power absorption was maximum for $\rho = 0.2 \ldots 0.3$ (figure 6.2.9a).

Although, in general, a dependence of the ion confinement on elongation is difficult to observe [83], in this particular shot the bulk ion temperature increases with elongation, a feature commonly observed for the electrons [173]. The line integrated density increases when κ rises, the power coupling between electrons and ions is therefore improved.
The behaviour of the suprathermal temperature is opposite, its value is decreasing, which may be ascribed to the density increase (paragraph 6.2.1). Contrary to the behaviour observed in the density scan, the suprathermal population strength is increasing, including its energy, although the temperature eventually drops. This indicates an improved fast ion confinement and a correlation of the fast ion proportion with the improving current drive efficiency, despite the density increase.

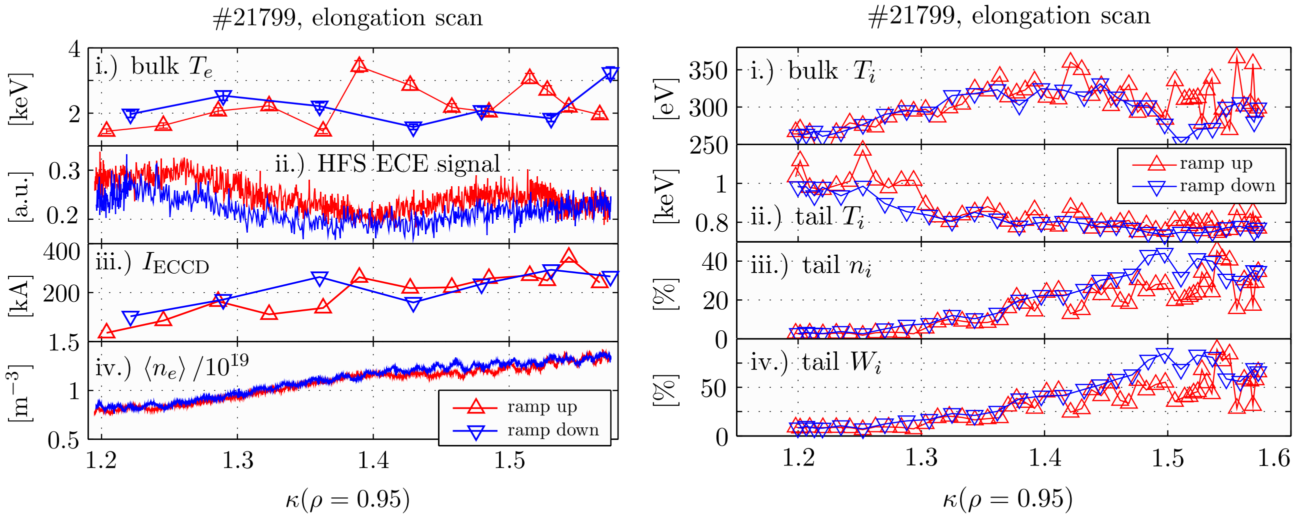

(a) κ scan: electron behaviour.

(b) κ scan: ion behaviour.

Figure 6.2.8: Dependence of the fast ion population parameters on the plasma elongation. (a) shows the destiny of the electrons, (b) of the ions.

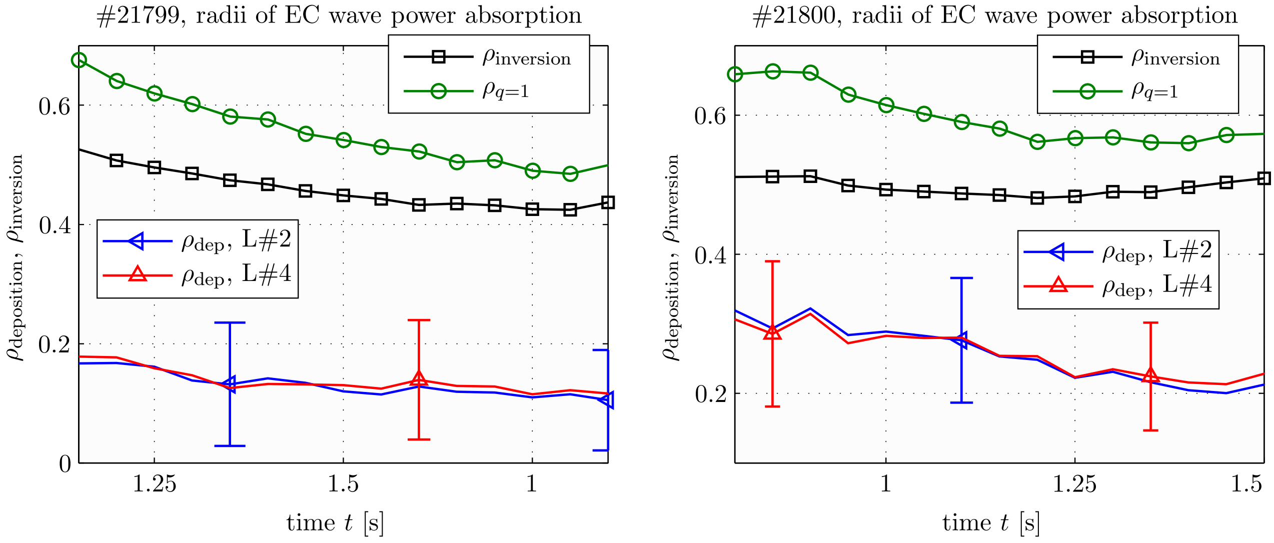

(a) κ-scan.

(b) δ scan.

Figure 6.2.9: Spatial arrangement of EC power deposition and sawtooth inversion radius for (a) the κ and (b) the δ parameter scans.

A scan of triangularity is shown in figure 6.2.10, where a gradual reversal of the triangularity, from $\delta = +0.3$ in $t = 0.8$ s to $\delta = -0.3$ in $t = 1.5$ s, was executed. The gyrotron configuration was as in discharge #21799. Collisionality is low and a decrease of T_i^b with δ is expected to take place (figure 4.10.2), but the low energy channels of the VNPA indicate no decrease (though, it should be recalled that this is the temperature at the edge and the CXRS measurement was not available for this discharge). Instead, the fast ion temperature increases by more than 60 %, although the bulk electron temperature doesn't change significantly and the electron density and driven current both decrease. Some correlation with the shown HFS ECE channel is also seen.

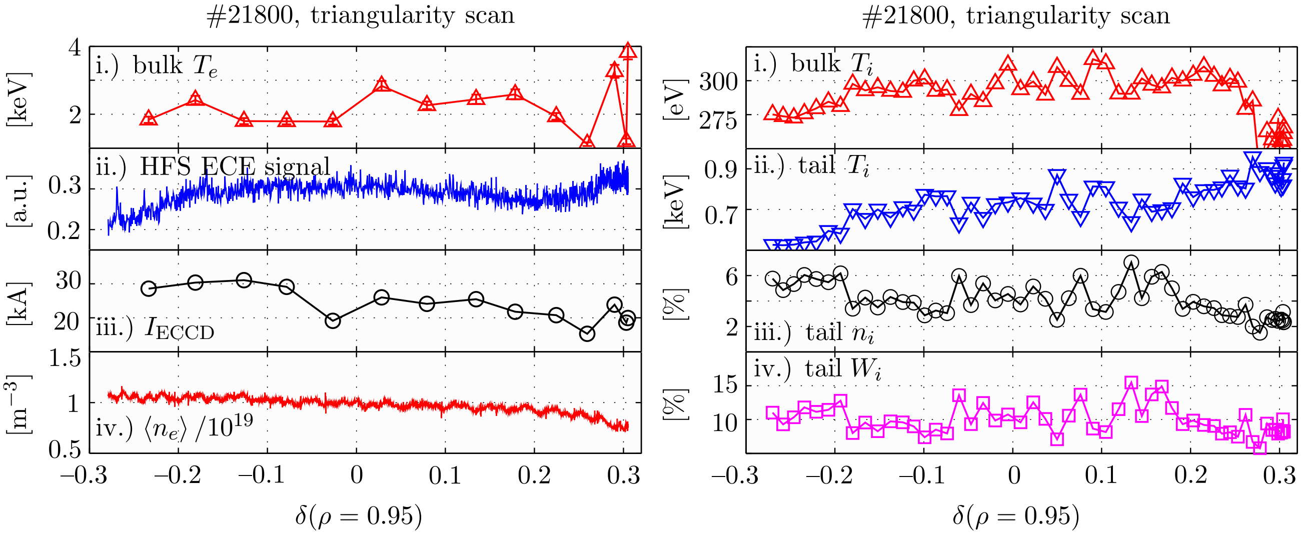

(a) δ scan: electron behaviour.

(b) δ scan: ion behaviour.

Figure 6.2.10: Dependence of the fast ion population parameters on the plasma triangularity. (a) shows the destiny of the electrons, (b) of the ions.

In both scans, the dependence of the fast ions on the plasma geometry parameters are opposite to the thermal ions. Note however, these experiments were carried out with a constant plasma current ($I_{\mathrm{p}} = 250$ kA), such that the inversion radius is shrinking during the evolution of δ and κ. The q-profiles are however flat for these discharges, on-axis $q_0 \sim 0.7$ on average, edge $q_a = 3 \ldots 4$ so all the EC power is well absorbed within the inversion radius (figure 6.2.9). As shown, the (pre-crash) $q = 1$ surface does not necessarily coincide with the inversion radius, especially with a flat q-profile where ρ_{inv} may be substantially smaller (see appendix B in [298]).

A reason for the two exceptions observed – higher suprathermal temperature at low κ and high δ – may be found in the improved stability of the internal kink, responsible for the triggering of the sawtooth oscillations (section 6.6). Shape investigations have shown that the sawteeth periods are longer at low κ and high δ [274]. With many parameters affecting the fast ion properties modified in these discharges, a proper assessment of the plasma shaping role is difficult to clarify.

Last but not least it should be mentioned that fast ions are found to have a suppressive effect on sawteeth on large machines with strong ion heating, e.g. ion cyclotron resonance heating (ICRH) on JET [299], and the stabilising effect was ascribed to fishbone modes (toroidal precession of the banana orbits of trapped fast ions). However, the fast ion energies on TCV are below the fishbone instability threshold that requires $T_i^s / T_i^b \gg R / r_{\mathrm{inv}}$ [300].

6.3 Fast ion localisation (vertical plasma scan)

The discharges executed in 2005–2006 shown so far were all placed at the vessel midplane to ensure the diagnosis of the hottest part of the plasma with the CNPA. The spatial location of the fast ion population was investigated with a sequence of plasma discharges displaced vertically on a shot-to-shot basis. The resulting CNPA 'pseudo chords' are shown in figure 6.3.1a. Discharge #33026 is a repeat of the on-axis counter-ECCD experiment #31177 (2 launchers with ECCD on-axis, 2 launchers ECRH off-axis). The chosen toroidal EC injection angle is a compromise between highest fast ion population and accessibility by the launcher configuration at all vertical plasma positions (however, plasmas placed between $z = 18$ and $z = 24$ cm are inaccessible to on-axis current drive). This equilibrium was then progressively moved upwards and the EC launcher angles adjusted such that the EC power deposition was as similar to the midplane shot as possible (these calculations were made before the experiment based on the model discharge). Note that slight changes in the launcher angles may result in strongly altered driven current or transport barrier conditions. If necessary, the angles were fine tuned by repetition of the discharge until the bulk electron density and temperature profiles were reasonably similar to those of the reference shot. The reproducibility of the fast ion population was verified with the VNPA (its vertical view line ensures the diagnosing of always the same plasma region), the corresponding VNPA charge exchange spectra are shown in figure 6.3.1b.

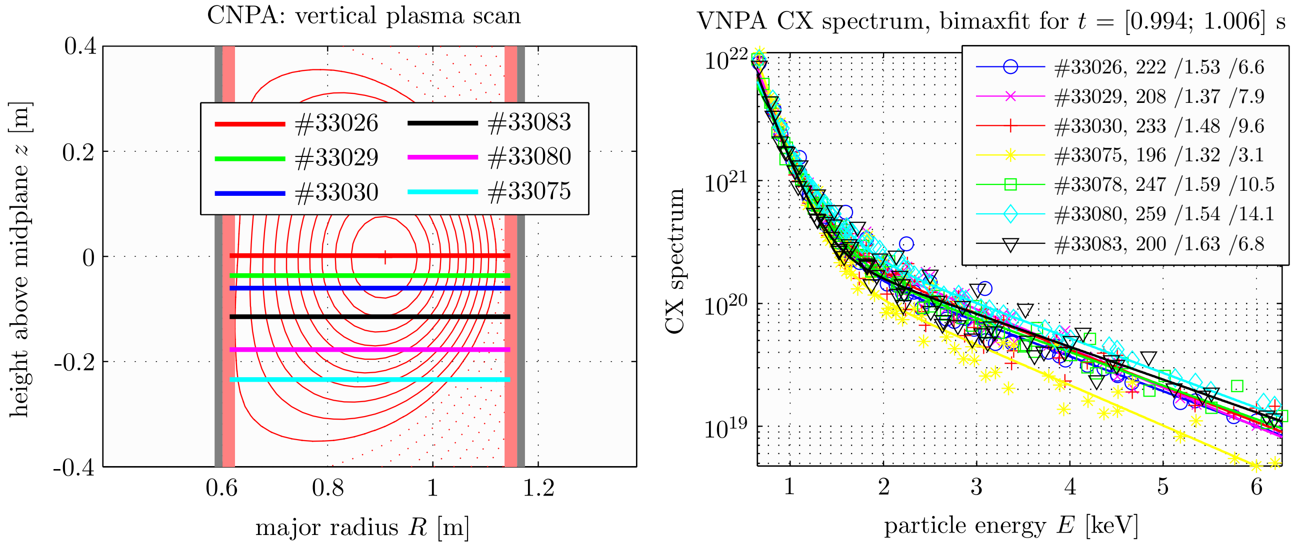

(a) pseudo chords. (b) VNPA CX spectra.

Figure 6.3.1: (a) Virtual CNPA view lines mapped to the equilibrium of discharge #33026 for a set of vertically displaced discharges. The nested surfaces indicate the normalised flux radii ρ_ψ, with a spacing of $\Delta\rho_\psi = 0.1$. (b) Charge exchange spectra measured with the VNPA. Ideally the spectra should overlap, as the discharges are designed to be identical (a part the vertical position). The legend values following the discharge numbers indicate the fit parameters, that is the bulk ion temperature (in eV), the suprathermal ion temperature (in keV) and the density ratio of supra-to-thermal population (in percent).

For each discharge, the steady-state fast ion population parameters were determined by averaging the CNPA charge exchange spectra over three measurements around $t = 1$ s, shown in figure 6.3.2 for hydrogen (a) and deuterium (b). The bi-Maxwellian fit parameters are again given in the legend labels. Inferred fast ion densities, as a function of the minimum normalised radius intercepted by the CNPA (figure 6.3.1a), are plotted in figure 6.3.3. Fast ions were found up to $z = 20$ cm ($\rho \approx 0.8$).

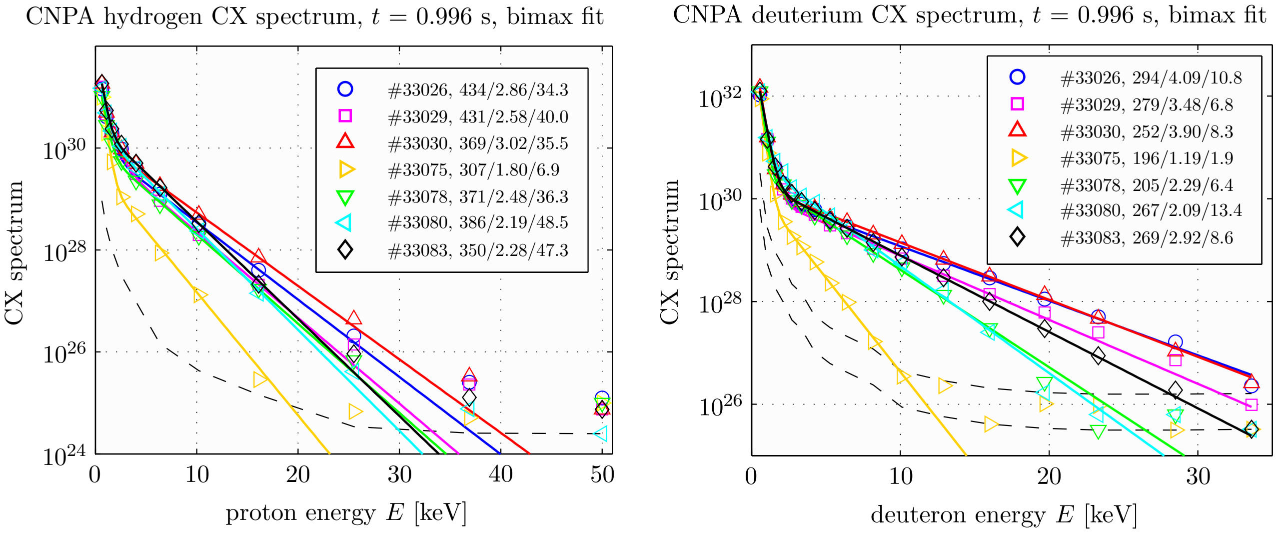

(a) Hydrogen. (b) Deuterium.

Figure 6.3.2: Bi-Maxwellian fit of the charge exchange spectrum of (a) hydrogen and (b) deuterium. The legend values following the discharge numbers indicate the fit parameters, namely the bulk ion temperature (in eV), the suprathermal ion temperature (in keV) and the density ratio of supra-to-thermal population (in percent).

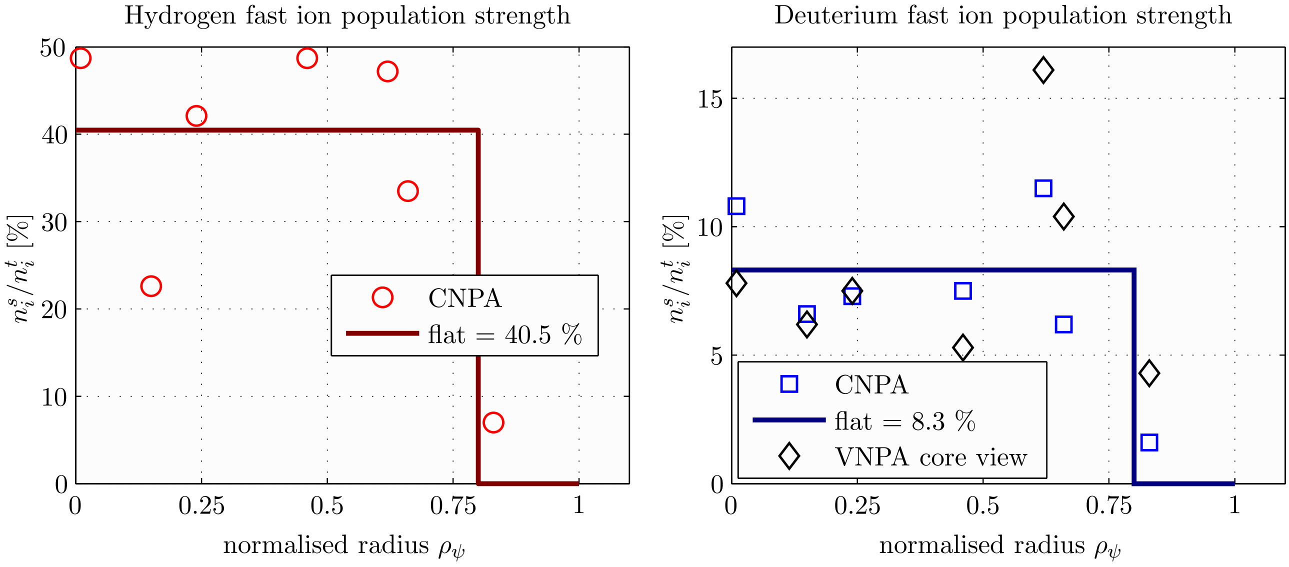

(a) Suprathermal hydrogen. (b) Suprathermal deuterium.

Figure 6.3.3: Definition of a radial profile of suprathermal ions for (a) hydrogen and (b) deuterium. The suprathermal population strength is difficult to reproduce among the discharges considered, a radially constant ratio between tail and bulk of the ion velocity distribution is a reasonable approximation. Respectively 40 % and 8 % of the hydrogen and deuterium ions populate the tail. No fast ions are found beyond $\rho = 0.8$.

These plots show that the fast ion populations were not extremely reproducible. The variation of fast ion density fraction measured by the CNPA at least follows the same trends as the ratio measured with the VNPA. The stronger fast ion population observed in discharge #33080 is due to stronger off-axis heating with a fifth gyrotron. Note that the injection of EC power in a L-mode plasma generally lowers the confinement time (*'power degradation'*) with respect to that for ohmic discharges and continues to degrade with increasing auxiliary heating power [301].

In plasmas with transport barriers however, there is no degradation of τ_E with power at least in part because the barrier is strengthened. As a result, the confinement of the fast ions also improves.
The population density ratio is, however, surprisingly constant over the radius, an average over the discharges probing $\rho < 0.8$ gives $n_i^s/n_i^b = 40$ % for hydrogen and $n_i^s/n_i^b = 8$ % for deuterium. The number of fast ions outside $\rho = 0.8$ decays rapidly. This is not a surprise, since the ion orbits have a Larmor radius, eq.(1.4.2), of approximately 1 cm at the outer midplane, that is about one third of the distance of the flux surface $\rho = 0.8$ to the outer wall (discharge #33026).

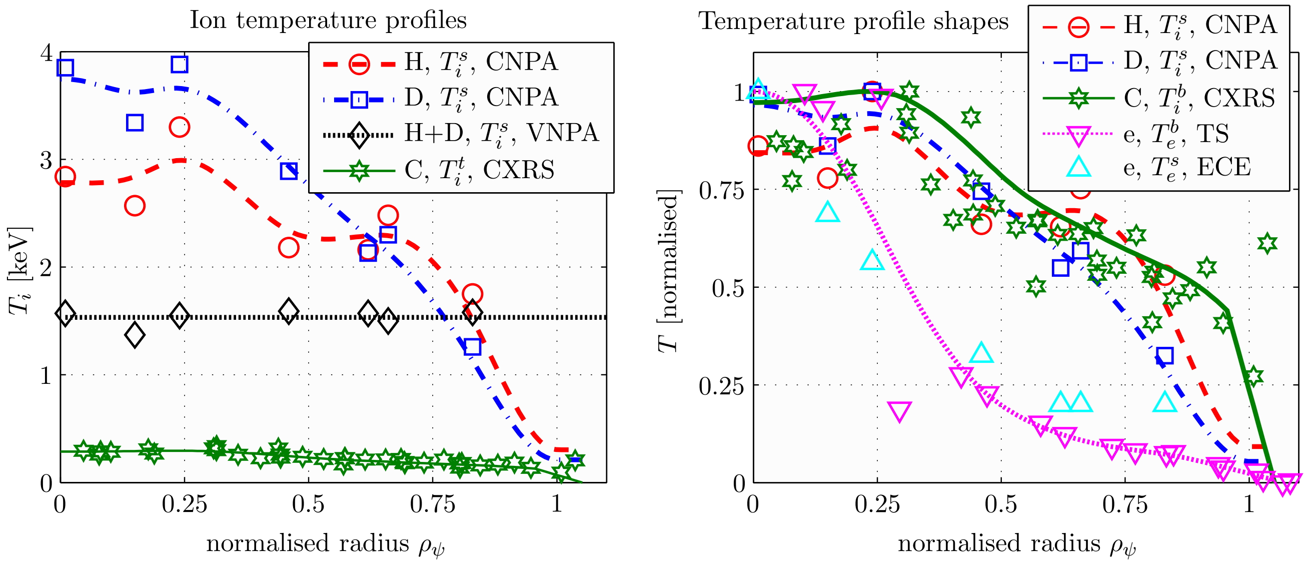

(a) T_i profile compilation.

(b) Temperature profile shapes.

Figure 6.3.4: (a) Measurement of the ion temperatures in the vertical plasma scan. For the suprathermal temperatures, each symbol represents a single discharge in its class. The interrupted lines show the profiles which were fitted to the measurements, these were then used in the *DOUBLE-TCV* simulation shown in figure 6.3.5. The VNPA looks through the centre of the plasma in all discharges. (b) Normalised profiles of electron and ion temperature, measured by CNPA (suprathermal ions), CXRS (thermal ions), high field side ECE (suprathermal electrons) and Thomson scattering (thermal electrons). The thermal and suprathermal profiles of particles having the same charge have the same shape, electron profiles are strongly peaked (transport barrier), ion profiles are broadly parabolic.

The measured fast ion temperatures were combined to give a T_i^s profile, shown in figure 6.3.4a. keV-ions are found up to the plasma edge. The VNPA does, of course, not measure against the radial position, so a 'profile' plotted as a function of the minimum radius intercepted by the CNPA is pretty flat, as expected. The scatter of the measured hydrogen T_i^s is larger, due to poorer statistics of the CNPA measurement.
Figure 6.3.4b shows normalised profiles of electrons and ions, such to compare their shapes. The profiles of thermal and suprathermal particles of the same particle type agree, those of the electrons (TS, ECE) are strongly peaked (due to the transport barrier) whereas the ion profiles (CNPA, CXRS) are broad. This may indicate that fast ions are subject to the same spatial confinement properties as bulk ions. The assembled profiles were interpolated as shown in the previous plots and input to *DOUBLE-TCV* for validation. In a single run, using the background plasma profiles and equilibrium of discharge #33026, the charge exchange spectra of all the 'virtual CNPA view lines' of the set of shots was modelled. The results are shown in figure 6.3.5. Bearing in mind that the discharges were not perfectly similar, the simulation fits well with the individual measurements.

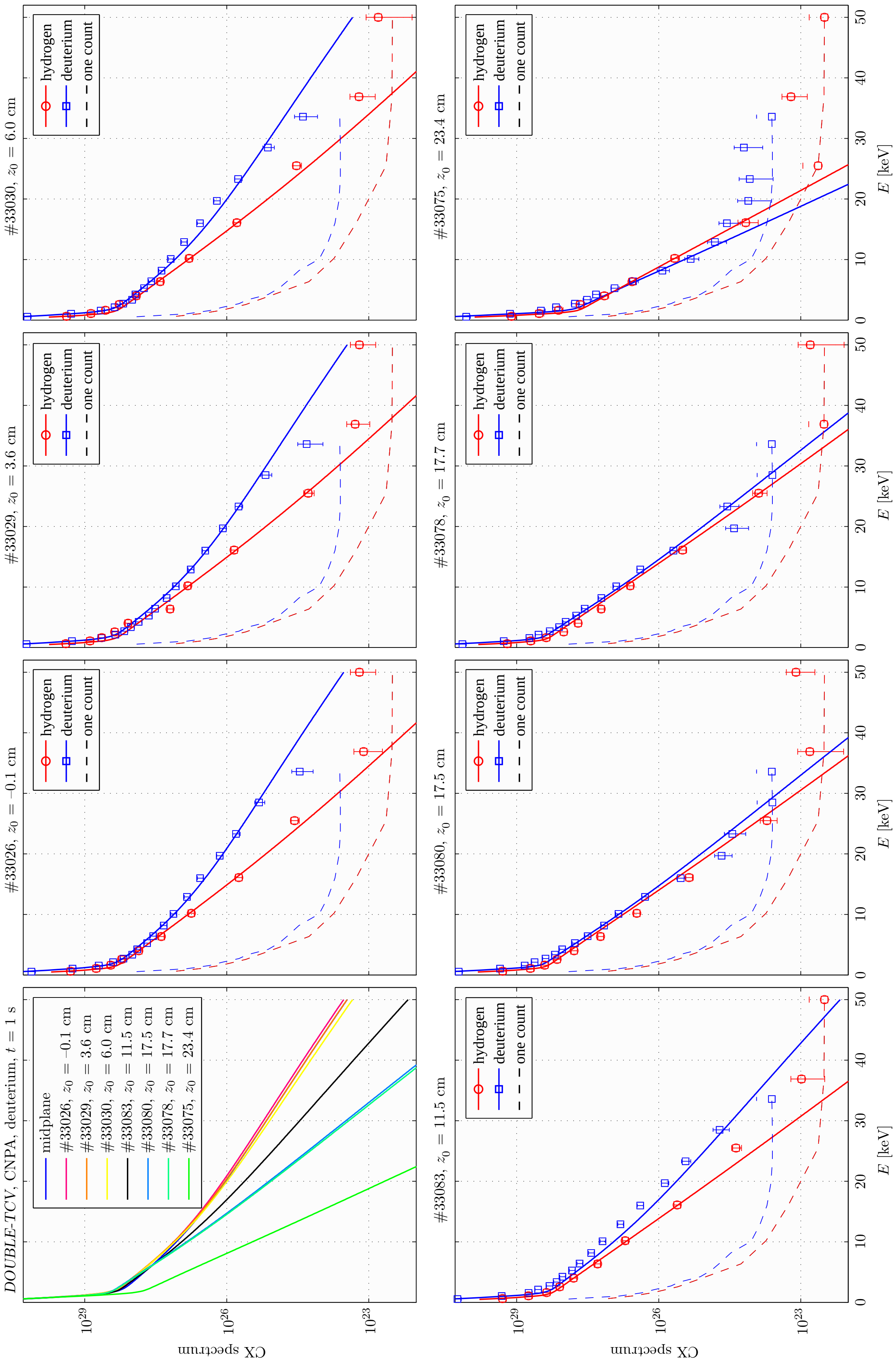

Figure 6.3.5: CNPA charge exchange spectra of hydrogen and deuterium for a set of discharges at various vertical positions. The spectra were modelled using *DOUBLE-TCV* and were calculated using the equilibrium and plasma profiles of discharge #33026 which was vertically centred at the midplane.

6.4 Steady-state fast ion populations

With ECH, after a transient phase where the fast ion population is building up – if the heating and plasma configuration do not change is not altered – the population parameters stabilise and steady-state is maintained throughout the duration of the auxiliary heating period. This is demonstrated in figure 6.1.8, or more clearly on figure 6.4.1a, where the fast ion population is unaltered from t = 1.25 s onwards. Discharge #31173 is similar to #31175 shown above. The fast variation of the deduced fast ion density evolution is due to uncertainties in the fit of the absolute charge exchange spectrum, with the fluctuations reflecting the error bar of the n_i^s retrieval process.

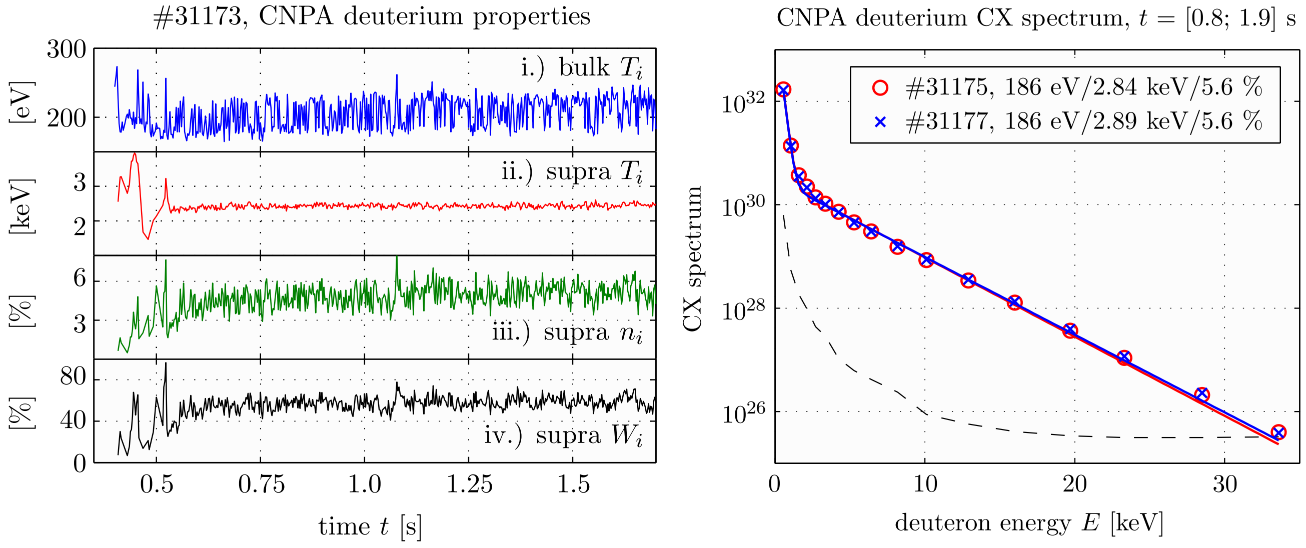

(a) Hydrogen spectra.

(b) Deuterium spectra.

Figure 6.4.1: (a) Steady-state fast ion population in discharge #31175. The plasma and heating parameters remain constant after t = 1.25 s.
(b) Discharges #31175 and #31177 were run according to the same model, they are thus supposed to exhibit identical fast ion populations. The charge exchange spectra were averaged over the whole steady state phase.

Conversely, the steady-state population parameters are highly reproducible. Figure 6.4.1b shows the deuterium charge exchange spectrum, averaged over t = [1.3; 1.9] s, for discharge #31175 and its repeat #31177. Identical plasma and auxiliary heating configuration engender identical fast ion population strength and temperature. This is in general not true for the initial evolution of the hot ion parameters up to the phase of steady-state.

To unfold further general parametric features of the fast ion population, a database of steady-state fast ion populations was constructed. Each entry was compiled from a single steady-state interval by averaging the charge exchange spectrum over several hundred of milliseconds before applying the bi-Maxwellian fit. Steady-state phases shorter than 100 ms were not included, together with plasmas designed to scan a particular parameter (i.e. those shown in the preceding sections). Early times of auxiliary heating were not considered, such to stabilise the EC driven current radial redistribution. The dataset currently consists of 25 TCV discharges (obtained between 2004 and 2007). As with the complete database (section 6.1.2), dependence of the fast ion parameters on plasma density, temperatures, inductive and non-inductive currents, total and local auxiliary heating powers, energy equipartition, plasma purity, loop voltage etc. were investigated. This was extended to include composite parameters, like collisionality or conductivity. Parameters showing an obvious impact on the fast ions are shown in figure 6.4.2.

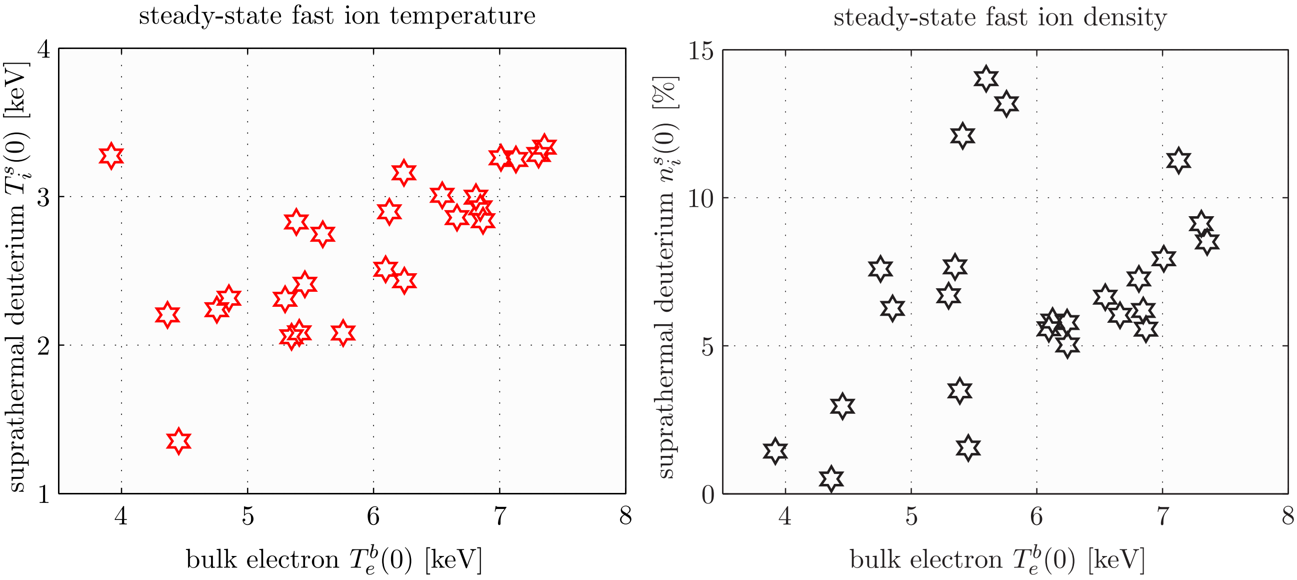

(a) Fast ion temperature.

(b) Fast ion density.

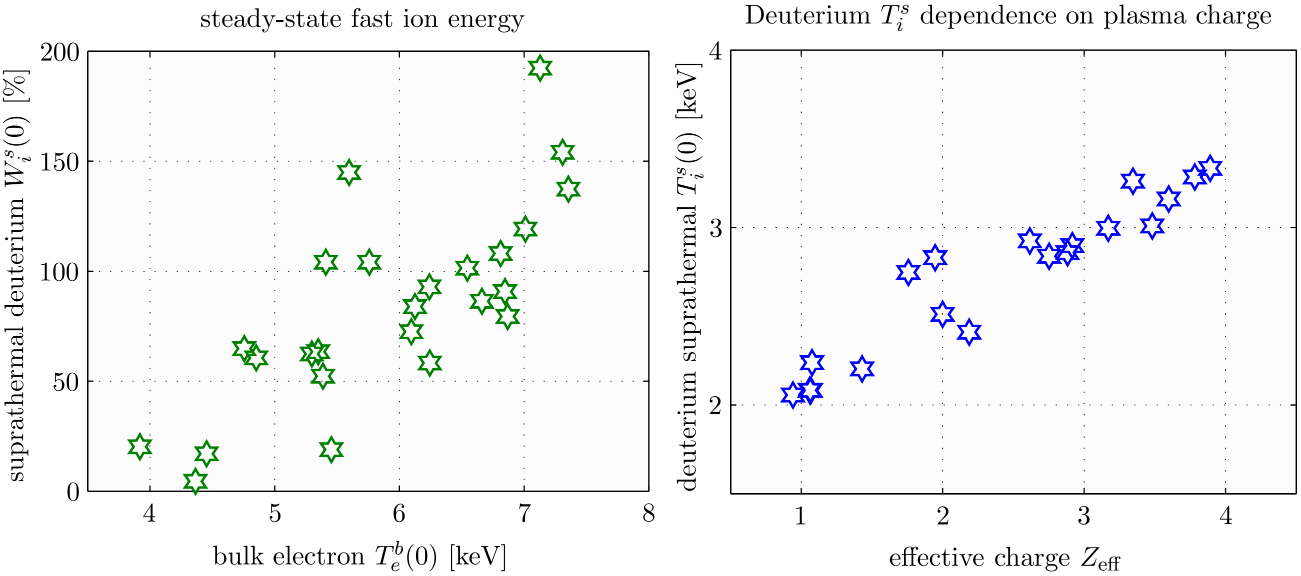

(c) Fast ion energy.

(d) Plasma purity.

Figure 6.4.2: (a), (b) and (c): Dependence of steady state fast deuterium parameters on the thermal bulk electron temperature (closest measurement to the magnetic axis with the Thomson scattering system). (d) Scaling of the suprathermal deuterium ion temperature with the effective plasma charge.

In steady-state, the suprathermal ion temperature scales with the bulk electron temperature, roughly $T_e^b \geqslant T_i^s > T_e^b/2$, where the first inequality is derived from the complete database (figure 6.1.4). The fast ion density and energy increase is quite linear with T_e^b, although the scatter of the density is more important. Below $T_e^b = \sim 3.5$ keV $\cong 10 \times T_i^b(0)$, the fast ion density is not measurable. The presence of impurities also raises the suprathermal ion temperature, with a linear Z_{eff} dependence. This dependence seems natural since on TCV the effective plasma charge increases with heating power [34].

The difference between the parameters of hydrogen and deuterium fast ions are interesting. The fast ion temperatures are generally close. In steady state, with long temporal averaging, the errors are reduced and the suprathermal temperatures of the two isotopes coincide (figure 6.4.3).

The fast ion densities, normalised by their respective bulk ion densities, are different, where, for hydrogen, the proportion of suprathermals to thermals can reach 1:2, whereas for deuterium the ratio doesn't exceed 1:3. Inspection of the respective suprathermal energies, now normalised to the total thermal ion energy, i.e. for deuterium,

$$\frac{W^s_{i,\mathrm{D}}}{W^b_{i,\mathrm{H}} + W^b_{i,\mathrm{D}}} \equiv w^s_{i,\mathrm{D}} = \frac{T^s_{i,\mathrm{D}}}{T^b_{i,\mathrm{D}}} \frac{n^s_{i,\mathrm{D}}}{n^b_{i,\mathrm{H}} + n^b_{i,\mathrm{D}}}, \tag{6.4.1}$$

shows that the fast deuterium stored energy exceeds the fast hydrogen energy by a factor 2, corresponding to the mass ratio of the two isotopes. This energy ratio doesn't depend on the plasma hydrogen content.

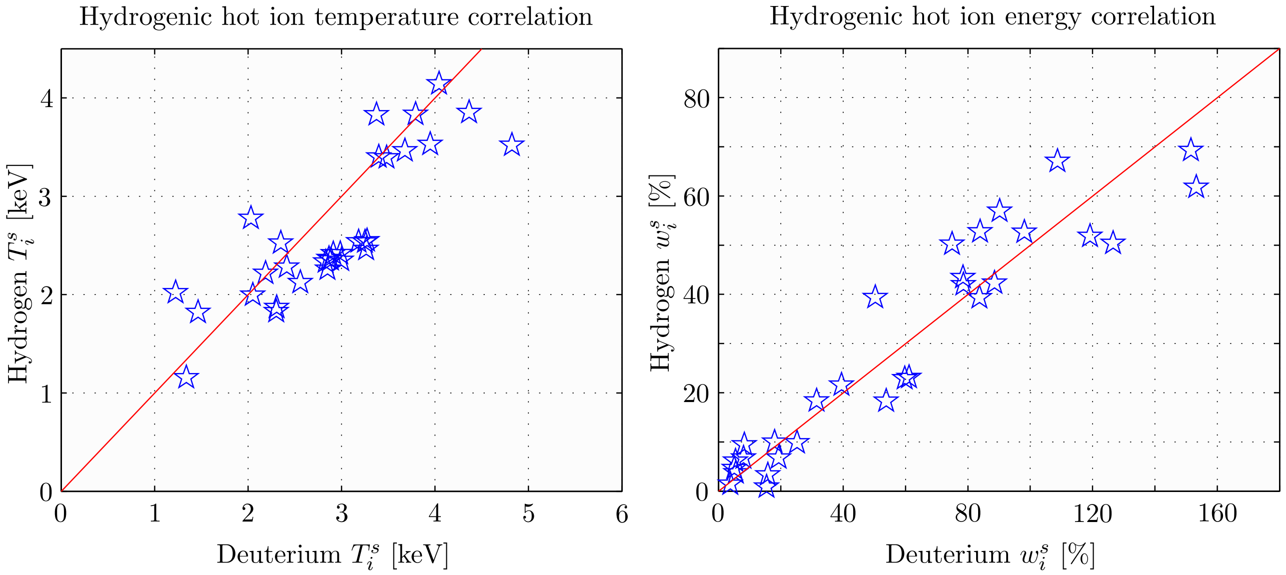

(a) Suprathermal temperatures. (b) Suprathermal energies.

Figure 6.4.3: Correlation between suprathermal temperature (a) and energy (b) of the fast hydrogen and deuterium ions. The straight lines indicate respectively $T^s_{i,\mathrm{D}} = T^s_{i,\mathrm{H}}$ and $w^s_{i,\mathrm{D}} = 2\,w^s_{i,\mathrm{H}}$.

6.5 Validation of the fast ion detection

In section 3.4 it was seen that the CNPA measurement is not exempt from parasitic contributions to the measured signal. As a consequence, the analysis of suprathermal ions only became reliable after completion of the diagnostic shield.

Effective shielding is demonstrated in figure 6.5.1, where a strong neutral flux (20 hits per millisecond) at the highest diagnosed deuterium energy ($E = 33$ keV) is shown. The auxiliary CNPA channels, monitoring X-ray (channel #31) and photon (channel #32) incidence on the channeltrons, do not measure anything other than the normal random hits during this period. The measured fluxes are therefore correctly ascribed to incoming neutrals.

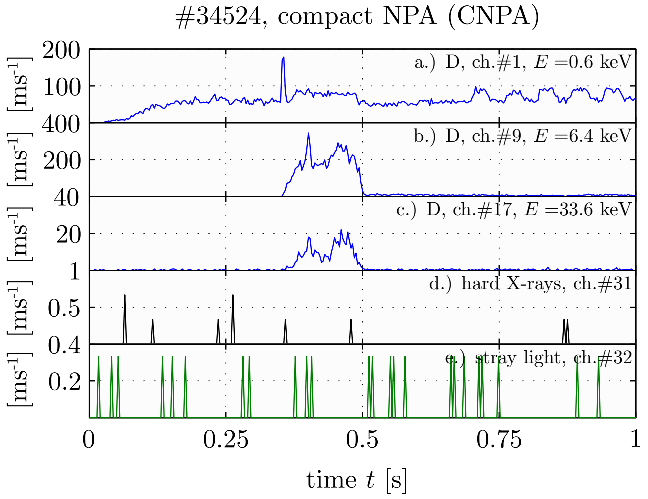

Figure 6.5.1: Monitoring of parasitic signals in the CNPA channels. Fast ions are present in the time interval $t = [0.35; 0.5]$ s, as the CNPA detectors #31 and #32 do not indicate any signal contribution due to stray light or hard X-rays.

However, to dispel any doubts about the existence of the suprathermal ion component, alternative measurements were considered that led to a series of experimental validation investigations. This includes cross checks with the neutron detector (sections 6.5.1.2 and 6.5.3), analysis of the fast ions resulting from the ionisation of neutral beam ions (section 6.5.1) and global considerations of the stored particle energy (section 6.5.2).

6.5.1 DNBI deposited fast ions

6.5.1.1 Steady-state classical slowing down ion energy distribution

The description of neutral beam ions deposited in a hot and dense plasma [70] requires consideration of the ionisation of the injected beam neutrals by collisions with plasma electrons and ions, subsequent drift motion in the confining magnetic field, the scattering and slowing down of the fast beam ions by small angle long range Coulomb collisions and charge-exchange collisions with plasma neutrals. Further, loss mechanisms like shine-through (incomplete ionisation) or orbit losses (particle collisions with the tokamak wall) may also not be negligible. An accurate analysis of the relaxation of the hot ion component requires a self-consistent solution of a set of non-linear Fokker-Planck equations for energetic ions and background plasma species [302]. Here we shall restrict this formidable task to an approximate description of the ion energy distribution in plasmas with DNBI neutrals at steady-state by solving a simplified Fokker-Planck equation, based on the following approximations: a.) the magnetic field is uniform; b.) the plasma particle energy distributions are Maxwellian and c.) the hot beam ion density is small with respect to the cold background plasma density. If, further, the hot ion velocity v_h is such that $v_{\mathrm{th}i} \ll v_h \ll v_{\mathrm{the}}$, with $v_{\mathrm{th}i}$ and v_{the} the thermal ion and electron velocities, the relevant equation for the hot ion distribution function f_{ih}, for a beam injected at an angle θ in respect to the direction of the magnetic field and switched on at $t = 0$, may be written [303]

$$\tau_s \frac{\partial f_{\mathrm{ih}}}{\partial t} = \frac{1}{v^2} \frac{\partial}{\partial v} \left\{ \left(v_c^3 + v^3 \right) f \right\} + \frac{m_i}{2\, m_h} \frac{v_c^3}{v^3} \frac{\partial}{\partial \mu} \left\{ \left(1 - \mu^2 \right) \frac{\partial f}{\partial \mu} \right\} + \tilde{S} \left(v - v_0 \right) \delta \left(\mu - \mu_0 \right) \tau_s, \tag{6.5.1}$$

where $\mu = v_\parallel / v = \cos\theta$, the index 0 refers to the nominal beam velocity, the index h refers to the beam species and

$$v_c = \sqrt[3]{\frac{3\sqrt{\pi} m_e}{4\, m_i}}\, v_{\mathrm{the}} \tag{6.5.2}$$

is the critical velocity, above which, during slowing down, the hot ion preferentially transfers its kinetic energy to the electrons instead of the plasma ions [304]. The solution of eq.(6.5.1) reaches steady state (for a stationary beam) on the time scale of the collisional slowing down time

$$\tau_s = \frac{m_i\, m_h\, v_c^3}{4\pi\, n_i\, Z_h^2\, e^4 \ln\Lambda}. \tag{6.5.3}$$

For a beam source yielding S fast ions per second and unit volume, of half width velocity spread $\Delta v \ll v_0$, i.e. a source of the form

$$\widetilde{S}(v - v_0) = \frac{S \exp\left(-\frac{(v - v_0)^2}{(\Delta v)^2}\right)}{v^2 \Delta v \sqrt{\pi}} \tag{6.5.4}$$

and considering velocities above v_c, the angular scattering term in eq.(6.5.1) may be dropped and the solution becomes

$$f_{i\mathrm{h}}(v, t, \mu) = \frac{\tau_s}{2} \frac{S\delta\left(\mu - \mu_0\right)}{v^3 + v_c^3} \left\{ \mathrm{erfc}\left[\frac{v - v_0}{\Delta v}\right] - \mathrm{erfc}\left[\frac{v^* - v_0}{\Delta v}\right] \right\}, \tag{6.5.5}$$

where

$$v^* = \sqrt[3]{\left(v^3 + v_c^3\right) \exp\left(\frac{3\, t}{\tau_s}\right) - v_c^3}. \tag{6.5.6}$$

The slowing down distribution function $f_{i\mathrm{h}}(E)$ scales therefore $\propto 1/E$.

Figures 6.5.2 and 6.5.3 show the application of this simplified fast ion distribution calculation to the parameters of discharge #33767, whose key plasma parameters are $n_e(0) = 5.1 \times 10^{19}$ m^{-3}, $T_e(0) = 900$ eV, $T_i(0) = 670$ eV; hydrogen DNBI beam with full energy $E_0 = 50.7$ keV and equivalent DNBI current $I_0 = 1.64$ A. Beam neutral attenuation and radial profile were calculated as explained in section 3.2.2. The ionised fractions of the four beam components, considering electron and ion impact ionisation, are shown in figure 6.5.2a, at the magnetic axis. Although the beam neutral density is maximum at approximately mid-radius, the fast ion production is highest close to the magnetic axis where the electron temperature is higher. A beam velocity spread of $\Delta v = 1$ km/s was assumed. The slowing-down time, eq.(6.5.3), is $\tau_s = 18.8$ ms and the critical energy, eq.(6.5.2), is $E_c = 13$ keV. The fast ion distribution function, calculated using eq.(6.5.5), together with the background plasma ion distribution, is shown in figure 6.5.2b. The discontinuities coinciding with the four beam components are clearly visible.

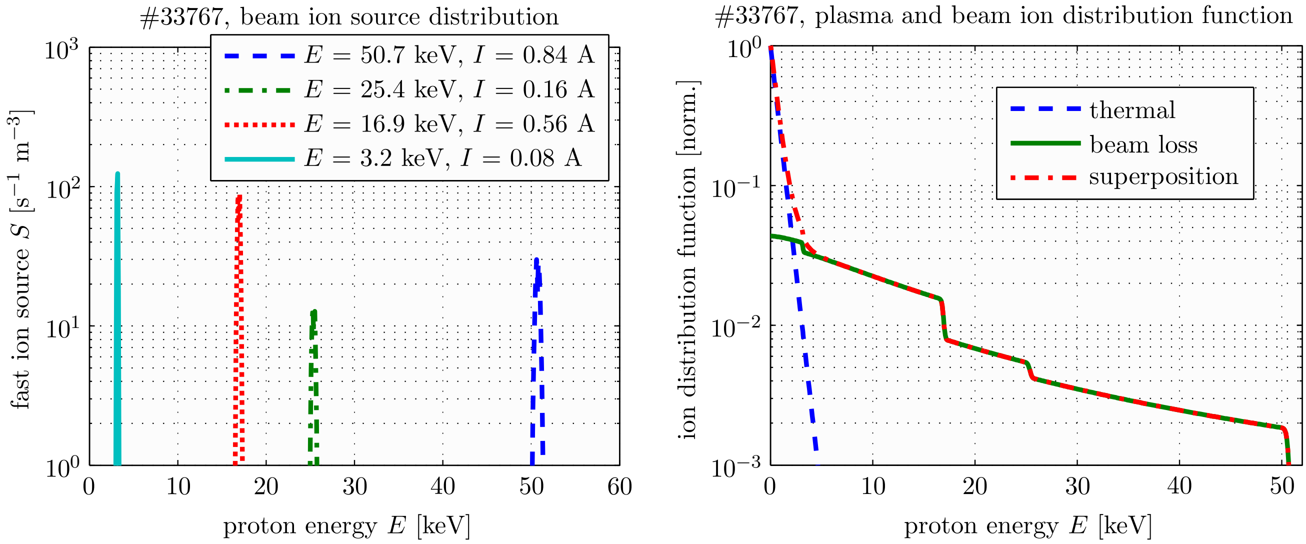

(a) Fast ion source. (b) Fast ion relaxation.

Figure 6.5.2: (a) Fast ion fuelling of the plasma with the beam, at the respective energies of the four beam components. The ion source density is representative for the conditions at the magnetic axis of discharge #33767, $t = 0.81$ s.
(b) Calculated fast ion slowing down distribution function due to the partial ionisation of the hydrogen diagnostic neutral beam at steady state. The ratio of beam to background plasma ions shown is valid at the magnetic axis.

f_{ih} was then discretised and used by *DOUBLE-TCV*, together with the other necessary available experimental information and the CNPA hydrogen neutral flux calculated for the time interval prior and during the DNBI beam blip (figure 6.5.3). The thick line represents the steady-state total ion distribution and reasonable absolute agreement is found.

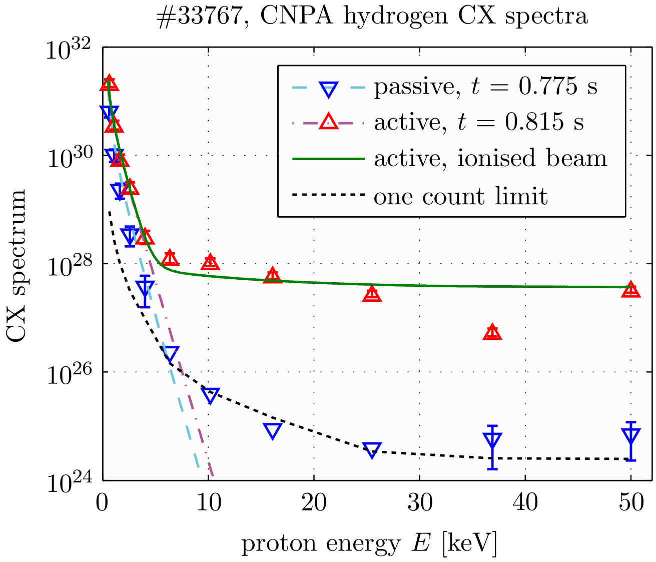

Figure 6.5.3: *DOUBLE-TCV* simulation of passive and active charge exchange without beam ionisation (dash-dotted curve) and by taking ionisation (full stroke) into account. The ion distribution function input to the code in the latter case corresponds to the one shown in figure 6.5.2b.

The CNPA data was averaged over the whole beam blip, which lasted for 28.5 ms. This is more than τ_s, such that steady-state conditions should be established.

For the sake of completeness, it should be mentioned that the transient behaviour of the beam deposited ions was studied with the (beam non-intersecting) VNPA by Karpushov et al. [305] by scanning electron density and temperature. The fast ion production was modelled with a code incorporating equations presumably similar to those presented in this section [306]. The slowing down of the ions was found to be classical, e.g the time delay between the start of beam injection and increase of the flux into the highest VNPA channel scales with n_e and T_e as τ_s does, that is the time required for the beam ions to slow down from the injection energy (50 keV) to the maximum energy diagnosed with the VNPA (6 keV).

6.5.1.2 Beam bombardment of the inner wall

The response of the neutron detector to fast ions was tested by injection of the neutral beam, operated exceptionally with D_2, in the empty torus. Without plasma, the beam is stopped at the inner vessel wall where fusion reactions may occur with the deuterium in the graphite wall surface. Here, the spatial distribution and energetic composition of the beam is well known at the impact surface, that is the vacuum profile calculated from eq.(3.2.5), and the birthplace of the neutrons produced by the D-D fusion reaction are also well localised, considerably simplifying the evaluation of the neutron rate impinging on the neutron detector.

Modelling of the neutron flux at the location of the neutron detector is shown for the 5 DNBI pulses of discharge #31700 in figure 6.5.4.

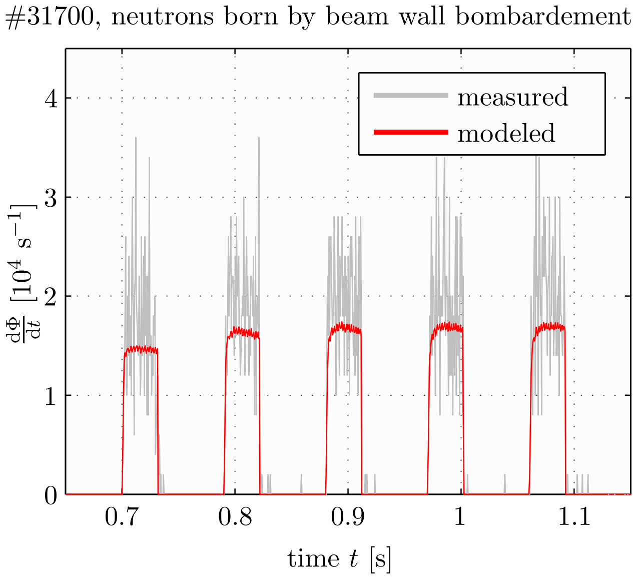

(a) Fusion in wall.

Figure 6.5.4: Measured (noisy curve) and modelled neutron detector response to the vessel wall bombardment by a deuterium neutral beam in the absence of a plasma.

The deuterium beam nominal energy was 26 keV and the total equivalent current reached 2 A. Agreement was achieved with the assumption of a deuterium absorption layer depth of 1 μm and a saturation of 0.4 (i.e. the number of deuterium atoms per carbon atom), values generally accepted by edge and wall plasma physicists [307].

6.5.2 Plasma particle energy balance

A further validation of the suprathermal ion population in the plasma was undertaken through an accurate assessment of the kinetic energies of the various plasma particles for comparison with the total measured energy. That is measured with a diamagnetic loop (DML) [66] (hardware components are illustrated in figure 6.5.5a).

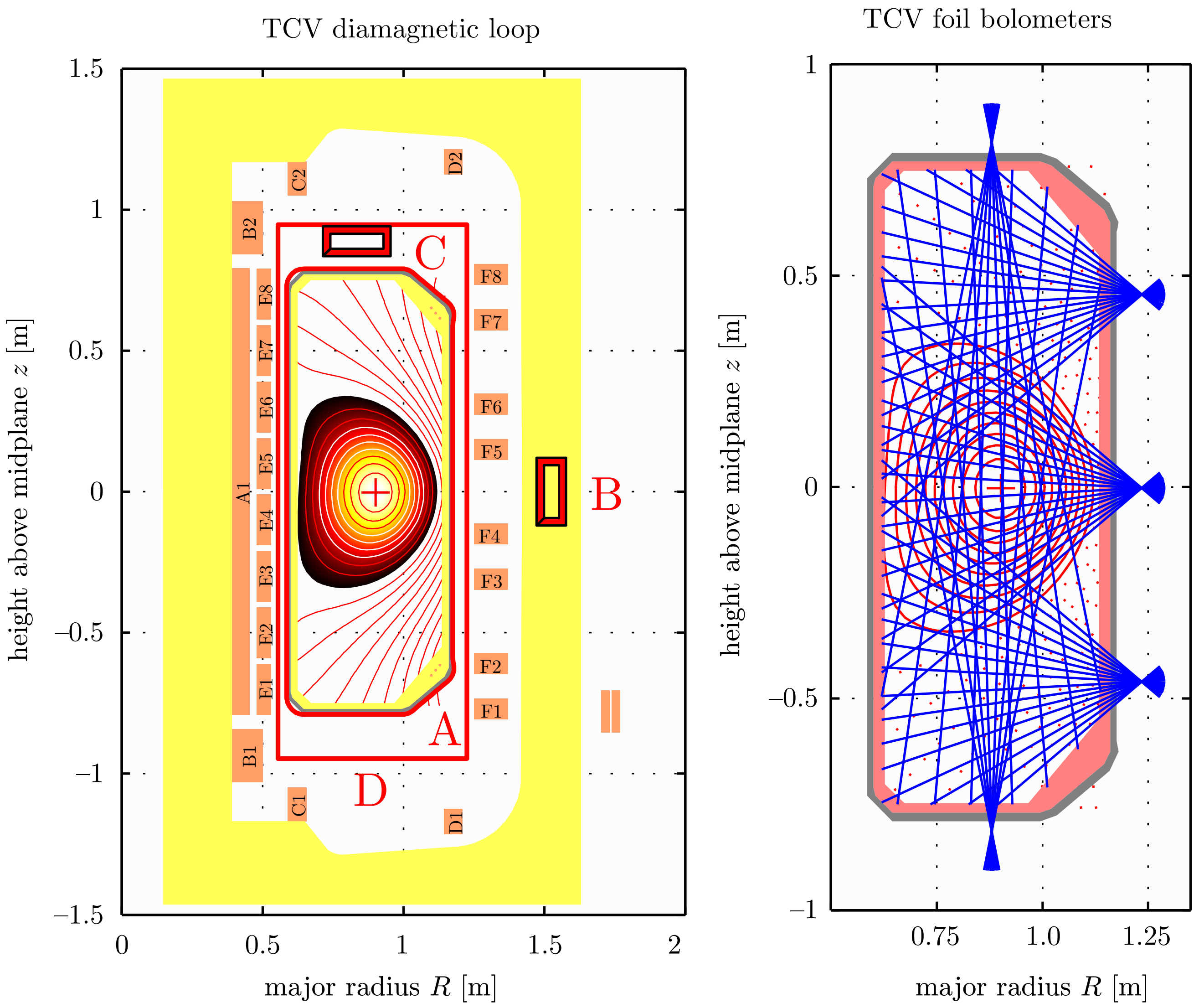

(a) DML layout on TCV.

(b) Metal foil bolometers.

Figure 6.5.5: (a) Arrangement of the loops for the diamagnetic measurement. A: vessel image current loop (bonded onto the vessel), B: current diffusion loop, C: compensation loop, D: diamagnetic loop. All parts are located in toroidal sector #1, the only sector without diagnostic ports.
(b) 5 cameras host an array of 8 miniaturised metal foil bolometers each which are used to measure the power radiated by impurities (the plasma is optically thin in the VUV and soft X-ray frequency range) and lost by neutrals. The incident power is obtained from the temperature rise of the absorber knowing its thermal capacity. Their thermal inertia limits the time resolution of the bolometer to approximately 10 ms.

A stable plasma configuration relies on an equilibrium between magnetic and kinetic pressure, there is therefore a relation between the equilibrium magnetic field and plasma energy (see appendix A in [308] for a derivation). More precisely, the latter is proportional to the toroidal diamagnetic flux, that is the difference in toroidal flux with and without plasma.

The diamagnetic flux is measured with the D loop encircling the exterior of the vacuum vessel and requires correction by a.) the C compensation loop to account for the flux from the toroidal coils, b.) the current diffusion in the toroidal coil conductor (B) and c.) the A loop wound on the vessel to assess the vessel image current. The loops B and C are multiturn such that their area encloses the same flux as the single-turn D loop.

The assessment of the energy stored in the thermal bulk electron and ion populations is relatively simple as the profiles of electron density and temperature and ion temperature are measured with good spatial resolution. The measurement of the plasma effective charge (X-rays), hydrogenic composition (CNPA) and plasma neutrality determine then the ion density profiles of the ionic species. The energy content of the suprathermal ion and electron population are by far more difficult to quantify because of the difficulties in deconvoluting the ECE frequency and NPA flux spectra in space and energy. In section 5.4.3.2 the suprathermal electron populations were precisely simulated for two time instants of discharge #34527. The total suprathermal energy is then

$$W_e^s = W_{\text{therm}}^s + W_{\text{trans}}^s = \sum_{k=1}^{K} \int \left[n_{e,k}^s \left(\frac{1}{2} T_{e\parallel,k}^s + T_{e\perp,k}^s + \frac{1}{2} m_e v_{d,k}^2 \right) \right] \mathrm{d}V, \tag{6.5.7}$$

where the summation is taken over all K suprathermal electron populations listed on page 155.

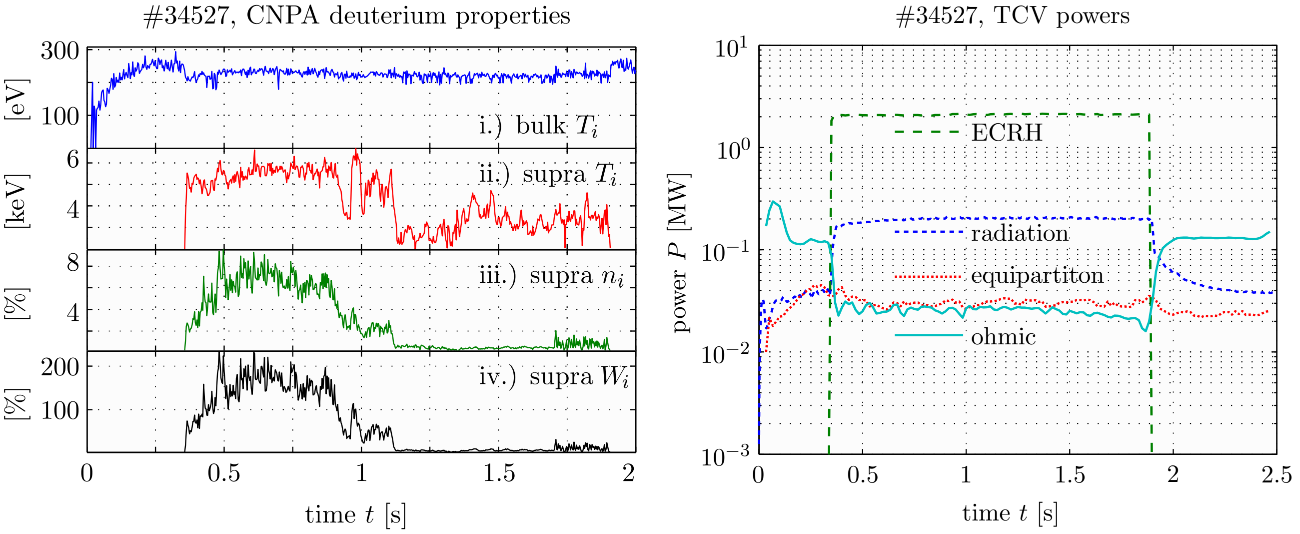

(a) Fast deuterium.

(b) Powers on TCV.

Figure 6.5.6: (a) Time traces of the deuterium ion parameters for discharge #34527. Notice the hot ion temperature, reaching the value of the bulk electron temperature (the electron properties for this discharge are shown in section 5.4.3.2).
(b) Ohmic and auxiliary heating, electron–ion equipartition and radiated powers of discharge #34527. The total radiated power is obtained from the local emissivities inside the plasma calculated by tomography treated by the minimum Fisher information method [309].

For the fast ions, we may use the result of section 6.3, i.e. take radially constant ratios between suprathermal and thermal ion temperature and density, with the latter truncated at $\rho = 0.8$. Time traces for the core fast ion parameters for discharge #34527 are shown in figure 6.5.6a. The populations are further assumed to be isotropic and, for the carbon impurity, no fast ion population is considered, that is

$$W_{i,\ell}^s = \frac{3}{2} \int n_{i,\ell}^s T_{i,\ell}^s \, \mathrm{d}V \qquad \ell \in [\mathrm{H}, \mathrm{D}]. \tag{6.5.8}$$

The heating, equipartition and radiation loss powers are shown in figure 6.5.6b. The equipartition power is calculated using the parameters of the bulk populations only. The radiation losses include also the power removed by neutrals leaving the plasma and was derived from the measurement of an array of 64 golden foil bolometers [310] which are probing a poloidal cross section with 5 pinhole cameras surrounding the vessel [311], shown in figure 6.5.5b. The total radiated power is then estimated with the fast computer tomography code *FABCAT* [312]. A considerable part of the power deposited by the EC waves is conducted by the plasma and heats the wall, releasing impurities (and other wall particles). These penetrate into the plasma where they, as shown on the trace of P_{rad}, strongly enhance the power losses by resonant line radiation during the auxiliary heating period. At the same time, the ohmic heating power drops by one third, with the enhanced plasma conductivity, the total plasma current remains approximately constant, whereas the loop voltage is strongly reduced (figure 6.5.7a). The reduced coupling between electrons and ions, expressed by the equipartition power, doesn't change during the auxiliary heating phase.

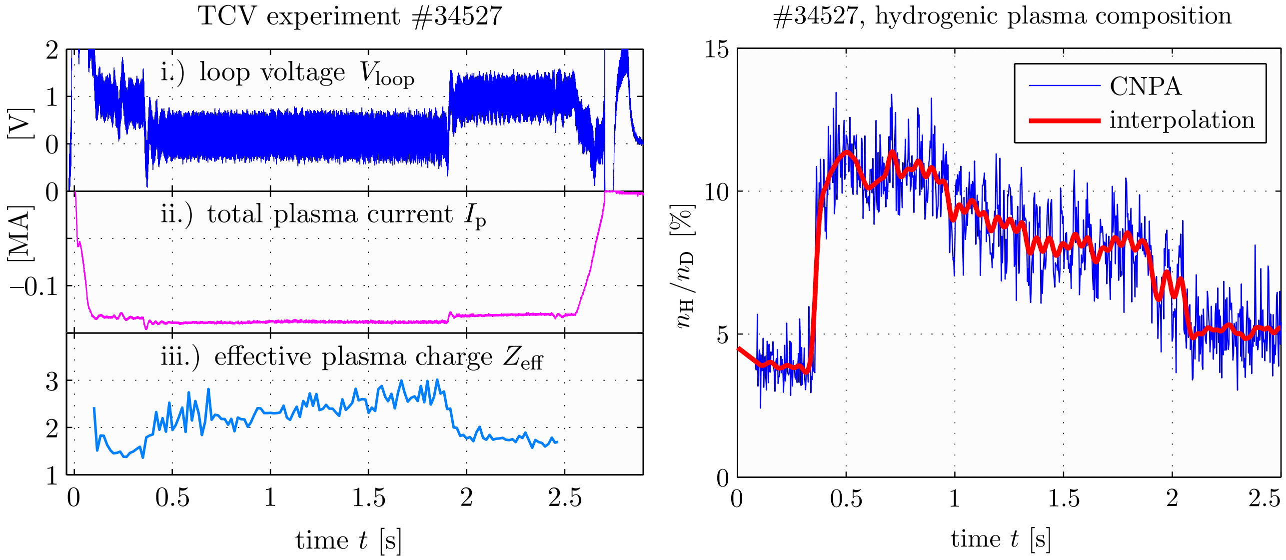

(a) Loop voltage and plasma current.

(b) Isotopic composition.

Figure 6.5.7: (a) Measured loop voltage and plasma current.
(b) Evolution of the hydrogenic composition of the plasma (calculated from the CNPA measurement). The thick line is a cubic spline interpolation of the measured neutral flux ratios.

The calculated energies of the individual particle species and populations are summarised in figure 6.5.8. The left figure shows the various ion energies. The carbon energy fraction is negligibly small, the thermal hydrogen energy is small but doubles with EC injection, because of enhanced wall desorbed fuelling (same reasoning as for the carbon density increase). This is confirmed by the CNPA measurement of the hydrogenic composition (figure 6.5.7b). During the phase of strong ion acceleration, i.e. for the period of pronounced counter-ECCD, the suprathermal deuterium content strongly exceeds its thermal counterpart. Now, the suprathermal hydrogen contains an important fraction of the total ion stored energy. In contrast to the fast ion population, the overall thermal ion energy is reduced during the gyrotron activity, as the energy transfer from electrons to ions is less effective and some of the bulk ions become suprathermal.

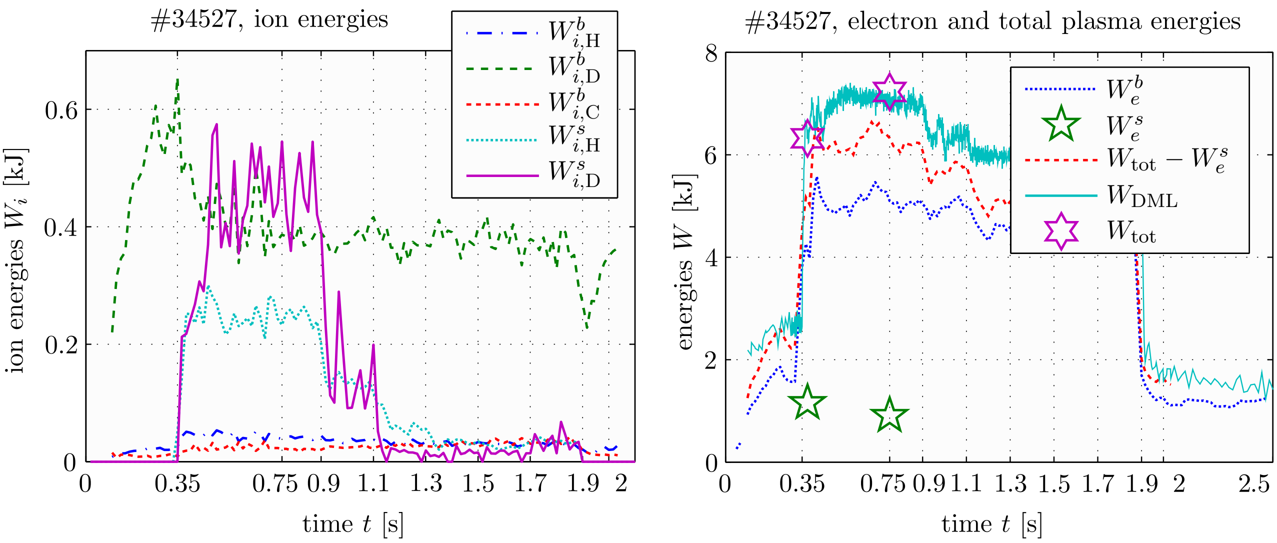

(a) Ion energies.

(b) Electron and total energies.

Figure 6.5.8: (a) Energy content of the hydrogen, deuterium and carbon ion populations in the plasma.
(b) Electron energy content and the total plasma energy measured with the diamagnetic loop (DML). The pentagrams indicate the suprathermal electron energy calculated from the *NOTEC-TCV* simulation (figure 5.4.9). The hexagrams represent the sum of total ion and electron energies.

As expected for a device with electron heating only, most of the energy is stored in the electrons (figure 6.5.8b), with the thermal bulk sustaining by far the most abundant portion (lowest trace). The available measurements enable us to calculate the sum of all particle energy quantities (middle curve) in time, except for the fast electrons (pentagrams). When the latter are summed (at the two times where *NOTEC-TCV* was run), excellent agreement with the DML measured total kinetic energy is found (hexagrams and top trace).

6.5.3 Comparison with neutron detector

The steep increase of the fusion cross section with energy (figure 1.1.2b) makes the neutron detector a highly sensitive diagnostic of plasmas contaminated with fast deuterium. The assessment of the spatial and energetic distribution of the fast ions with the CNPA (section 6.3) offers a possibility of predicting the neutron detector signal more accurately.
To this purpose, the profiles of thermal (figure 6.5.9a) and suprathermal deuterium temperature (figure 6.3.4a) and density (figure 6.3.3b) determined previously were projected onto a full toroidal grid of horizontal×vertical×toroidal = 28×65×50 grid points. A full calibration matrix describing the individual attenuation of neutrons by the tokamak structure elements on their journey to the neutron detector for each of these points was estimated. Assuming isotropic ion velocity distributions, the fusion reactivity was then numerically evaluated using the one dimensional integral over energy,

$$\langle \sigma v \rangle = \int \sigma(E)\, g(E)\, \mathrm{d}E, \tag{6.5.9}$$

where the function $g(E)$ for the bi-Maxwellian ion energy distribution function, eq.(6.1.2), is defined as [313]

$$g(E) = \frac{\sqrt{2}}{n^b_{\mathrm{iD}} + n^s_{\mathrm{iD}}} \frac{E}{\sqrt{\pi m}} \left\{ n^b_{\mathrm{iD}} \left(\frac{2}{T^b_{\mathrm{iD}}}\right)^{3/2} \exp\left(-\frac{E}{T^b_{\mathrm{iD}}}\right) + n^s_{\mathrm{iD}} \left(\frac{2}{T^s_{\mathrm{iD}}}\right)^{3/2} \exp\left(-\frac{E}{T^s_{\mathrm{iD}}}\right) \right\}.$$

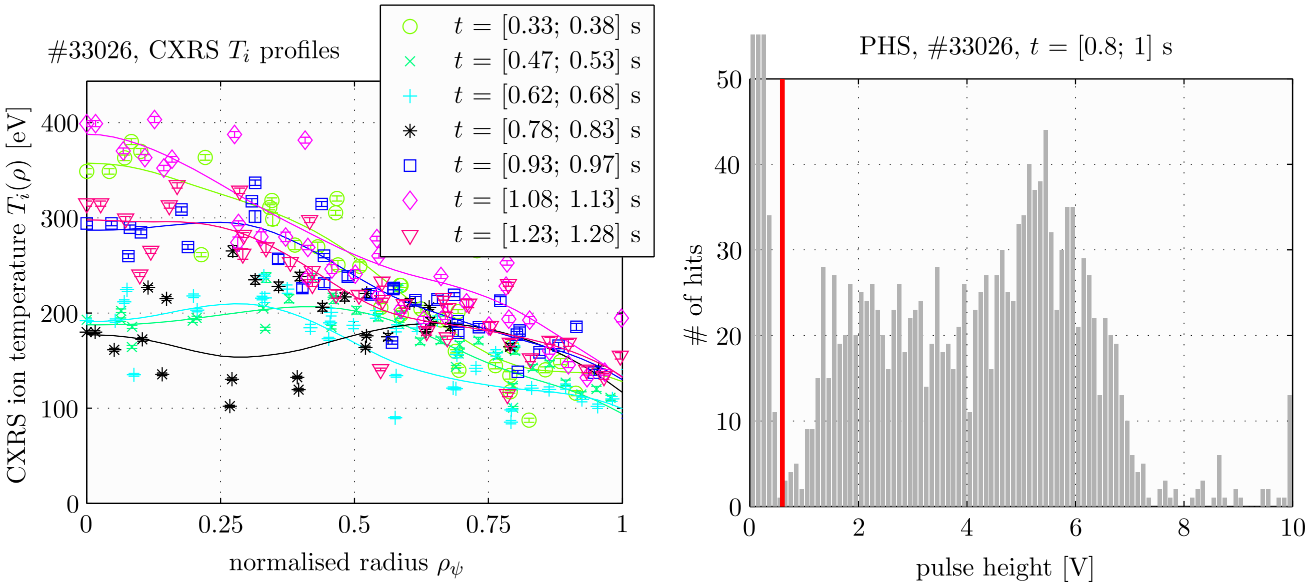

(a) Bulk ion temperature.

(b) Neutron detector PHS.

Figure 6.5.9: (a) Charge-exchange recombination spectroscopy bulk ion temperature profiles. The core ion temperature drops by a factor of two upon the start of EC injection and recovers once the gyrotron power flattop is reached.
(b) Pulse height spectrum of the neutron detector dominated by neutrons born in fusion reactions induced by the ions populating the suprathermal tail of the distribution function.

The resulting neutron yield profile valid at $t = 1$ s is shown in figure 6.5.10a.

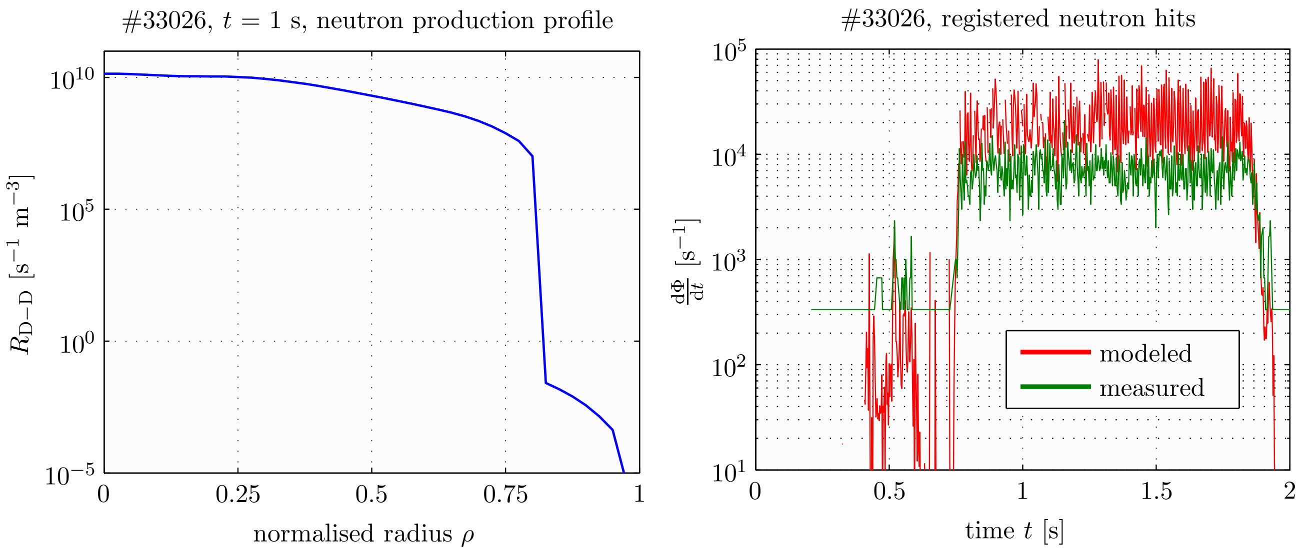

(a) Neutron yield profile.

(b) Neutron production trace.

Figure 6.5.10: (a) Numerically calculated neutron emission profile of discharge #33026 assuming the spatial profile of the bi-Maxwellian ion distribution function determined in section 6.3.
(b) Measurement and simulation of the neutrons registered with the neutron detector during the same discharge. Agreement within a factor of 2.

The discontinuity at $\rho = 0.8$ results from the truncated fast ion density profile. The measured neutron pulse height spectrum is shown in figure 6.5.9b and the benchmark of measured and calculated neutron detector counting rate is shown in figure 6.5.10b. Measurement and simulation, following this long process, agree within a factor of 2 !

6.6 Ion acceleration by sawteeth

In TCV plasmas exhibiting a fast ion population, a remarkable effect of the sawtooth crash on the ion distribution is observed. This is shown on figure 6.6.1, where the three top traces show DMPX soft X-ray channels at radii outside, very close to and just inside the inversion radius. The last plot shows time traces of a selection of the deuterium CNPA channels. With each sawtooth collapse (period $\Delta t \approx 12$ ms), the neutral flux is strongly enhanced (here the flux is tripled). This behaviour is observed on all CNPA channels, independent of energy. The discharge shown here uses the same model as for #30477 shown at the beginning of this chapter, except for a higher current ($I_{\mathrm{p}} = 160$ kA). An increase in current causes the core safety factor to drop below 1, eq.(1.5.4), and sawteeth appear.

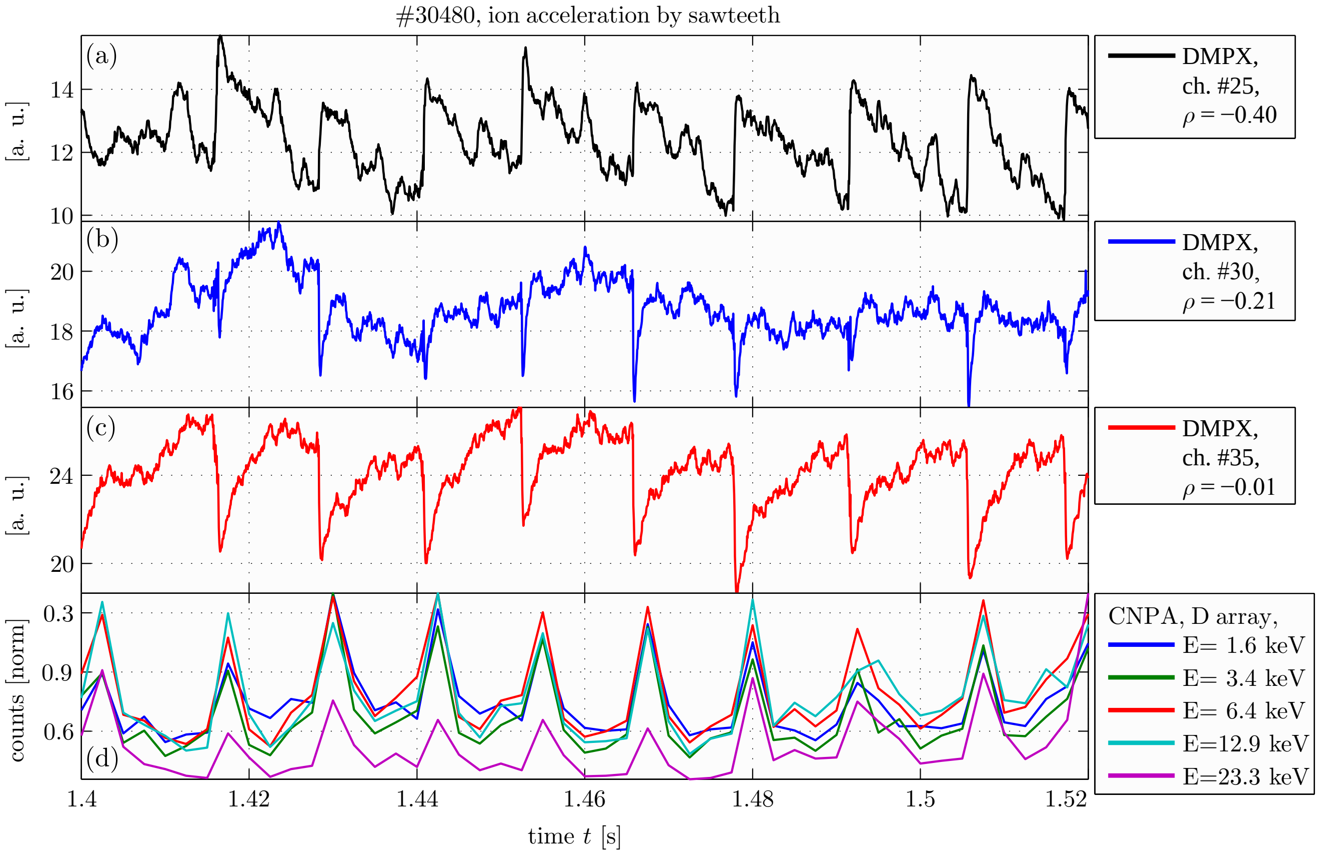

Figure 6.6.1: Traces (a) to (c) show time traces of the electron temperature of a sawteething plasma measured with the top detector of the DMPX. (c) looks at the magnetic axis, (b) at the inversion radius ($\rho = 0.2$) and (a) has a radius of tangency further outside. The characteristic sawtooth evolution is clearly visible. (d) shows time traces of the neutral particle flux encountered in deuterium channels #3, #6, #9, #12 and #15 of the CNPA. All CNPA channels show the same behaviour, that is a strong increase of the neutral flux immediately after the sawtooth crash.

Another example is shown in figure 6.6.2b (discharge #35502), where the launcher mirror angle of the co-injected ECCD was swept out and back in such a way that the current is initially driven inside ($t = 0.65$ s), later outside ($t = 0.8$ s) and finally again inside the $q = 1$ surface ($t = 0.9$ s). Shown are the core DMPX channel #29 and the CNPA deuterium channel #4. The local modification of the current profile engenders a change of the sawtooth period in the range 3...15 ms.

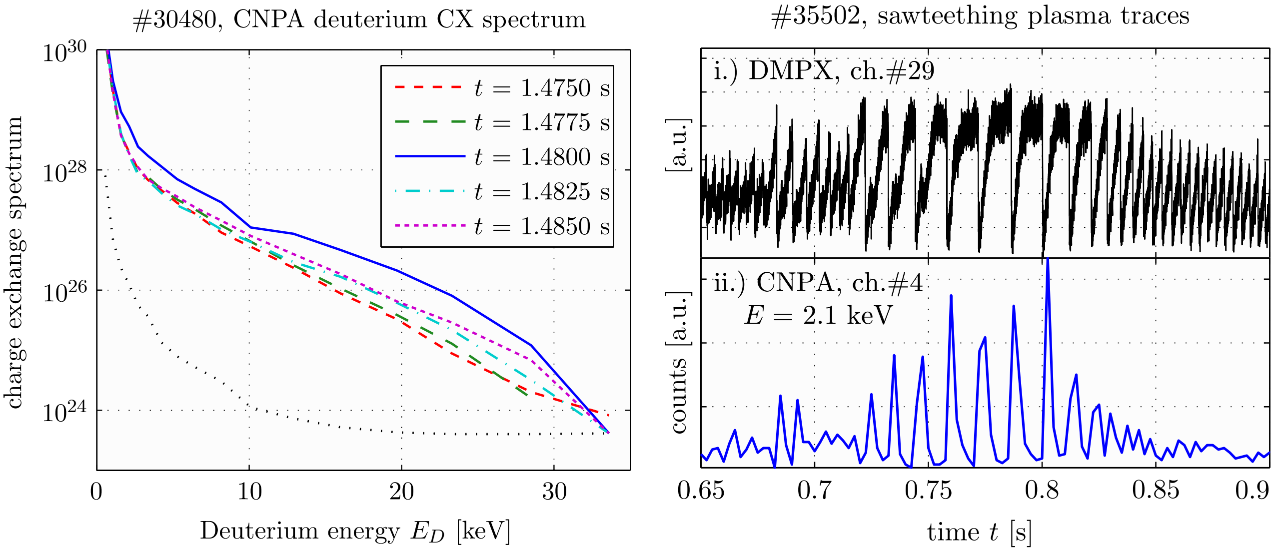

(a) One sawtooth cycle of #30480.

(b) Sweeping sawteeth #35502.

Figure 6.6.2: Left figure: Deuterium charge exchange spectrum prior, at (t = 1.48 s) and after the sawtooth crash. After the crash, the suprathermal population is strongly enhanced but decays within the CNPA time resolution to the strength measured before the crash.
Right figure: Sawteeth with varying period and amplitude.

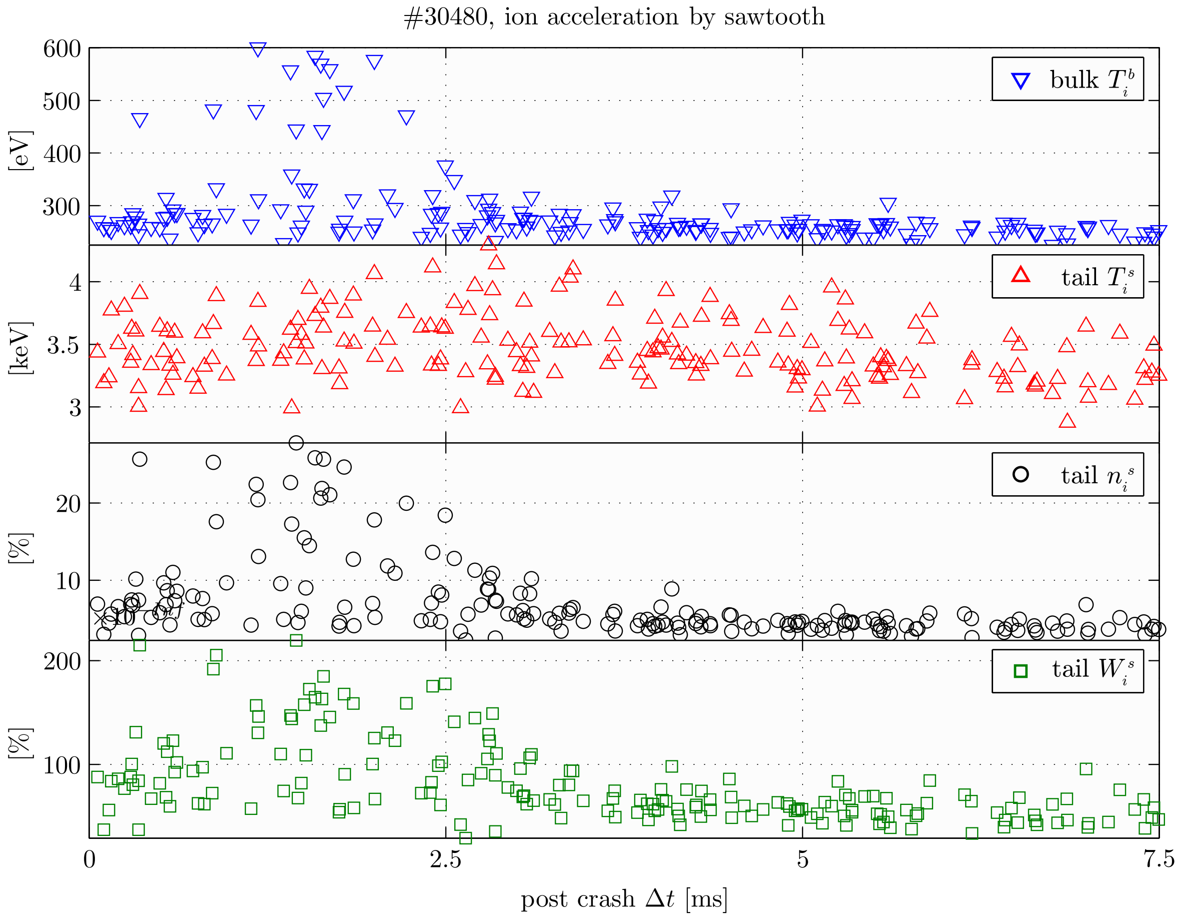

Figure 6.6.3: Representation of the CNPA measurement as a function of time after the sawtooth crash. The temperature of the suprathermal population is not modified, but its density transiently increases by a factor of five.

The evolution of the CNPA deuterium charge exchange spectrum during a complete sawtooth cycle is shown in figure 6.6.2a. The crash is initiated at $t = 1.4775$ s. The CNPA measurement at this time doesn't show yet any effect because its neutral flux was collected in the 2.5 ms preceding this time. The first measurement after the crash includes therefore the neutrals which have ventured the crash. Channel #11 ($E_\mathrm{D} = 10$ keV) saturates. The fast ion temperature is not substantially modified, with only the fast ion tail strength increased. This is more clearly seen on figure 6.6.3, where the usual ion parameters, calculated for each single CNPA measurement, are plotted against post crash time. The latter was determined from the core DMPX signal. Remind again that each CNPA measurement is accumulated in the 2.5 ms preceding the acquisition. The maximum ion response is seen in the spectrum measured up to 1.5 ms after the crash. The rise of the bulk temperature is due to the strong high temperature tail, that even contributes to the lowest energy channels. The tail temperature, whose scatter is indicated by the error bar, is not affected by the sawtooth.

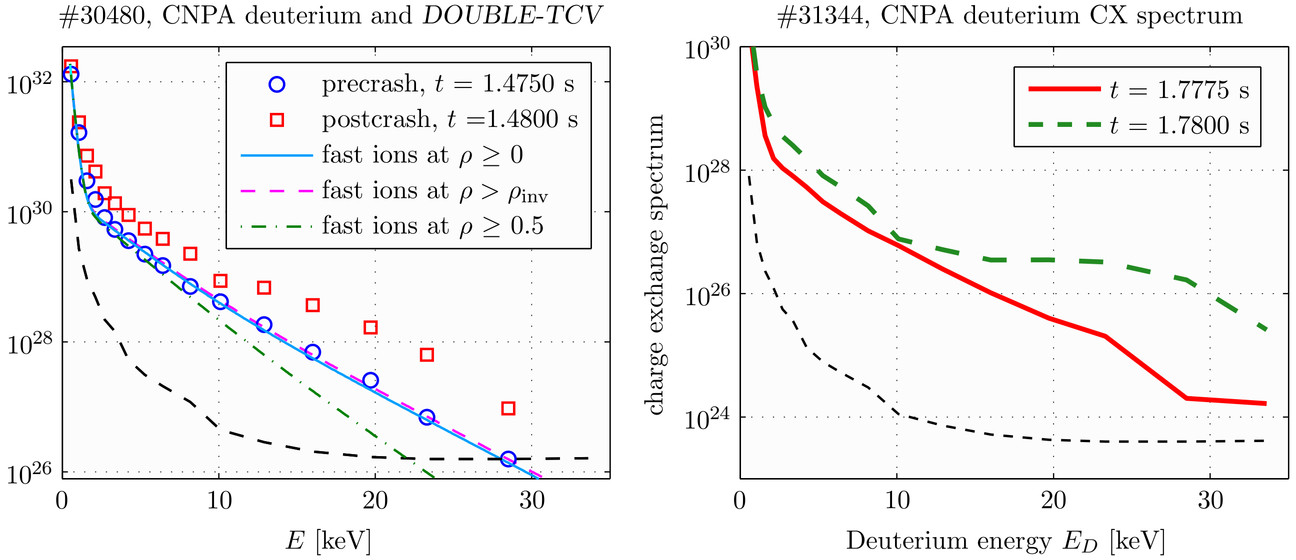

(a) Redistribution of fast ions.

(b) Distribution function oddities.

Figure 6.6.4: (a) Simulation of a possible post sawtooth crash fast ion distribution in space. The symbols show the CNPA measurement before and after the sawtooth crash. A displacement of the fast ions from the core to the location just outside the inversion radius does not lead to an enhanced neutral flux. Locations even further outside result in weaker neutral spectra because of sparser fast ion concentration. (b) Example of a strong impact of the reconnection event on the fast ion distribution function. The CNPA channel at $E = 10$ keV is again close to saturation.

One may think that the reconnection event expels fast ions from the core to the edge, where neutral particles are far more abundant, thereby leading to a higher NPA signal. To test for this possibility, the fast ion content of discharge #30480 was modelled with *DOUBLE-TCV* before the sawtooth crash ($t = 1.475$ s, $T_i^s(0) = 3$ keV, $n_i^s = 4$ %). During the crash, we then assume that all the fast ions within the inversion radius (here $\rho_\mathrm{inv} = 0.27$) are getting expelled to the location just outside ρ_inv as the q-profile is constant up to this radius such that there is no confinement within ρ_inv. The total number of fast ions to be displaced is obtained by integration of the fast ion density profile over the core volume. These ions displaced outside the reconnection site, gives a suprathermal hydrogen and deuterium fraction of 60 % and 12 % respectively, at $\rho = 0.3$. Inside this radius, the suprathermal temperature and density is set to zero (only the core profiles are of importance here). *DOUBLE-TCV* is then rerun with this arrangement, with the same profiles of the background plasma as before the crash.

This represents an upper limit in the estimation of the neutral flux since the postcrash electron density and temperature both increase outside the inversion radius, and the expulsed neutral flux attenuation is thus enhanced.

Figure 6.6.4a combines the simulation with the CNPA data and shows that the displacement of all core suprathermal ions to the reconnection site has a negligibly small effect on the resulting neutral flux spectrum. In fact, the fast ions occupy a rather small volume in the plasma core, when they are redistributed in radius, they are simply relocated into a much larger volume. The number of these fast ions which can reach the CNPA after neutralisation is therefore considerably reduced. Figure 6.6.4a illustrates also a fast ion relocation to $\rho = 0.5$, the resulting CX spectrum would be much weaker.

The enhancement of the high energy neutral flux requires, therefore, the acceleration of additional ions, on a very fast timescale. Stronger sawteeth result in a clear distortion of the neutral flux spectrum. This is not so clear with discharge #30480, but with #31344, shown in figure 6.6.4b, the high energy end of the distribution is clearly preferentially populated.

In contrast to the low density X2 heated discharges discussed here, in ohmic plasmas, even with large crash amplitudes, a perpendicular fast ion acceleration is not observed. For the acceleration mechanism to be effective, the fast ions need therefore already to have been present in the plasma before the crash.

6.7 Summary of the observations

From the previous sections it is clear that the ion acceleration observed on TCV is of anomalous, non-collisional nature. The fast time scales of ion heating need wave–particle interactions to be at play. The ion behaviour strongly correlates with the bulk electron temperature. The electron drift velocity, which is not readily ascertainable experimentally, seems to play a key role, as the fast ion parameters scale with the same parameters that describe the ECCD current drive efficiency (e.g. electron density, electron temperature).

To summarise, the fast ions

- are accelerated on a time scale of the order of some 100 μs and
- are thus the result of a non-collisional wave–particle interaction,
- appear to owe their existence to the presence of ECCD,
- are satisfactorily described by a suprathermal Maxwellian population,
- reach a state of equilibrium when the EC heating and the plasma parameters are steady-state,
- do only appear if the EC power is deposited inside the inversion radius,
- become more abundant upon internal magnetic reconnection events and
- their parameters depend on the plasma shape such that the fast ion confinement is improved if the internal kink is more stable

More specifically, the fast ion temperature

- transiently reaches, but doesn't exceed, the bulk electron temperature,
- is somewhat lower than $T_e^b(0)$ when the fast ion population is in steady-state,
- is identical for the hydrogenic species,
- becomes hotter when heavier impurities are admixed (although the current drive efficiency is expected to decrease),
- has a parabolic profile, of similar shape to the bulk profile

and the fast ion density

- increases linearly with the auxiliary heating power,
- scales with the inverse of the mass of the species considered,
- has a density fraction generally below 20 % of the bulk ion density and
- is a constant fraction of the bulk density profile, over the whole core plasma radius

6.8 Potential mechanism for anomalous ion acceleration

On the basis of the collected data the most likely process causing the ion energisation will now be identified. The theory of potential mechanisms leading to mostly perpendicular ion acceleration are quickly reviewed, discussed in the frame of TCV and possibly compared to studies carried out on other devices. The discussion is limited to mechanisms obviously involving EC waves, that is parametric decay (section 6.8.1) and current driven microinstabilities (section 6.8.2).

6.8.1 Parametric decay instabilities (PDI)

Parametric processes are nonlinear phenomena driven by large wave amplitudes, i.e. occurring in the vicinity of a resonance layer and are frequently observed in laboratory plasmas [314]. A widely studied example of a parametric decay instability is the three wave coupling process, where a high frequency electromagnetic pump wave (frequency ω_0, wave vector $\mathbf{k}_0$) of a power density exceeding a certain threshold, parametrically excites other waves. If the interaction takes place in space and time, the pump wave energy may be efficiently transferred to the new decay wave modes, one of which is electrostatic (low frequency) and the other is also electromagnetic, with frequency close to that of the pump wave. The process conserves energy and momentum, i.e.

$$\begin{cases} \omega_0 = \omega_{\mathrm{HF}} + \omega_{\mathrm{LF}} \\ \mathbf{k}_0 = \mathbf{k}_{\mathrm{HF}} + \mathbf{k}_{\mathrm{LF}} \end{cases} \tag{6.8.1}$$

In the frequency range of electron cyclotron pump waves, such a process takes place at the upper hybrid resonance layer (UHR). The electric field of an extraordinary EC wave is strongly enhanced (i.e. becomes quasi electrostatic) when the wave approaches the UHR layer, where the wave decays into an electrostatic lower-hybrid (LH) mode of frequency

$$\omega_{\mathrm{LH}} \simeq \frac{\omega_{\mathrm{p}i}}{\sqrt{1 + \left(\dfrac{\omega_{\mathrm{pe}}}{\Omega_{\mathrm{ce}}}\right)^2}} \tag{6.8.2}$$

and an electromagnetic electron Bernstein mode (discovered by Ira Bernstein [315]).

Parametric decay was theoretically [316] studied and observed (measurement of ω_{LF} and/or ω_{HF}) in numerous dense, hot and magnetised plasma experiments, e.g. Versator II [317] at MIT, FT-1 [318] at IOFFE, Wendelstein W7-A [319] in Garching and TCA [320, 321] in Lausanne. In all these experiments, the EC wave was launched quasi-perpendicularly to the magnetic field (where the three-wave interaction is strongest [184]), at the fundamental cyclotron frequency in X-mode, from the high field side (except in W7-A(‖)). ECR first-pass absorption in these experiments was generally quite weak (less than 50 %) such that a considerable fraction of the injected wave continued to propagate to the UHR, where the parametric process was identified (the electron Bernstein branch of the hot plasma dispersion relation is connected to the X-mode branch at the UHR). The UHR (where the pump wave frequency matches $\omega_{\mathrm{UH}}^2 = \omega_{\mathrm{pe}}^2 + \Omega_{\mathrm{ce}}^2$) is located on a curved layer close to the outer edge of the torii (see the illustration in figure 6.8.1). The Bernstein wave travels back to the vertical ECR plane in the core, where it is efficiently absorbed by the electrons [322] (even for perpendicular propagation, magnetic shear ensures that $k_\parallel \neq 0$, otherwise absorption would not take place). In those experiments where the ion temperature was measured, strong ion heating (fast ion tails) was found(**). The heating was attributed to the lower hybrid waves, which have phase velocities in the range of the ion velocities, such that the wave-particle interaction becomes effective and strongly damp the waves on the ions. The process depends on a threshold for decay, so the ion heating shows a strongly non-linear dependence on the pump wave power density [317].

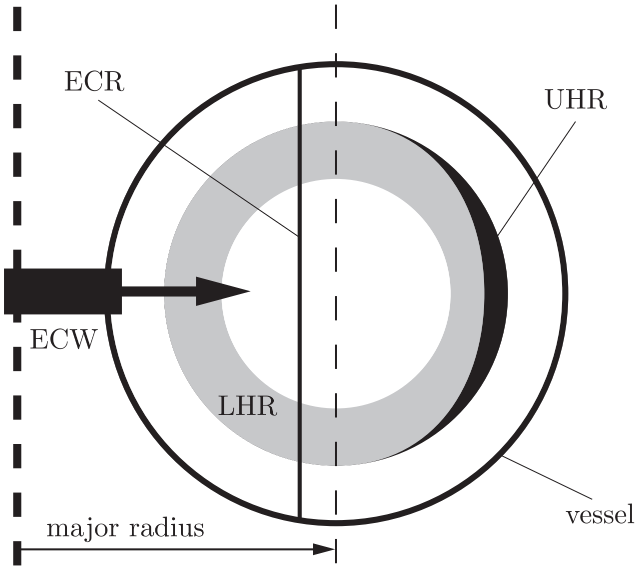

Figure 6.8.1: Sketch of the poloidal cross-section of the FT-1 tokamak. The electron cyclotron waves (ECW) are injected from the high field side, the electron cyclotron (ECR), upper-hybrid (UHR) and lower-hybrid (LHR) resonance layers are indicated by the labels.

With the EC injected with ordinary polarisation (this mode has a cut-off at half the density of the X-mode), no ion heating was observed(††).

(‖) In the stellerator the wave was launched from the low field side, in O-mode. The O-mode power was only absorbed by half upon first pass through the ECR layer and was reflected back from a polarisation twisting mirror mounted on the inner vessel wall.

(**) On TCA, the total ion stored energy increased by up to 60 % during ECRH. The fast ions have a tail temperature of $\lesssim$500 eV whereas the bulk ion temperatures range below 200 eV. The tail strength is strongest in low density discharges and the ratio between hot and cold ion population reaches 25 %.

(††) Except on TCA, where the O-wave was reflected at the wall and reentered the plasma in X-mode.

In FT-1 the necessary condition for ion heating, the accessibility of the UHR to the wave, was demonstrated by lowering the magnetic field, such that the UHR was moved outside the plasma and ion heating was no longer observed. On TCV, to allow the X2 EC waves access to the UHR, would require launching from the HFS since the UHR is shadowed from the LFS by the left hand cut-off (figure 5.2.4b) and PDI cannot occur. Injecting second harmonic ordinary mode (O2, with the wave electric field being parallel to the toroidal magnetic field) instead of X2 into a low density plasma could be possible, the former is not in cut-off and is generally poorly absorbed on its first pass through the plasma. One may eventually hope for a polarisation change upon reflection on the inner chamber wall, such that the UHR is reached from the HFS. However, low density O2 plasmas, due to the poor power absorption of less than 15 % [323], are of little interest on TCV and this polarisation was only attempted in the early days of the availability of the gyrotron sources. During O2 injection, the VNPA did not measure any difference in the charge exchange spectrum in respect to the ohmic phase(‡‡). There are however legitimate doubts over a wave polarisation change at the wall.

Recently, O2 was injected into high density TCV plasmas, such that the EC beam mode converts to extraordinary polarisation inside the plasma behind the UHR. These discharges are shortly reviewed in the next section.

6.8.1.1 Electron Bernstein wave heating (EBWH) and emission (EBE)

Electron Bernstein waves (EBW) [315] experience very localised damping on electrons in the region where the wave frequency matches the Doppler broadened electron cyclotron resonance frequency or its harmonics. Unlike the electromagnetic extraordinary and ordinary modes, the absorption remains strong even at high harmonics of the electron cyclotron frequency Ω_{ce}. EBW do not have any density cutoffs inside the plasma and can, therefore, access plasmas of arbitrary density for frequencies above Ω_{ce}. These features of EBW present a possibility of efficient means for electron cyclotron resonance heating and current drive in high beta plasmas, particularly in spherical tokamaks, where the X- and O-mode propagation into the plasma may only be assured at high Ω_{ce} harmonics, leading to weak damping of these modes inside the plasma. However, EBW are electrostatic wave modes and cannot exist in vacuum, thus requiring excitation by mode conversion from an externally launched electromagnetic mode.

In tokamaks, the first experimental demonstration of EBW heating was performed in 2001 on the WT-3 tokamak [324], where a wave was launched perpendicular to the magnetic field from the LFS in O-mode, which converted into X-mode by a polariser at the inner vessel wall and then reflected back towards the plasma. These experiments were made at low density, below the O-mode density cut-off. Similar studies were conducted on the COMPASS-D tokamak where EBW were used to drive noninductive currents (EBCD) [325], here the waves were injected using high field side launch.

When HFS launch or mode conversion outside the plasma are not available, a double-mode conversion process [326] offers a practical possibility for electron Bernstein wave heating (EBWH). At a particular launching angle, a quasicircularly polarised ordinary-mode (O-mode) wave converts to extraordinary (X) mode at the plasma cutoff. This mode conversion requires an O-wave oblique launch near an optimal angle. After this first mode conversion, the wave propagates back towards the plasma edge until it encounters the UHR layer, where a second mode conversion from X wave into the Bernstein (B) wave occurs. This conversion occurs with near 100 % efficiency in a hot plasma [326].

(‡‡) Discharges #14916, #14920.

For EBW's there is no density limit, they can propagate towards the plasma centre, where they are absorbed by the bulk electrons near the electron cyclotron resonance layer or, in the non-resonant case, by collisional multiple pass damping. This so-called O-X-B heating scheme was successfully demonstrated for the first time in the stellarator W7-AS [327], in the high-density high confinement mode as early as 1997.

The first tokamak demonstrating EBW in overdense plasmas at a density $n_e(0) \geqslant 10^{20}$ m^{-3}, that is above the O2 cutoff at about $n_e(0) = 8.7 \times 10^{-19}$ m^{-3}, was the Tokyo Spherical Tokamak 2 (TST-2) using the X-B scheme from the LFS with the X mode tunnelling through the evanescent layer with highly reduced density scale length due to a local limiter [328].

The first true tokamak double mode-conversion EBW experiment (O-X-B scheme) was performed on TCV, in an overdense H-mode [329] tokamak plasma [29, 330]. Absorbed-power fractions exceeding 60 % were reported.

The strong EBW absorption also implies that electron Bernstein waves are emitted (EBE) by a thermal plasma [331]. These waves can then mode convert to the X- then O-mode and be observed externally to the plasma (B-X-O conversion). On TCV, EBE was experimentally confirmed [332] by diagnosing overdense plasmas around the optimum toroidal angle window for the B-X-O conversion using the LFS ECE radiometer connected to the steerable mirror of the 7th launcher (section 5.3.5).

The analysis of the overdense TCV plasmas with certified EBWH with the VNPA(§§) did not however show any signature of anomalous ion heating.

6.8.2 Current driven turbulence (CDT)

The quest for plasma heating in excess of the classic Joule dissipation, driven by the wish to progress towards ignition, has always attracted large interest in the field of plasma physics. The actual research of turbulent plasma heating commenced with the reports about current driven, turbulent heating of dense plasmas to several hundreds of eV in linear configurations by the Russian team led by Babikin [333]. This team had achieved a very efficient coupling between their system and the external energy source, due to an apparent increase of the plasma resistance up to a level comparable with the impedance of the source. Very soon it was clear that the anomalous resistivity was a macroscopic manifestation of current-driven turbulence (CDT). Their results gave rise to strong research activity exploring CDT, with numerous projects, initially especially in the former Soviet union [334], culminating in a feasibility study to apply turbulent heating in a tokamak [335] and its ensuing experimental demonstration on the TRIAM-1 [336] and TORTUR [337] tokamaks.

CDT experiments are sometimes equipped with giant capacitor batteries, whose charge is dissipated into the plasma in microseconds. The toroidal electric fields driving the current range from small fractions to multiple thousands of the Dreicer electric field.
CDT is different to the beam-plasma interactions intensely studied at this time as it is the response of virtually all plasma particles to a large applied electric field. The anomalous plasma conductivity of CDT plasmas scales as $\sigma \sim 1/\sqrt{E}$ where E is the applied toroidal electric field.

(§§) owing to lack of viable plasma targets positioned at the vessel midplane, most of the discharges were placed at $z = 20$ cm, such that the CNPA is of no use.

The enhancement of the resistivity over the classical Spitzer-Härm value, eq.(1.6.2), was found to be independent of the machine (including tokamaks, e.g. TFR and Alcator), and scales [338] with the ratio of the applied electric field to the Dreicer field(¶¶), eq.(3.4.4),

$$\frac{\sigma_{\text{Spitzer}}}{\sigma_{\text{exp}}} \simeq 10 \frac{E}{E_{\text{Dreicer}}}. \tag{6.8.3}$$

Although such a scaling suggests that an universal mechanism is responsible for the turbulence, almost all known nonlinear processes, from weak quasi-linear to strong turbulence, have been identified in CDT experiments. Common to all experiments is a rapid plasma heating and collisionless dissipation, i.e. collisions do not play any role.

With time, many CDT theories have been proposed. The hydrodynamic Buneman-Budker instability [339], an ion–electron two stream instability, excited by strongly drifting electrons, leading to the scattering of the latter such that their run away is inhibited. A possible scenario is the following: When the external electric field is applied, the electron acceleration is initially very large and the Buneman-Budker instability may be driven unstable. The turbulence threshold requires $v_{\text{d}} > 8\, v_{\text{the}}$ and develops independently of the ratio of electron and ion temperature. As the turbulence develops (mode frequency $\omega \simeq \omega_{\text{pe}}/2\sqrt[3]{m_e/m_i}$) the large amplitude electric fields efficiently scatter the circulating electron trajectories and the net electron drift velocity therefore decreases and eventually thermalises the electron drift energy. The increase of the thermal electron energy then quenches the instability. If the electric field has not decayed yet, the electrons suffer further acceleration and the whole cycle may repeat again with the effect that the electron thermal and drift velocities steadily increase with each cycle, but their values remain close. Note that the anomalous resistivity becomes steady-state in some CDT experiments and the scaling, eq.(6.8.3), implies that the mean electron drift velocity stabilises at about $0.1\, v_{\text{the}}$. This oscillatory behaviour of the turbulence cycles have been reproduced in computer simulations [340–342]. The effect of the turbulence is such that the electrons are decoupling from the bulk distribution at a rate less effective than for free acceleration.

However, the Buneman instability requires giant electron drift speeds (with respect to the ions) and is difficult to achieve in turbulent heating experiments. The kinetic ion-acoustic instability is much less restrictive, and is a far more plausible mechanism at moderate drift velocities, but requires the ion temperature to be smaller than the electron temperature for destabilisation ($T_e > 3\, T_i$). The properties of the ion-acoustic instability are discussed in detail in section 6.8.2.2. In CDT experiments, the ion-acoustic turbulence (IAT) case corresponds to the so-called accelerative regime, with $E/E_{\text{Dreicer}} \leqslant 0.1$.

Another important turbulence phenomena observed in CDT experiments is the fan instability, which is driven by runaway electrons and grows when an electron temperature anisotropy appears such that $T_{\parallel e} \gg T_{\perp e}$. In CDT experiments the fan instability develops in the restricted runaway regime, e.g. for important applied electric fields $E/E_{\text{Dreicer}} > 0.1$. This instability is discussed in the next section.

The degree of magnetisation of the plasma, i.e. the ratio of electron plasma and electron cyclotron frequency, is a very important parameter of CDT as it influences the polarisation of the excited plasma modes.

(¶¶) The Dreicer field is the field by which an electron gains a drift velocity equal to the electron thermal speed within the electron–ion collision time.

6.8.2.1 Runaway beam instabilities

The formation of a runaway tail is frequently observed in tokamaks, especially at low densities. The runaway rate continuously grows when the toroidal electric field exceeds the Dreicer field [343]. As a result, the runaway electrons gain parallel energy and their distribution function becomes highly anisotropic, i.e. exhibits an extended tail along the direction of the magnetic field, such that $T_{e\parallel} \gg T_{e\perp}$. This anisotropy can be a cause of classical beam–plasma instabilities through the resonance at

$$\omega = k_\parallel v_\parallel - n\,\Omega_{ce}, \tag{6.8.4}$$

where n is an integer. The Čerenkov resonance $n = 0$ is stabilising as long as the distribution function is monotonically decreasing in the parallel direction. The lowest order anomalous Doppler resonance $n = +1$ is destabilising provided the anisotropy is sufficiently strong, i.e. [344]

$$k_\parallel \left|\frac{\partial f_e}{\partial v_\parallel}\right| < \frac{\Omega_{ce}}{v_\perp}\left|\frac{\partial f_e}{\partial v_\perp}\right|. \tag{6.8.5}$$

At the $n = 1$ resonance, there are several weakly damped directly excited natural modes (i.e. they do not depend on the evolution of the turbulence), including the magnetised electron plasma mode $\omega = (k_\perp/k)\,\omega_{\mathrm{pe}}$ and the lower hybrid mode, ω_{LH}, eq.(6.8.2), which propagates at highly oblique angles with respect to the magnetic field ($k_\perp \gg k_\parallel$).
The pioneering work of Parail and Pogutse [345, 346] has determined the linear instability mechanism of the so-called fan instability, which arises when runaway electrons interact with low frequency modes through the anomalous Doppler resonance provided that the electron beam velocity satisfies

$$v_b \gtrsim 3\left(\frac{\Omega_{\mathrm{ce}}}{\omega_{\mathrm{pe}}}\right)^{3/2} v_{\mathrm{the}}\sqrt{\frac{E_{\mathrm{Dreicer}}}{E}}. \tag{6.8.6}$$

The instability tends to isotropise the runaway beam in the velocity range $v_\parallel \simeq v_b \simeq \Omega_{\mathrm{ce}}/k_\parallel$. At the same time, the Čerenkov range, characterised by $v_\parallel \simeq \omega/k_\parallel$, tends to form a plateau through the quasi-linear wave–particle interaction. Since the damping rate due to the Čerenkov resonance is proportional to $\partial f_e/\partial v_\parallel$, the plateau formation makes Čerenkov damping less effective. Consequently, even after plateau formation, the instability continues to grow until the whole runaway beam becomes isotropised. At the same time, the isotropisation in the Doppler resonance range $v_\parallel \simeq \Omega_{\mathrm{ce}}/k_\parallel$ leads to the formation of a positive slope, $\partial f_e/\partial v_\parallel > 0$, through pitch angle scattering, and a ‘fast’ Čerenkov mode with a frequency $\omega \simeq \omega_{\mathrm{pe}}$ may be excited.
This interaction brakes the unimpeded acceleration of electrons by the applied electric field and may lead to anomalous ion heating [347]. The experiments conducted on the TM-3 tokamak [348] nicely fit into the fan instability model.

6.8.2.2 Ion-acoustic turbulence (IAT)

The current driven ion acoustic instability has been predicted at the end of the 1950ies by Jackson [349] and Jackson [350]. The onset of the ion-acoustic turbulence (IAT) may proceed in a way similar to the Buneman-Budker instability described above. Note that the latter goes continuously over into the ion-acoustic instability when the electron drift speed drops below the Buneman-Budker instability threshold. Approximative conditions for the onset of IAT are derived in appendix B (linear stability analysis).

The solution of the kinetic dispersion relation yields a mode frequency, eq.(B.2.12), of approximately

$$\omega^2(k) = \left(\omega_{\mathrm{p}i}^2\,\lambda_{\mathrm{D}i}^2 + 3\,v_{\mathrm{th}i}^2\right) k^2 \lesssim \omega_{\mathrm{p}i} \tag{6.8.7}$$

and, at low ion temperatures, such that the Landau wave damping on the ions is weak, a positive growth rate of the order of $\sqrt{m_e/m_i}$, eq.(B.3.4),

$$\gamma_{\mathbf{k}} = -\sqrt{\frac{\pi}{8}}\,\sqrt{\frac{m_e}{m_i}}\,k\,c_s\left[1 - \frac{u_k}{c_s} + \sqrt{\frac{m_i}{m_e}\left(\frac{T_e}{T_i}\right)^3}\,\exp\left(-\frac{T_e}{2\,T_i} - \frac{3}{2}\right)\right] \tag{6.8.8}$$

and shows that the instability is operative at a modest drift speed u_k, exceeding the ion sound speed c_s, eq.(B.2.14), particularly in a nonisothermal plasma having $T_e > T_i$. However, the excitation of ion modes decreases as the ion temperature becomes closer to the electron temperature, because of stronger ion Landau damping, which strongly influences the critical drift velocity. Note that Maxwellian distributions were assumed for electron and ion velocities, the instability threshold may markedly deviate for non-Maxwellian situations.
The linear destabilisation(***) of IAT was studied extensively in theory and was experimentally confirmed in mercury vapour [351, 352], helium [353] and argon [354, 355] discharges.

Since the early experiments on CDT, where the turbulence level substantially exceeds the linear regime, the key role played by IAT in non-linear effects like the creation of anomalous resistivity was recognised. Explanations of the experimental findings required knowledge of the turbulence spectrum at the saturation level of the instability. Investigations were undertaken, both analytically [356] and numerically [357]. Among the various models of IAT developed since the 1960s, the lowest order non-linear, e.g. quasi-linear formulations have proven the most successful. The most advanced analytical theory available today was developed by Bychenkov et al [358] and the numerical simulations of IAT most relevant for tokamak plasmas were probably (there have been attempts of various complexity by many researchers) achieved by Ishihara et al [359].

The early theoretical contributions to the understanding of IAT considered simplistic plasmas, e.g. in absence of a confining magnetic field, and are not applicable to tokamaks. Ions are practically unmagnetised ($\omega_{\mathrm{c}i} \ll \omega \lesssim \omega_{\mathrm{p}i}$) in tokamaks but electrons are magnetised (on TCV $\omega_{\mathrm{pe}} \simeq \omega_{\mathrm{ce}}$), introducing a privileged direction in the electron dynamics. Many theories considered therefore one-dimensional models for the turbulence evolution (e.g. [360] and [361]). These simulations suffered from a inability to explain the saturation of the turbulence. Appert et al [362] suggested that the saturation of the instability may rely intrinsically on the multidimensional nature of turbulence. Later, the inclusion of the induced scattering by ions (nonlinear Landau damping) was analytically shown [358] to play an essential role for the instability to acquire a quasi-steady state of turbulence. This was successfully confirmed employing a three-dimensional quasilinear approach by Ishihara et al [363]. The addition of the confining magnetic field strongly affects the evolution of the instability [359].

An important observation, practically always made in CDT experiments, is the formation of a high-energy tail in the ion energy distribution function. The formation of the tail was categorically ascribed as a manifestation of IAT, although quantitative estimations of the observed ion populations were rarely possible.

(***) When the fluctuation energy is small enough such that the linear stability analysis remains valid.

One common feature of the ion heating is that the ion tail temperature approaches the electron temperature after the dissipation of the heat pulse. The later numerical experiments always strived to reproduce the experimentally observed IAT induced ion energisation. The most recent works, which retain the ion dynamics self-consistently, give an account of the onset, growth and subsequent saturation of IAT and provide a quite satisfactory picture of the high complexity of ion heating. In fact, as the wave amplitude grows, bulk ions acquire a large sloshing energy, and time reversible nonresonant diffusion(†††) [364] may become significant. Cold bulk ions, which in the numerical analysis are assumed to have low temperature compared with electrons, diffuse towards the ion acoustic resonant region where $v \simeq c_S$, thus forming a high-energy ion tail with a temperature of order T_e. Once those ions reach the resonance region, strong resonant interaction takes place and significantly contributes to wave damping. In linear theory, the growth rate profile $\gamma(\mathbf{k})$ peaks in the direction of the electron drift, that is, in the direction of $\theta = 0$, where θ is the angle between $\mathbf{k}$ and $\mathbf{v}_\mathrm{d}$, the drift velocity. However, the saturated multidimensional ion acoustic turbulence spectra revealed in computer simulations often have a peak off axis, $\theta = 30 \ldots 50^\circ$. Resonant ions, which diffuse from the nonresonant region, preferentially damp the modes with small θ, because this is the direction of maximum growth rate, and thus most active diffusion takes place. Off-axis modes remain excited. Therefore, at saturation, the spectrum is dominated by modes having large propagation angles with respect to the electron drift velocity. This so-called anomalous k-spectrum was revealed by cross-correlation measurements [365, 366]. It should be noted that the mechanism of nonresonant diffusion is insensitive to the initial ion temperature. In the simulation of Ishihara [359], even with extreme ratios of ion and electron temperatures, e.g. $T_e = 100\,T_i$ initially, the high-energy ion tail formed at saturation has a population $n_i^s = 0.1 \ldots 0.2\,n_i^b$, which can only be explained by the nonresonant diffusion of bulk ions towards the resonant region.

One important aspect of IAT is its role played in creating anomalous resistivity. Being a particle–wave–particle interaction, with a single wave having simultaneous resonance interactions with electrons and ions, IAT is efficient for stabilising the electron drift speed thus quenching electron runaway. The resonance condition can be derived from quantum mechanics [367], whose energy and momentum conservation laws, for electrons and ions, are written

$$\begin{cases} \hbar\omega = m_e\, v_{e\|}\, \mathrm{d}v_{e\|}, \\ \hbar k_\| = m_e\, \mathrm{d}v_{e\|}, \\ \hbar\omega = m_i\, \mathbf{v}_i \cdot \mathrm{d}\mathbf{v}_i, \\ \hbar\mathbf{k} = m_i\, \mathrm{d}\mathbf{v}_i, \end{cases}$$

such that the resonance condition, by substitution,

$$\mathbf{k} \cdot \mathbf{v}_i = \omega = k_\| v_{e\|}, \tag{6.8.9}$$

which is three-dimensional for the ions but one-dimensional for the electrons, implying that the resonance of the wave with the ions is particularly broad. The oblique k-spectrum of the fluctuations ($k_\perp \gg k_\|$) upon the saturation of the instability indicates that longitudinal electron energy is transferred into mostly transverse energy of the resonating ions. The conservation of the longitudinal momentum, $m_i\, \mathrm{d}v_{i\|} + m_e\, \mathrm{d}v_{e\|} = 0$, shows that momentum is transferred from electrons to ions generating additional effective resistivity.

(†††) Occurs only when the wave amplitude is growing with time or the fluctuations have a finite (non-infinite) correlation time.

6.8.3 Anomalous ion acceleration on the Alcator tokamak

After TM-3 [348], Alcator was the second tokamak from which strong CDT was reported [368,369]. The results of their investigations of anomalous ion heating are of particular interest, since all imaginable acceleration mechanisms were assessed by Coppi et al [370].
Strongest ion heating was observed for low density operation, when an electric field not much smaller than the Dreicer field was applied such that the distribution of circulating electrons tends to slide away as a whole (this is the so-called 'slide-away' regime). Coppi elucidated IAT as a possible mechanism but its relevance was rejected because the measured spectrum of electromagnetic fluctuations was cut-off below the ion plasma frequency. More significance was then attributed to oblique lower hybrid modes excited by the runaway beam excited fan instability (section 6.8.2.1), destabilised by the measured anisotropy in the electron distribution function [371, 372].

REQUIREMENTS	**TCV**	**PDI**	**FAN**	**IAT**
Turbulence drive possibilities	ECCD, sawtooth	parametric decay	toroidal field	toroidal field, ECCD
plasma isothermicity	$T_e > T_i$	-	-	$T_e > T_i$
electron drift	weakly relativistic	-	relativistic	$v_d \gg c_s$
EC accessibility	X2 EC	UHR	-	-
MANIFESTATIONS	**TCV**	**PDI**	**FAN**	**IAT**
fluctuation frequency	$\omega \lesssim \omega_{\mathrm{pi}}$	$\omega \lesssim \omega_{\mathrm{pi}}$	$\omega \gtrsim \omega_{\mathrm{pi}}$	?
electron tail anisotropy	$T_{e\perp} > T_{e\parallel}$	?	$T_{e\perp} \ll T_{e\parallel}$	$T_{e\perp} < T_{e\parallel}$
ion tail anisotropy	?	?	oblique	oblique

Table 6.1: Comparison of requirements for turbulence onset and its manifests for PDT, fan instability and IAT. The first column represents the conditions and observations on TCV.

6.8.4 Anomalous ion acceleration on the TCV tokamak

Table 6.1 compares turbulence theory with TCV experiment. Due to the inaccessibility of the upper hybrid layer, section 6.8.1 already described the incompatibility of parametric decay mechanisms on TCV. Further, the fan instability cannot develop in TCV plasmas as the suprathermal electron temperature anisotropy is opposite to the requirement of destabilisation of the fan instability. Electron cyclotron heating contributes perpendicular energy to the electrons such that $T_{e\parallel} < T_{e\perp}$. IAT seems therefore the most plausible mechanism for the ion energisation on TCV. The electron drift speeds and the remarkable non-isothermicity of EC heated TCV plasmas, $T_e^b(0)/T_i^b(0) = 10 \ldots 40$, are compatible with conditions required for the onset of IAT. The conditions for onset of IAT were verified analytically [293]. The saturation of the suprathermal ion temperature at the value of the bulk electron temperature is further circumstantial evidence of IAT. In appendix B it is shown that ion-acoustic waves, in the limit of long wavelength, propagate at the ion sound speed. It is therefore expected that ions with velocity around the wave phase speed are strongly accelerated, this is roughly the velocity where the thermal and suprathermal NPA charge exchange spectra intersect, i.e. the knee energy,

$$E_{\mathrm{knee}} = \frac{3\left(\ln T_i^b - \ln T_i^s\right)/2 + \ln\left(n_i^s/n_i^b\right)}{1/T_i^s - 1/T_i^b}, \tag{6.8.10}$$

and thus $\sqrt{2\,E_{\mathrm{knee}}/m_i}$ is of order $\sqrt{T_e/m_i}$.

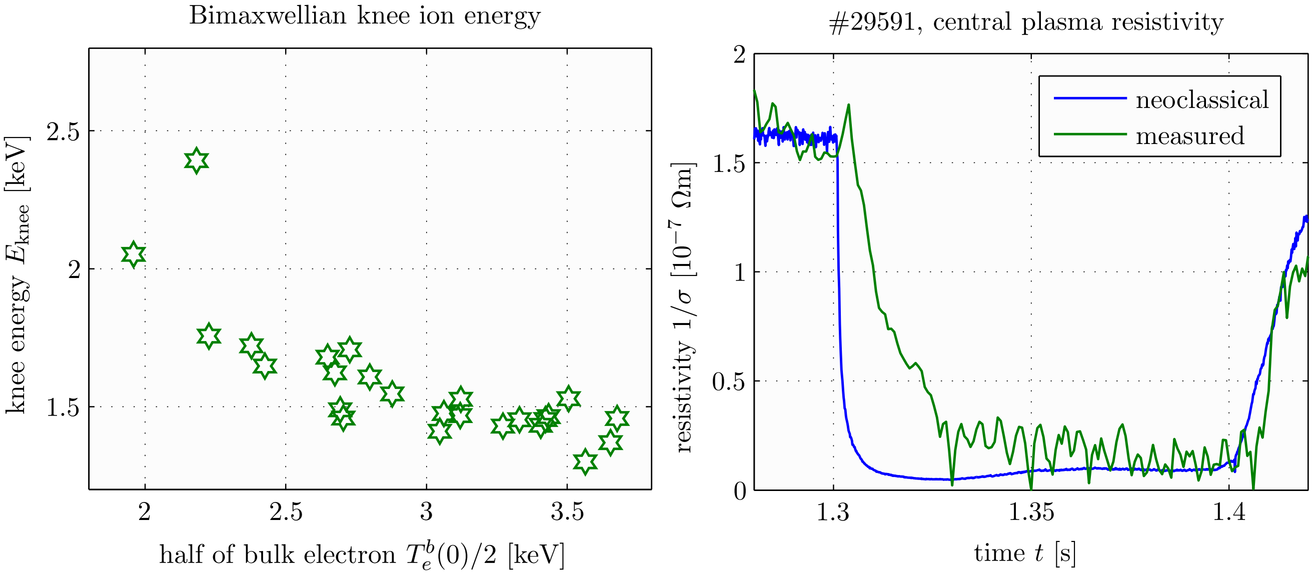

(a) Knee energy.

(b) Neoclassical conductivity.

Figure 6.8.2: (a) Comparison of the CNPA charge exchange knee energy, eq.(6.8.10), to the bulk electron temperature divided by 2. In the absence of non-resonant diffusion, $E_{\mathrm{knee}} = T_e/2$ is expected. (b) Neoclassical and measured plasma resistivity evolution for discharge #29591.

In figure 6.8.2a the knee energy of the steady-state fast ion database is plotted against half the bulk electron temperature and indeed, at weak turbulence (low electron temperature), knee and ion sound energy agree. For stronger turbulence, nonresonant diffusion is suspected to fill the increasing gap between knee and energy of strongest interaction (the latter increases linearly with electron temperature).

Now we should compare the turbulence saturation level (that is the tail population parameters at steady state) to theoretical predictions. However, the available analytical and numerical contributions to the scientific literature on IAT consider more extreme ratios of electron and ion temperatures. In order to study the linear and non-linear evolution of the turbulence, a numerical IAT code was implemented. Its description and the results of these calculations are the subject of chapter 7. But first, some aspects of the TCV observations require further discussion in the frame of IAT theory.

6.8.4.1 Anomalous resistivity

The anomalous resistivity observed in CDT experiments is proportional to the turbulence level W/nT [373],

$$\nu_c = \frac{n\,e^2}{m_e\,\sigma} \propto \frac{W}{n\,T}\,\omega_{\mathrm{pe}}, \tag{6.8.11}$$

where ν_c is the effective electron–ion momentum transfer collision frequency and W is the turbulent energy density. A measurement of σ gives therefore an estimation of the turbulence strength. The estimation of anomalous resistivity due to turbulence doesn't of course make much sense on TCV as the behaviour of the conductivity is obscured by the non-inductive current replacement in the ECCD experiments discussed before. However, σ may be calculated neoclassically and its value qualitatively compared to the measured conductivity. The neoclassical conductivity was calculated using the formulae in [58], including corrections for collision frequency and plasma charge and the temperature measured with the calibrated LFS ECE diagnostic.

The experimental resistivity is calculated from the measured loop voltage and from an estimation of the plasma current obtained with a set of poloidal magnetic field probes [65]. Time traces of the obtained resistivities for discharge #29591 (refer to figures 6.1.7–6.1.9) are plotted in figure 6.8.2b. The measured and calculated resistivities agree before the onset of turbulence ($t < 1.30$ s) and upon steady-state turbulence ($t > 1.36$ s). There is, however, an important discrepancy after the onset of the turbulence, where the measured resistivity decays much more slowly than the neoclassical estimation. The difference may be interpreted as due to anomalous resistivity.

6.8.4.2 Ion heating rate

The quasi-linear theory of ion acoustic turbulence predicts the ion heating in a hydrogen plasma to be proportional to the electron temperature increase [374],

$$\frac{\mathrm{d}T_i}{\mathrm{d}T_e} \simeq \frac{c_\mathrm{S}}{v_\mathrm{d}}. \tag{6.8.12}$$

In discharge #29591, shown in figure 6.1.7, the temperatures rise linearly for the first 30 ms of auxiliary heating.
The bulk electron temperature rises from initially 1.4 keV to 5 keV and the ion tail temperature tends to 4.5 keV. When eq.(6.8.12) is solved for these values, one gets an average electron drift speed of $v_\mathrm{d} = 2 \ldots 4 \times 10^5$ m/s, depending on the electron temperature used to evaluate the ion sound speed. *TORAY-GA* calculates a current drive density of $j_\mathrm{ECCD} = 0.95$ MA/m^{-3} peaking at $\rho = 0.2$, corresponding to a drift speed of $v_\mathrm{d} = j_\mathrm{ECCD}/n_e/e = 3 \times 10^5$ m/s. The observed ion heating rate is therefore compatible with IAT.

6.8.4.3 Ion mass

The measurement of the fluctuation power density on Alcator decreased in intensity when impurities were added. On TCV, T_i^s increases with higher Z_eff. The hydrogen population contains the double of the energy of the deuterium population, thus the energy (or pressure) increases as m_i, nevertheless, there are no indications of suprathermal carbon (CXRS measurement).
In TCV deuterium plasmas, hydrogen is a light ion impurity. With even small hydrogen fractions, the dispersion properties of the plasma are considerably modified [375]. But as the IAT saturation mechanism depends on the linear and nonlinear interaction of different types of ions with the wave, the fluctuation level may also be considerably changed depending upon the hydrogen contamination. Most of the theories on IAT consider a single ion species in the plasma, some analytical contributions investigated the modification of the IAT spectrum in presence of multiple ion species [376, 377]. However, the approximations made in these papers are not compatible(‡‡‡) with the ion mix on TCV.

A simple one-dimensional analysis [378] shows that, as the percentage of contamination of light ions increases, the phase velocity of the mode increases and therefore the number of heavy ions in resonance decreases. However, experiments seems to indicate the contrary, Nakamura et al [379] have measured the propagation of stimulated ion acoustic waves in Argon plasmas and found the ion acoustic phase velocity to decrease when helium was added...

We shall investigate the tail strength of hydrogen and deuterium numerically in section 7.5.

(‡‡‡) Equation eq.(2.4) in [377] is not satisfied for hydrogen/carbon or deuterium/carbon mixtures on TCV.

6.8.4.4 Hydrogen isotope ion temperature

On TCV, the hydrogen and deuterium temperatures seem to thermalise on a very fast scale (see figure 6.1.8, both T_i^s agree from the beginning). This is not the result of collisional heat equilibration because the hydrogen-deuterium heat exchange time,

$$\tau_{\mathrm{HD}} = \frac{3\,\varepsilon_0^2 \sqrt{m_p}\,(3\pi\,T_i^s)^{3/2}}{2\,n_{\mathrm{D}}^s\,e^4 \ln\Lambda}, \tag{6.8.13}$$

gives for the parameters of discharge #29591, i.e. $n_e = 2.5 \times 10^{19}\ \mathrm{m}^{-3}$, $T_e^b = 5$ keV, $n_D^s/n_D^b = 5$ %,

$$\tau_{\mathrm{HD}} = \frac{n_{\mathrm{H}}^s}{n_{\mathrm{D}}^s}\tau_{\mathrm{DH}} = 75\ \mathrm{ms}, \tag{6.8.14}$$

i.e. on a time scale to reach overall steady-state (after about 70 ms, see again figure 6.1.8). This indicates that the upper limit of the experimentally observed suprathermal temperature must be related to the quench of IAT.

6.8.4.5 Ion acceleration by sawteeth

Ion acceleration by internal reconnection has been observed in other laboratory plasmas. On the Madison Symmetric Torus (MST) reversed field pinch (RFP) in Wisconsin, quick bulk (200 μs) ion heating synchronised with a global magnetic reconnection event was investigated with charge exchange recombination spectroscopy and Rutherford scattering (RS) diagnostics [380]. The bulk ion temperatures increased by more than a factor of three (e.g. 300 eV to 1 keV), almost everywhere in radius (though there are multiple radial reconnection sites in a RFP). The ion heating amounts to at least 20 % of the released magnetic energy. The heating is stronger with higher current and weaker density (both trends are beneficial for the confinement) and if charge exchange losses are ignored, the peak temperatures reached by carbon (CXRS) and helium (RS) are the same. The ion heating is further isotropic [381]. The acceleration mechanism is not known, though the measured fluctuation power spectrum has shown some losses at ω_{ci}.

On the Mega-Ampere Spherical Tokamak (MAST) in Culham ion acceleration was observed (with an NPA) following each internal reconnection event (IRE) in ohmic discharges [382]. Here the acceleration was satisfactorily explained by ion runaway in the toroidal electric field generated by the IRE, following the theory developed by Furth and Rutherford [383]. The same mechanism is in fact at play in solar flares [384]. The ion runaway threshold requires the toroidal field to satisfy

$$E > \sqrt[3]{\frac{3\,m_e}{2\pi\,m_i}}E_{\mathrm{Dreicer}}. \tag{6.8.15}$$

This is the case on MAST, where the measured loop voltage spike is as high as 200 V, but not on TCV (section 5.4.4.3). In any case, this mechanism creates fast ion tails parallel to the magnetic field. Indeed, when the tangentially looking NPA was swung around to probe the MAST plasma perpendicularly, no ion acceleration was observed.

For TCV, an enhancement of IAT by the sawtooth crash could be envisaged. As shown in section 5.4.4.3, electrons are strongly accelerated by the crash field and one could think of these runaway electrons giving an additional boost to the turbulence, such that the enhanced fluctuation power accelerates more ions. The deformation of the ion distribution function at higher energies (see figure 6.6.4b) points again towards a wave–particle interaction. This possibility will be addressed in the numerical experiment of section 7.6.

6.8.4.6 Ion acceleration by edge localised modes (ELM)

It has been known for many years since the first demonstration on the ASDEX tokamak [329] that tokamak plasmas can undergo a sudden transition in the energy confinement time which is generally accompanied by a reduction in the deuterium visible light emission D_α (generated by the recombination of deuterium at the plasma edge) and is referred to as the H-mode [385]. The H-mode is frequently accompanied by bursts in magnetohydrodynamic (MHD) activity and in the D_α emission, known as edge localised modes (ELM), and this type of H-mode is referred to as the ELMy H-mode [386]. If ELMs do not appear, then the density often rises uncontrollably, sometimes leading to a major plasma current disruption. ELMs are easily detected as spikes in the D_α signal, corresponding to a sudden increase in the line-of-sight integral of the ionisation rate in the plasma edge, which is concurrent with the abrupt, momentary breach of the H-mode transport barrier.

Recently, the neutral particle spectra emitted from high density ELMy H-mode TCV plasmas, heated with intense EC waves at the third harmonic, were analysed and an anomalous time ordering of the ELM provoked neutral flux response on different NPA energy channels was found [387]. Other than in the X2 heated low density discharges, the high densities of the ELMy H-mode ($> 5 \times 10^{19}$ m^{-3}, $T_e \approx 2$ keV) bring about intense neutral fluxes into all channels of the VNPA(§§§). Good neutral counting statistics of several MHz allow diagnostic operation at sampling times as low as 50 μs (fixed energy setup). As shown in figure 6.8.3a, the VNPA flux traces steadily increase prior to the ELM (improved ion heating at high density accompanied by an improvement of the ion confinement) and when the ELM is triggered, a strong flux spike is seen in all channels. The latter was explained by a transient neutralisation target increase (neutral influx) due to enhanced plasma–wall interaction. The ion temperature (about $T_i \approx 800$ eV for the discharge shown) might be inferred with the VNPA from an energy interval below the energies required for the retrieval of the core ion temperature, eq.(4.3.13) and shows ion heating obviously resulting from the ELM/sawtooth crash (figure 6.8.3d). However, neither the post-crash increase in T_i nor the risen high energy fluxes (figure 6.8.3c) may be explained in terms of modified neutralisation probabilities (due to changes in the plasma profiles [388] or collisional electron–ion coupling).

Oddly the flux starts to increase on the high energy channels first (figure 6.8.3b). If this were due to the enhanced neutral influx from the plasma edge, we would expect the low energy channel signals to grow first, as these ions are neutralised at a radial position closer to the edge than the high energy ions (section 4.5.1). Considering the VNPA integration time of 50 μs, the maximum impact of the ELM crash on the ions occurs in a time $40 \leqslant t < 90$ μs. The data shown in figure 6.8.3b and 6.8.3d was extracted from a total of 19 sawteeth crashes in the time interval $t = 0.5 \ldots 0.7$ s (the VNPA acquisition interval is restricted as the acquisition memory has a capacity for 4096 samples only).

It is important to highlight that, in this type of operation, ELMs occur simultaneously with sawteeth (period about 20 ms). Coupling of ELMs and sawteeth are a common feature [389]. The sawteeth then enhance the energy lost per ELM by a factor 4 (with respect to ohmic H-mode ELMs without sawteeth). The time ordering of the VNPA channel response points again towards a wave–particle mechanism, as if initially the interaction takes place resonantly at high energy and the heated ions then slow down. Although the electron temperature is smaller ($T_e(0) = 1.1$ keV for the data of figure 6.8.3) than in the X2 heated discharges, there is still a chance that the sawtooth crash causes IAT, although the electron drift speeds must then be higher than in the low density discharges (figure B.3.1). An investigation of the electron dynamics in these discharges is difficult if not impossible, as the ECE diagnostics may not be used as the electron density is above the X2 cutoff.

(§§§) Note that such count rates push the CNPA inevitably into saturation.

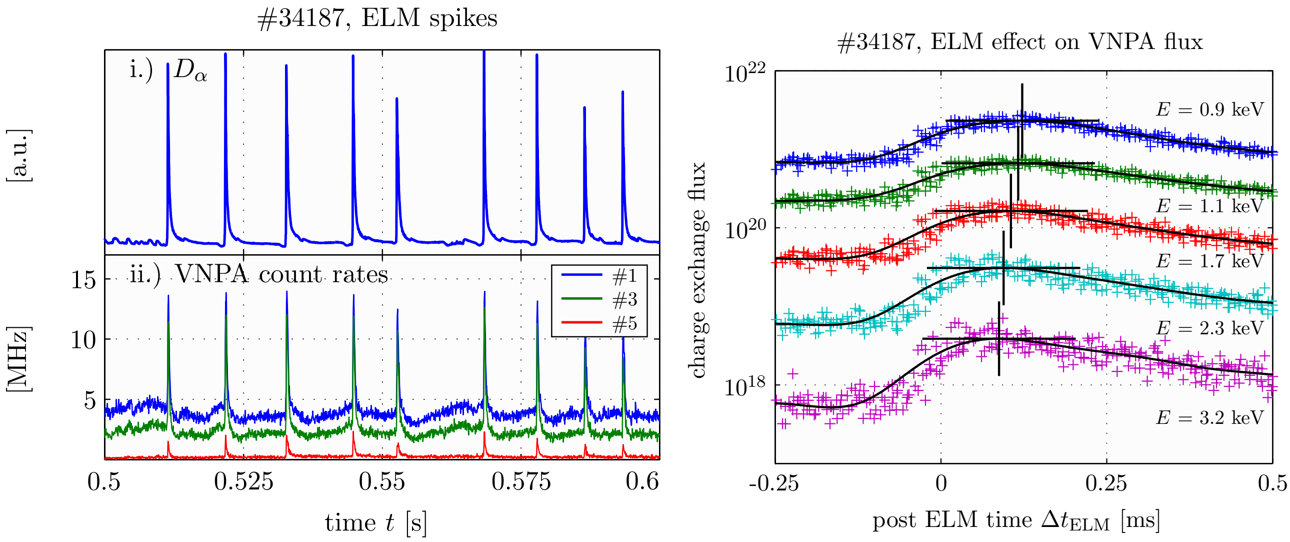

(a) Neutral flux spikes. (b) Neutral flux at ELM.

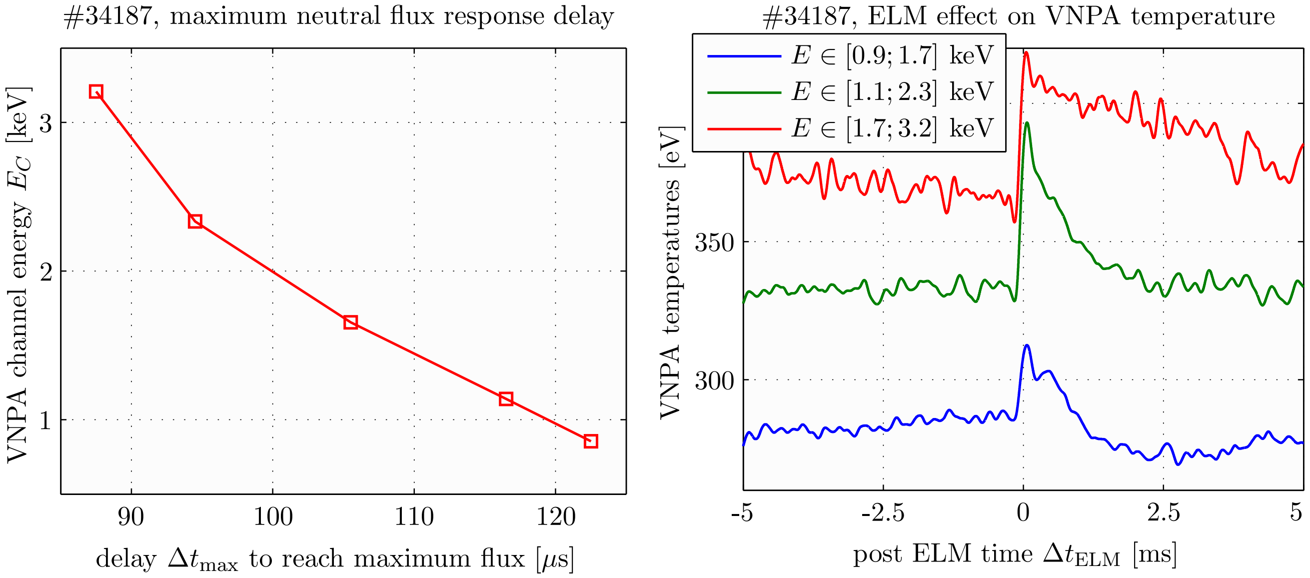

(c) Flux rise times. (d) VNPA temperatures.

Figure 6.8.3: (a) ELM spikes seen by the D_α photodiode and on some VNPA channels operated such as to receive neutrals at fixed energy. The ELM period is about 20 ms.
(b) Increase of the neutral flux at the ELM event. The data shown is a compilation from 19 ELMs in discharge #34187, e.g. the neutral pulses accumulated in the full VNPA acquisition time interval (0.5. . . 0.7 s). The VNPA measurements are coherently rearranged in respect to the ELM using the D_α spikes as conditional signal. The thick lines are cubic spline interpolations.
(c) The time to reach the maximum of the neutral flux response after the occurrence of the ELM is a decreasing function of energy.
(d) The flux trace fits shown in (b) were used to calculate temperatures from the slope of the charge exchange spectrum at various radial locations, which, due to the restricted VNPA energy range, correspond all to positions outside half radius.

6.9 Future experiments

Experiments presented and discussed hitherto were all conducted in 2005/2006. During the long TCV shutdown in 2007 substantial upgrades were made to the set of diagnostics relevant for the studies reported here. These aimed at making more relevant experiments to better track down the mechanism at play in the anomalous ion acceleration, e.g.

- ☞ The assessment of a potential temperature anisotropy (parallel versus perpendicular direction to the magnetic field) of the fast ion population,
- ☞ the measurement of the plasma electromagnetic emission spectrum for the identification of the relevant wave being destabilised,
- ☞ further improved measurements of oblique ECE emission, especially during sawtooth activity and
- ☞ the acquisition of a staggered NPA flux measurement synchronised with modulated ECRH, ECCD or sawteeth

Unfortunate circumstances(¶¶¶) have hindered the execution of any of these prepared experiments. As the thesis was overdue, it was decided to finish this work at the academic level with the material collected so far. Regarding the investments in time and fonds we may hope that these experiments may be carried out later in 2009. At the time of writing the tokamak operations are about to resume...
The new experimental possibilities and a non-exhaustive shopping list of the further envisagable studies are briefly outlined in the following subsections.

6.9.1 Toroidal orientation of the CNPA viewline

Anisotropic ion acceleration is a frequent process in nature, for example, the ion conics (suprathermal ions with peaked off-perpendicular pitch-angles) have largely been investigated in the magnetosphere from satellites in the northern dayside polar cusp [288] (at an altitude of 7600 km). These ions are believed to be produced in the upper ionosphere by an acceleration mechanism acting perpendicularly to the geomagnetic field [390]. Although ion acceleration was studied in laboratory plasmas for a long time, the potential anisotropy of ion pitch angle distribution was not addressed for many decades, diagnostics were mostly installed with a line of sight perpendicular to the main magnetic field. For the case of IAT, progress in theory permitted the calculation of the IAT spectra analytically [391, 392] and numerically [363] in two dimensions, revealing the anomalous $\mathbf{k}$-spectrum with the highly oblique mode at the saturation of the turbulence which is manifested by an anisotropic suprathermal ion temperature $T_{i\perp} \neq T_{i\parallel}$ (section 7.2). Even after this discovery, the pitch angle distribution of IAT has yet to be investigated in the laboratory.

(¶¶¶) Gyrotron operator availability and ITER project priority lead to the decision to modify the scientific program of TCV in early 2008 (machine restart in March). Experiments requiring electron cyclotron auxiliary heated plasmas were then postponed to summer. Operational difficulties after the summer break (troubles with plasma breakdown due to the fresh vessel first wall installed in 2007) required extended commissioning of the machine until into autumn. A first experimental session was finally scheduled for mid September, but shortly before being carried out, an accidentally destroyed vessel window (due to unwanted refraction of the EC beam) provoked an air leak and the dispersion of metal inside the tokamak. After repair and first wall cleaning the machine was restarted at the beginning of November. Our ultimate session was scheduled for November 15, but a high voltage transformer explosion on November 12 required again the suspension of TCV operation. A transformer replacement was completed in March 2009.

Dedicated experiments to investigate a universal mechanism of perpendicular ion acceleration were conducted on the Continuous Current Tokamak (CCT) at the University of California [393]. There, the neutral spectrometer has scanned the toroidal viewing angle and a strong anisotropy of the high energy flux was discovered ($E_\perp/E_\parallel \sim 100$). This was observed in various types of plasmas, produced by ECRH, radiofrequency (RF) or ohmic (using a breakdown oscillator). But the ratio T_e/T_i was low, $5\ldots7$ and the electron drift speeds did not exceed the ion sound speed by much, so the destabilisation of ion-acoustic waves is questionable.

On TCV the modified CNPA setup (section 3.3.3.1) is now awaiting T_i anisotropy studies to be carried out. We would like to investigate turbulent plasmas in directions perpendicular, co-aligned (view at 60° with respect to the magnetic field) and counter-aligned with the ECCD driven electron drift direction. For the last two measurements, a reversal of the toroidal magnetic field and plasma current direction would be desirable, such to investigate counter-ECCD plasmas in both cases. In order to work with comparable vessel conditions, the CNPA view line could be switched over a weekend break (two days are required for the air venting, displacement and subsequent depressurisation of the CNPA interior).

6.9.2 Low frequency wave receiver (LHPI antenna)

On Alcator, the low frequency fluctuation spectrum was measured with a spectrum analyser connected to an insulated piece of the limiter or a small molybdenum tipped probe positioned in the limiter shadow [368]. The low frequency spectrum was peaked at the ion plasma frequency with a small continuum extending up to $5\ldots10 \times \omega_{\mathrm{p}i}$. The fluctuation intensity at $\omega_{\mathrm{p}i}$ increases with the drift parameter $v_\mathrm{d}/v_{\mathrm{th}e}$. The appearance of the frequency peak correlates with the heating of the ions. The measured emission cut off below $\omega_{\mathrm{p}i}$ was taken as proof that the turbulence is not IAT. Note that for the Alcator plasmas $\omega_{\mathrm{pe}} \gg \Omega_{\mathrm{c}e}$, such that $\omega_{\mathrm{LH}} \approx \omega_{\mathrm{p}i}$ and lower hybrid modes excited by the fan instability propagate for $\omega > \omega_{\mathrm{p}i}$.

The measurement of the fluctuation emissions spectrum on TCV would help to confirm (or confound) the development of IAT. Mainly driven by the Bernstein wave heating experiments (section 6.8.1.1), a new Lower Hybrid Parametric Instability (LHPI) antenna to measure the lower hybrid decay wave branch of the X-B conversion (which is a potential loss channel for the electron Bernstein wave heating) was designed and installed in 2008. The detection of the LH wave should support electron Bernstein heating experiments, help in the optimisation of the EBW heating scheme (e.g the EC injection angle) and confirm the threshold nature of the parametric decay.

The antenna consists of a rectangular single loop-antenna (lateral width and length 5 cm and 6 cm respectively) of low self inductance connected to a coaxial conductor balanced by a sleeve (figure 6.9.1). The sleeve ensures the matching of the characteristic impedance of the antenna to the coaxial transmission line. Similar designs have previously been used on Wendelstein 7-AS [394] and MAST [395]. The system is optimised for the range of the expected LH frequencies, 100 MHz to 3 GHz. As on TCV $\omega_{\mathrm{pe}} \approx \Omega_{\mathrm{c}e}$, thus $\omega_{\mathrm{LH}} = \omega_{\mathrm{p}i}/\sqrt{2}$, the antenna is well suited to analyse the vicinity of the IAT frequency range. The antenna was installed on a upper lateral port and radially positioned to approach the plasma as much as possible whilst remaining behind the excursion of the magnetic field ripple (~1 cm) into the port (safety measure as the loop is made of stainless steel). The proximity to the plasma is of vital importance, as the electrostatic ion acoustic waves are evanescent in vacuum. For any attempt to measure the IAT spectrum, the plasma must be placed at $z = 21$ cm and moved as close as possible to the outer wall.

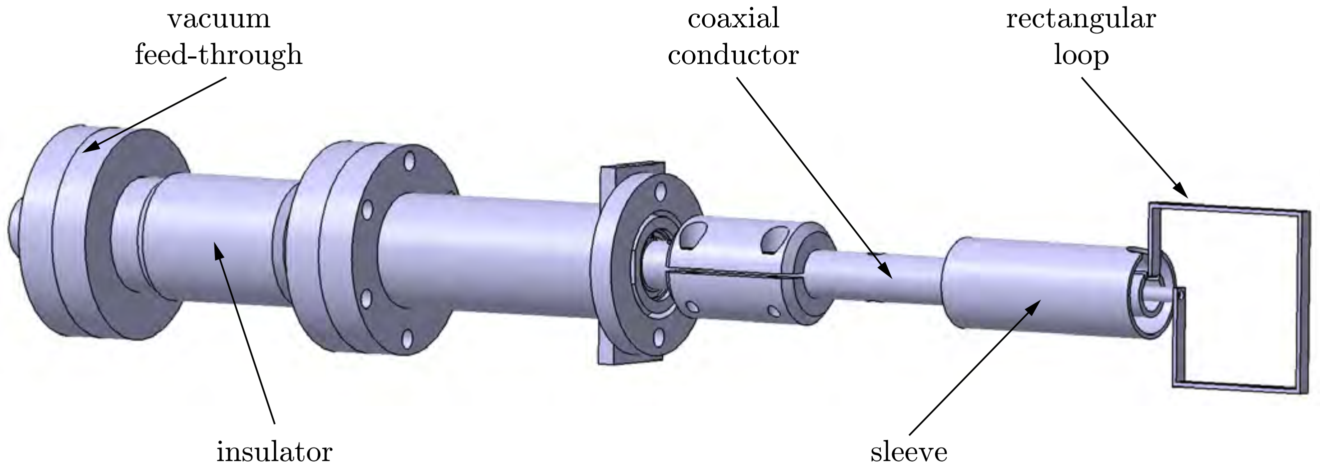

Figure 6.9.1: New low frequency wave probe (LHPI) and its coaxial feed on the TCV tokamak.

The coaxial conductor is fed through the vacuum, protected by a galvanic cell and connected to a spectrum analyser. Its video signals are acquired at 200 kHz and the device is configured remotely through the GPIB bus. The maximum sampling rate of one single frequency (no spectrum scanning) is $\sim$200 μs. Appendix C provides further details of the control and acquisition of the frequency power spectrum. Some preliminary spectrum acquisitions in ohmic plasmas were successfully achieved in 2008.

6.9.3 Oblique ECE antenna

A new radially displaceable mirror and a new receiver horn were procured in 2008. These will be installed behind the 7th launcher in summer 2009. Both are expected to improve the matching of the ECE to the waveguide. Oblique ECE measurements of a sawteething plasma would eventually help to determine the sawtooth induced electron drift to give a direct estimation of the toroidal crash field.

6.9.4 Digital controller of the CNPA acquisition trigger

The real time algorithm used to control the launcher mirror angle and thus the sawtooth period [227] may also come to use for the triggering of diagnostics. The output signal of this controller was rerouted to the CAMAC acquisition module of the CNPA, such to stop the acquisition as early as possible after the crash. The controller may then modify the sawteeth parameters (frequency and thus crash amplitude) to characterise the ion acceleration as a function of released magnetic energy. For discharges with short sawtooth periods, the CNPA flux measurement may then be averaged coherently to improve the particle counting statistics.

A more elaborate experimental session could then aim at progressively changing the vertical position of the plasma in a way to spatially scan the surroundings of the $q = 1$ surface with the oblique ECE and oblique CNPA view lines (as the electron acceleration is supposed to occur outside the inversion radius, in contrast to the ECCD electrons driving the IAT).

Chapter 7

Modelling of anomalous ion heating in ECCD current driven ion-acoustic turbulence on the TCV tokamak

This chapter describes the numerical experiments undertaken to understand the anomalous ion energisation on TCV described in the preceding chapter in terms of ion acoustic turbulence. A numerical approach was chosen because of doubts that an analytical model would be more adequate to study the quench of the instability [358].

First the equations describing the evolution of the electron and ion distribution functions in a plasma with IAT are described (section 7.1). These are then implemented in a numerical model based on finite difference equations (section 7.2). For parameters relevant for the plasma core of TCV, the onset, linear growth (section 7.1.2) and quasi-linear saturation (section 7.3) of IAT are then modelled for the case of a constant toroidal current. Section 7.4 investigates the saturation of IAT when the electron distribution function is replaced by f_e modelled with *CQL3D*, giving a more satisfactorily description of the electron populations on TCV. The energy sharing between hot hydrogen and deuterium is discussed in section 7.5 and the chapter concludes with the investigation of IAT driven by the sawtooth instability (section 7.6).

Early results of the numerical experiments were presented at the 49th Annual Meeting of the Division of Plasma Physics of the American Physical Society [396].

7.1 Ion acoustic turbulence in a magnetic field

Any study of turbulence relies on knowledge of the turbulent spectrum of the fluctuations of the electric field or potential, in space and time. In the case of IAT, the fluctuation spectrum governs the diffusion coefficients in the velocity space and thus determines the ion heating rates. From an experimental point of view, if measured, the k-spectrum of the fluctuations will provide the most relevant information on the nature of the instability. The large Čerenkov angle ion waves excited by a current will have a large angular spread, the problem is thus, necessarily, multidimensional. Due to the interplay of ion-acoustic waves with electrons and ions, a full description of the macroscopic manifests of IAT needs to follow both electron and ion velocity distribution functions in time, from the onset until the eventual quench of the turbulence. This usually requires numerical analysis because of complicated coupling among the diffusion equation and the growth or damping rate of each Fourier mode.

Quasi-linear theory has proven to correctly describe the physics of IAT experiments where the turbulence was driven by intense toroidal electric fields and higher order non-linearities were generally not required to explain the experimental observations [360,362]. In the quasi-linear analysis of the ion-acoustic instability, it has been found that saturation is mainly caused by the high-energy ion tail [363]. The formation of the high-energy ions is, in turn, largely due to nonresonant diffusion which transfers ions from the nonresonant to the resonant region [397,398].

The first solution of the quasilinear diffusion equation for a plasma immersed into an external magnetic field, was obtained by Fried and Ossakow [399], but their equations did not permit the ions to diffuse in velocity space. Rudakov [400] considered the wave–particle interaction at the electron cyclotron resonance (anomalous Doppler effect) which leads to cross-field heating of the electrons. The ECCD plasmas on TCV exhibit a strong perpendicular electron energisation (diagnosed with the perpendicularly viewing ECE diagnostics), which exceeds the direct EC energy transfer to the electrons in pure ECRH experiments (chapter 5). Dum [360], Appert [401] and Ishihara [361] performed one dimensional numerical studies which did not reproduce the quasi-steady saturation of the turbulence. Turbulence is three-dimensional by nature [402] and thus only three-dimensional considerations could successfully order the relevant saturation mechanism. Ishihara and Hirose [403] have so far realised the most complete (in terms of included physics) numerical simulation. The code presented in section 7.2 follows their approach. Although the turbulence mechanism at play in TCV plasmas may be assumed to develop similarly to the findings in the papers cited above, most of these simulations have either considered unrealistic mass ratios of ions and electrons or electron to ion temperature ratios (e.g. $T_e/T_i = 100$ in [403]) that are too far from the TCV situation. The simulations presented herein use an experimentally determined set of parameters.

As will be clearer in a moment, the evolution of current driven turbulence from onset towards saturation is quite complex and therefore any model need to be simplistic, i.e. the inclusion of all experimental features is generally impossible. Non-uniformities, e.g. gradients in density, temperature, drift velocity or energy and particle losses are neglected in the following. Often, the gradient along the magnetic field and therefore $k_\parallel$ are taken as constant, irrespective of the shear of the magnetic field in toroidal devices. However, the collective modes of CDT are mostly of sufficient high-frequency convective nature such that the parameter gradients are sufficiently constant over the short wavelength. Specifically, the ion-acoustic mode has a frequency spectrum in the range $\omega_{ci} \ll \omega \lesssim \omega_{pi}$ and thus the ions are essentially unmagnetised and the magnetic field plays a minor role in the ion dynamics resulting from the ion-acoustic turbulence.

7.1.1 Quasi-linear formulation

The following simplifications are made: The plasma is assumed to be spatially uniform and placed into a uniform magnetic field. This is a first approximation of the conditions on the magnetic axis in TCV, where the ECCD current is strongest and restricted to a narrow current channel at the gyrotron switch on (see section 5.4.3.2). The particle velocity distributions are initially approximated as Maxwellians. The hydrogenic ion populations are isotropic and cold, the electrons are drifting with a drift speed $v_{\rm de}$ being a fraction of the thermal electron speed, i.e.

$$f_e(v_\parallel, v_\perp, t=0) = n_e \left(\frac{m_e}{2\pi\, T_e(t=0)}\right)^{3/2} \exp\left(\frac{m_e}{2\, T_e(t=0)}\left(v_\perp^2 + \left(v_\parallel - v_{\rm de}\right)^2\right)\right) \qquad (7.1.1)$$

The current aligns with the main magnetic field. The drift speed exceeds the critical velocity for the excitation of IAT. The electrons are described as being magnetised, ($\omega_{\rm ce} \approx \omega_{\rm pe}$ for all TCV plasmas studied), whereas for the ions the cyclotron frequencies are not important.

The time evolution of the velocity distribution functions $f_\alpha(\mathbf{v},t)$ are characterised by the quasilinear diffusion equations [404], eq.(A.2.22), $\alpha \in e, i$

$$\frac{\partial f_\alpha}{\partial t} + \frac{q_\alpha}{m_\alpha}\mathbf{E}_0(t)\cdot\frac{\partial f_\alpha}{\partial \mathbf{v}} = \frac{\partial}{\partial \mathbf{v}}\cdot\underline{\mathbf{D}}_\alpha^{\mathrm{QL}}\cdot\frac{\partial f_\alpha}{\partial \mathbf{v}} \tag{7.1.2}$$

where $\mathbf{E}_0$ is an externally applied toroidal electric field. Toroidal symmetry leads to the parametrisation of the velocity and wave vector space in cylindrical geometry, with variables $(v_\perp, \phi_v, v_\parallel)$ and $(k_\perp, \phi_k, k_\parallel)$ respectively. Averaging over the angle $\varphi = \phi_v - \phi_k$ (that is, integrating over $\int_0^{2\pi} \mathrm{d}\varphi/2\pi$) and choosing a reference frame in which ions are freely accelerated, eqns.(7.1.2) become

$$\frac{\partial f_i(v_\perp, v_\parallel, t)}{\partial t} = \left(\frac{1}{v_\perp}\frac{\partial}{\partial v_\perp}v_\perp, \frac{\partial}{\partial v_\parallel}\right)\begin{pmatrix} D_{\perp\perp} & D_{\perp\parallel} \\ D_{\parallel\perp} & D_{\parallel\parallel}\end{pmatrix}_i \begin{pmatrix}\partial/\partial v_\perp \\ \partial/\partial v_\parallel\end{pmatrix} f_i(v_\perp, v_\parallel, t) \tag{7.1.3}$$

for the ions and

$$\begin{aligned}\frac{\partial f_e(v_\perp, v_\parallel, t)}{\partial t} = \left(\frac{1}{v_\perp}\frac{\partial}{\partial v_\perp}v_\perp, \frac{\partial}{\partial v_\parallel}\right)\begin{pmatrix} D_{\perp\perp} & D_{\perp\parallel} \\ D_{\parallel\perp} & D_{\parallel\parallel}\end{pmatrix}_e \begin{pmatrix}\partial/\partial v_\perp \\ \partial/\partial v_\parallel\end{pmatrix} f_e(v_\perp, v_\parallel, t) + \\ + \frac{e\,(m_e + m_i)}{m_e + m_i}E_0(t)\frac{\partial f_e(v_\perp, v_\parallel, t)}{\partial v_\parallel}\end{aligned} \tag{7.1.4}$$

for the electrons. The quasilinear diffusion tensor for singly charged, unmagnetised ions is written

$$\underline{\mathbf{D}}_i = \frac{8\pi\, e^2}{m_i^2}\sum_{\mathbf{k}}\frac{\mathbf{k}\mathbf{k}}{k^2}\mathscr{E}_{\mathbf{k}}(t)\left(\underbrace{\frac{\gamma_{\mathbf{k}}}{(\omega_{\mathbf{k}} - \mathbf{k}\cdot\mathbf{v})^2}}_{\underline{\mathbf{D}}_{\mathrm{NR}}} + \underbrace{\pi\,\delta\,(\omega_{\mathbf{k}} - \mathbf{k}\cdot\mathbf{v})}_{\underline{\mathbf{D}}_{\mathrm{R}}}\right) \tag{7.1.5}$$

and includes contributions of resonant ($\underline{\mathbf{D}}_{\mathrm{R}}$) and nonresonant ($\underline{\mathbf{D}}_{\mathrm{NR}}$) interactions, where

$$\mathscr{E}_{\mathbf{k}}(t) = \frac{|\mathbf{E}_{\mathbf{k}}(t)|^2}{8\pi} \tag{7.1.6}$$

is the spectral wave electric field energy density associated with the mode characterised by $\mathbf{k}$. The scalar product of wave and velocity vector is $\mathbf{k}\cdot\mathbf{v} = k_\perp v_\perp \cos\varphi + k_\parallel v_\parallel$ and the integration over φ was derived in [405] and becomes

$$\begin{aligned}\begin{pmatrix} D_{\perp\perp} \\ D_{\perp\parallel} \\ D_{\parallel\parallel}\end{pmatrix}_i = \sum_{\mathbf{k}}\frac{8\pi\, e^2}{m_i^2\, k^2}\mathscr{E}_{\mathbf{k}}(t)\left\{\frac{1}{\sqrt{(k_\perp v_\perp)^2 - (\omega_{\mathbf{k}} - k_\parallel v_\parallel)^2}}\begin{pmatrix}\left(\dfrac{\omega_{\mathbf{k}} - k_\parallel v_\parallel}{v_\perp}\right)^2 \\ \dfrac{k_\parallel\,(\omega_{\mathbf{k}} - k_\parallel v_\parallel)}{v_\perp} \\ k_\parallel^2\end{pmatrix} + \right. \\ \left. + \gamma_{\mathbf{k}}\left[\begin{pmatrix} 1/v_\perp^2 \\ 0 \\ 0\end{pmatrix} + \frac{|\omega_{\mathbf{k}} - k_\parallel v_\parallel|}{\left(\sqrt{(\omega_{\mathbf{k}} - k_\parallel v_\parallel)^2 - (k_\perp v_\perp)^2}\right)^3}\begin{pmatrix} 2\,k_\perp^2 - \left(\dfrac{\omega_{\mathbf{k}} - k_\parallel v_\parallel}{v_\perp}\right)^2 \\ \dfrac{k_\perp^2\, k_\parallel\, v_\perp}{\omega_{\mathbf{k}} - k_\parallel v_\parallel} \\ k_\parallel^2\end{pmatrix}\right]\right\}\end{aligned} \tag{7.1.7}$$

where the first term represents the resonant and the second the nonresonant parts.

According to quasilinear theory [404, 406], the wave energy evolves as

$$\frac{\partial \mathscr{E}_{\mathbf{k}}(t)}{\partial t} = 2\,\gamma_{\mathbf{k}}\,\mathscr{E}_{\mathbf{k}}(t) \tag{7.1.8}$$

Eq.(7.1.2) and eq.(7.1.8) constitute the set of quasilinear equations to be solved. The magnetised electron diffusion tensor is [238]

$$\begin{pmatrix} D_{\perp\perp} \\ \\ D_{\perp\parallel} \\ \\ D_{\parallel\parallel} \end{pmatrix}_e = \sum_{\mathbf{k}} \frac{8\pi^2\,e^2}{m_e^2\,k^2}\mathscr{E}_{\mathbf{k}}(t) \sum_{n=-\infty}^{\infty} J_n^2\left(\frac{k_\perp v_\perp}{\Omega_{ce}}\right)\delta\left(\omega_{\mathbf{k}} - k_\parallel v_\parallel - n\,\Omega_{ce}\right) \begin{pmatrix} \left(\dfrac{k_\perp n\,\Omega_{ce}}{v_\perp}\right)^2 \\ \dfrac{k_\parallel k_\perp n\,\Omega_{ce}}{v_\perp} \\ k_\parallel^2 \end{pmatrix} \tag{7.1.9}$$

and includes multiple cyclotron resonances, namely the Čerenkov resonance ($n = 0$), as well as normal ($n > 0$) and anomalous ($n < 0$) Doppler effects. Contributions to $\underline{\mathbf{D}}_e$ rapidly decrease with $|n|$, the calculation includes resonances within $n \pm 4$. The oscillation frequency $\omega_{\mathbf{k}}$ and quasilinear growth rate $\gamma_{\mathbf{k}}$ are determined from the real and imaginary parts of the dielectric response function, respectively

$$\begin{cases} \epsilon_r(\mathbf{k}, \omega_{\mathbf{k}}) = 0 \\ \gamma_{\mathbf{k}} = -\dfrac{\epsilon_i(\mathbf{k}, \omega_{\mathbf{k}})}{\partial \epsilon_r / \partial \omega_{\mathbf{k}}} = -\dfrac{\epsilon_i^{(e)}(\mathbf{k}, \omega_{\mathbf{k}}) + \epsilon_i^{(i)}(\mathbf{k}, \omega_{\mathbf{k}})}{\partial \epsilon_r / \partial \omega_{\mathbf{k}}} \end{cases} \tag{7.1.10}$$

with ϵ_r given by eq.(D.0.12), that is

$$\epsilon_r(\mathbf{k}, \omega_{\mathbf{k}}) = 1 - \frac{\omega_{\text{pi}}^2}{\omega^2} + \frac{\omega_{\text{pe}}^2}{k^2} \sum_{n=-\infty}^{+\infty} ⨍ \mathrm{d}^3 v \left(\frac{n\,\Omega_{\text{ce}}}{v_\perp}\frac{\partial f_e}{\partial v_\parallel} + k_\parallel \frac{\partial f_e}{\partial v_\parallel}\right) \frac{J_n^2(\frac{k_\perp v_\perp}{\Omega_{ce}})}{\omega - n\,\Omega_{\text{ce}} - k_\parallel v_\parallel} \tag{7.1.11}$$

where $⨍ f(\mathbf{v})\mathrm{d}^3 v$ denotes the Cauchy principal value integral and the ion and electron contributions to ϵ_i are respectively

$$\epsilon_i^{(i)}(\mathbf{k}, \omega_{\mathbf{k}}) = -\frac{\omega_{\text{pi}}^2}{k^2} \int \mathrm{d}^3 v \left(\frac{\omega_{\mathbf{k}} - k_\parallel v_\parallel}{v_\perp}\frac{\partial f_i}{\partial v_\perp} + k_\parallel \frac{\partial f_i}{\partial v_\parallel}\right) \frac{1}{\sqrt{(k_\perp v_\perp)^2 - \left(\omega_{\mathbf{k}} - k_\parallel v_\parallel\right)^2}} \tag{7.1.12}$$

and

$$\epsilon_i^{(e)}(\mathbf{k}, \omega_{\mathbf{k}}) = -\pi \frac{\omega_{\text{pe}}^2}{k^2} \sum_{n=-\infty}^{+\infty} \int \mathrm{d}^3\, v J_n^2\left(\frac{k_\perp v_\perp}{\Omega_{ce}}\right) \delta\left(\omega_{\mathbf{k}} - k_\parallel v_\parallel - n\,\Omega_{\text{ce}}\right) \left(\frac{n\,\Omega_{\text{ce}}}{v_\perp}\frac{\partial f_e}{\partial v_\parallel} + k_\parallel \frac{\partial f_e}{\partial v_\parallel}\right) \tag{7.1.13}$$

with

$$\left.\frac{\partial \epsilon_r}{\partial \omega}\right|_{\omega=\omega_{\mathbf{k}}} \approx \frac{2\,\omega_{\text{pi}}^2}{\omega_{\mathbf{k}}}. \tag{7.1.14}$$

The solutions of the equations presented in this section describe the time evolution of the electron and ion distribution functions under the influence of ion acoustic turbulence in a magnetic field. Note that only the turbulence is responsible for the coupling between the particle species (collisions are neglected).

7.1.2 IAT onset and linear growth

The conditions for the onset of IAT and subsequent linear growth are determined by the solution of the dielectric response function eq.(7.1.10). Figure 7.1.1 shows the resulting mode frequency and growth rate as a function of the wave number for a deuterium plasma of density $n = 2\times 10^{-19}$ m^{-3} ($\omega_{\mathrm{p}i} \approx 4\times 10^{9}$ rad/s) with $T_e/T_i = 35$ and a drift velocity $v_{\mathrm{de}}/v_{\mathrm{the}} = 0.3$ for different angles of propagation with respect to the direction of the toroidal magnetic field $B_{\mathrm{T}} = 1.425$ T. The density and magnetic field are typical for low density TCV discharges compatible for X2 EC injection and are such that $\omega_{\mathrm{ce}} = \omega_{\mathrm{pe}} \approx 2.5\times 10^{11}$ rad/s.

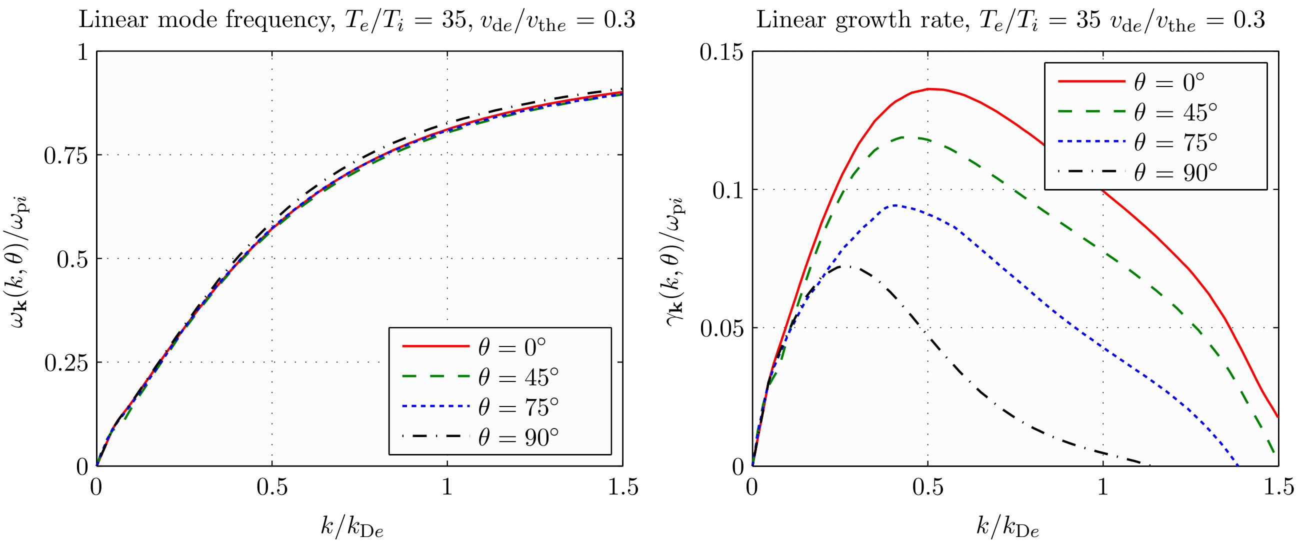

(a) Real solution of dispersion relation.

(b) Imaginary solution of dispersion relation.

Figure 7.1.1: Linear IAT frequency (a) and growth rate (b) for some angles of propagation with respect to the external magnetic field. The curves represent a deuterium plasma with degree of magnetisation $\omega_{\mathrm{ce}}/\omega_{\mathrm{pe}} = 1$, electron drift strength $v_{\mathrm{de}}/v_{\mathrm{the}} = 0.3$ and anisothermicity $T_e/T_i = 35$.

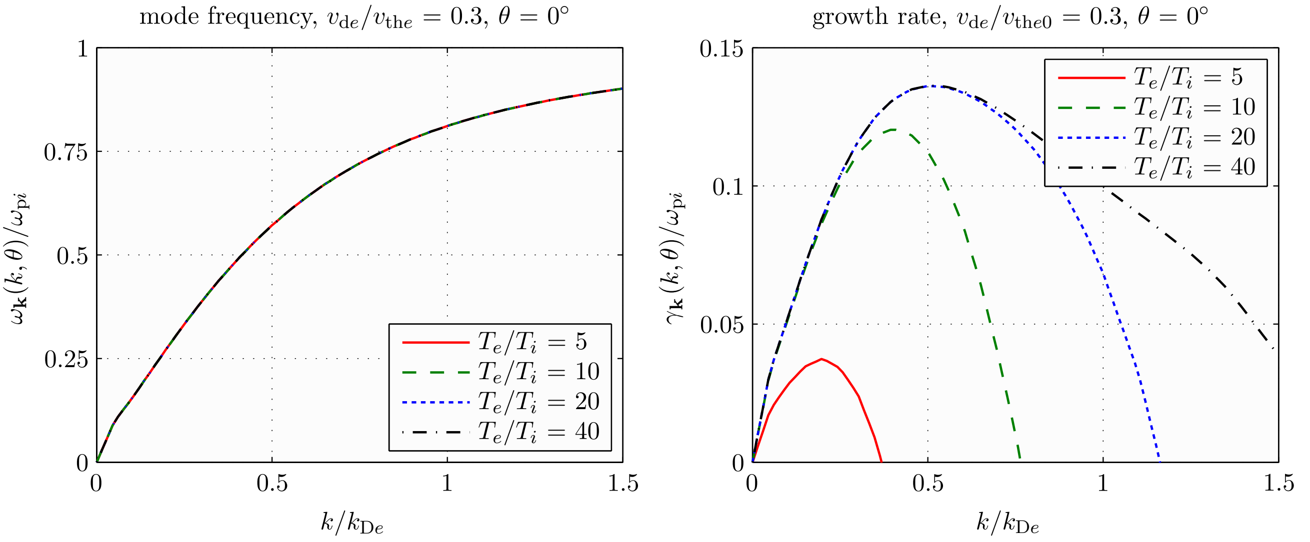

(a) Real solution of dispersion relation.

(b) Imaginary solution of dispersion relation.

Figure 7.1.2: Linear IAT frequency (a) and growth rate (b) for parallel propagation at various levels of anisothermicity. $v_{\mathrm{de}}/v_{\mathrm{the}} = 0.3$.

As expected, the maximum growth occurs for Fourier modes propagating along the main magnetic field. The oscillation frequency is almost insensitive to the direction of propagation and the maximum frequency is below the ion plasma frequency. Figure 7.1.2 illustrates the impact of the electron to ion temperature ratio, to which the mode frequency is insensitive, on the excitation of the turbulence. The figures represent mode propagation along the magnetic field and the drift velocity is again $v_{\mathrm{de}}/v_{\mathrm{the}} = 0.3$. The total growth rate is less than zero everywhere if $T_e/T_i < 2$. Its linear value doesn't exceed $\gamma_{\mathbf{k}}/\omega_{\mathrm{pi}} = 0.14$, even for still higher temperature ratios than those shown (i.e. typical for TCV low density X2 heated plasmas).

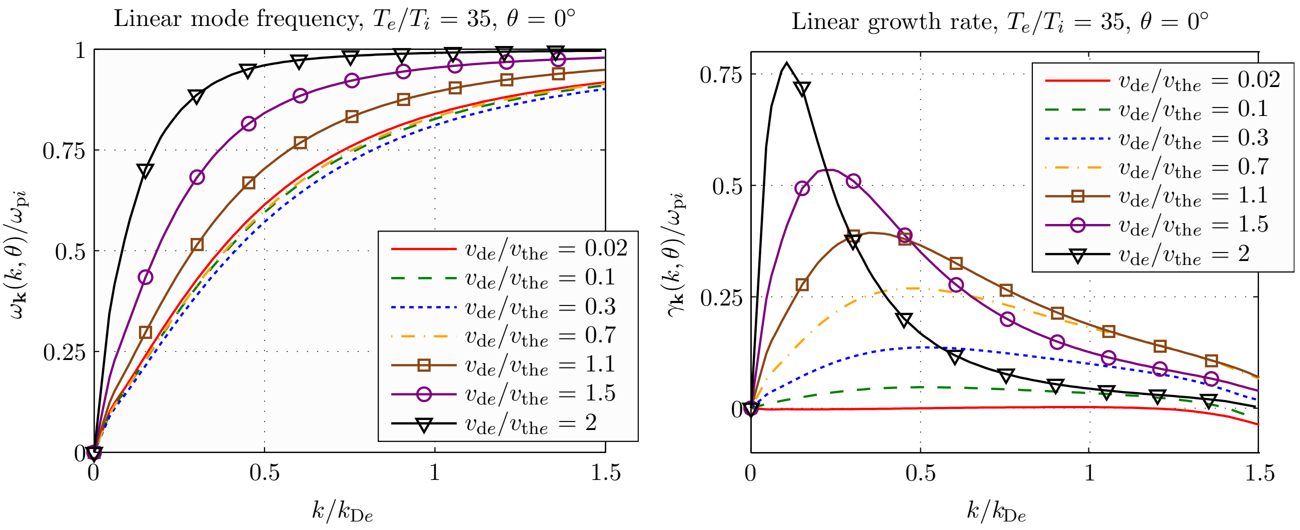
Linear mode frequency, $T_e/T_i = 35$, $\theta = 0°$

Linear growth rate, $T_e/T_i = 35$, $\theta = 0°$

(a) Real solution of dispersion relation.

(b) Imaginary solution of dispersion relation.

Figure 7.1.3: Linear IAT frequency (a) and growth rate (b) for parallel propagation for various electron drift speeds. $T_e/T_i = 35$.

Figure 7.1.3 finally shows how IAT is destabilised when the electron drift speed (shifted Maxwellian) is raised. All curves represent plasmas with $T_e/T_i = 35$ and modes with $\theta = 0$. With increasing v_{de}, the most unstable mode has a decreasing wave number and the growth rate becomes strongly enhanced. v_{de} also has an impact on the wave frequency.

The TCV plasmas discussed in the previous chapter are thus obviously unstable for ion acoustic turbulence. The initial growth of the turbulence is strongest for modes aligned with the confining magnetic field, is strongly enhanced the higher the electron drift speed and involves increasingly longer wave number when the ratio between electron and ion temperature increases.

7.2 Numerical implementation of an finite differences alternating direction implicit scheme for ion acoustic turbulence

To follow the evolution of f_e and f_i, the set of equations, eq.(7.1.3) to eq.(7.1.14), are now solved numerically using finite differences (FD). Similar to reference [359], the implementation uses the alternating-direction implicit (ADI) approach [407–409] promising better numerical stability and thus allowing for larger time steps. An explicit formulation of the technique is given in appendix E.

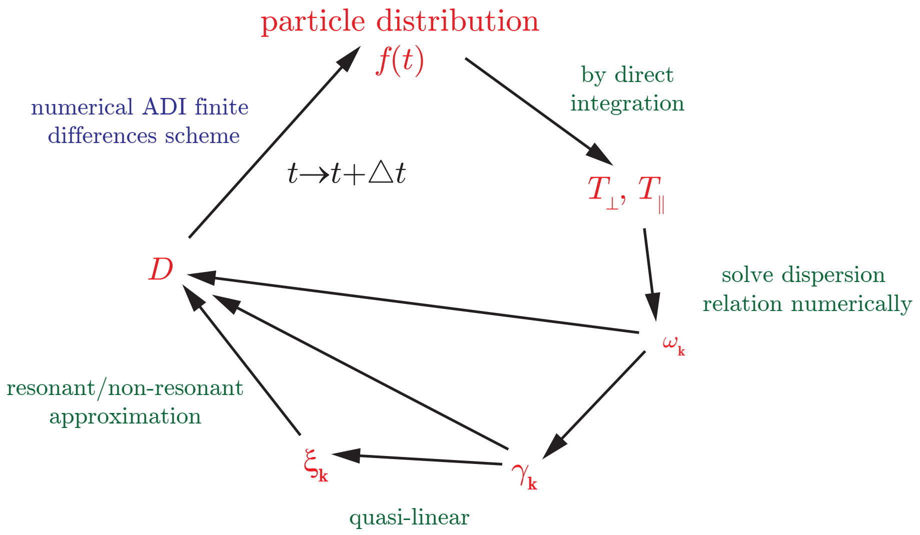

Figure 7.2.1: Iteration of the IAT code to solve the particle velocity distribution functions.

The solution of the real part of the exact dispersion relation, eq.(7.1.11), is a time consuming task. The mode frequency mostly depends on the anisotropy of the electron distribution function, that is, the exact solution is reasonably approximated by [410]

$$\epsilon_r(\mathbf{k}, \omega_{\mathbf{k}}) = 1 - \frac{\omega_{\mathrm{pi}}^2}{\omega^2} + \frac{k_{\mathrm{De}\parallel}^2}{k^2}\left(1 - \frac{2\, v_{\mathrm{de}}^2}{v_{\mathrm{the}\parallel}(t)} \exp\left(-\lambda\right) I_0(\lambda)\right) + \\ + \frac{k_{\mathrm{De}\perp}^2}{k^2}\left(1 - \frac{T_{e\perp}(t)}{T_{e\parallel}(t)}\right)\left(1 - \exp\left(-\lambda\right) I_0(\lambda)\right) \quad (7.2.1)$$

where $k_{\mathrm{De}\parallel}$ and $k_{\mathrm{De}\perp}$ are the electron Debye wave numbers evaluated respectively with the electron temperature parallel and perpendicular to the magnetic field respectively and where

$$\lambda = 2\left(\frac{k_\perp v_{e\perp}}{2\, \omega_{ce}}\right)^2 \quad (7.2.2)$$

and $I_0(\lambda)$ is the zeroth order modified Bessel function of argument λ. The time dependent temperatures appearing in eq.(7.2.1) are evaluated from

$$\begin{cases} T_{e\parallel}(t) = \dfrac{m_e}{n_e} \displaystyle\int \mathrm{d}^3v \left(v_\parallel - v_{\mathrm{de}}\right)^2 f_e(\mathbf{v}, t) \\ T_{e\perp}(t) = \dfrac{m_e}{2\, n_e} \displaystyle\int \mathrm{d}^3v\, v_\perp^2\, f_e(\mathbf{v}, t) \end{cases} \quad (7.2.3)$$

The code proceeds as illustrated in figure 7.2.1: With f_e and f_i known at time t, the instantaneous electron temperatures are obtained from eqns.(7.2.3), in order to solve the dispersion relation, eq.(7.2.1) and eq.(7.1.12) to eq.(7.1.14). The fluctuation energy is then updated through eq.(7.1.8) and the diffusion tensors, eq.(7.1.7) and eq.(7.1.9) calculated. $f_e(t + \Delta t)$ and $f_i(t + \Delta t)$ are finally determined by solving the quasilinear diffusion equations, eq.(7.1.3) and eq.(7.1.4) with the ADI method. In the calculation of the electron diffusion tensor, the singular delta function is approximated by a Lorentzian

$$\delta\left(\omega_{\mathbf{k}} - k_\parallel v_\parallel - n\, \Omega_{ce}\right) \approx \frac{1}{\pi} \frac{\eta}{\left(\omega_{\mathbf{k}} - k_\parallel v_\parallel - n\, \Omega_{ce}\right)^2 + \eta^2} \quad (7.2.4)$$

where the peak width was chosen $\eta = k_\parallel \Delta v_\parallel$ with $\Delta v_\parallel$ equal to the mesh size along $v_\parallel$ of the velocity grid.

Further, the separation of the ion diffusion tensor into resonant and nonresonant contributions leads to a divergence of $\underline{\mathbf{D}}_i$ at the boundary of the two regions. The correct value at $|\omega_{\mathbf{k}} - k_\parallel v_\parallel| \approx |k_\perp v_\perp|$ was worked out in reference [363] and is limited by

$$\left.\begin{pmatrix} D_{\perp\perp} \\ D_{\perp\parallel} \\ D_{\parallel\parallel} \end{pmatrix}_i\right|_{\substack{|\omega_{\mathbf{k}}-k_\parallel v_\parallel| \\ \approx |k_\perp v_\perp|}} \lesssim \frac{8\pi\, e^2}{m_i^2} \sum_{\mathbf{k}} \frac{\mathscr{E}_{\mathbf{k}}}{\gamma_{\mathbf{k}}\, k^2} \frac{1}{\gamma_{\mathbf{k}}^2 + 4\left(\omega_{\mathbf{k}} - k_\parallel v_\parallel\right)^2} \begin{pmatrix} k_\perp^2 \left(\left(\omega_{\mathbf{k}} - k_\parallel v_\parallel\right)^2 + \gamma_{\mathbf{k}}^2/2\right) \\ k_\perp k_\parallel \left(\omega_{\mathbf{k}} - k_\parallel v_\parallel\right)^2 \\ k_\parallel^2 \left(2\left(\omega_{\mathbf{k}} - k_\parallel v_\parallel\right)^2 + \gamma_{\mathbf{k}}^2\right) \end{pmatrix} \tag{7.2.5}$$

Damped modes prohibit nonresonant ions to diffuse [411, 412] and this is taken into account by replacing $\gamma_{\mathbf{k}}$ in eq.(7.1.7) by zero for all damped modes, as already used by Field and Fried [357] in 1964.

7.2.1 Parameter setup and grid configuration

Numerical simulations of ion waves in the frame of IAT are complicated by the fact that the time step has to be sufficiently small to follow the dynamics of the electrons, but the total simulation time must be long enough ($t \gg 1/\omega_{\mathrm{p}i}$) to reveal the asymptotic nonlinear behaviour of the instabilities. The ADI formulation improves the numerical stability such that time steps of $0.1/\omega_{\mathrm{p}i}$ give satisfactory results.

The velocity space is parameterised with a uniform mesh size of $\Delta v_e = 0.1\, v_{\mathrm{the}0}$ for the electrons and $\Delta v_i = 0.1\, c_{\mathrm{s}0}$ for the ions. The velocity grids extend to several multiples of the thermal electron velocity and ion sound velocity respectively. A typical simulation considers some hundred Fourier modes, covering the **k**-vector space confining the inverse volume where most of the waves are emitted. The code is currently implemented in Fortran and Matlab, quantities are described by four-dimensional matrices (describing the **v** and **k** spaces), such that the velocity space integrals and wave number space summations are facilitated by operations running along certain matrix dimensions.

The computer running the IAT code incorporates an Intel Core i7 (four physical CPU cores), featuring 12 GB of RAM. The abundant quantity of RAM permitted runs with larger numbers of Fourier modes and finer velocity space gridding. Such code runs did not exhibit a different evolution of the turbulence, the numerical stability of the reduced grid was thus considered sufficient and numerical divergence does not appear to occur.

The distribution functions are initially Maxwellians (isotropic for the ions, drifting for the electrons). The perpendicular derivatives of f at $v_\perp = 0$ are set to zero (cylindrical symmetry about $v_\parallel$) and the distribution itself is set to zero at the infinite velocity boundaries.
The fluctuation energy is initialised uniformly to a level that is a sufficiently small fraction of the thermal noise, such that the evolution at later times is independent of the initially chosen value (verified by comparison of the asymptotic turbulence behaviour at later times of simulations launched with different initial fluctuation levels). In the simulations shown in the following, this value was $\mathscr{E}_{\mathbf{k}}(t=0) = 1 \times 10^{-6}\, n_{e0}\, T_{e0}$.

7.3 Quasilinear turbulence growth and saturation studies

The initial evolution of IAT is characterised by the linear growth and frequency (section 7.1.2). When the wave amplitude grows, linear ω and γ are modified and the linear analysis is invalidated [357]. As already pointed out, an accurate description of IAT has to follow the evolution of the electron and ion distribution functions simultaneously. An exact description of f_e on the IAT timescale ($1/\omega_{\mathrm{pi}}$) during the start of injection of EC waves is however hopeless. A work around could be an approximation of the electron picture by the drifting Maxwellian, eq.(7.1.1), at least as an initial condition. As time advances, it may then be required that the current represented by the circulating electrons,

$$j(t) = n_e\, e \int f_e(\mathbf{v}, t)\, v_\parallel\, \mathrm{d}^3 v \tag{7.3.1}$$

remains constant. To achieve this, the external electric field E_0 in eq.(7.1.2) must grow in time. After each update of f_e, this field is found from $\partial j / \partial t = 0$, that is, using eq.(7.3.1) and eq.(7.1.2),

$$E_0(t) = -\frac{m_e}{n_e\, e} \int \mathrm{d}^3 v\, v_\parallel\, \frac{\partial}{\partial \mathbf{v}} \cdot \underline{\mathbf{D}}_e(\mathbf{v}, t) \cdot \frac{\partial f_e(\mathbf{v}, t)}{\partial \mathbf{v}} \tag{7.3.2}$$

This procedure was applied to model discharge #31188 presented in the following section. $E_0(t)$ is updated such to regulate a constant j, equal to the driven ECCD current. Section 7.4 will later demonstrate that this approach is not determinative on the long-term behaviour of the turbulence.

7.3.1 Discharge #31188

The IAT simulation results presented in the following were produced for the parameters of discharge #31188, whose electron distribution function was modelled using *CQL3D* (section 5.4.2.2) and reasonably approximated with a bi-Maxwellian (figure 5.4.3). The IAT code was therefore initialised with the following settings: Bulk $f_e^{(0)}$: $n_e^{(0)} = 2 \times 10^{-19}$ m^{-3}, $T_e^{(0)} = 6.5$ keV (both from the Thomson scattering diagnostic), $v_{\mathrm{de}}^{(0)} = 0$; Tail $f_e^{(1)}$, derived from the bi-Maxwellian *CQL3D* f_e fit: $n_e^{(1)}/n_e^{(0)} = 10$ %, $T_e^{(1)} = 15$ keV and $v_{\mathrm{de}}^{(1)} = 0.7\, v_{\mathrm{the}}$. The tail temperature is in agreement with the HFS ECE measurement. The deuterium ion population temperature is $T_i^{(0)} = 200$ eV (CXRS measurement), so $T_e/T_i \simeq 33$. Note that the drift speed of the tail population is $v_{\mathrm{de}}^{(1)} \simeq 30\, c_{s0}$, thus destabilising IAW or equivalently $v_{\mathrm{de}}^{(1)} \gtrsim 0.1\, c$, where the latter value is consistent with the *NOTEC-TCV* simulation (page 155). The simulation uses the time step of $\Delta t = 0.1/\omega_{\mathrm{pi}}$ and runs at least until the saturation of the turbulence is reached. Here the simulation was stopped after 6000 iterations, corresponding to 600 turbulence cycles, thus covering a time period of about 0.1 μs.

Figure 7.3.1 shows a compilation of plots illustrating the modelled evolution of the quantities in k-space, that is, from top to down, the mode frequency $\omega_{\mathbf{k}}$, IAW growth respectively damping rates (i.e. γ_e, γ_i and $\gamma_{\mathrm{tot}} = \gamma_e + \gamma_i$) and the resulting fluctuation spectrum $\mathscr{E}_{\mathbf{k}}$. With the appearance of the fast ions, the ion damping increases strongly, such that the total growth rate is completely governed by the ions. The absolute decrease of the electron growth rate is due to the increasing electron heating, that is the slope of the electron distribution function flattens and thus γ_e becomes weaker. The number of growing modes decreases during the turbulence growth and some time after the quench of the instability, there are only damped modes remaining and the turbulence energy starts to vanish. The velocity space diffusion tensors for the electrons and ions are shown in figures 7.3.4 and 7.3.5 respectively.

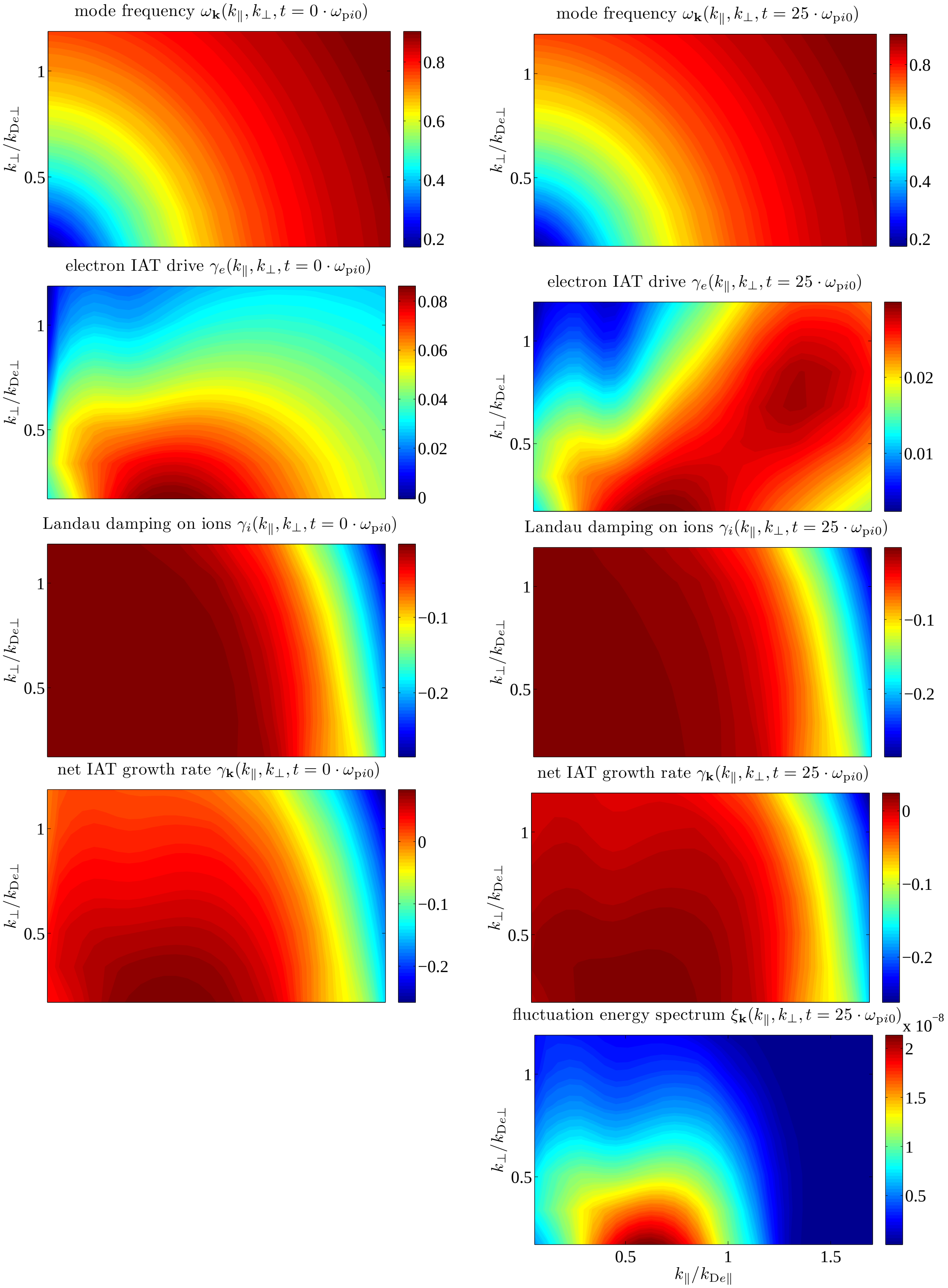

Figure 7.3.1: IAT simulation for TCV discharge #31188, t = 1.4 s. From top to down: mode frequency $\omega_{\mathbf{k}}$, electron IAW emission rate $\gamma_{e\mathbf{k}}$, ion IAW damping rate $\gamma_{i\mathbf{k}}$, total IAW growth rate $\gamma_{\mathbf{k}}$ and IAW energy density $\mathscr{E}_{\mathbf{k}}$. The time evolution of the turbulence is shown from left to right, that is at $\omega_{\mathrm{p}i} \cdot t$ = 0 (initial conditions) and 25. See the next figure for the continuation.

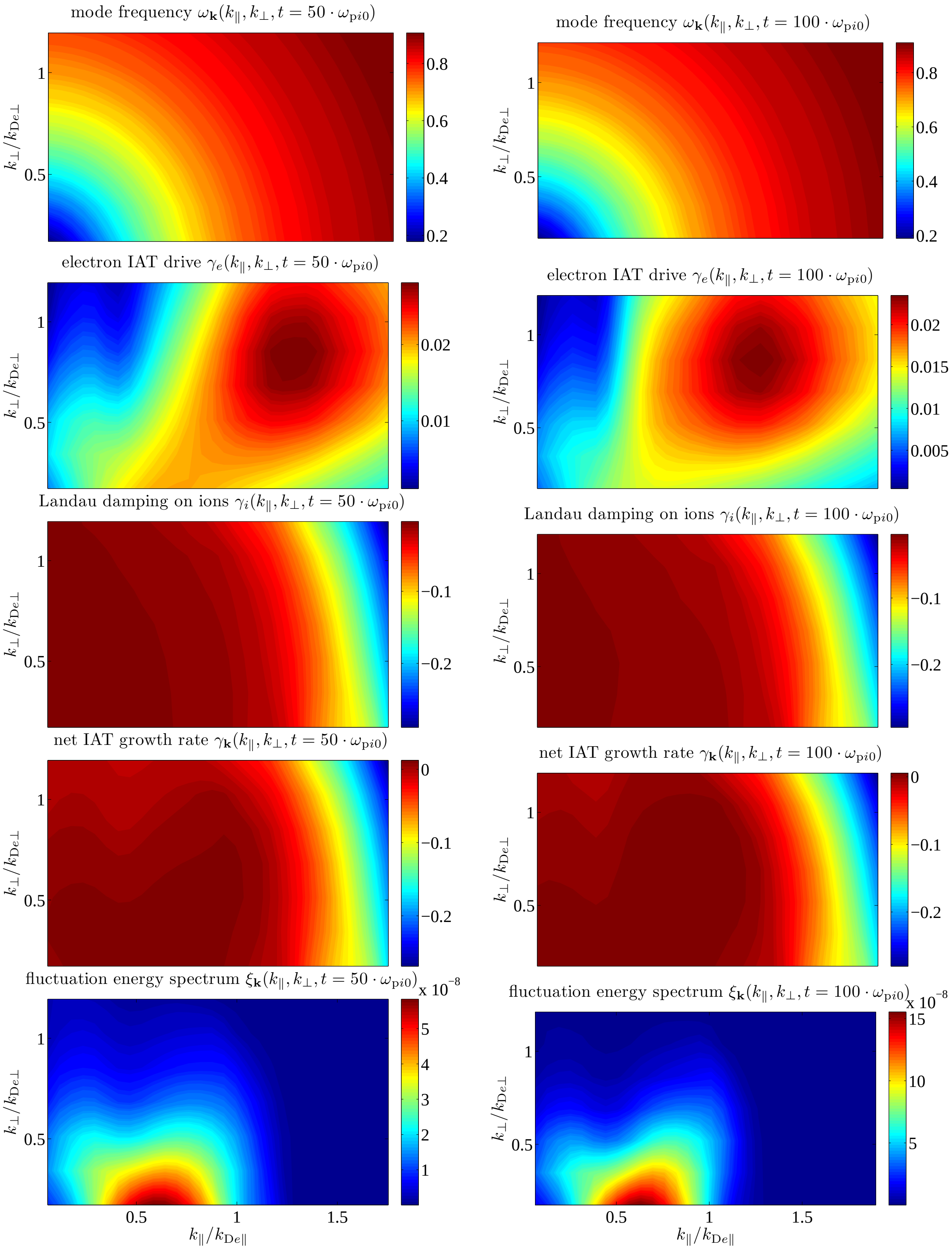

Figure 7.3.2: IAT simulation for TCV discharge #31188, $t = 1.4$ s. From top to down: mode frequency $\omega_{\mathbf{k}}$, electron IAW emission rate $\gamma_{e\mathbf{k}}$, ion IAW damping rate $\gamma_{i\mathbf{k}}$, total IAW growth rate $\gamma_{\mathbf{k}}$ and IAW energy density $\mathscr{E}_{\mathbf{k}}$. The time evolution of the turbulence is shown from left to right, that is at $\omega_{\mathrm{pi}} \cdot t = 50$ and 100. See the previous figure for the initial evolution and the next figure for the continuation.

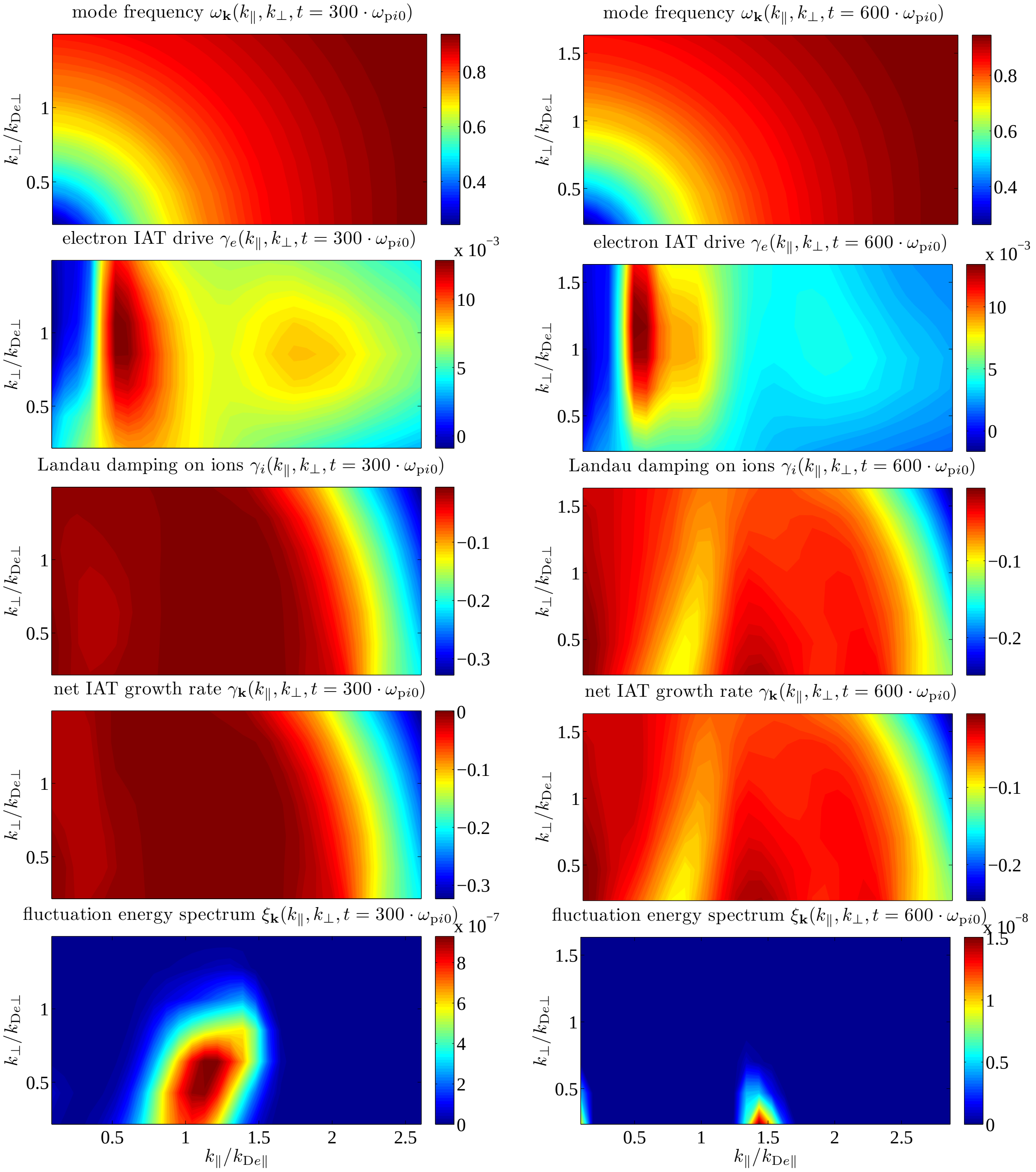

Figure 7.3.3: IAT simulation for TCV discharge #31188, t = 1.4 s. From top to down: mode frequency $\omega_{\mathbf{k}}$, electron IAW emission rate $\gamma_{e\mathbf{k}}$, ion IAW damping rate $\gamma_{i\mathbf{k}}$, total IAW growth rate $\gamma_{\mathbf{k}}$ and IAW energy density $\mathscr{E}_{\mathbf{k}}$. The time evolution of the turbulence is shown from left to right, that is at $\omega_{\mathrm{p}i} \cdot t$ = 300 and 600. See the previous figure for earlier times.

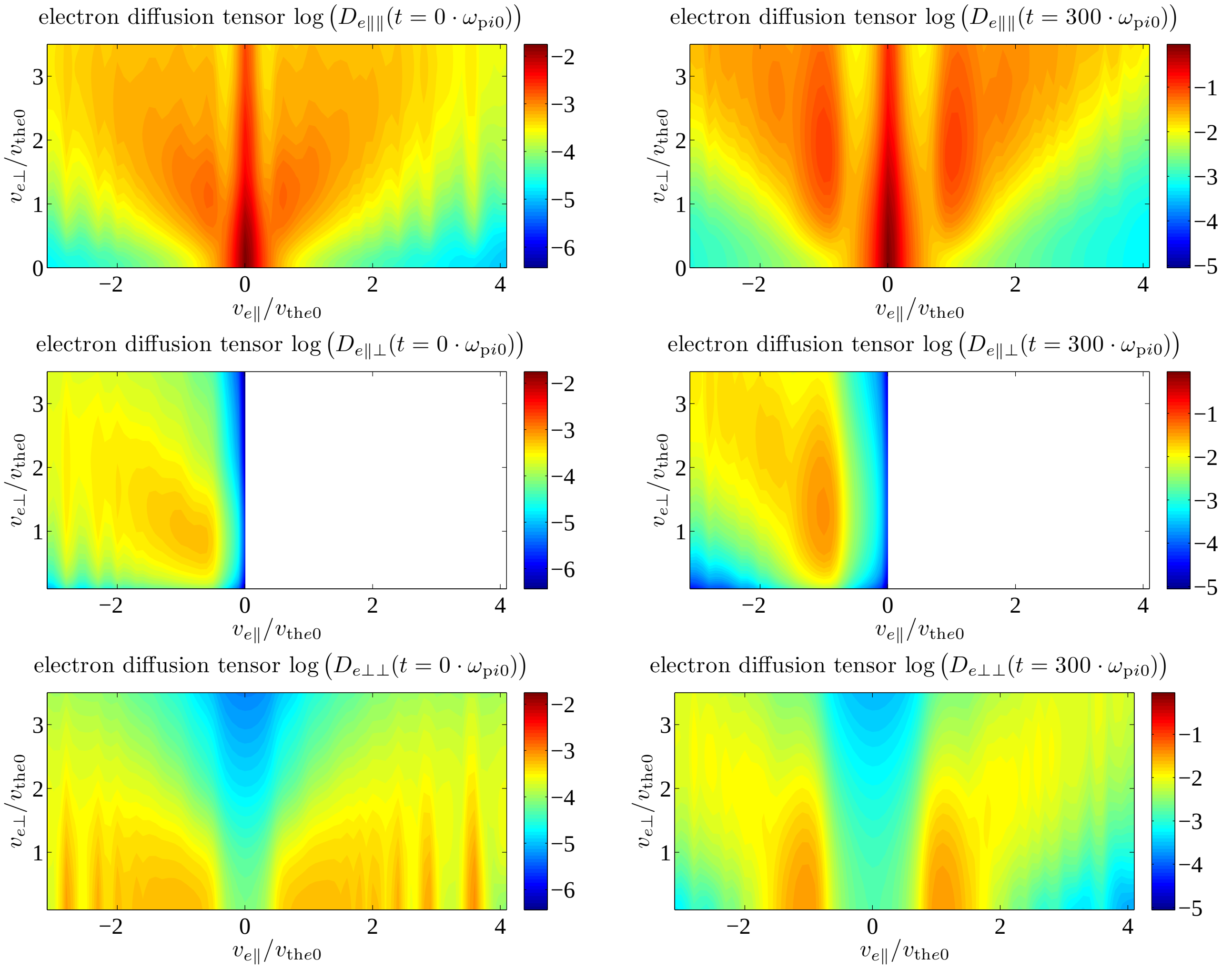
electron diffusion tensor $\log\left(D_{e\parallel\parallel}(t = 0 \cdot \omega_{\mathrm{pi}0})\right)$

electron diffusion tensor $\log\left(D_{e\parallel\parallel}(t = 300 \cdot \omega_{\mathrm{pi}0})\right)$

electron diffusion tensor $\log\left(D_{e\parallel\perp}(t = 0 \cdot \omega_{\mathrm{pi}0})\right)$

electron diffusion tensor $\log\left(D_{e\parallel\perp}(t = 300 \cdot \omega_{\mathrm{pi}0})\right)$

electron diffusion tensor $\log\left(D_{e\perp\perp}(t = 0 \cdot \omega_{\mathrm{pi}0})\right)$

electron diffusion tensor $\log\left(D_{e\perp\perp}(t = 300 \cdot \omega_{\mathrm{pi}0})\right)$

Figure 7.3.4: IAT simulation for TCV discharge #31188, $t = 1.4$ s. From top to down: electron diffusion tensor components $D_{e\parallel\parallel}$, $D_{e\parallel\perp}$ and $D_{e\perp\perp}$. The left column represents the diffusion at IAT onset ($\omega_{\mathrm{pi}} \cdot t$ = 0), the right column at quasilinear saturation ($\omega_{\mathrm{pi}} \cdot t = 300$).

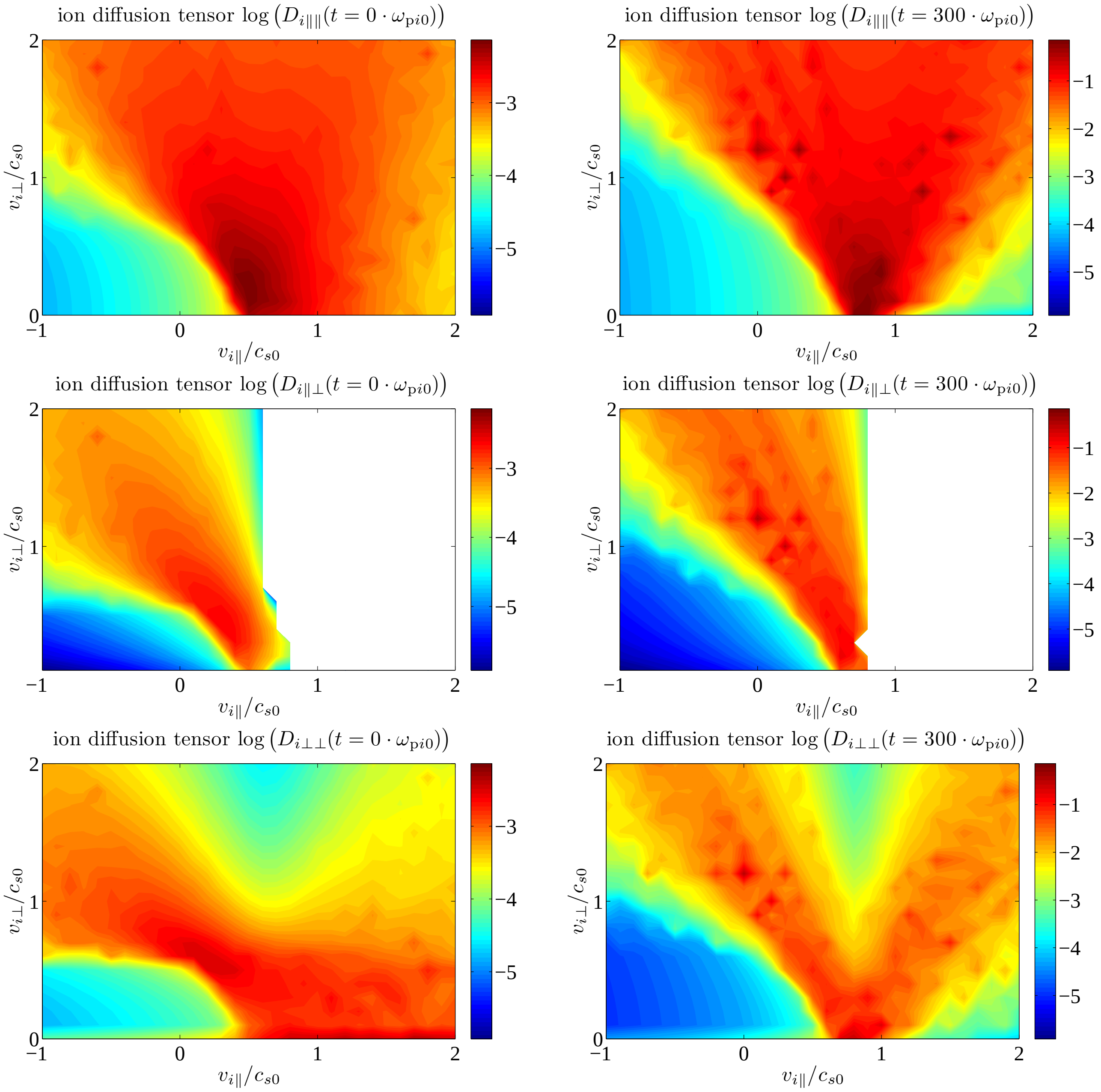

Figure 7.3.5: IAT simulation for TCV discharge #31188, $t = 1.4$ s. From top to down: ion diffusion tensor components $D_{i\|\|}$, $D_{i\|\perp}$ and $D_{i\perp\perp}$. The left column represents the diffusion at IAT onset ($\omega_{\mathrm{p}i} \cdot t = 0$), the right column at quasilinear saturation ($\omega_{\mathrm{p}i} \cdot t = 300$).

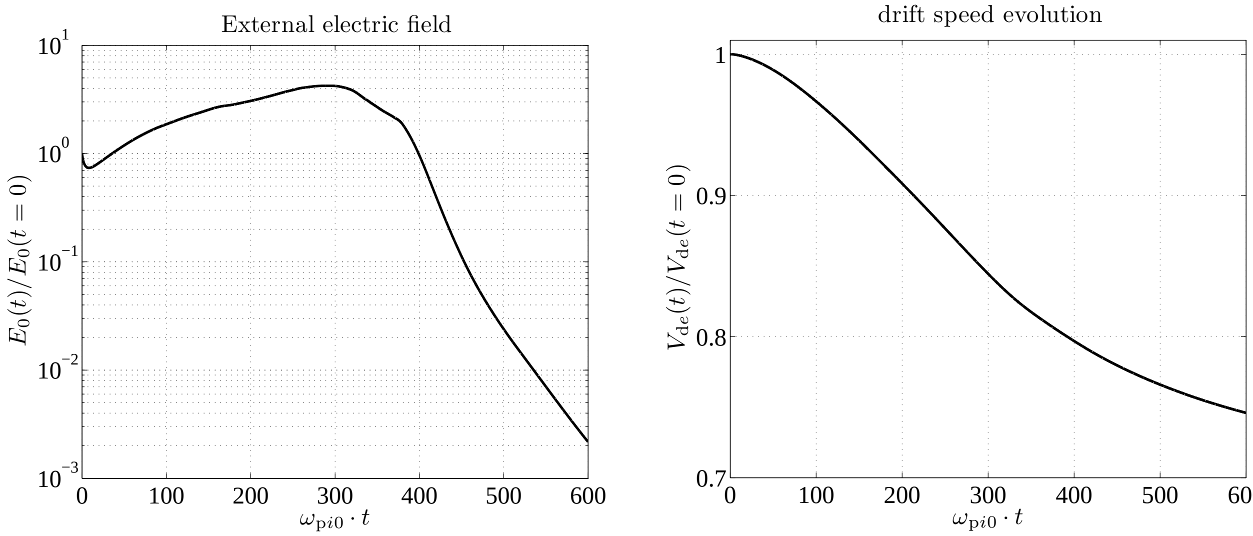

(a) constant current regulator (b) electron distribution drift

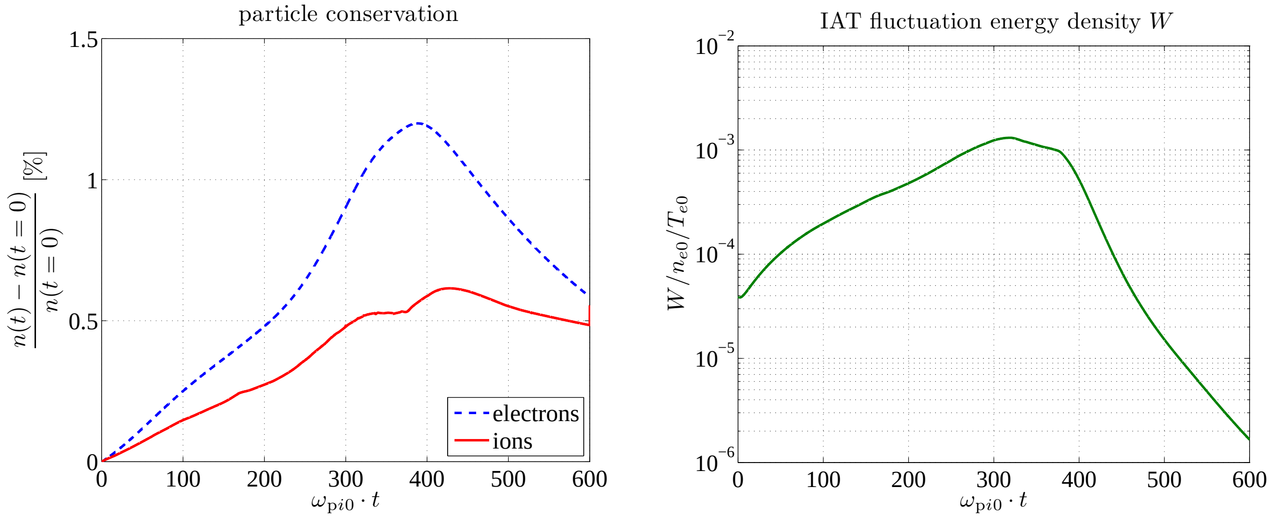

(c) simulation stability (d) IAW total wave energy

Figure 7.3.6: IAT simulation for TCV discharge #31188, $t = 1.4$ s. Time traces of (a) artificial toroidal electric field $E_0(t)$, (b) distribution function averaged electron drift velocity $v_{\mathrm{de}}(t)$, (c) number of particles involved in the IAT simulation and (d) total fluctuation energy density $W(t)$.

Figure 7.3.6 shows then time traces of the artificially applied external electric field (to maintain a constant toroidal current), average electron drift velocity, the particle conservation measuring the accuracy of the simulation and the total electric field energy density $W(t)$. The latter is obtained by summation of all Fourier modes: The number of modes with wave vector $\mathbf{k}$ in a large volume V is $V\mathrm{d}^3k/(2\pi)^3$, thus

$$W(t) = \sum_{\mathbf{k}} \mathscr{E}_{\mathbf{k}}(t) = \lim_{V\to\infty} \frac{V}{(2\pi)^3} \int 2\pi\, k_\perp\, \mathrm{d}k_\perp \int \mathrm{d}k_\parallel\, \mathscr{E}_{\mathbf{k}}(t) =$$

$$\lim_{\substack{\Delta k_\perp \to 0 \\ \Delta k_\parallel \to 0}} \frac{\pi}{(\Delta k_\perp)^2 \Delta k_\parallel} \sum_{k_\parallel} \sum_{k_\perp} 2\pi\, k_\perp\, \Delta k_\perp\, \Delta k_\parallel\, \mathscr{E}_{\mathbf{k}}(t) \quad (7.3.3)$$

$W(t)$ characterises the different stages of the turbulence, namely the onset ($\omega_{\mathrm{pi}} \cdot t = 0$) and linear growth (here up to approximately $\omega_{\mathrm{pi}} \cdot t = 25$), where the most unstable mode aligns with the direction of the current, $k_\parallel \approx 0.7\, k_{\mathrm{De}}$.

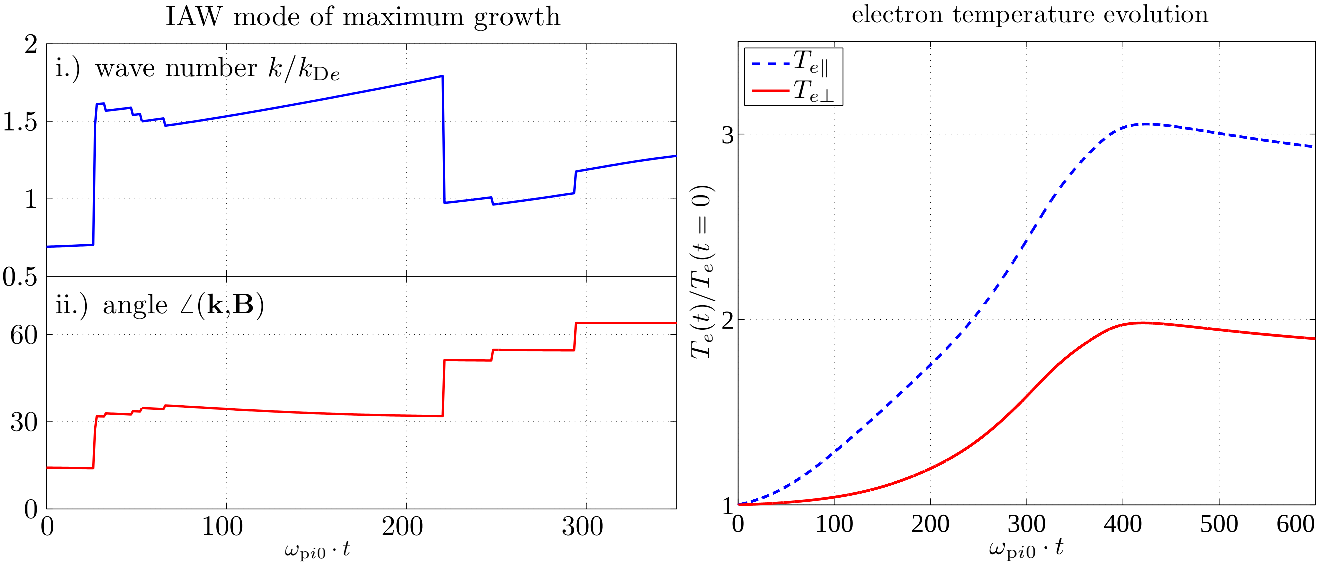

(a) most unstable mode. (b) simulated electron temperatures.

Figure 7.3.7: IAT simulation for TCV discharge #31188, $t = 1.4$ s.
(a) k-space coordinates of the most unstable mode, i.e. the norm of the wave vector (i) and its angle with respect to the toroidal magnetic field (ii).
(b) Electron heating, measured with the parallel and perpendicular electron temperatures, evaluated from the modelled electron distribution function.

Later the evolution is quasi-linear where the electrons would emit IAW at large wave numbers, but these are heavily damped by the ions ($\omega_{\mathrm{pi}} \cdot t = 50 \ldots 100$) and then the quasi-linear quench, where $W(t)$ saturates at a level of $\approx 1 \times 10^{-3}\, n_{e0}\, T_{e0}$ (around $\omega_{\mathrm{pi}} \cdot t = 300 \ldots 400$) and finally decays. At the saturation stage, the mode with highest growth $\gamma_{\mathbf{k}}$ is located at strongly oblique angles with respect to the direction of the current. The coordinates of the mode with maximum growth rate is shown in figure 7.3.7a, as a function of time.

Velocity space representations of the particle distribution functions are shown in figure 7.3.8 (during the growth of IAT) and 7.3.9 (at saturation). The electron distribution function becomes strongly distorted in the parallel direction (mainly due to the artificially applied electric field, continuously pushing more electrons into the runaway regime). The electron heating, measured with the virtual diagnostics by means of eqns.(7.2.3), are shown in figure 7.3.7b. The temperatures saturate only when the fluctuation energy is already decaying (after $\omega_{\mathrm{pi}} \cdot t = 400$). The parallel temperature triples, the perpendicular doubles. Note that the increase in T_e shown here is not due to the absorption of the EC waves (which are not part of the model) but due to anomalous resistivity generated by the turbulence (parallel direction) and the cross-field scattering of the electrons due to the cyclotron resonance (perpendicular direction).
The ion distribution function spreads at the very early stage by nonresonant diffusion and resonant interactions tend to flatten the distribution function around the resonance region located around $v_i/c_{s0} \approx 1$ where the tail is formed. The tail develops mostly in the parallel direction during the linear phase, later the distortion extends also into the perpendicular direction. Note that the counter-current distribution is mostly unaffected by the turbulence. The illustrations below the contour plots in figures 7.3.8 and 7.3.9 indicate the parallel and perpendicular integrals of the ion distribution function, eqns.(5.4.6), nicely highlighting the buildup of the suprathermal tail distribution.

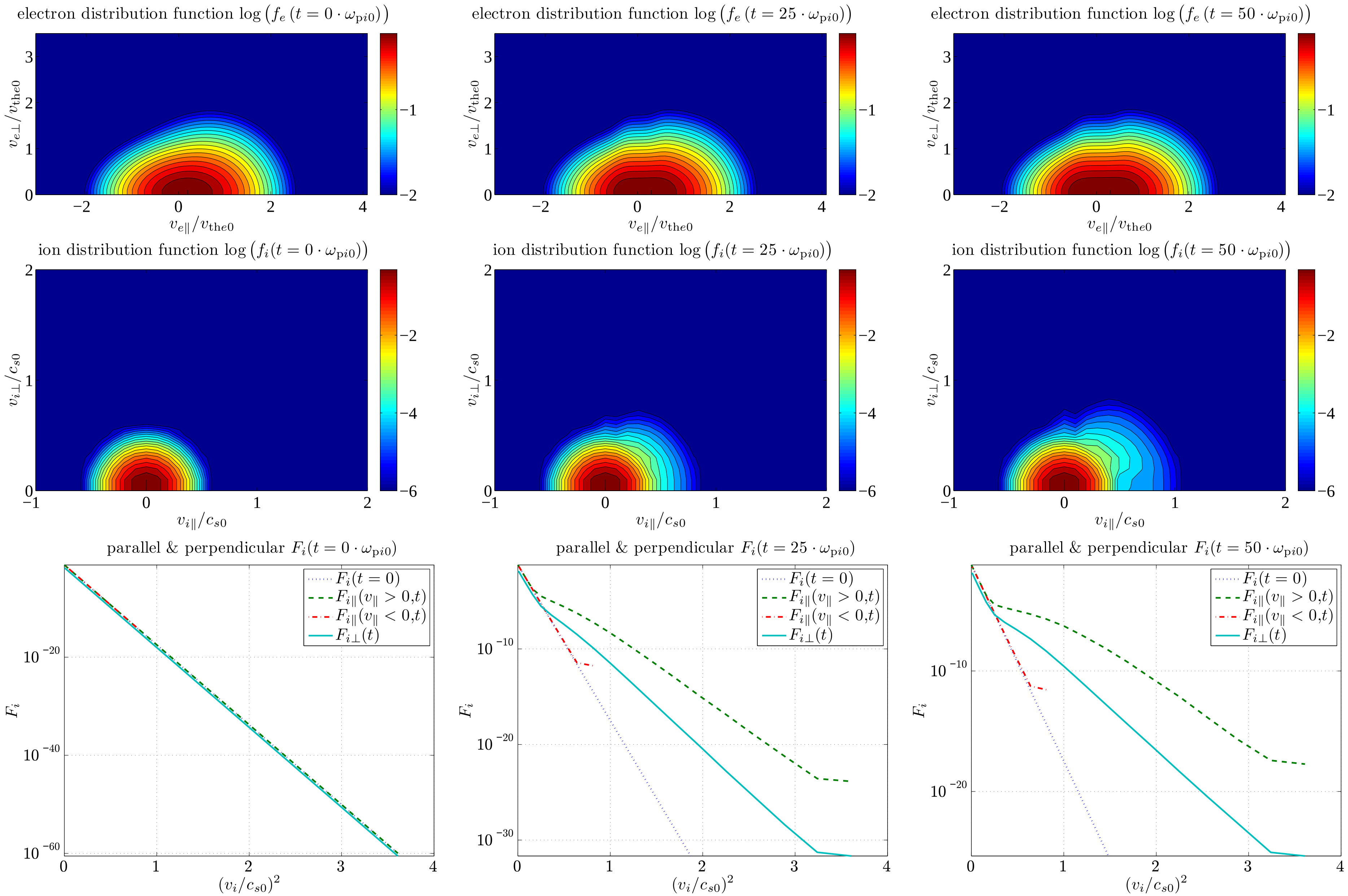

Figure 7.3.8: IAT simulation for TCV discharge #31188, $t = 1.4$ s. From top to down: Pitch angle maps of the electron f_e and ion f_i velocity distribution functions as well as parallel and perpendicular integrals of the latter. The time evolution of the velocity space diffusion is shown from left to right, that is at $\omega_{\mathrm{pi}} \cdot t = 0$, 25 and 50. See figure 7.3.9 for the continuation of the series.

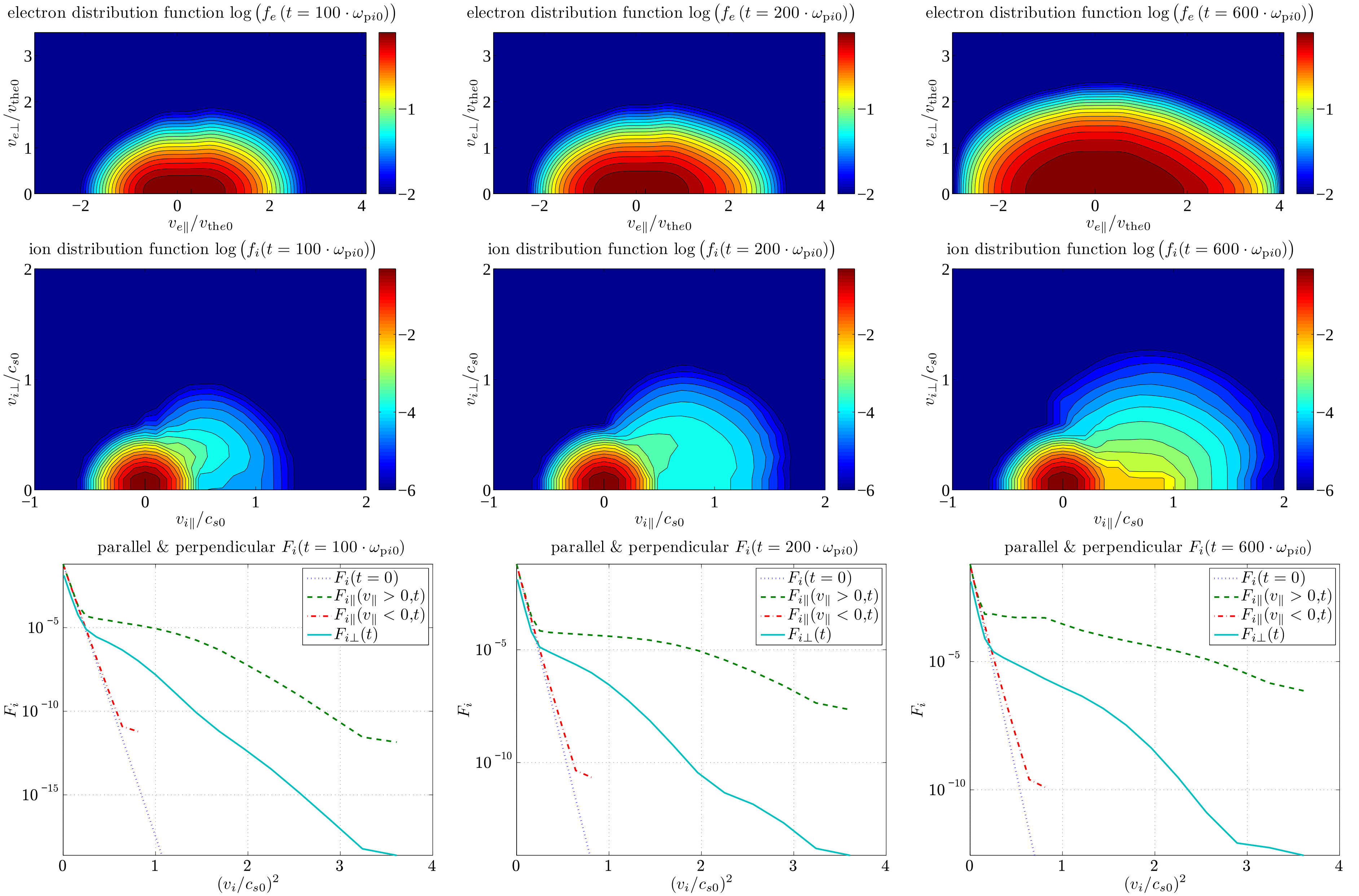

Figure 7.3.9: IAT simulation for TCV discharge #31188, $t = 1.4$ s. From top to down: Pitch angle maps of the electron f_e and ion f_i velocity distribution functions as well as parallel and perpendicular integrals of the latter. The time evolution of the velocity space diffusion is shown from left to right, that is at $\omega_{\mathrm{pi}}\cdot t = 100$, 200 and 600.

It is convenient to express the velocity space diffusion coefficients in terms of a tensor describing the characteristic time of diffusion $\underline{\boldsymbol{\tau}}_{\mathbf{k}}$,

$$\underline{\mathbf{D}}_i(\mathbf{v},t) = \frac{8\pi\, e^2}{m_i^2} \sum_{\mathbf{k}} \mathscr{E}_{\mathbf{k}}(t)\, \underline{\boldsymbol{\tau}}_{\mathbf{k}}(\mathbf{v},t) \tag{7.3.4}$$

as the dynamics of the ions in the velocity space is more instructively illustrated by $\tau_{\mathbf{k}}$ associated with the most unstable mode.

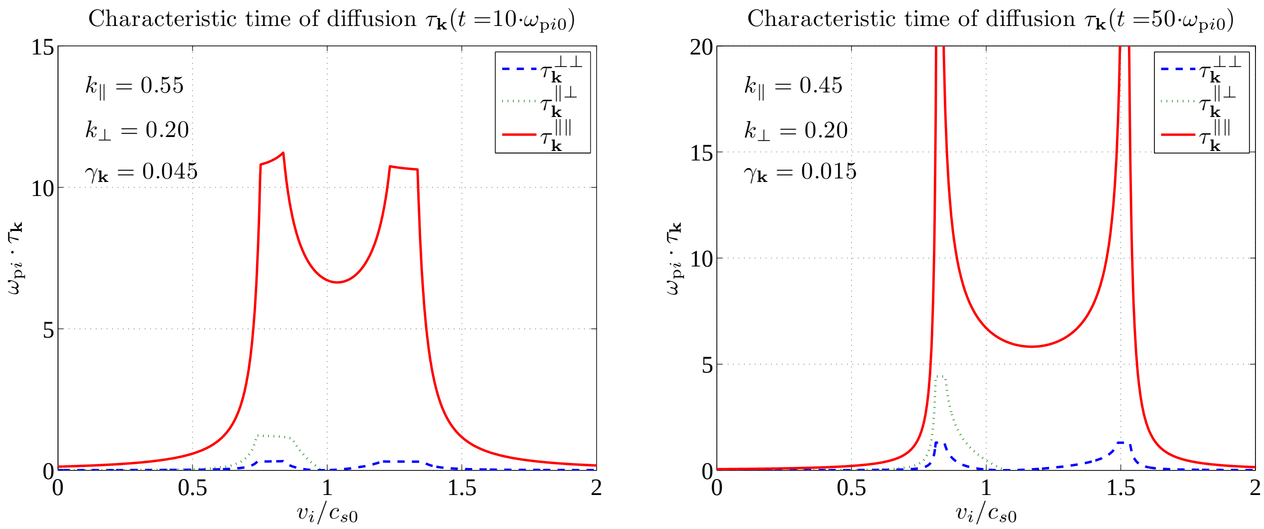

(a) at onset.

(b) during quasilinear growth.

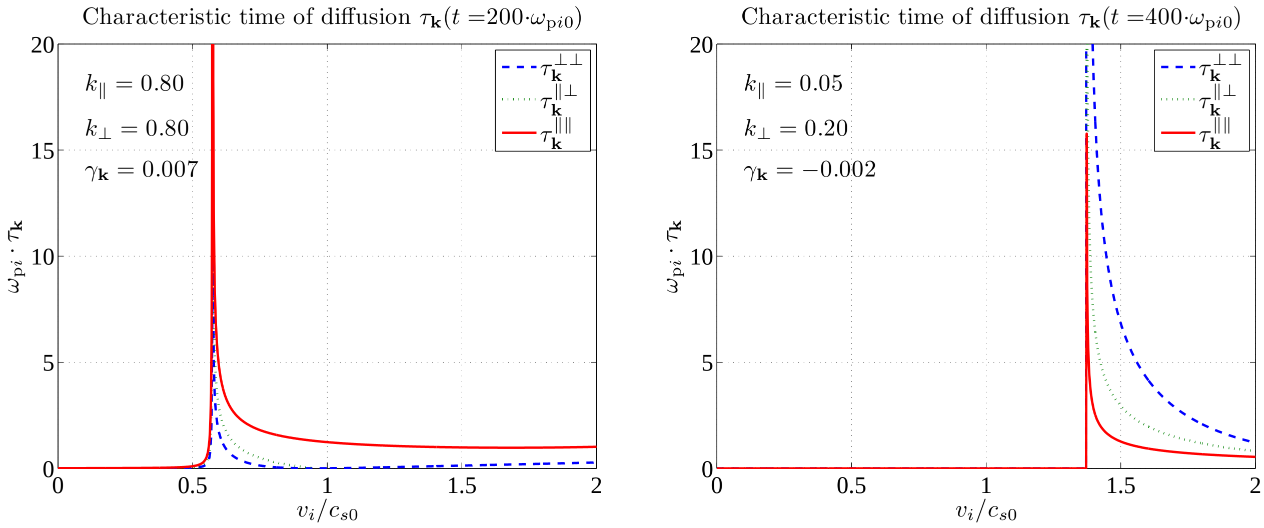

(c) at quasisaturation.

(d) saturated.

Figure 7.3.10: IAT simulation for TCV discharge #31188, $t = 1.4$ s. Characteristic time of ion diffusion in the velocity space of the most unstable IAW mode, whose coordinates and growth rate are indicated on each subfigure. (a) – (d) show the time instants $\omega_{pi}\cdot t = 10$, 50, 200 and 400 respectively. The resonant domain of diffusion locates between the two peaks in (a) and to the right of the characteristic time peaks in the other subfigures.

Figure 7.3.10 shows the characteristic ion diffusion time evaluated at velocities $v_{i\|} = v_{i\perp}$, as a function of $v = \sqrt{v_{i\|}^2 + v_{i\perp}^2}$. The resonant and nonresonant parts of the diffusion coefficients join smoothly together at the resonance boundaries. As shown, from the beginning, and throughout the quasilinear growth, the diffusion in the parallel direction dominates.

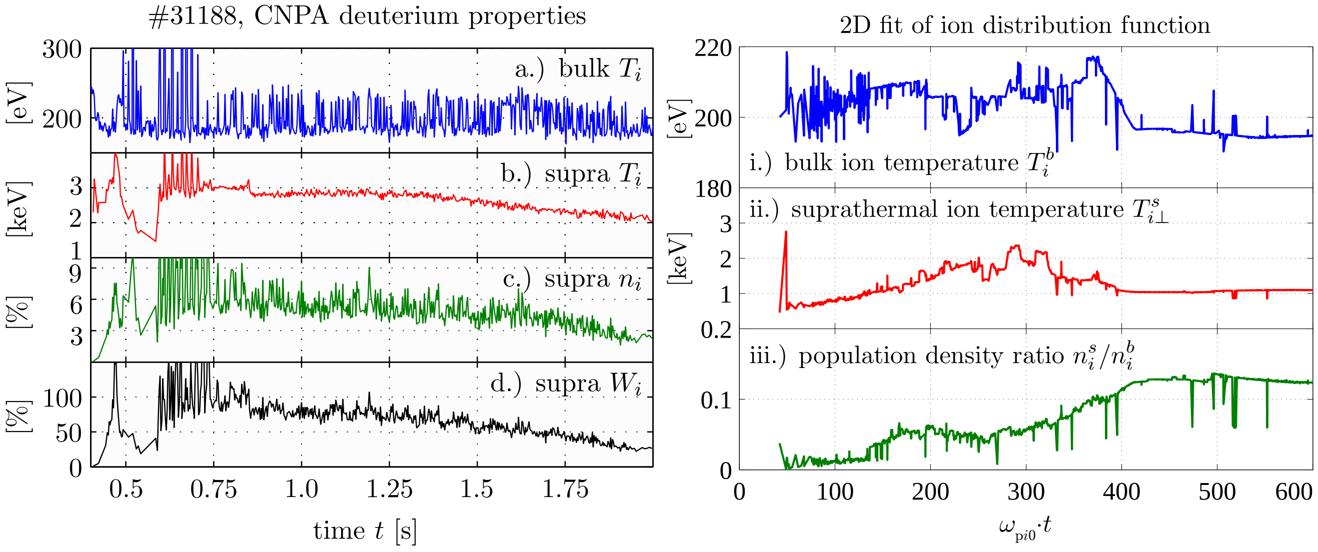

(a) experiment.

(b) simulation.

Figure 7.3.11: Comparison of the measured (#31188, CNPA) fast ion properties (a) to the simulation (b) of the fast ion production using the IAT code. The simulation is representative for the experimental time $t = 1.4$ s, when the electron distribution function was modelled with *CQL3D*.

This is clearly seen in the distribution function, the suprathermal tail first extends into the parallel direction. Diffusion into the perpendicular direction finally dominates at the quench of the turbulence and f_i starts to deform into the perpendicular velocities as well.

The ion distribution function is approximately described by a superposition of the thermal bulk with an anisotropic suprathermal tail. At each time step, f_i was fitted by two-dimensional unconstrained nonlinear minimisation with the function (isotropic bulk and anisotropic tail)

$$f_i(v_\perp, v_\parallel, t) = n_i^b \left(\frac{m_i}{2\pi\, T_i^b}\right)^{3/2} \exp\left(-\frac{m_i}{2}\left(\frac{v_{i\perp}^2 + v_{i\parallel}^2}{T_i^b}\right)\right) + \\ 2\, n_i^s \left(\frac{m_i}{2\pi}\right)^{3/2} \frac{1}{T_{i\perp}^s \sqrt{T_{i\parallel}^s}} \exp\left(-\frac{m_i}{2}\left(\frac{v_{i\perp}^2}{T_{i\perp}^s} + \frac{v_{i\parallel}^2}{T_{i\parallel}^s}\right)\right) \quad (7.3.5)$$

The resulting fast ion parameters are shown in figure 7.3.11 (right) where they are compared to the fast ion time traces measured with the CNPA (left). The bulk ion temperature barely changes, as in the experiment.

Note that the simulation is intended to model the turbulence for the electron properties at $t = 1.4$ s, although the onset of IAT already occurs at $t = 0.4$ s. The modelled hot perpendicular ion temperature steadily increases and upon saturation ($\omega_{\mathrm{pi}} \cdot t = 300$), exceeds 2 keV (ten times the bulk temperature). At the same time, the fast ion density is about 6 % of the total ion density. Both, T_i^s and n_i^s/n_i^b are close the experimentally observed values (3 keV and 5 % respectively). At later times, the simulation shows a cooling and strengthening of the tail population, but this will probably not be observed in the experiment where turbulence is driven continuously by ECCD.

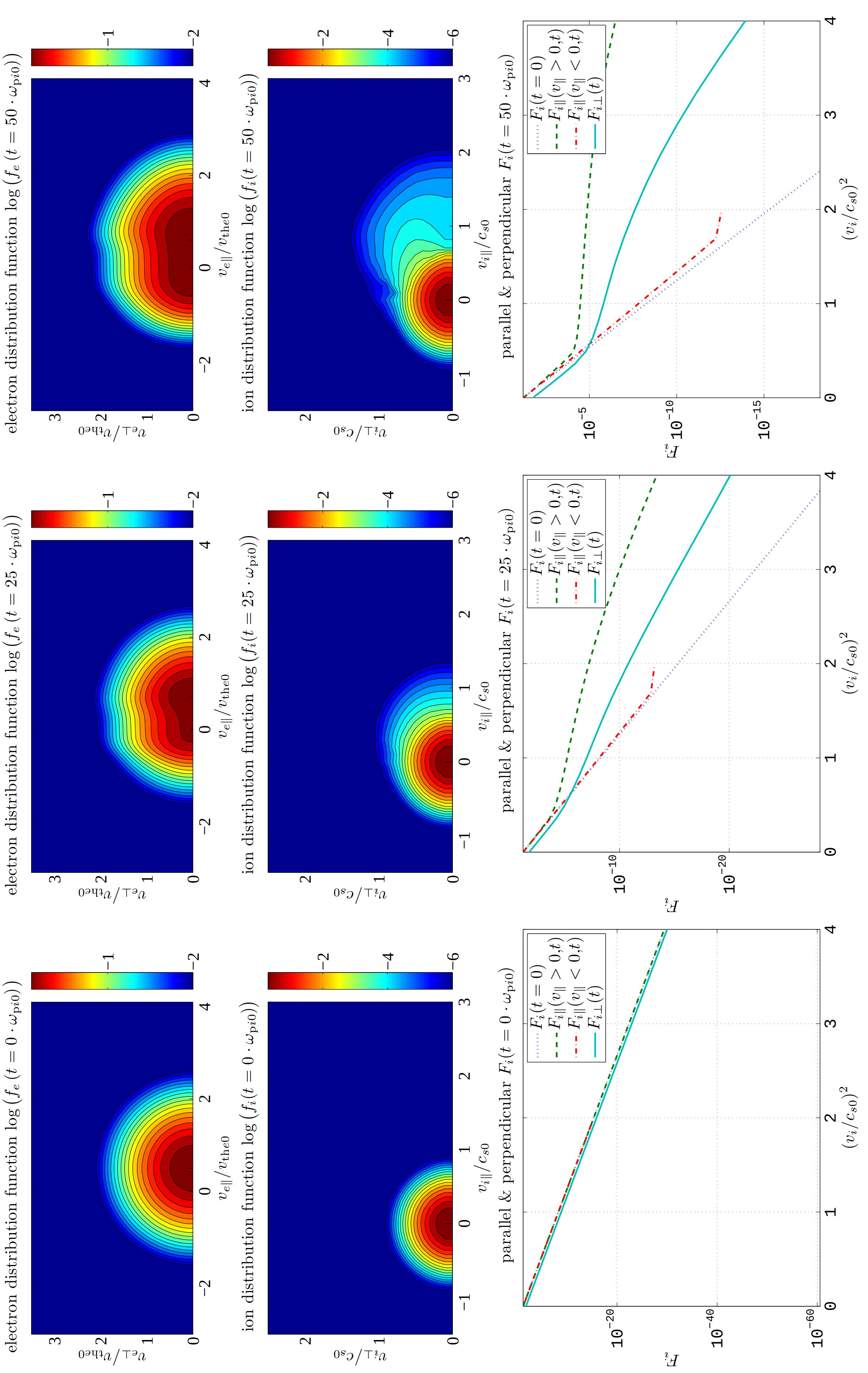

Figure 7.3.12: IAT simulation for TCV discharge #34527, $t = 0.37$ s. From top to down: Pitch angle maps of the electron f_e and ion velocity distribution functions f_i as well as parallel and perpendicular integrals of the latter. The time evolution of the velocity space diffusion is shown from left to right, that is at $\omega_{pi}\cdot t = 0$, 25 and 50. See figure 7.3.13 for the continuation of the series.

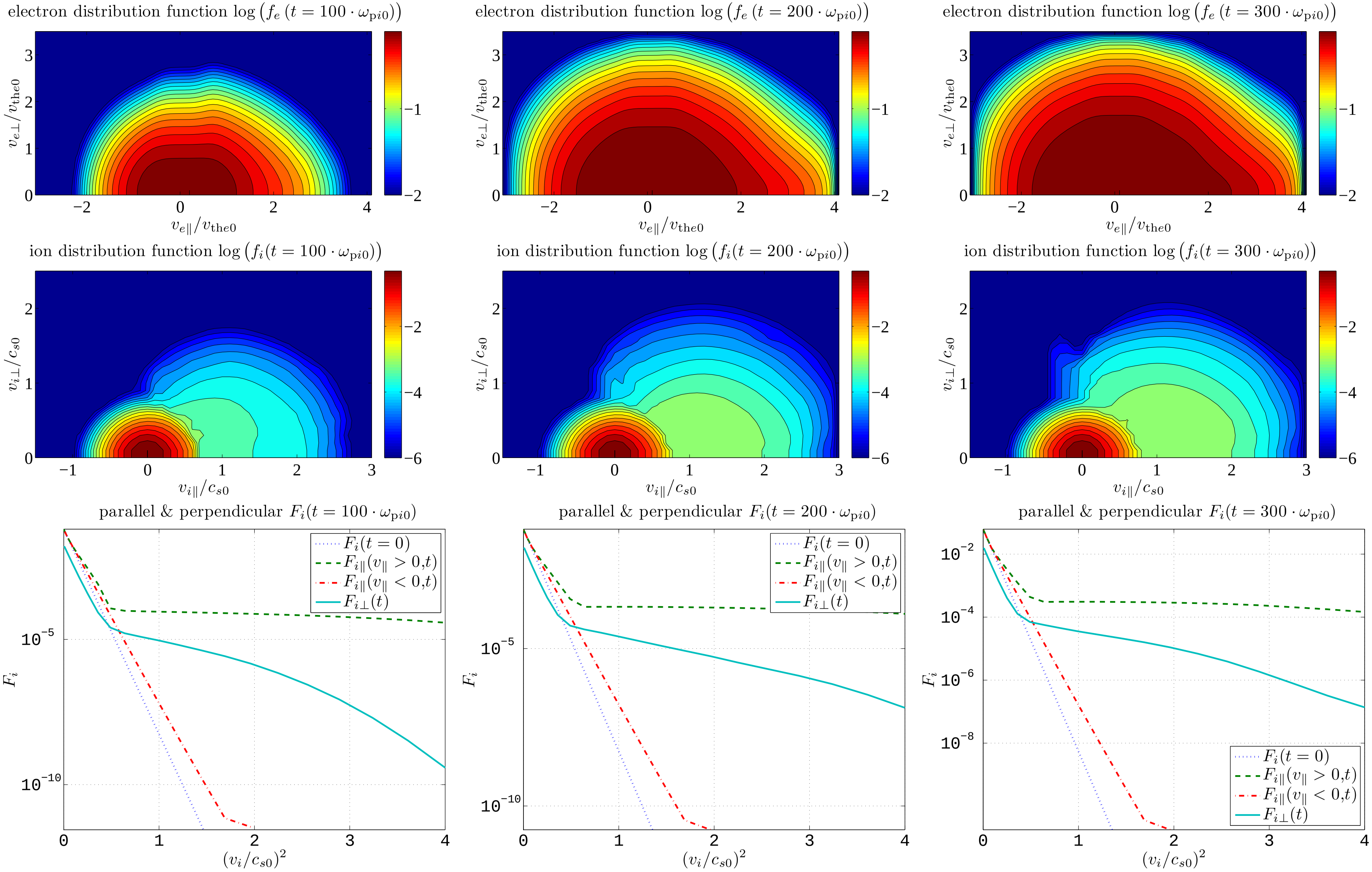

Figure 7.3.13: IAT simulation for TCV discharge #34527, $t = 0.37$ s. From top to down: Pitch angle maps of the electron f_e and ion velocity distribution functions f_i as well as parallel and perpendicular integrals of the latter. The time evolution of the velocity space diffusion is shown from left to right, that is at $\omega_{\mathrm{pi}} \cdot t = 100$, 200 and 300.

7.3.2 Discharge #34527

The *NOTEC-TCV* simulation of the ECE spectra immediately after switch-on of the gyrotrons in discharge #34527 has revealed a weakly relativistic current channel in the core of the plasma (page 155). To model this shot, instead of a bi-Maxwellian electron distribution function used for #31188 (previous figures), a single Maxwellian was chosen as initial condition. Otherwise the parameters are as stated on page 155, for $t = 0.37$ s.

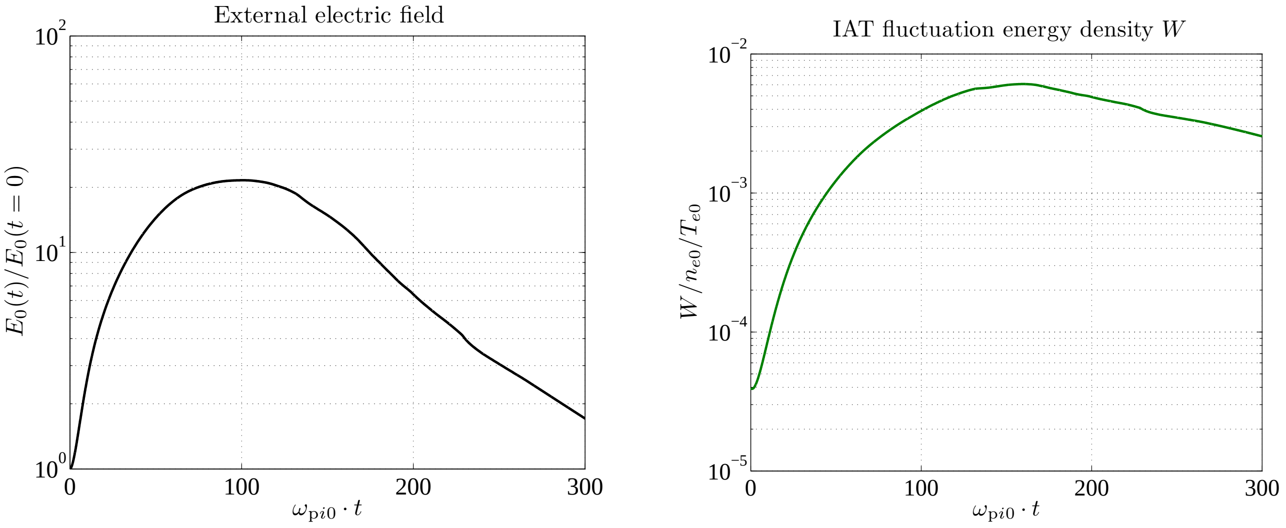

(a) auxiliary electric field (b) fluctuation intensity

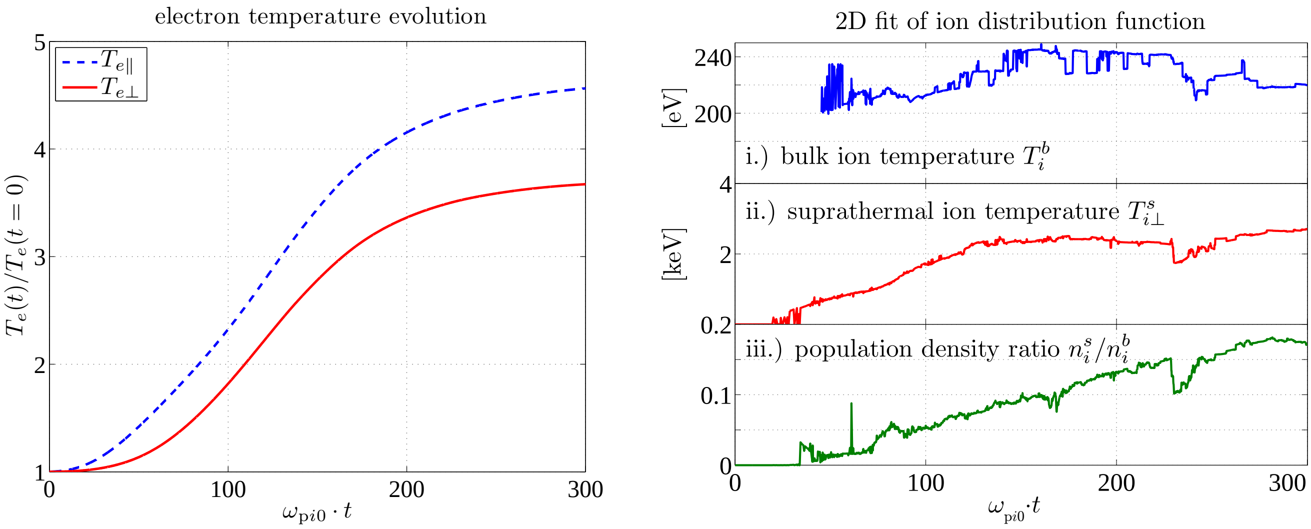

(c) electron heating (d) ion heating

Figure 7.3.14: IAT simulation for TCV discharge #34527, $t = 0.37$ s. Time traces of (a) the auxiliary toroidal electric field, (b) fluctuation energy density $W(t)$, (c) electron temperatures parallel and perpendicular to the magnetic field and (d) the modelled fast ion parameters.

The characteristics of the development of the turbulence are fairly similar to #31188, figures 7.3.12 and 7.3.13 show again the evolution of the particle distribution functions and figure 7.3.14 the fluctuation energy and electron temperature traces. The ion tail properties are shown in figure 7.3.14d, which must be compared to figure 6.5.6a.

Note that this simulation tries to model the transient phase ($t = 0.37$ s) after gyrotron switch on ($t = 0.35$ s). The measurement of the fast ion temperature reveals a quickly growing very hot value (> 5 keV at $t = 0.37$ s) which the simulation is not able to reproduce. The simulation, however, is initialised with an electron bulk temperature of 3.2 keV only (Thomson scattering measurement) and the IAT is not expected to yield a temperature $T_i^s > T_e^b$. The discrepancy is thus rather due to a wrong setup of the code than due to an inadequate model for the turbulence. Note that an important drift velocity (here $\beta = 0.4$) causes an initially rather strong level of turbulence (corresponds to the curves $v_{\mathrm{de}}/v_{\mathrm{the}} \simeq 1.5$ on figure 7.1.3) and the validity of quasilinear theory $\gamma_{\mathbf{k}} \ll \omega_{\mathbf{k}}$ may be violated. Modelling of the later, IAT saturated time instant $t = 0.75$ s (next section) is more successful.

7.4 IAT saturation level with static CQL3D electron description

The artificially applied electric field to maintain a constant current in the simulated plasma exceeds the real field (due to V_{loop}) by some multiples and the applicability of this trick to TCV experiments may rise some doubts. Instead of iterating the electron distribution function in the course of the turbulence excitation, the (steady-state) f_e modelled with *CQL3D* may be simply used as a static representation of the electrons. The *CQL3D* pitch angle map represents somehow the conditions at the saturation state of the turbulence, some features of the quasilinear dynamics of IAT may therefore not appear in such a simulation. Again for discharge #34527, but this time for the saturated turbulence case ($t = 0.7$ s), the *CQL3D* simulation is shown in figure 7.4.1. The simulation discussed in the following was then fed with this distribution, whereas the ion configuration was configured as previously.

With $f_{e,CQL3D}$ used in the IAT code, IAW are still destabilised. Figure 7.4.2 illustrates the impact of IAT on the ion velocity distribution. From the start, only strongly oblique modes can grow (this represents the saturation state of the simulation when f_e evolves under the influence of the turbulence, see figure 7.3.1, and this is in some sense natural as we have plugged a saturated state electron distribution into the code). As there are no growing field aligned modes, the parallel energisation of the ions during quasilinear growth does not occur.

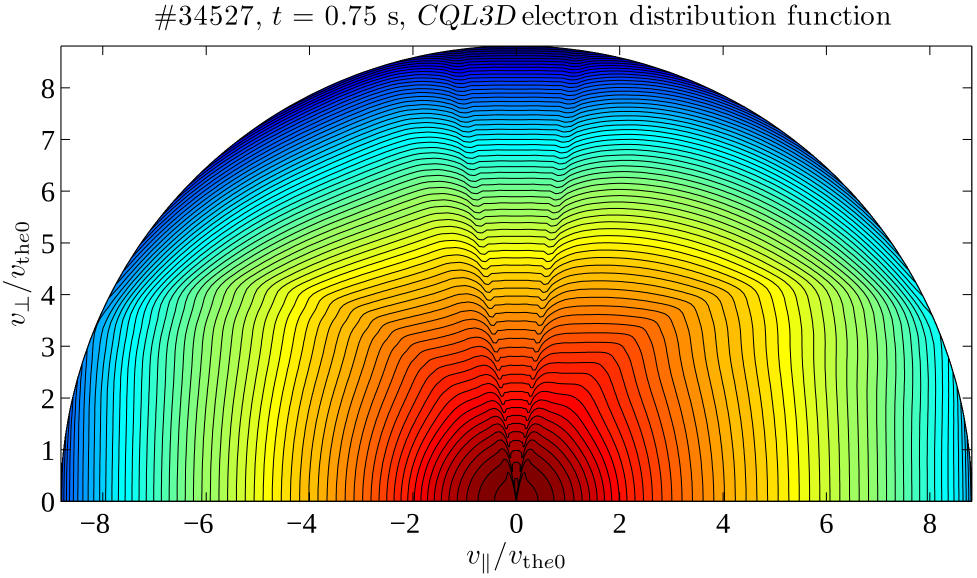

Figure 7.4.1: *CQL3D* modelled electron distribution function for discharge #34527, $t = 0.75$ s.

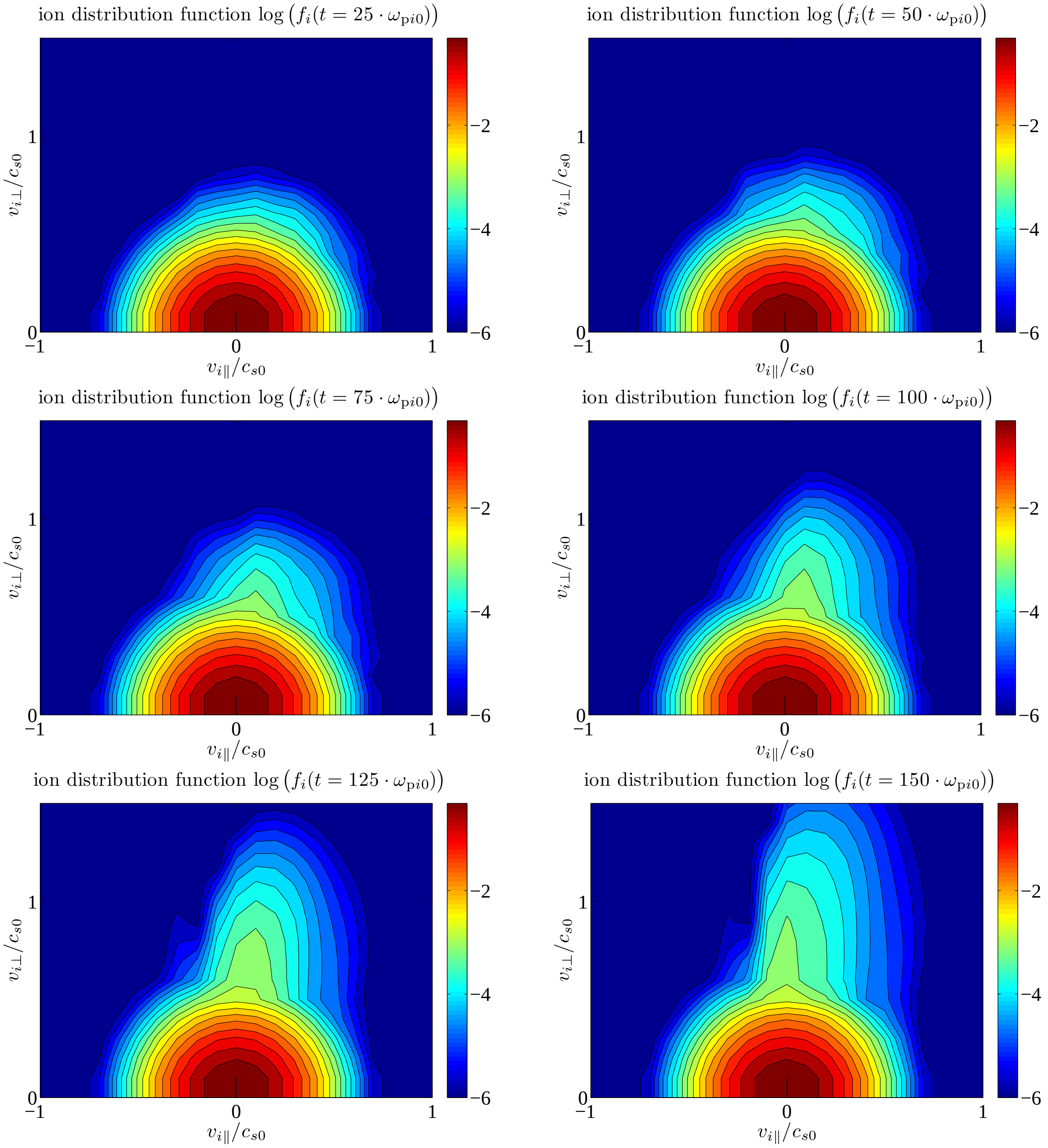

Figure 7.4.2: Evolution of the ion distribution function when the electron distribution function is taken from the *CQL3D* simulation without subsequent updates during the evolution of the turbulence.

The perpendicular ion distribution function $F_{i\perp}$ and its one-dimensional fit with a bi-Maxwellian are shown in figure 7.4.3. The fast ion temperature is now hot but the suprathermal population density is weak, however, these values are close to the experimental observation, see figure 6.5.6a, i.e. much closer than the simulation for $t = 0.37$ s where f_e is updated as presented in the previous section.

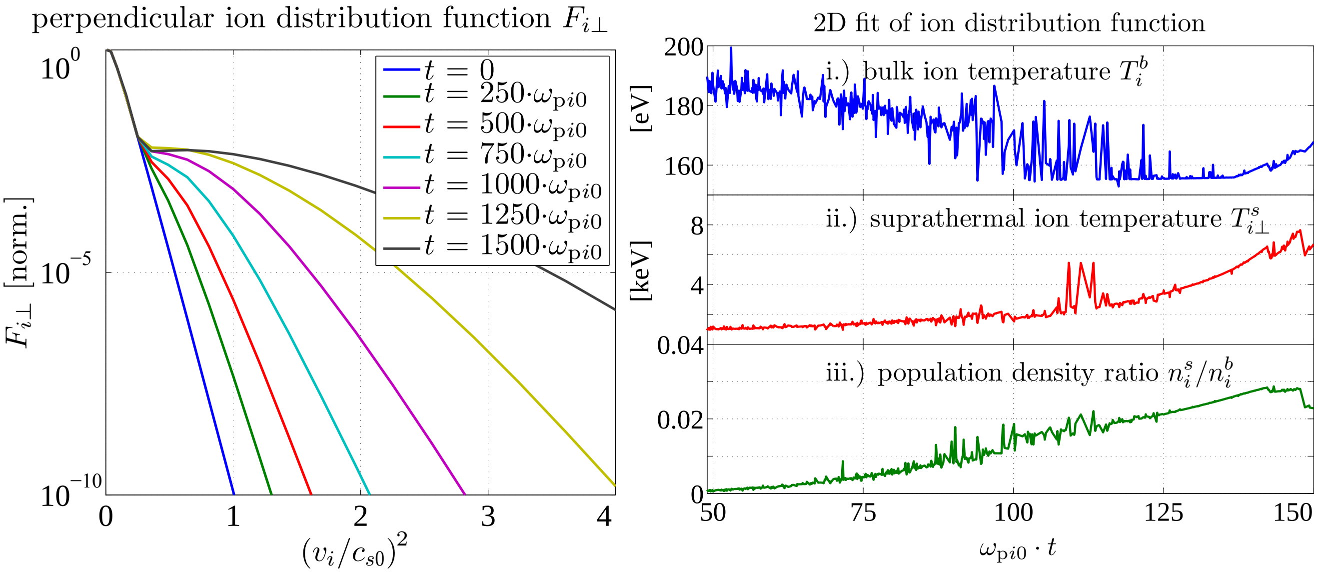

(a) perpendicular f_i (b) modelled suprathermal ions

Figure 7.4.3: (a) Parallel integral of the distribution function showing the heating and population of the perpendicular fast ion tail of the ion distribution function.
(b) 1D fit of the $F_{i\perp}$ shown in (a) with a bi-Maxwellian distribution. The scenario corresponds to discharge #34527, $t = 0.75$ s, the experimental fast ion parameters were shown in figure 6.5.6a.

7.5 Energy distribution among the ion species

Experiments on TCV indicate a suprathermal energy content of hydrogen at the half of the value of deuterium (section 6.4). This was numerically explored by replicating the set of equations treating deuterium also for hydrogen in the IAT code, such to advance f_i^{H} and f_i^{D} independently in time. The temperature setup of the ionic population is initialised with the same values for both isotopes and the bulk density ratio is that obtained with the CNPA (section 4.9.6.1), typically 10 %. Figure 7.5.1 shows the simulated ratio of suprathermal hydrogen to deuterium energy for the scenario of discharge #34527 (same setup as in the run shown in paragraph 7.3.2).

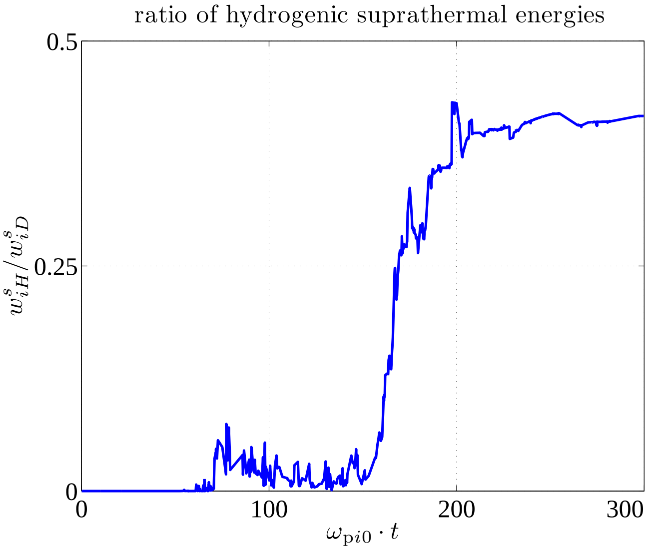

Figure 7.5.1: Ratio of modelled fast hydrogen to fast deuterium energy for the experimental parameters of discharge #34527. The hydrogen stored suprathermal energy is roughly half the deuterium stored energy. The total isotopic composition of this discharge is $n_i^{\mathrm{H}}/n_i^{\mathrm{D}} = 11$ % (CNPA measurement).

The suprathermal deuterium energy content indeed exceeds that of hydrogen by more than a factor of 2. The energy ratio observed in the simulation is independent of the chosen isotopic composition, as in the experiment.

7.6 Turbulence boost by sawtooth crash field

As mentioned in section 6.8.4.5, we shall now look again into the ion acceleration by sawteeth. When the IAT code is initiated with the electron and ion configuration of discharge #30480 (illustrations in section 6.6), that is an ion distribution function with a tail population (taken isotropic) of $T_i^s = 3.2$ keV and $n_i^s/n_i^b = 5$ %, IAT is not destabilised as long as $v_{\text{de}} < 0.2\, v_{\text{the}}$. This can be considered as the saturated state of the turbulence.

The effect of the sawtooth crash field is studied as follows: At the first time step, the electric field required to sustain the toroidal current is determined and, before the ADI equations are iterated, an additional electric field of 1...10 V/m is imposed. This additional field is kept constant, as the sawtooth crash phase is supposed to last for 100 μs (section 5.4.4.3), which is 1000× longer than the IAT simulation time window. With this additional field, IAT is indeed destabilised, although only weakly.

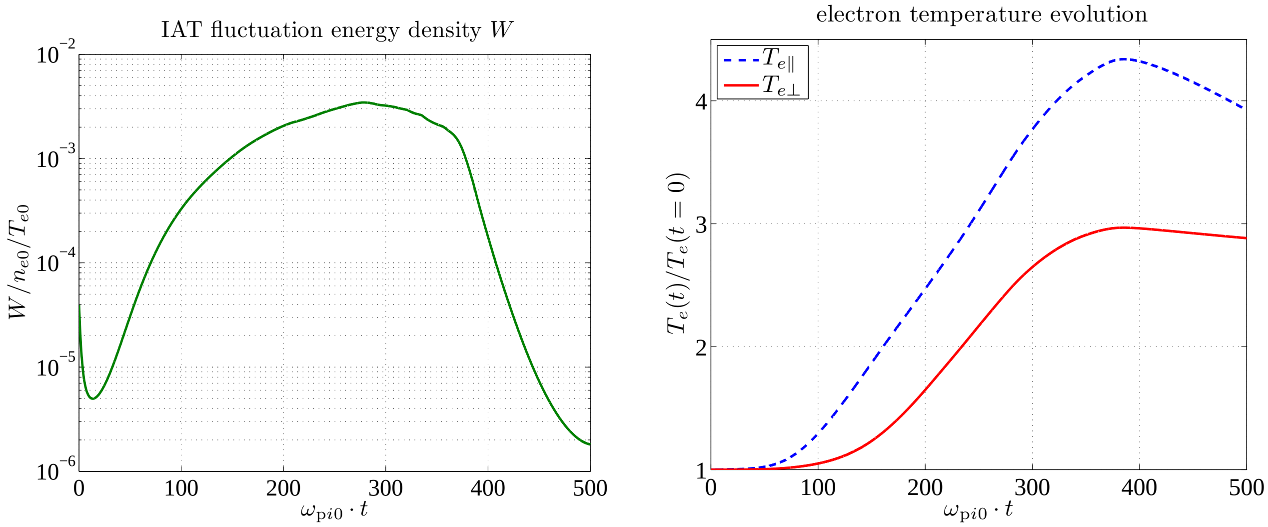

(a) fluctuation energy (b) electron heating

Figure 7.6.1: (a) Re-destabilisation of IAT by the sawtooth crash field in discharge #30480 with initially saturated IAT.
(b) Additional electron heating (with respect to the pre crash temperatures).

Excitation of IAT is shown in figure 7.6.1 and the fast ion tail feeding in figure 7.6.2 and are to be compared to figure 6.6.3. Experimentally, the cooling indicated in the simulation is not observed, but the strong enhancement of the number of fast ions is of clear evidence and agrees even quantitatively.
The electrons are also strongly heated, IAT may thus play the key role in the perpendicular energisation of the electrons, the enhancement of $T_{e\perp}$ by a factor of three (figure 7.6.1) corresponds to the increase of the HFS ECE temperature (figure 5.4.11) outside the inversion radius...

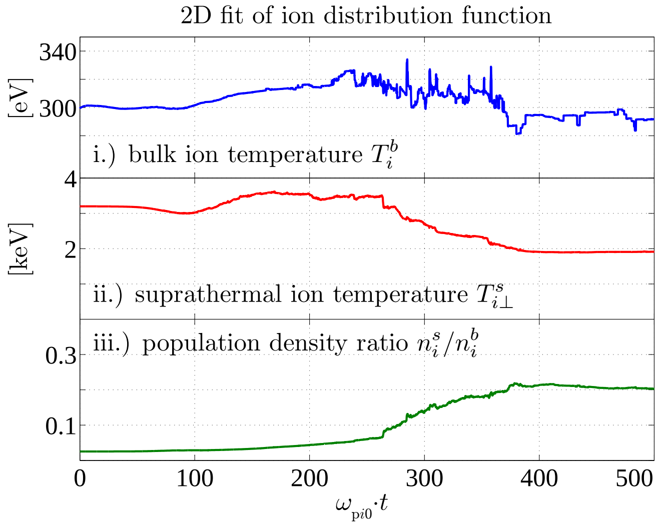

Figure 7.6.2: Fit of the modelled ion distribution function representative for discharge #30480. The ions are initially distributed by a bi-Maxwellian ($T_i^b = 300$ eV, $T_i^s = 3.2$ keV and $n_i^s/n_i^b = 5$ %), determined from the CXRS and CNPA measurements at $t = 1.4$ s.

7.7 Comment on the spatial location of IAT

The vertical plasma displacement experiment reported in section 6.3 revealed a large profile of fast ions in TCV. The spatial dimension was not addressed in the IAT code discussed in this chapter, as this would be a very difficult task. Instead, the following argument is proposed: IAW are preferentially damped by hot ions (this quenches the IAT), the IAW are thus rather absorbed at their birthplace or deeper plasma regions, the bulk and suprathermal ion temperature profiles decrease towards the edge and thus waves propagating outwards are damped more weakly with increasing minor radius. This has two consequences: First, the experimentally observed large suprathermal ion temperature profile is rather due to local IAW emission, that is, IAT is driven over a large fraction of the plasma radius. This is a plausible assumption as the suprathermal circulating fast ECCD electrons are found to diffuse strongly with radius (section 5.4.2.2). Second, the presence of IAW at the plasma edge may be detectable with the LHPI antenna (section 6.9.2) and ultimately prove the presence of IAT in TCV low density X2 EC heated plasmas.

7.8 Conclusion

Although rather simplistic, the IAT simulations are qualitatively in good agreement with the experimental observations on TCV. IAT is thus a good candidate to explain the fast ion acceleration in low density TCV plasmas with X2 electron cyclotron wave injection. In many situations, the perpendicular properties of the modelled suprathermal ion population agree also quantitatively with the CNPA measurements (ion density and temperature). Plasmas hosting very hot fast ions (the hottest fast ion temperatures observed range > 5 keV) require important electron drift speeds, such that the weak turbulence approach exploited here gets close to the limit of applicability.

Chapter 8

Summary and conclusions

This thesis primarily deals with some elements of the physics of plasma ions observed on the TCV tokamak. The properties of mostly hydrogenic ions were experimentally studied using two neutral particle analysers. The NPA were absolutely calibrated using active charge exchange measurements (injection of energetic neutrals with the diagnostic beam). The flexibility of the compact NPA diagnostic, collecting neutral particles along a horizontal view line, was enhanced by the addition of a viewing chord oriented obliquely with respect to the toroidal direction. The CNPA was equipped with a hard X-ray shield and commissioned for scientific measurement in scenarios where the diagnostic is exposed to plasmas potentially producing strong parasitic signals. With these upgrades, the diagnostic is currently available for reliable operation in all scenarios exploited thus far on TCV.

The quality of neutral particle emission spectrometry and the reliability of the NPA measured ion temperature was validated in plasmas with thermalised ions against the other ion diagnostics available on TCV, that is the neutral beam stimulated charge-exchange recombination spectroscopy diagnostic and a neutron survey monitor. The fuel and impurity ion species intrinsically contained in inductively heated thermal TCV plasmas are efficiently thermalised amongst each other, and the various ion temperature assessments were shown to agree within their error bars. The behaviour of the ions is found to follow the classical equipartition as long as the ion heating is dominated by collisional processes. In an original diagnostic exercise the spatial ion temperature profile was reconstructed using the single chord CNPA either by plasma displacement across the diagnostic line of sight or by extensive modelling of the NPA measured neutral flux by means of different neutralisation and neutral transport codes. Absolute neutral density profiles and the isotopic plasma ion composition are welcome products of these simulations. The consistent interpretation of the various NPA measurements made in TCV ohmic plasmas (chapter 4) show that the underlying ion physics in these discharges is well understood.

The phenomenon of clearly anomalous ion acceleration in TCV low density plasmas, when second harmonic electron cyclotron waves are injected, was studied in a series of dedicated plasmas. The observations show that the fast ion's properties are intimately linked to the parameters of the fast electrons, whose temperature, density and drift velocity (and the resulting ion acceleration) are strongest in plasmas with a non-inductively driven ECCD current.

As a consequence, it was necessary to correctly assess the fast electron properties. This was performed by both modelling the absorption of the electron cyclotron waves with the *CQL3D* code and by reverse-engineering of the parameters governing the emission of non-thermal EC radiation measured with the various ECE antennas on TCV using the raytracing code *NOTEC-TCV*.

The second approach demonstrated the importance of electrons circulating in the torus at weakly relativistic speeds, whose density may dominate the plasma core.

Upon the launch of the EC beam, the ion dynamics in the velocity space occur on time scales faster than 100 μs and must therefore be the product of wave–particle interactions. The properties of the suprathermal ions (T_i^s, n_i^s) reach steady-state conditions after a typical period of current redistribution if the ECRH and ECCD parameters are kept constant with time. The time resolution of the NPA is however (although by far better than any other ion diagnostic on TCV) two orders of magnitude too slow to study the details of the turbulence onset. The experimental investigations have therefore concentrated on the state of quasi-saturation of the fast ion population.

The NPA measurements are satisfactorily described adopting a bi-maxwellian ion velocity distribution function. The observed suprathermal population may comprise up to 30 % (deuterium) or the majority (hydrogen) of the ions of the respective isotope and behaves such that the deuterium stored suprathermal energy is twice that of hydrogen. The suprathermal temperatures of the hydrogenic species are equal and inferior (but close) to the temperature of the bulk electrons and thus exceed the thermal ion temperatures by a factor up to 35. The suprathermal ion profiles were experimentally probed by vertical plasma displacement. The density fraction of suprathermal to thermal ions is constant up to a normalised radius of $\rho = 0.8$ (confinement is lost beyond). The shape of the $T_i^s(\rho)$ profile is congruent to the thermal profile.

To understand the experimental data, the mechanisms potentially able to accelerate ions to suprathermal velocities reported in the scientific literature were reviewed. The ion energisation by the ion acoustic turbulence process, excited by the circulating electrons, was found to be compatible with the parameters of the TCV plasmas. To study IAT, the quasi-linear diffusion equation was numerically coded according to an alternating-direction implicit finite difference formulation. These advanced numerical simulations incorporate all experimentally known information and calculate the evolution of the ion velocity distribution function in plasmas with developed IAT. It was found that the simulations agree qualitatively and sometimes quantitatively with experiment. Virtual numerical and real experiment exhibit many properties inherent to IAT, namely

- ☞ the creation of the fast ion population with temperatures and densities of the same order as measured with the CNPA,
- ☞ the quench of the turbulence due to the fast ions and the achievement of a quasi steady-state and
- ☞ the acceleration of the ions into the direction perpendicular to the magnetic field during the quasilinear evolution of the IAT

These results suggest that IAT is a plausible candidate to explain the observed ion energisation. However, the most relevant experiments have yet to confirm this hypothesis, that is the measurement of the modelled anisotropy in pitch angle of the ion velocity distribution (CNPA biviewline setup) as well as the assessment of the turbulence fluctuation spectrum (LHPI antenna). It is currently hoped that these may be carried out during summer 2009.

Preliminary measurements of the effect of sawtooth crashes on the fast ions were performed and ion acceleration was observed. The IAT code has shown that the toroidal sawtooth crash electric field may enhance the saturation level of the turbulence and thus put more ions into the tail of the velocity distribution function. Future localised oblique ECE measurements may be able to provide a better estimation of the runaway electron current at the reconnection location and thus improve the modelling of the IAT stimulation by sawteeth.

To summarise, the physics involved in the acceleration of the ions is of puzzling complexity. The richness of observed phenomenons affecting the ions is rather spectacular (and passionate for the author) for a machine strongly emphasising on the physics of electrons (heating, confinement and diagnosis). Limited port access (complicating toroidally oblique particle measurements addressing the asymmetries in f_i) and the difficulty to probe the plasma SOL (variable plasma shape and position preventing the installation of an IAW antenna) make TCV an awkward machine on which to explore IAT. It may however be difficult (if not impossible) to drive IAT unstable on other present-day tokamaks, as strong auxiliary electron heating, settling $T_e \gg T_i$, is an indispensable ingredient. This remark includes ITER, whose presently anticipated operational scenarios target $T_i > T_e$ (thanks to fusion α's and NBI) without exception [413]. IAT is thus not, at least at present, thought to be ITER relevant.

To conclude, concerning the physics of ions in TCV, let us take the plunge and look ahead. Electron heating in the present relatively low density TCV plasmas doesn't allow for fusion reactor relevant ion heating by equipartition. Heating at higher plasma densities, together with the implementation of direct ion heating would considerably enlarge the attainable range of T_i/T_e. TCV is currently considering possible major upgrades [414] aiming at making the physics of fast ions (and related MHD) a major part of the scientific TCV programme:

☞ Deuterium heating beams providing a NBI power of about 3 MW (injection energy ∼35 keV), in conjunction with an increase of the X3 gyrotron power to 4.5 MW, would allow $T_i/T_e = 2$. For instance, this configuration would enable to directly test the ITER sawtooth stabilisation scheme [415, 416], that is the stabilising effect of fast ions can be controlled with ECRH/ECCD [417].

☞ Another upgrade includes the installation of active MHD antennas (∼50 kW) designed to drive a range of Alfvén wave-particle resonances, thus producing large fast ion populations. The main goal of this project is to study the still underexplored question of the transport of fusion α-particles induced by resonant wave–particle interactions.

The upgrades of the actuators would certainly also require upgrades of TCV's ion diagnostic set and setup.

Appendix A

The relativistic quasilinear diffusion equation

The quasilinear description of the wave-particle interaction assumes that two different time scales are at play, that is the distribution function $f(\mathbf{r}, \mathbf{p}, t)$ is separable in two parts, a volume averaged, slowly evolving [238, 418]

$$F(\mathbf{p}, t) = \langle f \rangle = \lim_{V \to \infty} \frac{1}{V} \int_V f(\mathbf{r}, \mathbf{p}, t) \mathrm{d}^3 r \tag{A.0.1}$$

and a rapidly varying part

$$\tilde{f}(\mathbf{r}, \mathbf{p}, t) = f(\mathbf{r}, \mathbf{p}, t) - F(\mathbf{p}, t) \tag{A.0.2}$$

where the latter is due to the interaction of the wave (perturbation fields $\tilde{\mathbf{E}}$, $\tilde{\mathbf{B}}$) with the particles. For the cyclotron the resonance interaction, the fast timescale is of the order of Ω_c^{-1}. This separation implies $\left\langle \tilde{f} \right\rangle = \left\langle \tilde{\mathbf{B}} \right\rangle = \left\langle \tilde{\mathbf{E}} \right\rangle = 0$. In what follows, $\mathbf{E} = 0$ and a homogenous background magnetic field B_0 is assumed, though this doesn't make the applicability of the model impossible to situations with weak spatial gradients of F and $\mathbf{B}_0$, as long as they may be considered as being constant over a Larmor radius (this is generally true for tokamaks).

As in a linear model, the evolution of f is governed by the Vlasov equation

$$\frac{\partial f(\mathbf{r}, \mathbf{p}, t)}{\partial t} + \mathbf{v} \cdot \frac{\partial f}{\partial \mathbf{r}} + q\left(\mathbf{E} + \mathbf{v} \wedge \mathbf{B}\right) \cdot \frac{\partial f}{\partial \mathbf{p}} = 0 \tag{A.0.3}$$

whose volume averaging removes the linear terms of the fluctuating quantities

$$\frac{\partial F(\mathbf{p}, t)}{\partial t} + q\left(\mathbf{v} \wedge \mathbf{B}_0\right) \cdot \frac{\partial F(\mathbf{p}, t)}{\partial \mathbf{p}} = -q \left\langle \left(\tilde{\mathbf{E}} + \mathbf{v} \wedge \tilde{\mathbf{B}}\right) \cdot \frac{\partial \tilde{f}(\mathbf{r}, \mathbf{p}, t)}{\partial \mathbf{p}} \right\rangle \tag{A.0.4}$$

Collisions are ignored because the wave, when propagating, interacts with many electrons simultaneously such that collective effects largely dominate. When it comes to absorption, collisional removal of electrons away from the resonance layer is negligible due to the low collision frequency in tokamaks.

A.1 Distribution function fluctuations $\tilde f$

First we want to find the solution for the distribution function fluctuations $\tilde f$, that is the rapidly evolving part of f. Subtracting the last two equations yields

$$\begin{aligned}\frac{\partial \tilde f(\mathbf{r},\mathbf{p},t)}{\partial t} + \mathbf{v}\cdot\frac{\partial \tilde f(\mathbf{r},\mathbf{p},t)}{\partial \mathbf{r}} + q\,(\mathbf{v}\wedge\mathbf{B}_0)\cdot\frac{\partial \tilde f(\mathbf{r},\mathbf{p},t)}{\partial \mathbf{p}} &= -q\left(\tilde{\mathbf{E}}+\mathbf{v}\wedge\tilde{\mathbf{B}}\right)\cdot\frac{\partial F(\mathbf{p},t)}{\partial \mathbf{p}} \\ &\quad - q\left[\left(\tilde{\mathbf{E}}+\mathbf{v}\wedge\tilde{\mathbf{B}}\right)\cdot\frac{\partial \tilde f(\mathbf{r},\mathbf{p},t)}{\partial \mathbf{p}} - \left\langle\left(\tilde{\mathbf{E}}+\mathbf{v}\wedge\tilde{\mathbf{B}}\right)\cdot\frac{\partial \tilde f(\mathbf{r},\mathbf{p},t)}{\partial \mathbf{p}}\right\rangle\right]\end{aligned} \tag{A.1.1}$$

The two last terms are second order perturbations and describe the reaction of the wave on $\tilde f$ and are thus representing the nonlinear mode-mode coupling of the waves which are neglected in the framework of quasilinear theory. Without these terms, eq.(A.1.1) becomes linear in $\tilde f$. Using the argument to separate fast and slow parts of f again, F may be considered as being static in respect to $\tilde f$.
As long as the fraction of particles trapped by the wave is small, eq.(A.1.1) is solved assuming that the particle orbits are not affected by the fluctuating fields of the wave, that is an integration along the unperturbed particle orbits. The formal solution writes, assuming $\tilde f = 0$ at $t \to -\infty$,

$$\tilde f(\mathbf{r},\mathbf{p},t) = \int_{-\infty}^{t} -q\left(\tilde{\mathbf{E}}(\mathbf{r}',t') + \mathbf{v}'\wedge\tilde{\mathbf{B}}(\mathbf{r}',t')\right)\cdot\frac{\partial F(\mathbf{v}',t')}{\partial \mathbf{p}'}\mathrm{d}t' \tag{A.1.2}$$

with $\mathbf{r}'$ and $\mathbf{v}'$ parameterised by the unperturbed equations of motion

$$\begin{cases}\dfrac{\mathrm{d}\mathbf{r}'}{\mathrm{d}t} &= \dfrac{\mathbf{p}'}{m\gamma'} \\ \dfrac{\mathrm{d}\mathbf{p}'}{\mathrm{d}t} &= q\left(\dfrac{\mathbf{p}}{m\gamma'}\wedge\mathbf{B}_0\right)\end{cases} \tag{A.1.3}$$

The EC wave is then assumed to be representable by a monochromatic plane wave, the fluctuating terms therefore read

$$\tilde{\mathbf{E}}(\mathbf{r},t) = \tilde{\mathbf{E}}(\mathbf{k},\omega)\exp\big(\mathrm{i}\,(\mathbf{k}\cdot\mathbf{r}-\omega t)\,\big) \tag{A.1.4}$$

$$\tilde{\mathbf{B}}(\mathbf{r},t) = \left(\frac{\mathbf{k}}{\omega}\wedge\tilde{\mathbf{E}}(\mathbf{k},\omega\right)\exp\big(\mathrm{i}\,(\mathbf{k}\cdot\mathbf{r}-\omega t)\,\big) \tag{A.1.5}$$

$$\tilde f(\mathbf{r},\mathbf{p},t) = \tilde f(\mathbf{k},\mathbf{p},\omega)\exp\big(\mathrm{i}\,(\mathbf{k}\cdot\mathbf{r}-\omega t)\,\big) \tag{A.1.6}$$

where the Faraday's law of induction, the first equation of the eqns.(5.1.1), was used to express the magnetic in terms of the electric field. The linearised solution of the relativistic Vlasov equation, eq.(A.1.2), then becomes

$$\begin{aligned}\tilde f(\mathbf{k},\mathbf{p},\omega) = -q\int_{-\infty}^{t}\exp\Big(\mathrm{i}\big(\mathbf{k}\cdot(\mathbf{r}'-\mathbf{r}) - \omega(t'-t)\big)\Big)\times \\ \left[\tilde{\mathbf{E}}(\mathbf{k},\omega) + \frac{\mathbf{v}'}{\omega}\wedge\Big(\mathbf{k}\wedge\tilde{\mathbf{E}}(\mathbf{k},\omega)\Big)\right]\cdot\frac{\partial F(\mathbf{v}',t')}{\partial \mathbf{p}'}\mathrm{d}t'\end{aligned} \tag{A.1.7}$$

The coordinates of the unperturbed trajectories, $\mathbf{r}'$ and $\mathbf{v}'$ are obtained by solving eq.(A.1.3) in cylindrical geometry, writing the cartesian coordinates

$$v_x = v_\perp\cos\phi \tag{A.1.8}$$

$$v_y = v_\perp\sin\phi \tag{A.1.9}$$

$$v_z = v_\parallel \tag{A.1.10}$$

with ϕ the gyroangle and $v_\parallel$ and $v_\perp$ the components respectively parallel and perpendicular to the background field $\mathbf{B}_0$. The solution of eq.(A.1.3) writes, employing the change of variable $t' \to t-t'$

$$\begin{aligned} p'_x &= p_\perp \cos\left(\tilde{\Omega}_{ce}(t-t') + \phi\right) && \text{(A.1.11)} \\ p'_y &= p_\perp \sin\left(\tilde{\Omega}_{ce}(t-t') + \phi\right) && \text{(A.1.12)} \\ p'_z &= p_\parallel && \text{(A.1.13)} \end{aligned}$$

with $\tilde{\Omega}_{ce}$ the relativistic gyrofrequency

$$\tilde{\Omega}_{ce} = \frac{\Omega_{ce}}{\gamma} \tag{A.1.14}$$

Integration yields

$$\begin{aligned} x' - x &= \frac{v_\perp}{\tilde{\Omega}_{ce}}\left(\sin\phi - \sin\left(\tilde{\Omega}_{ce}(t-t') + \phi\right)\right) && \text{(A.1.15)} \\ y' - y &= \frac{v_\perp}{\tilde{\Omega}_{ce}}\left(\cos\phi - \cos\left(\tilde{\Omega}_{ce}(t-t') + \phi\right)\right) && \text{(A.1.16)} \\ z' - z &= -v_\parallel(t-t') && \text{(A.1.17)} \end{aligned}$$

such that the exponential in eq.(A.1.7), using the Stix frame for the wave vector (figure 5.1.1), is then written as

$$\begin{aligned} &\exp\left(\mathrm{i}\big(\mathbf{k}\cdot(\mathbf{r}'-\mathbf{r}) - \omega(t'-t)\big)\right) = \\ &\qquad \exp\left(\mathrm{i}\left\{k_\perp \frac{v_\perp}{\tilde{\Omega}_{ce}}\left[\sin\phi - \sin\left(\phi + \tilde{\Omega}_{ce}(t-t')\right)\right] + (\omega - k_\parallel v_\parallel)(t-t')\right\}\right) \end{aligned} \tag{A.1.18}$$

Using the generating function of the Bessel function [419]

$$\exp\left(\mathrm{i}\xi\sin\phi\right) = \sum_{n=-\infty}^{+\infty} J_n(\xi)\exp\left(\mathrm{i}n\phi\right) \tag{A.1.19}$$

eq.(A.1.7) reads now

$$\begin{aligned} &\tilde{f}(\mathbf{k},\mathbf{p},\omega) = -q\sum_{n'=-\infty}^{+\infty} J'_n(\xi)\exp\left(\mathrm{i}n'\phi\right)\int_{-\infty}^{t}\mathrm{d}t'\exp\left(\mathrm{i}\big((\omega - k_\parallel v_\parallel)(t-t')\big)\right)\times \\ &\sum_{n=-\infty}^{+\infty} J_n(\xi)\exp\left(-\mathrm{i}n\big(\hat{\Omega}_{ce}(t-t')+\phi\big)\right)\left\{\left[\cos\left(\hat{\Omega}_{ce}(t-t')+\phi\right)\tilde{E}_x + \sin\left(\hat{\Omega}_{ce}(t-t')+\phi\right)\tilde{E}_y\right]\times\right. \\ &\qquad\left.\left(\frac{\partial F}{\partial p_\perp} + \frac{k_\parallel}{\gamma\omega m}\Xi F\right) + \left(\frac{\partial F}{\partial p_\parallel} - \cos\left(\hat{\Omega}_{ce}(t-t')+\phi\right)\frac{k_\perp}{\gamma\omega m}\Xi F\right)\tilde{E}_z\right\} \end{aligned} \tag{A.1.20}$$

where $\xi = k_\perp v_\perp/\hat{\Omega}_{ce}$the differential operator Ξ is defined as

$$\Xi = p_\perp\frac{\partial}{\partial p_\parallel} - p_\parallel\frac{\partial}{\partial p_\perp} \tag{A.1.21}$$

By using convenient recurrence relations of Bessel functions, namely

$$J_{n+1}(\xi) + J_{n-1}(\xi) = \frac{2\,n}{\xi} J_n \tag{A.1.22}$$

$$J_{n+1}(\xi) - J_{n-1}(\xi) = -2\,J_n' \tag{A.1.23}$$

and the exponential forms of the trigonometric functions, eq.(A.1.20) becomes

$$\tilde{f}(\mathbf{k},\mathbf{p},\omega) = -\mathrm{i}q \sum_{n'=-\infty}^{+\infty} \sum_{n=-\infty}^{+\infty} \frac{1}{\omega - n\hat{\Omega}_{ce} - k_\parallel v_\parallel} J_n'(\xi) \exp\big(\mathrm{i}(n'-n)\phi\big) \times \\ \left\{ \left[\frac{n\hat{\Omega}_{ce}}{k_\perp v_\perp} J_n(\xi)\tilde{E}_x + J_n'(\xi)\tilde{E}_y \right] \left(\frac{\partial F}{\partial p_\perp} + \frac{k_\parallel}{\gamma\omega m} \Xi F \right) + J_n(\xi)\tilde{E}_z \left(\frac{\partial F}{\partial p_\parallel} - \frac{n\hat{\Omega}_{ce}}{\gamma\omega m v_\perp} \Xi F \right) \right\} \tag{A.1.24}$$

where the polarisation of the electric field is, in the case of TCV, calculated using *Toray-GA*. $\tilde{f}$ depends on the gyro-phase through the exponential term. Generally the phase of angular velocity and wave vector are different such that, instead of the Stix frame, the true three-dimensional form of the wave vector has to be used. Writing the electric field components as

$$E_L = e_L \exp(-\mathrm{i}\phi)\,, \quad E_R = e_R \exp(+\mathrm{i}\phi)\,, \quad E_\parallel = \tilde{E}_z \tag{A.1.25}$$

where $e_L = \tilde{E}_x + \mathrm{i}\tilde{E}_y$ and $e_R = \tilde{E}_x - \mathrm{i}\tilde{E}_y$. Replacing the phase factor by the phase difference of the two vectors $\phi \to \phi - \varphi$, where φ is the angle between the xy-plane and $\mathbf{k}$, the desired form of the solution for $\tilde{f}$, eq.(A.1.24), as a function of F, results in

$$\tilde{f}(\mathbf{k},\mathbf{p},\omega) = -\mathrm{i}q \sum_{n'=-\infty}^{+\infty} \sum_{n=-\infty}^{+\infty} \frac{1}{\omega - n\hat{\Omega}_{ce} - k_\parallel v_\parallel} J_n'(\xi) \exp\big(\mathrm{i}(n'-n)(\phi-\varphi)\big) \times \\ \left\{ \left[\mathcal{E}\left(1 - \frac{k_\parallel v_\parallel}{\omega}\right) + J_n E_\parallel \frac{n\hat{\Omega}_{ce}}{\omega} \frac{v_\parallel}{v_\perp} \right] \frac{\partial F}{\partial p_\perp} + \left[\mathcal{E} \frac{k_\parallel v_\perp}{\omega} + J_n E_\parallel \left(1 - \frac{n\hat{\Omega}_{ce}}{\omega}\right) \right] \frac{\partial F}{\partial p_\parallel} \right\} \tag{A.1.26}$$

where $\mathcal{E} = 1/2\,(J_{n+} E_R + J_{n-1} E_L)$.

A.2 Modification of the plasma background distribution function F

Now lets determine the evolution of the background distribution function F, that is the slowly evolving part of f. The rapidly evolving part of the distribution function, eq.(A.1.26), needs to be inserted into the equation describing the slowly evolving part F, eq.(A.0.4). F doesn't change during one gyro-turn, such that the right term of eq.(A.0.4) is conveniently gyro-averaged, i.e.

$$\left\langle \tilde{f} \right\rangle_\phi = \frac{1}{2\pi} \int_0^{2\pi} \tilde{f}\,\mathrm{d}\phi \tag{A.2.1}$$

and from the self-correlation of the Fourier transform, applied to the average of two real quantities

$$\Big\langle A(\mathbf{r})B(\mathbf{r}) \Big\rangle = \lim_{V\to 0} \frac{1}{V} \int_k A^*(\mathbf{k})B(\mathbf{k})\,\mathrm{d}^3k \tag{A.2.2}$$

follows

$$\frac{\partial F(\mathbf{p},t)}{\partial t} = -q\lim_{V\to 0}\frac{1}{V}\int_k\frac{1}{2\pi}\int_0^{2\pi}\left[\tilde{\mathbf{E}}_k+\frac{\mathbf{v}}{\omega_k}\wedge\left(\mathbf{k}\wedge\tilde{\mathbf{B}}_k\right)\right]^*\cdot\frac{\partial\tilde{f}_k(\mathbf{k},\mathbf{p},t)}{\partial\mathbf{p}}\,\mathrm{d}\phi\,\mathrm{d}^3k \tag{A.2.3}$$

The next step is the calculation of the velocity space gradient of $\tilde{f}$, which, as $\tilde{f}$ depends on the gyro-phase, has a component in ϕ. In cylindrical coordinates, i.e.

$$\mathbf{p} = p_\perp\cos\phi\,\mathbf{e}_x+p_\perp\sin\phi\,\mathbf{e}_y+p_\parallel\mathbf{e}_z = p_\perp\mathbf{e}_\perp+p_\parallel\mathbf{e}_\parallel \tag{A.2.4}$$

$$\mathbf{k} = k_\perp\cos(\phi-\varphi)\mathbf{e}_\perp-k_\perp\sin(\phi-\varphi)\mathbf{e}_\phi+k_\parallel\mathbf{e}_\parallel \tag{A.2.5}$$

$$\begin{aligned}\tilde{\mathbf{E}} &= \left(\tilde{E}_x\cos\phi+\tilde{E}_y\sin\phi\right)\mathbf{e}_\perp+\left(-\tilde{E}_x\sin\phi+\tilde{E}_y\cos\phi\right)\mathbf{e}_\phi = \\ &= E_\perp\mathbf{e}_\perp+E_\phi\mathbf{e}_\phi+E_\parallel\mathbf{e}_\parallel\end{aligned} \tag{A.2.6}$$

$$\nabla_{\mathbf{p}} = \mathbf{e}_\perp\frac{\partial}{\partial p_\perp}+\mathbf{e}_\phi\frac{1}{p_\perp}\frac{\partial}{\partial\phi}+\mathbf{e}_\parallel\frac{\partial}{\partial p_\parallel} \tag{A.2.7}$$

the derivation results in

$$\begin{aligned}\frac{\partial F(\mathbf{p},t)}{\partial t} = -q\lim_{V\to 0}\frac{1}{V}\int_k\frac{1}{2\pi}\int_0^{2\pi}\Bigg\{&\left[E_\perp^*\left(1-\frac{v_\parallel k_\parallel}{\omega}\right)^*+E_\parallel\frac{v_\parallel k_\perp}{\omega}\cos\psi\right]\frac{\partial\tilde{f}}{\partial p_\perp}+\\ &\underbrace{\left[\left(-E_\perp\frac{v_\perp k_\perp}{\omega}-E_\parallel\frac{v_\parallel k_\perp}{\omega}\right)\sin\psi+E_\phi\left(1-\frac{v_\parallel k_\parallel}{\omega}-\frac{v_\perp k_\perp}{\omega}\cos\psi\right)\right]^*\frac{1}{p_\perp}\frac{\partial\tilde{f}}{\partial\phi}}_{U^*}+\\ &\left[E_\parallel\left(1-\frac{v_\perp k_\perp}{\omega}\cos\psi\right)+E_\perp\frac{v_\perp k_\parallel}{\omega}\right]^*\frac{\partial\tilde{f}}{\partial p_\parallel}\Bigg\}\,\mathrm{d}\phi\,\mathrm{d}^3k\end{aligned} \tag{A.2.8}$$

where $\psi=\phi-\varphi$. With the definition of the differential operators

$$S = \left(1-\frac{v_\parallel k_\parallel}{\omega}\right)\frac{\partial}{\partial p_\perp}+\frac{v_\perp k_\parallel}{\omega}\frac{\partial}{\partial p_\parallel} \tag{A.2.9}$$

$$T = \frac{k_\perp}{\omega}\left(v_\perp\frac{\partial}{\partial p_\parallel}-v_\parallel\frac{\partial}{\partial p_\perp}\right) \tag{A.2.10}$$

and

$$E_\perp = \frac{\big(E_L\exp(-\mathrm{i}\phi)+E_R\exp(\mathrm{i}\phi)\big)}{2} \tag{A.2.11}$$

the quasilinear equation may be written in compact form

$$\begin{aligned}\frac{\partial F(\mathbf{p},t)}{\partial t} = -q\lim_{V\to 0}\frac{1}{V}\int_k\frac{1}{2\pi}\int_0^{2\pi}\Bigg\{&\frac{\big(E_L\exp(-\mathrm{i}\phi)+E_R\exp(\mathrm{i}\phi)\big)^*}{2}S^*\tilde{f}+\\ &E_\parallel^*\frac{\partial\tilde{f}}{\partial p_\parallel}-\cos\psi E_\parallel^*T^*\tilde{f}+U^*\frac{1}{p_\perp}\frac{\partial\tilde{f}}{\partial\phi}\Bigg\}\,\mathrm{d}\phi\,\mathrm{d}^3k\end{aligned} \tag{A.2.12}$$

The term containing U is simplified using the fact that $\tilde{f}$ is periodic

$$\int_0^{2\pi}U^*\frac{1}{p_\perp}\frac{\partial\tilde{f}}{\partial\phi}\mathrm{d}\phi = -\int_0^{2\pi}\frac{\partial U^*}{\partial\phi}\frac{1}{p_\perp}\tilde{f}\mathrm{d}\phi \tag{A.2.13}$$

and with

$$\frac{\partial E_\perp}{\partial \phi} = E_\phi, \qquad \frac{\partial E_\phi}{\partial \phi} = -E_\perp \tag{A.2.14}$$

to

$$-\frac{\partial U}{\partial \phi} = \frac{(E_L \exp(-\mathrm{i}\phi) + E_R \exp(\mathrm{i}\phi))}{2}\left(1 - \frac{k_\parallel v_\parallel}{\omega}\right) + \cos(\phi-\varphi) E_\parallel \frac{k_\perp v_\parallel}{\omega} \tag{A.2.15}$$

such that the quasilinear equation becomes

$$\begin{aligned}\frac{\partial F(\mathbf{p},t)}{\partial t} &= -q \lim_{V\to 0}\frac{1}{V}\int_k \frac{1}{2\pi}\int_0^{2\pi}\left\{\frac{\left(E_L \exp(-\mathrm{i}\phi) + E_R \exp(\mathrm{i}\phi)\right)^*}{2}\times\right. \\ &\left[\left(1-\frac{k_\parallel v_\parallel}{\omega}\right)\frac{1}{p_\perp}\frac{\partial}{\partial p_\perp}\left(p_\perp \tilde{f}\right) + \frac{k_\parallel v_\perp}{\omega}\frac{\partial \tilde{f}}{\partial p_\parallel}\right] + \\ &\left. E_\parallel^*\left[\left(1-\frac{k_\perp v_\perp}{\omega}\cos(\phi-\varphi)\right)\frac{\partial \tilde{f}}{\partial p_\parallel} + \frac{k_\perp v_\parallel}{\omega}\cos(\phi-\varphi)\frac{1}{p_\perp}\frac{\partial}{\partial p_\perp}\left(p_\perp \tilde{f}\right)\right]\right\}\mathrm{d}\phi\,\mathrm{d}^3k\end{aligned} \tag{A.2.16}$$

The ϕ-integrals are of the form

$$\sum_{n'=-\infty}^{+\infty}\sum_{n=-\infty}^{+\infty} J_{n'}(\xi)\frac{1}{2\pi}\int_0^{2\pi}\exp\left(\mathrm{i}(n'-n)(\phi-\varphi)\right)\mathrm{d}\phi = \sum_{n=-\infty}^{+\infty} J_n \tag{A.2.17}$$

such that

$$\begin{aligned}\frac{\partial F(\mathbf{p},t)}{\partial t} = q \lim_{V\to 0}\frac{1}{V}\int_k &\left\{\frac{1}{p_\perp}\frac{\partial}{\partial p_\perp}p_\perp\left[\left(1-\frac{k_\parallel v_\parallel}{\omega}\right)\mathcal{E}^* + \frac{n\hat{\Omega}_{ce}}{\omega}\frac{v_\parallel}{v_\perp}E_\parallel^* J_n\right]\right. \\ &\left. + \frac{\partial}{\partial p_\parallel}\left[\frac{k_\parallel v_\perp}{\omega}\mathcal{E}^* + \left(1-\frac{n\hat{\Omega}_{ce}}{\omega}\right)E_\parallel^* J_n\right]\right\}\tilde{f}\mathrm{d}^3k\end{aligned} \tag{A.2.18}$$

Inserting the solution of $\tilde{f}$, eq.(A.1.26), the integral faces the problem of the pole in the denominator coming from the dielectric tensor. The pole is treated as a Cauchy principal value integral

$$\int_x^\infty \frac{1}{x-x_0}\mathrm{d}x = \mathrm{P.V.}\int_{x\neq x_0}\frac{1}{x-x_0}\mathrm{d}x + \mathrm{i}\pi\delta(x-x_0) \tag{A.2.19}$$

The second term, the residue, represents the resonant interaction between EC wave and electrons in the dielectric tensor. Neglecting the generally small non-resonant absorption represented by the principal value integral, i.e. going to the limit of resonant interaction, the pole in the $k_\parallel$ integration of eq.(A.2.18) is then replaced by

$$-\mathrm{i}\frac{1}{\omega - n\hat{\Omega}_{ce} - k_\parallel v_\parallel} \longrightarrow \pi\delta(\omega - n\hat{\Omega}_{ce} - k_\parallel v_\parallel) \tag{A.2.20}$$

such that

$$\begin{multline}
\frac{\partial F(\mathbf{p},t)}{\partial t} = q^2\pi \lim_{V\to 0}\frac{1}{V}\int_k \sum_{n=-\infty}^{+\infty}\left[\frac{1}{p_\perp}\frac{\partial}{\partial p_\perp}p_\perp\left(\mathcal{E}^* + \frac{v_\parallel}{v_\perp}E_\parallel^* J_n\right)\frac{n\hat{\Omega}_{\mathrm{ce}}}{\omega}\delta(\omega - n\hat{\Omega}_{\mathrm{ce}} - k_\parallel v_\parallel) + \right. \\
\left. \frac{\partial}{\partial p_\parallel}\left(\mathcal{E}^* + \frac{v_\parallel}{v_\perp}E_\parallel^* J_n\right)\frac{k_\parallel v_\perp}{\omega}\delta(\omega - n\hat{\Omega}_{\mathrm{ce}} - k_\parallel v_\parallel)\right]\times \\
\left[\left(\mathcal{E} + \frac{v_\parallel}{v_\perp}E_\parallel J_n\right)\frac{n\hat{\Omega}_{\mathrm{ce}}}{\omega}\frac{\partial F}{\partial p_\perp} + \left(\mathcal{E} + \frac{v_\parallel}{v_\perp}E_\parallel J_n\right)\frac{k_\parallel v_\perp}{\omega}\frac{\partial F}{\partial p_\parallel}\right]\mathrm{d}^3k \tag{A.2.21}
\end{multline}$$

This equation may be interpreted as a diffusion equation in velocity space

$$\frac{\partial F(\mathbf{p},t)}{\partial t} = \frac{\partial}{\partial \mathbf{p}}\cdot \mathbf{D}_{\mathrm{QL}}\cdot\frac{\partial F}{\partial \mathbf{p}} \tag{A.2.22}$$

with $\underline{\mathbf{D}}_{\mathrm{QL}}$ the quasilinear diffusion tensor

$$\underline{\mathbf{D}}_{\mathrm{QL}} = \begin{pmatrix} D_{\perp\perp} & D_{\perp\parallel} \\ D_{\parallel\perp} & D_{\parallel\parallel} \end{pmatrix} \tag{A.2.23}$$

whose components are

$$D_{\perp\perp} = \pi q^2 \lim_{V\to 0}\frac{1}{V}\int_k \sum_{n=-\infty}^{+\infty}\delta\left(\omega - n\hat{\Omega}_{ce} - k_\parallel v_\parallel\right)\left|\mathcal{E} + J_n E_\parallel\frac{v_\parallel}{v_\perp}\right|^2\left(\frac{n\hat{\Omega}_{ce}}{\omega}\right)^2\mathrm{d}^3k \tag{A.2.24}$$

$$D_{\parallel\parallel} = \pi q^2 \lim_{V\to 0}\frac{1}{V}\int_k \sum_{n=-\infty}^{+\infty}\delta\left(\omega - n\hat{\Omega}_{ce} - k_\parallel v_\parallel\right)\left|\mathcal{E} + J_n E_\parallel\frac{v_\parallel}{v_\perp}\right|^2\left(\frac{k_\parallel v_\perp}{\omega}\right)^2\mathrm{d}^3k \tag{A.2.25}$$

$$D_{\perp\parallel} = \pi q^2 \lim_{V\to 0}\frac{1}{V}\int_k \sum_{n=-\infty}^{+\infty}\delta\left(\omega - n\hat{\Omega}_{ce} - k_\parallel v_\parallel\right)\left|\mathcal{E} + J_n E_\parallel\frac{v_\parallel}{v_\perp}\right|^2\frac{n\hat{\Omega}_{ce}}{\omega}\frac{k_\parallel v_\perp}{\omega}\mathrm{d}^3k \tag{A.2.26}$$

$$D_{\parallel\perp} = D_{\perp\parallel} \tag{A.2.27}$$

Appendix B

The ion-acoustic instability and the ion-acoustic wave

Waves able to efficiently interact with plasma ions need phase velocities in the range of the ion velocities, i.e. $\omega/k \to v_{\mathrm{ions}}$. That is, electromagnetic waves are too fast, only electrostatic waves have phase velocities sufficiently small to cause strong interactions with the ions. The ion-acoustic wave is such an example and its dispersion relation shall be approximately solved in this appendix.

B.1 Kinetic dispersion relation

Starting point is, as always, the Maxwell equations. However, the magnetic field of an electrostatic wave is zero, only the Poisson equation is needed. In contrast to the fluid approach used in section 5.1, a kinetic description involving the Vlasov equation, accounting for particle effects, is adopted here. The self-consistent *Vlasov-Maxwell* system to solve (unknowns $\mathbf{E}$ and f) is

$$\begin{cases} \nabla \cdot \mathbf{E} = \dfrac{\rho}{\varepsilon_0} \\ \dfrac{\partial f_\alpha}{\partial t} + \mathbf{v} \cdot \dfrac{\partial f_\alpha}{\partial \mathbf{x}} + \dfrac{q_\alpha}{m_\alpha}(\mathbf{E} + \mathbf{v} \times \mathbf{B}) \cdot \dfrac{\partial f_\alpha}{\partial \mathbf{v}} = 0 \\ \rho = \displaystyle\sum_\alpha q_\alpha \int f_\alpha \, \mathrm{d}^3 v \\ \mathbf{j} = \displaystyle\sum_\alpha q_\alpha \int \mathbf{v} f_\alpha \, \mathrm{d}^3 v \end{cases} \tag{B.1.1}$$

where $\alpha \in [e, i]$ and for simplicity, the background plasma is considered as unmagnetised ($\mathbf{B}_0 = 0$), external electric field free ($\mathbf{E}_0 = 0$) and spatially uniform, $f_{\alpha 0} = f_{\alpha 0}(\mathbf{v})$. The perturbation due to the electrostatic wave ($\mathbf{E_1}, \mathbf{B_1} = 0$) is of the form

$$f_{\alpha 1}(\mathbf{x}, \mathbf{v}, t) = f_{\alpha 1}(\mathbf{v}) e^{\mathrm{i}(\mathbf{k} \cdot \mathbf{x} - \omega t)} \tag{B.1.2}$$

Linearisation of the system yields

$$\begin{cases} \dfrac{\partial f_{\alpha 1}}{\partial t} + \mathbf{v} \cdot \dfrac{\partial f_{\alpha 1}}{\partial \mathbf{x}} + \dfrac{q_\alpha}{m_\alpha} \mathbf{E}_1 \cdot \dfrac{\partial f_{\alpha 0}}{\partial \mathbf{v}} = 0 \\ \nabla \cdot \mathbf{E}_1 = \dfrac{1}{\varepsilon_0} \displaystyle\sum_\alpha q_\alpha \int f_{\alpha 1} \, \mathrm{d}^3 v \end{cases} \tag{B.1.3}$$

which is then Fourier transformed, i.e.

$$\begin{cases} -\mathrm{i}(\omega-\mathbf{k}\cdot\mathbf{v})f_{\alpha 1}+\dfrac{q_\alpha}{m_\alpha}\mathbf{E}_1\cdot\dfrac{\partial f_{\alpha 0}}{\partial\mathbf{v}}=0 \\ \mathrm{i}\mathbf{k}\cdot\mathbf{E}_1=\dfrac{1}{\varepsilon_0}\displaystyle\sum_\alpha q_\alpha\int f_{\alpha 1}\,\mathrm{d}^3v \end{cases} \tag{B.1.4}$$

It is convenient to use the electrostatic potential: $\mathbf{E}_1=-\nabla\phi$, i.e. in Fourier space $\mathbf{E}_1=-\mathrm{i}\mathbf{k}\phi$ in the first formula of eq.(B.1.4). Solve for

$$f_{\alpha 1}=-\phi\frac{q_\alpha}{m_\alpha}\frac{\mathbf{k}\cdot\frac{\partial f_{\alpha 0}}{\partial\mathbf{v}}}{\omega-\mathbf{k}\cdot\mathbf{v}} \tag{B.1.5}$$

and inject it in the second equation of eq.(B.1.4):

$$k^2\phi=-\frac{1}{\varepsilon_0}\sum_\alpha\frac{q_\alpha^2\phi}{m_\alpha}\int\frac{\mathbf{k}\cdot\frac{\partial f_{\alpha 0}}{\partial\mathbf{v}}}{\omega-\mathbf{k}\cdot\mathbf{v}}\,\mathrm{d}^3v \tag{B.1.6}$$

The resonance for $\omega=\mathbf{k}\cdot\mathbf{v}$, i.e. $v_{\mathrm{particles}}=\omega/k=v_{\mathrm{ph}}$ (phase velocity) is visible in the denominator. Eq.(B.1.6) may be rewritten as

$$\underbrace{1+\sum_\alpha\frac{q_\alpha^2}{\varepsilon_0 m_\alpha}\frac{1}{k^2}\int\frac{\mathbf{k}\cdot\frac{\partial f_{\alpha 0}}{\partial\mathbf{v}}}{\omega-\mathbf{k}\cdot\mathbf{v}}\,\mathrm{d}^3v}_{=:\,D(\omega,\mathbf{k})}=0 \tag{B.1.7}$$

where $D(\omega,\mathbf{k})=\det\underline{\boldsymbol{\epsilon}}(\omega,\mathbf{k})=0$ is the *dispersion function*. Choosing a geometry $\mathbf{k}=k\mathbf{e}_z$ (no loss of generality)

$$0=D(\omega,\mathbf{k})\equiv\epsilon(\omega,\mathbf{k})=\epsilon_r(\omega,\mathbf{k})+\mathrm{i}\epsilon_i(\omega,\mathbf{k})=1+\sum_\alpha\frac{q_\alpha^2}{m_\alpha\varepsilon_0 k^2}\underbrace{\int_{\mathcal{L}}\frac{k\frac{\partial f_{\alpha 0}}{\partial u}}{\omega-ku}\mathrm{d}^3v}_{\text{Landau integral}} \tag{B.1.8}$$

B.2 Low frequency wave mode

Without having to deal with the question on the integration path around the pole in the Landau integral [420] in eq.(B.1.8) the dispersion relation may be solved using the approximation (to be verified a posteriori)

$$v_{\mathrm{th}i}\ll\omega/k\ll v_{\mathrm{th}e} \tag{B.2.1}$$

that is, the singular denominator is approximated by the asymptotic expression

$$\frac{1}{\omega-ku}=\frac{1}{\omega}\left[1+\frac{ku}{\omega}+\left(\frac{ku}{\omega}\right)^2+\left(\frac{ku}{\omega}\right)^3\ldots\right] \tag{B.2.2}$$

for the ions and by the convergent series

$$\frac{1}{\omega-ku}\approx-\frac{1}{ku} \tag{B.2.3}$$

for the electrons. A neutral hydrogen plasma is considered in the following ($n_e = n_i = n_0$, $Z = 1$). An isotropic Maxwellian ion velocity distribution is assumed. The ion Landau integral evaluates to

$$\int_{-\infty}^{\infty} \frac{\mathrm{d}f_{0i}}{\mathrm{d}u} \frac{1}{\omega - ku} \,\mathrm{d}u \approx \int_{-\infty}^{\infty} \frac{\mathrm{d}f_{0i}}{\mathrm{d}u} \left[\frac{1}{\omega} + \frac{ku}{\omega^2} + \frac{(ku)^2}{\omega^3} + \frac{(ku)^3}{\omega^4}\right] \mathrm{d}u = -\frac{kn_i}{\omega^2} - 3\frac{k^3 n_i}{\omega^4} v_{\mathrm{th}i}^2 \tag{B.2.4}$$

where the first and third terms of the expansion are zero (f is an odd function). The second and forth term were integrated by parts and for the latter the second order moment of f,

$$v_{\mathrm{th}i}^2 = \int_{-\infty}^{\infty} u^2 f_{0i} \,\mathrm{d}u \tag{B.2.5}$$

was used.

For the electrons, a displaced Maxwellian, describing a net electron drift of velocity $\mathbf{v_d}$ with respect to the ions, is adopted

$$f_{e0}(\mathbf{v}) = \frac{1}{(2\pi)^{3/2} v_{\mathrm{the}}^3} \exp\left(-\frac{1}{2}\frac{(\mathbf{v} - \mathbf{v_d})^2}{v_{\mathrm{the}}^2}\right) \tag{B.2.6}$$

such that, for $u_k = \mathbf{k} \cdot \mathbf{v_d}/k \ll v_{\mathrm{the}}$,

$$\frac{\mathrm{d}f_{0e}}{\mathrm{d}u} = -\frac{u - u_k}{v_{\mathrm{the}}^2} f_{0e} \approx -\frac{u}{v_{\mathrm{the}}^2} f_{0e} \tag{B.2.7}$$

and thus the electron Landau integral becomes

$$\int_{-\infty}^{\infty} \frac{\mathrm{d}f_{0i}}{\mathrm{d}u} \frac{1}{\omega - ku} \,\mathrm{d}u \approx \frac{1}{kv_{\mathrm{the}}^2} \int_{-\infty}^{\infty} u\, f_{0e} \frac{\mathrm{d}u}{u} = \frac{n_e}{kv_{\mathrm{the}}^2} \tag{B.2.8}$$

The dispersion relation may therefore be written

$$\begin{aligned} D(\omega, k) \approx 1 - \frac{e^2\, n_i}{m_i\, \varepsilon_0} \frac{1}{\omega^2} \left(1 + 3\frac{k^2 v_{\mathrm{th}i}^2}{\omega^2}\right) + \frac{e^2\, n_e}{m_e\, \varepsilon_0} \frac{1}{k^2 v_{\mathrm{the}}^2} &= \\ 1 - \frac{\omega_{\mathrm{p}i}^2}{\omega^2} \left(1 + 3\frac{k^2 v_{\mathrm{th}i}^2}{\omega^2}\right) + \frac{\omega_{\mathrm{pe}}^2}{k^2 v_{\mathrm{the}}^2} &= 0 \end{aligned} \tag{B.2.9}$$

The solution $\omega = \omega(k)$ of the fourth order equation, using the Taylor approximation

$$\sqrt{1 + x} = 1 + \frac{1}{2}x \tag{B.2.10}$$

becomes

$$\omega^2(k) = \frac{\omega_{\mathrm{p}i}^2}{1 + 1/(\lambda_{\mathrm{De}}^2 k^2)} \left[1 + 3\left(k^2 \lambda_{\mathrm{D}i}^2 + \frac{\lambda_{\mathrm{D}i}^2}{\lambda_{\mathrm{De}}^2}\right)\right] \tag{B.2.11}$$

where $\lambda_{\mathrm{D}\alpha}$ are the particle Debye length, eq.(1.3.2). In the limit of large wave length $\lambda \sim 1/k$, i.e. much larger than λ_{D},

$$\omega^2(k) = \left(\omega_{\mathrm{p}i}^2 \lambda_{\mathrm{D}e}^2 + 3v_{\mathrm{th}i}^2\right) k^2 \tag{B.2.12}$$

The second term (corresponding to the higher order term in the development of the denominator of the ion Landau integral) is much smaller and therefore, at lowest order,

$$\omega^2(k) = c_S^2 k^2 \tag{B.2.13}$$

where

$$\frac{\omega_{\mathrm{p}i}^2}{\omega_{\mathrm{pe}}^2} v_{\mathrm{the}}^2 \equiv \frac{m_e}{m_i}\frac{T_e}{m_e} \equiv \frac{T_e}{m_i} = c_S^2 \tag{B.2.14}$$

is the ion sound speed.

B.3 Instability growth/damping rate

To lowest order

$$\frac{\partial \epsilon_r(\omega_r, k)}{\partial \omega_r} = 2\frac{\omega_{\mathrm{p}i}^2}{\omega_r^3} \tag{B.3.1}$$

and the imaginary part of ϵ,

$$\begin{aligned}
\epsilon_i(\omega, k) = -\pi \sum_\alpha \frac{e^2}{m_\alpha \varepsilon_0 k^2} \left.\frac{\mathrm{d}F_{0,\alpha}}{\mathrm{d}u}\right|_{u=\omega/k} = \\
\sqrt{\frac{2}{\pi}}\frac{e^2 n_0 \omega_r}{\varepsilon_0 k^3}\left[\frac{\exp\left(-\frac{\omega_r^2}{2\,k^2 v_{\mathrm{the}}^2}\right)}{m_e v_{\mathrm{the}}^3} + \frac{\exp\left(-\frac{\omega_r^2}{2\,k^2 v_{\mathrm{th}i}^2}\right)}{m_i v_{\mathrm{th}i}^3}\right] = \\
\sqrt{\frac{2}{\pi}}\frac{e^2 n_0}{\varepsilon_0 k^2}\left[\left(\frac{\omega_r}{k} - u_k\right)\frac{\exp\left(-\frac{\omega_r^2}{2\,k^2 v_{\mathrm{the}}^2}\right)}{m_e v_{\mathrm{the}}^3} + \frac{\omega_r}{k}\frac{\exp\left(-\frac{\omega_r^2}{2\,k^2 v_{\mathrm{th}i}^2}\right)}{m_i v_{\mathrm{th}i}^3}\right]
\end{aligned} \tag{B.3.2}$$

As $\omega_r/k = c_S \ll v_{\mathrm{the}}$, the exponential of the electron contribution is of order one. The damping rate is then found in the limit of resonant approximation,

$$\begin{aligned}
\gamma_{\mathbf{k}} \equiv -\frac{\epsilon_i(\omega_r, k)}{\partial \epsilon_r(\omega_r, k)/\partial \omega_r} = \\
-\sqrt{\frac{\pi}{8}}k\left.\left[\frac{\omega^4}{k^4 v_{\mathrm{th}i}^4}\exp\left(-\frac{1}{2}\frac{\omega^2}{k^2 v_{\mathrm{th}i}^2}\right) + \frac{\omega^3}{k^3 c_S^3}\sqrt{\frac{m_e}{m_i}}\left(\frac{\omega}{k} - u_k\right)\right]\right|_{\omega=\omega_r}
\end{aligned} \tag{B.3.3}$$

which reduces, in the limit of long wave length $\omega_r = k c_S$, to

$$\gamma_{\mathbf{k}} = -\sqrt{\frac{\pi}{8}}\sqrt{\frac{m_e}{m_i}}k c_S\left[1 - \frac{u_k}{c_S} + \sqrt{\frac{m_i}{m_e}\left(\frac{T_e}{T_i}\right)^3}\exp\left(-\frac{T_e}{2\,T_i} - \frac{3}{2}\right)\right] \tag{B.3.4}$$

where the last term is due to the ions, the others to the electrons. The first and last terms are stabilising, these represent the Landau damping on electrons and ions respectively. Eq.(B.3.4) demonstrates that if the magnetic field aligned electron drift speed is sufficiently important, $\gamma_{\mathbf{k}}$ may become positive and the wave then grows spontaneously. This is the current driven ion-acoustic instability. The growth rate $\gamma_{\mathbf{k}}/\omega_{\mathbf{k}}$ is proportional to $\sim \sqrt{m_e/m_i}$.

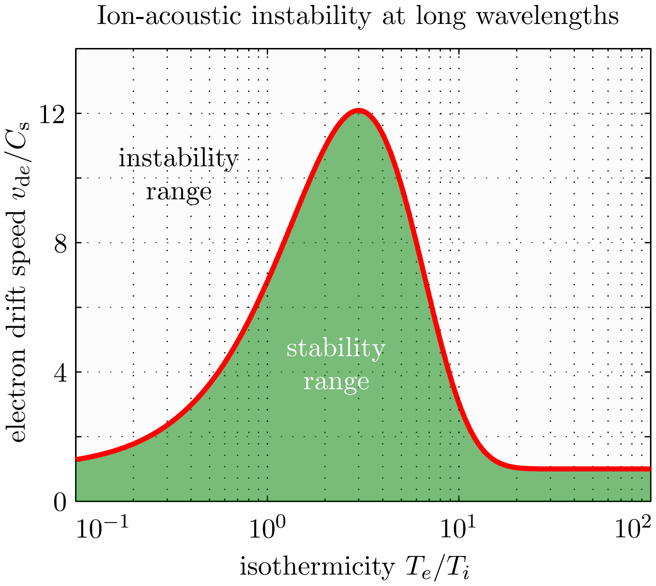

Figure B.3.1: Conditions for the ion-acoustic instability to occur in a hydrogen plasma at long wavelengths.

Figure B.3.1 shows the stability diagram for a hydrogen plasma as a function of the plasma non-isothermicity. Without streaming electrons ($u_k = 0$), the damping on ions and electrons is equally important for a temperature ratio of $T_e/T_i \sim 16$. If the ion damping is negligible (at low ion temperature) then the instability develops as soon as the electron drift speed exceeds the ion sound speed ($u_k > c_S$).

The initial assumption, eq.(B.2.1), must now be verified. Because of $c_S/v_{\mathrm{the}} = \sqrt{m_e/m_i} \ll 1$, the ion sound speed is smaller than the thermal electron speed, the second inequality $\omega/k = c_S \ll v_{\mathrm{the}}$ is therefore always fulfilled. This also implies, as the slope of the electron distribution function at the wave phase velocity is small, that the Landau damping on the electrons is weak. If, on the other hand, the ions are hot, $T_{i0} \sim T_{e0}$, then $\omega/k \sim c_S \to v_{\mathrm{th}i}$ and strong Landau damping of the wave on the ions is expected, such that the usual condition $|\gamma_k| \ll |\omega_k|$ for the applicability of the resonant approximation is verified. A requirement for the wave to exist is therefore $\sqrt{T_e/T_i} = c_S/v_{\mathrm{th}i} \ll 1$ as expressed by the first inequality in eq.(B.2.1).

Appendix C

Acquisition of the IAT fluctuation power spectrum

C.1 The spectrum analyser system

The device is a thirty years old Hewlett-Packard 71000 series analogue spectrum analyser system, routinely employed in the millimetre wave lab to test the equipment surrounding the gyrotrons. The analyser has a superheterodyne receiver where the local oscillator is swept through a range of frequencies. It contains little memory where traces and variables can be stored. The following modules are available:

Preselector HP70600A: The LHPI antenna signal is connected to the input of this module. It provides tracking preselection from 2.7 to 22 GHz. Low pass filtering is used below 2.9 GHz. The module contains a tunable filter that rejects all out-of-band frequencies from mixing with the local oscillator and creating unwanted responses at the IF frequencies. For the moderate frequency signals captured with the LHPI antenna this module mainly serves to protect the RF section (see below), as the latter doesn't have an RF input attenuator.

Local oscillator HP70900A: The local oscillator (LO) provides a swept LO signal in the range of 3–6.6 GHz. This module is the master controller of the spectrum analyser system. It contains the system firmware to control and coordinate measurements and is responsible for the output data delivery. This module has a GPIB bus interface.

Radiofrequency section HP70905B: The RF section converts the incoming RF signal from the preselector to a 21.4 MHz IF signal (by mixing with the LO signal). The supported RF frequency range is 50 kHz to 22 GHz.

External Mixer interface HP70907A: Provides the interface between external mixers and the spectrum analyser system. The module contains an LO amplifier, bias supply and downconversion circuitry to convert the 321.4 MHz input IF to a 21.4 MHz IF signal. The supported frequency range is 2.7 to 325 GHz. This module is not used for the LHPI signal analysis.

IF section HP70903: The intermediate frequency (IF) module processes the 21.4 MHz IF signal received from the RF section (or the external mixer interface). It contains resolution bandwidth filters, log amplifiers, detection circuitry and video filters. The resolution bandwidth is 100 kHz to 3 MHz.

Graphics display unit HP70206A: This independent full width module is the display and control interface to the spectrum analyser system. It contains a 9 inch CRT and has a GPIB bus controller.

The frequency resolution of the system is dependent on the resolution bandwidth setting Δf_{RBW} of the bandpass filter. Resolution comes into play because the IF filters are band-limited circuits that require finite times to charge and discharge. If the mixing products are swept through them too quickly, there will be a loss of signal amplitude. If one thinks about how long a mixing product stays in the passband of the IF filter (Δt_{PB}), that time is directly proportional to bandwidth and inversely proportional to the sweep in Hz per unit time $\Delta f / t_{\mathrm{ST}}$,

$$\Delta t_{\mathrm{PB}} = \Delta f_{\mathrm{RBW}} \frac{t_{\mathrm{ST}}}{\Delta f} \tag{C.1.1}$$

On the other hand, the rise time of a filter is inversely proportional to its bandwidth, $\Delta t_{\mathrm{PB}} \propto 1/\Delta f_{\mathrm{RBW}}$, thus

$$\Delta f_{\mathrm{RBW}} \propto \sqrt{\Delta f / t_{\mathrm{ST}}} \tag{C.1.2}$$

If the filter bandwidth (in Hz) is smaller than the square root of the LO sweep speed (in Hz/s), then the spectrum analyser will not produce meaningful results. Choosing a wider bandpass filter improves the signal-to-noise ratio at the expense of a decreased frequency resolution.
For example, the analysis of the frequency range 500 MHz to 2 GHz into 800 frequency bins requires the sweep period to be as long as 50 ms. The system may be used to measure one single frequency, the minimum sampling time is about 200 μs. For use with very weak signals, a pre-amplifier can be used, although harmonic and intermodulation distortion may lead to the creation of new frequency components that weren't present in the original signal.

C.2 Device remote setup and control

This system features an 8 bit GPIB (IEEE 488.1) interface with a bandwidth of 1 MByte/s for remote control and/or acquisition and is connected to a standard PC through a high-speed GPIB-USB-HS adapter (USB 2.0) from National Instruments.
A *MATLAB* GUI was developed to setup the device remotely using the Instrument Control Toolbox from Mathworks. All relevant parameters can be adjusted and all settings may be read back from the device for verification. A standard webcam captures still images of the display unit (to have a visual feedback of the signal trace displayed on screen and to read the occasional error messages printed there).

C.3 Spectrum acquisition over GPIB or DTACQ

The acquired frequency spectrum is getting digitised in the display unit of the spectrum analyser. The memory array is readable through the GPIB bus [421] and the *MATLAB* GUI may be used for this purpose (using the Data acquisition toolbox). The best data transfer speed is achieved when the data is read asynchronously in binary mode, making use of the end-of-sweep bit of the Service Request Enable Register. The data is stored as 16 bit integers which have to be transferred over the 8 bit GPIB bus in portions of 2 bytes each. However, the data transmission monopolises the spectrum analyser such that the next frequency sweep cannot start unless the data transfer has completed.

Figure C.3.1: 19 inch rack containing the GHz spectrum analyser mainframe HP70001A (middle) connected to the LHPI antenna. The PC (bottom) ensures the remote control of the analyser through the GPIB bus. The analog X- and Y-signals of the display unit (top) are digitised and acquired.

The sampling of the frequency range 500 MHz to 2 GHz with 800 points is thus prolonged from 50 ms to 180 ms or from 25 ms to 100 ms with 10 frequency points. In the single frequency acquisition mode, the sampling resolution decreases from 187 μs to only 50 ms.

The acquisition through the GPIB bus is thus too slow for the turbulence studies. Instead, the analogue X-Y video signal outputs of the local oscillator unit are acquired at 200 kHz using a DTACQ card (together with the calibrated time vector) and the frequency signal is reconstructed afterwards. Note that the system may be triggered externally but we currently use it in the free running mode such to achieve the best temporal resolution available.

Appendix D

Dielectric tensor of a magnetised plasma

The calculation of the dielectric tensor for a magnetised plasma follows the same lines as in section 5.1 and thus requires the calculation of the current using the perturbed distribution function. The perturbation of f was calculated in appendix A by integration of the Vlasov equation along the unperturbed orbits. The result, eq.(A.1.24), writes

$$\tilde{f}_e(\mathbf{k},\mathbf{v},\omega) = \frac{e}{m_e\omega}\sum_{n'=-\infty}^{+\infty}\sum_{n=-\infty}^{+\infty} J'_n(\xi)\frac{\exp\left(\mathrm{i}(n'-n)\phi\right)}{\omega - n\Omega_{ce} - k_\parallel v_\parallel}\tilde{\mathbf{A}}\cdot\tilde{E} \tag{D.0.1}$$

with the components of vector $\tilde{\mathbf{A}}$,

$$\begin{aligned}
\tilde{A}_x &= \left((\omega - k_\parallel v_\parallel)\frac{\partial F_e}{\partial v_\perp} + k_\parallel v_\perp\frac{\partial F_e}{\partial v_\parallel}\right)\frac{n}{\mathrm{i}\xi}J_n(\xi), && \text{(D.0.2)}\\
\tilde{A}_y &= \left((\omega - k_\parallel v_\parallel)\frac{\partial F_e}{\partial v_\perp} + k_\parallel v_\perp\frac{\partial F_e}{\partial v_\parallel}\right)J'_n(\xi), && \text{(D.0.3)}\\
\tilde{A}_z &= -\mathrm{i}\left(\frac{v_\parallel}{v_\perp}n\Omega_{ce}\frac{\partial F_e}{\partial v_\perp} + (\omega - n\Omega_{ce})\frac{\partial F_e}{\partial v_\parallel}\right)J_n(\xi) && \text{(D.0.4)}
\end{aligned}$$

Comparing the Ohm law, $\tilde{\mathbf{j}} = \underline{\boldsymbol{\sigma}}\cdot\tilde{\mathbf{E}}$ to eq.(D.0.1), the electron contribution to the conductivity tensor is therefore

$$\underline{\boldsymbol{\sigma}} = \frac{\varepsilon_0\omega_{\mathrm{pe}}^2}{\omega}\int \mathrm{d}^3v\,\mathbf{v}\left(\sum_{n'=-\infty}^{+\infty}\sum_{n=-\infty}^{+\infty} J'_n(\xi)\frac{\exp\left(\mathrm{i}(n'-n)\phi\right)}{\omega - n\Omega_{ce} - k_\parallel v_\parallel}\right)\tilde{\mathbf{A}} \tag{D.0.5}$$

where the components of the velocity vector are defined in eq.(A.1.10). The trigonometric functions are then again produced through eq.(A.1.19) and gyroaveraging, eq.(A.2.1), using the property eq.(A.2.17), eq.(D.0.5) finally yields

$$\underline{\boldsymbol{\sigma}} = -\mathrm{i}\frac{\varepsilon_0\omega_{\mathrm{pe}}^2}{\omega}\int \mathrm{d}^3v\sum_{n=-\infty}^{+\infty}\frac{1}{\omega - n\Omega_{ce} - k_\parallel v_\parallel}\mathbf{V}:\tilde{\mathbf{A}} \tag{D.0.6}$$

with

$$\mathbf{V} = \begin{pmatrix} \mathrm{i}\dfrac{n\Omega_{ce}}{k_\perp}J_n(\xi) \\ v_\perp J'_n(\xi) \\ \mathrm{i}v_\parallel J_n(\xi) \end{pmatrix} \tag{D.0.7}$$

Using the properties eq.(A.1.22), eq.(A.1.23) and further

$$\sum_{n=-\infty}^{\infty} J_n^2(\xi) \quad = \quad 1 \tag{D.0.8}$$

$$\sum_{n=-\infty}^{\infty} \Big(nJ_n(\xi)\Big)^2 \quad = \quad \frac{\xi^2}{2} \tag{D.0.9}$$

in the conductivity tensor, the dielectric tensor, eq.(5.1.9), then becomes

$$\underline{\boldsymbol{\epsilon}}(\mathbf{k},\omega) = \left(1 - \frac{\omega_{\mathrm{pi}}^2}{\omega^2}\right)\mathbb{1} + \\ - \frac{\omega_{\mathrm{pe}}^2}{\omega} \sum_{n=-\infty}^{+\infty} \int \mathrm{d}^3 v \left(\frac{n\Omega_{ce}}{v_\perp}\frac{\partial F_e}{\partial v_\parallel} + k_\parallel \frac{\partial F_e}{\partial v_\parallel}\right) \frac{\mathbf{V} : \mathbf{V}^\dagger}{\omega - n\Omega_{ce} - k_\parallel v_\parallel} \tag{D.0.10}$$

where $\mathbf{V}^\dagger$ denotes the complex conjugate and transpose of $\mathbf{V}$. Here we are interested in electrostatic waves with small wavelength such that the hypothesis of a purely longitudinal electric field is not plain wrong. That is, the electrostatic approximation, through projection of the dielectric tensor on the vector k,

$$\epsilon(\mathbf{k},\omega) \equiv \frac{\mathbf{k}\cdot\underline{\boldsymbol{\epsilon}}(\mathbf{k},\omega)\cdot\mathbf{k}}{k^2} = 0 \tag{D.0.11}$$

yields the dielectric function

$$\epsilon(\mathbf{k},\omega) = \left(1 - \frac{\omega_{\mathrm{pi}}^2}{\omega^2}\right) + \\ - \frac{\omega_{\mathrm{pe}}^2}{k^2} \sum_{n=-\infty}^{+\infty} \int \mathrm{d}^3 v \left(\frac{n\Omega_{ce}}{v_\perp}\frac{\partial F_e}{\partial v_\parallel} + k_\parallel \frac{\partial F_e}{\partial v_\parallel}\right) \frac{J_n^2(\xi)}{\omega - n\Omega_{ce} - k_\parallel v_\parallel} \tag{D.0.12}$$

where the relation

$$\sum_{n=-\infty}^{+\infty} nJ_n^2 = 0 \tag{D.0.13}$$

was used.

Appendix E

Alternating-direction implicit difference equation method applied to IAT

The projection of the distribution function onto a grid in v-space, such that indexes j and k refer to mesh points $(v_\perp, v_\parallel)$ of a grid of size $\Delta v_\perp$ and $\Delta v_\parallel$ respectively, is represented by

$$f^n_{j.k} = f(j\Delta v_\perp, k\Delta v_\parallel, n\Delta t) \tag{E.0.1}$$

and the ADI scheme for the quasilinear diffusion equation, eq.(7.1.3), for the case of the ions, is then

$$\begin{aligned}\frac{f_i^{n+1/2} - f_i^n}{\Delta t/2} &= \\ &D^n_{i\parallel\parallel}\frac{\partial^2 f_i^{n+1/2}}{\partial v_\parallel^2} + C^n_\parallel \frac{\partial f_i^{n+1/2}}{\partial v_\parallel} + 2D^n_{i\parallel\perp}\frac{\partial^2 (f_i^{n+1/2} + f_i^n)}{\partial v_\parallel \partial v_\perp} + C^n_\perp \frac{\partial f_i^n}{\partial v_\perp} + D^n_{i\perp\perp}\frac{\partial^2 f_i^n}{\partial v_\perp^2}\end{aligned} \tag{E.0.2}$$

and

$$\begin{aligned}\frac{f_i^{n+1} - f_i^{n+1}}{\Delta t/2} = D^n_{i\parallel\parallel}\frac{\partial^2 f_i^{n+1/2}}{\partial v_\parallel^2} + C^n_\parallel \frac{\partial f_i^{n+1/2}}{\partial v_\parallel} \\ + 2D^n_{i\parallel\perp}\frac{\partial^2 (f_i^{n+1/2} + f_i^{n+1})}{\partial v_\parallel \partial v_\perp} + C^n_\perp \frac{\partial^2 f_i^{n+1}}{\partial v_\perp^2} + D^n_{i\perp\perp}\frac{\partial^2 f_i^{n+1}}{\partial v_\perp^2}\end{aligned} \tag{E.0.3}$$

with

$$C^n_\parallel = \left(\frac{\partial D^n_{i\parallel\parallel}}{\partial v_\parallel} + \frac{D^n_{i\perp\parallel}}{v_\perp} + \frac{\partial D^n_{i\perp\parallel}}{\partial v_\perp}\right) \tag{E.0.4}$$

and

$$C^n_\perp = \left(\frac{\partial D^n_{i\parallel\perp}}{\partial v_\parallel} + \frac{D^n_{i\perp\perp}}{v_\perp} + \frac{\partial D^n_{i\perp\perp}}{\partial v_\perp}\right) \tag{E.0.5}$$

For the first half time step, eq.(E.0.2), the derivation is implicit into the parallel and explicit into the perpendicular direction, whereas the situation is opposite for the second time step, eq.(E.0.3).

The derivatives are calculated as usual

$$\begin{cases} \dfrac{\partial f}{\partial v_\parallel} = \dfrac{f_{j,k+1} - f_{j,k-1}}{2\Delta v_\parallel} \\ \dfrac{\partial f}{\partial v_\perp} = \dfrac{f_{j+1,k} - f_{j-1,k}}{2\Delta v_\perp} \\ \dfrac{\partial^2 f}{\partial v_\parallel^2} = \dfrac{f_{j,k+1} - 2f_{j,k} + f_{j,k-1}}{\Delta v_\parallel^2} \\ \dfrac{\partial^2 f}{\partial v_\perp^2} = \dfrac{f_{j+1,k} - 2f_{j,k} + f_{j-1,k}}{\Delta v_\perp^2} \end{cases} \tag{E.0.6}$$

and the mixed derivative, due to the mixture of implicit and explicit derivation into the two directions, requires to combine the two time instants f^n and $f^{n+1/2}$ such that [422]

$$\frac{\partial^2 (f_i^{n+1/2} + f_i^n)}{\partial v_\parallel \partial v_\perp} = \frac{f^{n+1/2}_{j,k+1} - f^{n+1/2}_{j,k-1} - f^{n+1/2}_{j-1,k+1} + f^{n+1/2}_{j-1,k-1} + f^n_{j+1,k+1} - f^n_{j+1,k-1} - f^n_{j,k+1} + f^n_{j,k-1}}{2\Delta v_\parallel v_\perp} \tag{E.0.7}$$

and

$$\frac{\partial^2 (f_i^{n+1/2} + f_i^{n+1})}{\partial v_\parallel \partial v_\perp} = \frac{f^{n+1/2}_{j+1,k} - f^{n+1/2}_{j-1,k} - f^{n+1/2}_{j+1,k-1} + f^{n+1/2}_{j-1,k-1} + f^{n+1}_{j+1,k+1} - f^{n+1}_{j-1,k+1} - f^{n+1}_{j+1,k} + f^{n+1}_{j-1,k}}{2\Delta v_\parallel v_\perp} \tag{E.0.8}$$

Eq.(E.0.2) may then be rewritten as

$$\begin{aligned} &- \left\{ \frac{D^n_{i,\parallel\parallel}(j,k)}{\Delta v_\parallel^2} + \frac{C^n_{i\parallel}(j,k)}{2\Delta v_\parallel} + \frac{D^n_{i,\parallel\perp}(j,k)}{2\Delta v_\parallel \Delta v_\perp} \right\} f_i^{n+1/2}(j,k+1) + \\ &\left\{ \frac{2}{\Delta t} + \frac{2D^n_{i\parallel\parallel}(j,k)}{\Delta v_\parallel^2} \right\} f_i^{n+1/2}(j,k) \\ &\qquad + \left\{ -\frac{D^n_{i,\parallel\parallel}(j,k)}{\Delta v_\parallel^2} + \frac{C^n_{i\parallel}(j,k)}{2\Delta v_\parallel} + \frac{D^n_{i,\parallel\perp}(j,k)}{2\Delta v_\parallel \Delta v_\perp} \right\} f_i^{n+1/2}(j,k-1) = \varphi_i^n(j,k) \end{aligned} \tag{E.0.9}$$

where

$$\begin{aligned} \phi^n_{j,k} = \frac{2}{\Delta t} f^n_{j,k} &+ \frac{D_{i,\parallel\perp}(j,k)}{2\Delta v_\parallel \Delta v_\perp} \left\{ -f^{n+1/2}_{j-1,k+1} + f^{n+1/2}_{j-1,k-1} + f^n_{j+1,k+1} - f^n_{j+1,k-1} - f^n_{j,k+1} + f^n_{j,k-1} \right\} \\ &+ \frac{C^n_{i\perp}(j,k)}{2\Delta v_\perp} \left\{ f^n_{j+1,k} - f^n_{j-1,k} \right\} + \frac{D^n_{i\perp\perp}(j,k)}{\Delta v_\perp^2} \left\{ f^n_{j+1,k} - 2f^n_{j,k} + f^n_{j-1,k} \right\} \end{aligned} \tag{E.0.10}$$

or equivalently in matrix form

$$\underline{\mathbf{G}}^n f_i^{n+1/2} = \underline{\boldsymbol{\varphi}}^n \tag{E.0.11}$$

with $\underline{\mathbf{G}}$ being tridiagonal and the algebraic system is solved through the LU decomposition of matrix $\underline{\mathbf{G}}$(*). The solution for the second time step proceeds analogously. A single time step Δt of the computation does thus comprise the alternating solution of the successive time steps eq.(E.0.2) and eq.(E.0.3) on a time interval $\Delta t/2$ each. The equations for the advancing of the distribution function of the electrons is then straightforward, with the only difference of additional terms involving the external electric field E_0.

(*) In fact, although the matrix $\underline{\boldsymbol{\varphi}}$ contains terms at the advanced time $t = (n+1/2)\Delta t$, the boundary condition $\partial f/\partial v_\perp(v_\perp = 0)$ permits to start the calculation at $v_\perp = 0$. As the calculation advances in $v_\perp$, the value of f at the advanced time is already known at the preceding $v_\perp$ and $\underline{\boldsymbol{\varphi}}$ is therefore known.
Noting A, B and C the matrix describing the lower off-, upper off- and diagonal part of $\underline{\mathbf{G}}$, the recurrence relations for $f^{n+1/2}$ write

$$\begin{cases} E(j,k) = \dfrac{A(j,k)}{B(j,k) - C(j,k)E(j,k)} \\[2ex] F(j,k) = \dfrac{\varphi(j,k) + C(j,k)F(j,k-1)}{B(j,k) - C(j,k)E(j,k-1)} \\[2ex] f^{n+1/2}(j,k) = E(j,k)f^{n+1/2}(j,k+1) + F(j,k) \end{cases} \tag{E.0.12}$$

That is, as the calculation advances in the perpendicular direction, the parallel index k is swept out (calculation of F) and back in (calculation of f).

Appendix F

Neutral particle analysis on the Joint European Torus (JET)

F.1 Introduction

At the beginning of his thesis, the author was seconded a couple of times to the Joint European Torus (JET), located in Culham, close to Oxford (Great Britain) which is currently the largest operational tokamak in the world. These visits aimed at learning the physics of neutral particle analysis and later helping the responsible officer in addressing issues preventing the diagnostic unleashing its full potential [423]. Lost bits of the neutralisation code (section F.4) were reimplemented and used to assess the accuracy of the fast ion temperature calculation (section F.5). The acquired skills were then capitalised on the NPA data analysis of a couple of JET experiments, namely the proton-triton (pT) fusion [424] and the tornado mode [425] sessions. Note that initial plans intended to devote a considerable part of this thesis to topics of the fast ion physics at JET. JET suffered repeated delays of machine restart (finally more than one year) due to technical problems and at a certain point it was decided to abandon further participation in JET experiments and to concentrate the research activities on TCV.

F.2 The JET tokamak

The reactor was financed and built by the members of the Euratom association and its experimental campaigns are supported by a large international network of collaborations. JET was designed to investigate reactor relevant physics, such as advanced heating schemes (neutral beams, ICRH and fusion α-particle production), fast ion confinement and plasma-wall interactions. Experiments started in 1983. The most impressive achievement of JET is certainly the production of a D–T fusion power exceeding 16 MW ($Q \approx 0.7$) during more than 1 s in 1997 [426]. The main JET parameter are stated in table F.1.

JET features three auxiliary heating technologies, namely 8 neutral beam sources injecting H or D (energy 120 keV) [427], four ion-cyclotron resonance heating antennas (frequency range 23–56 MHz) [428] and a lower-hybrid current drive system (operating at 3.7 GHz) [429].

F.3 High energy neutral particle analyser KF-1

JET features a low energy NPA KR-2 [169, 430] (installed at the horizontal midplane) and a high energy NPA KF-1 [431] measuring fluxes propagating vertically ($R = 3.07$ m). KF-1 is a GEMMA-2M device manufactured by IOFFE. KF-1 is a key diagnostic for the investigation

Parameter	**Symbol**	**Value**
major radius	R_0	2.96 m
maximum minor radius	a	1.25 m
internal height of vessel	h	2.1 m
aspect ratio	$\epsilon = R_0/a$	$\sim$0.35
toroidal magnetic field on axis	$B_{\phi 0} = B_\phi(R_0)$	$\leqslant 3.45$ T
plasma current	I_p	< 6 MA
plasma elongation	κ_{JET}	1.6
Flattop pulse length	T	20 s
RF heating power (ion-cyclotron frequency heating)	P_{ICRH}	$\leqslant 22$ MW
RF heating power (lower-hybrid frequency heating)	P_{LH}	$\leqslant 7$ MW
NBI heating power	P_{NBI}	$\leqslant 24$ MW

Table F.1: System parameters of the JET tokamak.

of fast ions produced by the neutral beam or radiofrequency heating systems. The acceptance cone of the NPA is narrow, such that only ions with pitch angles $v_z/v_\phi \gtrsim 200$ contribute to the measurement, corresponding to ions whose banana orbit tips align with the KF-1 viewline (see figure F.3.1.a). KF-1 has 8 detection channels with energies $E \in [0.2; 3.5]$ MeV, is of the $\mathbf{E} \parallel \mathbf{B}$ type and can be set up to analyse H, D, T, ^{3}He or α-particles (^{4}He). The incoming flux is reionised using a carbon foil stripper. The detection lines are inorganic CsI(Tl) scintillators coupled to Hamamatsu R7600 photomultipliers. Unfortunately these are strongly sensitive to neutrons, whose fluencies may reach intense levels on JET (especially during D-T plasma mix operation, $\Phi \simeq 10^{18}$ neutrons/sec). Each channel is therefore equipped with a 16 bin pulse height analyser, permitting a compensation for the parasitic neutron counts by a post-shot analysis (see figure F.3.1.b).

F.4 Impurity induced neutralisation (*IIN*)

For protons in the MeV range, contrary to the keV energies diagnosed on TCV, neutralisation is strongly enhanced (high reaction cross-section) by charge-exchange reactions with hydrogen-like (charge Z–1) and helium-like (charge Z–2) intrinsic impurity ions, especially carbon, beryllium and helium on JET. This mechanism was experimentally observed on JET and led to the development of the impurity induced neutralisation model (*IIN*) [432, 433]. The *IIN* code available at JET includes radiative recombination with electrons, charge exchange reactions with impurities, thermal deuterium and NBI atoms and equates a system of steady-state ion density balance equations for bare, [H]-, and [He]-like impurities. The required input parameters are impurity (He, Be, C) density ratios, their respective confinement times, the ion temperature T_i, the electron density n_e, the thermal deuterium density $n_{\mathrm{D}}^{\mathrm{thermal}}$ and the effective charge Z_{eff}.
As pointed out in [433], the main source of uncertainty in the determination of the fast ion distribution function is the [H]-like electron donor density in the plasma core, that causes an uncertainty of 45 % in the neutralisation probability, eq.(4.3.3). From eq.(4.3.5), the error bar on $f_i^{\mathrm{fast}}(E)$ is about 50 % assuming a measurement with good counting statistics (e.g. Poisson uncertainty < 5 %).
The fast ion perpendicular temperature $\overline{T_{i\perp}^{\mathrm{fast}}}$ is inferred from the fast ion distribution function using Stix's expression [434] for ICRF heated ions and therefore the perpendicular fast ion temperature can be inferred from the slope of the logarithm of the fast ion distribution function,

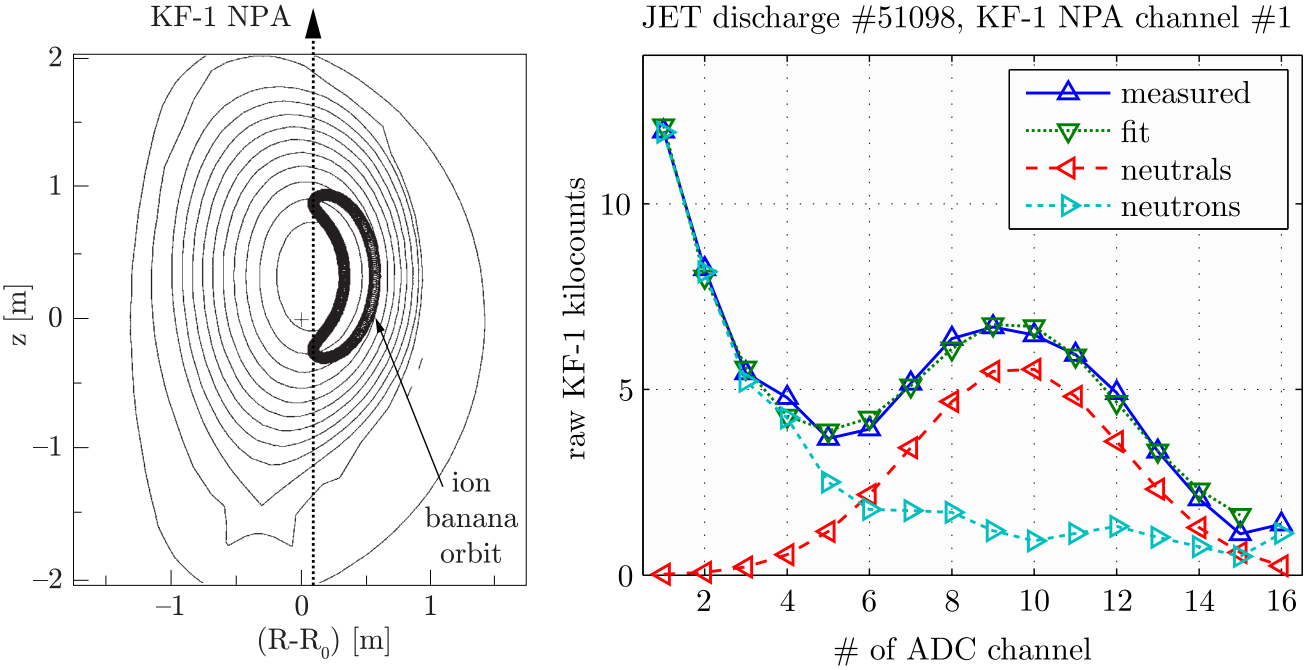

(a) KF-1 sight line.

(b) Neutron signal rejection.

Figure F.3.1: (a) View line of JET's KF-1 high energy NPA.
(b) Fit of the measured KF-1 high energy NPA pulse height spectrum with a gaussian (neutrals) and a decaying exponential (neutrons).

eq.(4.3.11), that is

$$-\frac{1}{\overline{T_{i\perp}^{\text{fast}}}} = \frac{\partial}{\partial E} \ln \left(\frac{\overline{f_i^{\text{fast}}}(E)}{\sqrt{E}} \right) \tag{F.4.1}$$

where the bars over the quantities $\overline{f_i^{\text{fast}}}(E)$ and $\overline{T_{i\perp}^{\text{fast}}}(E)$ stand for line-of-sight integrated values. The central fast ion perpendicular temperature $T_{i\perp}^{\text{fast}}(r=0)$ is then given by the formula from [435], i.e.

$$T_{i\perp}^{\text{fast}}(r=0) \simeq \overline{T_{i\perp}^{\text{fast}}}(E^*) \left(1 + \frac{\overline{T_{i\perp}^{\text{fast}}}(E^*)}{2E^*} \right) \tag{F.4.2}$$

where E^* is the median energy of the NPA measurements.
The error bars on $T_{i\perp}^{\text{fast}}$ are fairly low, since the main source of uncertainty on the temperature is the measured C^5-ions charge exchange cross-section (20 %), resulting in [433] an uncertainty of ≈10 %. From the line integrated fast ion distribution function, it is straightforward to deduce f_i^{fast} by integrating $f_i(E)$ over the energy range of the measurement. The method used to calculate f_i^{fast} implies that the error bars be set similarly to that of the fast ion distribution, i.e. ∼50 % [433].

F.5 Reliability of the KF-1 T_i^{fast} measurement

Fast ion densities and temperatures may also be calculated from γ-ray and neutron spectroscopy data on JET. In the past these measurements did not agree very well with the NPA and in particular the inference of T_i^{NPA} was suspected to be incorrectly calculated. Efforts were therefore undertaken [436] to study the sensitivity of JET's code calculating the neutralisation probability

on its various input parameters and its impact on $f_i^{\text{fast}}(E)$, $T_{i,\perp}^{\text{fast}}$ and n_i^{fast} such to assess the robustness of this calculation. The input parameters have been varied within their error bars.
For this purpose the plasma discharge #61260 from the 2003 trace tritium campaign C11 has been analysed during the time interval $t = [47.55; 48.45]$ s, where only ICRF heating ($P = 4$ MW) tuned to the H-minority at its 1st harmonic was present. The statistical error in the counts is below 3 % for this time interval, magnetic field $B_T = 3.4$ T, plasma current $I_{\text{p}} = 1.8$ MA, $T_e = 7$ keV and $n_e = 3 \times 10^{19}$ m^{-3} in the plasma core.

F.5.1 Fast ion distribution function and fast ion density

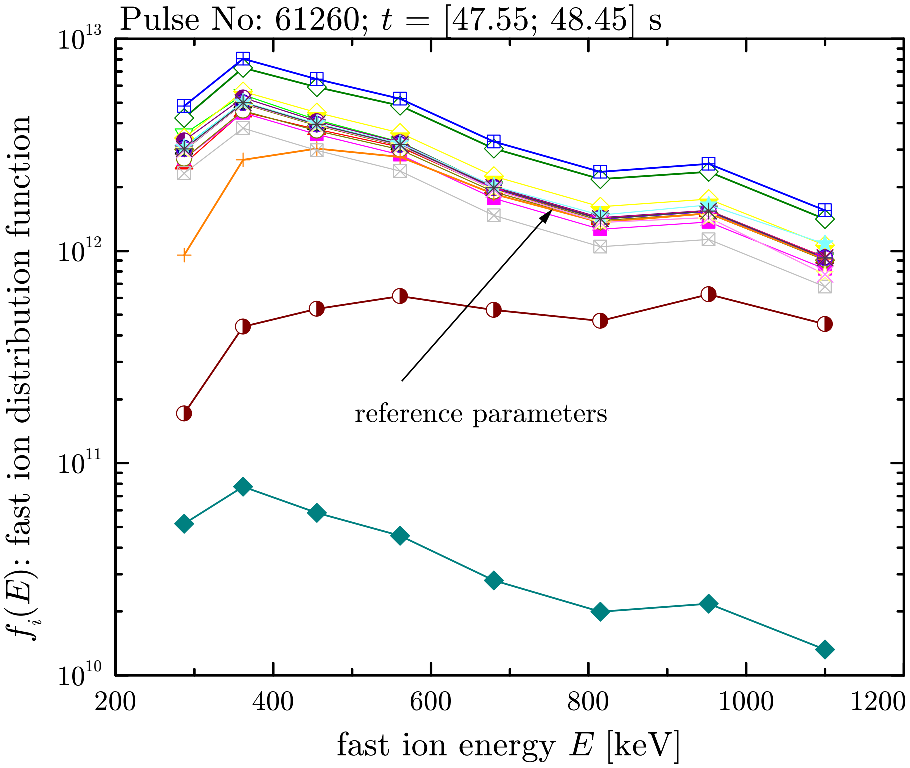

Figure F.5.1: Neutralisation code input parameter impact on the calculation of the fast ion distribution function. △ represents the calculation of the neutralisation probability using the reference parameters, the other curves were calculated by modification of one single input parameter. For the legend, refer to table F.2.

Figure F.5.1 shows a compilation of such a procedure and its effect on the inferred fast ion distribution function. The modified parameters and their associated error bars were the following: The relative impurity concentrations (Be/C and He/C ratio ±100 %), the thermal deuterium density $n_{\text{D}} \pm 100$ %, the electron density $n_e \pm 20$ %, the empirical impurity confinement times τ for Beryllium, Helium and Carbon ±100 %, the ion temperature $T_i \pm 10$ %, the effective charge $Z_{\text{eff}} \pm 30$ % and the statistical Poisson uncertainty of the fast neutral counts N_i.
It is found that the modification of most of the input parameters, within their error bars, doesn't strongly affect the absolute value of the fast ion distribution function. Large changes result when decreasing the impurity confinement times towards zero, but this does not make physically sense (see section F.5.4). The confinement of carbon and – to a minor extent – Beryllium change the neutralisation probability and therefore f_i^{fast} by 2 and 1 order of magnitude respectively. The modification of the shape of f_i^{fast} by changing τ_{Be} or τ_{He} is due to the strong energy dependence of the cross-sections for charge exchange [433]. Z_{eff} affects neutralisation and reionisation, which is also seen in f_i^{fast}. Table F.2 shows the values of the resulting n_i^{fast} (last column).

modified input parameter	$\frac{\Delta T_\perp(r=0)}{T_\perp^{\mathrm{ref}}(r=0)}$ [%]	$\frac{\Delta n_i^{\mathrm{fast}}}{n_i^{\mathrm{fast}}}$ [%]
▲: Be/C ratio → +100 %	5.6	−3.2
▽: Be/C ratio → −80 %	−4.5	2.9
▼: He/C ratio → +100 %	0.4	−0.1
□: He/C ratio → −100 %	−0.4	0.1
■: n_D thermal → +100 %	−0.6	−10.7
⬘: n_D thermal → −100 %	0.7	13.6
⬖: n_e → +20 %	−0.8	−1.7
○: n_e → −20 %	3.8	−5.2
●: reduced n_e at boundary	0.1	−0.4
◐: τ_{Be} → +100 %	−2.4	2.3
◑: τ_{Be} → −99 %	1630.9	−76.8
◇: τ_{C} → +100 %	2.2	51.2
◆: τ_{C} → −99 %	−4.0	−98.6
⊕: τ_{He} → +100 %	−0.2	0.1
+: τ_{He} → −99 %	39.5	−15.7
⊗: T_i → +10 %	0.0	−0.5
×: T_i → −10 %	0.1	0.6
⊠: Z_{eff} → +30 %	−2.0	−25.4
⊞: Z_{eff} → −30 %	2.0	64.4
☆: $N_i \rightarrow N_i - 1/\sqrt{N_i}$	−8.7	−2.9
★: $N_i \rightarrow N_i + 1/\sqrt{N_i}$	8.7	2.9

Table F.2: The impact of input parameter modification on the fast ion temperature. With the reference parameters, the central $T_{i\perp}^{\mathrm{fast}}(r=0)$ was 555 keV and the line integrated fast ion density $\overline{n_i^{\mathrm{fast}}} = 2.3\times10^{18}\ \mathrm{m}^{-3}$.

F.5.2 Cross-check of the fast ion density n_i^{fast} with other diagnostics

n_i^{fast} may also be determined from the ratio of the spectroscopic emission line intensities of the hydrogenic species (assuming $n_{\mathrm{D}} \approx n_e$, with ICRF tuned to the hydrogen minority),

$$\alpha = \frac{\mathrm{H}_\alpha}{\mathrm{H}_\alpha + \mathrm{D}_\alpha + \mathrm{T}_\alpha} \qquad \Rightarrow \qquad n_i^{\mathrm{fast}} \approx \frac{\alpha}{1-\alpha} \tag{F.5.1}$$

or the fast ion energy,

$$W_{\mathrm{fast}} = \frac{4}{3}\Big(W_{\mathrm{DIA}} - W_{\mathrm{MHD}}\Big) \tag{F.5.2}$$

$$W_{\mathrm{fast}} = 4\pi^2\, R_0 \int_0^a r\,\kappa(r)\, n_i^{\mathrm{fast}}(r) \left[T_{i\perp} + \frac{1}{2}T_{i\parallel}\right] \mathrm{d}r \tag{F.5.3}$$

where W_{DIA} is the plasma energy measured by the diamagnetic loop and W_{MHD} is calculated by the equilibrium reconstruction code *EFIT* [437] using magnetic measurements and MHD calculations. The integral in eq.(F.5.3) uses gaussian profiles with width of $\Delta = 0.3$ m with the usual assumption that $T_{i\parallel} = 0.1{\cdot}T_{i\perp}$. Such considerations show agreement within the error bars (±30 %) with the density inferred from the fast ion distribution function.

F.5.3 Fast ion temperature $T_{i,\perp}^{\text{fast}}$

Since most of the input parameters only affect the absolute value of f_i^{fast}, the effect on the inferred $T_{i\perp}^{\text{fast}}$ (depending on the slope of f_i^{fast} only) is rather weak (refer again to table F.2). Apart from the two non-physical impurity confinement times τ_{C} and $\tau_{\text{Be}} \to 0$, the inferred $T_{i\perp}^{\text{fast}}$ is indeed found to be insensitive to the modified parameters, with changes below 10 %.

F.5.4 Impurity confinement times

To better understand the impact of τ, a further scan of these parameters was performed. For JET $\tau \gtrsim 1$ s, see the simple estimation in [433]. Figure F.5.2 shows how $T_{i\perp}^{\text{fast}}$ and n_i^{fast} are altered when modifying τ in the range of $0 - -2$ s. It is found that around $\tau \approx 1$ s the modifications by a scan of τ_{Be} and τ_{He} are negligibly small. Another picture is obtained when modifying τ_{C}, where no saturation of n_i^{fast} is observed. Other than for helium and beryllium, the cross-section for charge exchange of carbon with background atoms is two orders of magnitude smaller at low energy. The radial carbon transport described by τ_{C} is therefore more important in the calculation of the ionisation balance. **$T_{i\perp}^{\text{fast}}$ is, however, not affected at all**, due to the small energy dependence of the charge exchange cross section at low energy. To conclude, this exercise outlined the reliable and robust measurement of the fast ion perpendicular temperature $T_{i\perp}$ using experimental data from the high energy NPA KF1. The crude *IIN*-model permits to calculate the fast ion density n_i^{fast} with 50 % of accuracy, with a refined analysis of the neutralisation calculation input parameter the error bars may be reduced well below. The inference of n_i^{fast} from NPA data is in agreement with edge spectroscopy measurements. Other causes for the differences in the values of fast ion densities and temperatures inferred from different diagnostics on JET must be search for, such as selective species heating (ICRF or NBI), or spatial (location) and velocity anomalies (pitch-angle anisotropy), which all usually occur in JET. Diagnostics should thus not be blamed for disagreement, but rather considered as complementary, as these differences provide precious information about the configuration of the various fast ion populations.

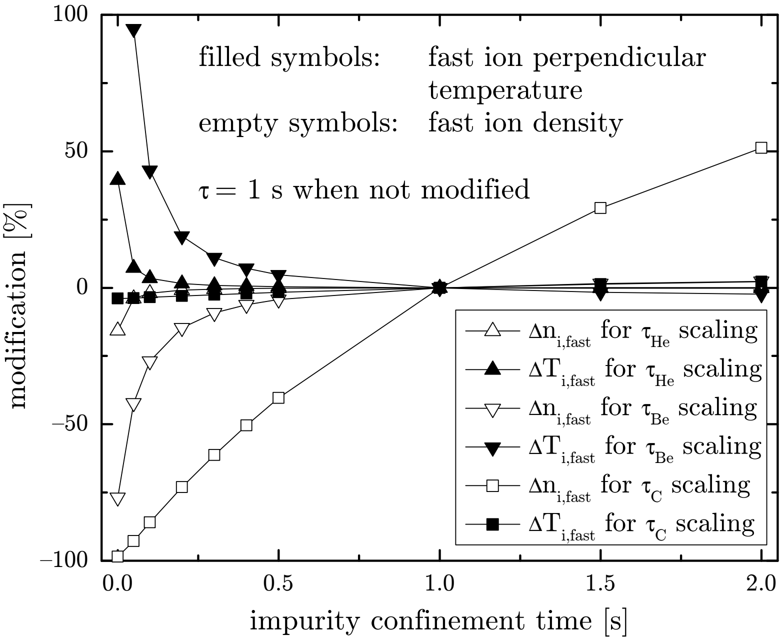

Figure F.5.2: n_i^{fast} and $T_{i,\perp}^{\text{fast}}$ as a function of the different τ.

Appendix G

The CRPP intranet wiki (CRPPwiki)

G.1 Motivation

The management of documentation of the scientific activities at the Centre de Recherches en Physique des Plasmas (CRPP) [438] was frequently object of lamentation in the past. Many scientific tasks, in particular the activities concerning the tokamak à configuration variable (TCV) [439], involve a large number of collaborators and nevertheless, if at all, documentation was mostly pursued individually. There was a growing number of voices calling for a decent platform of collaborative knowledge exchange. An internal knowledge management base where everybody involved in a project could contribute to its documentation was missed badly. Some scientists serviced their private personal web pages – or even personal web servers. Whenever a colleague was leaving, most of the documentation was either lost or, if stored on our servers, could not be updated and expanded. With time, the quantity of obsolete information became a serious problem. An easily maintainable and feedable, barrier-free and up-to-date documentation system became thus an urgent need.

A part-time job of the main author was the administration of the web servers hosted at CRPP. Driven by mostly personal needs, a wiki system was installed on the intranet server [440] in 2006 and a small group of mostly PhD students started to use it. The almost unlimited potential of the system was rapidly perceived and, by popular request, the system (baptised CRPPwiki) was chosen to replace the whole existing intranet web by the end of 2007.

G.2 Wiki approach

Initially, several platforms suitable for collaborative teamworking were evaluated. Rapidly, the evaluation focused on products incorporating the wiki(*) philosophy [441]. A wiki is probably the most simple content management system (CMS) available on the market. A wiki enables documents to be written collaboratively, using a Web browser. The structure and formatting of wiki pages are specified with a simplified markup language, sometimes known as “wikitext”. A wiki is thus essentially a database for creating, browsing, and searching through information. A defining characteristic of wiki technology is the ease with which pages can be created and updated. Generally, there is no review before modifications are accepted. Wikis revolutionised the way information is collected, updated and shared and was rapidly adopted in open and closed networks (e.g. corporate intranets) [442].

(*) “Wiki” is a Hawaiian word for “fast”.

G.3 Choice of the system: MediaWiki

A large number of solutions faithfully implementing the wiki concept are currently available [443], some of them target specialised applications. After having carefully tested some of the most promising candidates, we have finally chosen the MediaWiki software [444], which was introduced back in 2002. Although not being the most versatile system for technical documentation purposes, its large dispersal and neat development are good warrants for longevity and support of the platform. MediaWiki features all projects of the Wikimedia foundation, including the largest wiki ever available, the popular encyclopedia Wikipedia [445], currently holding approximately 3 million articles and thus being one of the world's largest web sites. MediaWiki is written in the PHP programming language, and can use either the MySQL (our choice) or PostgreSQL relational database management system. MediaWiki is distributed under the terms of the GNU General Public License [446], making it free and open source software. MediaWiki provides a rich core feature set and its code base contains various "hooks" using callback functions to attach additional code in an extensible way providing additional functionality. This allows developers to write extensions without modifying the core or having to submit their code for review. The CRPPwiki has been augmented by various extensions, some of them will be shortly discussed in the sections hereafter.
Outstanding scalability is achieved through multiple layers of caching and database replication. MediaWiki supports rich content generated through specialised syntax. For example, the software comes with support for rendering mathematical formulas using LaTeX.

G.4 Authorship and access control

On the wiki, the authors are authenticated against the official, centralised EPFL LDAP directory using the wiki LDAP plug-in [447]. The server hosting the wiki [440] is freely browsable from computers connected to the IP network subnets attributed to the CRPP. From outside, the server is protected with the EPFL authentication and access control tool Tequila [448], granting server access for all CRPP members over a SSL protected communication channel. This way of access is frequently employed by the collaborators hosted in the CRPP satellite laboratories at the Paul Scherrer institute (PSI) in Villigen and people who are travelling or working from home. Tequila has the ability of federated authentication and supports single sign-on. This means that the authentication is transparent for all applications protected by Tequila. For example, a user who has logged into the intranet server using Tequila is then automatically authenticated in the wiki software. Contributors to external collaborations who are not employed by CRPP/EPFL are accredited inside the EPFL LDAP tree as guests, who are then granted access to the application using an individual Tequila rule. These people edit the wiki content from their home laboratory or on their portable computer through a wireless connection when they are on visit in CRPP.

To ensure full transparency of authorship, anonymous editing has been prohibited on the CRPPwiki. Imposed restrictions on the structure or information held by the wiki are kept to a strict minimum such to guarantee a democratic wiki space, to maximally stimulate and facilitate contributions and not to regiment the authors. Some pages edited by the administrative department containing legal text (e.g. internal regulations) are however protected against (abusive or unintentional) alteration(†). A selected group of people are granted access to edit their content.

(†) Using the `$wgGroupPermissions` directive in the MediaWiki configuration file `LocalSettings.php`

The administration of the wiki is currently shared among five people which have the bureaucrat permission status. Questions about the organisation of a wiki page or differences of opinion on its content are preferentially sorted out on the discussion tab associated with that page. So far we did not need moderators to clear away insoluble problems not willing to converge towards a consensus.

The team of wiki managers follows the evolution of the content of the wiki (through the *recent changes* special page, which is also available as Atom or RSS feed through the news extension [449]) and helps to clean up fragmented, duplicate or erroneous information.

G.5 Wiki structure

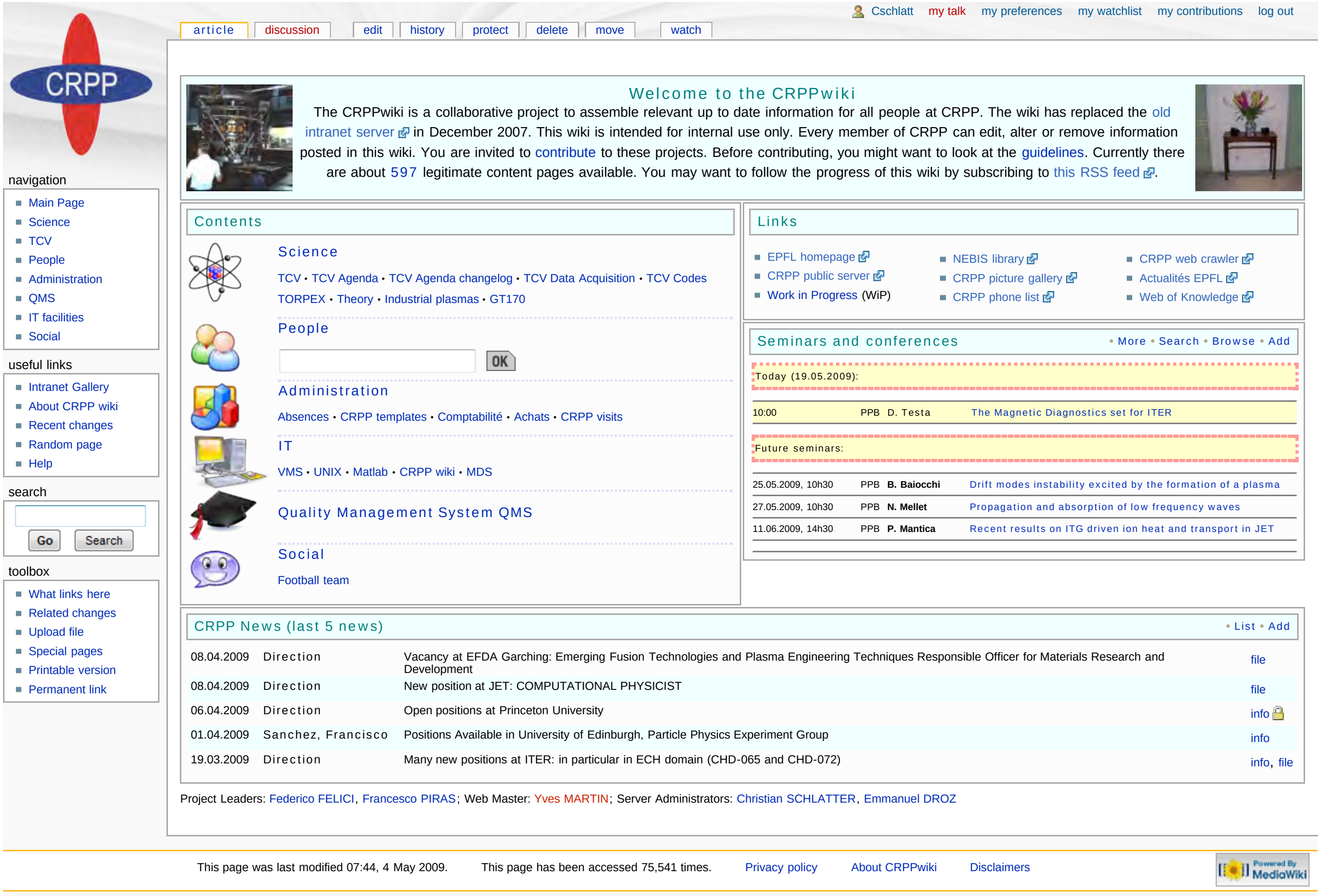

Welcome to the CRPPwiki

The CRPPwiki is a collaborative project to assemble relevant up to date information for all people at CRPP. The wiki has replaced the old intranet server in December 2007. This wiki is intended for internal use only. Every member of CRPP can edit, alter or remove information posted in this wiki. You are invited to contribute to these projects. Before contributing, you might want to look at the guidelines. Currently there are about 597 legitimate content pages available. You may want to follow the progress of this wiki by subscribing to this RSS feed.

Contents

Science

TCV • TCV Agenda • TCV Agenda changelog • TCV Data Acquisition • TCV Codes
TORPEX • Theory • Industrial plasmas • GT170

People

Administration

Absences • CRPP templates • Comptabilité • Achats • CRPP visits

IT

VMS • UNIX • Matlab • CRPP wiki • MDS

Quality Management System QMS

Social

Football team

Links

- EPFL homepage
- CRPP public server
- Work in Progress (WiP)
- NEBIS library
- CRPP picture gallery
- CRPP phone list
- CRPP web crawler
- Actualités EPFL
- Web of Knowledge

Seminars and conferences

Today (19.05.2009):

10:00	PPB	D. Testa	The Magnetic Diagnostics set for ITER

Future seminars:

25.05.2009, 10h30	PPB	**B. Baiocchi**	Drift modes instability excited by the formation of a plasma
27.05.2009, 10h30	PPB	**N. Mellet**	Propagation and absorption of low frequency waves
11.06.2009, 14h30	PPB	**P. Mantica**	Recent results on ITG driven ion heat and transport in JET

CRPP News (last 5 news)

08.04.2009	Direction	Vacancy at EFDA Garching: Emerging Fusion Technologies and Plasma Engineering Techniques Responsible Officer for Materials Research and Development	file
08.04.2009	Direction	New position at JET: COMPUTATIONAL PHYSICIST	file
06.04.2009	Direction	Open positions at Princeton University	info 🔒
01.04.2009	Sanchez, Francisco	Positions Available in University of Edinburgh, Particle Physics Experiment Group	info
19.03.2009	Direction	Many new positions at ITER: in particular in ECH domain (CHD-065 and CHD-072)	info, file

Project Leaders: Federico FELICI, Francesco PIRAS; Web Master: Yves MARTIN; Server Administrators: Christian SCHLATTER, Emmanuel DROZ

This page was last modified 07:44, 4 May 2009. This page has been accessed 75,541 times. Privacy policy About CRPPwiki Disclaimers

Figure G.5.1: The CRPP intranet main page dynamically displays content from different database queries, in particular the scientific seminar schedule. The main entries in the content box on the left link to thematic portals and subportals.

Wikis generally have a flat structure, that is all pages are independent of each other. The information on different pages is therefore essentially interconnected by links.

We have created a certain number of thematic portals for the different fields of activity in the institute. Examples are: Science, with subportals of all experimental facilities at CRPP (TCV, TORPEX, SULTAN, GTS170 etc.), people, IT, administration or special interest (e.g. football team, PhD corner). The main portals are linked to from the wiki home page (see screenshot).

MediaWiki however provides many features beyond hyperlinks for structuring content. One of the earliest features is namespaces. Namespaces can be viewed as folders which separate different basic types of information or functionality. E.g. TCV is an own namespace on CRPPwiki.

In addition to namespaces, content can be ordered using subpages (SubPageList2 extension, [450]). This simple feature provides automatic breadcrumbs from a page of the pattern `[[Page title/Subpage title]]` to the component before the slash. Pages may be attributed to one or more categories (e.g. public relations). A query for content may then be limited to a certain category. A particulary useful extension is the CategoryTree extension [451], which is an AJAX based gadget to display the category structure of a wiki, e.g. all diagnostics probing ion properties on the tokamak (see figure G.5.2).

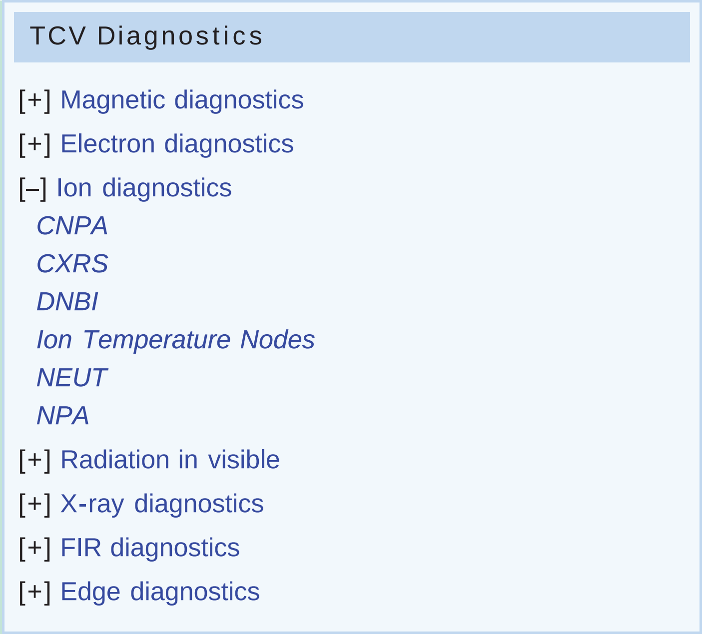

TCV Diagnostics

[+] Magnetic diagnostics
[+] Electron diagnostics
[–] Ion diagnostics
  CNPA
  CXRS
  DNBI
  Ion Temperature Nodes
  NEUT
  NPA
[+] Radiation in visible
[+] X-ray diagnostics
[+] FIR diagnostics
[+] Edge diagnostics

Figure G.5.2: AJAX featured, collapsible category tree. The example shown illustrates the diagnostics categories on the TCV tokamak, the ion diagnostic tree is expanded.

Each wiki author has its personal wiki page created automatically upon his first login. Historically the CRPP collaborators had their personal Apache user pages on the public and intranet web servers (`http://crpplocal.epfl.ch/~username`), which were mostly written in more or less sophisticated HTML. Many scientists have now migrated their web space onto the wiki, where they maintain their to-do lists, work-in-progress tasks and personal log books.

G.6 Content management

The wiki essentially is a CMS and thus the wiki content author should not be concerned with the formatting of the layout of a page (apart its hierarchical structure). MediaWiki can be easily templated. A certain number of models were created for the standardised rendering of special page layouts, e.g. for the portals or for page collections comprising pages edited by different people (like the TCV port window portraits or diagnostic factsheet pages, see section G.8.3), such to facilitate navigation, ensure the visual integrity and help in the creation of pages incorporating a more complex structure. The models of these pages are normally maintained by the wiki administrators.

G.7 CRPPwiki specials

G.7.1 Math typesetting and advanced plotting

The required steps to enable the usage of LaTeX to render mathematical equations on the wiki is straightforward [452]. LaTeX fragments are placed between `<math></math>` tags and are converted to PNG inserts by the `texvc` script included in the MediaWiki distribution. `texvc` makes use of the standard TeX installation of the web server (in our case TeTeX on a Fedora Linux).

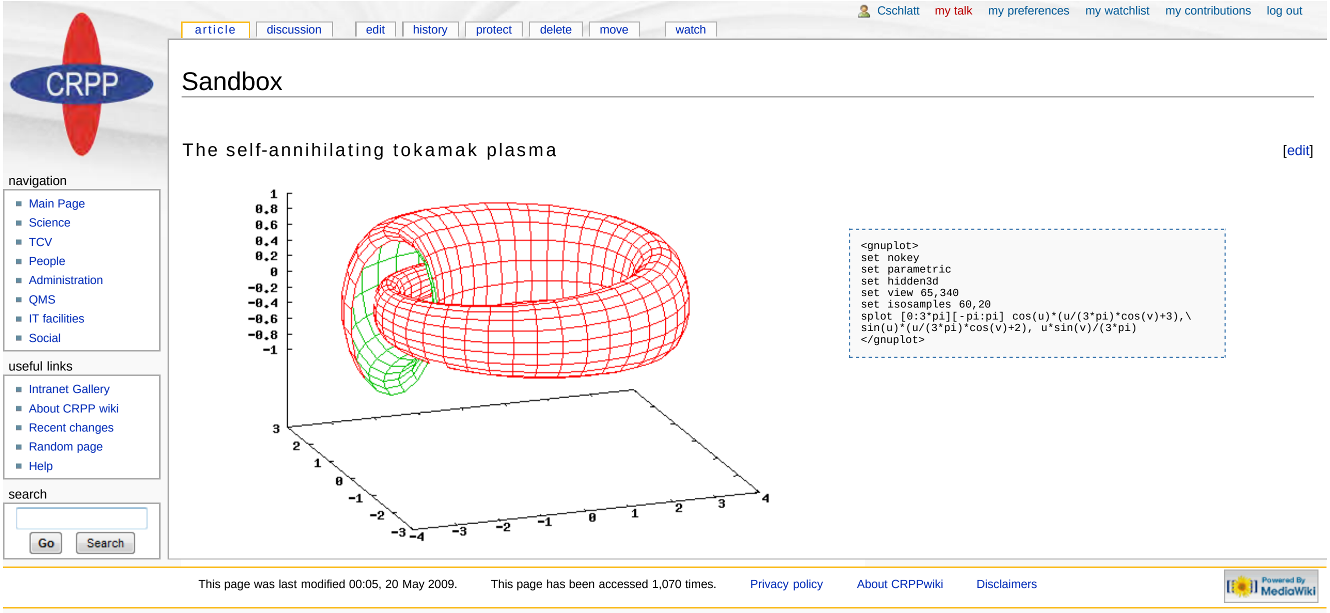

Sandbox

The self-annihilating tokamak plasma

```
<gnuplot>
set nokey
set parametric
set hidden3d
set view 65,340
set isosamples 60,20
splot [0:3*pi][-pi:pi] cos(u)*(u/(3*pi)*cos(v)+3),\
sin(u)*(u/(3*pi)*cos(v)+2), u*sin(v)/(3*pi)
</gnuplot>
```

This page was last modified 00:05, 20 May 2009. This page has been accessed 1,070 times. Privacy policy About CRPPwiki Disclaimers

Figure G.7.1: Inline rendering of Gnuplot figures.

Formidable support for the inline generation of 2D or 3D figures is provided through the Gnuplot extension [453].

G.7.2 Hyperlink consolidation

A bot of the Python wikipedia robot framework [454] crawls the wiki every weekend and reports broken external links on the associated discussion tabs of the concerned pages. It will only report dead links if they have been found off line at least two times. This should prevent users from removing links just because of a temporary server failure. A summary of all found dead links is compiled on a dedicated wiki page. These are then occasionally fixed by the wiki managers. If available, the bot reports include a link to the Internet Archive Wayback Machine [455], so that important references can be kept (should no replacement link be known).

G.7.3 Inline interpretation of HTML and PHP

The wiki may be considerably enhanced by adding HTML and PHP functionality, that is, any HTML or PHP code embedded into a wiki page is interpreted by the web server. Note that doing so on a public wiki would be a foolish idea, as this would make the system vulnerable for the injection of malicious code. In our network the (generally trusted) wiki authors are informed of this potential danger. In the case of maximum disaster (deletion of the wiki database), the wiki content may be almost entirely restored from backups, which are performed three times a day.

HTML support[‡] was initially provided to facilitate and promote the migration of HTML web content into the wiki. In the meantime the wiki authors have learnt the wiki markup language and wiki pages created recently do not make use of HTML anymore.

A small hack of the wiki source code allows PHP code embedded within `<php></php>` tags to be executed. It is sufficient to append the following function at the end of the Setup.php file in the includes subdirectory:

```
function ParsePHPTag($Content)
{
 global $wgOut;
 $wgOut->enableClientCache(false);
 ob_start();
 eval($Content);
 $Result = ob_get_contents();
 ob_end_clean();
 return($Result);
}
$wgParser->setHook('php','ParsePHPTag');
```

Some new PHP web applications developed by CRPP (e.g. a collaborative management of tasks to more efficiently share/organise the work in progress or a scientific pin board to help in the preparation of journal and conference contributions) are directly deployed inside the wiki.

G.7.4 Gallery back end

Superseding the rather basic feature set of the MediaWiki software to manage graphic content, we use an external host for figures, photos, illustrations and videos. These files are thus first uploaded to the CRPP intranet gallery, featured by the open source web based photo album organiser Gallery2 [456], where they are categorised into an album hierarchy. Gallery2 supports all regular features of state of the art picture databases like keywording, slideshows, user commenting, EXIF support and renders/displays a large collection of file formats.
The gallery contains mainly scientific material, serving for publications or internal technical documentation, but is also the place to hold pictures taken at social events in relation with CRPP. The collection of files is currently growing towards a respectable scientific figure archive.

We use the Gallery2wiki hack [457] to make Gallery2 a back end for MediaWiki, providing an easy-to-use interface to select an item from the gallery and insert it into the wiki page. Gallery2 calculates a number of smaller resolutions (down to thumbnail size) than the dimension of the file uploaded and all these are readily available on the wiki. The dimension of the item to be displayed by default is selected upon insertion into the wiki page, the visitor of a page may then change the picture size inline by clicking on the target resolution displayed in the upper right hand corner of the picture (see screenshot G.7.3).

This solution has the advantage of storing all graphic material in one single place and to display the same object at various locations.

[‡] `$wgRawHtml = true;` in `Localsetting.php`.

Figure G.7.2: Picture from the Gallery2 shown on the wiki. The resizer panel on the top left lets the visitor choose various precalculated picture resolutions (from thumbnail to original size) to change the displayed picture dimensions inside the wiki page.

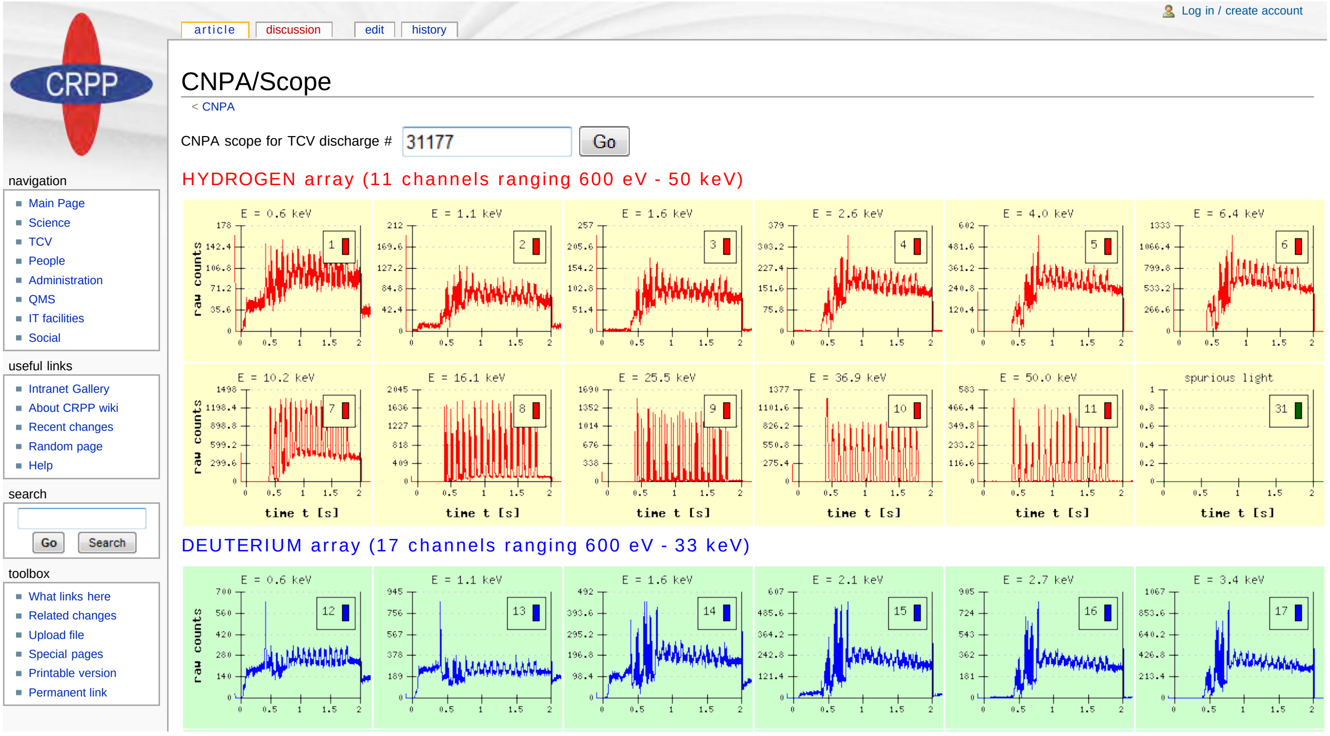

CNPA/Scope

< CNPA

CNPA scope for TCV discharge # 31177 Go

HYDROGEN array (11 channels ranging 600 eV - 50 keV)

DEUTERIUM array (17 channels ranging 600 eV - 33 keV)

Figure G.7.3: Web scope showing time traces of the neutral particle flux escaping the plasma, measured with the compact neutral particle analyser (CNPA). The PNG bitmaps are produced on-the-fly and embedded into the wiki page.

G.7.5 Web scope

The experimental data measured with the large collection of diagnostics available on TCV are acquired and stored into a single, self-descriptive, hierarchical structure MDSplus database [458] traditionally employed in nuclear fusion facilities. The web server is able to retrieve data from this database using a API written in PHP. A set of specialised functions were developed to process data, explore the database tree (traverser) and plot time traces inline on the wiki. The traces are produced on-the-fly using the PHPlot graph library [459]. This interface was conceived for the purpose of illustrating the documentation (there are better tools for the scientific data analysis).

Figure G.7.3 shows the traces of some energy channels of the compact neutral particle analyser (CNPA), a spectrometer recording the flux of neutral particle escaping from the plasma commonly used to calculate the plasma core ion temperature from the slope of the neutral flux spectrum [47].

G.7.6 AJAX connectivity

Most PHP distributions come now with out-of-the-box support for Asynchronous JavaScript and XML (AJAX), considerably enhancing connectivity between the wiki and MySQL databases using Web 2.0 technology(§). For example, we use AJAX featured wiki pages to browse through (or for the rendering of different views of) the TCV agenda (figure G.7.4), which is the directory of the daily allocation of the scientific program simultaneously used for the planning of the tokamak operator personnel. Other examples are the interfaces to query the internal news and job offer database or our internal seminar archive holding presentation abstracts and files.

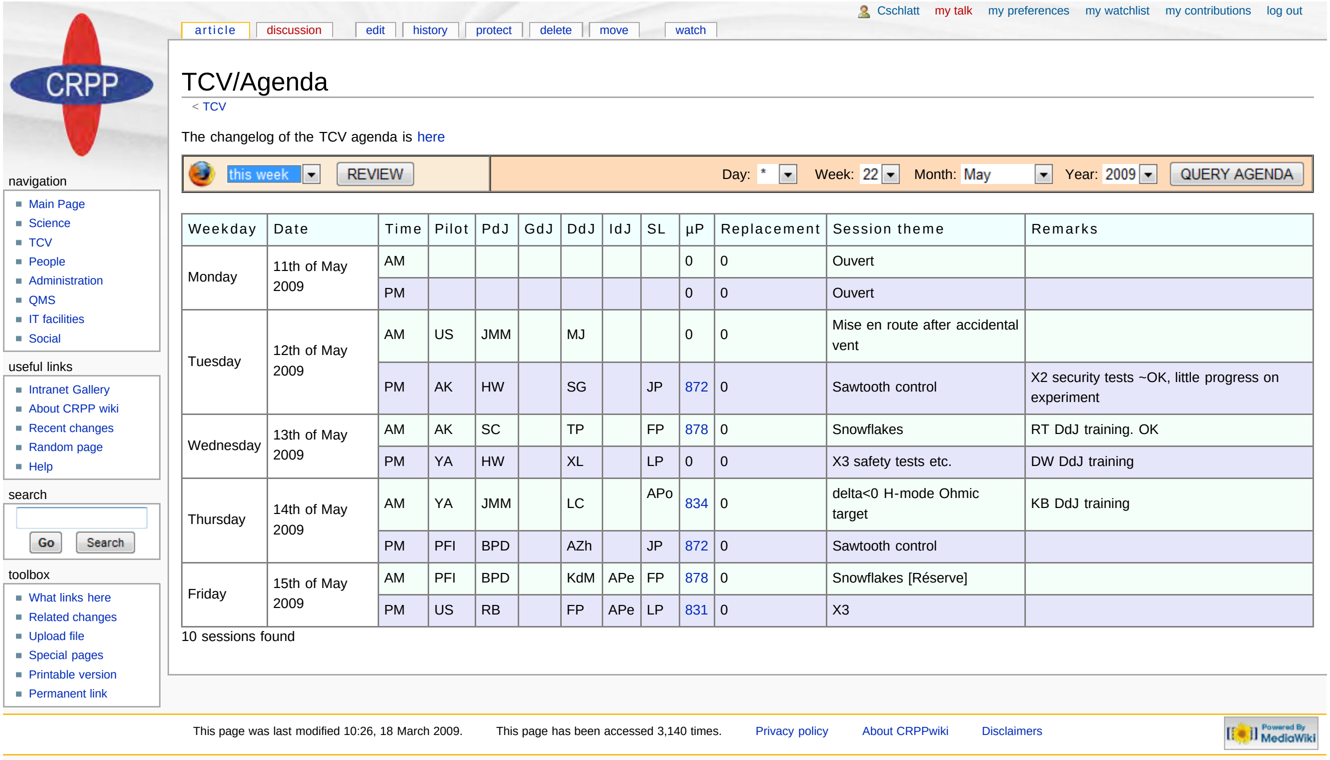

TCV/Agenda

< TCV

The changelog of the TCV agenda is here

Day: * Week: 22 Month: May Year: 2009

Weekday	Date	Time	Pilot	PdJ	GdJ	DdJ	IdJ	SL	μP	Replacement	Session theme	Remarks
Monday	11th of May 2009	AM							0	0	Ouvert	
		PM							0	0	Ouvert	
Tuesday	12th of May 2009	AM	US	JMM		MJ			0	0	Mise en route after accidental vent	
		PM	AK	HW		SG		JP	872	0	Sawtooth control	X2 security tests ~OK, little progress on experiment
Wednesday	13th of May 2009	AM	AK	SC		TP		FP	878	0	Snowflakes	RT DdJ training. OK
		PM	YA	HW		XL		LP	0	0	X3 safety tests etc.	DW DdJ training
Thursday	14th of May 2009	AM	YA	JMM		LC		APo	834	0	delta<0 H-mode Ohmic target	KB DdJ training
		PM	PFI	BPD		AZh		JP	872	0	Sawtooth control	
Friday	15th of May 2009	AM	PFI	BPD		KdM	APe	FP	878	0	Snowflakes [Réserve]	
		PM	US	RB		FP	APe	LP	831	0	X3	

10 sessions found

This page was last modified 10:26, 18 March 2009. This page has been accessed 3,140 times. Privacy policy About CRPPwiki Disclaimers

Figure G.7.4: AJAX featured TCV agenda displaying the weakly scientific programme and used as roaster for the people involved in the operation of the machine.

(§) Such that only parts of the web page have to be reloaded in the browser of the visitor. AJAX functionality is enabled on the wiki through `$wgUseAjax = true;` in `LocalSettings.php`.

G.8 Usage and experience examples

G.8.1 Scientific program preparation and experimental session documentation

One condition for approval of a scientific experiment to be conducted on TCV – in the following referred to as a mission – is the creation and maintenance of a wiki mission page. Templates were made available to assist in giving these pages a good start. They must contain exhaustive information about the experiment (which risks to be dropped from the scientific program if documentation is considered insufficient) and are supposed to reflect the current state of progress (experiments generally include multiple sessions spread over several weeks or month). Such pages thus continuously evolve, from the first idea of the experiment, during its thorough preparation and planning, providing valuable information for the colleagues and the members of the team piloting the tokamak. During the experiment, the session leader collects the information about operation, technical problems and so on, which is then fed into the page little by little when first results become available. Different people in the tokamak control room may contribute information (the wiki can handle multiple edits of a page by different people). After the experiments, updates on the progress and outcomes of the data analysis are reported and a table for a selection of the "best plasma shots" may be constructed by insertion of a realtime query of the official TCV logbook [460]. Once the mission is completed the scientist reports the obtained results and conclusions and posts links to the relevant scientific publications.

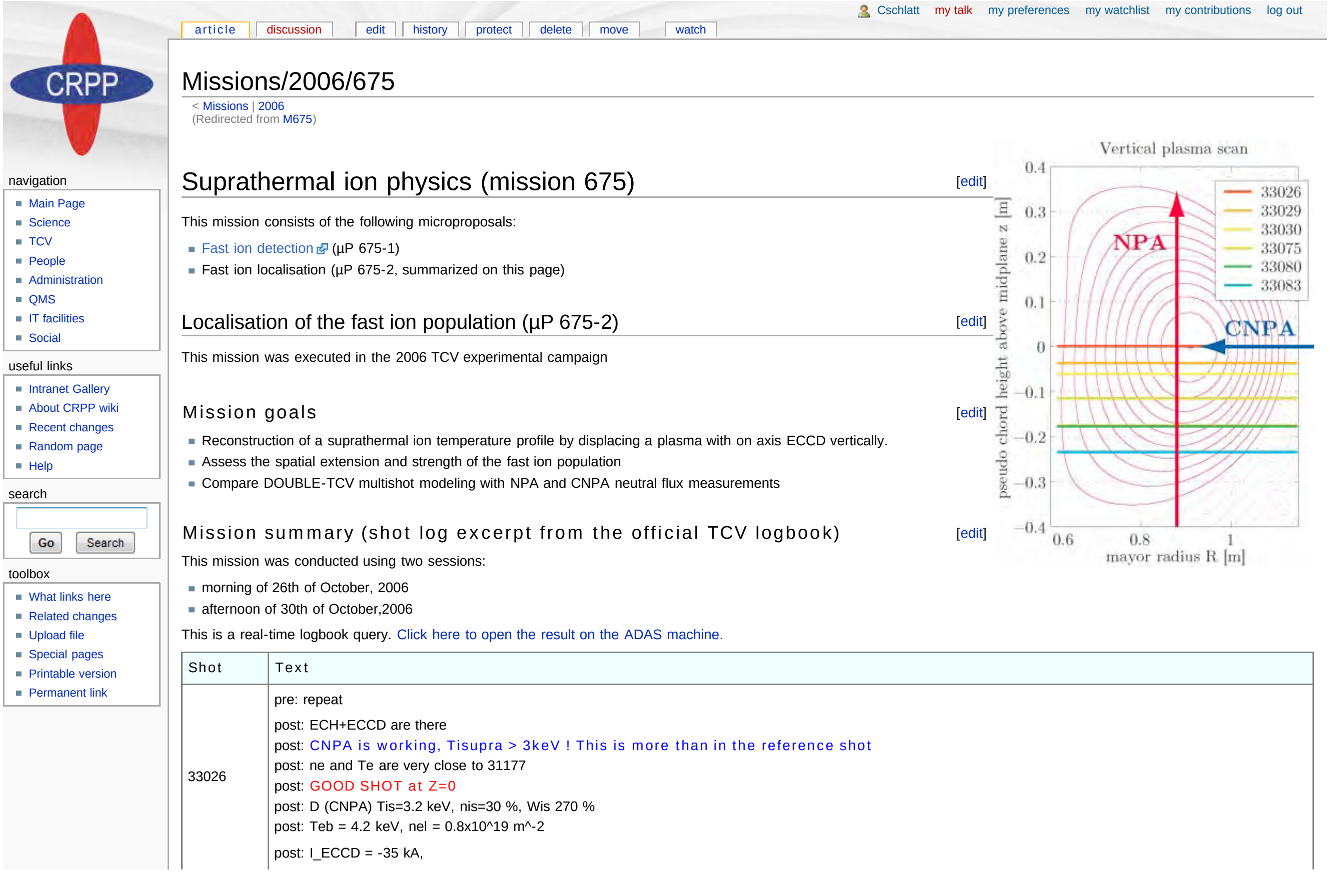

Missions/2006/675

< Missions | 2006
(Redirected from M675)

Suprathermal ion physics (mission 675)

This mission consists of the following microproposals:

- Fast ion detection (µP 675-1)
- Fast ion localisation (µP 675-2, summarized on this page)

Localisation of the fast ion population (µP 675-2)

This mission was executed in the 2006 TCV experimental campaign

Mission goals

- Reconstruction of a suprathermal ion temperature profile by displacing a plasma with on axis ECCD vertically.
- Assess the spatial extension and strength of the fast ion population
- Compare DOUBLE-TCV multishot modeling with NPA and CNPA neutral flux measurements

Mission summary (shot log excerpt from the official TCV logbook)

This mission was conducted using two sessions:

- morning of 26th of October, 2006
- afternoon of 30th of October,2006

This is a real-time logbook query. Click here to open the result on the ADAS machine.

Shot	Text
33026	pre: repeat post: ECH+ECCD are there post: CNPA is working, Tisupra > 3keV ! This is more than in the reference shot post: ne and Te are very close to 31177 post: GOOD SHOT at Z=0 post: D (CNPA) Tis=3.2 keV, nis=30 %, Wis 270 % post: Teb = 4.2 keV, nel = 0.8x10^19 m^-2 post: I_ECCD = -35 kA,

Figure G.8.1: Mission page describing the design, planning, reports and results of an experiment on the TCV tokamak (only the first part of the page is shown). The table is constructed from a customised query of the official experiment logbook.

G.8.2 Turntable for conference organisers

The wiki very successfully propelled the intranet of the local organising committee (LOC) [461], composed of a team of 20 scientists from CRPP, of the IAEA fusion energy conference (FEC), held in Geneva in October 2008 [462]. The wiki was used to manage the tasks and responsibilities of the LOC members, providing an internal information platform, served for the collaborative editing of text and to host the documents.

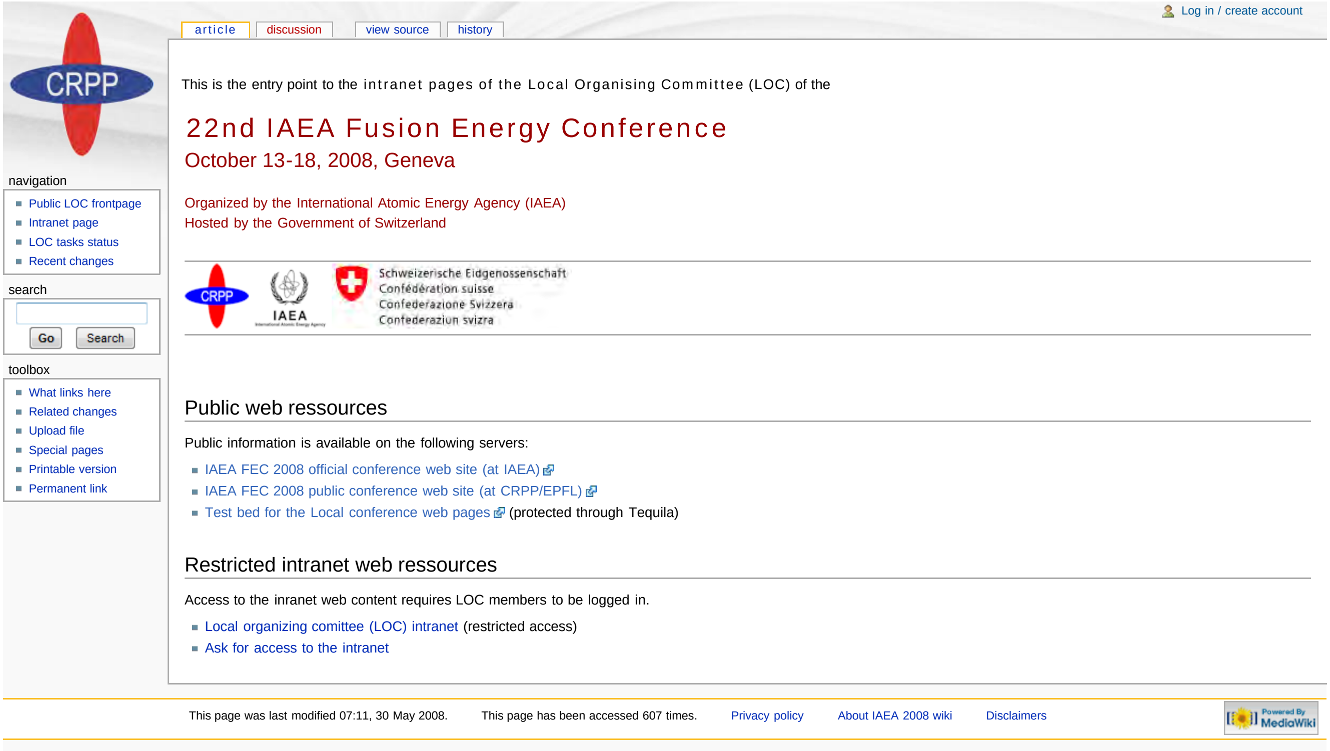

This is the entry point to the intranet pages of the Local Organising Committee (LOC) of the

22nd IAEA Fusion Energy Conference

October 13-18, 2008, Geneva

Organized by the International Atomic Energy Agency (IAEA)
Hosted by the Government of Switzerland

Public web ressources

Public information is available on the following servers:

- IAEA FEC 2008 official conference web site (at IAEA)
- IAEA FEC 2008 public conference web site (at CRPP/EPFL)
- Test bed for the Local conference web pages (protected through Tequila)

Restricted intranet web ressources

Access to the inranet web content requires LOC members to be logged in.

- Local organizing comittee (LOC) intranet (restricted access)
- Ask for access to the intranet

This page was last modified 07:11, 30 May 2008. This page has been accessed 607 times. Privacy policy About IAEA 2008 wiki Disclaimers

Figure G.8.2: Entry point to the wiki of the local organising committee of the IAEA fusion energy conference. Read access to all other pages of this wiki requires a valid user account.

G.8.3 TCV diagnostic manual

The construction of a comprehensive manual of the diagnostics on TCV was one of the first projects launched on the wiki. In its current form, each diagnostic is documented with

- a mandatory factsheet page. This page provides a short description of the diagnostic, its operational status, lists the measured parameters, the physical location on the tokamak, the responsible officer and his deputy and describes the nodes in the MDSplus database holding the relevant data and the tools for data retrieval, data visualisation (scopes) and advanced data analysis codes (mostly written in MATLAB). The header of the CNPA factsheet page is shown in figure G.8.3.

A set of optional, more or less templated subpages, may then be filled additionally. These pages specifically address

- the physics principles at the base of the diagnosis (educational aspects),
- the detailed description of the subsystems of the diagnostic (complete hardware documentation of the electrical system, electronics, mechanics, vacuum systems, acquisition and control modules and software),

- ☞ the configuration of the diagnostic (operational aspects like how to switch it on, change a parameter, solve standard problems),
- ☞ a chronological hardware logbook documenting the history of the implementation, maintenance and upgrades of the diagnostic on TCV and
- ☞ a web scope of some key signal traces (see section G.7.5).

Part of this diagnostic information is stored in a separate MySQL database, whose content is entirely filled and updated through the wiki. This data may then appear on several of the aforementioned pages and serves to compile up-to-date reports (e.g. the list of currently operational diagnostics). TCV counts currently more than 35 distinct diagnostics whose documentation has now approached a satisfactory level. Note that such diagnostic pages are also created for new diagnostics which are not yet available for exploitation (or whose construction is maybe not even agreed). This also serves for the purpose to address all aspects of project management (feasibility study, cost analysis, CRPP services resource and responsibility planning etc.) and ensures an excellent scope of documentation right from the first day of availability of the diagnostic on the tokamak torus.

G.8.4 Redaction of abstracts and paper preprints involving multiple authors

Scientific publications involving multiple authors generally undergo multiple modifications suggested by several co-authors. Writing such a text on the wiki considerably simplifies and accelerates its production, as the corrections are directly made on the text without the need to send them first to the main author. This document was developed in this way.

G.9 Conclusions

The wiki is well on the way to become the brain holding all relevant information about our institute and, as no content is never really deleted, is in the same time the archive of our accomplished work. The evolution of the ongoing projects is readily available through the page history feature, such that all past revisions of a wiki page may be retrieved at any time. The wiki is even compatible with the requirements of quality management, the MediaWiki permanent link feature may be used to snapshot the status of a project at a given time.

The wiki was received with enthusiasm at CRPP and had an spectacular start. Some units of CRPP, e.g. the departments providing services (electronics lab, IT support) had (and some still have) some reservations concerning the unlimited collaborative aspect of the wiki approach, fearing the loss of control over the substantiality of their contributions to the documentation and project reports. Since then many of the prejudice and doubts have evaporated and most of the collaborators jumped on to the club of privileged wiki agitators. The wiki currently holds more than 2000 pages created by a crowd of more than 100 authors. In 20 month of existence the wiki has proven its suitability for everyday documentation purposes and especially for the activities involving the TCV tokamak, we already crossed the point from where it is hard to imagine life without it...

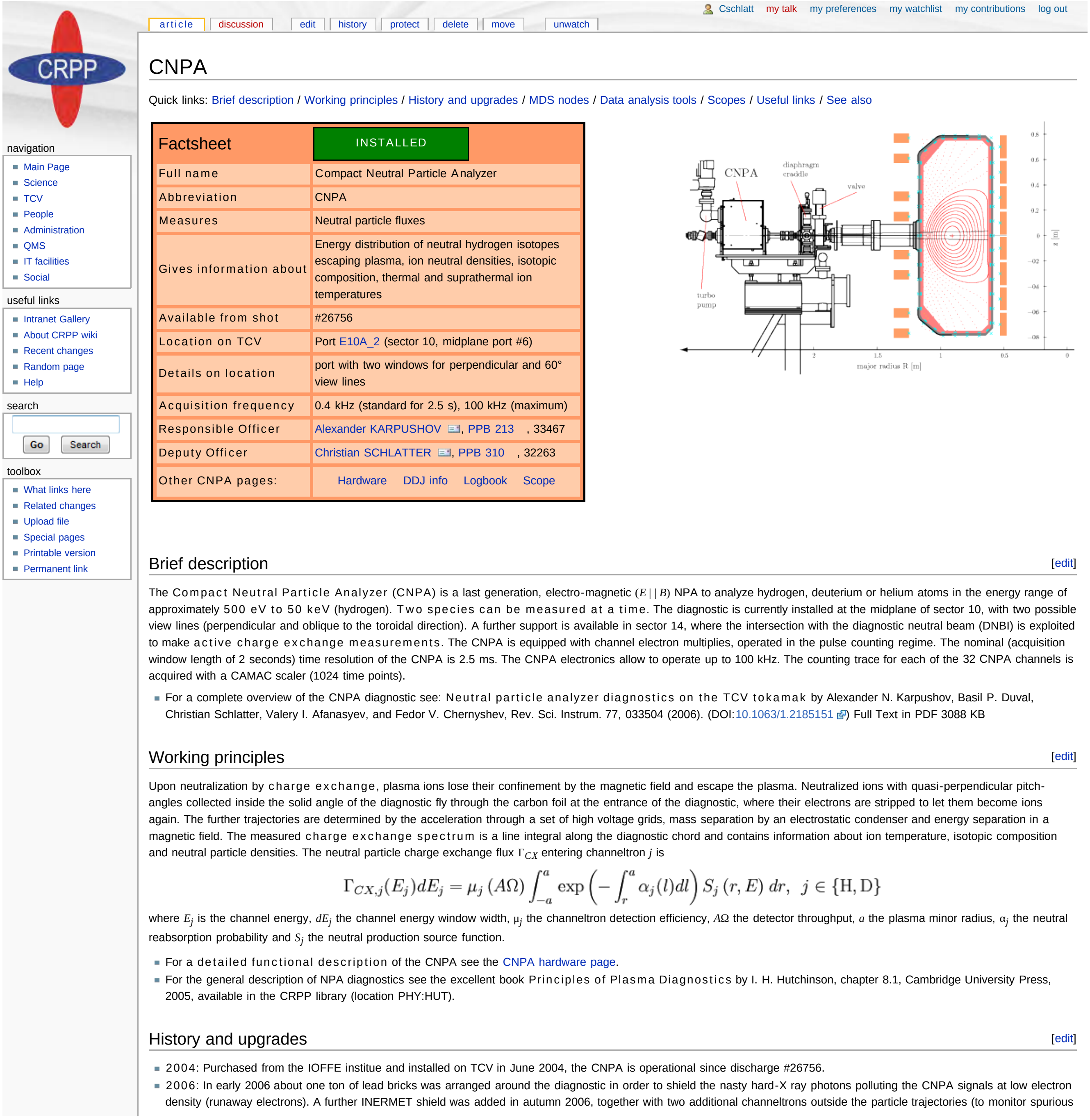

CNPA

Quick links: Brief description / Working principles / History and upgrades / MDS nodes / Data analysis tools / Scopes / Useful links / See also

Factsheet	INSTALLED
Full name	Compact Neutral Particle Analyzer
Abbreviation	CNPA
Measures	Neutral particle fluxes
Gives information about	Energy distribution of neutral hydrogen isotopes escaping plasma, ion neutral densities, isotopic composition, thermal and suprathermal ion temperatures
Available from shot	#26756
Location on TCV	Port E10A_2 (sector 10, midplane port #6)
Details on location	port with two windows for perpendicular and 60° view lines
Acquisition frequency	0.4 kHz (standard for 2.5 s), 100 kHz (maximum)
Responsible Officer	Alexander KARPUSHOV, PPB 213 , 33467
Deputy Officer	Christian SCHLATTER, PPB 310 , 32263
Other CNPA pages:	Hardware DDJ info Logbook Scope

Brief description [edit]

The Compact Neutral Particle Analyzer (CNPA) is a last generation, electro-magnetic ($E \,||\, B$) NPA to analyze hydrogen, deuterium or helium atoms in the energy range of approximately 500 eV to 50 keV (hydrogen). Two species can be measured at a time. The diagnostic is currently installed at the midplane of sector 10, with two possible view lines (perpendicular and oblique to the toroidal direction). A further support is available in sector 14, where the intersection with the diagnostic neutral beam (DNBI) is exploited to make active charge exchange measurements. The CNPA is equipped with channel electron multiplies, operated in the pulse counting regime. The nominal (acquisition window length of 2 seconds) time resolution of the CNPA is 2.5 ms. The CNPA electronics allow to operate up to 100 kHz. The counting trace for each of the 32 CNPA channels is acquired with a CAMAC scaler (1024 time points).

- For a complete overview of the CNPA diagnostic see: Neutral particle analyzer diagnostics on the TCV tokamak by Alexander N. Karpushov, Basil P. Duval, Christian Schlatter, Valery I. Afanasyev, and Fedor V. Chernyshev, Rev. Sci. Instrum. 77, 033504 (2006). (DOI:10.1063/1.2185151) Full Text in PDF 3088 KB

Working principles [edit]

Upon neutralization by charge exchange, plasma ions lose their confinement by the magnetic field and escape the plasma. Neutralized ions with quasi-perpendicular pitch-angles collected inside the solid angle of the diagnostic fly through the carbon foil at the entrance of the diagnostic, where their electrons are stripped to let them become ions again. The further trajectories are determined by the acceleration through a set of high voltage grids, mass separation by an electrostatic condenser and energy separation in a magnetic field. The measured charge exchange spectrum is a line integral along the diagnostic chord and contains information about ion temperature, isotopic composition and neutral particle densities. The neutral particle charge exchange flux Γ_{CX} entering channeltron j is

$$\Gamma_{CX,j}(E_j)dE_j = \mu_j\,(A\Omega)\int_{-a}^{a}\exp\left(-\int_r^a \alpha_j(l)dl\right) S_j\,(r,E)\,dr,\quad j\in\{\mathrm{H},\mathrm{D}\}$$

where E_j is the channel energy, dE_j the channel energy window width, μ_j the channeltron detection efficiency, $A\Omega$ the detector throughput, a the plasma minor radius, α_j the neutral reabsorption probability and S_j the neutral production source function.

- For a detailed functional description of the CNPA see the CNPA hardware page.
- For the general description of NPA diagnostics see the excellent book Principles of Plasma Diagnostics by I. H. Hutchinson, chapter 8.1, Cambridge University Press, 2005, available in the CRPP library (location PHY:HUT).

History and upgrades [edit]

- 2004: Purchased from the IOFFE institue and installed on TCV in June 2004, the CNPA is operational since discharge #26756.
- 2006: In early 2006 about one ton of lead bricks was arranged around the diagnostic in order to shield the nasty hard-X ray photons polluting the CNPA signals at low electron density (runaway electrons). A further INERMET shield was added in autumn 2006, together with two additional channeltrons outside the particle trajectories (to monitor spurious

Figure G.8.3: Diagnostic factsheet for the Compact Neutral Particle Analyser (CNPA) installed on the TCV tokamak. The data shown in the factsheet table is extracted from a database.

Bibliography

[1] **"World Consumption of Primary Energy by Energy Type and Selected Country Groups**," Energy Information Administration, U.S. Department of Energy, Tech. Rep., July 31, 2006.

[2] **"Crude oil - The supply outlook**," Report to the Energy Watch Group, Tech. Rep., October 2007.

[3] J. Schindler and W. Zittel, **"Zukunft der weltweiten Erdölversorgung**," Ludwig-Bölkow-Systemtechnik GmbH, Ottobrunn, Deutschland, Tech. Rep., May 2008.

[4] **"Key world energy statistics**," International energy agency (IEA), Paris, Tech. Rep., 2007.

[5] C. of the European Communities, **"Renewable Energy Roadmap: Renewable Energies in the 21st century; building a sustainable future**," Commission of the European Communities, Communication from the Commission to the European Parliament and the Council 848, January 2007.

[6] **"Uranium resources and nuclear energy**," Energy Watch Group, Tech. Rep., December 2006, background paper prepared by the Energy Watch Group.

[7] K. Tuček, J. Carlsson, and H. Wider, **"Comparison of sodium and lead-cooled fast reactors regarding reactor physics aspects, severe safety and economical issues**," *Nuclear Engineering and Design*, vol. 236, no. 14–16, pp. 1589–1598, August 2006, proceedings of the 13th International Conference on Nuclear Energy and the 13th International Conference on Nuclear Energy, Beijing, China, May 16–20, 2005.

[8] M. G. Haines, **"Fifty years of controlled fusion research**," *Plasma Physics and Controlled Fusion*, vol. 38, no. 5, pp. 643–656, May 1996, historical perspective review paper.

[9] C. Seife, ***Sun in a Bottle: The Strange History of Fusion and the Science of Wishful Thinking***, N. Y. Penguin Group, Ed. Viking Adult, October 2008.

[10] International Atomic Energy Agency (IAEA), **"Fifty years of Magnetic Confinement Fusion Research – A Retrospective**," printed, Vienna, Austria, September 2008, booklet published on the occasion of the 22nd IAEA Fusion Energy Conference (FEC) held in Geneva, October 13–18, 2008, celebrating fifty years of nuclear fusion research.

[11] G. Brumfiel, **"Fusion dreams delayed**," *Nature*, vol. 459, pp. 488–489, May 2009.

[12] **"Energy, Electricity and Nuclear Power Estimates for the Period up to 2030**," International Atomic Energy Agency (IAEA), Vienna, Austria, Tech. Rep., July 2006, Reference Data Series No. 1.

[13] M. P. Fewell, **"The atomic nuclide with the highest mean binding energy,"** *American Journal of Physics*, vol. 63, no. 7, pp. 653–658, July 1995.

[14] M. Chadwick, P. Oblovzinský, M. Herman, N. Greene, R. McKnight, D. Smith, P. Young, R. MacFarlane, G. Hale, S. Frankle, A. Kahler, T. Kawano, R. Little, D. Madland, P. Moller, R. Mosteller, P. Page, P. Talou, H. Trellue, M. White, W. Wilson, R. Arcilla, C. Dunford, S. Mughabghab, B. Pritychenko, D. Rochman, A. Sonzogni, C. Lubitz, T. Trumbull, J. Weinman, D. Brown, D. Cullen, D. Heinrichs, D. McNabb, H. Derrien, M. Dunn, N. Larson, L. Leal, A. Carlson, R. Block, J. Briggs, E. Cheng, H. Huria, M. Zerkle, K. Kozier, A. Courcelle, V. Pronyaev, and S. van der Marck, **"ENDF/B-VII.0: Next Generation Evaluated Nuclear Data Library for Nuclear Science and Technology,"** *Nuclear Data Sheets*, vol. 107, no. 12, pp. 2931–3118, December 2006. URL: http://www.sciencedirect.com/science/journal/00903752

[15] A. Einstein, **"Ist die Trägheit eines Körpers von seinem Energieinhalt abhängig?"** *Annalen der Physik*, vol. 323, no. 13, pp. 639–641, November 1905, Vierte Folge, Band 18, Dreizehntes Heft.

[16] B. H. Duane, **"Fusion Cross Section Theory,"** Brookhaven National Laboratory, Tech. Rep. BNWL-1685, 1972.

[17] M. I. K. Santala, M. J. Mantsinen, L. Bertalot, S. Conroy, V. Kiptily, S. Popovichev, A. Salmi, D. Testa, Y. Baranov, P. Beaumont, P. Belo, J. Brzozowski, M. Cecconello, M. deBaar, P. deVries, C. Gowers, J.-M. Noterdaeme, C. Schlatter, and S. E. Sharapov, **"Proton-triton nuclear reaction in ICRF heated plasmas in JET,"** *Plasma Physics and Controlled Fusion*, vol. 48, no. 8, pp. 1233–1253, August 2006.

[18] J. Wesson, ***Tokamaks***. Oxford: Clarendon Press, 2004.

[19] J. D. Lawson, **"Some Criteria for a Power Producing Thermonuclear Reactor,"** *Proceedings of the Physical Society of London. Section B, Mathematical and Physical Sciences*, vol. 70, no. 1, pp. 6–10, January 1957.

[20] G. E. Moore, **"Cramming more components onto integrated circuits,"** *Electronics*, vol. 38, no. 8, pp. 114–117, April 1965.

[21] J. P. Freidberg, ***Plasma Physics and Fusion Energy***. Cambridge University Press, February 2007.

[22] F. F. Chen, ***Introduction to plasma physics and controlled fusion*, 2nd ed.** New York: Springer Verlag, 2006, vol. 1: Plasma and Physics.

[23] URL: http://www.tokamak.info

[24] L. Spitzer, Jr. and R. Härm, **"Transport Phenomena in a Completely Ionized Gas,"** *Physical Review*, vol. 89, no. 5, pp. 977–981, March 1953.

[25] J. Huba, ***NRL Plasma Formulary***. Washington, DC 20375: Naval Research Laboratory, 2007. URL: http://wwwppd.nrl.navy.mil/nrlformulary/

[26] J. Adam, **"Review of Tokamak plasma heating by wave damping in the ion cyclotron range of frequency,"** *Plasma Physics and Controlled Fusion*, vol. 29, no. 4, pp. 443–472, April 1987.

[27] V. Erckmann and U. Gasparino, **“Electron cyclotron heating and current drive in toroidal fusion plasmas**,” *Plasma Physics and Controlled Fusion*, vol. 36, no. 12, pp. 1869–1962, December 1994, review article.

[28] R. Koch, **“The Ion Cyclotron, Lower Hybrid and Alfvén Wave Heating Methods**,” *Fusion Science and Technology*, vol. 53, no. 2T, pp. 194–201, February 2008.

[29] A. Mück, L. Curchod, Y. Camenen, S. Coda, T. P. Goodman, H. P. Laqua, A. Pochelon, L. Porte, and F. Volpe, **“Demonstration of Electron-Bernstein-Wave Heating in a Tokamak via O-X-B Double-Mode Conversion**,” *Physical Review Letters*, vol. 98, no. 17, p. 175004 (4pp), April 2007.

[30] F. Hofmann, J. B. Lister, W. Anton, S. Barry, R. Behn, S. Bernel, G. Besson, F. Buhlmann, R. Chavan, M. Corboz, M. J. Dutch, B. P. Duval, D. Fasel, A. Favre, S. Franke, A. Heym, A. Hirt, C. Hollenstein, P. Isoz, B. Joye, X. Llobet, J.-C. Magnin, B. Marlétaz, P. Marmillod, Y. Martin, J.-M. Mayor, J.-M. Moret, C. Nieswand, P.-J. Paris, A. Perez, Z. A. Pietrzyk, R. A. Pitts, A. Pochelon, R. Rage, O. Sauter, G. Tonetti, M. Q. Tran, F. Troyon, D. J. Ward, and H. Weisen, **“Creation and control of variably shaped plasmas in TCV**,” *Plasma Physics and Controlled Fusion*, vol. 36, no. 12B, pp. B277–B287, December 1994.

[31] F. Piras, S. Coda, I. Furno, J.-M. Moret, R. A. Pitts, O. Sauter, B. Tal, G. Turri, A. Bencze, B. P. Duval, F. Felici, A. Pochelon, and C. Zucca, **“Snowflake divertor plasmas on TCV**,” *Plasma Physics and Controlled Fusion*, vol. 51, no. 5, p. 055009 (8pp), May 2009.

[32] F. Troyon, R. Gruber, H. Saurenmann, S. Semenzato, and S. Succi, **“MHD-Limits to Plasma Confinement**,” *Plasma Physics and Controlled Fusion*, vol. 26, no. 1A, pp. 209–216, January 1984.

[33] M. Greenwald, J. L. Terry, S. M. Wolfe, S. Ejima, M. G. Bell, S. M. Kaye, and G. H. Neilson, **“A new look at density limits in tokamaks**,” *Nuclear Fusion*, vol. 28, no. 12, pp. 2199–2207, December 1988.

[34] H. Weisen, J.-M. Moret, S. Franke, I. Furno, Y. Martin, M. Anton, R. Behn, M. J. Dutch, B. P. Duval, F. Hofmann, B. Joye, C. Nieswand, Z. A. Pietrzyk, and W. V. Toledo, **“Effect of plasma shape on confinement and MHD behaviour in the TCV tokamak**,” *Nuclear Fusion*, vol. 37, no. 12, pp. 1741–1758, December 1997.

[35] R. Behn, S. Franke, and Z. A. Pietrzyk, **“The Thomson Scattering diagnostic on the TCV tokamak**,” in *Proceedings of the 21th EPS conference on Controlled Fusion and Plasma Physics*, Montpellier, France, 1994.

[36] R. Behn, S. Franke, Z. A. Pietrzyk, M. Anton, C. Nieswand, H. Weisen, and B. Marlétaz, **“The Thomson Scattering diagnostic on the TCV tokamak**,” in *Proceedings of the 7th International Symposium on Laser-Aided Plasma Diagnostics (LAPD-7), December 5–8, 1995*, M. Muruoka, Ed., Fukuoka, Japan, 1995, pp. 392–397.

[37] S. Franke, **“Application of Thomson scattering at 1.06 μm as a diagnostic for spatial profile measurements of electron temperature and density on the TCV tokamak**,” PhD thesis, Ecole polytechnique fédérale de Lausanne (EPFL), CH-1015 Lausanne, Switzerland, 1997, no. 1654, also available as Lausanne Report LRP 756/97.

[38] R. Behn, J. H. Rommers, R. A. Pitts, Z. A. Pietrzyk, R. Chavan, and B. Marlétaz, **"A Thomson scattering diagnostic for measurements in the divertor region of TCV**," *Review of Scientific Instruments*, vol. 70, no. 1, pp. 768–771, January 1999.

[39] S. Barry, C. Nieswand, and S. L. Prunty, **"Far-infrared polarimetry on the TCV tokamak**," in *Proceedings of the* 8^{th} *International Symposium on Laser-aided Plasma Diagnostics (LAPD-8), September 22–26, 1997*, Doorwerth, The Netherlands, 1997, pp. 313–318.

[40] S. Barry, **"The extension of the FIR interferometer of TCV to a polarimeter and measurements of the Faraday rotation caused by the poloidal magnetic field**," PhD thesis, National University of Ireland, Cork, Ireland, 1999, also available as Lausanne Report LRP 638/99.

[41] L. Zehnder, **"Ein neuer Interferenzrefraktor**," *Zeitschrift für Instrumentenkunde*, vol. 11, pp. 275–285, 1891.

[42] L. Mach, **"Über einen Interferenzrefraktor**," *Zeitschrift für Instrumentenkunde*, vol. 12, pp. 89–93, 1892.

[43] T. D. de Wit, A.-L. Pecquet, J.-C. Vallet, and R. Lima, **"The biorthogonal decomposition as a tool for investigating fluctuations in plasmas**," *Physics of Plasmas*, vol. 1, no. 10, pp. 3288–3300, October 1994.

[44] I. Furno, H. Weisen, C. Carey, C. Angioni, R. Behn, E. Fable, and A. Zabolotsky, **"A new method for the inversion of interferometry data using basis functions derived from singular value decomposition of local measurements in tokamak plasmas**," *Plasma Physics and Controlled Fusion*, vol. 47, no. 1, pp. 49–69, January 2005.

[45] G. Bekefi, **"Radiation processes in plasmas**," ser. Wiley series in plasma physics. John Wiley and Sons, New York-London-Sidney, 1966.

[46] H. Weisen, **"Measurement and modelling of light impurity behaviour in TCV**," in *Proceedings of the* 23^{rd} *EPS Conference on Controlled Fusion and Plasma Physics, Kiev, Ukraine*, 1996.

[47] I. H. Hutchinson, ***Principles of plasma diagnostics*, 2nd ed.** Cambridge, United Kingdom: Cambridge University Press, 2002.

[48] E. R. Pike and S. Sarkar, ***The quantum theory of radiation***, ser. International series of monographs on physics. Oxford Clarendon Press, 1995, vol. 86.

[49] S. von Goeler, **"Diagnostics for fusion experiments**," in *Proceedings of the International School of Plasma Physics, September 4–16, 1978*, ser. Course on Diagnostics for Fusion Experiments, E. Sindoni and C. Wharton, Eds., International School of Plasma Physics and Association CNR-Euratom. Pergamon Press, Oxford, United Kingdom, 1979.

[50] A. V. Sushkov and D. E. Kravtsov, **"Modernisation of the T-10 tokamak X-ray imaging diagnostic**," in *Proceedings of the* 30^{th} *EPS Conference on Controlled Fusion and Plasma Physics, St. Petersburg, July 7–11, 2003*, ser. Europhysics Conference Abstracts (ECA), vol. 27A. European Physical Society (EPS), 2003, pp. P–2.63.

[51] A. Sushkov, V. Andreev, Y. Camenen, A. Pochelon, I. Klimanov, A. Scarabosio, and H. Weisen, **"High-resolution multiwire proportional soft X-ray diagnostic measurements on TCV,"** *Review of Scientific Instruments*, vol. 79, no. 2, p. 023506 (5pp), February 2008, part 1. URL: http://link.aip.org/link/?RSINAK/79/023506/1

[52] M. Anton, M. J. Dutch, and H. Weisen, **"Relative calibration of photodiodes in the soft X-ray spectral range,"** *Review of Scientific Instruments*, vol. 66, no. 7, pp. 3762–3769, July 1995.

[53] G. Arnoux, **"Détermination du Z_{eff} par mesure du Bremsstrahlung sur TCV,"** Master's thesis, Ecole polytechnique fédérale de Lausanne, Lausanne, Switzerland, February 2001.

[54] A. Weller, D. Pasini, A. W. Edwards, R. D. Gill, and R. Granetz, **"Modelling of soft X-ray emission from JET plasmas,"** JET Joint Undertaking, Abingdon, Oxon OX14 3EA, United Kingdom, JET internal report 10, 1987, JET-IR(87)10.

[55] G. Elwert, **"Über die Ionisationsprozesse und Rekombinationsprozesse in einem Plasma und die Ionisationsformel der Sonnenkorona,"** *Zeitschrift für Naturforschung, section A-A, Journal of physical sciences*, vol. 7, no. 6, pp. 432–439, 1952.

[56] H. Weisen, D. Pasini, A. Weller, and A. W. Edwards, **"Measurement of light impurity densities and Z_{eff} in JET using X-ray tomography,"** *Review of Scientific Instruments*, vol. 62, no. 6, pp. 1531–1538, June 1991.

[57] F. L. Hinton and C. Oberman, **"Electrical conductivity of plasma in a spatially inhomogeneous magnetic field,"** *Nuclear Fusion*, vol. 9, no. 4, p. 319, April 1969.

[58] S. P. Hirshman, R. J. Hawryluk, and B. Birge, **"Neoclassical conductivity of a Tokamak plasma,"** *Nuclear Fusion*, vol. 17, no. 6, pp. 611–614, June 1977.

[59] F. L. Hinton and R. D. Hazeltine, **"Theory of plasma transport in toroidal confinement systems,"** *Reviews of Modern Physics*, vol. 48, no. 2, pp. 239–308, April 1976.

[60] O. Sauter, C. Angioni, and Y. Lin-Liu, **"Neoclassical conductivity and bootstrap current formulas for general axisymmetric equilibria and arbitrary collisionality regime,"** *Physics of Plasmas*, vol. 6, no. 7, pp. 2834–2839, July 1999.

[61] M. Bernard, **"Mesure de la charge effective et de la concentration d'impuretés dans le plasma de TCV,"** Master's thesis, Ecole polytechnique fédérale de Lausanne, Lausanne, Switzerland, February 2006.

[62] P. A. Davidson, ***An introduction to magnetohydrodynamics***. Cambridge University Press, 2001.

[63] F. Hofmann and G. Tonetti, **"Tokamak equilibrium reconstruction using Faraday-rotation measurements,"** *Nuclear Fusion*, vol. 28, no. 10, pp. 1871–1878, October 1988.

[64] F. Hofmann, **"FBT – A free-boundary tokamak equilibrium code for highly elongated and shaped plasmas,"** *Computer Physics Communications*, vol. 48, no. 2, pp. 207–221, February 1988.

[65] J.-M. Moret, F. Buhlmann, D. Fasel, F. Hofmann, and G. Tonetti, **"Magnetic measurements on the TCV Tokamak**," *Review of Scientific Instruments*, vol. 69, no. 6, pp. 2333–2348, June 1998.

[66] J.-M. Moret, F. Buhlmann, and G. Tonetti, **"Fast single loop diamagnetic measurements on the TCV tokamak**," *Review of Scientific Instruments*, vol. 74, no. 11, pp. 4634–4643, November 2003.

[67] S. Y. Abdul-Rassak and E. W. Laing, **"Transport coefficients for a two-temperature equal-mass plasma in a uniform magnetic field**," *Journal of Plasma Physics*, vol. 52, no. 2, pp. 309–319, October 1994.

[68] O. G. Bakunin, ***Turbulence and diffusion: scaling versus equations***, ser. Springer series in synergetics. Springer Verlag, Berlin, 2008.

[69] W. Dorland, G. W. Hammett, T. S. Hahm, and M. A. Beer, **"Nonlinear gyrofluid model of ITG turbulence**," in *Proceedings of the U.S./Japan Workshop on Ion Temperature Gradient-Driven Turbulent Transport, January 1993*, ser. AIP conference proceedings, W. Horton, A. Wootton, and M. Wakatani, Eds., no. 284, Austin, Texas, USA, January 1994, pp. 344–367.

[70] E. Speth, **"Neutral beam heating of fusion plasmas**," *Reports on Progress in Physics*, vol. 52, no. 1, pp. 57–121, January 1989.

[71] R. C. Isler, **"An overview of charge-exchange spectroscopy as a plasma diagnostic**," *Plasma Physics and Controlled Fusion*, vol. 36, no. 2, pp. 171–208, February 1994.

[72] A. A. Ivanov, G. F. Abdrashitov, V. S. Belkin, A. I. Gorbovsky, V. I. Davydenko, P. P. Deichuli, A. N. Dranichnikov, V. A. Kapitonov, V. Y. Kremyansky, V. V. Mishagin, A. A. Podminogin, V. Y. Savkin, I. V. Shikhovtsev, N. V. Stupishin, A. V. Sitnikov, A. S. Medvedko, Y. A. Evtushenko, V. V. Kolmogorov, I. I. Averbuch, and R. Uhlemann, **"Diagnostic neutral beam injectors for large plasma physics experiments**," *Fusion Technology*, vol. 35, no. 1T, pp. 180–184, January 1999, proceedings of the International Conference on Open Magnetic Systems for Plasma Confinement, Budker Institute of Nuclear Physics, Novosibirsk, Russian Federation, July 27–31, 1998.

[73] V. G. Kiptily, F. E. Cecil, and S. S. Medley, **"Gamma-ray diagnostics of high temperature magnetically confined fusion plasmas**," *Plasma Physics and Controlled Fusion*, vol. 48, no. 8, pp. R59–R82, August 2006.

[74] G. K. Woodgate, ***Elementary Atomic Structure*, 2nd ed.** Great Clarendon Street, Oxford OX2 6DP: Oxford University Press, 1980.

[75] W. M. Solomon, K. H. Burrell, P. Gohil, R. J. Groebner, and L. R. Baylor, **"Extraction of poloidal velocity from charge exchange recombination spectroscopy measurements**," *Review of Scientific Instruments*, vol. 75, no. 10, pp. 3481–3486, October 2004, proceedings of the 15^{th} Topical Conference on High-Temperature Plasma Diagnostics.

[76] R. E. Bell and E. J. Synakowski, **"New understanding of poloidal rotation measurements in a Tokamak plasma**," in *Proceedings of the Twelfth Topical Conference on Atomic Processes in Plasmas*, ser. AIP Conference Proceedings, vol. 547, November 2000, pp. 39–52.

[77] J. Mlynár, A. N. Shukaev, P. Bosshard, B. P. Duval, A. A. Ivanov, M. Kollegov, V. V. Kolmogorov, X. Llobet, R. A. Pitts, and H. Weisen, **"Diagnostic Neutral Beam Injector at the TCV Tokamak**," CRPP/EPFL, CH-1015 Lausanne, LRP 710, October 2001.

[78] A. N. Karpushov, G. F. Abdrashitov, I. I. Averboukh, P. Bosshard, I. Condrea, B. P. Duval, A. A. Ivanov, V. V. Kolmogorov, J. Mlynár, A. Perez, I. V. Shikhovtsev, A. N. Shukaev, and H. Weisen, **"Upgrade of the diagnostic neutral beam injector for the TCV tokamak**," *Fusion Engineering and Design*, vol. 66-68, pp. 899–904, September 2003, proceedings of the 22$^{\text{nd}}$ Symposium on Fusion Technology.

[79] A. N. Karpushov, Y. Andrebe, B. P. Duval, and A. Bortolon, **"The diagnostic neutral beam injector with arc-discharge plasma source on the TCV Tokamak**," *Fusion Engineering and Design*, 2009, contributed paper presented at the 25th Symposium on Fusion Technology (SOFT), Rostock, Germany, September 15–19, 2008. Article in press.

[80] R. J. Fonck, D. S. Darrow, and K. P. Jaehnig, **"Determination of plasma-ion velocity distribution via charge-exchange recombination spectroscopy**," *Physical Review A*, vol. 29, no. 6, pp. 3288–3309, June 1984.

[81] R. Uhlemann, R. S. Hemsworth, G. Wang, and H. Euringer, **"Hydrogen and deuterium ion species mix and injected neutral beam power fractions of the TEXTOR-PINIs for 20-60 kV determined by Doppler shift spectroscopy**," *Review of Scientific Instruments*, vol. 64, no. 4, pp. 974–982, April 1993.

[82] J. Mlynár, **"TCV DNBI Profile and Attenuation Studies with Code Manual**," Centre de Recherches en Physique des Plasmas (CRPP), CRPP/EPFL, station 13, CH-1015 Lausanne, Switzerland, Lausanne Report LRP 692/01, 2001.

[83] P. Bosshard, **"Confinement ionique dans le tokamak TCV mesuré par spectroscopie d'échange de charge**," Ph.D. dissertation, Ecole polytechnique fédérale de Lausanne (EPFL), CH-1015 Lausanne, Switzerland, March 2003, no 2723, LRP 750.

[84] A. Zabolotskiy, **"Particle transport in tokamak plasmas**," PhD thesis, Ecole polytechnique fédérale de Lausanne (EPFL), CH-1015 Lausanne, Switzerland, 2005, no. 3252, also available as Lausanne Report LRP 814/2006.

[85] M. Tunklev, P. Breger, K. Günther, M. von Hellermann, R. König, M. O'Mullane, and K.-D. Zastrow, **"Modelling of passive charge exchange emission and neutral background density deduction in JET**," *Plasma Physics and Controlled Fusion*, vol. 41, no. 8, pp. 985–1004, August 1999.

[86] International Atomic Energy Agency (IAEA). (2008, September) **Atomic and molecular data**. Internet. International Atomic Energy Agency (IAEA). Vienna, Austria. Version 3.1.1. URL: http://www-amdis.iaea.org/ALADDIN/

[87] A. de Chambrier, A. Heym, F. Hofmann, B. Joye, R. Keller, A. Lietti, J. B. Lister, P. D. Morgan, N. J. Peacock, A. Pochelon, and M. F. Stamp, **"Measurements of electron and ion heating by Alfvén waves in the TCA Tokamak**," *Plasma Physics*, vol. 25, no. 9, pp. 1021–1036, September 1983.

[88] A. de Chambrier, **"Mesures de la température ionique dans le plasma du tokamak TCA en présence de chauffage par ondes Alfvén**," PhD thesis, Ecole polytechnique

fédérale de Lausanne (EPFL), CH-1015 Lausanne, Switzerland, 1988, no. 712, also available as Lausanne Report LRP 345/88.

[89] A. D. Cheetham, A. Heym, F. Hofmann, K.Hruska, R. Keller, A. Lietti, J. B. Lister, A. Pochelon, H. Ripper, A. Simik, and A. Tuszel, **"Design and construction of the TCV tokamak,"** in *Fusion Technology 1980*, R. Hancox, Ed., vol. 1. Pergamon Press, Oxford, United Kingdom, 1981, pp. 601–607, proceedings of the 11th symposium on fusion technology (SOFT), Oxford, September 15–19, 1980.

[90] A. de Chambrier, G. A. Collins, C. Hollenstein, B. Joye, J. B. Lister, J.-M. Moret, S. Nowak, A. Pochelon, and W. C. Simm, **"Target plasma conditions in TCA,"** Centre de Recherches en Physique des Plasmas, Ecole polytechnique fédérale de Lausanne, CH-1015 Lausanne, Switzerland, Lausanne Report (LRP) 241/84, November 1984.

[91] A. de Chambrier, B. P. Duval, J. B. Lister, F. J. Mompeán, and J.-M. Moret, **"The ion temperature evolution on TCA during Alfvén wave heating and in non-stationary Ohmic conditions,"** *Plasma Physics and Controlled Fusion*, vol. 31, no. 4, pp. 527–547, April 1989.

[92] A. N. Karpushov, B. P. Duval, C. Schlatter, V. I. Afanasyev, and F. V. Chernyshev, **"Neutral particle analyzer diagnostics on the TCV Tokamak,"** *Review of Scientific Instruments*, vol. 77, no. 3, p. 033504 (13pp), March 2006.

[93] V. Afrosimov, I. Gladkovskii, Y. S. Gordeev, I. F. Kalinkevich, and N. Fedorenko, **"Method of investigation of the flux of atoms emitted by a plasma,"** *Soviet Physics - Technical Physics*, vol. 5, no. 12, pp. 1378–1388, June 1961.

[94] S. S. Medley, A. J. H. Donné, R. Kaita, A. I. Kislyakov, M. P. Petrov, and A. L. Roquemore, **"Contemporary instrumentation and application of charge exchange neutral particle diagnostics in magnetic fusion energy experiments,"** *Review of Scientific Instruments*, vol. 79, no. 1, p. 011101 (16pp), January 2008, invited Review Article.

[95] A. I. Kislyakov, A. J. H. Donné, L. I. Krupnik, S. S. Medley, and M. P. Petrov, **"Particle Diagnostics,"** *Fusion Science and Technology*, vol. 53, no. 2, pp. 577–603, February 2008, chapter 8 of the special issue on Plasma Diagnostics for Magnetic Fusion Research.

[96] V. I. Afanasyev, M. I. Mironov, S. V. Konovalov, A. V. Khudoleev, M. P. Petrov, S. S. Kozlovsky, V. G. Nesenevich, B. V. Lyublin, S. Y. Petrov, A. I. Kislyakov, F. V. Chernyshev, and A. D. Melnik, **"Neutral particle analysis on ITER and requirements for DEMO,"** in *Burning plasma diagnostics*, ser. AIP conference proceedings, F. P. Orsitto, G. Gorini, E. Sindoni, and M. Tardocchi, Eds., vol. 988, Varenna, Italy, 2008, pp. 177–184, proceedings of the International Conference on Burning Plasma Diagnostics, September 24–28, 2007.

[97] ***Five-channel energy and mass analyser of atomic particles***, A. F. Ioffe Physico-Technical Institute of the Academy of Science of the USSR, Leningrad, 1974.

[98] A. B. Izvozchikov, M. P. Petrov, S. Y. Petrov, F. V. Chernyshev, and I. V. Shustov, **"The Akord-12 multichannel analyzer for simultaneous recording of the energy spectra of hydrogen and deuterium atoms,"** *Soviet Physics - Technical Physics*, vol. 37, no. 2, pp. 201–204., 1992.

[99] V. V. Afrosimov, E. L. Berezovskii, I. P. Gladkovskii, A. I. Kislyakov, M. P. Petrov, and V. A. Sadovnikov, **"Multichannel energy and mass analyzer for atomic particles**," *Soviet Physics - Technical Physics*, vol. 20, no. 1, pp. 33–37, July 1975, translated from Zhurnal Tekhnicheskoi Fiziki, vol. 45, no. 1, pp. 56–63, 1975.

[100] A. N. Karpushov, B. P. Duval, C. Schlatter, H. Weisen, V. I. Afanasyev, F. V. Chernyshev, and M. I. Mironov, **"Determination of the Radial Profile of Hydrogen Isotope Composition in TCV plasmas**," in *32nd EPS Conference on Plasma Physics and Controlled Fusion combined with the 8th International Workshop on Fast Ignition of Fusion Targets, Tarragona, June 27– July 1, 2005*, ser. Europhysics Conference Abstracts, B. v. M. C. Hidalgo, Ed., vol. 29C, Asociación EURATOM-CIEMAT para Fusión, Madrid. Tarragona: The European Physical Society, 2005, pp. P–4.097.

[101] F. V. Chernyshev, V. I. Afanasyev, A. V. Dech, M. Kick, A. I. Kislyakov, S. S. Kozlovskii, A. Kreter, M. I. Mironov, M. P. Petrov, and S. Y. Petrov, **"A Compact Neutral-Particle Analyzer for Plasma Diagnostics**," *Instruments and Experimental Techniques*, vol. 47, no. 2, pp. 214–220, March 2004.

[102] F. V. Chernyshev, V. I. Afanasyev, A. V. Detch, M. Kick, A. I. Kislyakov, S. S. Kozlovski, A. Kreter, M. I. Mironov, M. P. Petrov, and S. Y. Petrov, **"Compact Neutral Particle Analyzer for Plasma Diagnostics**," in *Proceedings of the 30th EPS Conference on Controlled Fusion and Plasma Physics, St. Petersburg, July 7–11, 2003*, ser. Europhysics Conference Abstracts (ECA), S. L. R. Koch, Ed., vol. 27A. St. Petersburg: European Physical Society (EPS), 2003, pp. P–4.71.

[103] T. Ozaki, P. Goncharov, E. Veschev, S. Sudoa, T. Seki, and N. Tamura, **"High-energy neutral particle measurements simulating α-particle diagnostics in Large Helical Device**," *Fusion Engineering and Design*, vol. 82, no. 5–14, pp. 1251–1257, October 2007, proceedings of the 24th Symposium on Fusion Technology (SOFT), Warsaw, Poland, September 2006.

[104] R. Balbin, S. Petrov, J. Fontdecaba, K. J. McCarthy, V. Vargas, J. Carmona, J. Guasp, and D. Makarin, **"First Measurements of High-Energy Charge-Exchange Neutrals Using Compact Neutral Particle Analyser in TJ-II Stellarator**," in *Proceedings of the 32nd EPS Conference on Plasma Physics and Controlled Fusion combined with the 8th International Workshop on Fast Ignition of Fusion Targets, Tarragona, June 27–July 1, 2005*, ser. Europhysics Conference Abstracts (ECA), C. Hidalgo and B. van Milligen, Eds., vol. 29C, no. D-5.001, Asociación EURATOM-CIEMAT para Fusión, Madrid. Tarragona: European Physical Society (EPS), 2005, pp. D–5.001.

[105] E. D. Mezonlin, S. Roberson, C. Raynor, R. Appartaim, I. J. A. Johnson, V. I. Afanasyev, S. S. Kozlovsky, J. M. Moller, D. N. Hill, E. B. Hooper, H. S. McLean, and R. D. Wood, **"Neutral particle analyzer measurements on the SSPX spheromak**," *Review of Scientific Instruments*, vol. 78, no. 5, p. 053504 (7pp), May 2007.

[106] W. Schneider, M. Turnyanskiy, F. Chernyshev, V. Afanasyev, M. Kick, and T. Richert, **"Comparison of the IOFFE neutral particle analyser with the Princeton analyser on the Mega Amp Spherical Tokamak**," *Vacuum*, vol. 83, no. 4, pp. 752–756, November 2008, proceedings of the "Symposium on Vacuum based Science and Technology" in conjunction with the 6th Annual DVG-Meeting, Greifswald, September 5–7, 2007.

[107] V. K. Liechtenstein, T. M. Ivkova, E. D. Olshanski, R. Golser, W. Kutschera, P. Steier, C. Vockenhuber, R. Repnow, R. von Hahn, M. Friedrich, and U. Kreissig, **"Recent investigations and applications of thin diamond-like carbon (DLC) foils,"** *Nuclear Instruments and Methods in Physics Research Section A*, vol. 521, no. 1, pp. 197–202, March 2004.

[108] **Channeltron electron multiplier handbook for mass spectrometry applications**. Web. Burle Technologies, Inc. 1000 New Holland Avenue, Lancaster, PA 17601-5688 U.S.A. URL: http://www.burle.com/cgi-bin/byteserver.pl/pdf/ChannelBook.pdf

[109] URL: http://www.sjuts.com/

[110] J. A. Stillerman, T. W. Fredian, K. A. Klare, and G. Manduchi, **"MDSplus data acquisition system,"** *Review of Scientific Instruments*, vol. 68, no. 1, pp. 939–942, January 1997.

[111] ***Compact Neutral Particle Analyser, CNPA-03, Technical description and instruction manual***, Ioffe Physical-Technical Institute, Institution of the Russian Academy of Sciences, 26, Politechnicheskaya street, St.Petersburg 194021, Russian Federation, 2003.

[112] Y. V. Gott and A. G. Motlich, **"Comparative characteristics of atomic particle stripping analysers with solid and gaseous targets,"** *Nuclear Instruments and Methods*, vol. 155, no. 3, pp. 443–447, October 1978.

[113] S. von Goeler, J. Stevens, S. Bernabei, M. Bitter, T. K. Chu, F. Jobes, K. Hill, W. Hooke, J. C. Hosea, H. Hsuan, E. Mazzucato, E. Meservey, R. W. Motley, and S. Sesnic, **"Perpendicular Bremsstrahlung emission of suprathermal electrons,"** *Review of Scientific Instruments*, vol. 57, no. 8, pp. 2130–2132, August 1986.

[114] A. Fasoli, **"Relaxation process and plasma resistivity,"** lecture notes of the Plasma Physics II course at EPFL, October 2007.

[115] H. Dreicer, **"Electron and Ion Runaway in a Fully Ionized Gas. I,"** *Physical Review*, vol. 115, no. 2, pp. 238–249, July 1959.

[116] Y. Peysson, S. Coda, and F. Imbeaux, **"Hard X-ray CdTe tomography of tokamak fusion plasmas,"** *Nuclear Instruments and Methods in Physics Research Section A: Accelerators, Spectrometers, Detectors and Associated Equipment*, vol. 458, no. 1, pp. 269–274, February 2001.

[117] S. Gnesin and S. Coda, **"Design of a tomographic hard X-ray spectrometer for suprathermal electron studies with ECRH,"** in *Burning plasma diagnostics*, ser. AIP conference proceedings, F. P. Orsitto, G. Gorini, E. Sindoni, and M. Tardocchi, Eds., vol. 988, 2008, pp. 222–225, international Conference on Burning Plasma Diagnostics, Varenna, Italy, September 24-28, 2007.

[118] S. Gnesin, S. Coda, J. Decker, and Y. Peysson, **"Suprathermal electron studies in the TCV tokamak: Design of a tomographic hard X-ray spectrometer,"** *Review of Scientific Instruments*, vol. 79, no. 10, p. 10F504 (5pp), October 2008, proceedings of the 17^{th} topical conference on high-temperature plasma diagnostics, May 11–15, 2008, Albuquerque, New Mexico, USA. URL: http://link.aip.org/link/?RSI/79/10F504/1

[119] Y. Peysson and F. Imbeaux, **“Tomography of the fast electron Bremsstrahlung emission during lower hybrid current drive on TORE SUPRA**,” *Review of Scientific Instruments*, vol. 70, no. 10, pp. 3987–4007, October 1999.

[120] S. Coda, S. Alberti, P. Blanchard, T. P. Goodman, M. A. Henderson, P. Nikkola, Y. Peysson, and O. Sauter, **“Electron cyclotron current drive and suprathermal electron dynamics in the TCV tokamak**,” *Nuclear Fusion*, vol. 43, no. 11, pp. 1361–1370, November 2003, special issue on Electron Cyclotron Wave Physics and Technology.

[121] J. H. Hubbell and S. M. Seltzer. (2004) **Tables of X-Ray Mass Attenuation Coefficients and Mass Energy-Absorption Coefficients**. Internet. National Institute of Standards and Technology. Gaithersburg, MD. URL: http://physics.nist.gov/xaamdi

[122] Plansee, **“DENSIMET® und INERMET® Wolframlegierungen**,” A-6600 Reutte, Tirol, Austria, March 2008, http://www.plansee.com.

[123] O. N. Jarvis, **“Neutron measurement techniques for tokamak plasmas**,” *Plasma Physics and Controlled Fusion*, vol. 36, no. 2, pp. 209–244, February 1994.

[124] H. Brysk, **“Fusion neutron energies and spectra**,” *Plasma Physics*, vol. 15, no. 7, pp. 611–617, July 1973.

[125] H.-S. Bosch and G. Hale, **“Improved formulas for fusion cross-sections and thermal reactivities**,” *Nuclear Fusion*, vol. 32, no. 4, pp. 611–631, April 1992, erratum in Nuclear Fusion, vol. 33, p. 1919, no. 12, December 1993.

[126] ——, **“Improved formulas for fusion cross-sections and thermal reactivities (erratum)**,” *Nuclear Fusion*, vol. 33, no. 12, p. 1919, December 1993, erratum of Nuclear Fusion, vol. 32, no. 4, pp. 611–631, April 1992.

[127] H. Knoepfel and D. A. Spong, **“Runaway electrons in toroidal discharges**,” *Nuclear Fusion*, vol. 19, no. 6, pp. 785–826, June 1979.

[128] J. Mlynár, G. Bonheure, A. Murari, L. Bertalot, M. Angelone, M. Pillon, S. Conroy, G. Ericsson, J. Källne, and S. Popovichev, **“Progress in neutron diagnostics at JET**,” *Czechoslovak Journal of Physics*, vol. 56, no. 2, pp. B118–B124, October 2006.

[129] L. Hively, **“Convenient computational forms for Maxwellian reactivities**,” *Nuclear Fusion*, vol. 17, no. 4, pp. 873–876, April 1977.

[130] G. Lehner and F. Pohl, **“Reaktionsneutronen als Hilfsmittel der Plasmadiagnostik**,” *Zeitschrift für Physik A Hadrons and Nuclei*, vol. 207, no. 1, pp. 83–104, February 1967.

[131] W. J. Price, ***Nuclear radiation detection*, second edition ed.** McGraw-Hill, New York, 1964.

[132] **Canberra Industries, Inc.** 800 Research Parkway, Meriden, CT 06450, U.S.A. URL: http://www.canberra.com/products/1132.asp

[133] P. Bosshard, **“Mesure de la température ionique par comptage des neutrons de fusion**,” Travail pratique de diplôme, Ecole polytechnique fédérale de Lausanne (EPFL), CH-1015 Lausanne, Switzerland, February 1997.

[134] E. A. Lorch, **“Neutron Spectra of ^{241}Am/B, ^{241}Am/Be, ^{241}Am/F, ^{242}Cm/Be, ^{238}Pu/13C and ^{252}Cf isotopic neutron sources**,” *The International Journal of Applied Radiation and Isotopes*, vol. 24, no. 10, pp. 585–591, October 1973.

[135] J. Greenborg, **“Neutron Attenuation Mechanisms in Concrete Shielding**,” *Journal of Materials JMLSA*, vol. 4, no. 2, pp. 251–281, June 1969.

[136] M. F. A. Harrison, **“Role of atomic and molecular processes in fusion research**,” *Physics reports - Review section of physics letters*, vol. 37, no. 2, pp. 59–81, February 1978, introductory paper.

[137] E. F. Gurnee and J. L. Magee, **“Interchange of charge between gaseous molecules in resonant and near-resonant processes**,” *The Journal of Chemical Physics*, vol. 26, no. 5, pp. 1237–1248, May 1957.

[138] Y. S. Gordeev, A. N. Zinovev, and M. P. Petrov, **“Recombination of hydrogen in a quasi-stationary thermonuclear plasma**,” *JETP Letters*, vol. 25, no. 4, pp. 204–207, February 1977.

[139] S. A. Cohen and H. F. Dylla, **“O-H charge-exchange in cold, dense hydrogen plasmas**,” *Nuclear Fusion*, vol. 18, no. 1, pp. 5–8, January 1978.

[140] M. Wischmeier, **“Simulating divertor detachment in the TCV and JET tokamaks**,” PhD thesis, Ecole polytechnique fédérale de Lausanne (EPFL), CH-1015 Lausanne, Switzerland, 2004, no. 3176, also available as Lausanne Report LRP 799/05.

[141] G. Haas and H.-S. Bosch, **“In vessel pressure measurement in nuclear fusion experiments with ASDEX gauges**,” *Vacuum*, vol. 51, no. 1, pp. 39–46, September 1998.

[142] D. Reiter, ***The EIRENE code user manual*, version 11 ed.**, KFA, Jülich, 2005.

[143] J. Hughes, D. Mossessian, J. Terry, B. LaBombard, and D. Stotler, **“Experimental diagnosis and kinetic computation of neutral penetration in the Alcator C-Mod edge plasma**,” Portland, Maine, USA, 2004, contributed poster presented at the 16th International Conference on Plasma Surface Interactions in Controlled Fusion Devices, May 24–28, 2004.

[144] B. LaBombard, **“KN1D: A 1-D Space, 2-D Velocity, Kinetic Transport Algorithm for Atomic Molecular Hydrogen in an Ionizing Plasma**,” MIT Plasma Science and Fusion Center (PSFC), 175 Albany St., Cambridge, MA 02139, USA, PSFC Research Report PSFC/RR-01-9, 2001.

[145] J.-M. Moret, **“A software package to manipulate space dependencies and geometry in magnetic confinement fusion**,” *Review of Scientific Instruments*, vol. 76, no. 7, p. 073507 (5pp), July 2005.

[146] R. A. Pitts, B. P. Duval, A. Loarte, J.-M. Moret, J. A. Boedo, D. Coster, I. Furno, J. Horacek, A. S. Kukushkin, D. Reiter, J. Rommers, and the TCV Team, **“Divertor geometry effects on detachment in TCV**,” *Journal of Nuclear Materials*, vol. 290, pp. 940–946, March 2001, proceedings of the 14th International Conference on Plasma-Surface Interactions in Controlled Fusion Devices, Rosenheim, Germany, May 22–26, 2000.

[147] R. J. Goldston, **"Diagnostics for hot plasmas using hydrogen neutral beams,"** in *Diagnostics for fusion reactor conditions*, P. E. Stott, D. K. Akulina, G. G. Leotta, E. Sidoni, and C. Wharton, Eds., vol. I. Villa Monastero, Varenna, Italy: Commission of the european communities, Pergamon Press, September 1982, pp. 263–287, proceedings of the course held at the international school of plasma physics, September 6–17, 1982.

[148] R. K. Janev, W. D. Langer, J. K. Evans, and J. D. E. Post, **"Elementary Processes in Hydrogen-Helium Plasmas. Cross Sections and Reaction Rate Coefficients."** ser. Springer Series on Atoms and Plasmas. Springer-Verlag Heidelberg, New York, London, Paris, Tokyo, November 1987, vol. 4.

[149] P. R. Bevington and D. K. Robinson, ***Data reduction and error analysis for the physical sciences*, 3rd ed.** Boston: McGraw-Hill book company, 2003.

[150] W. H. Press, S. A. Teukolsky, W. T. Vetterling, and B. P. Flannery, ***Numerical recipes for Fortran 77, The Art of Scientific Computing*, second edition ed.** Cambridge: Cambridge University Press, 2001.

[151] C. Schlatter, B. P. Duval, and A. N. Karpushov, **"Reconstruction of Hydrogenic Ion Temperature Profiles on TCV,"** in *Proceedings of the 32nd EPS Conference on Plasma Physics and Controlled Fusion combined with the 8th International Workshop on Fast Ignition of Fusion Targets, Tarragona, Spain, June 27–July 1, 2005*, ser. Europhysics Conference Abstracts (ECA), B. v. M. C. Hidalgo, Ed., vol. 29C, no. P-1.050, Asociación EURATOM-CIEMAT para Fusión, Madrid. Tarragona: European Physical Society (EPS), 2005.

[152] S. S. Medley, R. E. Bell, M. P. Petrov, A. L. Roquemore, and E. V. Suvorkin, **"Initial neutral particle analyzer measurements of ion temperature in the National Spherical Torus Experiment,"** *Review of Scientific Instruments*, vol. 74, no. 3, pp. 1896–1899, March 2003.

[153] A. I. Kislyakov, M. P. Petrov, and E. V. Suvorkin, **"Measurement of the isotope composition of ITER-FEAT plasma by means of neutral particle diagnostics,"** *Plasma Physics and Controlled Fusion*, vol. 43, no. 12, pp. 1775–1783, December 2001.

[154] **A. B. Izvozchikov**, PhD thesis, A. F. Ioffe Physico-Technical Institute, Leningrad, Sowjet Union, 1980.

[155] M. I. Mironov, ***DOUBLE-TCV: Simulation of CX fluxes emitted by tokamak plasma***, IOFFE Physico-Technical Institute, St. Petersburg, Russian Federation, 2006.

[156] **HDF Hierarchical Data Format**. URL: http://hdf.ncsa.uiuc.edu/

[157] **A. Bortolon**, private communication, 2006.

[158] A. A. Ivanov, V. I. Davidenko, P. P. Deichuli, A. Kreter, V. V. Mishagin, A. A. Podminogin, I. V. Shikhovtsev, B. Schweer, and R. Uhlemann, **"Radio frequency ion source for plasma diagnostics in magnetic fusion experiments,"** *Review of Scientific Instruments*, vol. 71, no. 10, pp. 3728–3735, October 2000.

[159] P. P. Deichuli, A. A. Ivanov, and N. V. Stupishin, **"Long-pulse arc-discharge plasma source with cold cathode for diagnostic neutral beam injector,"** *Review of Scientific Instruments*, vol. 79, no. 2, p. 02C106 (3pp), February 2008, proceedings of the 12th International Conference on Ion Sources, August 26–31, 2007, Jeju Isl, South Korea.

[160] C. Schlatter, B. P. Duval, and A. N. Karpushov, **"Reconstruction of ion temperature profiles from single chord NPA measurements on the TCV tokamak**," *Plasma Physics and Controlled Fusion*, vol. 48, no. 12, pp. 1765–1785, December 2006.

[161] H. P. Eubank, P. Noll, and F. Tappert, **"Plasma density measurements with atomic beams**," *Nuclear Fusion*, vol. 5, no. 1, pp. 68–72, March 1965.

[162] V. V. Afrosimov, M. P. Petrov, and V. A. Sadovnikov, **"Measurement of the local values of the ion temperature in a tokamak using charge exchange of plasma ions with a jet of hydrogen atoms**," *JETP Letters*, vol. 18, no. 8, pp. 300–302, 1973.

[163] G. Schilling, T. A. Kozub, S. S. Medley, and K. M. Young, **"TFTR diagnostic neutral beam**," *Review of Scientific Instruments*, vol. 57, no. 8, pp. 2060–2062, August 1986, part 2.

[164] W. L. Rowan, R. D. Bengtson, R. V. Bravenec, H. He, J. Jagger, D. M. Patterson, D. W. Ross, P. M. Valanju, A. J. Wootton, E. S. Marmar, J. H. Irby, J. A. Snipes, and J. L. Terry, **"Neutral beam diagnostics for Alcator C-Mod**," *Review of Scientific Instruments*, vol. 68, no. 1, pp. 300–303, January 1997, 11th Topical Conference on High-Temperature Plasma Diagnostics, May 12–16, 1996, Monterey, California, USA.

[165] L. Q. Hu, B. N. Wan, C. D. Hu, B. H. Liu, Z. W. Wu, J. Huang, W. L. Rowan, H. Huang, and K. Gentle, **"Neutral beam diagnostics for the HT-7 tokamak**," *Review of Scientific Instruments*, vol. 75, no. 10, pp. 3496–3498, October 2004, proceedings of the 15th Topical Conference on High-Temperature Plasma Diagnostics, April 19–22, 2004, San Diego, California, USA.

[166] K. J. McCarthy, R. Balbin, A. Lopez-Fraguas, A. Garcia, J. M. Carmona, J. Sanchez, and A. A. Ivanov, **"Diagnostic neutral beam injector and associated diagnostic systems for the TJ-II stellarator device**," *Review of Scientific Instruments*, vol. 75, no. 10, pp. 3499–3501, October 2004, proceedings of the 15th Topical Conference on High-Temperature Plasma Diagnostics, April 19–22, 2004, San Diego, California, USA.

[167] R. D. Hazeltine and F. L. Waelbroeck, **"Frontiers in physics**," in *The Framework of Plasma Physics*, P. Books, Ed. Reading, Massachusetts: Westview Press, 1998, vol. 100.

[168] P. R. Thomas, P. Andrew, B. Balet, D. Bartlett, J. Bull, B. de Esch, A. Gibson, C. Gowers, H. Guo, G. Huysmans, T. Jones, M. Keilhacker, R. Koenig, M. Lennholm, P. Lomas, A. Maas, F. Marcus, F. Nave, V. Parail, F. Rimini, J. Strachan, K. D. Zastrow, and N. Zornig, **"Observation of alpha heating in JET DT plasmas**," *Physical Review Letters*, vol. 80, no. 25, pp. 5548–5551, June 1998.

[169] V. I. Afanasyev, A. Gondhalekar, P. Y. Babenko, P. Beaumont, P. de Antonis, A. V. Detch, A. I. Kislyakov, S. S. Kozlovskij, M. I. Mironov, M. P. Petrov, S. Y. Petrov, F. V. Tschernyshev, C. H. Wilson, and the EFDA-JET team, **"Neutral particle analyzer/isotope separator for measurement of hydrogen isotope composition of JET plasmas**," *Review of Scientific Instruments*, vol. 74, no. 4, pp. 2338–2352, April 2003.

[170] I. Condrea, R. A. Pitts, B. P. Duval, S. M. Ahmed, A. Zabolotsky, M. Wischmeier, A. N. Karpushov, J. Horacek, Y. R. Martin, and J. Mlynár, **"Helium Discharge Operation in TCV**," in *Proceedings of the 29th EPS Conference on Plasma Physics and Controlled Fusion, Montreux, Switzerland, June 17–21, 2002*, ser. Europhysics Conference Abstracts

(ECA), R. Behn and C. Varandas, Eds., vol. 26B, no. P-2.079. European Physical Society (EPS), 2002, contributed paper.

[171] P. Bosshard, B. P. Duval, A. N. Karpushov, and J. Mlynár, **"Ion Temperature Behaviour and Ion Contribution to the Power Balance Measured by CXRS in Ohmic and ECR Heated Plasmas on TCV**," in *Proceedings of the 29th EPS Conference on Plasma Physics and Controlled Fusion, Montreux, Switzerland, June 17–21, 2002*, ser. Europhysics Conference Abstracts (ECA), R. Behn and C. Varandas, Eds., vol. 26B, no. P-4.120. European Physical Society (EPS), 2002.

[172] A. Pochelon, Y. Camenen, A. Marinoni, S. Brunner, S. Coda, I. Furno, J. Graves, A. Martynov, S. Medvedev, F. Piras, H. Reimerdes, O. Sauter, A. Scarabosio, S. Alberti, P. Angelino, R. Behn, A. Bortolon, A. Bottino, L. Curchod, K. Daouk, B. P. Duval, A. Fasoli, T. P. Goodman, M. A. Henderson, F. Hofmann, S. Jolliet, A. N. Karpushov, X. Lapillonne, J. B. Lister, Y. Martin, J.-M. Moret, J. I. Paley, R. A. Pitts, L. Porte, F. Ryter, L. Sulmoni, A. Sushkov, G. Tonetti, L. Villard, M. Q. Tran, H. Weisen, and the TCV Team, **"Physics Insight and Performance Benefit in MHD and Energy Transport from Plasma Shaping Experiments in the TCV Tokamak**," in *Proceedings of the 22nd IAEA Fusion Energy Conference, Geneva, Switzerland, October 13–18, 2008*, International Atomic Energy Agency (IAEA), Ed., no. EX/P5-15. Vienna, Austria: International Atomic Energy Agency (IAEA), 2009.

[173] J.-M. Moret, S. Franke, H. Weisen, M. Anton, R. Behn, B. P. Duval, F. Hofmann, B. Joye, Y. Martin, C. Nieswand, Z. A. Pietrzyk, and W. van Toledo, **"Influence of plasma shape on transport in the TCV Tokamak**," *Physical Review Letters*, vol. 79, no. 11, pp. 2057–2060, September 1997.

[174] F. Hofmann, R. Behn, S. Coda, T. P. Goodman, M. Henderson, P. Lavanchy, P. Marmillod, Y. Martin, A. Martynov, J. Mlynár, J.-M. Moret, A. Pochelon, H. Reimerdes, O. Sauter, S. Alberti, C. Angioni, K. Appert, J. Bakos, P. Blanchard, P. Bosshard, R. Chavan, I. Condrea, A. Degeling, B. P. Duval, D. Fasel, J.-Y. Favez, A. Favre, I. Furno, P. Gomez, P. Gorgerat, J.-P. Hogge, P.-F. Isoz, B. Joye, I. Klimanov, J. B. Lister, X. Llobet, J.-C. Magnin, A. Manini, B. Marlétaz, J.-M. Mayor, P. Nikkola, P.-J. Paris, A. Perez, Z. A. Pietrzyk, V. Piffl, R. A. Pitts, A. Scarabosio, E. Scavino, A. Sushkov, G. Tonetti, M. Q. Tran, H. Weisen, and A. Zabolotsky, **"Stability and energy confinement of highly elongated plasmas in TCV**," *Plasma Physics and Controlled Fusion*, vol. 43, no. 12A, pp. A161–A173, December 2001, invited paper presented at the 28th EPS Conference on Controlled Fusion and Plasma Physics.

[175] A. Pochelon, T. P. Goodman, M. Henderson, C. Angioni, R. Behn, S. Coda, F. Hofmann, J.-P. Hogge, N. Kirneva, A. A. Martynov, J.-M. Moret, Z. A. Pietrzyk, F. Porcelli, H. Reimerdes, J. Rommers, E. Rossi, O. Sauter, M. Q. Tran, H. Weisen, S. Alberti, S. Barry, P. Blanchard, P. Bosshard, R. Chavan, B. P. Duval, Y. V. Esipchuck, D. Fasel, A. Favre, S. Franke, I. Furno, P. Gorgerat, P.-F. Isoz, B. Joye, J. B. Lister, X. Llobet, J.-C. Magnin, P. Mandrin, A. Manini, B. Marlétaz, P. Marmillod, Y. Martin, J.-M. Mayor, J. Mlynár, C. Nieswand, P.-J. Paris, A. Perez, R. A. Pitts, K. A. Razumova, A. Refke, E. Scavino, A. Sushkov, G. Tonetti, F. Troyon, W. van Toledo, and P. Vyas, **"Energy confinement and MHD activity in shaped TCV plasmas with localized electron cyclotron heating**," *Nuclear Fusion*, vol. 39, no. 11Y, pp. 1807–1818, November 1999, Proceedings of the 17th IAEA Fusion Energy Conference (FEC), Yokohama, Japan, October 19–24, 1998. Special issue 2.

[176] Y. Camenen, A. Pochelon, A. Bottino, S. Coda, F. Ryter, O. Sauter, R. Behn, T. P. Goodman, M. A. Henderson, A. N. Karpushov, L. Porte, and G. Zhuang, **"Electron heat transport in shaped TCV L-mode plasmas**," *Plasma Physics and Controlled Fusion*, vol. 47, no. 11, pp. 1971–1987, November 2005.

[177] Y. Camenen, A. Pochelon, R. Behn, A. Bottino, A. Bortolon, S. Coda, A. N. Karpushov, O. Sauter, and G. Zhuang, **"Impact of plasma triangularity and collisionality on electron heat transport in TCV L-mode plasmas**," *Nuclear Fusion*, vol. 47, no. 7, pp. 510–516, July 2007.

[178] A. Marinoni, S. Brunner, Y. Camenen, S. Coda, J. P. Graves, X. Lapillonne, A. Pochelon, O. Sauter, L. Villard, and the TCV team, **"The effect of plasma triangularity on turbulent transport: Modelling TCV experiments by linear and non-linear gyrokinetic simulations**," *Plasma Physics and Controlled Fusion*, vol. 51, no. 5, p. 055016 (19pp), May 2009.

[179] L. A. Artsimovich, **"Tokamak devices**," *Nuclear Fusion*, vol. 12, no. 2, pp. 215–252, March 1972, review paper.

[180] A. Zabolotsky, H. Weisen, and A. N. Karpushov, **"Influence of particle sources on electron density peaking in TCV and JET**," *Nuclear Fusion*, vol. 46, no. 5, pp. 594–607, May 2006.

[181] F. Wagner, **"Neutral particle diagnostics for ohmically and auxiliary heated tokamaks**," *Journal of Vacuum Science and Technology*, vol. 20, no. 4, pp. 1211–1217, April 1982.

[182] S. L. Davis, D. Mueller, and C. J. Keane, **"Mass resolving charge-exchange system on the poloidal divertor experiment**," *Review of Scientific Instruments*, vol. 54, no. 3, pp. 315–327, March 1983.

[183] T. H. Stix, ***Waves in plasmas***. New York: Springer Verlag, 1992.

[184] M. Bornatici, R. Cano, O. de Barbieri, and F. Engelmann, **"Electron cyclotron emission and absorption in fusion plasmas**," *Nuclear Fusion*, vol. 23, no. 9, pp. 1153–1257, September 1983.

[185] M. Brambilla, **"International series of monographs on physics**," in *Kinetic theory of plasma waves: Homogenous plasmas*. Oxford: Clarendon Press, 1998, vol. 96.

[186] C. J. Edgcombe, ***Gyrotron oscillators: Their principles and pratice***. Taylor & Francis, London, November 1993.

[187] V. V. Alikaev, G. A. Bobrovskii, V. I. Poznyak, K. A. Razumova, V. V. Sannikov, Y. A. Sokolov, and A. A. Shmarin, **"ECR plasma heating in the TM-3 tokamak in magnetic fields up to 25kOe**," *Soviet Journal of Plasma Physics*, vol. 2, no. 3, pp. 212–215, May–June 1976, translation of Fizika Plazmy.

[188] T. P. Goodman, S. Alberti, M. A. Henderson, A. Pochelon, and M. Q. Tran, **"Design and installation of the electron cyclotron wave system for the TCV tokamak**," in *Proceedings of the 19th Symposium on Fusion Technology (SOFT), September 16–20, 1996, Lisbon, Portugal*, C. Varandas, Ed., vol. 1. North-Holland Publishing Company, August 1997, pp. 565–568.

[189] T. P. Goodman and the TCV team, **"Experience in integrated control of the multi-megawatt electron cyclotron heating system on the TCV tokamak: the first decade**," *Nuclear Fusion*, vol. 48, no. 5, p. 054011 (14pp), May 2008.

[190] S. Alberti, A. Arnold, E. Borie, G. Dammertz, V. Erckmann, P. Garin, E. Giguet, S. Illy, G. L. Cloarec, Y. L. Goff, R. Magne, G. Michel, B. Piosczyk, C. Tran, M. Q. Tran, M. Thumm, and D. Wagner, **"European high-power CW gyrotron development for ECRH systems**," *Fusion Engineering and Design*, vol. 53, no. 1–4, pp. 387–397, January 2001, IAEA Technical Committee Meeting on 'ECRH Physics and Technology for Fusion Devices' and the 11th Joint Workshop on Electron Cyclotron Emission and Electron Cyclotron Resonance Heating, Oh-arai, Japan, October 4–8, 1999.

[191] T. P. Goodman, M. A. Henderson, J.-P. Hogge, Z. A. Pietrzyk, A. Pochelon, and O. Sauter, **"Poloidally Asymmetric Plasma Response during ECRH Experiments in TCV**," in *Proceedings of the 26th EPS Conference on Controlled Fusion and Plasma Physics, June 14–18, 1999*, ser. Europhysics Conference Abstracts (ECA), R. M. Pick, Ed., vol. 23J. Maastricht, The Netherlands: European Physical Society (EPS), 1999, pp. 1101–1104.

[192] M. A. Henderson, T. P. Goodman, J.-P. Hogge, Z. A. Pietrzyk, A. Pochelon, and O. Sauter, **"Poloidally asymmetric plasma response with ECH deposition near $q = 1$ in TCV**," *Fusion Engineering and Design*, vol. 53, no. 1–4, pp. 241–248, January 2001, proceedings of the IAEA Technical Committee Meeting on 'ECRH Physics and Technology for Fusion Devices' and 11th Joint Workshop on Electron Cyclotron Emission and Electron Cyclotron Resonance Heating (EC-11): October 4–8, 1999, Oh-arai, Japan.

[193] G. Wentzel, **"Eine Verallgemeinerung der Quantenbedingungen für die Zwecke der Wellenmechanik**," *Zeitschrift für Physik A Hadrons and Nuclei*, vol. 38, no. 6–7, pp. 518–529, June 1926.

[194] H. A. Kramers, **"Wellenmechanik und halbzahlige Quantisierung**," *Zeitschrift für Physik A Hadrons and Nuclei*, vol. 39, no. 10–11, pp. 828–840, October 1926.

[195] L. Brillouin, **"La mécanique ondulatoire de Schrödinger; une méthode générale de resolution par approximations successives**," *Comptes rendus hebdomadaires des séances de l'Académie des sciences*, vol. 183, pp. 24–26, 1926, Académie des sciences.

[196] M. Born and E. Wolf, ***Principles of Optics: Electromagnetic Theory of Propagation, Interference and Diffraction of Light*, 6th ed.** Cambridge University Press, 1997.

[197] T. P. Goodman, M. A. Henderson, F. Perthuisot, Z. A. Pietrzyk, A. Pochelon, M. Q. Tran, J.-P. Hogge, J.-M. Moret, O. Sauter, W. van Toledo, and K. A. Razumova, **"Influence of Polarization in ECCD Experiments in TCV**," in *Proceedings of the 2nd Europhysics Topical Conference on Radio Frequency Heating and Current Drive of Fusion Devices, Brussels, Belgium, January 20–23, 1998*, ser. Europhysics Conference Abstracts (ECA), J. Jacquinot, G. van Oost, and R. R. Weynants, Eds., vol. 22A. European Physical Society (EPS), 1998, pp. 245–248, contributed paper.

[198] V. V. Alikaev and V. V. Parail, **"Current drive by electron cyclotron waves**," *Plasma Physics and Controlled Fusion*, vol. 33, no. 13, pp. 1639–1656, November 1991, proceedings of the 18th EPS conference on Controlled Fusion and Plasma Physics, June 3–7, 1991.

[199] N. J. Fisch and A. H. Boozer, **"Creating an Asymmetric Plasma Resistivity with Waves**," *Physical Review Letters*, vol. 45, no. 9, pp. 720–722, September 1980.

[200] C. F. F. Karney and N. J. Fisch, **"Currents driven by electron-cyclotron waves**," *Nuclear Fusion*, vol. 21, no. 12, pp. 1549–1557, December 1981.

[201] O. Sauter, R. Behn, S. Coda, I. Furno, T. P. Goodman, M. Henderson, F. Hofmann, J.-P. Hogge, C. Nieswand, Z. A. Pietrzyk, A. Pochelon, H. Reimerdes, and J. Rommers, **"Current and Pressure Profile Control using ECCD and ECH in TCV**," in *Proceedings of the 26th EPS Conference on Controlled Fusion and Plasma Physics, Maastricht, June 14–18, 1999*, ser. Europhysics Conference Abstracts (ECA), vol. 23J. European Physical Society (EPS), 1999, pp. 1105–1108.

[202] O. Sauter, M. A. Henderson, F. Hofmann, T. Goodman, S. Alberti, C. Angioni, K. Appert, R. Behn, P. Blanchard, P. Bosshard, R. Chavan, S. Coda, B. P. Duval, D. Fasel, A. Favre, I. Furno, P. Gorgerat, J.-P. Hogge, P.-F. Isoz, B. Joye, P. Lavanchy, J. B. Lister, X. Llobet, J.-C. Magnin, P. Mandrin, A. Manini, B. Marlétaz, P. Marmillod, Y. Martin, J.-M. Mayor, A. A. Martynov, J. Mlynár, J.-M. Moret, C. Nieswand, P. Nikkola, P. Paris, A. Perez, Z. A. Pietrzyk, R. A. Pitts, A. Pochelon, G. Pochon, A. Refke, H. Reimerdes, J. Rommers, E. Scavino, G. Tonetti, M. Q. Tran, F. Troyon, and H. Weisen, **"Steady-State Fully Noninductive Current Driven by Electron Cyclotron Waves in a Magnetically Confined Plasma**," *Physical Review Letters*, vol. 84, no. 15, pp. 3322–3325, April 2000.

[203] M. Kikuchi and M. Azumi, **"Experimental evidence for the bootstrap current in a tokamak**," *Plasma Physics and Controlled Fusion*, vol. 37, no. 11, pp. 1215–1238, November 1995, review article.

[204] A. G. Peeters, **"The bootstrap current and its consequences**," *Plasma Physics and controlled Fusion*, vol. 42, no. 12B, pp. B231–B242, December 2000, invited paper of the 27th European Physical Society (EPS) Conference on Controlled Fusion and Plasma Physics, Budapest, Hungary, June 12–16.

[205] S. Coda, T. P. Goodman, M. A. Henderson, O. Sauter, R. Behn, A. Bottino, Y. Camenen, E. Fable, A. Martynov, P. Nikkola, A. Scarabosio, G. Zhuang, and C. Zucca, **"High-bootstrap, noninductively sustained electron internal transport barriers in the Tokamak à Configuration Variable**," *Physics of Plasmas*, vol. 12, no. 5, May 2005, proceedings of the 46th Annual Meeting of the Division of Plasma Physics of the American-Physical-Society, Savannah, Georgia, November 15–19, 2004.

[206] S. Coda, O. Sauter, M. A. Henderson, and T. P. Goodman, **"Full Bootstrap Discharge Sustainment in Steady State in the TCV Tokamak**," in *Proceedings of the 22nd IAEA Fusion Energy Conference (FEC), October 13–18, 2008, Geneva, Switzerland*, International Atomic Energy Agency (IAEA), Ed., no. EX/2-3. Vienna, Austria: International Atomic Energy Agency (IAEA), 2008, invited paper.

[207] R. H. Cohen, **"Effect of trapped electrons on current drive**," *Physics of Fluids*, vol. 30, no. 8, pp. 2442–2449, August 1987.

[208] K. Matsuda, **"Ray tracing study of the electron-cyclotron current drive in DIII-D using 60 GHz**," *IEEE transactions on plasma science*, vol. 17, no. 1, pp. 6–11, February 1989.

[209] Y. Lin-Liu, O. Sauter, R. Harvey, V. Chan, T. Luce, and R. Prater, **"Modeling of Trapped Electron Effects on Electron Cyclotron Current Drive for Recent DIII-D Experiments,"** in *Proceedings of the 26th EPS Conference on Controlled Fusion and Plasma Physics, June 14–18, 1999*, ser. Europhysics Conference Abstracts (ECA), R. Pick, Ed., vol. 23J, no. P3.078. Maastricht, The Netherlands: European Physical Society (EPS), 1999, pp. 1245–1248, contributed poster.

[210] J. E. Kinsey and M. Choi, ***The TORAY Electron Cyclotron Heating and Current Drive Code*, 1st ed.**, General Atomics, La Jolla, California, 92186, April 2003.

[211] A. Manini, J.-M. Moret, F. Ryter, and the ASDEX Upgrade Team, **"Signal processing techniques based on singular value decomposition applied to modulated ECH experiments,"** *Nuclear Fusion*, vol. 43, no. 6, pp. 490–511, June 2003.

[212] A. J. Lichtenberg, S. Sesnic, and A. W. Trivelpiece, **"Measurement of the Synchrotron Radiation Spectrum from a Hot Plasma,"** *Physical Review Letters*, vol. 13, no. 13, pp. 387–388, September 1964.

[213] A. E. Costley, R. J. Hastie, J. W. M. Paul, and J. Chamberlain, **"Electron Cyclotron Emission from a Tokamak Plasma: Experiment and Theory,"** *Physical Review Letters*, vol. 33, no. 13, pp. 758–761, September 1974.

[214] S. Coda, **"Diagnostic techniques for measuring suprathermal electron dynamics in plasmas,"** *Review of Scientific Instruments*, vol. 79, no. 10, October 2008, invited review paper presented at the 17th topical conference on high-temperature plasma diagnostics. URL: http://link.aip.org/link/?RSINAK/79/10F501/1

[215] D. J. Griffiths, ***Introduction to electrodynamics*, 3rd ed.** Upper Saddle River, New Jersey: Prentice Hall, 1999.

[216] The TFR group and I. Fidone, **"Asymmetric electron cyclotron emission from superthermal electrons in the TFR tokamak,"** *Physical Review Letters A*, vol. 24, no. 5, pp. 2861–2864, November 1981.

[217] S. Preische, P. C. Efthimion, and S. M. Kaye, **"Radially localized measurements of superthermal electrons using oblique electron cyclotron emission,"** *Physics of Plasmas*, vol. 3, no. 11, pp. 4065–4073, November 1996.

[218] ——, **"Oblique electron cyclotron emission for electron distribution studies,"** *Review of Scientific Instruments*, vol. 68, no. 1, pp. 409–414, January 1997, invited paper.

[219] H. J. Hartfuss, T. Geist, and M. Hirsch, **"Heterodyne methods in millimetre wave plasma diagnostics with applications to ECE, interferometry and reflectometry,"** *Plasma Physics and Controlled Fusion*, vol. 39, no. 11, pp. 1693–1769, November 1997, review article.

[220] P. Blanchard, **"Etudes du rayonnement suprathermique émis lors du chauffage cyclotronique électronique du plasma du tokamak TCV,"** PhD thesis, Ecole polytechnique fédérale de Lausanne (EPFL), CH-1015 Lausanne, Switzerland, July 2002, no. 2606, also available as Lausanne Report LRP 730/02.

[221] I. Klimanov, L. Porte, S. Alberti, P. Blanchard, A. Fasoli, and T. P. Goodman, **"Electron cyclotron emission spectrometry on the Tokamak à Configuration Variable,"** *Review of Scientific Instruments*, vol. 76, no. 9, September 2005.

[222] I. Klimanov, **"Reconstruction of the electron distribution function during ECRH/ECCD and magnetic reconnection events in a tokamak plasma**," PhD thesis, Ecole polytechnique fédérale de Lausanne (EPFL), CH-1015 Lausanne, Switzerland, January 2006, no. 3432, also available as Lausanne Report LRP 813/06.

[223] T. P. Goodman, V. S. Udintsev, I. Klimanov, A. Mueck, O. Sauter, and C. Schlatter, **"First measurements of oblique ECE with a real-time movable line of sight on TCV**," *Fusion Science and Technology*, vol. 53, no. 1, pp. 196–207, January 2008, conference paper presented at the 14th Joint Workshop on Electron Cyclotron Emission and Electron Cyclotron Resonance Heating, Santorini, Greece, May 9–12, 2006.

[224] Y. Camenen, F. Hofmann, A. Pochelon, A. Scarabosio, S. Alberti, G. Arnoux, P. Blanchard, S. Coda, T. Goodman, M. Henderson, E. Nelson-Melby, L. Porte, and O. Sauter, **"Current profile tailoring using localized electron cyclotron heating in highly elongated TCV plasmas**," *Nuclear Fusion*, vol. 47, no. 7, pp. 586–598, July 2007.

[225] J. P. Graves, C. Angioni, R. V. Budny, R. J. Buttery, S. Coda, L. G. Eriksson, C. G. Gimblett, T. P. Goodman, R. J. Hastie, M. A. Henderson, H. R. Koslowski, M. J. Mantsinen, A. Martynov, M. L. Mayoral, A. Mueck, M. F. F. Nave, O. Sauter, and E. Westerhof, **"Sawtooth control in fusion plasmas**," *Plasma Physics and Controlled Fusion*, vol. 47, no. 12B, pp. B121–B133, December 2005, special issue of the invited papers from the 32nd European Physical Society (EPS) Conference on Plasma Physics, Tarragona, Spain, June 27–July 1, 2005.

[226] J. I. Paley and S. Coda, **"Real time control of the plasma current and elongation in tokamaks using ECRH actuators**," *Plasma Physics and Controlled Fusion*, vol. 49, no. 10, pp. 1735–1746, October 2007.

[227] J. I. Paley, F. Felici, S. Coda, T. P. Goodman, and F. Piras, **"Real time control of the sawtooth period using EC launchers**," *Plasma Physics and Controlled Fusion*, vol. 51, no. 5, p. 055010 (9pp), May 2009.

[228] F. M. Levinton, M. C. Zarnstorff, S. H. Batha, M. Bell, R. E. Bell, R. V. Budny, C. Bush, Z. Chang, E. Fredrickson, A. Janos, J. Manickam, A. Ramsey, S. A. Sabbagh, G. L. Schmidt, E. J. Synakowski, and G. Taylor, **"Improved Confinement with Reversed Magnetic Shear in TFTR**," *Physical Review Letters*, vol. 75, no. 24, pp. 4417–4420, December 1995.

[229] C. Gormezano, A. C. C. Sips, T. C. Luce, S. Ide, A. Becoulet, X. Litaudon, A. Isayama, J. Hobirk, M. R. Wade, T. Oikawa, R. Prater, A. Zvonkov, B. Lloyd, T. Suzuki, E. Barbato, P. Bonoli, C. K. Phillips, V. Vdovin, E. Joffrin, T. Casper, J. Ferron, D. Mazon, D. Moreau, R. Bundy, C. Kessel, A. Fukuyama, N. Hayashi, F. Imbeaux, M. Murakami, A. Polevoi, and H. S. John, **"Steady state operation**," *Nuclear Fusion*, vol. 47, no. 6, pp. S285–S336, June 2007, chapter 6 of the special issue on the progress in ITER physics basis.

[230] R. C. Wolf, **"Internal transport barriers in tokamak plasmas**," *Plasma Physics and Controlled Fusion*, vol. 45, no. 1, pp. R1–R91, January 2003, review article.

[231] S. Coda, E. Asp, E. Fable, T. P. Goodman, O. Sauter, V. S. Udintsev, R. Behn, M. A. Henderson, A. Marinoni, G. P. Turri, C. Zucca, and the TCV team, **"The physics of electron internal transport barriers in the TCV tokamak**," *Nuclear Fusion*, vol. 47, no. 7, pp. 714–720, July 2007.

[232] M. A. Henderson, Y. Camenen, S. Coda, T. P. Goodman, P. Nikkola, A. Pochelon, O. Sauter, and the TCV Team, **"Rapid and Localized Electron Internal-Transport-Barrier Formation During Shear Inversion in Fully Noninductive TCV Discharges**," *Physical Review Letters*, vol. 93, no. 21, November 2004.

[233] P. H. Rebut, P. P. Lallia, and M. L. Watkins, **"The critical temperature gradient model of plasma transport: Applications to JET and future tokamaks**," in *Plasma Physics and Controlled Nuclear Fusion Research 1988. Proceedings of the twelfth International Conference on Plasma Physics and Controlled Nuclear Fusion Research, Nice, France, October 12–19, 1988*, ser. Nuclear Fusion Supplement 1989, International Atomic Energy Agency (IAEA), Ed., vol. 2. Vienna, Austria: International Atomic Energy Agency (IAEA), October 1989, pp. 191–200, IAEA-CN-50/D-IV-1.

[234] T. P. Goodman, R. Behn, Y. Camenen, S. Coda, E. Fable, M. A. Henderson, P. Nikkola, J. Rossel, O. Sauter, A. Scarabosio, C. Zucca, S. Alberti, P. Amorim, Y. Andrèbe, K. Appert, G. Arnoux, A. Bortolon, A. Bottino, R. Chavan, I. Condrea, E. Droz, B. P. Duval, P. Etienne, D. Fasel, A. Fasoli, B. Gulejová, J.-P. Hogge, J. Horacek, P.-F. Isoz, B. Joye, A. N. Karpushov, S. H. Kim, I. Klimanov, P. Lavanchy, J. B. Lister, X. Llobet, T. Madeira, J.-C. Magnin, A. Marinoni, J. Márki, B. Marlétaz, P. Marmillod, Y. Martin, A. Martynov, M. Maslov, J.-M. Mayor, J.-M. Moret, A. Mück, P. J. Paris, I. Pavlov, A. Perez, R. A. Pitts, A. Pochelon, L. Porte, C. Schlatter, K. Schombourg, H. Shidara, M. Siegrist, U. Siravo, A. V. Sushkov, G. Tonetti, M. Q. Tran, H. Weisen, M. Wischmeier, A. Zabolotsky, G. Zhuang, and A. Zhuchkova, **"Safety factor profile requirements for electron ITB formation in TCV**," *Plasma Physics and Controlled Fusion*, vol. 47, no. 12B, pp. B107–B120, December 2005, special issue of the invited papers from the 32nd European Physical Society (EPS) Conference on Plasma Physics, Tarragona, Spain, June 27–July 1, 2005.

[235] M. A. Henderson, R. Behn, S. Coda, I. Condrea, B. P. Duval, T. P. Goodman, A. N. Karpushov, Y. Martin, A. Martynov, J.-M. Moret, P. Nikkola, L. Porte, O. Sauter, A. Scarabosio, G. Zhuang, and the TCV team, **"Control of electron internal transport barriers in TCV**," *Plasma Physics and Controlled Fusion*, vol. 46, no. 5A, pp. A275–A284, May 2004, special issue of the 9th IAEA Technical committee meeting on H-mode physics and transport barriers.

[236] P. Nikkola, **"The effect of electron transport on electron cyclotron current drive in tokamak plasmas**," PhD thesis, Ecole polytechnique fédérale de Lausanne (EPFL), CH-1015 Lausanne, Switzerland, 2004, no. 3048, also available as Lausanne Report LRP 793/04.

[237] N. J. Fisch, **"Conductivity of rf-heated plasma**," *Physics of Fluids*, vol. 28, no. 1, pp. 245–247, January 1985.

[238] C. F. Kennel and F. Engelmann, **"Velocity space diffusion from weak plasma turbulence in a magnetic field**," *Physics of Fluids*, vol. 9, no. 12, pp. 2337–2388, December 1966.

[239] A. G. Peeters and D. Strintzi, **"The Fokker-Planck equation, and its application in plasma physics**," *Annalen der Physik*, vol. 17, no. 2–3, pp. 142–157, February 2008.

[240] R. W. Harvey and M. G. McCoy, **"The CQL3D Fokker–Planck Code**," in *Proceedings of the IAEA Technical Committee Meeting on Advances in Simulation and Modeling of Thermonuclear Plasmas, Montreal, Canada, 1992*, International Atomic Energy Agency

(IAEA), Ed. Vienna, Austria: International Atomic Energy Agency (IAEA), 1993, pp. 489–526, also available as General Atomics Report GA-A20978, 1992.

[241] R. W. Harvey, O. Sauter, R. Prater, and P. Nikkola, **"Radial transport and electron-cyclotron-current drive in the TCV and DIII-D tokamaks**," *Physical Review Letters*, vol. 88, no. 20, May 2002.

[242] S. Coda, S. Alberti, P. Blanchard, I. Klimanov, J.-M. Moret, and P. Weber, **"Dynamical Studies of Suprathermal Electron Relaxation by Modulated ECCD**," in *Proceedings of the 30th EPS Conference on Controlled Fusion and Plasma Physics, St. Petersburg, Russian Federation, July 7–11, 2003*, ser. Europhysics Conference Abstracts (ECA), vol. 27A, no. P-3.134. European Physical Society (EPS), 2003.

[243] S. Coda, Y. Peysson, L. Delpech, T. P. Goodman, M. A. Henderson, J.-P. Hogge, X. Llobet, B. Marlétaz, Z. A. Pietrzyk, A. Pochelon, G. Pochon, O. Sauter, and H. Weisen, **"Measurements of Hard X–Ray Emission Profiles in the TCV Tokamak during Electron Cyclotron Heating and Current Drive**," in *Proceedings of the 26th EPS Conference on Controlled Fusion and Plasma Physics, June 14–18, 1999*, ser. Europhysics Conference Abstracts (ECA), vol. 23J. Maastricht, The Netherlands: European Physical Society (EPS), 1999, pp. 1097–1100.

[244] S. Coda, I. Klimanov, S. Alberti, G. Arnoux, P. Blanchard, and A. Fasoli, **"The effect of ECRH on the electron velocity distribution function**," *Plasma Physics and Controlled Fusion*, vol. 48, no. 12B, pp. B359–B369, December 2006.

[245] P. Nikkola, O. Sauter, R. Behn, S. Coda, I. Condrea, T. Goodman, M. Henderson, and R. Harvey, **"Modelling of the electron cyclotron current drive experiments in the TCV tokamak**," *Nuclear Fusion*, vol. 43, no. 11, pp. 1343–1352, November 2003.

[246] P. Blanchard, H. Weisen, S. Alberti, S. Coda, P. Gomez, and T. Goodman, **"Measurements of electron cyclotron emission from non-Maxwellian electron distributions in TCV plasmas with ECH and ECCD**," in *Proceedings of the 28th EPS Conference on Controlled Fusion and Plasma Physics, June 18–22, 2001*, ser. Europhysics Conference Abstracts (ECA), C. Silva, C. Varandas, and D. Campbell, Eds., vol. 25A, no. P1.077, Instituto Superior Tecnico, Centro de Fusao Nuclear. Madeira Tecnopolo, Funchal, Portugal: European Physical Society (EPS), December 2001, pp. 309–312.

[247] R. W. Harvey, M. G. McCoy, and G. D. Kerbel, **"Power Dependence of Electron-Cyclotron Current Drive for Low- and High-Field Absorption in Tokamaks**," *Physical Review Letters*, vol. 62, no. 4, pp. 426–429, January 1989.

[248] G. Zhuang, R. Behn, I. Klimanov, P. Nikkola, and O. Sauter, **"Influence of non-Maxwellian velocity distributions during ECRH and ECCD on electron temperature measurements by Thomson scattering**," *Plasma Physics and Controlled Fusion*, vol. 47, no. 9, pp. 1539–1558, September 2005.

[249] P. Blanchard, S. Alberti, S. Coda, H. Weisen, P. Nikkola, and I. Klimanov, **"High field side measurements of non-thermal electron cyclotron emission on TCV plasmas with ECH and ECCD**," *Plasma Physics and Controlled Fusion*, vol. 44, no. 10, pp. 2231–2249, October 2002.

[250] R. M. J. Sillen, M. A. F. Allaart, W. J. Goedheer, and A. Kattenberg, **"NOTEC, a code to simulate electron cyclotron emission spectra of plasmas which include non-thermal populations**," Associate EURATOM-FOM, FOM-Instituut voor Plasmafysica, Rijnhuizen, Nieuwegein, Nederland, Rijnhuizen Report 86-165, October 1987.

[251] V. S. Udintsev, **"Electron Temperature Dynamics of TEXTOR Plasmas**," PhD thesis, University of Utrecht, The Netherlands, November 2003.

[252] V. S. Udintsev, M. J. van de Pol, A. J. H. Donné, J. W. Oosterbeek, and A. Krämer-Flecken, **"New ECE diagnostics for the TEXTOR-94 tokamak**," *Review of Scientific Instruments*, vol. 72, no. 1, pp. 359–362, January 2001, Proceedings of the 13th Topical Conference on High-Temperature Plasma Diagnostics, Tucson, Arizona, June 18–22, 2000.

[253] V. S. Udintsev, G. Turri, E. Asp, C. Schlatter, T. P. Goodman, O. Sauter, H. Weisen, P. Blanchard, S. Coda, B. P. Duval, E. Fable, A. Gudozhnik, P. F. Isoz, M. A. Henderson, I. Klimanov, X. Llobet, P. Marmillod, A. Mueck, L. Porte, H. Shidara, G. Giruzzi, M. Goniche, and F. Turco, **"Recent Electron Cyclotron Emission Results on TCV**," *Fusion Science and Technology*, vol. 52, no. 2, pp. 161–168, August 2007.

[254] D. B. Batchelor, R. C. Goldfinger, and H. Weitzner, **"Ray Tracing Near the Electron Cyclotron Frequency with Application to EBT**," *IEEE transactions on plasma science*, vol. PS-8, no. 2, pp. 78–89, June 1980.

[255] T. P. Goodman, V. S. Udintsev, F. Felici, C. Zucca, and C. Schlatter, **"Co- and Counter viewing oblique ECE measurements during ECH and ECCD on the TCV tokamak**," in *Proceedings of the 34th EPS Conference on Plasma Physics, July 2–6, 2007*, ser. Europhysics Conference Abstracts (ECA), P. Gkasior and J. Wołowski, Eds., vol. 31F, no. P-2.147. Warsaw, Poland: European Physical Society (EPS), 2007.

[256] S. Alberti, T. Goodman, M. Henderson, A. Manini, J.-M. Moret, P. Gomez, P. Blanchard, S. Coda, O. Sauter, Y. Peysson, and the TCV team, **"Full absorption of third harmonic ECH in TCV tokamak plasmas in the presence of second harmonic ECCD**," *Nuclear Fusion*, vol. 42, no. 1, pp. 42–45, January 2002.

[257] I. Furno, C. Angioni, F. Porcelli, H. Weisen, R. Behn, T. P. Goodman, M. A. Henderson, Z. A. Pietrzyk, A. Pochelon, H. Reimerdes, and E. Rossi, **"Understanding sawtooth activity during intense electron cyclotron heating experiments on TCV**," *Nuclear Fusion*, vol. 41, no. 4, pp. 403–420, April 2001.

[258] S. von Goeler, W. Stodiek, and N. Sauthoff, **"Studies of Internal Disruptions and m=1 Oscillations in Tokamak Discharges with Soft X-Ray Techniques**," *Physical Review Letters*, vol. 33, no. 20, pp. 1201–1203, November 1974. URL: http://link.aps.org/doi/10.1103/PhysRevLett.33.1201

[259] V. A. Vershkov and S. V. Mirnov, **"Role of impurities in current Tokamak experiments**," *Nuclear Fusion*, vol. 14, no. 3, pp. 383–395, June 1974.

[260] B. B. Kadomtsev, **"On disruptive instability in tokamaks**," *Fizika Plazmy*, vol. 1, no. 5, pp. 710–715, September-October 1975, in russian.

[261] A. Sykes and J. A. Wesson, **"Relaxation Instability in Tokamaks**," *Physical Review Letters*, vol. 37, no. 3, pp. 140–143, July 1976.

[262] J. Birn and E. R. Priest, Eds., ***Reconnection of Magnetic Fields: Magnetohydrodynamics and Collisionless Theory and Observations*, 1st ed.** Cambridge University Press, 2007.

[263] D. Biskamp, ***Magnetic reconnection in plasmas*, 1st ed.**, ser. Cambridge Monographs on Plasma Physics, W. Grossman, D. Papadopoulos, R. Sagdeev, and K. Schindler, Eds. Cambridge University Press, 2000, vol. 3.

[264] H. Soltwisch, "**Current distribution measurement in a tokamak by FIR polarimetry**," *Review of Scientific Instruments*, vol. 57, no. 8, pp. 1939–1944, August 1986.

[265] R. J. Hastie, "**Sawtooth Instability in Tokamak Plasmas**," *Astrophysics and Space Science*, vol. 256, no. 1–2, pp. 177–204, March 1997.

[266] S. Migliuolo, "**Theory of ideal and resistive $m = 1$ modes in tokamaks**," *Nuclear Fusion*, vol. 33, no. 11, pp. 1721–1754, November 1993.

[267] I. Furno, "**Fast transient transport phenomena measured by soft X-ray emission in TCV tokamak plasmas**," PhD thesis, Ecole polytechnique fédérale de Lausanne (EPFL), CH-1015 Lausanne, Switzerland, 2001, no. 2434, also available as Lausanne Report LRP 703/01.

[268] B. Coppi, R. Galvão, R. Pellat, M. Rosenbluth, and P. Rutherford, "**Resistive internal kink modes**," *Soviet Journal of Plasma Physics*, vol. 2, no. 6, pp. 533–535, November 1976.

[269] F. Porcelli, D. Boucher, and M. N. Rosenbluth, "**Model for the sawtooth period and amplitude**," *Plasma Physics and Controlled Fusion*, vol. 38, no. 12, pp. 2163–2186, December 1996.

[270] F. Porcelli, E. Rossi, G. Cima, and A. Wootton, "**Macroscopic Magnetic Islands and Plasma Energy Transport**," *Physical Review Letters*, vol. 82, no. 7, pp. 1458–1461, February 1999.

[271] F. Porcelli, A. Airoldi, C. Angioni, A. Bruschi, P. Buratti, F. Califano, S. Cirant, I. Furno, D. Grasso, E. Lazzaro, A. A. Martynov, M. Ottaviani, F. Pegoraro, G. Ramponi, E. Rossi, O. Sauter, C. Tebaldi, and O. Tudisco, "**Modelling of macroscopic magnetic islands in tokamaks**," *Nuclear Fusion*, vol. 41, no. 9, pp. 1207–1218, September 2001.

[272] F. Porcelli, S. Annibaldi, D. Borgogno, P. Buratti, F. Califano, R. Coelho, E. Giovannozzi, D. Grasso, E. Lazzaro, F. Pegoraro, M. Ottaviani, and A. Smolyakov, "**Predicting the behaviour of magnetic reconnection processes in fusion burning plasma experiments**," *Nuclear Fusion*, vol. 44, no. 2, pp. 362–371, February 2004.

[273] H. Reimerdes, A. Pochelon, O. Sauter, T. P. Goodman, M. A. Henderson, and A. Martynov, "**Effect of triangular and elongated plasma shape on the sawtooth stability**," *Plasma Physics and Controlled Fusion*, vol. 42, no. 6, pp. 629–639, June 2000.

[274] A. Pochelon, F. Hofmann, H. Reimerdes, C. Angioni, R. Behn, R. Duquerroy, I. Furno, P. Gomez, T. Goodman, M. Henderson, A. Martynov, P. Nikkola, O. Sauter, and A. Sushkov, "**Plasma shape effects on sawtooth/internal kink stability and plasma shaping using electron cyclotron wave current profile tailoring in TCV**," *Nuclear Fusion*, vol. 41, no. 11, pp. 1663–1669, November 2001.

[275] O. Sauter, C. Angioni, D. Boucher, I. Furno, A. Pochelon, and F. Porcelli, **"Sawtooth period simulations of TCV discharges**," in *Theory of fusion plasmas*, ser. International school of plasma physics Piero Caldirola, J. W. Connor, E. Sindoni, and J. Vaclavik, Eds., vol. 18. Joint Varenna-Lausanne International Workshop on the Theory of Fusion Plasmas, Varenna, Italy, August 31–September 4, 1998, 1999, pp. 403–408.

[276] H. Reimerdes, I. Furno, F. Hofmann, A. Martynov, A. Pochelon, and O. Sauter, **"Sawtooth behaviour in highly elongated TCV plasmas**," *Plasma Physics and Controlled Fusion*, vol. 48, no. 11, pp. 1621–1632, November 2006.

[277] M. A. Henderson, S. Alberti, C. Angioni, G. Arnoux, R. Behn, P. Blanchard, P. Bosshard, Y. Camenen, S. Coda, I. Condrea, T. P. Goodman, F. Hofmann, J.-P. Hogge, A. N. Karpushov, A. Manini, A. Martynov, J.-M. Moret, P. Nikkola, E. Nelson-Melby, A. Pochelon, L. Porte, O. Sauter, S. M. Ahmed, Y. Andrèbe, K. Appert, R. Chavan, A. Degeling, B. P. Duval, P. Etienne, D. Fasel, A. Fasoli, J.-Y. Favez, I. Furno, J. Horacek, P. Isoz, B. Joye, I. Klimanov, P. Lavanchy, J. B. Lister, X. Llobet, J.-C. Magnin, B. Marlétaz, P. Marmillod, Y. Martin, J.-M. Mayor, J. Mylnar, P. J. Paris, A. Perez, Y. Peysson, R. A. Pitts, D. Raju, H. Reimerdes, A. Scarabosio, E. Scavino, S. H. Seo, U. Siravo, A. Sushkov, G. Tonetti, M. Q. Tran, H. Weisen, M. Wischmeier, A. Zabolotsky, and G. Yhuang, **"Recent results from the electron cyclotron heated plasmas in Tokamak à Configuration Variable (TCV)**," *Physics of Plasmas*, vol. 10, no. 5, pp. 1796–1802, May 2003, invited paper at the 44th Annual Meeting of the APS division of Plasma Physics, November 11–15, 2002, Orlando, Florida, United States of America.

[278] Z. A. Pietrzyk, C. Angioni, R. Behn, S. Coda, T. P. Goodman, M. A. Henderson, F. Hofmann, J.-P. Hogge, J.-M. Moret, A. Pochelon, H. Reimerdes, O. Sauter, and H. Weisen, **"Central electron temperature enhancements due to sawtooth stabilization during counter electron cyclotron current drive in Tokamak à Configuration Variable**," *Physics of Plasmas*, vol. 7, no. 7, pp. 2909–2914, July 2000.

[279] C. Angioni, T. Goodman, M. Henderson, and O. Sauter, **"Effects of localized electron heating and current drive on the sawtooth period**," *Nuclear Fusion*, vol. 43, no. 6, pp. 455–468, June 2003.

[280] P. Savrukhin, **"Generation of Suprathermal Electrons during Magnetic Reconnection at the Sawtooth Crash and Disruption Instability in the T-10 Tokamak**," *Physical Review Letters*, vol. 86, pp. 3036–3039, 2001.

[281] I. Klimanov, S. Alberti, P. Blanchard, S. Coda, A. Fasoli, and G. Zhuang, **"Reconstruction of the electron distribution function during ECCD and magnetic reconnection events**," October 2003, poster presented at the 45th Annual APS Division of Plasma Physics Meeting 2003, Albuquerque, New Mexico, USA.

[282] I. Klimanov, A. Fasoli, and T. P. Goodman, **"Generation of suprathermal electrons during sawtooth crashes in a tokamak plasma**," *Plasma Physics and Controlled Fusion*, vol. 49, no. 3, pp. L1–L6, March 2007, brief communication.

[283] H. Dreicer, **"Electron and Ion Runaway in a Fully Ionized Gas. II**," *Physical Review*, vol. 117, no. 2, pp. 329–342, January 1960.

[284] W. W. Heidbrink and G. J. Sadler, **"The behaviour of fast ions in tokamak experiments**," *Nuclear Fusion*, vol. 34, no. 4, pp. 535–615, April 1994, see also the corrigendum in Nuclear Fusion, vol. 35, no. 2, p. 243, February 1995.

[285] A. Fasoli, C. Gormenzano, H. Berk, B. Breizman, S. Briguglio, D. Darrow, N. Gorelenkov, W. Heidbrink, A. Jaun, S. Konovalov, R. Nazikian, J.-M. Noterdaeme, S. E. Sharapov, K. Shinohara, D. Testa, K. Tobita, Y. Todo, G. Vlad, and F. Zonca, **"Progress in the ITER Physics Basis, chapter 5: Physics of energetic ions**," *Nuclear Fusion*, vol. 47, no. 6, pp. S264–S284, June 2007.

[286] J. A. Miller, P. J. Cargill, E. A. Gordon, G. D. Holman, B. R. Dennis, T. N. LaRosa, R. M. Winglee, S. G. Benka, and S. Tsuneta, **"Critical issues for understanding particle acceleration in impulsive solar flares**," *Journal of Geophysical Research, Space Physics*, vol. 102, no. A7, pp. 14 631–14 659, July 1997.

[287] L. O. Drury, **"Acceleration of cosmic rays**," *Contemporary Physics*, vol. 35, no. 4, pp. 231–242, July 1994.

[288] R. D. Sharp, R. G. Johnson, and E. G. Shelley, **"Observation of an Ionospheric Acceleration Mechanism Producing Energetic (keV) Ions Primarily Normal to the Geomagnetic Field Direction**," *Journal of Geophysical Research - Space Physics*, vol. 82, no. 22, pp. 3324–3328, August 1977.

[289] P. C. Thonemann, E. P. Butt, R. Carruthers, A. N. Dellis, D. W. Fry, A. Gibson, G. N. Harding, D. J. Lees, R. W. P. McWhirter, R. S. Pease, S. A. Ramsden, and S. Ward, **"Production of high temperatures and nuclear reactions in a gas discharge**," *Nature*, vol. 181, no. 4604, pp. 217–220, 1958.

[290] T. P. Goodman, M. A. Henderson, Z. A. Pietrzyk, A. Pochelon, M. Tran, J.-P. Hogge, J.-M. Moret, H. Reimerdes, O. Sauter, and W. van Toledo, **"Observations of up–down differences in plasma response during ECRH on TCV**," in *Proceedings of the Joint 1998 International Congress on Plasma Physics and the 25th EPS Conference on Controlled Fusion and Plasma Physics, June 29–July 3, 1998*, P. Pavlo, Ed., vol. 22C. Praha, Czech Republic: European Physical Society, 1998, pp. 1324–1327.

[291] A. N. Karpushov, S. Coda, and B. P. Duval, **"Observation of suprathermal ions in the TCV during ECH and ECCD**," in *Proceedings of the* 30th *EPS Conference on Controlled Fusion and Plasma Physics, St. Petersburg, July 7–11, 2003*, ser. Europhysics Conference Abstracts (ECA), R. Koch and S. Lebedev, Eds., vol. 27A. European Physical Society (EPS), 2003, p. P3.123.

[292] A. N. Karpushov, B. P. Duval, T. P. Goodman, and C. Schlatter, **"Non-Maxwellian Ion Energy Distribution in ECH-heated plasmas on TCV**," in *Proceedings of the 33rd EPS Conference on Plasma Physics, Rome, Italy, June 19–23, 2006*, ser. Europhysics Conference Abstracts (ECA), F. D. Marco and G. Vlad, Eds., vol. 30I, no. P-1.152. European Physical Society (EPS), 2006, contributed poster.

[293] C. Schlatter, B. P. Duval, A. N. Karpushov, E. Asp, S. Coda, and V. S. Udintsev, **"Conditions for anomalous energy and momentum transfer from electrons to ions in ECCD discharges on TCV**," in *Proceedings of the 33rd EPS Conference on Plasma Physics, Rome, Italy, June 19–23, 2006*, no. P-1.149, 2006, contributed paper.

[294] T. P. Donaldson, **"Theory of foil-absorption techniques for plasma X-ray continuum measurements**," *Plasma Physics*, vol. 20, no. 12, pp. 1279–1289, December 1978.

[295] E. Westerhof, R. W. Polman, G. M. D. Hogeweij, J. Lok, E. Min, A. A. M. Oomens, F. C. Schüller, and the RTP Team, **"Further analysis of the electron cyclotron current drive experiments on RTP**," *Fusion Engineering and Design*, vol. 53, no. 1–4, pp. 259–266, January 2001.

[296] P. Nikkola and O. Sauter, **"Numerical and experimental studies of electron cyclotron current drive efficiency in plasmas with nearly zero ohmic current**," in *Theory of fusion plasmas: Proceedings of the joint Varenna-Lausanne international workshop on theory of fusion plasmas held at Villa Monastero, Varenna, Italy, August 28–September 1, 2000*, J. W. Connor, Ed., Istituto di Fisica del Plasma Piero Caldirola del CNR-Milano and Centre de Recherches en Physique des Plasmas CRPP-EPFL. Bologna: Editrice Compositori, 2000.

[297] H. Weisen, I. Furno, S. Alberti, C. Angioni, K. Appert, R. Behn, P. Blanchard, P. Bosshard, S. Coda, I. Condrea, A. Degeling, B. P. Duval, P. Gomez, T. P. Goodman, M. A. Henderson, F. Hofmann, J.-P. Hogge, B. Joye, J. B. Lister, X. Llobet, A. Manini, Y. Martin, A. Martynov, J.-M. Mayor, E. Minardi, J. Mlynár, J.-M. Moret, P. Nikkola, Z. A. Pietrzyk, R. A. Pitts, A. Pochelon, H. Reimerdes, J. H. Rommers, O. Sauter, E. Scavino, G. Tonetti, M. Q. Tran, and A. Zabolotsky, **"Shape dependence of sawtooth inversion radii and profile peaking factors in TCV L mode plasmas**," *Nuclear Fusion*, vol. 42, no. 2, pp. 136–142, February 2002.

[298] Z. A. Pietrzyk, A. Pochelon, T. Goodman, M. Henderson, J.-P. Hogge, H. Reimerdes, M. Tran, R. Behn, I. Furno, J.-M. Moret, C. Nieswand, J. Rommers, O. Sauter, W. van Toledo, H. Weisen, F. Porcelli, and K. Razumova, **"Behaviour of central plasma relaxation oscillations during localized electron cyclotron heating on the TCV tokamak**," *Nuclear Fusion*, vol. 39, no. 5, pp. 587–611, May 1999.

[299] D. J. Campbell, D. F. H. Start, J. A. Wesson, D. V. Bartlett, V. P. Bhatnagar, M. Bures, J. G. Cordey, G. A. Cottrell, P. A. Dupperex, A. W. Edwards, C. D. Challis, C. Gormezano, C. W. Gowers, R. S. Granetz, J. H. Hammen, T. Hellsten, J. Jacquinot, E. Lazzaro, P. J. Lomas, N. L. Cardozo, P. Mantica, J. A. Snipes, D. Stork, P. E. Stott, P. R. Thomas, E. Thompson, K. Thomsen, and G. Tonetti, **"Stabilization of Sawteeth with Additional Heating in the JET Tokamak**," *Physical Review Letters*, vol. 60, no. 21, pp. 2148–2151, May 1988.

[300] F. Porcelli, **"Fast particle stabilisation**," *Plasma Physics and Controlled Fusion*, vol. 33, no. 13, pp. 1601–1620, November 1991, invited paper at the 18th European Physical Society Plasma Physics Division Conference on Controlled Fusion and Plasma Physics, June 3–7, 1991.

[301] ITER Physics Expert Group on Disruptions, Plasma Control, and MHD and ITER Physics Basis Editors, **"ITER Physics Basis, chapter 3: MHD stability, operational limits and disruptions**," *Nuclear Fusion*, vol. 39, no. 12, pp. 2251–2389, December 1999.

[302] A. Pankin, G. Bateman, R. Budny, A. Kritz, D. McCune, A. Polevoi, and I. Voitsekhovitch, **"Numerical techniques used in Neutral Beam Injection modules**," *Computer Physics Communications*, vol. 164, no. 1–3, pp. 421–427, December 2004, proceedings of the 18th International Conferene on the Numerical Simulation of Plasmas, Falmouth, USA, September 7–10, 2003.

[303] J. G. Cordey and M. J. Houghton, **"Problems associated with injection of a high-energy neutral beam into a plasma**," *Nuclear Fusion*, vol. 13, no. 2, pp. 215–220, March 1973.

[304] T. H. Stix, **"Heating of toroidal plasmas by neutral injection**," *Plasma Physics*, vol. 14, no. 4, pp. 367–384, April 1972.

[305] A. N. Karpushov, P. Bosshard, B. P. Duval, and J. Mlynár, **"Relaxation of the DNBI Deposited Particles in the TCV Plasmas**," in *Proceedings of the 29th EPS Conference on Plasma Physics and Controlled Fusion, Montreux, Switzerland, June 17–21, 2002*, ser. Europhysics Conference Abstracts, vol. 26B, 2002, pp. P–4.119.

[306] A. N. Karpushov, A. Anikeev, K. Noack, and S. Strogalova, **"Integrated transport code system for multicomponent high-β plasmas in the gas-dynamic trap**," in *Proceedings of the 27th EPS Conference on Controlled Fusion and Plasma Physics, Budapest, June 12–16, 2000*, ser. Europhysics Conference Abstracts (ECA), vol. 24B. European Physical Society (EPS), 2000, pp. 920–923.

[307] **R. A. Pitts**, private communication, April 2006.

[308] A. Manini, J.-M. Moret, S. Alberti, T. P. Goodman, and M. A. Henderson, **"Modulated ECH power absorption measurements using a diamagnetic loop in the TCV tokamak**," *Plasma Physics and Controlled Fusion*, vol. 44, no. 2, pp. 139–157, February 2002.

[309] M. Anton, H. Weisen, M. Dutch, W. von der Linden, F. Buhlmann, R. Chavan, B. Marletaz, P. Marmillod, and P. Paris, **"X-ray tomography on the TCV tokamak**," *Plasma Physics and Controlled Fusion*, vol. 38, no. 11, pp. 1849–1878, November 1996.

[310] K. F. Mast, J. C. Vallet, C. Andelfinger, P. Betzler, H. Kraus, and G. Schramm, **"A low noise highly integrated bolometer array for absolute measurement of VUV and soft X-radiation**," *Review of Scientific Instruments*, vol. 62, no. 3, pp. 744–750, March 1991.

[311] J. Mlynár, I. Furno, B. Joye, and A. Refke, **"Bolometry on the TCV Tokamak**," Centre de recherches en physique des plasmas, Ecole polytechnique fédérale de Lausanne, CH-1015 Lausanne, Switzerland, Internal CRPP report INT 196/99, 1999.

[312] C. Schlatter and J. Mlynár, **"Fast-Algorithm Bolometric Computer Aided Tomography (FABCAT)**," CRPP-EPFL, CH-1015 Lausanne, Switzerland, Internal report INT 205/02, 2002.

[313] G. Lapenta and P. Quarati, **"Analysis of non-Maxwellian fusion reaction rates with electron screening**," *Zeitschrift für Physik A Hadrons and Nuclei*, vol. 346, no. 3, pp. 243–250, September 1993.

[314] M. Porkolab and R. P. H. Chang, **"Nonlinear wave effects in laboratory plasmas: A comparison between theory and experiment**," *Reviews of Modern Physics*, vol. 50, no. 4, pp. 745–795, October 1978.

[315] I. B. Bernstein, **"Waves in a plasma in a magnetic field**," *Physical Review*, vol. 109, no. 1, pp. 10–21, January 1958.

[316] J. A. Heikkinen and S. J. Karttunen, **"Parametric scattering in electron-cyclotron resonance heating**," *Physics of Fluids*, vol. 29, no. 4, pp. 1120–1126, April 1986.

[317] F. S. McDermott, G. Bekefi, K. E. Hackett, J. S. Levine, and M. Porkolab, **"Observation of the parametric decay instability during electron cyclotron resonance heating on the Versator II tokamak**," *Physics of Fluids*, vol. 25, no. 9, pp. 1488–1490, September 1982.

[318] D. G. Bulyginsky, V. K. Gusev, V. V. Djachenko, M. A. Irzak, M. Y. Kantor, M. M. Larionov, L. S. Levin, G. A. Serebreny, and N. V. Shustova, **"ECR-Heating of plasma in FT-1 tokamak and its influence on the ion component**," in *Proceedings of the 11th European Conference on Controlled Fusion and Plasma Physics, Aachen, Germany, September 5–9, 1983*, ser. Europhysics Conference Abstracts (ECA), S. Methfessel, Ed., vol. 7D, part I, no. E34. European Physical Society (EPS), 1983, pp. 457–460, contributed paper.

[319] V. Erckmann, G. Janzen, W. Kasparek, G. Müller, E. Räuchle, P. Schüller, K. Schwörer, M. Thumm, R. Wilhelm, and the W VII-A team, **"Wave absorption and transport studies on ECR-heated stellerator plasmas in W VII-A**," in *Plasma physics and Controlled Nuclear Fusion research 1984*, ser. Nuclear Fusion Supplement, International Atomic Energy Agency (IAEA), Ed., vol. 2, no. IAEA-CN-44/D-I-5, 1985, pp. 419–429, proceedings of the tenth IAEA conference, London, September 12–19, 1984.

[320] Z. A. Pietrzyk, A. Pochelon, R. Behn, A. Bondeson, M. Dutch, T. P. Goodman, M. Q. Tran, and D. R. Whaley, **"Electron cyclotron resonance heating on the TCA tokamak**," *Nuclear Fusion*, vol. 33, no. 2, pp. 197–209, February 1993.

[321] A. Pochelon, T. P. Goodman, D. Whaley, M. Q. Tran, A. Perrenoud, D. Reinhard, B. Jödicke, H. G. Mathews, W. Kasparek, and M. Thumm, **"39GHz ECRH system for breakdown studies on the TCA tokamak**," in *Fusion Technology 1990*, B. E. Keen, M. Huguet, and R. Hemsworth, Eds., vol. 2. Elsevier science publishers, 1991, pp. 1075–1079, proceeding of the 16th Symposium on Fusion Technology (SOFT), London, United Kingdom, September 3–7, 1990.

[322] T. H. Stix, **"Radiation and absorption via mode conversion in an inhomogenous collision-free plasma**," *Physical Review Letters*, vol. 15, no. 23, pp. 878–882, December 1965.

[323] M. A. Henderson, T. P. Goodman, R. Behn, S. Coda, J.-P. Hogge, Y. Martin, Y. Peysson, Z. A. Pietrzyk, A. Pochelon, O. Sauter, and M. Q. Tran, **"Recent Results in ECH and ECCD experiments in the TCV tokamak**," Centre de Recherches en Physique des Plasmas (CRPP), CH-1015 Lausanne, Switzerland, Lausanne Report LRP 643/99, August 1999, paper presented at the Fourth International Workshop on Strong Microwaves in Plasmas, August 1–8, 1999, Nizhny Novgorod, Russia.

[324] T. Maekawa, T. Kobayashi, S. Yamaguchi, K. Yoshinaga, H. Igami, M. Uchida, H. Tanaka, M. Asakawa, and Y. Terumichi, **"Doppler-Shifted Cyclotron Absorption of Electron Bernstein Waves via $N_{\|}$-Upshift in a Tokamak Plasma**," *Physical Review Letters*, vol. 86, no. 17, pp. 3783–3786, April 2001.

[325] V. Shevchenko, Y. Baranov, M. O'Brien, and A. Saveliev, **"Generation of Noninductive Current by Electron-Bernstein Waves on the COMPASS-D Tokamak**," *Physical Review Letters*, vol. 89, no. 26, p. 265005 (4pp), December 2002.

[326] J. Preinhaelter and V. Kopecký, "**Penetration of high-frequency waves into a weakly inhomogenous magnetized plasma at oblique incidence and their transformation to Bernstein modes**," *Journal of Plasma Physics*, vol. 10, pp. 1–12, August 1973, part 1.

[327] H. P. Laqua, V. Erckmann, H. J. Hartfuß, H. Laqua, and the W7-AS Team ECRH Group, "**Resonant and Nonresonant Electron Cyclotron Heating at Densities above the Plasma Cutoff by O-X-B Mode Conversion at the W7-AS Stellarator**," *Physical Review Letters*, vol. 78, no. 18, pp. 3467–3470, May 1997.

[328] S. Shiraiwa, K. Hanada, M. Hasegawa, H. Idei, H. Kasahara, O. Mitarai, K. Nakamura, N. Nishino, H. Nozato, M. Sakamoto, K. Sasaki, K. Sato, Y. Takase, T. Yamada, , H. Zushi, and the TST-2@K Group, "**Heating by an Electron Bernstein Wave in a Spherical Tokamak Plasma via Mode Conversion**," *Physical Review Letters*, vol. 96, no. 18, p. 185003 (4pp), May 2006.

[329] F. Wagner, G. Becker, K. Behringer, D. Campbell, A. Eberhagen, W. Engelhardt, G. Fussmann, O. Gehre, J. Gernhardt, G. v. Gierke, G. Haas, M. Huang, F. Karger, M. Keilhacker, O. Klüber, M. Kornherr, K. Lackner, G. Lisitano, G. G. Lister, H. M. Mayer, D. Meisel, E. R. Müller, H. Murmann, H. Niedermeyer, W. Poschenrieder, H. Rapp, and H. Röhr, "**Regime of Improved Confinement and High Beta in Neutral-Beam-Heated Divertor Discharges of the ASDEX Tokamak**," *Physical Review Letters*, vol. 49, no. 19, pp. 1408–1412, November 1982.

[330] A. Mück, Y. Camenen, S. Coda, L. Curchod, T. P. Goodman, H. P. Laqua, K. Mason, R. Patterson, A. Pochelon, L. Porte, and V. S. Udintsev, "**Electron Bernstein Wave Heating and Emission in the TCV Tokamak**," in *Proceedings of the 33rd European Physical Society Conference on Plasma Physics, Rome, Italy, June 19–23, 2006*, ser. Europhysics Conference Abstracts (ECA), F. D. Marco and G. Vlad, Eds., vol. 30I. European Physical Society (EPS), 2006.

[331] A. K. Ram, A. Bers, and C. N. Lashmore-Davies, "**Emission of electron Bernstein waves in plasmas**," *Physics of Plasmas*, vol. 9, no. 2, pp. 409–418, February 2002.

[332] A. Mück, Y. Camenen, S. Coda, L. Curchod, T. P. Goodman, H. P. Laqua, A. Pochelon, L. Porte, V. S. Udintsev, F. Volpe, and the TCV Team, "**Electron Bernstein Wave Heating and Emission in the TCV Tokamak**," *Fusion Science and Technology*, vol. 52, no. 2, pp. 221–229, August 2007.

[333] M. V. Babykin, P. P. Gavrin, E. K. Zavoiskii, L. I. Rudakov, and V. A. Skoryupin, "**Stability of a turbulently heated plasma during adiabatic compression**," *Soviet Journal of Experimental and Theoretical Physics (JETP)*, vol. 20, pp. 1073–??, 1965.

[334] H. de Kluiver, "**Current-driven turbulence in plasmas**," FOM-Instituut voor Plasmafysica, Rijnhuizen, Jutphaas, Nederland, Rijnhuizen report 77-106, October 1977.

[335] A. Hirose, H. W. Piekaar, and H. M. Skarsgard, "**Turbulent heating of a large toroidal plasma**," *Nuclear Fusion*, vol. 16, no. 6, pp. 963–969, June 1976.

[336] K. Toi, N. Hiraki, K. Nakamura, O. Mitarai, Y. Kawai, and S. Itoh, "**Observation of bulk-ion heating in a tokamak plasma by application of positive and negative current pulses in TRIAM-1**," *Nuclear Fusion*, vol. 20, no. 9, pp. 1169–1172, September 1980.

[337] H. D. Kluiver, B. D. Groot, H. J. van der Meiden, F. B. Hendriks, A. W. Kolfschoten, T. Oyevaar, J. W. J. Verschuur, N. J. L. Cardozo, H. W. van der Ven, C. J. Barth, and W. P. G. van Velthoven, **"High-temperature, high-beta plasma heating by weak turbulence in the TORTUR tokamak**," *Physics Letters A*, vol. 94, no. 3–4, pp. 156–159, March 1983.

[338] H. de Kluiver, N. F. Perepelkin, and A. Hirose, **"Experimental results on current-driven turbulence in plasmas - a survey**," *Physics Reports (Review section of Physics Letters)*, vol. 199, no. 6, pp. 281–381, January 1991.

[339] O. Buneman, **"Dissipation of Currents in Ionized Media**," *Physical Review*, vol. 115, no. 3, pp. 503–517, August 1959.

[340] O. Ishihara and A. Hirose, **"Nonlinear Saturation of the Buneman Instability**," *Physical Review Letters*, vol. 44, no. 21, pp. 1404–1407, May 1980.

[341] O. Ishihara, A. Hirose, and A. B. Langdon, **"Nonlinear evolution of Buneman Instability**," *Physics of Fluids*, vol. 24, no. 3, pp. 452–464, March 1981.

[342] A. Hirose, O. Ishihara, and A. B. Langdon, **"Nonlinear evolution of Buneman instability: II. Ion dynamics**," *Physics of Fluids*, vol. 25, no. 4, pp. 610–616, April 1982.

[343] J. W. Connor and R. J. Hastie, **"Relativistic limitations of runaway electrons**," *Nuclear Fusion*, vol. 15, no. 3, pp. 415–424, June 1975.

[344] B. B. Kadomtsev and O. P. Pogutse, **"Electric conductivity of a plasma in a strong magnetic field**," *Soviet Journal of Experimental and Theoretical Physics (JETP)*, vol. 26, no. 6, pp. 1146–1150, June 1968.

[345] V. V. Parail and O. P. Pogutse, **"Instability of the runaway-electron beam in a tokamak**," *Soviet Journal of Plasma Physics*, vol. 2, no. 2, pp. 125–129, March–April 1976.

[346] ——, **"The kinetic theory of runaway electron beam instability in a tokamak**," *Nuclear Fusion*, vol. 18, no. 3, pp. 303–314, 1978.

[347] ——, **"Fan instability and anomalous ion heating**," *JETP Letters*, vol. 31, no. 3, pp. 151–154, February 1980.

[348] G. A. Bobrovskij, E. I. Kuznetsov, and K. A. Razumova, **"Dependence of transport coefficients on plasma parameters in the tokamak installation**," *Soviet Journal of Experimental and Theoretical Physics (JETP)*, vol. 32, no. 4, pp. 599–605, April 1971.

[349] J. D. Jackson, **"Longitudinal plasma oscillations**," *Journal of Nuclear Energy. Part C, Plasma Physics, Accelerators, Thermonuclear Research*, vol. 1, no. 4, pp. 171–189, 1960.

[350] E. A. Jackson, **"Drift Instabilities in a Maxwellian Plasma**," *Physics of Fluids*, vol. 3, no. 5, pp. 786–792, September 1960.

[351] H. Tanaca, M. Koganei, and A. Hirose, **"Dispersion Relation of Ion Waves in Mercury-Vapor Discharges**," *Physical Review Letters*, vol. 16, no. 24, pp. 1079–1081, June 1966.

[352] H. Tanaca, A. Hirose, and M. Koganei, **"Ion-Wave Instabilities in Mercury-Vapor Plasma**," *Physical Review*, vol. 161, no. 1, pp. 94–101, September 1967.

[353] M. Yamada and M. Raether, **"Saturation of the Ion-Acoustic Instability in a Weakly Ionized Plasma**," *Physical Review Letters*, vol. 32, no. 3, pp. 99–102, January 1974.

[354] M. Bitter and P. J. Paris, **"Current driven weak ion acoustic turbulence in a magnetized plasma**," *Physics of Fluids*, vol. 21, no. 4, pp. 609–616, April 1978.

[355] Y. Kawai, C. Hollenstein, and M. Guyot, **"Ion acoustic turbulence in a large-volume plasma**," *Physics of Fluids*, vol. 21, no. 6, pp. 970–974, June 1978.

[356] L. I. Rudakov and L. V. Korablev, **"Quasilinear theory of current instability in a plasma**," *Soviet Journal of Experimental and Theoretical Physics (JETP)*, vol. 23, no. 1, pp. 145–152, July 1966.

[357] E. C. Field and B. D. Fried, **"Solution of the Kinetic Equation for an Unstable Plasma in an Electric Field**," *Physics of Fluids*, vol. 7, no. 12, pp. 1937–1951, December 1964.

[358] V. Y. Bychenkov, V. P. Silin, and S. A. Uryupin, **"Ion-acoustic turbulence and anomalous transport**," *Physics Reports (Review section of Physics Letters)*, vol. 164, no. 3, pp. 119–215, July 1988.

[359] O. Ishihara and A. Hirose, **"Turbulent heating and anomalous k-spectrum in the quasilinear evolution of current-driven ion-acoustic instability in a magnetic field**," *Physics of Fluids*, vol. 27, no. 2, pp. 364–376, February 1984.

[360] C. T. Dum, R. Chodura, and D. Biskamp, **"Turbulent Heating and Quenching of the Ion Sound Instability**," *Physical Review Letters*, vol. 32, no. 22, pp. 1231–1234, June 1974.

[361] O. Ishihara and A. Hirose, **"Quasilinear Mechanism of High-Energy Ion-Tail Formation in the Ion-Acoustic Instability**," *Physical Review Letters*, vol. 46, no. 12, pp. 771–774, March 1981.

[362] K. Appert and J. Vaclavik, **"Tail formation by nonresonant interaction of ions with ion-acoustic turbulence**," *Plasma Physics*, vol. 23, no. 9, pp. 763–774, September 1981.

[363] O. Ishihara and A. Hirose, **"High-energy ion tail formation in the ion-acoustic instability – Three-dimensional quasilinear approach**," *Physics of Fluids*, vol. 26, no. 1, pp. 100–105, January 1983.

[364] P. A. Sturrock, **"Kinematics of Growing Waves**," *Physical Review*, vol. 112, no. 5, pp. 1488–1503, December 1958.

[365] W. Gekelman and R. L. Stenzel, **"Ion sound turbulence in a magnetoplasma**," *Physics of Fluids*, vol. 21, no. 11, pp. 2014–2023, November 1978.

[366] R. L. Stenzel and W. Gekelman, **"Dynamics of test particles in a turbulent magnetoplasma**," *Physics of Fluids*, vol. 21, no. 11, pp. 2024–2031, November 1978.

[367] B. Coppi, M. N. Rosenbluth, and R. N. Sudan, **"Nonlinear interactions of positive and negative energy modes in rarefied plasmas (I)**," *Annals of Physics*, vol. 55, no. 2, pp. 207–247, November 1969.

[368] G. J. Boxman, B. Coppi, L. C. J. M. de Kock, B. J. H. Meddens, A. A. M. Oomens, L. T. M. Ornstein, D. S. Pappas, R. R. Parker, L. Pieroni, S. E. Segre, F. C. Schüller, and R. J. Taylor, **"Low and high density operation of Alcator**," in *Proceedings of the 7th European Conference on Controlled Fusion and Plasma Physics, Lausanne, Switzerland, September 1–5, 1975*, ser. Europhysics Conference Abstracts (ECA), vol. II, Centre de Recherches en Physique des Plasmas (CRPP), Ecole polytechnique fédérale de Lausanne (EPFL). European Physical Society (EPS), 1975, pp. 14–23, invited paper.

[369] A. A. M. Oomens, L. T. M. Ornstein, R. R. Parker, F. C. Schüller, and R. J. Taylor, **"Observation of High-Frequency Radiation and Anomalous Ion Heating on Low-Density Discharges in Alcator**," *Physical Review Letters*, vol. 36, no. 5, pp. 255–257, February 1976.

[370] B. Coppi, F. Pegoraro, R. Pozzoli, and G. Rewoldt, **"Slide-away distributions and relevant collective modes in high-temperature plasmas**," *Nuclear Fusion*, vol. 16, no. 2, pp. 309–328, February 1976.

[371] B. Coppi, F. Pegoraro, and G. Rewoldt, **"Anomalous Ion Heating and Thermal Energy Transport**," in *Proceedings of the 7th European Conference on Controlled Fusion and Plasma Physics, Lausanne, Switzerland, 1–5 September 1975*, ser. Europhysics Conference Abstracts (ECA), vol. I, Centre de Recherches en Physique des Plasmas (CRPP), Ecole polytechnique fédérale de Lausanne (EPFL). European Physical Society (EPS), 1975, p. 170, contributed poster.

[372] B. Coppi, G. Lampis, F. Pegoraro, L. Pieroni, and S. Segre, **"Saturation of Lower Hybrid Modes in the Slide-away Regime**," *Lettere al nuovo cimento della Società Italiana di Fisica*, vol. 15, no. 3, pp. 88–90, June 1976, serie 2.

[373] R. Z. Sagdeev and A. Galeev, **"Frontiers in physics**," in *Nonlinear plasma theory*, T. M. O'Neil and D. L. Book, Eds. Benjamin, New York, 1969, vol. 34.

[374] A. A. Galeev and R. Z. Sagdeev, **"Current instabilities and anomalous resistivity of plasma**," in *Basic plasma physics*, ser. Handbook of Plasma Physics, A. A. Galeev and R. N. Sudan, Eds. Amsterdam: North-Holland Physics Publishing, 1984, vol. 2, ch. 6.1, pp. 271–303, part 6.

[375] B. D. Fried, R. B. White, and T. K. Samec, **"Ion Acoustic Waves in a Multi-Ion Plasma**," *Physics of Fluids*, vol. 14, no. 11, pp. 2388–2392, November 1971.

[376] V. P. Silin and S. A. Uryupin, **"Ion-acoustic turbulence in a plasma with two species of ions**," *Soviet Journal of Experimental and Theoretical Physics (JETP)*, vol. 75, no. 1, pp. 41–46, July 1992.

[377] I. V. Kuzora, V. P. Silin, and S. A. Uryupin, **"Turbulent Ion Heating in a Plasma with Two Ion Species**," *Plasma Physics Reports*, vol. 30, no. 4, pp. 307–317, April 2004.

[378] H. C. Jain and S. R. Sharma, **"Resistivity Phenomena in Multi-Ion Plasma with Ion Acoustic Turbulence**," *Physica Scripta*, vol. 21, no. 2, pp. 191–193, 1980.

[379] Y. Nakamura, M. Nakamura, and T. Itoh, **"Observation of Two Ion-Acoustic Waves in an Argon-Helium Plasma**," *Physical Review Letters*, vol. 37, no. 4, pp. 209–212, July 1976.

[380] S. Gangadhara, D. Craig, D. A. Ennis, D. J. D. Hartog, G. Fiksel, and S. C. Prager, **"Ion heating during reconnection in the Madison Symmetric Torus reversed field pinch**," *Physics of Plasmas*, vol. 15, no. 5, May 2008.

[381] D. J. D. Hartog and D. Craig, **"Isotropy of ion heating during a sawtooth crash in a reversed-field pinch**," *Plasma Physics and controlled Fusion*, vol. 42, no. 12, pp. L47–L53, December 2000.

[382] P. Helander, L.-G. Eriksson, R. J. Akers, C. Byrom, C. G. Gimblett, and M. R. Tournianski, **"Ion Acceleration during Reconnection in MAST**," *Physical Review Letters*, vol. 89, no. 23, December 2002.

[383] H. P. Furth and P. H. Rutherford, **"Ion Runaway in Tokamak Discharges**," *Physical Review Letters*, vol. 28, no. 9, pp. 545–548, February 1972.

[384] G. D. Holman, **"DC electric field acceleration of ions in solar flares**," *The Astrophysical Journal*, vol. 452, no. 1, pp. 451–456, October 1995, part 1.

[385] T. A. team, **"The H-mode of ASDEX**," *Nuclear Fusion*, vol. 29, no. 11, pp. 1959–2040, November 1989.

[386] A. W. Degeling, Y. R. Martin, P. E. Bak, J. B. Lister, and X. Llobet, **"Dynamics of edge localized modes in the TCV tokamak**," *Plasma Physics and controlled Fusion*, vol. 43, no. 12, pp. 1671–1698, December 2001.

[387] A. N. Karpushov, B. P. Duval, and C. Schlatter, **"Ion Temperature Fluctuations in ELMy H-mode of the X3 EC-heated Plasmas on TCV**," in *PLASMA 2007: International Conference on Research and Applications of Plasmas, Greifswald, Germany, October 16–19, 2007*, ser. AIP Conference Proceedings, H.-J. Hartfuss, M. Dudeck, J. Musielok, and M. J. Sadowski, Eds., vol. 993, 2007, pp. 219–222.

[388] R. Behn, A. Alfier, S. Y. Medvedev, G. Zhuang, R. Pasqualotto, P. Nielsen, Y. Martin, and the TCV team, **"Edge profiles of electron temperature and density during ELMy H-mode in ohmically heated TCV plasmas**," *Plasma Physics and Controlled Fusion*, vol. 49, no. 8, pp. 1289–1308, August 2007.

[389] M. Nave, S. Ali-Arshad, B. Alper, B. Balet, H. D. Blank, D. Borba, C. Challis, M. V. Hellermann, T. Hender, G. Huysmans, W. Kerner, G. Kramer, F. Porcelli, J. O'Rourke, L. Porte, G. Sadler, P. Smeulders, A. Sips, P. Stubberfield, D. Stork, R. Reichle, J. Wessom, and W. Zwingmann, **"MHD activity in JET hot ion H mode discharges**," *Nuclear Fusion*, vol. 35, no. 4, pp. 409–429, April 1995.

[390] P. M. Kintner, J. Vago, S. Chesney, R. L. Arnoldy, K. A. Lynch, C. J. Pollock, and T. E. Moore, **"Localized lower hybrid acceleration of ionospheric plasma**," *Physical Review Letters*, vol. 68, no. 16, pp. 2448–2451, April 1992.

[391] V. Y. Bychenkov, V. P. Silin, and S. A. Uryupin, **"Anisotropic turbulent heating of ions**," *Soviet Journal of Experimental and Theoretical Physics (JETP)*, vol. 15, no. 3, pp. 173–176, March 1989.

[392] V. Y. Bychenkov, V. N. Novikov, V. P. Silin, and S. A. Uryupin, **"Anisotropic ion heating and evolution of the ion-acoustic turbulence spectrum of a plasma in a strong electric field**," *Soviet Journal of Experimental and Theoretical Physics (JETP)*, vol. 15, no. 12, pp. 847–850, December 1989.

[393] J. D. Evans, G. J. Morales, and R. J. Taylor, **“Observation of Perpendicular Ion Acceleration in Toroidal Plasmas**,” *Physical Review Letters*, vol. 69, no. 10, pp. 1528–1531, September 1992.

[394] H. P. Laqua and H. J. Hartfuss, **“Electron Bernstein wave emission from an overdense plasma at the W7-AS stellarator**,” *Physical Review Letters*, vol. 81, no. 10, pp. 2060–2063, September 1998.

[395] V. Shevchenko, G. Cunningham, A. Gurchenk, E. Gusakov, B. Lloyd, M. O’Brien, A. Saveliev, A. Surkov, F. Volpe, and M. Walsh, **“Electron Bernstein wave studies in MAST**,” in *17th Topical Conference on Radio Frequence Power in Plasmas, Clearwater, Florida, May 7–9, 2007*, ser. AIP conference proceedings, P. M. Ryan and D. A. Rasmussen, Eds., vol. 933. American institute of physics, 2007, pp. 323–330.

[396] C. Schlatter, B. P. Duval, A. N. Karpushov, and T. P. Goodman, **“Ion-Acoustic Turbulence in ECCD-driven TCV plasmas**,” in *Bulletin of the American Physical Society*, vol. 52, no. 11. American Physical Society (APS), November 2007, 49th Annual Meeting of the Division of Plasma Physics (DPP), November 12–16, 2007, Orlando, Florida, USA.

[397] C. Wharton, P. Korn, D. Prono, S. Robertson, P. Auer, and C. T. Dum, **“New results in turbulent heating**,” in *Plasma Physics and Controlled Nuclear Fusion Research 1971*, ser. Proceedings series, International Atomic Energy Agency (IAEA), Ed., vol. 2, no. IAEA-CN-28/E-2, Vienna, Austria, November 1971, pp. 25–36, proceedings of the fourth international conference on plasma physics and controlled nuclear fusion research held by the International Atomic Energy Agency at Madison, USA, June 17–23, 1971.

[398] H. de Kluiver, C. J. Barth, H. J. B. M. Brocken, J. J. L. Caarls, B. de Groot, H. W. Kalfsbeek, H. W. Piekaar, A. Ravestein, W. R. Rutgers, B. de Stigter, H. W. H. van Andel, and H. W. van der Ven, **“Plasma heating by current-driven turbulence in the Tokamak Tortur I**,” in *Plasma Physics and Controlled Nuclear Fusion Research 1978*, ser. Nuclear Fusion Supplement, International Atomic Energy Agency (IAEA), Ed., vol. 2, no. IAEA-CN-37/Y-4-1. Vienna, Austria: International Atomic Energy Agency (IAEA), May 1979, pp. 639–648, proceedings of the seventh International Conference on Plasma Physics and Controlled Nuclear Fusion Research held by the International Atomic Energy Agency at Innsbruck, Austria, August 23–30, 1978.

[399] B. D. Fried and S. L. Ossakow, **“Kinetic Equation for an Unstable Plasma in Parallel Electric and Magnetic Fields**,” *Physics of Fluids*, vol. 9, no. 12, pp. 2428–2435, December 1966.

[400] L. I. Rudakov, **“Nature of turbulent heating in Tokamak TM-3 device**,” *Soviet Journal of Experimental and Theoretical Physics (JETP)*, vol. 33, no. 6, pp. 1148–1151, December 1971.

[401] K. Appert and J. Vaclavik, **“Quasilinear theory of the current-driven ion-acoustic turbulence in a weakly ionized plasma**,” *Physics of Fluids*, vol. 22, no. 3, pp. 454–461, March 1979.

[402] R. L. Stenzel, **“Experiments on current-driven three-dimensional ion sound turbulence. Part II: Wave dynamics**,” *Physics of Fluids*, vol. 21, no. 1, pp. 99–108, January 1978.

[403] O. Ishihara and A. Hirose, **"Quasilinear Evolution of Current-Driven Ion-Acoustic Instability in a Magnetic Field**," *Physical Review Letters*, vol. 50, no. 22, pp. 1783–1786, May 1983.

[404] W. E. Drummond and D. Pines, **"Non-linear stability of plasma oscillations**," in *Nuclear Fusion Supplement 1962*, ser. Plasma Physics and Controlled Nuclear Fusion Research, no. part 3, 1962, pp. 1049–1057, conference proceedings, Salzburg, Austria, September 4–9, 1961.

[405] A. A. Vedenov and D. D. Ryutov, **"Quasilinear effects in two-stream instabilities**," in *Reviews of plasma physics*, M. A. Leontovich, Ed. Consultants Bureau, New York, London, 1975, vol. 6, pp. 1–76.

[406] N. A. Krall and A. W. Trivelpiece, ***Principles of plasma physics***, ser. International series in pure and applied physics. New York: McGraw-Hill book company, 1973.

[407] D. W. Peaceman and J. H. H. Rachford, **"The numerical solution of parabolic and elliptic differential equations**," *Journal of the Society for Industrial and Applied Mathematics*, vol. 3, no. 1, pp. 28–41, March 1955.

[408] J. Jim Douglas, **"Alternating direction methods for three space variables**," *Numerische Mathematik*, vol. 4, no. 1, pp. 41–63, December 1962.

[409] J. Jim Douglas and J. E. Gunn, **"A general formulation of alternating direction methods. Part I. Parabolic and Hyperbolic problems**," *Numerische Mathematik*, vol. 6, no. 1, pp. 428–453, December 1964.

[410] Г. В. Гордеев, **"Колебания плазмы в магнитном поле**," *Журнал зкспериментальной и теоретической физики*, vol. 23, no. 6, pp. 660–668, 1952.

[411] S. E. Bodner, **"Quasi-linear theory in the non-resonant region**," *Journal of Plasma Physics*, vol. 5, no. 1, pp. 141–144, January 1971.

[412] A. N. Kaufman, **"Reformulation of quasi-linear theory**," *Journal of Plasma Physics*, vol. 8, no. 1, pp. 1–5, August 1972.

[413] C. Gormezano, A. C. C. Sips, T. C. Luce, S. Ide, A. Becoulet, X. Litaudon, A. Isayama, J. Hobirk, M. R. Wade, T. Oikawa, R. Prater, A. Zvonkov, B. Lloyd, T. Suzuki, E. Barbato, P. Bonoli, C. K. Phillips, V. Vdovin, E. Joffrin, T. Casper, J. Ferron, D. Mazon, D. Moreau, R. Bundy, C. Kessel, A. Fukuyama, N. Hayashi, F. Imbeaux, M. Murakami, A. R. Polevoi, and H. E. S. John, **"Progress in the ITER Physics Basis: Steady state operation**," *Nuclear Fusion*, vol. 47, no. 6, pp. S1–S17, June 2007, chapter 6 of the special issue on the Progress in the ITER Physics Basis.

[414] A. Fasoli and the TCV Team, **"Overview of Physics Research on the TCV Tokamak**," in *Proceedings of the 22nd IAEA Fusion Energy Conference (FEC), October 13–18, 2008, Geneva, Switzerland*, International Atomic Energy Agency (IAEA), Ed., no. OV/1-1. Vienna, Austria: International Atomic Energy Agency (IAEA), 2008, invited paper.

[415] I. T. Chapman, S. D. Pinches, L. C. Appel, R. J. Hastie, T. C. Hender, S. Saarelma, S. E. Sharapov, I. Voitsekhovitch, and J. P. Graves, **"Modeling sawtooth stabilization by energetic ions from neutral beam injection**," *Physics of Plasmas*, vol. 14, no. 7, p. 070703 (4pp), July 2007. URL: http://link.aip.org/link/?PHP/14/070703/1

[416] I. T. Chapman, I. Jenkins, R. V. Budny, J. P. Graves, S. D. Pinches, S. Saarelma, and JET EFDA Contributors, **"Sawtooth control using off-axis NBI,"** *Plasma Physics and Controlled Fusion*, vol. 50, no. 4, p. 045006 (15pp), April 2008. URL: http://stacks.iop.org/0741-3335/50/045006

[417] I. T. Chapman, S. D. Pinches, J. P. Graves, R. J. Akers, L. C. Appel, R. V. Budny, S. Coda, N. J. Conway, M. de Bock, L.-G. Eriksson, R. J. Hastie, T. C. Hender, G. T. A. Huysmans, T. Johnson, H. R. Koslowski, A. Kramer-Flecken, M. Lennholm, Y. Liang, S. Saarelma, S. E. Sharapov, I. Voitsekhovitch, the MAST and TEXTOR Teams, and JET EFDA Contributors, **"The physics of sawtooth stabilization,"** *Plasma Physics and Controlled Fusion*, vol. 49, no. 12B, pp. B385–B394, December 2007. URL: http://stacks.iop.org/0741-3335/49/B385

[418] I. Lerche, **"Quasilinear Theory of Resonant Diffusion in a Magneto-Active, Relativistic Plasma,"** *Physics of Fluids*, vol. 11, no. 8, pp. 1720–1727, August 1968.

[419] M. Abramowitz and I. A. Stegun, ***Handbook of Mathematical Functions with Formulas, Graphs, and Mathematical Tables*, ninth dover printing, tenth gpo printing ed.** New York: Dover Publications, 1964.

[420] L. D. Landau, **"On the vibrations of the electronic plasma,"** *Journal of Physics USSR*, vol. 10, pp. 25–34, 1946.

[421] H. Packard, ***Programming Manual of the HP 70000 Modular Spectrum Analyzer HP 70900B Local Oscillator Source-Controlled Modules*, a.0.0 ed.**, Hewlett Packard, 1400 Fountaingrove Parkway, Santa Rosa, California, USA, March 1994.

[422] J. Killeen and K. D. Marx, **"Plasma Physics,"** in *Methods in computational physics: Advances in research and applications*, B. Alder, S. Fernbach, and M. Rotenberg, Eds. Academic Press, New York, 1970, vol. 9.

[423] C. Schlatter, **"Investigation of problems related to KF-1,"** EFDA-JET, Culham, Oxford, UK, Internal report, February 2006, report on the High Level Commissioning prior to the C15 JET experimental campaign.

[424] D. S. Testa, M. Cecconello, C. Schlatter, and JET-EFDA contributors, **"The dependence of the proton–triton thermo-nuclear fusion reaction rate on the temperature and total energy content of the high-energy proton distribution function,"** *Nuclear Fusion*, vol. 49, no. 6, p. 062004 (9pp), June 2009. URL: http://dx.doi.org/10.1088/0029-5515/49/6/062004

[425] S. E. Sharapov, B. Alper, V. G. Kiptily, S. Hacquin, and C. Schlatter, **"Energetic Ion-driven instabilities on JET and on MAST,"** in *Bulletin of the American Physical Society*, vol. 51, no. 7. American Physical Society (APS), 2006, p. BI1.00005, invited talk presented at the 48th Annual Meeting of the Division of Plasma Physics (DPP), 30 October – 3 November 2006, Philadelphia, Pennsylvania, USA.

[426] M. Keilhacker, A. Gibson, C. Gormezano, P. J. Lomas, P. R. Thomas, M. L. Watkins, P. Andrew, B. Balet, D. Borba, C. D. Challis, I. Coffey, G. A. Cottrell, H. P. L. D. Esch, N. Deliyanakis, A. Fasoli, C. W. Gowers, H. Y. Guo, G. T. A. Huysmans, T. T. C. Jones, W. Kerner, R. W. T. Konig, M. J. Loughlin, A. Maas, F. B. Marcus, M. F. F. Nave, F. G. Rimini, G. J. Sadler, S. E. Sharapov, G. Sips, P. Smeulders, F. X. Soldner, A. Taroni,

B. J. D. Tubbing, M. G. von Hellermann, D. J. Ward, and the JET Team, **"High fusion performance from deuterium-tritium plasmas in JET**," *Nuclear Fusion*, vol. 32, no. 2, pp. 209–234, February 1999.

[427] E. Thompson, D. Stork, H. P. L. de Esch, and the JET team, **"The use of neutral beam heating to produce high performance fusion plasmas, including the injection of tritium beams into the Joint European Torus (JET)**," *Physics of Fluids B: Plasma Physics*, vol. 5, no. 7, pp. 2468–2480, July 1993.

[428] D. F. H. Start, J. Jacquinot, V. Bergeaud, V. P. Bhatnagar, S. W. Conroy, G. A. Cottrell, S. Clement, G. Ericsson, L.-G. Eriksson, A. Fasoli, V. Fuchs, A. Gondhalekar, C. Gormezano, G. Gorini, G. Grosshoeg, K. Guenther, P. J. Harbour, R. F. Heeter, L. D. Horton, A. C. Howman, H. J. Jackel, O. N. Jarvis, J. Kallne, C. N. L. Davies, K. D. Lawson, C. G. Lowry, M. J. Mantsinen, F. B. Marcus, R. D. Monk, E. Righi, F. G. Rimini, G. J. Sadler, G. Saibene, R. Sartori, B. Schunke, S. E. Sharapov, A. C. C. Sips, M. F. Stamp, M. Tardocchi, and P. van Belle, **"Bulk ion heating with ICRH in JET DT plasmas**," *Nuclear Fusion*, vol. 39, no. 3, pp. 321–336, March 1999, special issue of JET articles relating to results from the JET deuterium-tritium experiments.

[429] M. Lennholm, Y. Baranov, J. A. Dobbing, A. Ekedahl, P. Finburg, B. Fischer, C. Gormezano, C. Gowers, A. Kaye, J. Plancoulaine, F. G. Rimini, J. Romero, P. Schild, A. Sips, F. Smits, and F. X. Soldner, **"Operation of the 3.7 GHz LHCD system in JET**," in *16th IEEE/NPSS Symposium on Fusion Engineering (SOFE), Champaign, Illinois, USA, October 1–5, 1995 - Seeking a new energy era*, G. H. Miley and C. Elliot, Eds., vol. 1, 1995, pp. 754–757.

[430] G. Bracco, G. Betello, S. Mantovani, A. Moleti, B. Tilia, and V. Zanza, **"Design and calibration of the JET time of flight neutral particle analyzer with high noise rejection capability**," *Review of Scientific Instruments*, vol. 63, no. 12, pp. 5685–5697, December 1992.

[431] A. B. Izvozchikov, A. V. Khudoleev, M. V. Petrov, S. Y. Petrov, S. S. Kozlovskij, S. Corti, and A. Gondhalekar, **"Charge-exchange Diagnostic of Fusion Alpha Particles and ICRF Driven Minority Ions in MeV Energy Range in JET Plasma**," Joint European Torus (JET), Culham, Oxford, UK, JET Laboratory Report JET-R(91)12, December 1991.

[432] A. A. Korotkov and A. Gondhalekar, **"Impurity induced neutralization of MeV energy protons in JET plasmas**," in *Proceedings of the 21st EPS conference on controlled fusion and plasma physics*, E. Joffrin, P. Platz, and P. E. Stott, Eds. Geneva: The European Physical Society, 1994, pp. 266–268, volume 18B, part I.

[433] A. A. Korotkov, A. Gondhalekar, and A. J. Stuart, **"Impurity induced neutralization of megaelectronvolt energy protons in JET plasmas**," *Nuclear Fusion*, vol. 37, no. 1, pp. 35–51, January 1997.

[434] T. H. Stix, **"Fast-wave heating of a two-component plasma**," *Nuclear Fusion*, vol. 15, no. 5, pp. 737–754, October 1975.

[435] K. G. McClements, R. O. Dendy, and A. Gondhalekar, **"Interpretation of measurements of ICRF heated minority proton distributions in JET**," *Nuclear Fusion*, vol. 37, no. 4, pp. 473–480, April 1997.

[436] C. Schlatter, D. S. Testa, M. Cecconello, A. Murari, and M. I. K. Santala, **"Error estimation and parameter dependence of the calculation of the fast ion distribution function, temperature, and density using data from the KF-1 high energy neutral particle analyzer on Joint European Torus**," *Review of Scientific Instruments*, vol. 75, no. 10, pp. 3547–3549, October 2004.

[437] L. L. Lao, J. R. Ferron, R. J. Groebner, W. Howl, H. S. John, E. J. Strait, and T. S. Taylor, **"Equilibrium analysis of current profiles in tokamaks**," *Nuclear Fusion*, vol. 30, no. 6, pp. 1035–1049, June 1990.

[438] **CRPP public web page**. URL: http://crpp.epfl.ch

[439] **Description of the TCV tokamak**. URL: http://crpp.epfl.ch/crpp_tcv.html

[440] **CRPP intranet portal**. URL: http://crpplocal.epfl.ch/

[441] **Wiki design principles**. URL: http://c2.com/cgi-bin/wiki?WikiDesignPrinciples

[442] D. Tapscott and A. D. Williams, ***Wikinomics: How Mass Collaboration Changes Everything***. New York: Portfolio, May 2008, expanded edition.

[443] **Comparison of wiki software**. URL: http://en.wikipedia.org/wiki/Comparison_of_wiki_software

[444] **MediaWiki home page**. URL: http://www.mediawiki.org/

[445] **Wikipedia – The free encyclopedia**. URL: http://www.wikipedia.org/

[446] **GNU General Public License**. URL: http://en.wikipedia.org/wiki/GNU_General_Public_License

[447] **LDAP authentication for MediaWiki**. URL: http://www.mediawiki.org/wiki/Extension:LDAP_Authentication

[448] C. Lecommandeur, **"Tequila – A distributed web authentication and access control tool**," in *Proceedings of the EUNIS 2005 conference, Manchester, June 21–24, 2005*. European University Information Systems (EUNIS), 2005, contributed paper.

[449] **News extension for MediaWiki**. URL: http://www.mediawiki.org/wiki/Extension:News

[450] **Subpage list extension for MediaWiki**. URL: http://www.mediawiki.org/wiki/Extension:SubPageList2

[451] **Category tree extension for MediaWiki**. URL: http://www.mediawiki.org/wiki/Extension:CategoryTree

[452] **How to use TeX on MediaWiki**. URL: http://www.mediawiki.org/wiki/Manual:Enable_TeX

[453] **Gnuplot extension for MediaWiki**. URL: http://www.mediawiki.org/wiki/Extension:Gnuplot

[454] **The Python wikipediabot**. URL: http://meta.wikimedia.org/wiki/Using_the_python_wikipediabot

[455] **The Internet WayBackMachine**. URL: http://web.archive.org/

[456] **Gallery2 project home page**. URL: http://gallery.menalto.com/

[457] **Gallery2wiki hack snippet**. URL: http://www.transarte.net/mediawiki/index.php/Gallery2wiki

[458] **MDS+ web site**. URL: http://www.mdsplus.org

[459] **PHPlot project page**. URL: http://phplot.sourceforge.net/

[460] **The TCV logbook**. URL: http://adas.epfl.ch/perl/logbook.pl

[461] **The 2008 FEC LOC wiki**. URL: http://www.fec2008.ch/wiki/index.php/Main_Page

[462] **Web page of the 22nd IAEA Fusion Energy Conference (FEC)**. URL: www.fec2008.ch

Remerciements

Nous voilà à la fin d'un périple qui a duré finalement six ans ! C'était une belle histoire, certes aussi avec quelques périodes moins joyeuses, mais, je ne regrette rien. Ce travail n'aurait bien sûr pas été possible sans l'aide et la collaboration d'un grand nombre de personnes, toujours compétentes et disponibles pour donner un coup de main. Cet espace est malheureusement insuffisant pour remercier toutes les personnes qui ont contribué à la réussite de cette aventure.

Commençons avec Basil, directeur de thèse, on dirait, fait sur mesure. Tes racines anglaises/-greques expliquent certainement ton humour (incessant) et ta vitesse de réflexion parfois un peu gênant pour un bernois fonctionnant (dit-on) au ralenti. Tu étais toujours soucieux et engagé dans ton désir de former des physiciens ouverts et critiques d'esprit. J'ai beaucoup apprécié ton horizon et intéret très marqués pour les choses autres que la physique (des plasmas ou autre). J'ai le sentiment qu'on a probablement plus discuté d'informatique que d'autre chose dans ton bureau, dont la porte n'a jamais été fermée, malgré que tu es très sollicité. Tu joues un rôle clé dans l'institut, parfois involontairement trop en coulisses et du coup à mon avis ton travail n'est malheureusement pas assez valorisé par nous tous. Je te remercie pour ta franchise inconditionnelle et ton insistance quand nos avis divergeaient. Bien sûr tu avais presque (hmm) toujours raison ! J'ai eu une immense chance de pouvoir effectuer ma thèse sous ta surveillance. Rapidement tu sembles m'avoir fait entièrement confiance dans ce que je faisais et tu m'a accordé toute la liberté de travailler et progresser à ma façon. Je te dis ici encore une fois infiniment merci pour tout.

Puis Alexander, le sibérien, qui passe à l'action sans tourner autour du pot. Tu es carrément omniprésent à la salle de commande de TCV et tu as une capacité incroyable de sauter sur chaque occasion d'aider à la résolution d'un problème technique quelconque. Tu m'as été d'une immense aide, surtout au début de la thèse, car tu avais appris la spectrometrie des neutres deux ans avant que je me lance dans l'aventure au CRPP et j'ai bien pu profiter de tes compétences dans ce domaine. A mon arrivée, tu venais de passer commande de l'analyseur de neutres compacte (CNPA), qui devenait rapidement mon diagnostic préféré de TCV. Malgré que tu étais le responsable des NPA, tu m'a accordé main libre pour mes activités, en particulier les tests, l'installation et l'optimisation de l'écran de blindage contre les rayons X durs, ainsi que la conception du nouveau support du CNPA. Les soins que tu as apportés aux diagnostiques m'ont évité beaucoup de travail de « bidouillage » parfois jugé ingrat autour du tokamak.

Mes déviations dans le monde des émissions éléctroniques cyclotroniques ont été un succès grâce à Tim, merci pour ton aide et assistance pour la partie chauffage électronique. Merci également à Victor, pour la partie diagnostique ECE et le code NOTEC, que tu avais amené au CRPP.

Duccio, qui m'a fait découvrir ce drôle de monde à Culham, qui m'a présenté à plein de scientifiques à JET et qui m'a appris à utiliser KF-1 sur un tokamak où les ions sont vraiment chauds.

Pierre et Xavier, pour avoir satisfait toutes mes demandes informatiques.

Federico, Francesco, James et Yves pour avoir eu le courage d'oser l'idée folle d'enrichir le CRPP avec l'esprit wiki.

Les quelques personnes des services qui m'ont apporté une aide précieuse, notamment Pascal et Omar (technique du vide), Philippe, Blaise et Severino, pour leur coup de main pour faire marcher l'esclave du CNPA ou un simple ventilateur de salle de bain. Puis Claude, le supermécano de toutes les belles mécaniques, plus précisément de Porsche et Tokamak, qui, avec tant de créativité, résolvait tout problème de support pour le CNPA. Et encore Guy, qui devait lutter fort contre CATIA, pour en sortir tous les dessins techniques demandés.

Les bonnes âmes de l'administration, en particulier Edith, qui a toujours écouté avec bienveillance les soucis des doctorants et qui a souvent facilité les démarches péniblement administratives, ainsi que Paula, Nadia, Véronique, Heidi, Céline et Séverine.

Mes collègues de bureau, dans l'ordre d'apparition : Laura, Alexei, Sasha et Francesco. Surtout aussi pour ne pas avoir parlé uniquement de physique.

Tous les doctorants du CRPP, pour avoir partagé les peines et pour tous ces apéros qu'on a vu passer, Alban, Alberto, Alessandro B. (qui m'a initié à fumer la pipe), Alessandro M., Alexei, Andrea, Andreas (hallo Kaninchen), Andrey, Barbora, Costanza, Christian, David, Davoud, Edgar, Emiliano, Etienne, Federico, Francesca, Francesco (à quand le prochain verre de Cannonau ?), Gennady, Gilles, Hannes, Igor, Kees, Jonathan, Jan, Janos, Loic, Lucia, Lukas, Marco (merci pour les nombreux services de taxi entre JET et Oxford), Mario, Martin, Mattia, Misha, Nicolas, Paolo, Patrick, Pavel, Petri, Robert, Sébastien, Sergi, Silvano (cassa manna !), Stefan, Sudheer, Sun Hee, Theo, Thibaut, Xavier et Yann.

Les membres de la direction du CRPP, notamment Quang, qui, autour d'un repas cosaque à Moscou, m'invitait à rejoindre son institut. Kurt, sans qui je n'aurais probablement pas été engagé au CRPP, Ambrogio, de me confier son enseignement de la physique des plasma en son absence, ou encore Yves, pour les causettes bien sympathiques dans le régional Renens–Vevey.

Les rapporteurs de thèse, Sergei Sharapov, Marco Cecconello, Ambrogio Fasoli et Olivier Schneider.

Samuel, ami et colocataire pendant une bonne partie de cette thèse, pour avoir partagé les plaisirs et les mélancolies des thésards à l'EPFL autour d'innombrables bières.

Et bien sûr Roxane, toi mon amour, tu as pris le risque de sortir avec moi et tu as donc dû subir maintes fois les effets secondaires que peut provoquer un tel travail. Tu n'as pas perdu confiance en moi et tu as fait preuve de beaucoup de patience pendant cette dernière année. Ce qui compte, tu es toujours là – merci mon coeur !

Ma famille et mes amis, qui comprenaient rarement ce dont je parlais ou ce que je faisais, mais qui semblent avoir gardé confiance que cette histoire prendrait bien fin un jour.

Et tous ceux que j'ai oublié de mentionner. Je réalise que vous tous, l'ambiance, la multilinguisme et la pluridisciplinarité de la planète CRPP vont me manquer.

Christian SCHLATTER

Ecole polytechnique fédérale de Lausanne
Centre de Recherches en Physique des Plasmas
Building PPB, office 310, station 13
CH-1015 Lausanne SWITZERLAND

Phone: +41 (0)21 693 2263
Fax: +41 (0)21 693 5176
Email: `ch.schlatter@a3.epfl.ch`
Homepage: `http://crpp.epfl.ch/~slater`

Personal

Born on June 3d, 1975.

Swiss Citizen.

Education

Ph.D. Physics, Ecole polytechnique fédérale de Lausanne, 2009.
Dissertation: **Turbulent ion heating in TCV tokamak plasmas**

M.A. Physics, Ecole polytechnique fédérale de Lausanne, 2003.
Dissertation: **Radiation loss studies on T-10 tokamak using AXUV-detectors**

B.S. Physics, Ecole polytechnique fédérale de Lausanne, 2001.

High-school, Berner Maturitätsschule für Berufstätige, 1998.

Degree in Electronics, Lehrwerkstätten der Stadt Bern, 1996.

Employment

Centre de Recherches en Physique des Plasmas, Research assistant, 2003–2009.

Lehrwerkstätten der Stadt Bern, Professional school teacher, 1996–1998.

Lehrwerkstätten der Stadt Bern, trainee, 1992–1996.

International collaborations

Seconded to the Joint European Torus (JET) of the European Fusion Development Agreement (EFDA), Culham, UK, 2003–2006 (various stays)

Master diploma work on the T-10 tokamak at Nuclear Fusion Institute (NFI), Russian Research Centre “Kurchatov” (KIAE), Moscow, Russian Federation, 2002–2003 (6 month).

Publications

Refereed Journal Articles

C. Schlatter et al., **Reconstruction of ion temperature profiles from single chord NPA measurements on the TCV tokamak**, *Plasma Physics and Controlled Fusion*, vol. 48, no. 12, pp. 1765–1785, December 2006.

C. Schlatter et at., **Error estimation and parameter dependence of the calculation of the fast ion distribution function, temperature, and density using data from the KF-1 high energy neutral particle analyzer on Joint European Torus**, *Review of Scientific Instruments*, vol.75, no. 10, pp. 3547–3549, October 2004.

D. S. Testa, including C. Schlatter, **The dependence of the proton–triton thermo-nuclear fusion reaction rate on the temperature and total energy content of the high-energy proton distribution function**, *Nuclear Fusion*, vol. 49, no. 6, art. 062004 (9pp), June 2009.

V. S. Udintsev, including C. Schlatter, **Recent electron cyclotron emission results on TCV**, *Fusion Science and Technology*, vol. 52, no. 2, pp. 161–168, August 2007.

M. I. K. Santala, including C. Schlatter, **Proton-triton nuclear reaction in ICRF heated plasmas in JET**, *Plasma Physics and Controlled Fusion*, vol. 48, no. 8, pp. 1233–1253, August 2006.

A. N. Karpushov, including C. Schlatter, **Neutral particle analyzer diagnostics on the TCV tokamak**, *Review of Scientific Instruments*, vol. 77, no. 3, paper 033504, 13 pages, March 2006.

T. P. Goodman, including C. Schlatter, **First measurements of oblique ECE with a real-time movable line-of-sight on TCV**, *Fusion Science and Technology*, vol. 53, no. 1, pp. 196–207, January 2006.

T. P. Goodman, including C. Schlatter, **Safety factor profile requirements for electron ITB formation in TCV**, *Plasma Physics and Controlled Fusion*, vol. 47, no. 12B, pp. B107–B120, December 2005.

Proceedings

C. Schlatter at al., **Ion-Acoustic Turbulence in ECCD-driven TCV plasmas**, in Bulletin of the American Physical Society, vol. 52, no. 11, 2007. Poster presented at the 49th Annual Meeting of the Division of Plasma Physics (DPP), November 12–16, 2007, Orlando, Florida, USA.

C. Schlatter et al., **Conditions for anomalous energy and momentum transfer from electrons to ions in ECCD discharges on TCV**, in Proceedings of the 33rd EPS Conference on Plasma Physics, Rome, Italy, 19–23 June 2006, no. P-1.149, 2006, contributed paper.

C. Schlatter et al., **Reconstruction of hydrogenic ion temperature profiles on TCV**, in 32nd EPS Conference on Plasma Physics and Controlled Fusion combined with the 8th International Workshop on Fast Ignition of Fusion Targets, Tarragona, 27 June - 1 July 2005, B. v. M. C. Hidalgo, Ed., Asociación EURATOM-CIEMAT para Fusión, Madrid. Tarragona: The European Physical Society, 2005, p. P1.050, europhysics Conference Abstracts, volume 29C.

C. Schlatter et al., **Error analysis and parametric study of the JET high energy NPA**, poster presented at the 15th Topical Conference High-Temperature Plasma Diagnostics (HTPD), San Diego, California, USA, April 19–22, 2004.

A. N. Karpushov, including C. Schlatter, **Ion temperature fluctuations in ELMy H-mode of the X3 EC-heated plasmas on TCV**, in PLASMA 2007: International Conference on Research and Applications of Plasmas, Greifswald, Germany, 16–19 October 2007, ser. AIP Conference Proceedings, H.-J. Hartfuss, M. Dudeck, J. Musielok and M. J. Sadowski, Eds., vol. 993, 2007, pp. 219–222.

T. P. Goodman, including C. Schlatter, **Co- and counter viewing oblique ECE measurements during ECH and ECCD on the TCV tokamak**, 34th EPS Conference on Plasma Physics, 2–6 July, 2007, Europhysics Conference Abstracts (ECA), vol. 31F, no. P-2.147. Warsaw, Poland: European Physical Society (EPS), 2007.

S. E. Sharapov, including C. Schlatter, **Energetic Ion-driven instabilities on JET and on MAST**, in Bulletin of the American Physical Society, vol. 51, no. 7, BI1.00005, November 2006. Invited talk held at the 48th Annual Meeting of the Division of Plasma Physics (DPP), October 30–November 3, 2006, Philadelphia, Pennsylvania, USA.

A. Zabolotsky, including C. Schlatter, **Particle and Impurity Transport in Electron-Heated Discharges in TCV**, contributed paper EX/P3-7 presented at the 21th IAEA Fusion Energy Conference, Chengdu, China, October 16–21, 2006.

A. N. Karpushov, including C. Schlatter, **Non-maxwellian ion energy distribution in ECH-heated plasmas on TCV**, in Proceedings of the 33rd EPS Conference on Plasma Physics, Rome, Italy, 19–23 June 2006, ser. Europhysics conference abstracts (ECA), F. D. Marco and G. Vlad, Eds., vol. 30I, no. P-1.152. European Physical Society (EPS), 2006, contributed paper.

J. B. Lister, including C. Schlatter, **Creating an XML Driven Data Bus between Fusion Experiments**, in Proceedings of the 10th International Conference on Accelerator and Large Experimental Physics Control Systems (ICALEPCS), Geneva, Switzerland, October 10–14, 2005.

A. N. Karpushov, including C. Schlatter, **Determination of the radial profile of hydrogen isotope composition in TCV plasmas**, in 32nd EPS Conference on Plasma Physics and Controlled Fusion combined with the 8th International Workshop on Fast Ignition of Fusion Targets, Tarragona, 27 June - 1 July 2005, ser. Europhysics Conference Abstracts, B. v. M. C. Hidalgo, Ed., vol. 29C, Asociación EURATOM-CIEMAT para Fusión, Madrid. Tarragona: The European Physical Society, 2005, contributed paper P-4.097.

M. I. K. Santala, including C. Schlatter, **pT fusion by RF-heated protons in JET trace tritium discharges**, in Procceedings of the 31st EPS Conference on Plasma Physics, ser. Europhysics Conference Abstracts (ECA), vol. 28G, London, UK, June 28–July 2, 2004. Contributed paper P-5.163.

N. N. Timchenko, including C. Schlatter, **Radiation Losses Study on the Tokamak T-10 Using AXUV-Detectors**, in Proceedings of the 30th EPS Conference on Controlled Fusion and Plasma Physics, ser. Europhysics Conference Abstracts (ECA), vol. 27A, St. Petersburg, Russian Federation, July 7–11, 2003. Contributed paper P-2.74.

Д.В. Сарычев, including К. Шлаттер, **ИЗУЧЕНИЕ РАДИАЦИОННЫХ ПОТЕРЬ ПЛАЗМЫ ТОКАМАКА Т-10 С ПОМОЩЬЮ AXUV-ДЕТЕКТОРОВ**, paper MC–2–28, presented at the XXX Звенигородская конференция по физике плазмы и УТС, 24–28 февраля 2003 г.

Unpublished

C. Schlatter, **Gamma ray spectrometry in tokamaks**, CRPP-EPFL, CH-1015 Lausanne, Switzerland, Internal report INT 212/06, September 2006.

C. Schlatter, **Stability of the internal kink mode for the JET plasma scenarios described by an extended energy principle including kinetic additions**, CRPP-EPFL, CH-1015 Lausanne, Switzerland, Internal report 210/04, October 2004.

C. Schlatter et al., **Fast-algorithm bolometric computer aided tomography (FABCAT)**, CRPP-EPFL, CH-1015 Lausanne, Switzerland, Internal report INT 205/02, February 2002.

C. Schlatter, **$\mathbf{C}_\alpha$-circles**, technical report, Laboratory for Computation and Visualization in Mathematics and Mechanics (LCVM^2), IMRI-EPFL, CH-1015 Lausanne, Switzerland, July 2002.

C. Schlatter, **Study of magnetic flux shaped base functions for tomography**, CRPP-EPFL, CH-1015 Lausanne, Switzerland, Internal report INT 208/02, June 2002.

C. Schlatter, **Philipp Lenard et la physique aryenne**, Projet Science-Technique-Société (STS), EPFL, April 2002.

C. Schlatter, **Calibration strategies for high resolution liquid flow sensors**, technical report, internship at Sensirion, the sensor company, Zürich, October 2001.

C. Schlatter, **Wenn plötzlich das Licht ausbleibt... Deutung und Wahrnehmung des Phänomens der Sonnenfinsternis im Laufe der Menschheitsgeschichte**, semester project in the frame of the lecture 'Histoire des sciences', EPFL, May 1999.

Miscellaneous

Computer skills

Matlab, Fortran, C++, PHP, SQL, LaTeX, Linux, Windows

Last updated: Thursday 6th August, 2009

http://www.slatersoft.com/